

Metal(III)-Water Interactions

by

Philip Tregenna-Piggott

**A thesis presented in partial fulfilment of the
requirements for the Doctor of Philosophy degree
of the University of London.**

**Department of Chemistry
University College London
1993**

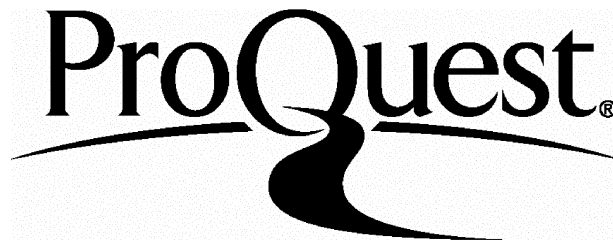
ProQuest Number: 10106670

All rights reserved

INFORMATION TO ALL USERS

The quality of this reproduction is dependent upon the quality of the copy submitted.

In the unlikely event that the author did not send a complete manuscript and there are missing pages, these will be noted. Also, if material had to be removed, a note will indicate the deletion.



ProQuest 10106670

Published by ProQuest LLC(2016). Copyright of the Dissertation is held by the Author.

All rights reserved.

This work is protected against unauthorized copying under Title 17, United States Code.
Microform Edition © ProQuest LLC.

ProQuest LLC
789 East Eisenhower Parkway
P.O. Box 1346
Ann Arbor, MI 48106-1346

***To my mother, brother and late grandmother Yaya.
In gratitude of all your moral and financial support.***

ABSTRACT

This thesis is devoted to the study of metal(III)-water interactions by a variety of physical techniques. Studies are undertaken in the solid state where the trivalent hexa-aqua-cation is held rigidly within the lattice, thus facilitating its study.

The $\text{RbM}^{\text{III}}(\text{SO}_4)_2 \cdot 12\text{H}_2\text{O}$ alums, where M^{III} is Al, Ga, In, Ti, V, Cr, and Fe, have been characterised by Raman spectroscopy. The Ti and V rubidium alums are of a different structural modification to the other alums studied. This is related to a change in the mode of water co-ordination leading to a larger trigonal field stabilisation energy for the Ti and V hexa-aqua-cations.

The Raman spectra of the $\text{RbTi}(\text{SO}_4)_2 \cdot 12\text{H}_2\text{O}$ alum are anomalous. Soft modes are observed indicating the onset of a phase transition. The Raman spectra are interpreted in conjunction with the published EPR and magnetic data for the $[\text{Ti}(\text{OH}_2)_6]^{3+}$ cation. A model in which the $[\text{Ti}(\text{OH}_2)_6]^{3+}$ cation is subject to a dynamic Jahn-Teller distortion, freezing out into a static distortion at temperatures approaching 4 K, is proposed.

A polarised neutron diffraction experiment has been performed on $\text{CsMo}(\text{SO}_4)_2 \cdot 12\text{D}_2\text{O}$. This is the first report of such a study for any trivalent hexa-aqua-cation. Information on the spatial spin distribution within the $[\text{Mo}(\text{OD}_2)_6]^{3+}$ cation is obtained. Spin density is found to occupy t_{2g} -like orbitals on the metal with some spin transferred to the ligand where it is concentrated in a molecular orbital normal to the plane of the water molecule. Negative spin is also found in the molybdenum-oxygen bonding region indicative of electron correlation effects. These observations are interpreted in terms of simple concepts of chemical bonding.

ACKNOWLEDGEMENTS

I would like to express my sincerest thanks and affection to my supervisor Stephen Peter Best for all his encouragement, kindness and tolerance.

Throughout the course of my Ph.D I have had the opportunity to work with many people on a variety of projects. The work-up of the Polarised Neutron Diffraction data would not have been possible without Philip Reynolds of the University of Western Australia. I would also like to thank Bruce Forsyth of the Rutherford and Appleton Laboratory for fruitful discussions as well as Gary McIntyre and Francis Tusset, our local contacts at the Institut Laue Langevin, Grenoble, for their assistance in collecting the data.

Special thanks goes to Frank Mabbs and David Collison of Manchester University whom have given me a great deal of help and assistance in relation to the EPR work. Equally, I would like to thank John Maher of Bristol University, Rob Deeth of Bath University, and Peter Bratt of University College London, whom have devoted much time to the collection of the EPR and ESEEM data.

I am indebted to Sean Howard of Cardiff University who, amongst many other things, performed a number of very useful *ab initio* calculations on systems which I have been studying. A big thankyou also goes to Paul Mallinson of Glasgow University, for making possible the refinement of the PND data with the program 'MOLLY', and sharing his expertise in the field of deformation density. I am also grateful to John Crangle of the University of Sheffield for access to the SQUID magnetometer and also to Mike Thompson, of Birkbeck College, and John Walsh, of Royal Holloway and Bedford New College, for access to their ICP-AES spectrometers.

I am also appreciative to Mike Hursthouse and all his group from Cardiff University in view of our attempts to determine the charge density distribution within the caesium chromium alum. I also acknowledge Ian Wood of University College London, for operating the powder X-ray diffractometer and plotting out the spectra.

I would like to thank the numerous members of the technical support facilities within the department whom have given me much assistance throughout my years as a student. Special thanks goes to Dick Waymark for his valiant efforts, time again, in filling the Oxford MD4 cryostat with liquid helium.

I would also like to thank Slava, Chris, Peter, David, Frank, Hiro, Navjot, Elliot, Dan O, Dan G, Rob, John, Suzanne, Niels, Dave, Christian, Dietrich, Uwe and Stewart for their companionship and good humour over the years. Special thanks goes to Socrates for freedom of travel.

Table of Contents

Title page	i
Dedication	ii
Abstract	iii
Acknowledgements	iv
Table of contents	vi
List of Tables	ix
List of Figures	xii

CHAPTER ONE 1

Introduction

1.1	Media in which to study metal(III)-water interactions.	1
1.2	Structure of the alums.	2
1.3	Origin of the trigonal field for the $[M(OH_2)_6]^{3+}$ cation within the alum lattice.	7
1.4	Aims of this work.	10
	References.	11

CHAPTER TWO 13

Single Crystal Raman Study of the Rubidium Alums

2.1	Introduction.	13
2.2	Theory of Raman Scattering.	13
2.3	Preparation of the rubidium alums.	18
2.4	Techniques used to produce large single crystals.	21
2.5	Preparation of, and techniques for cooling crystals for single crystal Raman experiments.	23
2.6	The Raman spectrometer.	25
2.7	Vibrational analysis.	27

2.8	Intensity determination.	31
2.9	Assignment of the Single Crystal Raman Spectra of the Rubidium Alums Between 275 and 1200 cm⁻¹.	34
2.10	Assignment of the Single Crystal Raman Spectra of the Rubidium Alums Between 10 and 275 cm⁻¹.	60
2.11	Single Crystal Raman Spectra Between 1200 and 4000 cm⁻¹.	82
2.12	Discussion.	85
	References.	89

CHAPTER THREE

91

Electronic Structure of [V(OH₂)₆]³⁺

3.1	Background.	91
3.2	Electronic structure of [V(OH₂)₆]³⁺ within the mixed alum system Rb{V/Ga}(SO₄)₂.12H₂O.	96
3.3	Electronic structure of [V(OH₂)₆]³⁺ within TiV(SO₄)₂.12H₂O.	125
	References.	134

CHAPTER FOUR

136

Electronic Structure of [Ti(OH₂)₆]³⁺

4.1	Review.	136
4.2	Previous assumptions of the symmetry and electronic structure of the [Ti(OH₂)₆]³⁺ cation.	138
4.3	The sign of the trigonal field.	143
4.4	Jahn-Teller theory.	146
4.5	Raman spectra of CsTi(SO₄)₂.12H₂O and RbTi(SO₄)₂.12H₂O.	151
4.6	Magnetic data.	157
4.7	Concluding remarks.	165
	References	167

CHAPTER FIVE		170
Polarised Neutron Diffraction Study of CsMo(SO₄)₂.12D₂O		
5.1	Introduction.	170
5.2	Theory of Neutron Scattering.	170
5.3	Experimental.	176
5.4	Programs used to refine the data.	182
5.5	Results of the Refinements.	187
5.6	Discussion.	215
5.7	Spin paramagnetism of CsM^{III}(SO₄)₂.12D₂O alums of Ti, Ru, V, Mo, Cr, and Fe at low temperatures and strong magnetic fields.	221
	References.	225

CHAPTER SIX		227
Electronic Structure of [Cr(OH₂)₆]³⁺		
6.1	Introduction.	227
6.2	Synthesis of single crystals of [Cr(OH₂)₆]³⁺ doped into M^IGa(SO₄)₂.12H₂O [M^I = Cs or Rb].	227
6.3	Techniques employed for the execution of single crystal EPR experiments.	228
6.4	CW EPR.	229
6.5	The spin echo phenomenon.	261
6.6	Electronic and emission spectra of chromium(III) within the alum lattice.	279
	References.	283

APPENDICES		284
A	Single crystal Raman spectra of Rubidium alums, between 1200 and 4000 cm⁻¹.	285
B	Inductively coupled Plasma - Atomic Emission Spectroscopy.	293

List of Tables

2.7.1	Results of site group analysis of alum lattice.	28
2.7.2	Raman activities for the different scattering experiments.	31
2.9.1	Vibrational Frequencies and assignments for RbAl(SO ₄) ₂ .12H ₂ O, between 275 and 1200 cm ⁻¹ .	35
2.9.2	Vibrational Frequencies and assignments for RbAl(SO ₄) ₂ .12D ₂ O, between 275 and 1200 cm ⁻¹ .	37
2.9.3	Vibrational Frequencies and assignments for RbIn(SO ₄) ₂ .12H ₂ O, between 275 and 1200 cm ⁻¹ .	42
2.9.4	Vibrational Frequencies and assignments for RbGa(SO ₄) ₂ .12H ₂ O, between 275 and 1200 cm ⁻¹ .	44
2.9.5	Vibrational Frequencies and assignments for RbFe(SO ₄) ₂ .12H ₂ O, between 275 and 1200 cm ⁻¹ .	46
2.9.6	Vibrational Frequencies and assignments for RbCr(SO ₄) ₂ .12H ₂ O, between 275 and 1200 cm ⁻¹ .	48
2.9.7	Vibrational Frequencies and assignments for RbV(SO ₄) ₂ .12H ₂ O, between 275 and 1200 cm ⁻¹ .	52
2.9.8	Vibrational Frequencies and assignments for RbV(SO ₄) ₂ .12D ₂ O, between 275 and 1200 cm ⁻¹ .	54
2.9.9	Vibrational Frequencies and assignments for RbTi(SO ₄) ₂ .12H ₂ O, between 275 and 1200 cm ⁻¹ .	58
2.10.1	Vibrational Frequencies and assignments for RbAl(SO ₄) ₂ .12H ₂ O, between 20 and 275 cm ⁻¹ .	61
2.10.2	Vibrational Frequencies and assignments for RbAl(SO ₄) ₂ .12D ₂ O, between 20 and 275 cm ⁻¹ .	63
2.10.3	Vibrational Frequencies and assignments for RbIn(SO ₄) ₂ .12H ₂ O, between 20 and 275 cm ⁻¹ .	66
2.10.4	Vibrational Frequencies and assignments for RbGa(SO ₄) ₂ .12H ₂ O, between 20 and 275 cm ⁻¹ .	68
2.10.5	Vibrational Frequencies and assignments for RbFe(SO ₄) ₂ .12H ₂ O, between 20 and 275 cm ⁻¹ .	70

2.10.6	Vibrational Frequencies and assignments for RbCr(SO ₄) ₂ ·12H ₂ O, between 20 and 275 cm ⁻¹ .	72
2.10.7	Vibrational Frequencies and assignments for RbV(SO ₄) ₂ ·12H ₂ O, between 20 and 275 cm ⁻¹ .	74
2.10.8	Vibrational Frequencies and assignments for RbV(SO ₄) ₂ ·12D ₂ O, between 20 and 275 cm ⁻¹ .	76
2.10.9	Vibrational Frequencies and assignments for RbTi(SO ₄) ₂ ·12H ₂ O, between 20 and 275 cm ⁻¹ .	80
2.11.1	Vibrational Frequencies and assignments for RbV(SO ₄) ₂ ·12H ₂ O, between 1200 and 4000 cm ⁻¹ .	83
3.2.1	Vibrational Frequencies and assignments for Rb{V/Ga}(SO ₄) ₂ ·12H ₂ O (45.5 (1) % V and 54.5 (1) % Ga), between 20 and 275 cm ⁻¹ .	104
3.2.2	Vibrational Frequencies and assignments for Rb{V/Ga}(SO ₄) ₂ ·12H ₂ O (45.5 (1) % V and 54.5 (1) % Ga), between 275 and 1200 cm ⁻¹ .	106
3.2.3	Energy levels for [V(OH ₂) ₆] ³⁺ under the action of a trigonal field (with E _g ground term) and spin-orbit coupling.	116
3.3.1	Chemical and physical properties of a selected number of aqua cations in solution.	126
3.3.2	Vibrational Frequencies and assignments for TlV(SO ₄) ₂ ·12H ₂ O, between 20 and 275 cm ⁻¹ .	128
3.3.3	Vibrational Frequencies and assignments for TlV(SO ₄) ₂ ·12H ₂ O, between 275 and 1200 cm ⁻¹ .	130
3.3.4	Vibrational Frequencies and assignments for TlV(SO ₄) ₂ ·12H ₂ O, between 1200 and 4000 cm ⁻¹ .	132
4.1.1	Summary of some of the g values that have been obtained for CsTi(SO ₄) ₂ ·12H ₂ O by EPR and magnetic susceptibility measurements.	136
4.2.1	First- and second-order Zeeman coefficients for three Kramers doublets derived from ² T _{2g} term after perturbation by trigonal field and spin-orbit coupling.	142

5.3.1	Data collection and analysis parameters for the neutron diffraction study of CsMo(SO₄)₂.12D₂O.	179
5.3.2	Atomic fractional cell coordinates and thermal parameters for CsMo(SO₄)₂.12D₂O.	180
5.3.3	Bond lengths and angles which define the coordination environments for CsMo(SO₄)₂.12X₂O (X = H or D).	181
5.5.1	Comparison between experimental structure factors and those calculated in ASRED Refinement 1.	190
5.5.2	Comparison between experimental structure factors and those calculated in ASRED Refinement 5.	197

List of Figures

- 1.2.1** Disposition of the three distinct structural subunits, $[M^I(OH_2)_6]^+$, $[M^{III}(OH_2)_6]^{3+}$ and $[SO_4]^{2-}$ along a crystallographic three-fold axis of a caesium β alum. 4
- 1.2.2** Stereo-chemistry of the monovalent cation in:
- (a) The β alum of $CsFe(SO_4)_2 \cdot 12H_2O$
- (b) The α alum of $CsFe(SeO_4)_2 \cdot 12H_2O$. 5
- 1.2.3** Mode of water co-ordination to the trivalent cation in:
- (a) The β alum of $CsFe(SO_4)_2 \cdot 12H_2O$
- (b) The α alum of $CsFe(SeO_4)_2 \cdot 12H_2O$. 6
- 1.3.1** Relationship between the molecular structure and the energies of the t_{2g} (O_h) orbitals for a hexa-aqua-cation on a site of trigonal symmetry with trigonal planar water co-ordination. 9
- 2.2.1** (a) Scattering of radiation by gaseous sample.
- (b) Origin of the vibration Raman effect. 14
- 2.4.1** The crystal growing apparatus. 22
- 2.5.1** Vertical cross-section through Oxford MD4 cryostat. 24
- 2.6.1** Spectral response of the GaAs and Bi-alkalai photomultiplier tubes. 26
- 2.7.1** Schematic representations of the internal modes of MX_6 and AB_4 species, and the external modes of water. 29
- 2.7.2** The alignment of the crystal axes with respect to the laboratory axes. 30
- 2.8.1** ν_1MO_6 region of $RbV(SO_4)_2 \cdot 12D_2O$. 33
- 2.9.1** Single crystal Raman spectra of $RbAl(SO_4)_2 \cdot 12H_2O$, between 275 and 1200 cm^{-1} . 36
- 2.9.2** Single crystal Raman spectra of $RbAl(SO_4)_2 \cdot 12H_2O$, between 275 and 1200 cm^{-1} . 38
- 2.9.3** Single crystal Raman spectra of $RbIn(SO_4)_2 \cdot 12H_2O$, between 275 and 1200 cm^{-1} . 43
- 2.9.4** Single crystal Raman spectra of $RbGa(SO_4)_2 \cdot 12H_2O$, between 275 and 1200 cm^{-1} . 45

2.9.5	Single crystal Raman spectra of $\text{RbFe}(\text{SO}_4)_2 \cdot 12\text{H}_2\text{O}$, between 275 and 1200 cm^{-1} .	47
2.9.6	Single crystal Raman spectra of $\text{RbCr}(\text{SO}_4)_2 \cdot 12\text{H}_2\text{O}$, between 275 and 1200 cm^{-1} .	49
2.9.7	Single crystal Raman spectra of $\text{RbV}(\text{SO}_4)_2 \cdot 12\text{H}_2\text{O}$, between 275 and 1200 cm^{-1} .	53
2.9.8	Single crystal Raman spectra of $\text{RbV}(\text{SO}_4)_2 \cdot 12\text{D}_2\text{O}$, between 275 and 1200 cm^{-1} .	55
2.9.9	Single crystal Raman spectra of $\text{RbTi}(\text{SO}_4)_2 \cdot 12\text{H}_2\text{O}$, between 275 and 1200 cm^{-1} .	59
2.10.1	Single crystal Raman spectra of $\text{RbAl}(\text{SO}_4)_2 \cdot 12\text{H}_2\text{O}$, between 15 and 300 cm^{-1} .	62
2.10.2	Single crystal Raman spectra of $\text{RbAl}(\text{SO}_4)_2 \cdot 12\text{D}_2\text{O}$, between 10 and 300 cm^{-1} .	64
2.10.3	Single crystal Raman spectra of $\text{RbIn}(\text{SO}_4)_2 \cdot 12\text{H}_2\text{O}$, between 20 and 300 cm^{-1} .	67
2.10.4	Single crystal Raman spectra of $\text{RbGa}(\text{SO}_4)_2 \cdot 12\text{H}_2\text{O}$, between 10 and 300 cm^{-1} .	69
2.10.5	Single crystal Raman spectra of $\text{RbFe}(\text{SO}_4)_2 \cdot 12\text{H}_2\text{O}$, between 25 and 300 cm^{-1} .	71
2.10.6	Single crystal Raman spectra of $\text{RbCr}(\text{SO}_4)_2 \cdot 12\text{H}_2\text{O}$, between 25 and 300 cm^{-1} .	73
2.10.7	Single crystal Raman spectra of $\text{RbV}(\text{SO}_4)_2 \cdot 12\text{H}_2\text{O}$, between 25 and 300 cm^{-1} .	75
2.10.8	Single crystal Raman spectra of $\text{RbV}(\text{SO}_4)_2 \cdot 12\text{D}_2\text{O}$, between 10 and 300 cm^{-1} .	77
2.10.9	Single crystal Raman spectra of $\text{RbTi}(\text{SO}_4)_2 \cdot 12\text{H}_2\text{O}$, between 15 and 300 cm^{-1} .	81
2.11.1	Single crystal Raman spectra of $\text{RbV}(\text{SO}_4)_2 \cdot 12\text{H}_2\text{O}$, between 1200 and 4000 cm^{-1} .	84
2.12.1	The F_g component of the $\nu_3(\text{SO}_4)^{2-}$ mode for the rubidium sulphate α - and β -alums, $\text{RbM}^{\text{III}}(\text{SO}_4)_2 \cdot 12\text{H}_2\text{O}$.	86

3.1.1	Splitting of ${}^3T_{1g}$ term (d^2 transition metal complex) by a trigonal field and spin-orbit coupling.	92
3.1.2	Electronic Raman band (${}^3E_g \leftarrow {}^3A_g$) for $[V(OH_2)_6]^{3+}$ in $RbV(SO_4)_2 \cdot 12H_2O$ recorded at 82 and 4.2 K.	93
3.1.3	Simulation of the ${}^3E_g \leftarrow {}^3A_g$ electronic Raman transition recorded for $RbV(SO_4)_2 \cdot 12H_2O$.	95
3.2.1	Photographs of crystals of $RbV(SO_4)_2 \cdot 12H_2O$ and $[V(OH_2)_6]^{3+}$ doped into $RbGa(SO_4)_2 \cdot 12H_2O$ grown using the single crystal growing apparatus.	98
3.2.2	Photographs of crystals made by co-crystallising $RbV(SO_4)_2 \cdot 12H_2O$ with $RbGa(SO_4)_2 \cdot 12H_2O$.	99
3.2.3	Electronic spectra of α and β $Rb\{Ga/V\}(SO_4)_2 \cdot 12H_2O$ mixed crystals.	101
3.2.4	A correlation diagram for a d^2 ion in an octahedral environment.	102
3.2.5	Single crystal Raman spectra of $Rb\{V/Ga\}(SO_4)_2 \cdot 12H_2O$ (45.5 (1) % V and 54.5 (1) % Ga) between 10 and 300 cm^{-1} .	105
3.2.6	Single crystal Raman spectra of $Rb\{V/Ga\}(SO_4)_2 \cdot 12H_2O$ (45.5 (1) % V and 54.5 (1) % Ga) between 275 and 1200 cm^{-1} .	107
3.2.7	Single crystal Raman spectra of $Rb\{V/Ga\}(SO_4)_2 \cdot 12H_2O$ (45.5 (1) % V and 54.5 (1) % Ga) between 1200 and 4000 cm^{-1} .	108
3.2.8	$\nu_1 MO_6$ region of $Rb\{V/Ga\}(SO_4)_2 \cdot 12H_2O$ (45.5 (1) % V and 54.5 (1) % Ga)	109
3.2.9	$\nu_1 MO_6$ region of $Rb\{V/Ga\}(SO_4)_2 \cdot 12H_2O$ (25.3 (2) % V and 74.7 (2) % Ga)	111
3.2.10	Single crystal Raman spectra of various $M^I\{V/Ga\}(SO_4)_2 \cdot 12H_2O$ alums of differing trivalent cation composition.	
	(a) Spectra of $A_g + E_g$ activity showing the region containing the electronic Raman transition	
	(b) Spectra of F_g activity showing the region containing $\nu_3(SO_4)^{2-}$	112
3.2.11	Single crystal Raman spectra of α $Rb\{V/Ga\}(SO_4)_2 \cdot 12H_2O$ alum between -100 and 100 cm^{-1} (6.6 (6) % V and 93.4 (6) % Ga)	114

3.2.12	Single crystal Raman spectra between -100 and 100 cm^{-1} showing bands of $A_g + E_g$ activity for:	
	(a) α $\text{Rb}\{\text{V/Ga}\}(\text{SO}_4)_2 \cdot 12\text{H}_2\text{O}$ (6.6 (6) % V and 93.4 (6) % Ga)	
	(b) $\text{RbV}(\text{SO}_4)_2 \cdot 12\text{H}_2\text{O}$; (c) $\text{RbGa}(\text{SO}_4)_2 \cdot 12\text{H}_2\text{O}$	115
3.2.13	Powder X-ray diffraction pattern for $\text{RbV}(\text{SO}_4)_2 \cdot 12\text{H}_2\text{O}$	120
3.2.14	Plot of unit cell dimension against $1/2[\cos^2\theta/\theta + \cos^2\theta/\sin\theta]$ for high angle reflections of $\text{RbV}(\text{SO}_4)_2 \cdot 12\text{H}_2\text{O}$.	121
3.2.15	Powder X-ray diffraction pattern for $\text{Rb}\{\text{V/Ga}\}(\text{SO}_4)_2 \cdot 12\text{H}_2\text{O}$ (45.5 (1) % V and 54.5 (1) % Ga)	122
3.2.16	Plot of unit cell dimension against vanadium composition for the $\text{Rb}\{\text{V/Ga}\}(\text{SO}_4)_2 \cdot 12\text{H}_2\text{O}$ β alum system.	123
3.3.1	Single crystal Raman spectra of $\text{TIV}(\text{SO}_4)_2 \cdot 12\text{H}_2\text{O}$, between 10 and 300 cm^{-1} .	129
3.3.2	Single crystal Raman spectra of $\text{TIV}(\text{SO}_4)_2 \cdot 12\text{H}_2\text{O}$, between 275 and 1200 cm^{-1} .	131
3.3.3	Single crystal Raman spectra of $\text{TIV}(\text{SO}_4)_2 \cdot 12\text{H}_2\text{O}$, between 1200 and 4000 cm^{-1} .	133
4.1.1	(a) EPR spectrum of Ti^{3+} doped into the CsAlSH alum recorded by Y. H. Shing and D. Walsh.	
	(b) Schematic energy level diagram, after Shing and Walsh, showing energy levels of Ti^{3+} when doped into $\text{CsAl}(\text{SO}_4)_2 \cdot 12\text{H}_2\text{O}$.	139
4.2.1	Splitting of T_g term (T_b) for $[\text{Ti}(\text{OH}_2)_6]^{3+}$ in an axial field.	140
4.3.1	Schematic diagrams showing three configurations which are found to be adopted by $[\text{M}(\text{OH}_2)_6]^{3+}$ cations.	144
4.3.2	Relationship between the molecular structure and the energies of the A_g and E_g orbital terms for the $[\text{Ti}(\text{OH}_2)_6]^{3+}$ cation lying on a site of trigonal symmetry.	147
4.4.1	(a) Potential-energy surface for an electronic E term linearly coupled to E displacements.	
	(b) Equipotential section of potential-energy surface for $E \otimes e$ problem taking into account quadratic and cubic terms of the vibronic hamiltonian.	150

4.4.2	Energy levels of the ground state $E \otimes e$ problem, taking into account tunnelling splitting, with the external magnetic field directed along a distortion axis.	152
4.5.1	Single crystal Raman spectra of $\text{RbTi}(\text{SO}_4)_2 \cdot 12\text{H}_2\text{O}$ showing bands of E_g symmetry between -100 and 250 cm^{-1} at temperatures of 80 , 125 , and 200 K .	153
4.5.2	Single crystal Raman spectra of $\text{RbTi}(\text{SO}_4)_2 \cdot 12\text{H}_2\text{O}$ showing bands of all symmetries between -100 and 250 cm^{-1} at temperatures of 4 , 15 , 70 , and 190 K .	154
4.5.3	Single crystal Raman spectra of $\text{RbTi}(\text{SO}_4)_2 \cdot 12\text{H}_2\text{O}$ showing bands of E_g symmetry between 250 and 1200 cm^{-1} at temperatures of 4 , 80 , and 125 K .	156
4.6.1	Plot of effective magnetic moment against temperature for $\text{CsTi}(\text{SO}_4)_2 \cdot 12\text{H}_2\text{O}$ in the temperature range $80 - 300 \text{ K}$ with the best theoretical fit achieved by Figgis, Lewis and Mabbs.	159
4.6.2	Plot of effective magnetic moment against temperature for $\text{CsTi}(\text{SO}_4)_2 \cdot 12\text{H}_2\text{O}$ in the temperature range $80 - 300 \text{ K}$ with the best theoretical fit achieved for data set 1.	160
4.6.3	Plot of effective magnetic moment against temperature for $\text{CsTi}(\text{SO}_4)_2 \cdot 12\text{H}_2\text{O}$ in the temperature range $80 - 300 \text{ K}$ with the best theoretical fit achieved for data set 2.	161
4.6.4	Plot of inverse susceptibility against temperature for $\text{CsTi}(\text{SO}_4)_2 \cdot 12\text{D}_2\text{O}$.	163
5.2.1	(a) Variation of the amplitude form factor f , for the Mn^{2+} ion, with $(\sin\theta/\lambda)$. (b) Values of the product $\lambda \cdot q$ for the upward and downward neutron polarisation states when a magnetic field produces alignment of the spins.	174
5.3.1	Molecular structure of the $[\text{Mo}(\text{OD}_2)_6]^{3+}$ cation within the $\text{CsMo}(\text{SO}_4)_2 \cdot 12\text{D}_2\text{O}$ alum.	178
5.3.2	A schematic representation of a polarised neutron diffractometer.	183

5.3.3	Plot of magnetic structure factors, obtained for $\text{CsMo}(\text{SO}_4)_2 \cdot 12\text{D}_2\text{O}$ against $\sin\theta/\lambda$	184
5.5.1	ASRED refinement 1: Experimental structure factors.	188
5.5.2	ASRED refinement 2: Experimental structure factors.	192
5.5.3	ASRED refinement 3: Experimental structure factors.	194
5.5.4	ASRED refinement 4: Experimental structure factors.	195
5.5.5	ASRED refinement 5: Experimental structure factors.	196
5.5.6	ASRED refinement 6: Experimental structure factors.	200
5.5.7	ASRED refinement 7: Experimental structure factors.	201
5.5.8	ASRED refinement 8: Experimental structure factors.	202
5.5.9	ASRED refinement 9: Experimental structure factors.	203
5.5.10	ASRED refinement 10: Experimental structure factors.	205
5.5.11	ASRED refinement 11: Theoretical structure factors.	206
5.5.12	ASRED refinement 12: Theoretical structure factors.	207
5.5.13	ASRED refinement 13: Theoretical structure factors.	208
5.5.14	ASRED refinement 14: Theoretical structure factors.	209
5.5.15	The symmetry allowed multipoles for an atom on a site of trigonal symmetry.	211
5.5.16	MOLLY refinement A: Experimental structure factors.	213
5.5.17	MOLLY refinement B: Theoretical structure factors.	214
5.6.1	Schematic diagram showing the orbital interactions which mediate the covalency and spin polarisation effects within the $[\text{Mo}(\text{OD}_2)_6]^{3+}$ cation.	216
5.6.2	Spin distribution about the water molecule in the $[\text{Mo}(\text{OD}_2)_6]^{3+}$ and $[\text{V}(\text{OD}_2)_6]^{2+}$ cations.	219
5.7.1	Plot of magnetic moment per ion vs H/T for $\text{CsM}^{\text{III}}(\text{SO}_4)_2 \cdot 12\text{D}_2\text{O}$ where $\text{M}^{\text{III}} = \text{Ti, Ru, V, Mo, Cr, and Fe}$.	223
6.4.1	Energy level diagram of Cr^{3+} doped into the $\text{CsGa}(\text{SO}_4)_2 \cdot 12\text{H}_2\text{O}$ lattice, showing the magnetic dipole allowed transitions within the $^4\text{A}_{2g}$ manifold.	231
6.4.2	Orientated single crystal cw-EPR spectra of $^{50}\text{Cr}(^{17}\text{OH}_2)_6]^{3+}$ doped into $\text{CsGa}(\text{SO}_4)_2 \cdot 12\text{H}_2\text{O}$. BetbGa_ data set.	234

6.4.3	Schematic diagram showing the orientation of the principal ZFS direction for the four paramagnets within the unit cell when a (111) face is normal to the field direction.	245
6.4.4	Principal ZFS directions of the four paramagnets within the unit cell shown as projections in plane A. The illustrated orientation of the magnetic unit cell is that found in spectrum BetbGa_4.	247
6.4.5	Principal ZFS directions of the four paramagnets within the unit cell shown as projections in plane A. The illustrated orientation of the magnetic unit cell is that found in spectrum BetbGa_9.	248
6.4.6	Orientated single crystal cw-EPR spectra of $[^{50}\text{Cr}(^{17}\text{OH}_2)_6]^{3+}$ doped into $\text{CsGa}(\text{SO}_4)_2 \cdot 12\text{H}_2\text{O}$. BetaGa_ data set.	249
6.4.7	Two limiting orientations of the magnetic unit cell with respect to the field direction when one of the 4 principal ZFS directions is aligned with the field.	260
6.5.1	(a) The inhomogeneously broadened EPR band (b) The precision of the spin packet about the field direction (c) Alignment of the bulk magnetisation along the field direction.	263
6.5.2	Schematic diagram showing the origin of the two-pulse echo in the rotating frame of reference.	265
6.5.3	Energy level diagram for $S = I = 1/2$ where the nuclear Zeeman interaction is much greater than the hyperfine interaction.	267
6.5.4	Two-pulse echo absorption sweep of $[^{50}\text{Cr}(^{17}\text{OH}_2)_6]^{3+}$ doped into $\text{CsGa}(\text{SO}_4)_2 \cdot 12\text{H}_2\text{O}$.	270
6.5.5	Three-pulse electron spin echo nuclear modulation spectra recorded for $[^{50}\text{Cr}(^{17}\text{OH}_2)_6]^{3+}$ doped into $\text{CsGa}(\text{SO}_4)_2 \cdot 12\text{H}_2\text{O}$ at 2812 G.	271
6.5.6	Fourier transforms of the electron spin echo nuclear modulation spectra recorded for $[^{50}\text{Cr}(^{17}\text{OH}_2)_6]^{3+}$ doped into $\text{CsGa}(\text{SO}_4)_2 \cdot 12\text{H}_2\text{O}$ at 2812 G.	272
6.5.7	Three-pulse electron spin echo nuclear modulation spectra recorded for $[^{50}\text{Cr}(^{17}\text{OH}_2)_6]^{3+}$ doped into $\text{CsGa}(\text{SO}_4)_2 \cdot 12\text{H}_2\text{O}$ at 3419 G.	273

6.5.8	Fourier transforms of the electron spin echo nuclear modulation spectra recorded for $[^{50}\text{Cr}(^{17}\text{OH}_2)_6]^{3+}$ doped into $\text{CsGa}(\text{SO}_4)_2 \cdot 12\text{H}_2\text{O}$ at 3419 G.	274
6.5.9	Three-pulse electron spin echo nuclear modulation spectra recorded for $[^{50}\text{Cr}(^{17}\text{OH}_2)_6]^{3+}$ doped into $\text{CsGa}(\text{SO}_4)_2 \cdot 12\text{H}_2\text{O}$ at 4240 G.	275
6.5.10	Fourier transforms of the electron spin echo nuclear modulation spectra recorded for $[^{50}\text{Cr}(^{17}\text{OH}_2)_6]^{3+}$ doped into $\text{CsGa}(\text{SO}_4)_2 \cdot 12\text{H}_2\text{O}$ at 4240 G.	276
6.6.1	Luminescence from (a) $\text{RbCr}(\text{SO}_4)_2 \cdot 12\text{H}_2\text{O}$, (b) $\text{CsCr}(\text{SO}_4)_2 \cdot 12\text{H}_2\text{O}$	280
6.6.2	Energy level diagram for d^3 configuration in octahedral symmetry.	281
A.1	Single crystal Raman spectra of $\text{RbV}(\text{SO}_4)_2 \cdot 12\text{D}_2\text{O}$, between 1200 and 4000 cm^{-1} .	285
A.2	Single crystal Raman spectra of $\text{RbTi}(\text{SO}_4)_2 \cdot 12\text{H}_2\text{O}$, between 1200 and 4000 cm^{-1} .	286
A.3	Single crystal Raman spectra of $\text{RbCr}(\text{SO}_4)_2 \cdot 12\text{H}_2\text{O}$, between 1200 and 4000 cm^{-1} .	287
A.4	Single crystal Raman spectra of $\text{RbGa}(\text{SO}_4)_2 \cdot 12\text{H}_2\text{O}$, between 1200 and 4000 cm^{-1} .	288
A.5	Single crystal Raman spectra of $\text{RbFe}(\text{SO}_4)_2 \cdot 12\text{H}_2\text{O}$, between 1200 and 4000 cm^{-1} .	289
A.6	Single crystal Raman spectra of $\text{RbAl}(\text{SO}_4)_2 \cdot 12\text{H}_2\text{O}$, between 1200 and 4000 cm^{-1} .	290
A.7	Single crystal Raman spectra of $\text{RbAl}(\text{SO}_4)_2 \cdot 12\text{D}_2\text{O}$, between 1200 and 4000 cm^{-1} .	291
A.8	Single crystal Raman spectra of $\text{RbIn}(\text{SO}_4)_2 \cdot 12\text{H}_2\text{O}$, between 1200 and 4000 cm^{-1} .	292
B.1	Schematic diagram of a conventional simultaneous ICP system.	294

INTRODUCTION

1.1 Media in which to study metal(III)-water interactions

Because of the undoubted importance of the role of metal-water interactions in aqueous chemistry, the nature of the metal-water bond has been and is currently a subject of intensive study.

Information on the nature of the metal-water bond from studies in aqueous media is limited. Contact shift studies, by means of magnetic resonance of proton¹ and oxygen-17 nuclei²⁻⁴ have been used to deduce both the extent of unpaired electron density transferred to the water ligand, and the spatial characteristic of the orbital that the unpaired electron occupies for various paramagnetic ions in solution. However, considerable differences exist between the models proposed by different authors. Neutron diffraction studies have determined the co-ordination number and the orientation of the water molecules to various metal cations in solution.⁵ This form of study has focused mainly on mono and di-valent cations. Until recently the only trivalent cations studied were those of the lanthanide cations.^{6,7} However a neutron diffraction study of $[\text{Cr}(\text{OH}_2)_6]^{3+}(\text{aq})$ has recently been reported.⁸ This work suggests that the first hydration shell of Cr^{3+} contains six water molecules with the oxygen and hydrogen atoms situated at 1.98 (2) and 2.60 (3) Å respectively from the Cr^{3+} centre. The mode of water co-ordination is determined by estimation of the O-H bond length from previous neutron diffraction studies of trivalent hexa-aqua-cations in the solid state.⁹⁻¹¹ By obtaining a mean value for the O-H bond of 0.99 Å, the mode of water co-ordination is estimated to be trigonal pyramidal with the plane of the water molecule tilted by 34 (6)^o out of the CrO_4 plane.

In contrast, the water molecule in a crystalline hydrate is considerably more constrained. The metal-water interaction is affected greatly by restrictions imposed by both crystallographic symmetry and hydrogen bonding. However, this also facilitates the study of the metal-water interaction which is why most studies have concentrated on the solid state.

$^{63}\text{Cu}(^{17}\text{OD}_2)_6^{3+}$ doped into the zinc Tutton salt: $\text{K}_2\text{Zn}(\text{SO}_4)_2 \cdot 6\text{D}_2\text{O}$ enriched to 16% in oxygen-17 isotope has been studied by Electron Paramagnetic Resonance, at 20 K, using X-band frequency microwave radiation.¹² The oxygen-17 hyperfine tensors are obtained, from which, a value of 1/6 is calculated for the 2s/2p ratio of the molecular orbital containing the unpaired electron.

Polarised neutron diffraction experiments have also been performed on a number of paramagnetic $[\text{M}(\text{OH}_2)_6]^{2+}$ cations within the ammonium Tutton salt lattice.^{13,14} These studies allow the magnetisation density within the aqua-complex to be determined. Hence, information regarding covalency and electron-electron correlation effects is obtained.

As yet, there are no reports of any analogous studies undertaken, using either resonance or diffraction techniques, to examine the nature of the metal(III)-water bond.

In the work presented here, metal(III) hexa-aqua-cations have been studied within the alum system: $\text{M}^{\text{III}}\text{M}^{\text{III}}(\text{SO}_4)_2 \cdot 12\text{H}_2\text{O}$. The caesium alum lattice, in particular, has been shown to be highly ordered¹⁵ and can accommodate some unstable hexa-aqua-cations such as Mn^{3+} ,¹⁵ Co^{3+} ¹⁵ and Mo^{3+} ¹⁶ and so provides an excellent framework in which to study metal(III)-water interactions.

1.2 Structure of the alums

In 1935, structural studies undertaken by Lipson^{17,18} showed that the alums could be disposed into three distinct classes which he designated α , β , and γ , all belonging to the primitive cubic space group $\text{Pa}\bar{3}$. He noted that the alum type was related to the size of the monovalent cation. Whereas most alums had the α structure, those with large monovalent cations, such as caesium, had the β structure. The only example of the γ class, $\text{NaAl}(\text{SO}_4)_2 \cdot 12\text{H}_2\text{O}$, was found for the small sodium cation. Lipson used the co-ordination number of the monovalent cation to designate alum type. In the α and β alums, the monovalent cation is surrounded by 12 oxygen atoms, six from water molecules and three each from two sulphate ions. Lipson infers that the β alum structure differs essentially from the α structure in having direct bonds from the SO_4 groups to the monovalent cation. The disposition of the three distinct

structural subunits of $[M^I(OH_2)_6]^+$, $[M^{III}(OH_2)_6]^{3+}$ and $[SO_4]^{2-}$, which lie along the crystallographic three-fold axes, is shown for a caesium β alum in figure 1.2.1. In the unique γ alum of $NaAl(SO_4)_2 \cdot 12H_2O$ the sulphate is inverted from its position shown in figure 1.2.1 such that the single oxygen is now directed towards the monovalent cation.

The stereochemistry of the monovalent cation has shown to give a reliable classification of the alum type.¹⁵ In the β alums, the water molecules co-ordinated to the monovalent cation lie in a plane and together with the 6 surrounding oxygen atoms from the two sulphate ions define a cuboctahedral array as illustrated in figure 1.2.2 (a). In the α alums, the water molecules form a puckered ring which together with the sulphate groups define an elongated icosahedron as shown in figure 1.2.2 (b). The hole created by the twelve oxygens of a cuboctahedron is larger than that of the corresponding icosahedron and hence β alums occur with larger mono-valent cations than the α alums.

Recent neutron diffraction studies of α^{10} and $\beta^{10,19}$ alums have shown that the stereochemistry of the trivalent cation is also indicative of alum type. Figure 1.2.3 shows the mode of water co-ordination to iron(III) in $CsFe(SO_4)_2 \cdot 12H_2O$, a β alum (fig. 1.2.3 (a)), and in $CsFe(SeO_4)_2 \cdot 12H_2O$, an α alum (fig. 1.2.3 (b)). In both alum types, the $M^{III}O_6$ core is approximately octahedral; the overall symmetry of the hexa-aqua-cation for both α and β modifications being S_6 . In the β alums, the hydrogen atoms define a plane with the metal-oxygen bond vector so that the mode of water co-ordination is trigonal planar. The plane of the water molecule in the β alums is twisted with respect to the MO_6 framework by an angle of between 19 and 22°. In the α alum of $CsFe(SeO_4)_2 \cdot 12H_2O$, the plane of the water molecule is tilted out of the MO_4 plane by 18.6 (10)° so that the mode of water co-ordination is trigonal pyramidal.

Both the M^I and M^{III} cations lie on sites of S_6 symmetry within the unit cell. The co-ordinating water molecules are crystallographically equivalent and lie in general positions. The sulphur atom and one of its oxygen atoms lie on sites of C_3 symmetry. The other three oxygen atoms of sulphate are crystallographically equivalent and lie in general positions.

Figure 1.2.1

Disposition of the three distinct structural units, $[M^I(OH_2)_6]^+$, $[M^{III}(OH_2)_6]^{3+}$ and $[SO_4]^{2-}$ along a crystallographic three-fold axis of a caesium β alum. (After S. P. Best [20]).

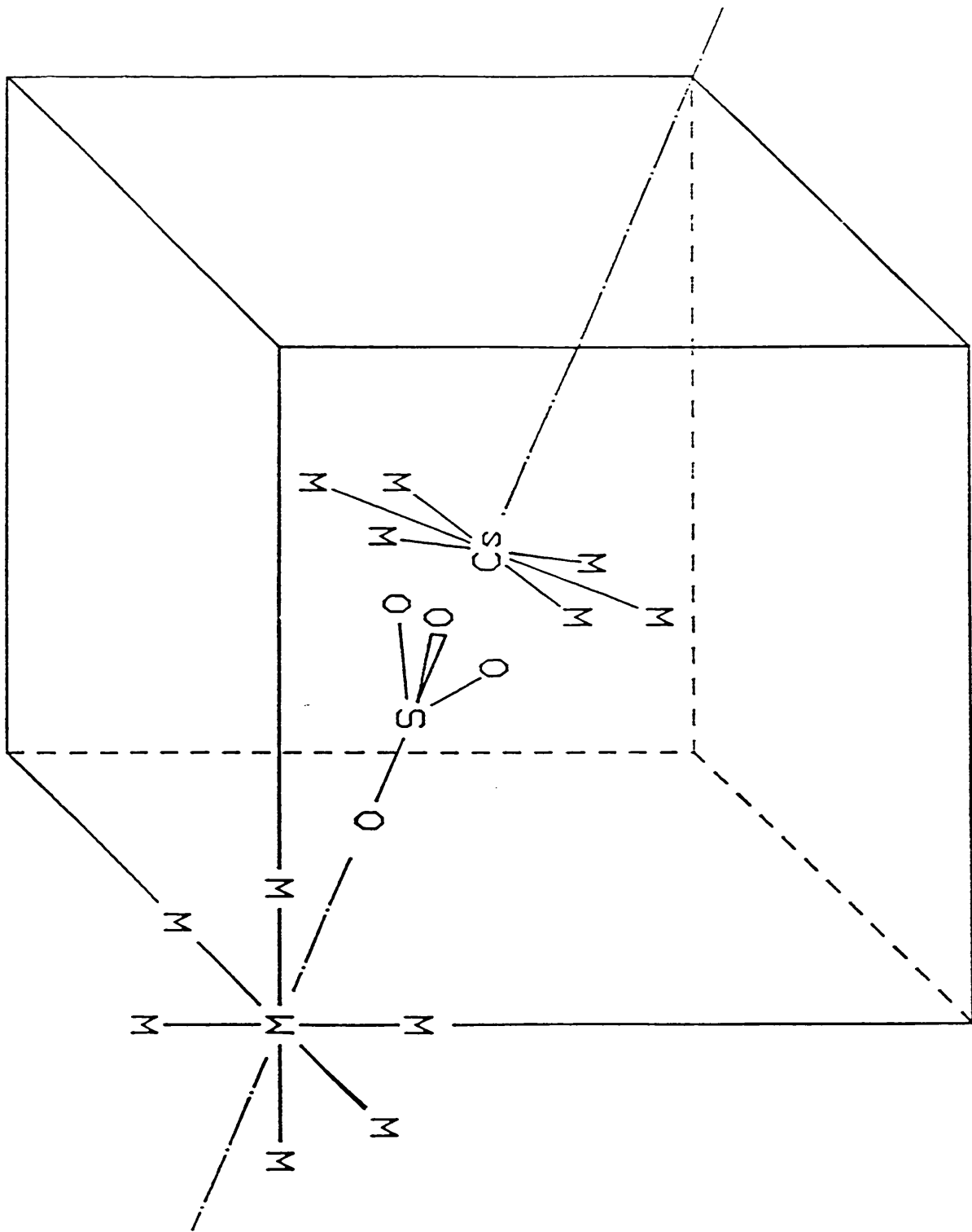


Figure 1.2.2

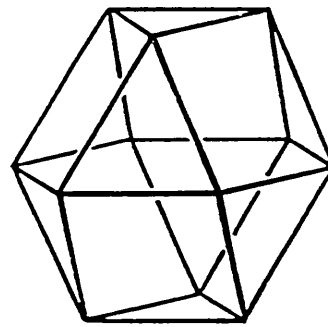
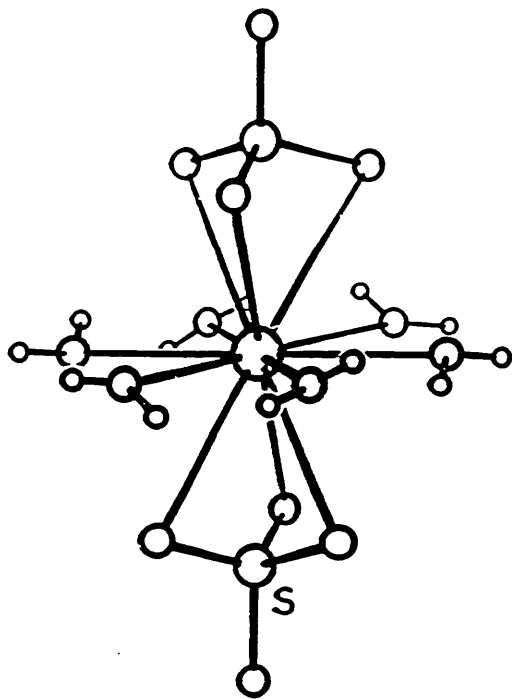
Stereo-chemistry of the monovalent cation in:

(a) The β alum of $\text{CsFe}(\text{SO}_4)_2 \cdot 12\text{H}_2\text{O}$

(b) The α alum of $\text{CsFe}(\text{SeO}_4)_2 \cdot 12\text{H}_2\text{O}$

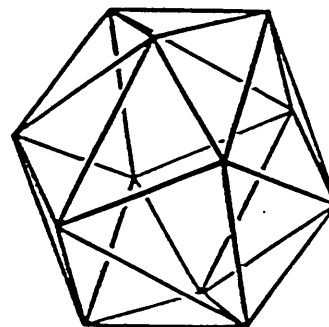
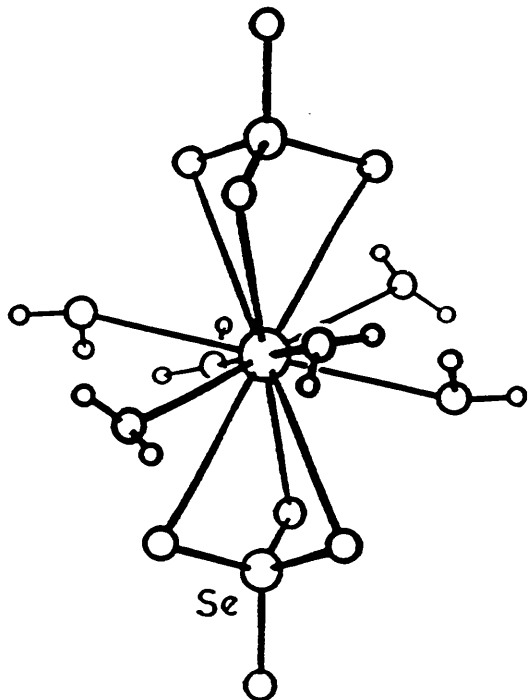
(After S. P. Best and J. B. Forsyth [10]).

β



Cuboctahedron

α



Icosahedron

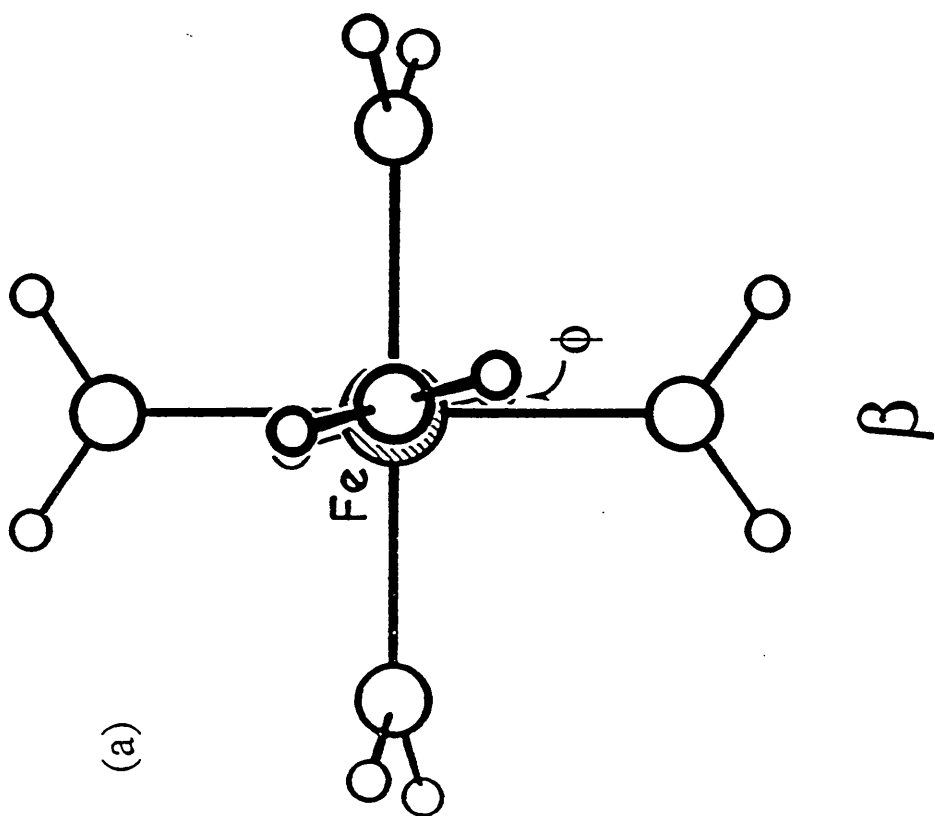
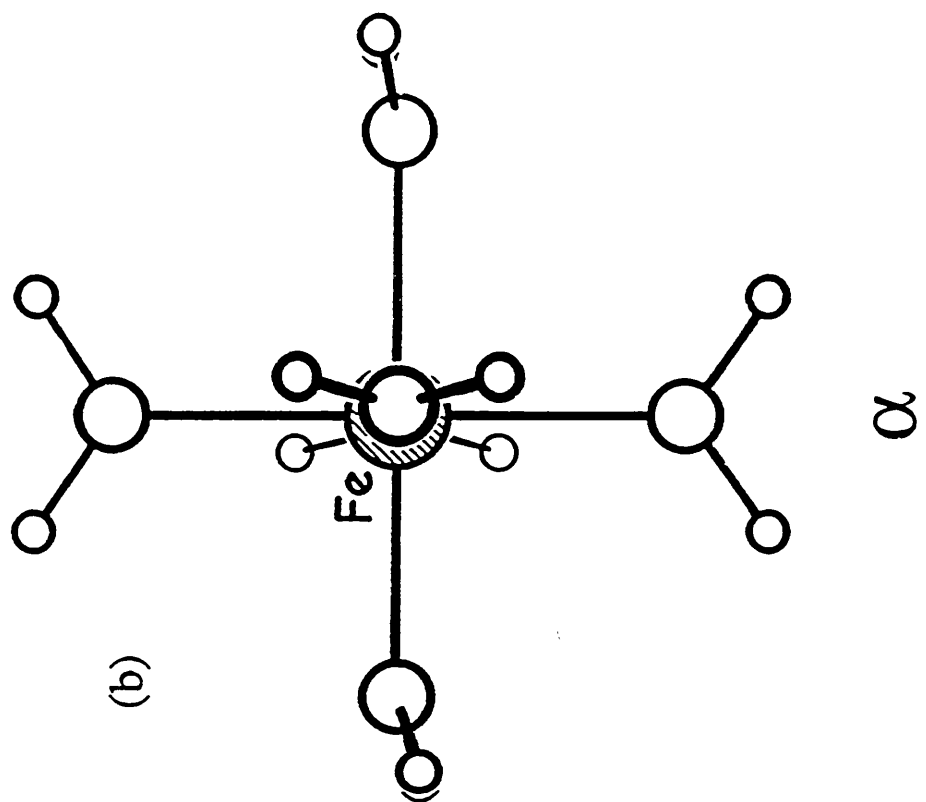
Figure 1.2.3

Schematic diagram showing the mode of water co-ordination to the trivalent cation in:

(a) The β alum of $\text{CsFe}(\text{SO}_4)_2 \cdot 12\text{H}_2\text{O}$

(b) The α alum of $\text{CsFe}(\text{SeO}_4)_2 \cdot 12\text{H}_2\text{O}$

The angle by which the plane of the water molecule is twisted away from the MO_6 framework, ϕ , is found to be $18.6^\circ(10)$ for the iron(III) hexa-aqua-cation within the β alum of $\text{CsFe}(\text{SO}_4)_2 \cdot 12\text{H}_2\text{O}$ (After S. P. Best and J. B. Forsyth [10]).



1.3 Origin of the trigonal field for the $[M(OH_2)_6]^{3+}$ cation within the alum lattice.

The factors that affect both the magnitude and sign of the trigonal field for the $[M(OH_2)_6]^{3+}$ cation within the alum lattice were first investigated by Van Vleck²¹ as part of the early development of crystal field theory. At the time of writing, Van Vleck was aware of susceptibility²² and relaxation²³ measurements on the ammonium vanadium sulphate alum which suggested that the $[V(OH_2)_6]^{3+}$ cation was subject to a trigonal distortion leaving the non-degenerate trigonal term lowest in energy. In view of Lipson's crystallographic measurements on the alums indicating that the $M^{III}O_6$ core was approximately octahedral, Van Vleck postulated 3 possible causes for the origin of the trigonal field within the alum lattice:

(I) The direct effect of the field from distant atoms. The term "distant atoms" describing atoms beyond the first co-ordination sphere.

(II) The indirect action of the field from distant atoms. This describes the effect whereby the distant atoms distort the water ligands from their octahedral arrangement leading to a non-cubic field.

(III) The Jahn-Teller effect. According to Jahn and Teller,²⁴ an orbitally degenerate ground term will be unstable with respect to an asymmetric nuclear displacement that will act to lift the degeneracy. Therefore the ground term degeneracy of a transition metal cation in a cubic field will have repercussions on the arrangement of the surrounding water molecules so that they are no longer cubically grouped.

Van Vleck concluded that (I) does not yield a sufficiently large splitting and that (III) is also not the principal cause of the trigonal field, based on a crystal field analysis. (II) is postulated as the primary cause of the trigonal field splitting for Ti^{3+} , V^{3+} , and Cr^{3+} . In addition it is suggested that the trigonal field splitting is amplified by (III) for Ti^{3+} and V^{3+} both of which have orbitally degenerate cubic ground terms. Although Van Vleck's analysis is confined to a simple crystal field point-charge treatment, the essence of the discussion is quite general and can be related to more

recent ligand field models.

The relationship between the electronic and molecular structures of trivalent cations has been examined by Best and Forsyth in a recent neutron diffraction study of a number of β alums.¹⁹ The angle by which the plane of the water molecule is twisted away from the MO_6 framework, ϕ (shown for $[Fe(OH_2)_6]^{3+}$ in fig. 1.2.3 (a)) is found to be dependent upon the electronic structure of the trivalent cation. The results of this study are summarised in figure 1.3.1. The magnitude of the trigonal field is related to the angle ϕ by the equation:

$$\delta = |3e_{\pi}\sin(2\phi)| \quad 1.3.1$$

which is derived from the angular overlap model^{25,26} (a.o.m.). δ is the absolute magnitude of the trigonal field splitting and e_{π} is an a.o.m. parameter related to the metal-ligand π interaction.

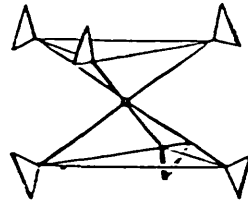
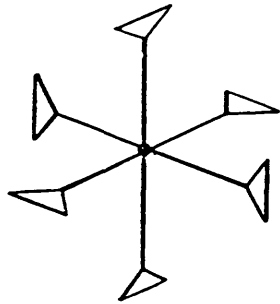
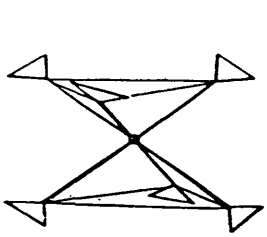
When ϕ is zero, the cation possesses T_h symmetry and the degeneracy of the t_{2g} (O_h) orbitals is accommodated. As ϕ increases, the symmetry of the cation approaches either the all-vertical (ϕ defined as positive) or all-horizontal (ϕ defined as negative) D_{3d} structure, depending on which direction the water molecules are rotated relative to the three-fold axis. In the all-vertical D_{3d} structure, the hydrogen atoms lie in the D_{3d} mirror planes that contain the oxygen atoms. Conversely, in the all-horizontal D_{3d} structure, the bond vector joining two hydrogen atoms of one water molecule is perpendicular to the D_{3d} mirror planes that contain the oxygen atoms. The model predicts that when ϕ is positive the a_g component of the t_{2g} (O_h) orbitals is lowest in energy. When ϕ is negative, the e_g component is lowest in energy. The trivalent hexa-aqua-cation is constrained within the alum lattice to have S_6 symmetry with ϕ negative such that the e_g component of the t_{2g} (O_h) orbitals is lowest lying. Where there is no electronic stabilisation to be gained from the trigonal field splitting, such as for Cr^{3+} and Fe^{3+} which have d^3 and high-spin d^5 electron configurations respectively, ϕ is found to be $\approx -19^\circ$. For Ru^{3+} , which has the low-spin d^5 electron configuration, $\phi \approx -22^\circ$. It is suggested that the primary cause of the trigonal field is the indirect action of distant atoms on the first co-ordination sphere about the metal(III) centre *viz.* hydrogen bonding constraints. For trivalent cations whose

Figure 1.3.1

Relationship between the molecular structure and the energies of the t_{2g} (O_h) orbitals for a hexa-aqua-cation on a site of trigonal symmetry with trigonal planar water coordination. The relative energies of the a_g and e_g components of the t_{2g} (O_h) orbitals were calculated using the equation:

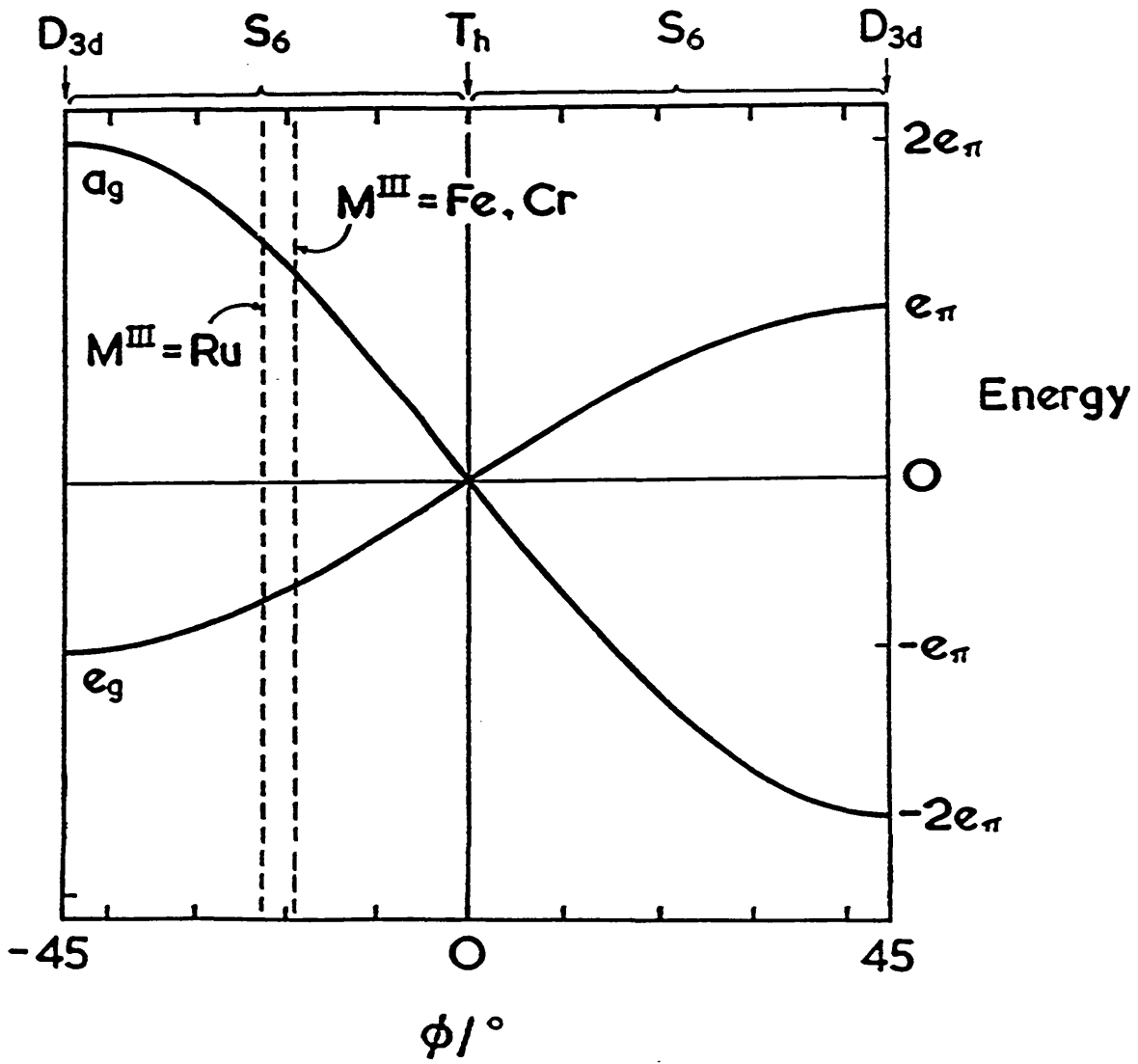
$$\delta = |3e_{\pi}\sin(2\phi)| \quad 1.3.1$$

which is derived from the angular overlap model^{26,27} (a.o.m.) δ is the absolute magnitude of the trigonal field splitting and e_{π} is an a.o.m. parameter related to the metal-ligand π interaction normal to the plane of the water molecule. (After Best and Forsyth [19]. Schematic diagrams of hexa-aqua-cations after Cotton *et al.* [11]).



all-horizontal

all-vertical



electronic structures are stabilised by a larger trigonal field splitting such as Ru^{3+} , the trigonal field is amplified by the Jahn-Teller effect. The findings of Best and Forsyth¹⁹ are therefore in accordance with the predictions made by Van Vleck over 50 years earlier.

The underlying assumption of this model is that the metal-ligand π interaction is anisotropic with the dominant interaction being normal to the water molecule. If the dominant interaction were in the plane of the water molecule then the relative orbital energies would be reversed from their positions shown in 1.3.1. Indirect evidence for the predominant metal-ligand π interaction being normal to the plane is found from the low temperature electronic spectrum of $\text{NH}_4\text{V}(\text{SO}_4)_2 \cdot 12\text{H}_2\text{O}$. The transition energies obtained by Hitchman *et al.*²⁷ have been interpreted in conjunction with the published magnetic susceptibility data²⁸ using the angular overlap model. In the communication it is reported that agreement with experiment can be obtained only if the π bonding in the plane of the water molecule is considerably weaker than that perpendicular to the plane.

1.4 Aims of this work

The broad aims of this work are to determine directly the anisotropy of the π interaction *viz.* resonance and diffraction techniques, and to examine the relationship between the electronic structure of the tervalent hexa-aqua-cation and the overall alum structure.

Techniques which can simultaneously give information on both the geometric and the electronic structure of a complex have been extensively employed. The two main techniques that have been utilised in this work are Raman spectroscopy, and neutron diffraction. For brevity, the alums $\text{M}^{\text{I}}\text{M}^{\text{III}}(\text{SO}_4)_2 \cdot 12\text{H}_2\text{O}$, $\text{M}^{\text{I}}\text{M}^{\text{III}}(\text{SeO}_4)_2 \cdot 12\text{H}_2\text{O}$, and $\text{M}^{\text{I}}\text{M}^{\text{III}}(\text{SO}_4)_2 \cdot 12\text{D}_2\text{O}$ are abbreviated to $\text{M}^{\text{I}}\text{M}^{\text{III}}\text{SH}$, $\text{M}^{\text{I}}\text{M}^{\text{III}}\text{SeH}$, and $\text{M}^{\text{I}}\text{M}^{\text{III}}\text{SD}$ respectively throughout this work.

REFERENCES

1. M. Bose, *Progress in NMR Spectroscopy*, Ed. J. W. Emsley, J. Feeney, and L. H. Sutcliffe, Pergamon, New York, **4**, (1969).
2. J. P Hunt, *Coord. Chem. Rev.* **7**, 1, (1970).
3. A. M. Chmelmick and D. Fiat, *J. Mag. Res.*, **8**, 325, (1972).
4. A. M. Chmelmick and D. Fiat, *J. Am. Chem. Soc.*, **93**, 2875, (1971).
5. G. W. Neilson, *Neutron diffraction studies of aqueous electrolyte solutions in Water and aqueous solutions*, Ed. G. W. Neilson & J. E. Enderly Adam Hilger, *Colston papers*, **37**, (1985).
6. A. H. Narten and R. L. Hahn, *Science*, **217**, 1249 (1982).
7. B. K. Annis, R. L. Hahn and A. H. Narten, *J. Chem. Phys.*, **82**, 2086 (1985).
8. R. D. Broadbent, G. W Neilson, and M Sandstrom, *J. Phys. : Condensed Matter*, **4**, 639, (1992).
9. G. E. Bacon and W. E. Gardner, *Proc. R. Soc. Lond.*, **A246**, 78 (1958).
10. S. P. Best and J. B. Forsyth., *J. Chem. Soc., Dalton Trans.*, 395 (1990).
11. F. A. Cotton, C. K. Fair, G. E. Lewis, G. N. Mott, F. K. Ross, A. J. Schultz, and J. Williams, *J. Am. Chem. Soc.*, **106**, 5319, (1984).
12. D. Getz and B. L. Silver, *J. Chem. Phys.*, **61**, 630 (1974).
13. R. J. Deeth, B. N. Figgis, J. B. Forsyth, E. S. Kucharski, and P. A. Reynolds, *Proc. R. Soc. Lond.*, **A 421**, 153 (1989).
14. B. N. Figgis, J. B. Forsyth, E. S. Kucharski, P. A. Reynolds and F. Tasset, *Proc. R. Soc. Lond.*, **A 428**, 113 (1990).
15. J. K. Beattie, S. P. Best, B. W. Skelton, and A. H. White, *J. Chem. Soc., Dalton Trans.*, 2105 (1981).
16. M. Brorson and M. Gajhede, *Inorg. Chem.*, **26**, 2109 (1987).
17. H. Lipson, *Phil. Mag.*, **19**, 887 (1935).
18. H. Lipson, *Proc. R. Soc. Lond.*, Ser A, **151**, 347 (1935).
19. S. P. Best and J. B. Forsyth, *J. Chem. Soc., Dalton Trans.*, 1721 (1990).
20. S. P. Best, Ph.D Thesis, Sydney University, (1983).
21. J. H. Van Vleck, *J. Chem. Phys.*, **7**, 61 (1939).
22. J. Van der Handel and A. Siegart, *Physica*, **4**, 871 (1937).

23. C. G. Gorter, *Physica*, **3**, 1006 (1936).
24. H. A. Jahn and E. Teller, *Proc. R. Soc. Lond.*, **161**, 220 (1937).
25. C. Daul and A. Goursot, *Inorg. Chem.*, **24**, 3554, (1985).
26. E. Larson and D. T. Cromer, *Acta Crystallogr.*, **22**, 793, (1967).
27. M. A. Hitchman, R. G. McDonald, P. W. Smith, and R. Stranger, *J. Chem. Soc., Dalton Trans.*, 1393 (1988).
28. B. N. Figgis, J. Lewis, and F. E. Mabbs, *J. Chem. Soc.*, **112**, 2480 (1963).

Single Crystal Raman Study of the Rubidium Alums

2.1 Introduction

Vibrational spectra are sensitive both to intra- and inter-molecular force constants and give complementary information to crystallographic data. Single crystal Raman studies of the caesium alums have previously been performed which include an assignment of the spectra between 250 and 1200 cm^{-1} .¹⁻⁵

Orientated single crystal Raman spectra for the alums $\text{RbM}^{\text{III}}(\text{SO}_4)_2 \cdot 12\text{H}_2\text{O}$ ($\text{M}^{\text{III}} = \text{Ti, V, Cr, Fe, Al, Ga or In}$) and $\text{RbM}^{\text{III}}(\text{SO}_4)_2 \cdot 12\text{D}_2\text{O}$ ($\text{M}^{\text{III}} = \text{Al or V}$), recorded between 10 and 4000 cm^{-1} , are presented. Whereas the caesium alums are predominately of the β modification,⁶ the morphology of the rubidium alums suggest they are predominately of the α modification.⁷ The study was undertaken to investigate how the field about the trivalent hexa-aqua-cation alters with change of alum type and also how the structure of the alum may be correlated to the electronic structure of the trivalent cation. The caesium alum study is used as the basis for assignment of the vibrational spectra of the rubidium alums.

2.2 Theory of Raman Scattering

When radiation of frequency ν_0 and intensity I_0 interacts with a circulation of freely orientated molecules, a small proportion of radiation is scattered in all directions (fig. 2.2.1 (a)).

The scattered radiation is of two forms:

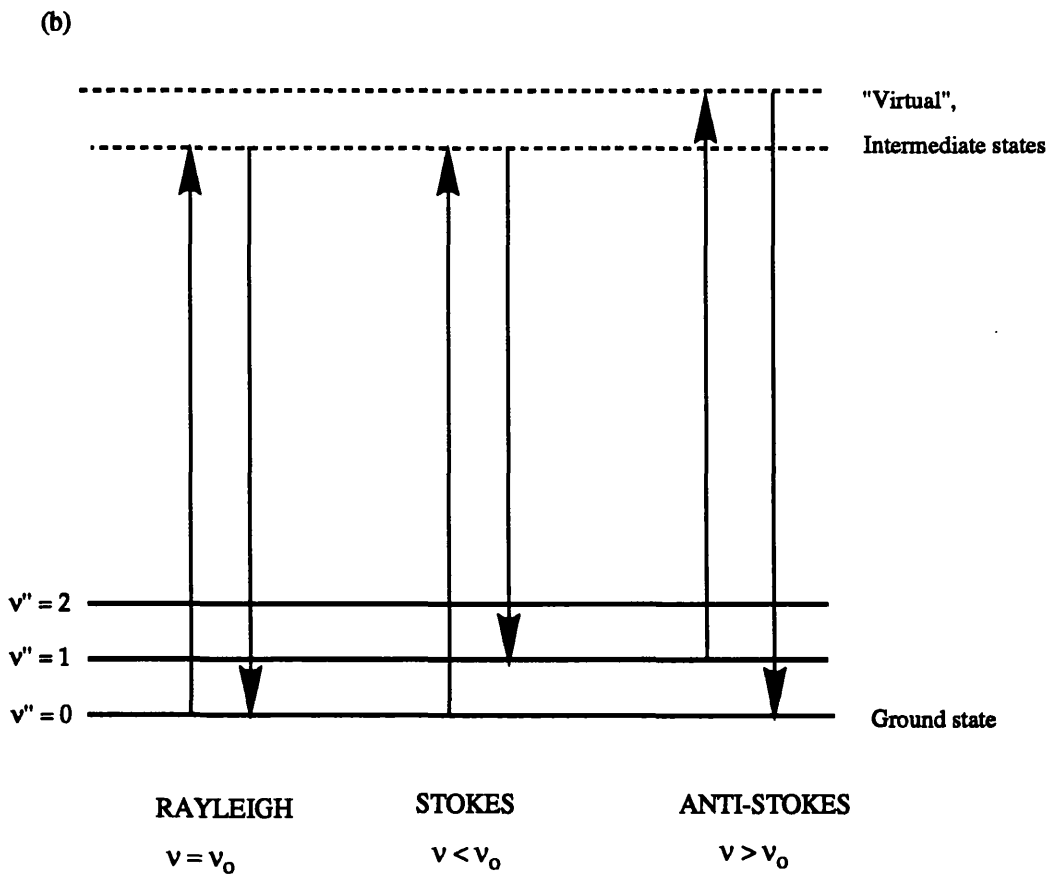
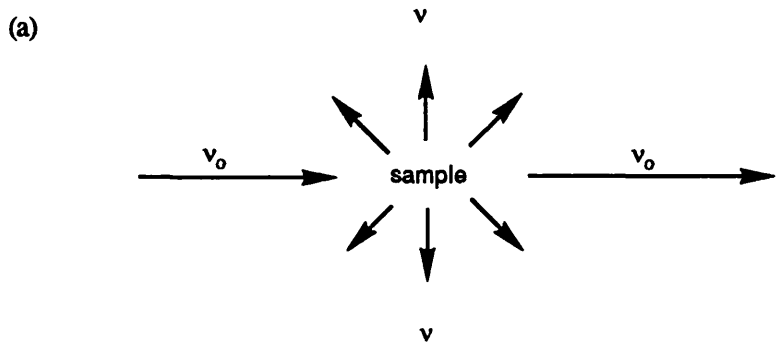
1. Rayleigh - Elastic Scattering.

This is of frequency ν_0 with intensity $I_{\text{Rayleigh}} \approx 10^{-5}I_0$. I increases as a function of $\nu_0^4\alpha_0^2$, where α_0 is the polarisability of the molecule at equilibrium.

Figure 2.2.1

(a) Scattering of radiation by gaseous sample

(b) Origin of the Vibration Raman Effect



2. Raman - Inelastic Scattering.

The frequency of the scattered radiation ν is different to that of the incoming radiation.

$$\nu = \nu_0 \pm \nu_i \quad 2.2.1$$

ν_i is a transition frequency of the molecule corresponding to vibrational/rotational /electronic transitions. Raman scattering is a much weaker effect than Rayleigh scattering. $I_{\text{Raman}} \approx 10^{-8}I_0$. For a vibrational transition, the intensity of Raman scattering depends on ν_0 , ν_i and on the rate of change of the polarisability with the normal co-ordinate Q_i , at equilibrium position.

$$I \propto (\nu_0 - \nu_i)^4 \left(\frac{d\alpha}{dQ_i}\right)_0^2 \quad \text{Stokes Lines} \quad 2.2.2$$

$$I \propto (\nu_0 + \nu_i)^4 \left(\frac{d\alpha}{dQ_i}\right)_0^2 \quad \text{Anti-Stokes Lines} \quad 2.2.3$$

Origin of the Vibration Raman effect

Figure 2.2.1 (b) is a schematic diagram showing the vibrational Raman effect. For bands which are termed 'the Stokes lines', the laser excites a molecule from the ground vibrational state to an upper, non-stationary, 'virtual' state; radiation of frequency of $(\nu_0 - \nu_i)$ is emitted when the molecule returns to the first excited vibrational state. The anti-Stokes bands originate from a molecule already existing in an excited vibrational state. The molecule is excited from the first excited vibrational state to an upper, 'virtual' state and returns to its ground vibrational state. Radiation of frequency $\nu_0 + \nu_i$ is emitted in this process.

The occupancy of the excited vibrational states is governed by the Boltzmann distribution. The ratio of intensities of the anti-Stokes and Stokes lines is therefore:

$$\frac{I_{AS}}{I_S} = \left(\frac{\nu_0 + \nu_i}{\nu_0 - \nu_i}\right)^4 \cdot \exp\left(\frac{-h\nu_i}{kT}\right)$$

2.2.4

Equation 2.2.4 was used to calculate the temperature of the crystals studied in

the series of experiments presented here. Since the Stokes and anti-Stokes lines are symmetrically spaced about the central Rayleigh line, their positions are used to calibrate the spectrometer.

Mechanism of Raman Scattering

Classical Approach:

When radiation is incident with a molecule, the electric field associated with the incident radiation induces a dipole moment in the molecule:

$$\mu = \mu_0 + \{ \alpha.E + 1/2! \beta.E^2 + 1/3! \gamma.E^3 \} \quad 2.2.5$$

where the total dipole moment μ is equal the first term μ_0 which represents the static dipole moment plus the second term in brackets which corresponds to the induced dipole moment μ_{ind} .

μ = dipole moment Cm

E = electric field strength Vm^{-1}

α = polarisability $CV^{-1}m^2$

β = hyperpolarisability $CV^{-2}m^3$

γ = 2nd hyperpolarisability $CV^{-3}m^4$

Typical Values:

$$\alpha \approx 10^{-40} CV^{-1}m^2$$

$$\beta \approx 10^{-50} CV^{-2}m^3$$

$$\gamma \approx 10^{-61} CV^{-3}m^4$$

Almost no conventional laser, operating in continuous wave mode, has enough electric field strength to make β significant. So we can write:

$$\mu_{ind} = \alpha.E \quad 2.2.6$$

α is a second rank tensor, such that:

$$\begin{pmatrix} (\mu_{ind})_x \\ (\mu_{ind})_y \\ (\mu_{ind})_z \end{pmatrix} = \begin{pmatrix} \alpha_{xx} & \alpha_{xy} & \alpha_{xz} \\ \alpha_{yx} & \alpha_{yy} & \alpha_{yz} \\ \alpha_{zx} & \alpha_{zy} & \alpha_{zz} \end{pmatrix} \begin{pmatrix} E_x \\ E_y \\ E_z \end{pmatrix} \quad 2.2.7$$

The electric field, E is a periodic function of time, t, given by:

$$E = E_0 \cos(2\pi\nu_0 t) \quad 2.2.8$$

Molecular polarisability depends on the displacement co-ordinate Q_1 . For a diatomic molecule, α is approximately a linear function of displacement.

$$\alpha = \alpha_0 + (d\alpha/dQ_1)_0 Q_1 + 1/2 (d^2\alpha/dQ_1^2)_0 Q_1^2 + \dots \quad 2.2.9$$

Q_1 = displacement co-ordinate (= 0 at equilibrium)

α_0 = polarisability in equilibrium configuration.

The third term is responsible for the appearance of overtones and combination bands in the Raman spectrum. The expression for μ_{ind} , considering the first order phonon spectrum only, now becomes:

$$\mu_{ind} = \{ \alpha_0 + (d\alpha/dQ_1)_0 Q_1 \} E_0 \cos(2\pi\nu_0 t) \quad 2.2.10$$

The displacement Q_1 is a function of time and the frequency of displacement which is the vibrational frequency of the molecule.

$$Q_1 = Q_1^0 \cos(2\pi\nu_1 t) \quad 2.2.11$$

μ_{ind} can now be written as:

$$\begin{aligned} \mu_{ind} &= E_0 \alpha_0 \cos(2\pi\nu_0 t) + E_0 Q_1^0 (d\alpha/dQ_1)_0 \cos(2\pi\nu_0 t) \cos(2\pi\nu_1 t) \equiv \\ \mu_{ind} &= E_0 \alpha_0 \cos(2\pi\nu_0 t) + 1/2 E_0 Q_1^0 (d\alpha/dQ_1)_0 \{ \cos 2\pi(\nu_0 + \nu_1)t + \cos 2\pi(\nu_0 - \nu_1)t \} \\ &= \{ \text{Rayleigh} \} \quad \quad \quad \{ \text{Anti-Stokes} \quad + \quad \text{Stokes} \} \quad 2.2.12 \end{aligned}$$

The intensity of a Raman band associated with the transition between the states i and f , observed at 90° , of one freely oriented molecule is given by:

$$I\left(\frac{\pi}{2}\right) = \frac{10^8 \pi^2}{\epsilon_0^2} I_0 (\nu_0 \pm \nu_{fi})^4 \sum_{\rho\sigma} [\alpha_{\rho\sigma}]_{fi} [\alpha_{\rho\sigma}]_{fi}^*$$

2.2.13

ϵ_0 = permittivity of free space (Fm^{-1})

I_0 = Intensity of the incident radiation (Wm^{-2})

ν_0 = exciting line wavenumber (cm^{-1})

ν_{fi} = wavenumber (cm^{-1}) of the Raman transition $f \leftarrow i$

$[\alpha_{\rho\sigma}]_{fi}$ = ρ, σ th component of the polarisability tensor.

$\rho, \sigma = x, y$ or z ; the space-fixed co-ordinate axes.

Classically, $[\alpha_{\rho\sigma}]_{fi}$ corresponds to $d\alpha_{\rho\sigma}/dQ$. As ν_0 approaches the frequency of an electronic transition ν_e , the classical description is unable to account for the observed spectrum. As $\nu_0 \rightarrow \nu_e$ an enormous increase in the intensity of a particular band, associated with the chromophore, can be observed along with an apparent breakdown in the harmonic oscillator selection rules, such that overtones may be appear with intensities comparable with that of the fundamental.

The Kramers-Heisenberg-Dirac dispersion formula, is a quantum-mechanical expression for $[\alpha_{\rho\sigma}]_{fi}$, over the entire frequency range and is given by the following sum over all vibronic states of the molecule:

$$[\alpha_{\rho\sigma}]_{fi} = \frac{1}{\hbar c} \sum_E \left[\frac{\langle F | \mu_\rho | E \rangle \langle E | \mu_\sigma | I \rangle}{\nu_{IE} - \nu_0 + i\Gamma_E} + \frac{\langle F | \mu_\sigma | E \rangle \langle E | \mu_\rho | I \rangle}{\nu_{FE} + \nu_0 + i\Gamma_E} \right]$$

2.2.14

I, F and E are the initial, final and intermediate states respectively.

$\langle F | \mu_\rho | E \rangle$ and $\langle E | \mu_\sigma | I \rangle$ are the electric dipole transition moments along the directions ρ and σ from $F \leftarrow E$ and $I \rightarrow E$ respectively. The term $i\Gamma_E$ is a damping constant which prevents the denominator at resonance from reaching zero and which represents the finite lifetime and 'sharpness' of the intermediate state.

At resonance, ν_0 , the laser excitation wavenumber equals the wavenumber of an electronic transition = ν_{IE} . The second term in brackets then becomes negligible compared to the first term. Off resonance, both terms have to be considered.

2.3 Preparation of the rubidium alums.

i) RbAlSH and RbAlSD

$\text{Al}_2(\text{SO}_4)_3$ was dissolved, on a steam bath, in sulphuric acid (2 mol dm^{-3}). Rb_2CO_3 was added in stoichiometric proportion to give a solution approximately 1 mol dm^{-3} in sulphuric acid. The alum crystallised on cooling. The product was recrystallised from sulphuric acid (1 mol dm^{-3}).

RbAlSD was prepared by recrystallising RbAlSH in a sealed vessel under dry nitrogen from D_2SO_4 (1 mol dm^{-3}). The product was again recrystallised from D_2SO_4 (1 mol dm^{-3}) to increase the deuterium concentration. The deuterium enrichment from this procedure is estimated to be greater than 99%.

ii) RbTiSH

Titanium(III) solutions are very susceptible to oxidation, solutions were therefore handled in an atmosphere of argon or nitrogen to prevent oxidation.

Mixing of deoxygenated solutions of Rb_2SO_4 and $\text{Ti}_2(\text{SO}_4)_3$ (15% w/v), both in sulphuric acid (1 mol dm^{-3}), gave a violet solution which on cooling gave violet crystals of RbTiSH. RbTiSH has a high solubility and is extremely susceptible to aerial oxidation. It is probably for these reasons that past attempts to synthesise the alum have been unsuccessful.^{8,9} Left open to air at room temperature, the formation of the white compound of TiO_2 on the crystal surface is noticeable within 5 minutes. Crystals of RbTiSH can, however, be handled at 5°C for short periods of time. RbTiSH should be stored under Argon or nitrogen below -5°C .

iii) RbVSH

Solutions of vanadium(III) are also susceptible to oxidation and were handled under an atmosphere of argon or nitrogen to prevent oxidation to the stable vanadium (IV) vanadyl ion $[\text{VO}(\text{H}_2\text{O})_5]^{2+}$. The first step in the preparation of this alum was the dissolution of vanadium trichloride in deoxygenated sulphuric acid (1 mol dm^{-3}). The dissolution is exothermic and leaves a significant quantity of insoluble impurity which was filtered and discarded before the next stage of the preparation. The resulting solution was then added in excess to a deoxygenated solution of Rb_2SO_4 in sulphuric

acid (1 mol dm^{-3}). The deep green solution was left to cool to room temperature overnight. The resulting solution gave very large deep blue crystals. The solution was kept at 2°C until crystallisation was complete. The product was recrystallised from sulphuric acid (1 mol dm^{-3}). Crystals of RbVSH are stable in air for short periods of time. Crystals of RbVSH should be stored under an inert gas below 5°C to prevent oxidation.

iv) RbCrSH

Hydrous chromic nitrate was dissolved in sulphuric acid (1 mol dm^{-3}) and a solution of rubidium sulphate applied in stoichiometric proportion. Crystals of RbCrSH were formed on cooling which were recrystallised from sulphuric acid (1 mol dm^{-3}).

v) RbFeSH

Hydrous ferric nitrate was dissolved in sulphuric acid (1 mol dm^{-3}) and a solution of rubidium sulphate added in stoichiometric proportion. Crystals of RbFeSH were formed on cooling which were recrystallised from sulphuric acid (1 mol dm^{-3}).

vi) RbGaSH

Gallium metal was refluxed in sulphuric acid (6 mol dm^{-3}) over a period of several weeks. When dissolution was complete, rubidium carbonate was added to the clear solution in stoichiometric proportion; the alum subsequently crystallised on cooling. The colourless octahedral crystals were recrystallised from sulphuric acid (1 mol dm^{-3}).

vii) RbInSH

This alum was made by application of rubidium carbonate to a solution of indium sulphate formed from dissolution of the metal in sulphuric acid (*ca.* 10 mol dm^{-3}) on a steam bath.

RbInSH is extremely deliquescent. A large excess of both $[\text{SO}_4]^{2-}_{\text{aq}}$ and $[\text{Rb}(\text{OH})_6]^{+}_{\text{aq}}$ were needed in order for the alum to crystallise. The alum was recrystallised from sulphuric acid (1 mol dm^{-3}) which was saturated with Rb_2SO_4 .

2.4 Techniques used to produce large single crystals

The crystal growing apparatus used to produce large single crystals is shown in figure 2.4.1. The apparatus was first developed for use in the caesium alum study.¹

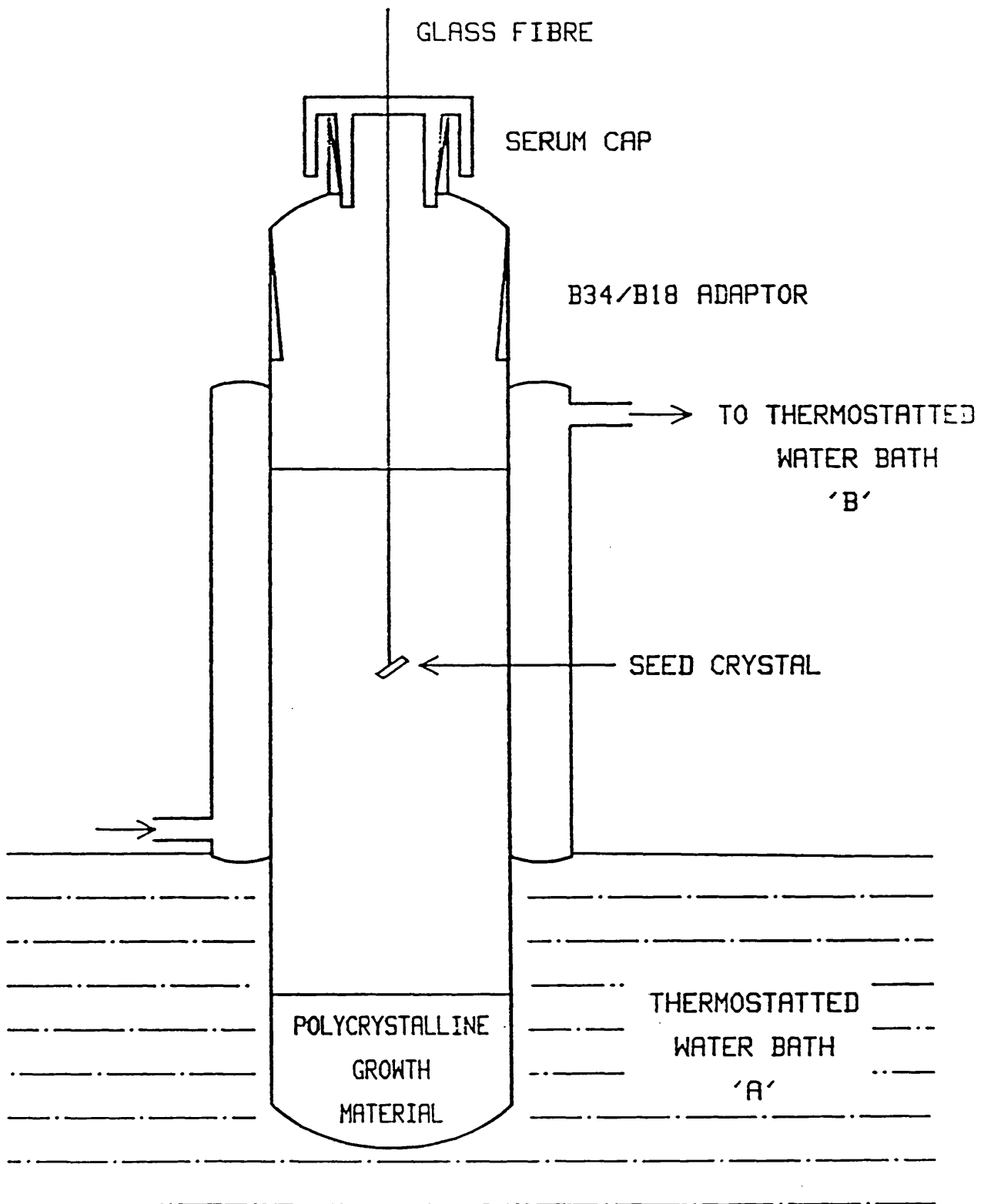
The seed crystal is placed in a saturated solution containing crystalline material of the alum. The solution is contained in glassware, the top half of which is surrounded by a thermostatted water jacket and connected to thermostatted water bath 'B'. The apparatus is placed in a thermostatted water bath 'A' so that the bottom half of the glassware, which is not surrounded by the water jacket is completely immersed. Thermostatted water bath 'B' is set at a lower temperature than bath 'A'. The density of aqueous solutions generally rises as the temperature is lowered, this has the effect of setting up convection currents in the solution aiding the mass transport of material to the crystal. Since the alums have a large positive coefficient of solubility, the solution around the crystal is super saturated and material is deposited onto the crystal.

The overall and relative temperatures of the two baths were optimised according to the solubility characteristics of the alum. The rate of deposition of material will be related to these factors. The rate of deposition must be sufficiently slow to allow the orderly deposition of growth material onto the crystal faces without leading to crystal defects. The temperature gradient must, however, be sufficiently large to maintain convection currents within the apparatus. Temperature gradients between 4 and 15 degrees were found to be suitable for the alums. Large single crystals of up to 20 mm along an edge were grown by this method. The crystal growing time varied between 4 days and 4 weeks.

For air sensitive solutions a sintered glass frit was incorporated into the bottom of the apparatus and attached to a source of argon or nitrogen.

FIGURE 2.4.1

The crystal growing apparatus (after S. P. Best [1]).



2.5 Preparation of, and techniques for cooling crystals for single crystal Raman measurements.

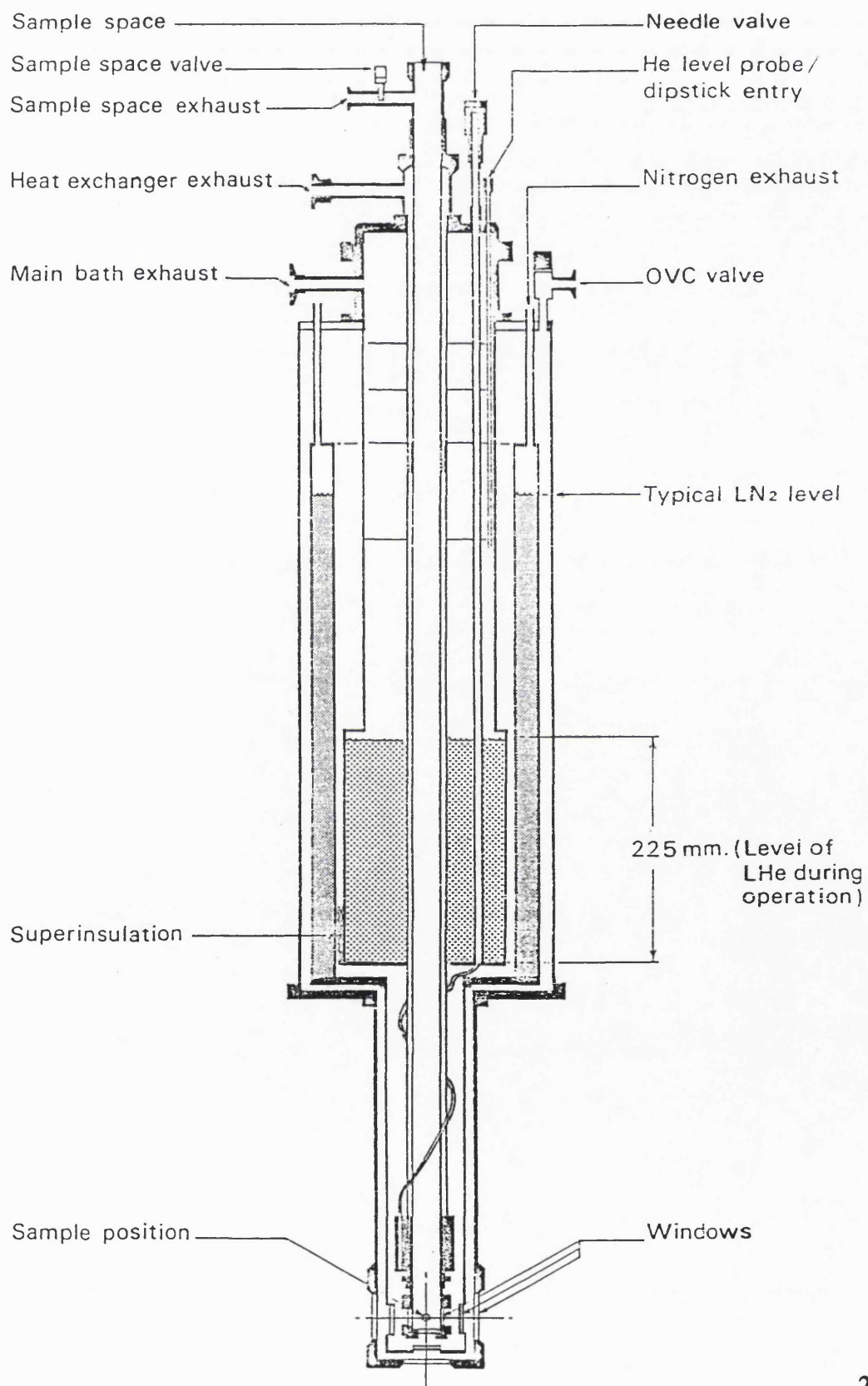
For single crystal Raman experiments, faces are required normal to the excitation and collection directions. The criteria for selecting these directions follow from the symmetry of the unit cell. For the alums, these directions, which are expressed in terms of the crystallographic axes, can be easily identified from the crystal morphology and are selected so as to allow the identification of the symmetry species. Optically clear crystals, free of defects required for the single crystal Raman experiment were mounted on a small goniometer using an epoxy resin ('Araldite Rapid') and faces of the crystal cut using a diamond saw. The cut crystal was then removed from the goniometer and the faces polished on a Hyprocel cloth using 1 micron Hyprez Diamond compound. The crystal was subsequently glued to a two circle goniometer head designed for use in either one of the liq. N₂ or liq. He cryostats that were used in this study.

For the liquid nitrogen cryostat, the goniometer head was attached to a copper cooling block and the area around the crystal evacuated. The crystals were cooled by the conduction of the copper block, the other side of which was in contact with liquid nitrogen. In order to prevent damage of the crystal surface through dehydration, liquid nitrogen was added to the cryostat soon after the atmosphere around the crystal had begun to be evacuated. For crystals of TlVSH and RbTiSH, this procedure was not adequate to prevent extensive damage of the crystal surface with severe loss of signal (in the case of RbTiSH TiO₂ formed on the surface) This problem was overcome by filling the space around the sample with dry He gas before cooling. After *ca.* 20 minutes, in which time the sample was presumed to have cooled down to a temperature close to 77 K, the helium gas was evacuated from the cryostat. This method inevitably leads to frosting on the outside of the cryostat. The O-rings were kept from freezing by use of a domestic hair drier.

The other cryostat used was the Oxford MD4 Bath cryostat shown schematically in figure 2.5.1. The cryostat is essentially a reservoir of coolant, He or N₂, which is used to cool the sample by contact with He gas within the sample chamber by means of a copper block acting as a heat exchanger. The coolant is

FIGURE 2.5.1

Vertical cross-section through Oxford MD4 cryostat (After Oxford Instruments Limited, instruction manual for Bath cryostat MD4 (1988)).



insulated from the atmosphere by use of superinsulating material and an outer reservoir of liquid nitrogen. The space surrounding the outer reservoir was evacuated down to pressures of *ca.* 10^{-6} Torr. The main advantage of this cryostat is that by evacuating the volume around the heat exchanger the cryogen is rapidly cooled and frozen. Sample temperatures as low as 62 K were achieved with liquid nitrogen as the coolant.

After the sample is cooled in one of the two cryostats, the cryostat is secured such that the desired crystal axes are aligned with the laboratory axes of the Raman experiment.

2.6 The Raman Spectrometer

The appropriate laser excitation line was chosen so as to be well away from any absorption maxima of the sample. In order to obtain a complete data set, it was necessary to obtain spectra with the electric vector of the laser beam rotated through $\pi/2$ radians. This was achieved by use of lens known as a half wave plate. The laser beam was focused onto the sample using a condensing lens. The scattered radiation was collected using a compound lens and focused onto the slits of the spectrometer. The radiation was also passed through a polaroid film, which was used to analyze the radiation, and a scrambler which depolarises the radiation before entry into the spectrometer. This is necessary because of polarisation bias inherent in the spectrometer. The scattered radiation was analyzed using a Spex R6 double monochromator and measured with either a Burle GaAs photo multiplier tube (PMT) or a Hamamatsu bi-alkali PMT. The GaAs tube was maintained in a cooled housing unit to reduce the dark current which varied from 20 to 80 counts/second. The bi-alkali tube has the advantage that it does not need cooling, the dark current is generally lower at around 4 counts/second. The spectral response of the two photomultiplier tubes differ greatly as shown in figure 2.6.1. The Raman spectra of RbAlSH and RbAlSD were collected using 406 nm excitation and a Hamamatsu bi-alkali PMT. All other spectra were measured using a Burle GaAs PMT.

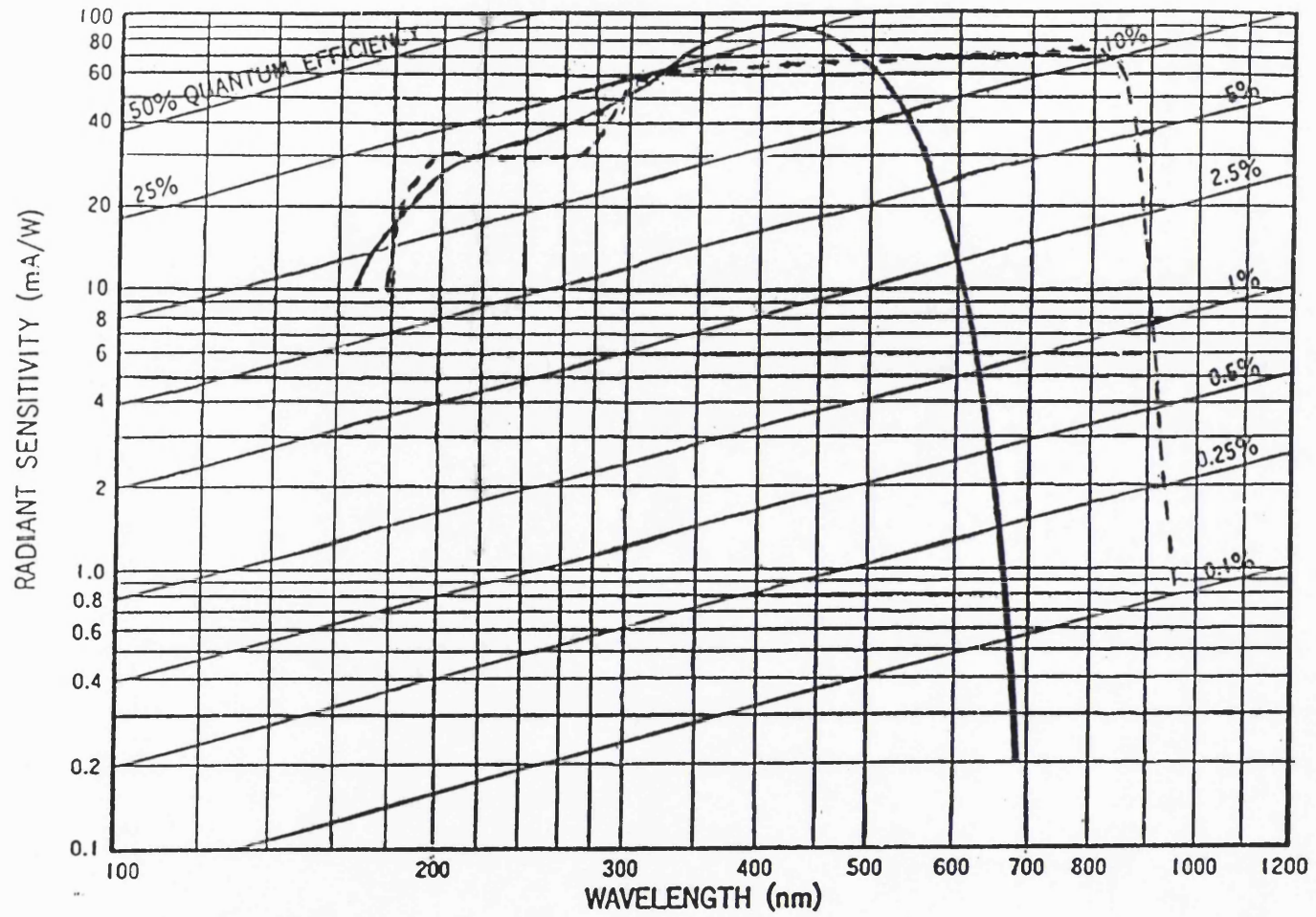


Figure 2.6.1

Spectral Response of the
GaAs ----- and
Bi-alkali -----
photomultiplier tubes.

2.7 Vibrational Analysis

The number and symmetry properties of the vibrational modes associated with a given molecular species within the alum lattice can be found using well established group theoretical techniques.^{10,11} In this method, the different molecular species are identified and their unperturbed symmetry correlated to the site symmetry and then the unit cell symmetry (giving rise to factor group coupling). Since the alums are an isomorphous series of crystals, the analysis is equivalent for both the α and β alums. Such an analysis has already been performed^{1,2} and will not be further discussed. The results are given in table 2.7.1. Schematic representations of the internal modes of the MO_6 and SO_4 species as well as the external modes of water are presented in figure 2.7.1. The alums crystallise with a cubic unit cell of symmetry $\text{Pa}\bar{3}$ (Hermann-Mauguin) or T_h (Schoenflies). For the T_h point group, the A_g , E_g , and F_g modes are Raman active, the F_u modes are infrared active and the A_u and E_u modes are inactive.

Oriented single crystal Raman experiments allow the A_g , E_g and F_g modes to be separated. With the co-ordinate system aligned along the crystallographic axes, experiments of the type $X'(\alpha \beta)Y'$, where X' and Y' are related to X , Y by a rotation about Z of $\pi/4$ radians, were chosen since a complete data set could be obtained this way without reorientation of the crystal. Experiments of the type $X'(\alpha \beta)Y'$ correspond to radiation polarised in the α designation relative to the crystallographic axes entering the crystal in the X' direction, being scattered at 90° and leaving the crystal through the Y' direction where, by use of a polaroid, only radiation polarised in the β designation is allowed to reach the monochromator. This is illustrated in figure 2.7.2

The activities of the Raman bands for each scattering experiment are given in table 2.7.2.

TABLE 2.7.1

Results of site group analysis of alum lattice (after S. P. Best [1])

MOLECULAR SPECIES	MODE	A_g	E_g	F_g	A_u	E_u	F_u
$M(OH_2)_6^{3+}$	U_1	1		1			
	U_2		1	2			
	U_3				1	1	3
	U_4				1	1	3
	U_5	1	1	3			
	U_6				1	1	3
	rock	1	1	3	1	1	3
	wag	1	1	3	1	1	3
	twist	1	1	3	1	1	3
	rot	1	1	3			
	tr				1	1	3
$M(OH_2)_6^+$	U_1	1		1			
	U_2		1	2			
	U_3				1	1	3
	U_4				1	1	3
	U_5	1	1	3			
	U_6				1	1	3
	rock	1	1	3	1	1	3
	wag	1	1	3	1	1	3
	twist	1	1	3	1	1	3
	rot	1	1	3			
	tr				1	1	3
SO_4^{2-}	U_1	1		1	1		1
	U_2		1	2		1	2
	U_3	1	1	3	1	1	3
	U_4	1	1	3	1	1	3
	rot	1	1	3	1	1	3
	tr	1	1	3	1	1	3
$H_2O(I)$	U_1	1	1	3	1	1	3
	U_2	1	1	3	1	1	3
	U_3	1	1	3	1	1	3
$H_2O(II)$	U_1	1	1	3	1	1	3
	U_2	1	1	3	1	1	3
	U_3	1	1	3	1	1	3

Figure 2.7.1

Schematic representations of the internal modes of MX_6 and AB_4 species, and the internal modes of water (after S. P. Best [1])

a) Normal modes of an octahedral MX_6 molecule (point group O_h).

b) Normal modes of a tetrahedral AB_4 molecule (point group T_d)

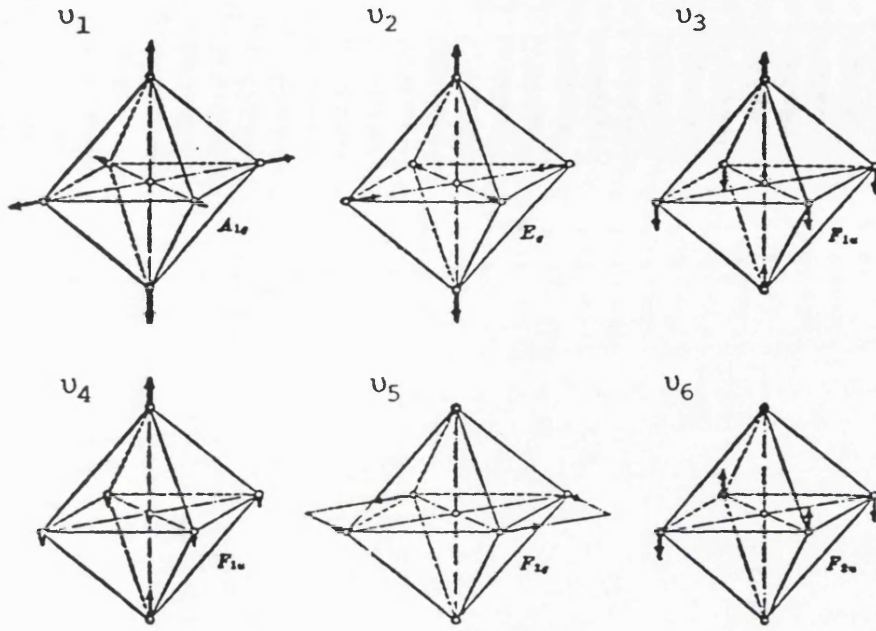
Only one component of each degenerate vibration is shown.

(After G. Herzberg [12])

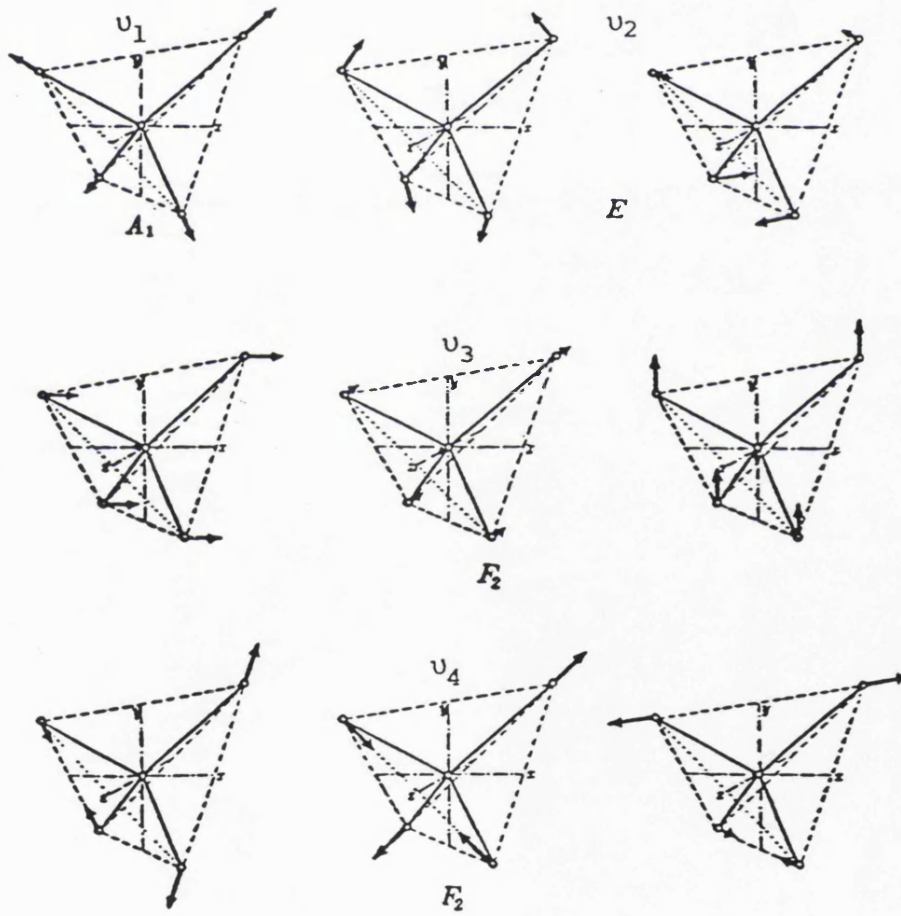
c) The external modes of water. The metal-water bond is along the twisting axis.

(After T. E. Jenkins and J. Lewis, [13])

a)



b)



c)

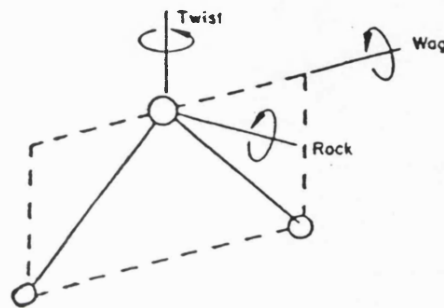
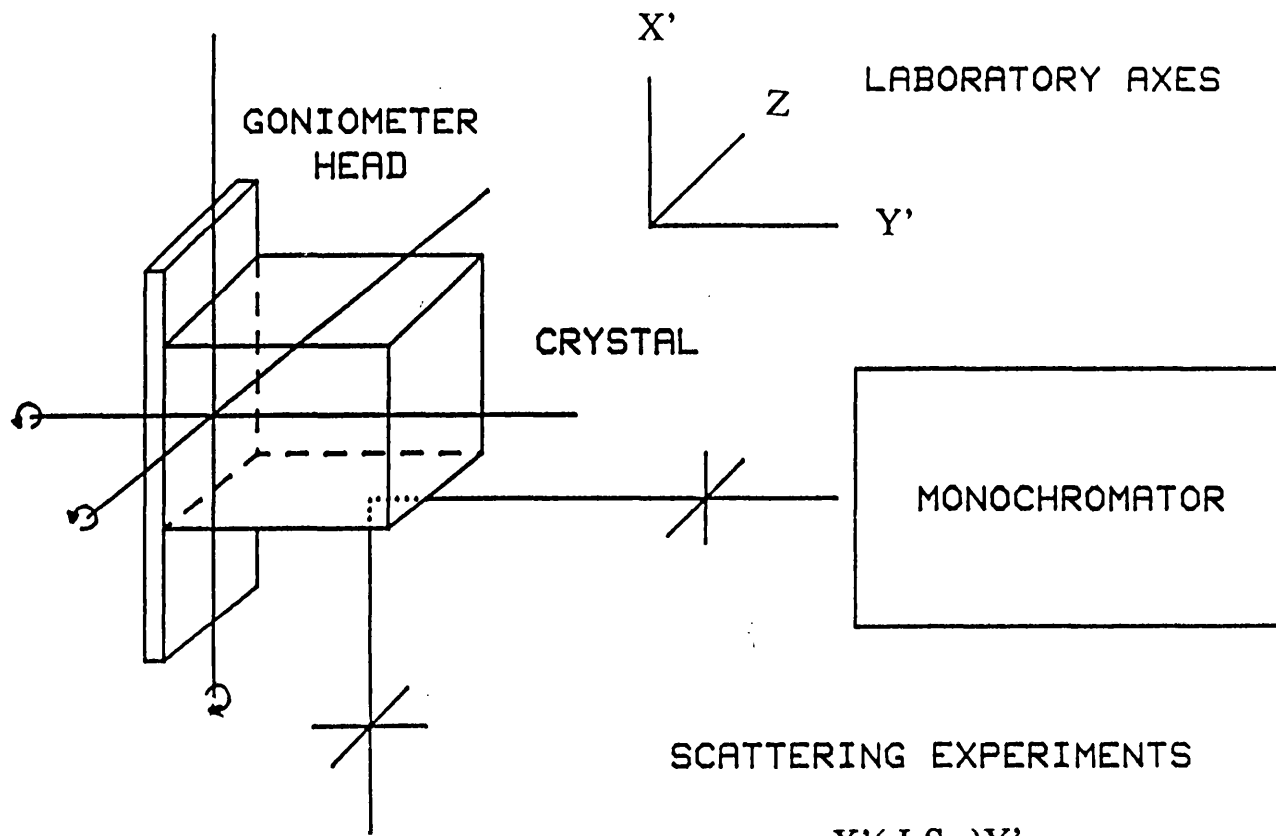


Figure 2.7.2

The alignment of the crystal axes with respect to the laboratory axes (After S. P. Best [1])



X'(IS)Y'

Y'X'

ZX'

ZZ

Y'Z

Table 2.7.2. Raman activities for the different scattering experiments

Scattering Experiment	Activity
X'(Z Z)Y'	$A_g + E_g$
X'(Z X')Y'	F_g
X'(Y'X')Y'	E_g

X', Y' are related to X, Y by a rotation of $\pi/4$ radians about Z.

The scattering tensor is symmetric

2.8 Intensity determination

In order to determine the activity of a Raman band, its intensity in the three Raman experiments listed in table 2.7.2 must be determined. The intensity of a Raman band is proportional to the area under the band. Thus, ideally a phonon mode of E_g symmetry should occur with the same peak areas in the X'(Z Z)Y' and X'(Y'X')Y' scattering experiments and with negligible intensity in the X'(Z X')Y' scattering experiment. Since the band profile will remain unchanged, the intensity ratio of a band measured in two different scattering experiments will be related to the ratio of the peak heights. The peak heights, measured on an arbitrary scale, are listed in the vibrational frequency and intensity tables that follow. Since the full width at half height (f.w.h.h.) for each phonon mode may in principle be different, this method is not applicable to comparing the relative intensities of different phonon modes. In practice, the peak heights of bands within a spectrum will depend on how well the incoming radiation is focused onto the sample, the quality of the crystal from which the radiation is scattered, and how well the scattered radiation is focused onto the slits of the monochromator. Consequently, the optimum signal achieved will differ in different scattering experiments. Bands of E_g symmetry will have different relative

intensities in the $X'(ZZ)Y'$ and $X'(Y'X')Y'$ scattering experiments. However, the relative intensities for each band of E_g symmetry should be the same for the two scattering experiments.

Owing to imperfect alignment and inefficiencies of both polariser and analyzer, "leakage" of bands into spectra where their activity is forbidden does occur. In regions of the spectra where bands occur in close proximity to one another, the band contours were estimated fitting the spectrum to Lorentzian/Gaussian sum functions. This is illustrated in figure 2.8.1 which shows the Raman spectrum of RbVSD between 446 and 530 cm^{-1} in the $X'(ZZ)Y'$ scattering experiment. This method allows a better estimate of the wavenumber and intensity of the Raman bands to be determined.

Towards the end of completing the collection of the spectra, it was noted that the collection lens showed a small, but significant, degree of chromaticity, i.e. the focal length of the collection lens is dependent on the wavelength of scattered radiation. This means that relative intensities of the observed Raman bands are dependent on which peak in the spectrum was used to optimise the signal. This was corrected for by measuring the relative intensities of two peaks well separated in wavenumber, in a spectrum of CsGaSH, optimising on each peak in turn. The corrected intensity for all the data points in the spectra were calculated using the expression:

$$\text{Counts}_{\text{cor}} = \text{counts}_{\text{obs}}(1 + (\text{displacement of peak from position where signal optimised}/1000 \text{ cm}^{-1})) \quad 2.8.1$$

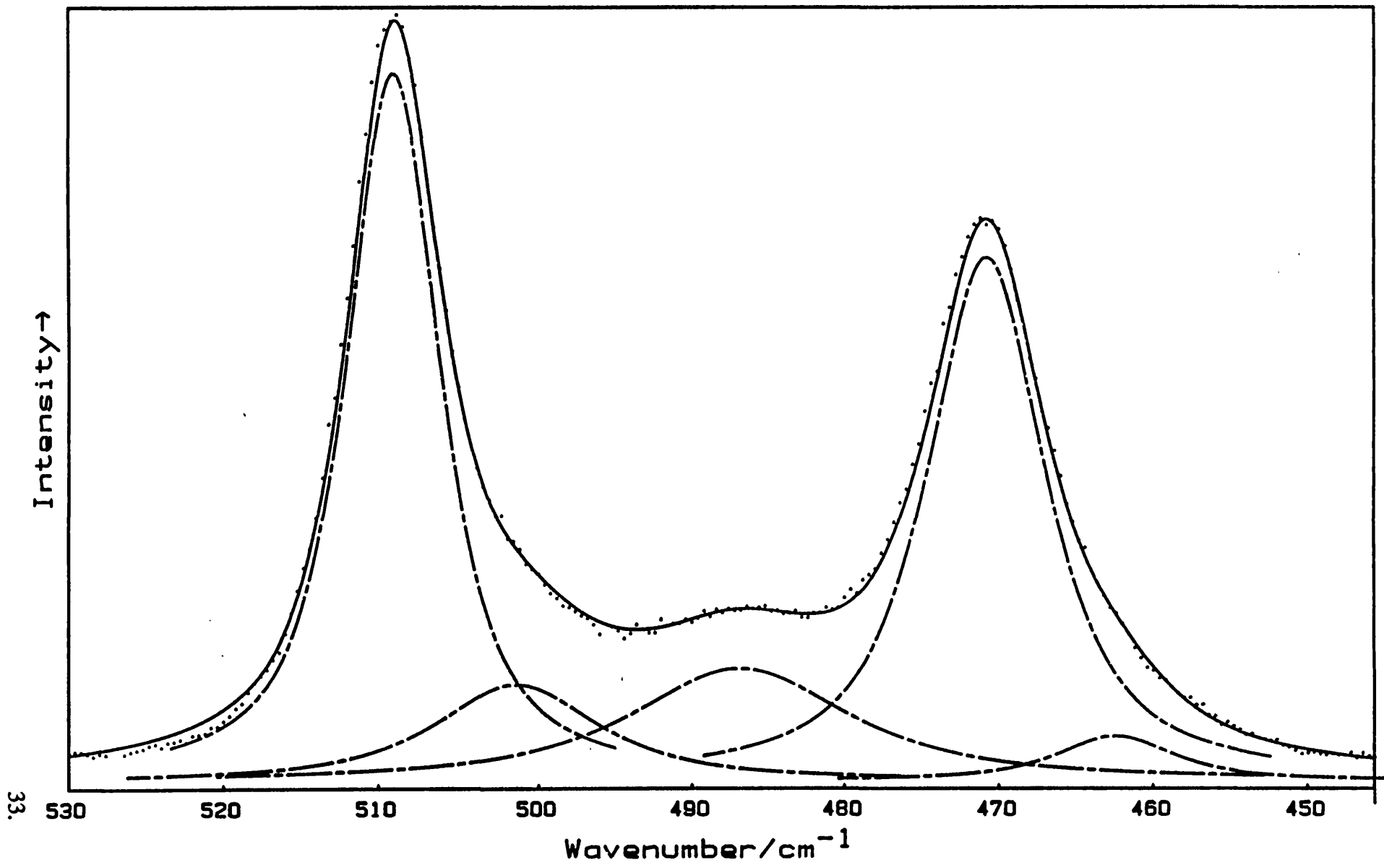
This correction proved to be adequate for a range of conditions.

Figure 2.8.1

$\nu_1\text{MO}_6$ region of $\text{RbV}(\text{SO}_4)_2 \cdot 12\text{D}_2\text{O}$ extracted from figure. 2.9.8.

Peak Positions and Parameters

PEAK POSITION	HEIGHT (0 - 100)	LORENZIAN (100)/ GAUSSIAN (0) MIX	FULL WIDTH HALF HEIGHT	SYMMETRY	ASSIGNMENT
461 cm^{-1}	6	80	9	F_2	
469 cm^{-1}	70	80	9.2	E_g	
485 cm^{-1}	15.2	80	17	A_g	
500 cm^{-1}	13	80	12.6	E_g	ρ_4
508 cm^{-1}	95	80	7.2	A_g	$\nu_1\text{VO}_6$



33.

2.9 Assignment of the Single Crystal Raman Spectra of the Rubidium alums between 275 and 1200 cm⁻¹

A) Assignment of the Spectra of RbAlSH and RbAlSD in the region 275 to 1200 cm⁻¹.

From previously published spectra of the caesium alums²⁻⁵ the vibrational modes expected to be found in the region 275 to 1200 cm⁻¹ are i) the internal modes of the trivalent hexa-aqua-cation; ii) the internal modes of sulphate; iii) the external modes of water, the rocks, wags and twists.

The group theoretical analysis predicts that $11A_g + 11E_g + 33F_g$ vibrational bands should be found for the forenamed molecular groupings. $4A_g + 11E_g + 19F_g$ bands are observed for the hydrate in this region. The difference between the expected and observed number of bands is attributed to vanishingly weak intensities in the case of the A_g and some of the F_g bands; some F_g bands are also likely to be accidentally degenerate where the factor group splitting is too small to be resolved. For the deuteriate, the spectra is greatly complicated by the presence of overtone and combination bands principally arising from the external modes of D₂O.

The key spectrum in the assignment of the internal modes is the E_g spectrum since each asymmetric normal co-ordinate is expected to have one E_g component and all E_g bands are observed. A listing of vibrational frequencies and assignments for the alums RbAlSH and RbAlSD are given in tables 2.9.1 and 2.9.2 respectively.

(i) The internal modes of $[Al(OH_2)_6]^{3+}$ and $[Al(OD_2)_6]^{3+}$

$\nu_1(AlO_6)$. One A_g and one F_g band are predicted for this mode. $\nu_1(AlO_6)$ has been assigned to a band, occurring with A_g activity, at 542 cm⁻¹ for the CsAlSH β alum; $\nu_1(AlO_6)$ for RbAlSH is expected to be found close to this value. The A_g band at 545 cm⁻¹ for RbAlSH is in close agreement with this expectation, the presence of a corresponding band at 519 cm⁻¹ for the deuteriate confirms the assignment. The ratio ν_D/ν_H is 0.95 in excellent agreement to that expected (0.949). A weak F_g band is also observed for both the hydrate and the deuteriate, coincident with the position of the A_g component in each case, and this is tentatively assigned to $\nu_1(AlO_6)$.

TABLE 2.9.1

Vibrational Frequencies and assignments for $\text{RbAl}(\text{SO}_4)_2 \cdot 12\text{H}_2\text{O}$ between 275 and 1200 cm^{-1} .

ν/cm^{-1}		$X'(Z Z)Y'$	$X'(Y'X')Y'$	$X'(Z X')Y'$	assignment
336	E_g	26	11		$\nu_5(\text{AlO}_6)$
338	F_g			94	
354	F_g			13	
440	E_g	131	57		$\nu_2(\text{SO}_4)$
441	F_g			273	
460	F_g	13	9	265	+
471	F_g			71	
473	E_g	263	113		$\nu_2(\text{AlO}_6)$
516	F_g	23	8	77	ρ_6
522	E_g	29	10		
523	F_g			145	
545	$A_g (+F_g?)$	77		11	$\nu_1(\text{AlO}_6)$
599	E_g	213	95	7	ρ_5
608	F_g	9	4	196	
615	F_g	9	4	180	
623	F_g	23	9	321	
639	$E_g (+F_g?)$	223	108	33	$\nu_4(\text{SO}_4)$
712	F_g			20	ρ_4
714	E_g	114	48		
729	F_g			9	
781	E_g	10	5		ρ_3
785	F_g			14	
789	A_g	5			
869	F_g		1	28	ρ_2
875	A_g	13			
891	E_g	16	7		
893	F_g			32	
935	F_g			2	ρ_1
940	E_g	23	17		
977	A_g	18			$\nu_1(\text{S}^{16}\text{O}_3^{18}\text{O})$
992	A_g	7368	111	173	
1087	F_g			20	$\nu_3(\text{SO}_4)$
1100	E_g	170	87		
1110	F_g			45	
1136	F_g	35	20	325	

Figure 2.9.1

Single crystal Raman spectra of $\text{RbAl}(\text{SO}_4)_2 \cdot 12\text{H}_2\text{O}$ between 275 and 1200 cm^{-1} .

Sensitivities: $X'(Z Z)Y'$ 108796 counts sec^{-1} ; $X'(Y'X')Y'$ 1821 counts sec^{-1} ;

$X'(Z X')Y'$ 4028 counts sec^{-1} (72 (1) K; step size 0.4 cm^{-1} ; spectral bandwidth

2.9 cm^{-1} at 600 cm^{-1} ; integration time: $X'(Z Z)Y'$ and $X'(Y'X')Y'$, 4 seconds; $X'(Z$

$X')Y'$ 5 seconds. 406 nm radiation, 50 mw power at sample).

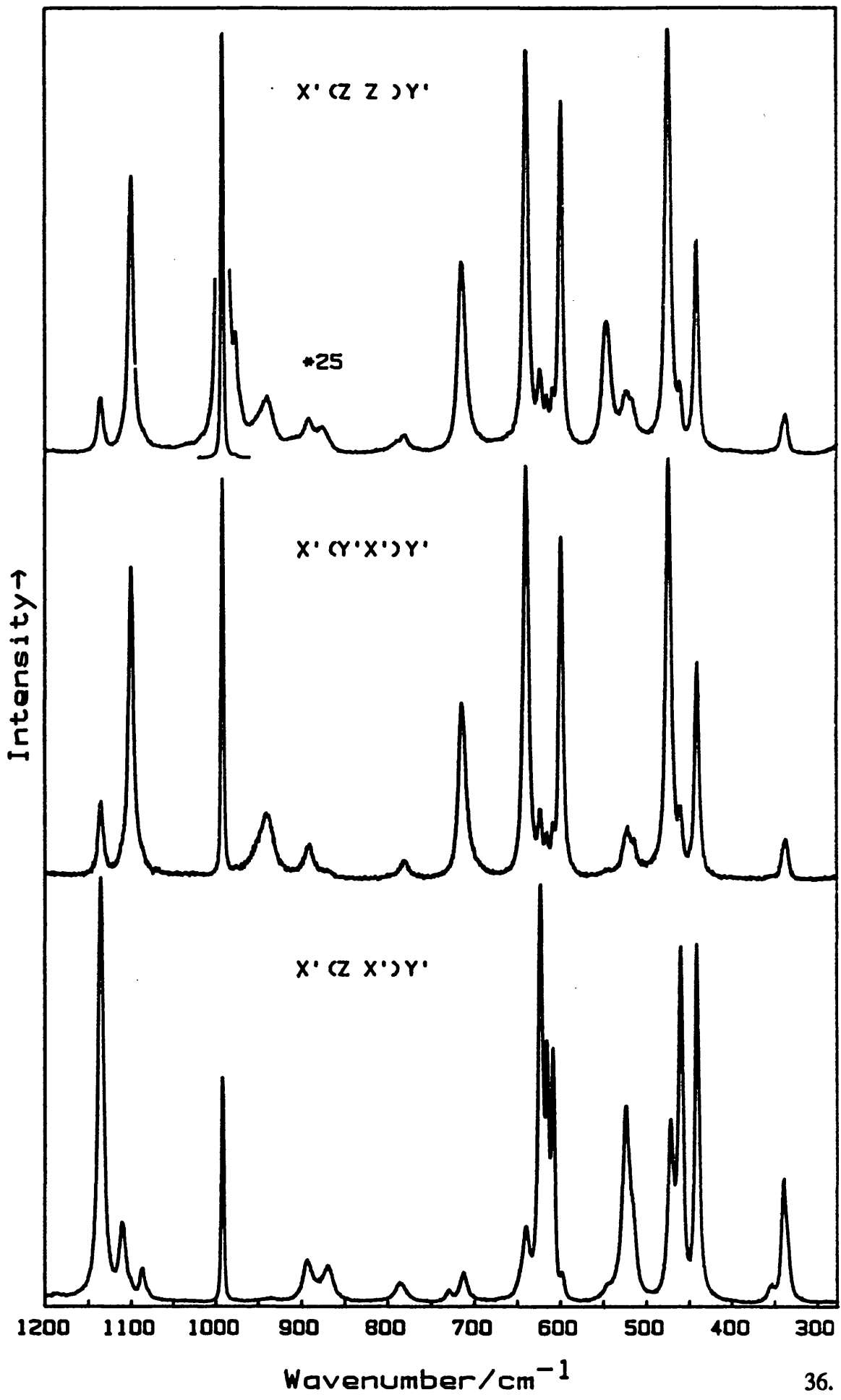


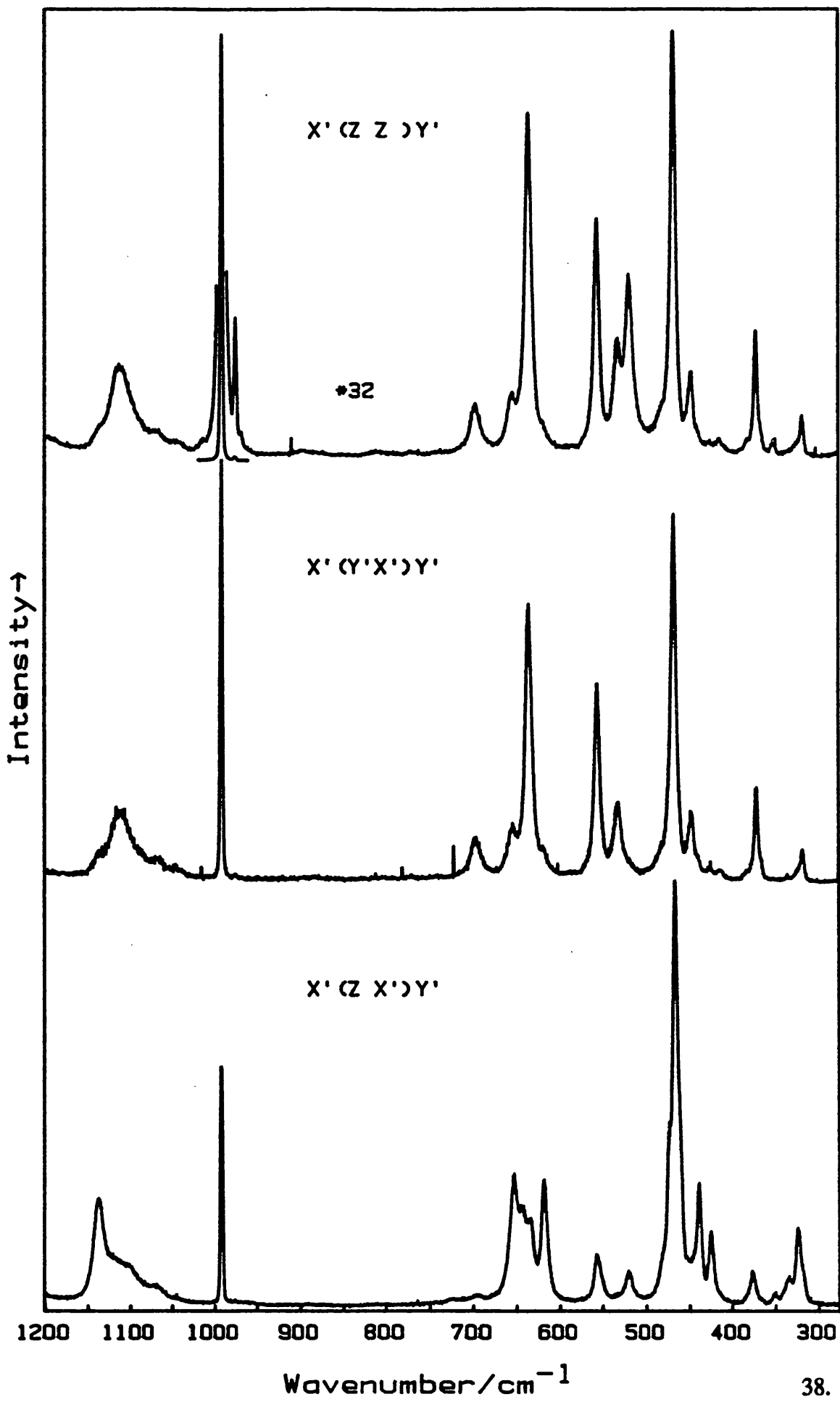
TABLE 2.9.2

Vibrational Frequencies and assignments for $\text{RbAl}(\text{SO}_4)_2 \cdot 12\text{D}_2\text{O}$ between 275 and 1200 cm^{-1} .

ν/cm^{-1}		$X'(Z Z)Y'$	$X'(Y'X')Y'$	$X'(Z X')Y'$	assignment
317	E_g	23	8		$\nu_2(\text{AlO}_4)$
323	F_g	3	3	43	
325	E_g	5	6		?
334	F_g			16	
350	F_g			6	
351	$A_g + F_g$	6			
365	E_g	11	4		
371	E_g		51	30	ρ_6
376	F_g			19	
413	E_g	6	2		
424	F_g	2	2	32	ρ_5+
438	F_g	4	1	53	
447	E_g	39	13		$\nu_2(\text{AlO}_4) +$
466	F_g			251	
467	E_g	223	91		$\nu_2(\text{SO}_4)$
473	F_g			22	
482	$E_g + F_g$	15	12	23	
519	$A_g (+F_g?)$	83		16	$\nu_1(\text{AlO}_4)$
532	E_g	45	17		ρ_4
555	E_g	115	46		ρ_3
556	F_g			28	
618	F_g	1	1	72	
636	E_g	183	67		$\nu_4(\text{SO}_4)$
636	F_g			12	
643	F_g			26	
653	F_g			76	
655	E_g	17	6		ρ_2
695	F_g			3	
697	E_g	24	9		ρ_1
724	F_g			2	
738	E_g	1	2		
743	F_g			1	
771	E_g	1	1		
808	F_g			1	
810	E_g	2	2		$\nu_{\text{D}_2\text{O}}$
875	$E_g?$	1	?	?	
891	$F_g?$			1	
897	E_g	2	2		
962	$F_g?$			1	
969	A_g	1			
976	A_g	70	2	1	$\nu_1(\text{S}^{16}\text{O}_3^{16}\text{O})$
991	A_g	7401	105	141	$\nu_1(\text{SO}_4)$
1014	A_g	2			
1044	E_g	2	2		
1045	$F_g?$			1	$\nu_2(\text{SO}_4)$
1068	E_g	3	2	?	
1069	F_g			2	+
1101	F_g			22	
1113	E_g	44	17		$\nu_{\text{D}_2\text{O}}$
1136	F_g	12	6	61	

Figure 2.9.2

Single crystal Raman spectra of $\text{RbAl}(\text{SO}_4)_2 \cdot 12\text{D}_2\text{O}$ between 275 and 1200 cm^{-1} .
Sensitivities: $X'(Z Z)Y'$ 113152 counts sec^{-1} ; $X'(Y'X')Y'$ 1628 counts sec^{-1} ;
 $X'(Z X')Y'$ 3912 counts sec^{-1} (67 (1) K; step size 0.4 cm^{-1} ; spectral bandwidth
2.9 cm^{-1} at 600 cm^{-1} ; integration time 4 seconds; 406 nm radiation, 50 mw power
at sample).



$\nu_2(\text{AlO}_6)$. Previous room temperature single crystal Raman Studies of RbAlSH ,¹⁴ assign $\nu_2(\text{SO}_4)$ at 473 cm^{-1} and $\nu_2(\text{AlO}_6)$ at *ca.* 440 cm^{-1} for E_g bands found in the hydrate. However, comparison of the low temperature spectra of RbAlSH with that of CsAlSeH^2 (also an α alum), shows the position of the band at 473 cm^{-1} to be unchanged on substitution of selenate for sulphate, suggesting that this band should not be assigned to $\nu_2(\text{SO}_4)$. The E_g band at 473 cm^{-1} along with the F_g component at 471 cm^{-1} in the hydrate are good candidates for assignment to $\nu_2(\text{AlO}_6)$. $\nu_2(\text{SO}_4)$ is also expected in this region. The E_g band at 440 cm^{-1} and the F_g band at 441 cm^{-1} are assigned to $\nu_2(\text{SO}_4)$.

$\nu_2(\text{MO}_6)$ and $\nu_2(\text{SO}_4)$ were found to be strongly coupled in the spectra of the caesium β alums. The extent of coupling of these two modes in RbAlSH is further discussed with respect to the Raman spectra of the other rubidium α alums.

The E_g component of an external mode is found at 599 cm^{-1} in the hydrate and this would be expected to occur at *ca.* 440 cm^{-1} in the deuteriate. The positions and intensities of the E_g and F_g bands found between 400 and 500 cm^{-1} in the deuteriate indicate that there is strong coupling owing to the high density of bands and ordering of the local modes is not attempted.

$\nu_3(\text{AlO}_6)$. The E_g band at 336 cm^{-1} along the F_g bands at 338 cm^{-1} and 354 cm^{-1} are assigned to $\nu_3(\text{AlO}_6)$, these bands occur at 317 cm^{-1} , 323 cm^{-1} , and 334 cm^{-1} for the deuteriate. The shifts on deuteration of 0.94 to 0.96 are what we would expect for this, the last Raman active internal mode of AlO_6 to be assigned.

(ii) The internal modes of sulphate

The intense bands occurring with A_g symmetry at 992 cm^{-1} in the hydrate, and, at 991 cm^{-1} in the deuteriate are assigned to $\nu_1(\text{SO}_4)$. A band of A_g symmetry arising from the $\nu_1(\text{S}^{16}\text{O}_3^{18}\text{O})$ mode is expected and is found at 977 and 976 cm^{-1} for the hydrate and deuteriate respectively. This band is expected to occur with intensity 0.75% of that of the $\nu_1(\text{SO}_4)$ mode. The height of the $\nu_1(\text{S}^{16}\text{O}_3^{18}\text{O})$ band cannot be measured accurately in the spectrum of the hydrate because of the extent of the wing of $\nu_1(\text{SO}_4)$. For the deuteriate, the height of $\nu_1(\text{S}^{16}\text{O}_3^{18}\text{O})$ is 0.8% of that found for $\nu_1(\text{SO}_4)$.

$\nu_2(\text{SO}_4)$ Already discussed with respect to $\nu_2(\text{AlO}_6)$.

$\nu_3(\text{SO}_4)$. For the deuteriate, the band positions for $\nu_3(\text{SO}_4)$ are coincident with bands designated as $\nu_{\text{D}_2\text{O}}$, which arise as a consequence of either overtones, bending modes or combination bands associated with D_2O . Assignments are therefore from the hydrate.

One A_g , one E_g and three F_g bands are predicted. From previous vibrational studies¹⁻⁵ $\nu_3(\text{SO}_4)$ is expected in the region between 1000 and 1200 cm^{-1} . An E_g component is found to lie at 1100 cm^{-1} and may be coincident with the A_g component. Three F_g components are also found occurring at 1087 cm^{-1} , 1110 cm^{-1} , and 1136 cm^{-1} , these bands are assigned as $\nu_3(\text{SO}_4)$.

$\nu_4(\text{SO}_4)$. Bands found with E_g activity at 639 cm^{-1} for the hydrate and 636 cm^{-1} for the deuteriate are assigned to this mode. F_g modes are found close by. All other remaining bands in the hydrate being accounted for as external modes of water by their shifts on deuteration. In the deuteriate, $\nu_4(\text{SO}_4)$ lies very close in position to an external mode of water; assignment of the F_g modes in this region is ambiguous.

(iii) The external modes of water (water librations)

The remaining bands in the Raman spectra occurring between 250 and 1200 cm^{-1} are due to the external modes of water, the rocks, wags, and twists, which correspond to hindered rotations around the three axes of inertia (see fig. 2.7.1).

Each of the six external modes of water has an E_g component. Since there are six E_g bands unaccounted for in the spectrum of the hydrate, the assignment is simply one to one. F_g and A_g (when observed) components are found close by. The intensities and positions of external modes in the deuteriate occurring in the 300 - 500 cm^{-1} spectral region are greatly affected by coupling owing to high density of bands arising from different modes.

The six external modes are labelled ρ_1 - ρ_6 in order of decreasing wavenumber. Examination of the X-ray^{6,15,16} and neutron diffraction¹⁷⁻²⁰ structures of the alums show that the hydrogen bonds extending out from the water co-ordinated to metal(III) are the strongest in the lattice. ρ_1 - ρ_3 are therefore likely to be associated with water molecules co-ordinated to the trivalent cation and ρ_4 - ρ_6 with water molecules co-ordinated to the monovalent cation.

An examination of the sensitivity of the external modes to deuteration, the

metal-ligand bond length the stereochemistry of water co-ordination and also the relative intensities of the external modes in the infrared and Raman spectra, has led to an assignment of the external modes of water co-ordinated to the trivalent cation.⁵ ρ_1 is assigned as the rocking motion, ρ_2 to the twisting motion and ρ_3 as the wagging motion. The assignments are very tentative however and no attempt has been made to order the external modes of the monovalent cation. The water molecules lie on sites of C_1 symmetry. Model calculations predict that in the absence of symmetry restrictions, a mixture of the wagging and twisting rotary motions is likely to occur.²¹ In view of this, the nomenclature ρ_1 - ρ_6 is retained here.

B) Assignment of RbInSH, RbGaSH, RbFeSH, and RbCrSH between 275 and 1200 cm^{-1} .

In broad terms the assignments of these rubidium α alums follow from the assignment of RbAlSH and are given in tables 2.9.3 - 2.9.6.

(i) The internal modes of $[M(\text{OH}_2)_6]^{3+}$

$\nu_1(\text{MO}_6)$. Strong A_g bands found at 500, 538, 526 and 540 cm^{-1} for the indium, gallium, iron and chromium alums, are assigned as $\nu_1(\text{MO}_6)$ respectively. The A_g bands are all found well away from other E_g modes and are consistent with the values of $\nu_1(\text{MO}_6)$ found for the caesium β alums.³

$\nu_2(\text{MO}_6)$ and $\nu_2(\text{SO}_4)$. With the exception of $\nu_2(\text{SO}_4)$, there is insignificant change in the position of the bands which are associated with the internal modes of sulphate for RbInSH, RbFeSH, RbGaSH, and RbCrSH. The wavenumber of $\nu_2(\text{SO}_4)$, however, is dependent on the trivalent cation, indicative of strong coupling effects. The spectra of RbCrSH is markedly different from the other rubidium sulphate α alums in this region. $\nu_2(\text{CrO}_6)$ is found at 503 cm^{-1} , much higher than for the other rubidium α alums. $\nu_2(\text{SO}_4)$ is found at 447 cm^{-1} . Since $\nu_2(\text{CrO}_6)$ is far removed from $\nu_2(\text{SO}_4)$, an estimate of the uncoupled wavenumber of $\nu_2(\text{SO}_4)$ can be estimated from the spectrum of RbCrSH where the coupling is assumed to be minimal. Uncoupled

TABLE 2.9.3

Vibrational Frequencies and assignments for $\text{RbIn}(\text{SO}_4)_2 \cdot 12\text{H}_2\text{O}$ between 275 and 1200 cm^{-1} .

ν/cm^{-1}		$X'(Z Z)Y'$	$X'(Y'X')Y'$	$X'(Z X')Y'$	assignment
294	$F_g + E_g$	23	21	109	$\nu_5(\text{InO}_6)$
305	$(A_g \text{ or } E_g)$	23	Sh?		
318	F_g			25	
352	$E_g ?$		17		
424	F_g			94	$\nu_2(\text{SO}_4)$
426	E_g	35	27		
457	F_g			185	+
461	F_g			173	
464	E_g	151	107		$\nu_2(\text{InO}_6)$
474	A_g	Sh			
494	F_g			68	
500	A_g	345	28		$\nu_1(\text{InO}_6)$
529	F_g		18	59	ρ_6
585	E_g	84	61		ρ_5
609	F_g		38	196	
612	F_g		38	164	
625	E_g	209	152	4	$\nu_4(\text{SO}_4)$
636	F_g			32	
691	F_g			28	
701	E_g	85	59		ρ_4
728	$E_g ?$		22		
775	E_g	25	21		ρ_3
779	F_g			21	
864	$F_g (+E_g)$		22	26	ρ_2
893	F_g			30	
894	E_g	38	28		
923	E_g	49	34		ρ_1
976	A_g	79			$\nu_1(\text{S}^{16}\text{O}_3^{18}\text{O})$
992	A_g	4439	214	116	
1086	F_g			32	$\nu_3(\text{SO}_4)$
1098	E_g	95	70		
1107	F_g			76	
1132	F_g	29	35	256	

Figure 2.9.3

Single crystal Raman spectra of $\text{RbIn}(\text{SO}_4)_2 \cdot 12\text{H}_2\text{O}$ between 275 and 1200 cm^{-1} .

Sensitivities: $X'(Z Z)Y'$ 110578 counts sec^{-1} ; $X'(Y'X')Y'$ 5030 counts sec^{-1} ;

$X'(Z X')Y'$ 6624 counts sec^{-1} (87 (3) K; step size 0.4 cm^{-1} ; integration time 4 seconds; 514 nm radiation, 30 mw power at sample).

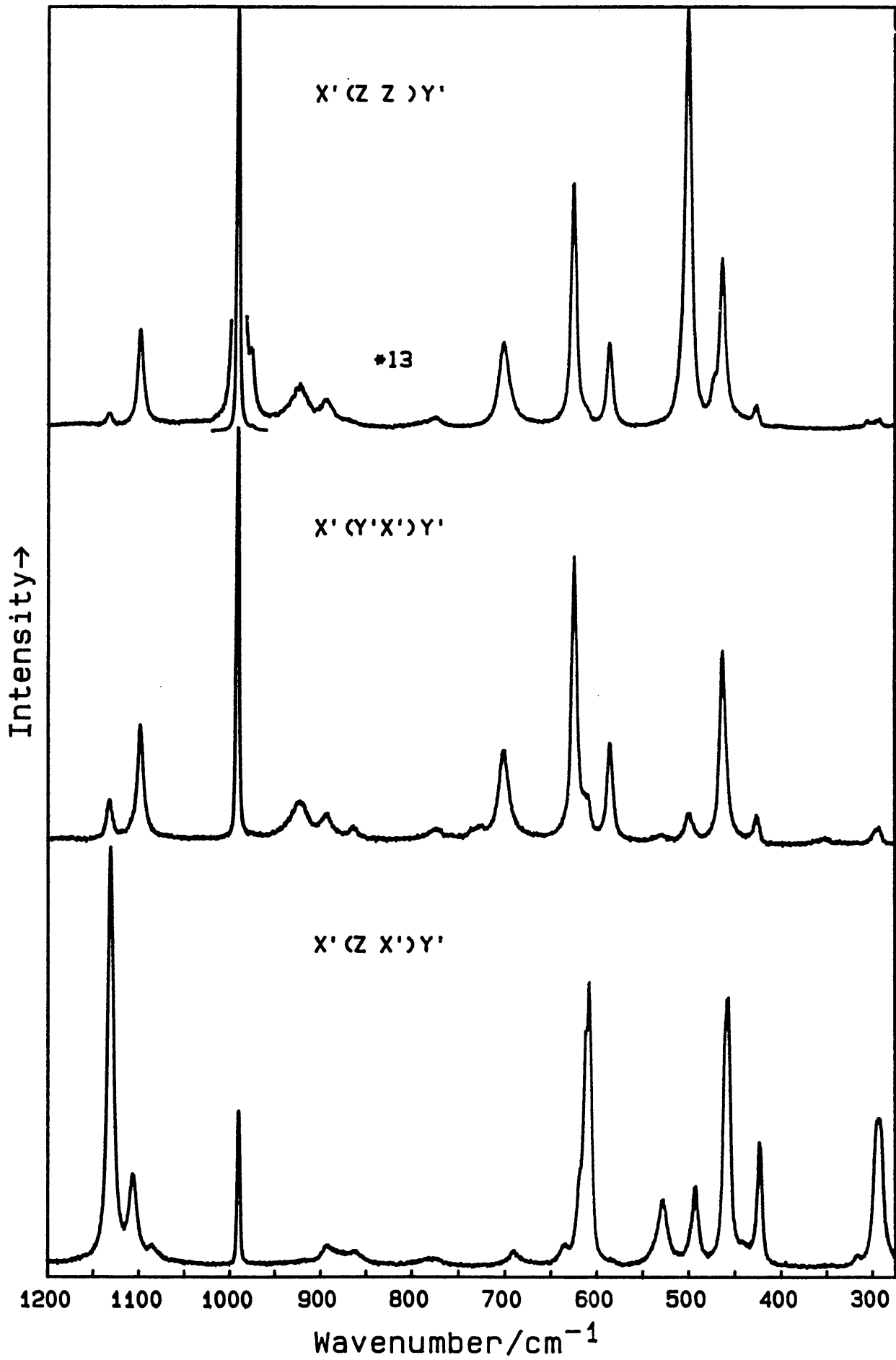


TABLE 2.9.4

Vibrational Frequencies and assignments for $\text{RbGa}(\text{SO}_4)_2 \cdot 12\text{H}_2\text{O}$ between 275 and 1200 cm^{-1} .

ν/cm^{-1}		$X'(Z Z)Y'$	$X'(Y'X')Y'$	$X'(Z X')Y'$	assignment
317	F_g			9	 $\nu_5(\text{GaO}_6)$
319	E_g	7	6		
326	$A_g ?$	8			
320	F_g			7	
338	F_g			9	
432	E_g	45	41		 $\nu_2(\text{SO}_4)$ + $\nu_2(\text{GaO}_6)$
432	F_g			67	
450	F_g			4	
461	F_g			108	
465	E_g	146	123		
465	F_g			80	
519	E_g	23	11		 ρ_6
517	F_g			29	
522	F_g			41	
538	$A_g (+F_g?)$	311	8	13	$\nu_1(\text{GaO}_6)$
594	E_g	186	155	5	ρ_5
604	F_g	2	1	14	
617	F_g	38	35	182	
632	$F_g?$			10	
633	E_g	267	221		$\nu_4(\text{SO}_4)$
645	F_g			3	 ρ_4
704	F_g			7	
708	E_g	131	98		
776	E_g	6	6		 ρ_3
777	F_g			3	
866	F_g		1	9	 ρ_2
872	A_g	7			
887	F_g			3	
898	E_g	26	22		
898	F_g			13	
933	E_g	30	29		ρ_1
977	A_g	47		1	$\nu_1(\text{S}^{16}\text{O}_3^{18}\text{O})$
993	A_g	13095	280	260	
1020	A_g			2	?
1087	F_g			9	 $\nu_3(\text{SO}_4)$
1100	E_g	153	118		
1109	F_g			24	
1123	RL	11	22	15	
1135	F_g	31	39	168	

Figure 2.9.4

Single crystal Raman spectra of $\text{RbGa}(\text{SO}_4)_2 \cdot 12\text{H}_2\text{O}$ between 275 and 1200 cm^{-1} .
Sensitivities: $X'(Z Z)Y'$ 260761 counts sec^{-1} ; $X'(Y'X')Y'$ 5814 counts sec^{-1} ;
 $X'(Z X')Y'$ 5282 counts sec^{-1} (63 (2) K; step size 0.4 cm^{-1} ; spectral bandwidth
1.7 cm^{-1} at 600 cm^{-1} ; integration time 3 seconds; 514 nm radiation, 80 mw power
at sample).

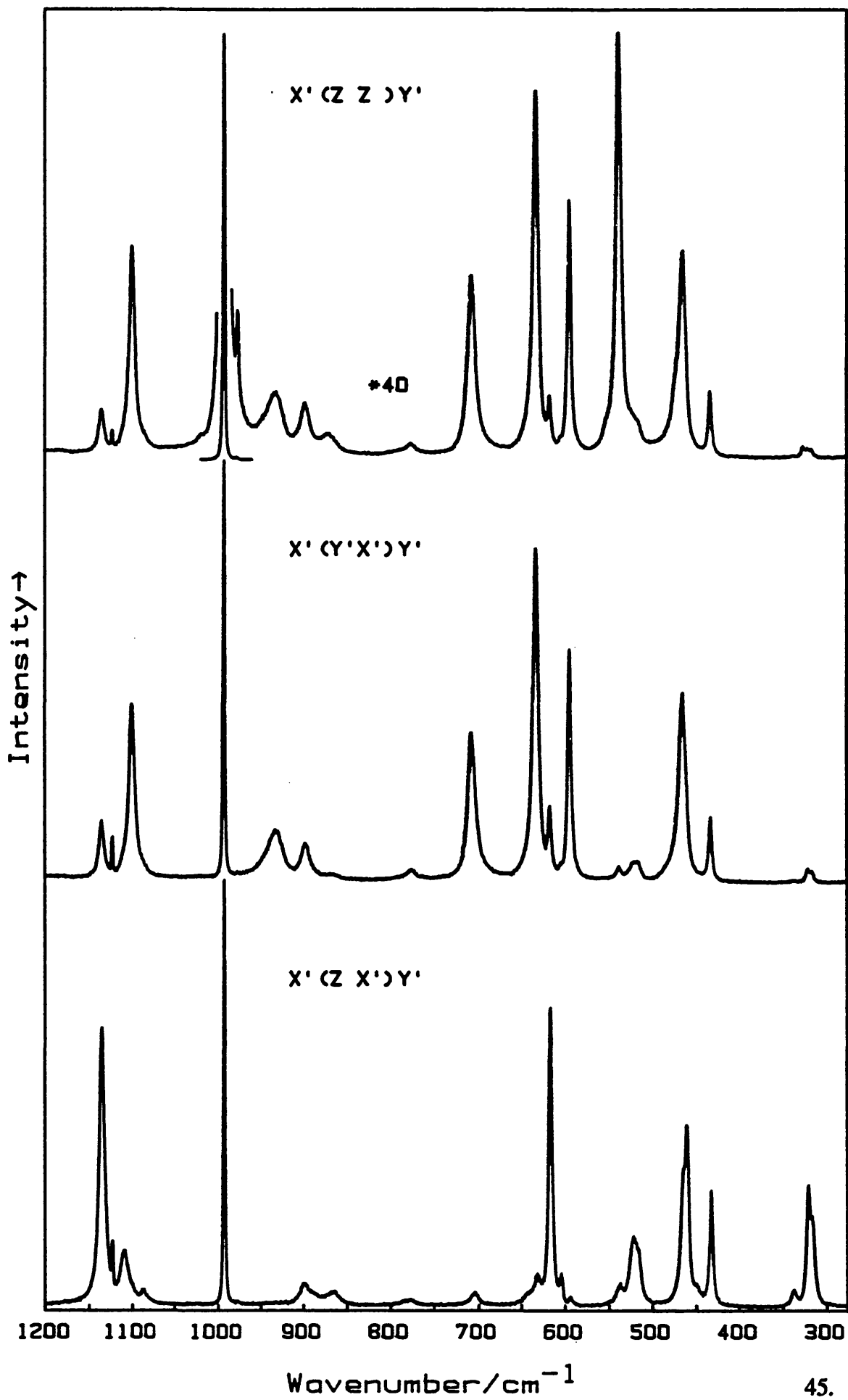


TABLE 2.9.5

Vibrational Frequencies and assignments for $\text{RbFe}(\text{SO}_4)_2 \cdot 12\text{H}_2\text{O}$ between 275 and 1200 cm^{-1} .

ν/cm^{-1}		$X'(Z Z)Y'$	$X'(Y'X')Y'$	$X'(Z X')Y'$	assignment
304	F_g			251	$\nu_5(\text{FeO}_6)$
305	E_g	46	59		
310	F_g		8	233	
316	A_g	18			
330	F_g	2	3	16	
435	E_g	50	46		$\nu_2(\text{SO}_4)$ + $\nu_2(\text{FeO}_6)$
435	F_g			139	
460	F_g	10	16	214	
470	E_g	138	121	16	
515	E_g ?	?	13		ρ_6
515	F_g			53	
526	A_g	1121	43		$\nu_1(\text{FeO}_6)$
530	F_g			49	
594	E_g	387	338	17	ρ_5
604	F_g			40	
616	F_g	40	53	290	
632	E_g	434	389	38	$\nu_4(\text{SO}_4)$
641	F_g			15	
701	F_g			15	ρ_4
705	E_g	155	84		
780	E_g	14	10		ρ_3
783	F_g			17	
855	F_g		2	26	ρ_2
862	A_g	14			
879	E_g	17	11		
880	F_g			29	
930	E_g	17	17	?	ρ_1
941	A_g	10			
976	A_g	43	1	1	$\nu_1(\text{S}^{16}\text{O}_3^{18}\text{O})$
991	A_g	14488	387	142	$\nu_1(\text{SO}_4)$
1083	F_g			13	$\nu_3(\text{SO}_4)$
1096	E_g	170	106		
1106	F_g	37	29	220	
1132	F_g	57	56	652	

Figure 2.9.5

Single crystal Raman spectra of $\text{RbFe}(\text{SO}_4)_2 \cdot 12\text{H}_2\text{O}$ between 275 and 1200 cm^{-1} .
Sensitivities: $X'(Z Z)Y'$ 222380 counts sec^{-1} ; $X'(Y'X')Y'$ 7954 counts sec^{-1} ;
 $X'(Z X')Y'$ 11446 counts sec^{-1} (72 (2) K; step size 0.4 cm^{-1} ; spectral bandwidth
1.92 cm^{-1} at 600 cm^{-1} ; integration time 4 seconds; 488 nm radiation, 80 mw power
at sample).

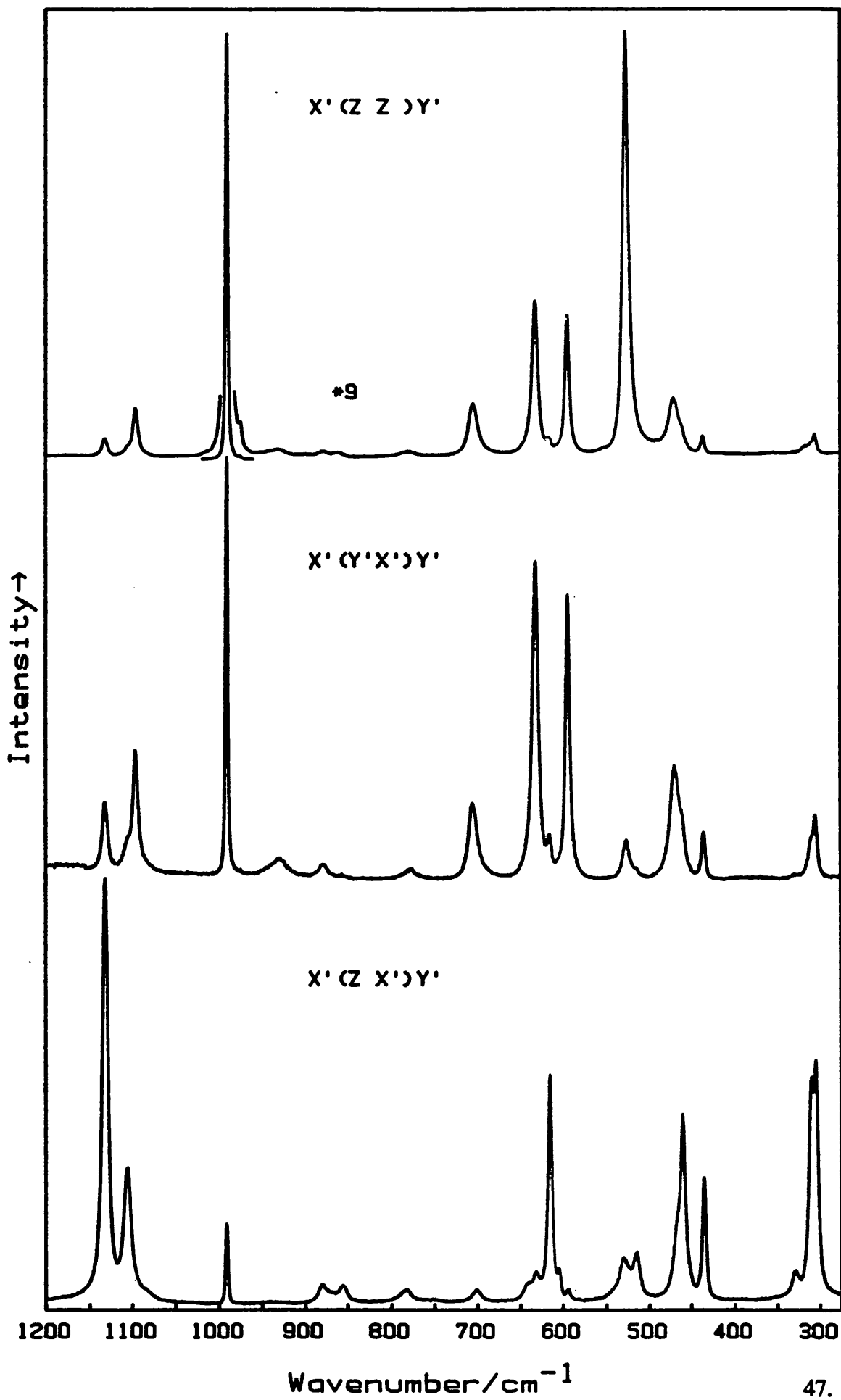


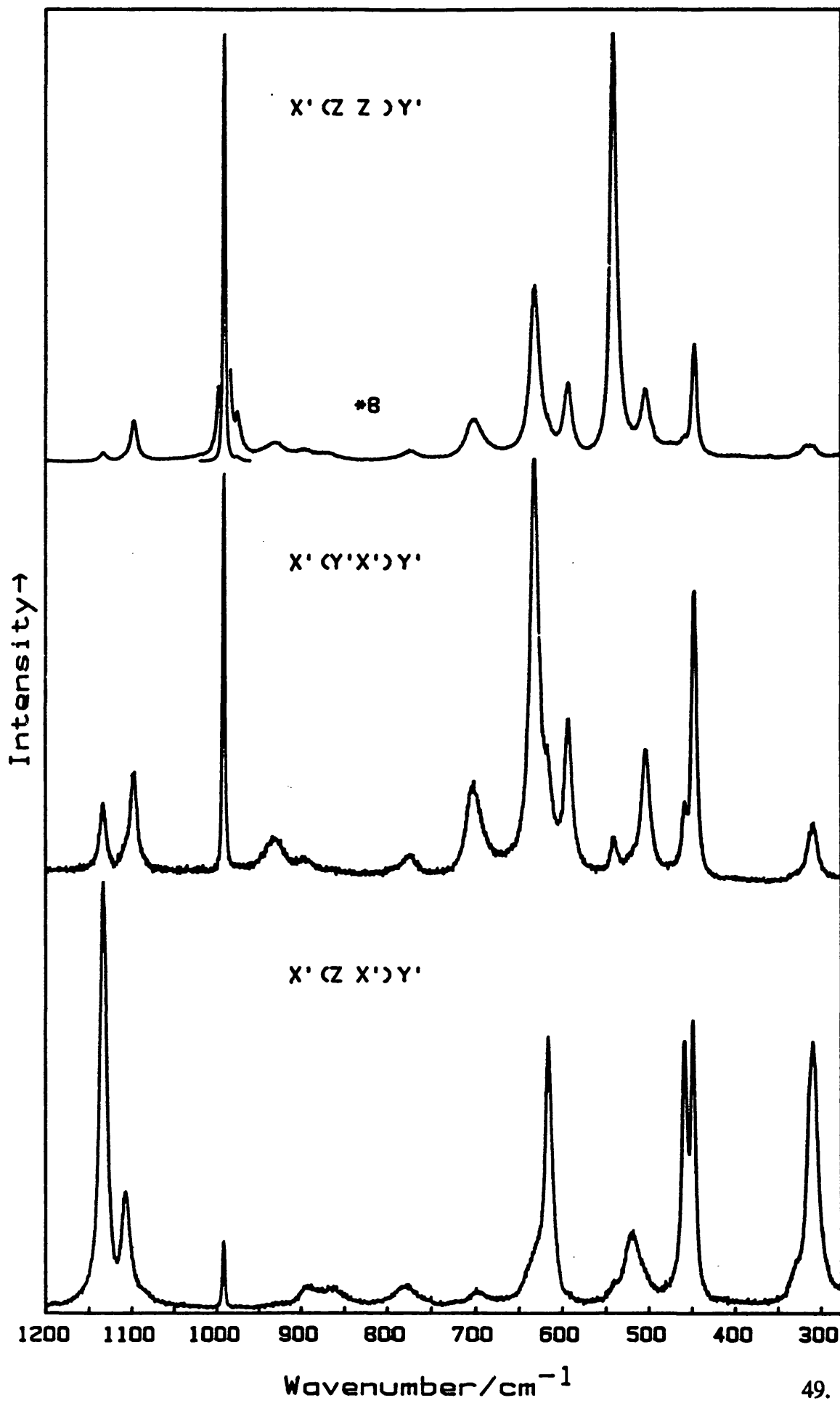
TABLE 2.9.6

Vibrational Frequencies and assignments for $\text{RbCr}(\text{SO}_4)_2 \cdot 12\text{H}_2\text{O}$ between 275 and 1200 cm^{-1} .

ν/cm^{-1}		$X'(Z Z)Y'$	$X'(Y'X')Y'$	$X'(Z X')Y'$	assignment
308	E_g	13	14		$\nu_3(\text{CrO}_6)$
309	F_g			81	
312	F_g			65	
316	A_g	13			
330	F_g	2	2	13	
447	E_g	123	74		$\nu_2(\text{SO}_4)$
449	F_g			91	
458	F_g	15	18	83	
503	E_g	52	31		$\nu_2(\text{CrO}_6)$
520	F_g		sh	20	ρ_6
540	A_g	165	21	6	$\nu_1(\text{CrO}_6)$
592	E_g	78	44		ρ_5
616	F_g	13	31	87	
631	E_g	191	117	16	$\nu_4(\text{SO}_4)$
698	F_g			4	ρ_4
701	E_g	42	24		
726	F_g			1	
753	F_g			2	ρ_3
774	E_g	10	5		
780	F_g			6	
864	F_g			4	ρ_2
872	A_g	6			
893	F_g			5	
896	E_g	8	3		
929	F_g			1	ρ_1
932	E_g	13	8		
976	A_g	21	2	1	$\nu_1(\text{S}^{16}\text{O}_3^{18}\text{O})$
992	A_g	3977	115	22	$\nu_1(\text{SO}_4)$
1082	F_g		2	5	$\nu_3(\text{SO}_4)$
1098	E_g	46	27		
1107	F_g			38	
1133	F_g	9	20	139	

Figure 2.9.6

Single crystal Raman spectra of $\text{RbCr}(\text{SO}_4)_2 \cdot 12\text{H}_2\text{O}$ between 275 and 1200 cm^{-1} .
Sensitivities: $X'(Z Z)Y'$ 61307 counts sec^{-1} ; $X'(Y'X')Y'$ 1871 counts sec^{-1} ;
 $X'(Z X')Y'$ 2155 counts sec^{-1} (100 (10) K; step size 0.4 cm^{-1} ; spectral bandwidth
2.7 cm^{-1} at 600 cm^{-1} ; integration time 4 seconds; 476 nm radiation, 60 mw power
at sample).



wavenumbers for the $\nu_2(\text{MO}_6)$ mode are estimated by subtracting the uncoupled $\nu_2(\text{SO}_4)$ wavenumber (447 cm^{-1}) from the sum of the E_g components of the coupled $\nu_2(\text{MO}_6)$ and $\nu_2(\text{SO}_4)$ modes. For aluminium, indium, gallium and iron, uncoupled $\nu_2(\text{MO}_6)$ wavenumbers are calculated as 466, 443, 450, and 458 cm^{-1} respectively. The corresponding values of $\nu_2(\text{MO}_6)$, calculated in the same way for the caesium β alums,³ are 464, 444, 450 and 456 cm^{-1} . The similar values suggest little change in the strength of the field immediately around the trivalent cation on change of alum type.

$\nu_3(\text{MO}_6)$. This mode is identifiable as the cluster of bands between 300 and 400 cm^{-1} . The E_g components are found at 294 cm^{-1} (In) 319 cm^{-1} (Ga), 308 cm^{-1} (Cr) and 305 cm^{-1} (Fe).

(ii) The internal modes of sulphate.

The A_g band arising from $\nu_1(\text{SO}_4)$ is found at 992 (In) 991 (Fe) 992 (Cr) and 993 (Ga). These values being close to that found for RbAlSH of 992 cm^{-1} . The form and position of $\nu_3(\text{SO}_4)$ and $\nu_4(\text{SO}_4)$ are likewise easily identified by comparison with the spectra of RbAlSH and are assigned accordingly. $\nu_2(\text{SO}_4)$ has already been discussed with $\nu_2(\text{MO}_6)$.

(iii) External modes of water.

The E_g components of the external modes are all found and are again labelled in order of decreasing wavenumber. Comparison of the external modes found for the rubidium sulphate α alums of Al, Cr, and Fe with the caesium selenate alum counterparts^{2,3} show that there is negligible change in band position for the external modes labelled ρ_1 and ρ_3 which are associated with the trivalent hexa-aqua-cation (in the caesium selenate alums, ρ_2 is strongly coupled to $\nu_3(\text{SeO}_4)$).^{2,3} The water librations are very sensitive to the structural environment, suggesting that the strength and directional order of the hydrogen bonds extending from the water co-ordinated to the metal(III) centre remain essentially unchanged from $\text{RbM}^{\text{III}}\text{SH}$ to $\text{CsM}^{\text{III}}\text{SeH}$.

(C) Assignment of $\text{RbV}(\text{SO}_4)_2 \cdot 12\text{H}_2\text{O}$ between 275 and 1200 cm^{-1}

$4A_g + 10E_g + 12F_g$ bands are found for the hydrate and $4A_g + 15E_g + 15F_g$ bands for the deuteriate.

(i) Internal modes of $[\text{V}(\text{OH}_2)_6]^{3+}$ and $[\text{V}(\text{OD}_2)_6]^{3+}$.

$\nu_1(\text{VO}_6)$. As for the α alums, the group theoretical analysis predicts that one band of A_g symmetry and one of F_g symmetry should arise from this mode. For the caesium vanadium alum, the A_g component has been assigned to a band at 525 cm^{-1} .³ The A_g bands, found at 531 cm^{-1} for RbVSH, and at 508 cm^{-1} for RbVSD, are assigned to $\nu_1(\text{VO}_6)$. The ν_D/ν_H ratio of 0.957 is higher than expected. Additionally, $\nu_1(\text{VO}_6)$ is found 6 cm^{-1} higher in RbVSH compared to CsVSH. The V-O bond distances in the CsVSH and RbVSH alums are found to be identical (1.992(6) Å in CsVSH⁶ and 1.996(3) in RbVSH¹⁵). The significant difference in the band position of $\nu_1(\text{VO}_6)$ is rather curious therefore since a good inverse relation is found between $M^{\text{III}}\text{-O}$ bond length and $\nu_1(\text{MO}_6)^{3+}$ stretching frequency.³ A possible explanation for the change in band position of $\nu_1(\text{VO}_6)$ is that this mode is found to be almost coincident with an external mode of water in the RbVSH alum. It is possible, therefore, that the position of $\nu_1(\text{VO}_6)$ may alter because of coupling effects. However, this explanation is not adequate in explaining the anomalous position of the $\nu_1(\text{VO}_6)$ mode in the spectra of the deuteriate. No F_g band is found nearby that shifts by the expected ratio on deuteration. F_g bands that are found nearby are accounted for by the external modes of water.

$\nu_2(\text{VO}_6)$. This mode, along with $\nu_2(\text{SO}_4)$, is expected between 400 and 500 cm^{-1} . An E_g band is found at 431 cm^{-1} in RbVSH. A band of E_g activity, is found at 410 cm^{-1} in the spectrum of RbVSD. The ratio ν_D/ν_H for the bands is 0.95 suggesting assignment to $\nu_2(\text{VO}_6)$. This leaves the bands at 475 cm^{-1} in the hydrate and at 470 cm^{-1} in the deuteriate for assignment to $\nu_2(\text{SO}_4)$. The change in relative intensities of the two E_g modes on deuteration suggests there is coupling of the two modes. In addition assignment of the two E_g bands to uncoupled components of $\nu_2(\text{VO}_6)$ and $\nu_2(\text{SO}_4)$ is not supported by the vibrational analysis of the Raman spectra of the caesium β alums.³ The Raman

TABLE 2.9.7

Vibrational Frequencies and assignments for $\text{RbV}(\text{SO}_4)_2 \cdot 12\text{H}_2\text{O}$,
between 275 and 1200 cm^{-1} .

ν/cm^{-1}		$X'(Z Z)Y'$	$X'(Y'X')Y'$	$X'(Z X')Y'$	assignment
306	F_g		20	114	$\nu_3(\text{VO}_6)$
311	E_g	80	73		
333	F_g	2	15	60	
431	E_g	900	656		$\nu_2(\text{SO}_4^{2-})$
434	F_g			90	
465	F_g			71	$\nu_2\text{VO}_6$
475	E_g	332	246	17	
531	A_g	443			$\nu_1(\text{VO}_6)$
533	E_g	?	53		ρ_6
535	F_g			21	
568	E_g	142	94		ρ_5
609	F_g	38	38	47	$\nu_4(\text{SO}_4)$
624	F_g			40	
626	E_g	191	144		
681	E_g	70	34		ρ_4
722	F_g			3	ρ_3
739	F_g			5	
755	E_g	253	145	3	
796	$E_g?$	1	4		
865	A_g	15			ρ_2
878	E_g	67	38		
884	F_g			2	
922	$F_g?$			1	ρ_1
958	$F_g?$			1	
961	A_g	55			
973	A_g	107			$\nu_1(\text{S}^{16}\text{O}_3^{18}\text{O})$
989	A_g	9136	169	23	$\nu_1(\text{SO}_4)$
1088	F_g			34	$\nu_3(\text{SO}_4)$
1092	E_g	118	78		
1101	F_g			9	

Figure 2.9.7

Single crystal Raman spectra of $\text{RbV}(\text{SO}_4)_2 \cdot 12\text{H}_2\text{O}$ between 275 and 1200 cm^{-1} .
Sensitivities: $X'(Z Z)Y'$ 141237 counts sec^{-1} ; $X'(Y'X')Y'$ 10220 counts sec^{-1} ;
 $X'(Z X')Y'$ 1840 counts sec^{-1} (79 (5) K; step size 0.4 cm^{-1} ; spectral bandwidth
2.96 cm^{-1} at 600 cm^{-1} ; integration time 4 seconds; 457 nm radiation, 50 mw power
at sample).

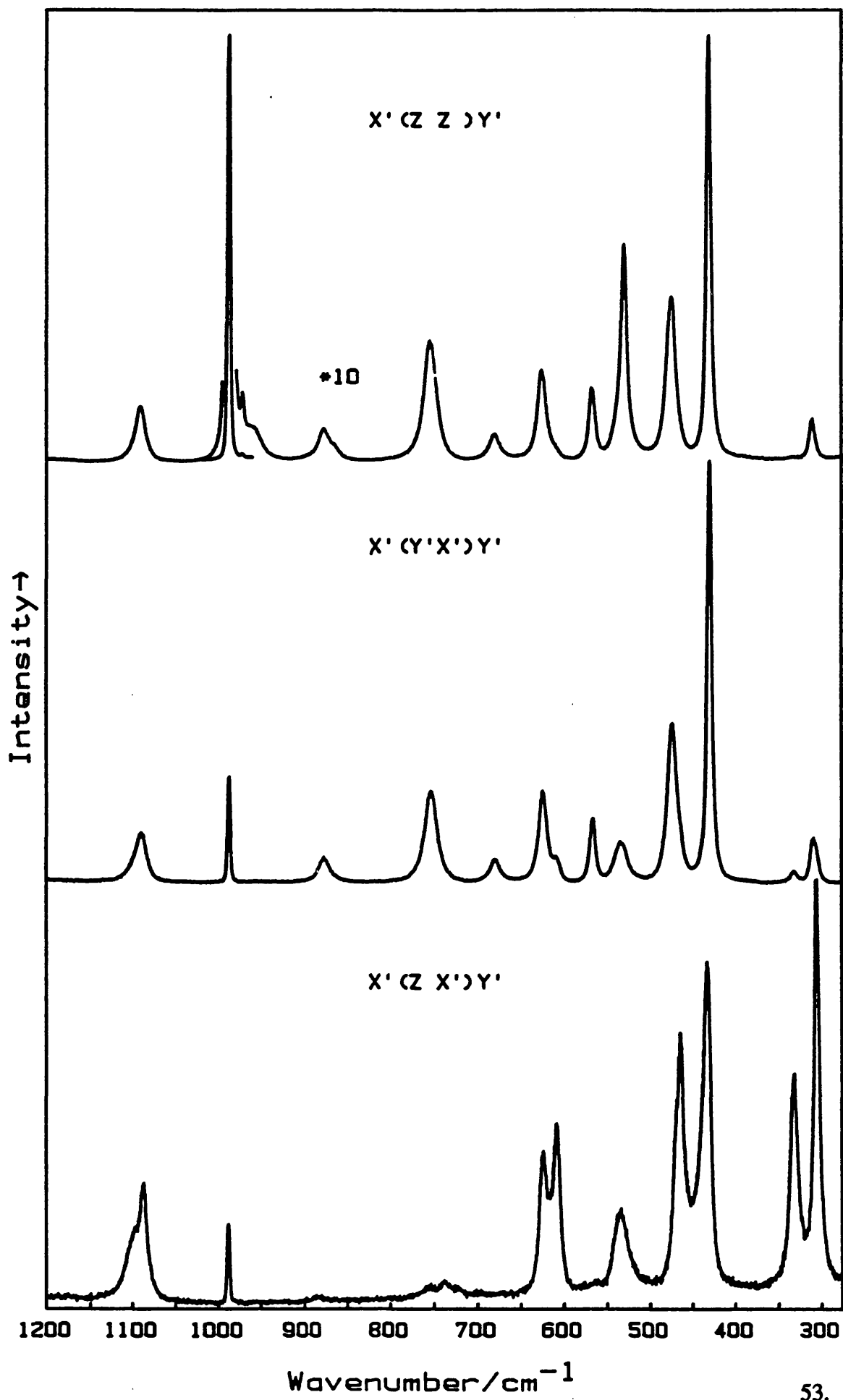


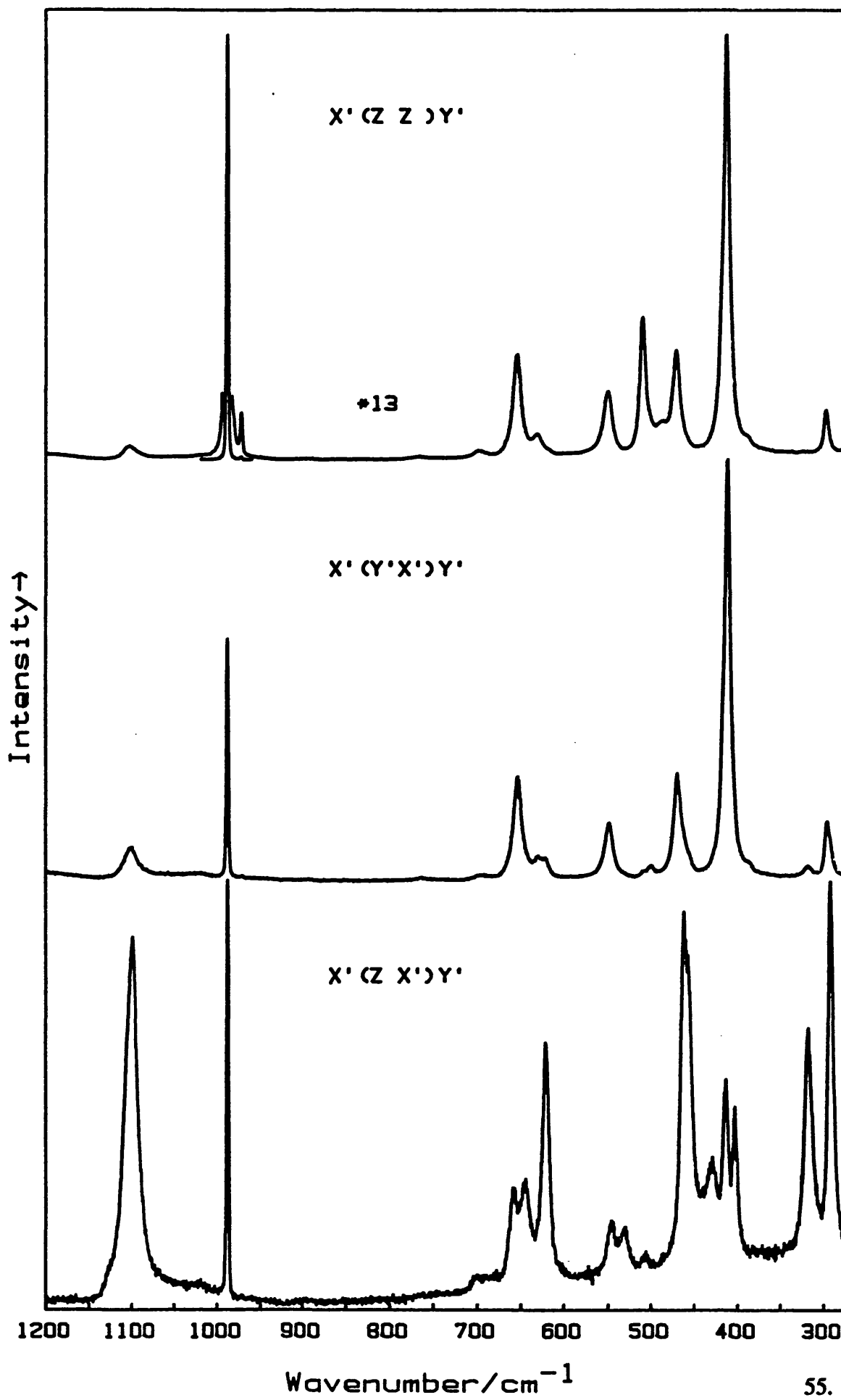
TABLE 2.9.8

Vibrational Frequencies and assignments for $\text{RbV}(\text{SO}_4)_2 \cdot 12\text{D}_2\text{O}$ between 275 and 1200 cm^{-1} .

ν/cm^{-1}		$X'(Z Z)Y'$	$X'(Y'X')Y'$	$X'(Z X')Y'$	assignment
292	F_g		33	91	$\nu_5(\text{VO}_6)$
295	E_g	95	70		
318	F_g	2	12	55	
387	E_g	31	13		ρ_6
403	F_g			37	
410	E_g	946	500		$\nu_2(\text{SO}_4^{2-})$
416	E_g	sh	sh		
413	F_g			44	ρ_5
456	F_g			30	
462	F_g		37	86	$\nu_2\text{VO}_6$
469	E_g	231	125		
485	A_g	55			ρ_4
500	E_g	42	14		
507	$F_g?$			3	
508	A_g	306	9		$\nu_1(\text{VO}_6)$
531	F_g			10	ρ_3
546	F_g			13	
548	E_g	136	65		
621	F_g		6	59	ρ_2
630	E_g	50	28		
646	F_g			24	$\nu_4(\text{SO}_4)$
653	E_g	235	123		
658	F_g			23	
682	$F_g?$			1	ρ_1
694	E_g	?	6		
697	A_g	15			
700	F_g			3	
764	$E_g(+F_g?)$	6	3	1	
852	$E_g(+F_g?)$	1	1	1	
864	E_g	1	1		
892	E_g	2	1		
898	F_g			1	
971	A_g	93	3	1	$\nu_1(\text{S}^{16}\text{O}_3^{18}\text{O})$
988	A_g	12439	288	102	$\nu_1(\text{SO}_4)$
1020	E_g	2	3	2	
1099	F_g			88	$\nu_3(\text{SO}_4)$
1102	E_g	30	34		
1128	F_g			3	

Figure 2.9.8

Single crystal Raman spectra of $\text{RbV}(\text{SO}_4)_2 \cdot 12\text{D}_2\text{O}$ between 275 and 1200 cm^{-1} .
Sensitivities: $X'(Z Z)Y'$ 191082 counts sec^{-1} ; $X'(Y'X')Y'$ 7780 counts sec^{-1} ;
 $X'(Z X')Y'$ 1593 counts sec^{-1} (81 (6) K; step size 0.4 cm^{-1} ; spectral bandwidth
2.22 cm^{-1} at 600 cm^{-1} ; integration time 4 seconds; 457 nm radiation, 60 mw power
at sample).



spectrum of RbVSH is practically identical both in position and profile with that of CsVSH. Comparison of the spectra of CsVSH with that of CsCrSH led to an estimate of 454 cm^{-1} for $\nu_2(\text{VO}_6)$ using the method of subtracting the uncoupled $\nu_2(\text{SO}_4)$ value (obtained from the spectra of CsCrSH) from the sum of the E_g components of the coupled $\nu_2(\text{VO}_6)$ and $\nu_2(\text{SO}_4)$ modes.³ Analysis of the spectra of the caesium alums suggests, therefore, that assignment of the band found at 431 cm^{-1} in RbVSH to the uncoupled component of $\nu_2(\text{VO}_6)$ is not correct. Ordering of the $\nu_2(\text{VO}_6)$ and $\nu_2(\text{SO}_4)$ modes is not attempted.

$\nu_3(\text{VO}_6)$. $A_g + E_g + 3F_g$ bands are expected for this mode. By comparison with the spectral assignment of CsVSH,³ the E_g band at 311 cm^{-1} and the F_g bands at 306 and 333 cm^{-1} are assigned as $\nu_3(\text{VO}_6)$ for the hydrate with the bands shifting for the deuteriate to 295 cm^{-1} (E_g) and 292 and 318 cm^{-1} (F_g) ν_D/ν_H being 0.95 .

(ii) The internal modes of sulphate

$\nu_1(\text{SO}_4^{2-})$. The totally symmetric stretch is found to be very intense and occurs at 989 cm^{-1} for the hydrate and 988 cm^{-1} for the deuteriate, the difference being less than experimental error. The expected F_g component in both cases is either vanishingly weak or is coincident with the A_g component and cannot be distinguished from the leakage of the A_g component into the other polarisations.

$\nu_2(\text{SO}_4^{2-})$. The assignment of this mode has already been discussed with respect to the $\nu_2(\text{VO}_6)$ phonon mode.

$\nu_3(\text{SO}_4^{2-})$. The cluster of bands occurring at around 1100 cm^{-1} are assigned to $\nu_3(\text{SO}_4^{2-})$. The position and intensity of these bands are analogous to the bands occurring for the $\nu_3(\text{SO}_4^{2-})$ mode in the caesium β alums. The bands are assigned from the hydrate, since, in the deuteriate, overtone and combination bands, principally arising from external modes of D_2O , occur in this region. The E_g component occurs at 1092 cm^{-1} . F_g components are found at 1088 , 1101 cm^{-1} .

$\nu_4(\text{SO}_4^{2-})$. $A_g + E_g + 3F_g$ bands are expected. The only remaining E_g band which does not shift significantly on deuteration occurs at 626 cm^{-1} for the hydrate. The F_g bands at 609 and 626 cm^{-1} are also assigned to $\nu_4(\text{SO}_4^{2-})$. In the spectra of the deuteriate, an external mode is found nearby and is involved in coupling with the $\nu_4(\text{SO}_4^{2-})$ mode. The E_g band at 630 cm^{-1} and the F_g band 621 cm^{-1} are assigned as

primarily arising from this mode.

(iii) The external modes of co-ordinated water

The external modes are again not assigned specifically but are labelled ρ_1 - ρ_6 in order of decreasing wavelength. The expected shift ratio is approximately 0.73 and the corresponding bands are found in the deuteriate, with the exception of ρ_1 which is only found with A_g symmetry in the hydrate.

(D) Assignment of RbTiSH between 275 and 1200 cm^{-1}

The spectra of this alum is analogous to the spectra of CsTiSH indicating that RbTiSH is also of the β modification. As with the Raman spectra of CsTiSH, some of the phonon modes between 275 and 1200 cm^{-1} show considerable broadening, most noticeable in the external water modes. Band broadening of the external modes of water is commonly associated with dynamic disorder of the water molecules.²²⁻²⁴ The Raman spectra of RbTiSH are discussed in detail in chapter 4. The internal modes of sulphate are found close in wavenumber and with similar relative intensities to those of CsVSH. There is also little difference in the position and intensities of the internal modes of $[\text{Ti}(\text{OH}_2)_6]^{3+}$ for the caesium and the rubidium alums indicating little change in environment of the trivalent hexa-aqua-cation on change of monovalent cation.

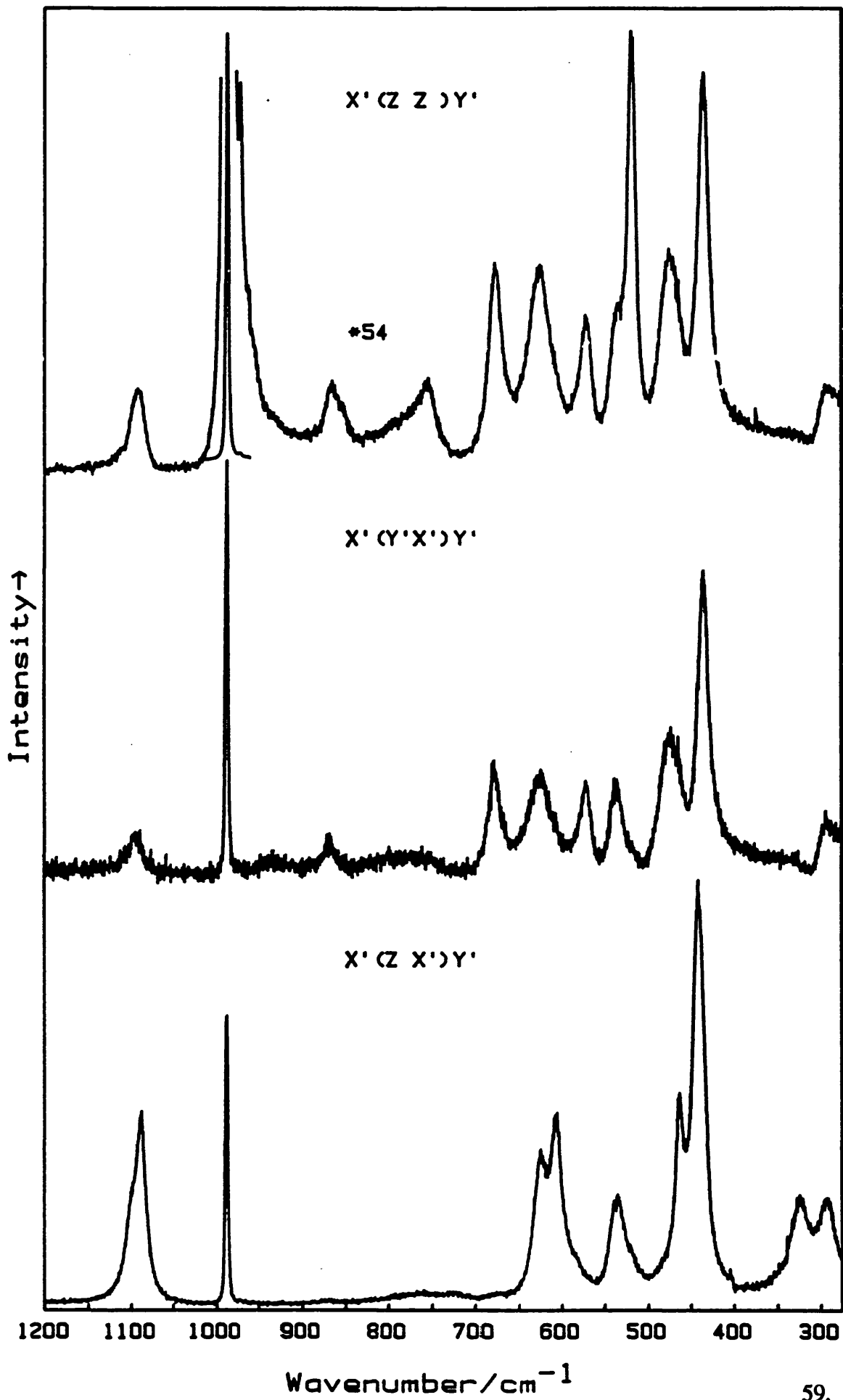
TABLE 2.9.9

Vibronic Frequencies and assignments for $\text{RbTi}(\text{SO}_4)_2 \cdot 12\text{H}_2\text{O}$,
between 275 and 1200 cm^{-1} .

ν/cm^{-1}		$X'(Z Z)Y'$	$X'(Y'X')Y'$	$X'(Z X')Y'$	assignment
292	F_g			20	$\nu_5(\text{TiO}_6)$
294	E_g	8	4		
324	F_g			21	
435	E_g	44	22		$\nu_2(\text{SO}_4^{2-})$ + $\nu_2(\text{TiO}_6)$
441	F_g			102	
463	F_g			46	
473	E_g	22	10		
518	A_g	50	3	3	$\nu_1(\text{TiO}_6)$
536	$E_g + F_g$	14	5	20	ρ_6
570	E_g	15	7		ρ_5
607	F_g			46	$\nu_4(\text{SO}_4)$
623	F_g			35	
625	E_g	21	7		
677	E_g	23	9	1	ρ_4
724	F_g			1	ρ_3
755	A_g	10	1		
763	F_g			2	
797	E_g	4	2		
854	A_g	4			ρ_2
866	E_g	7	4		
872	F_g			1	
932	E_g	1	2		ρ_1
961	A_g	2?			
988	A_g	2883	33	72	$\nu_1(\text{SO}_4)$
1092	E_g	10	4		$\nu_3(\text{SO}_4)$
1088	F_g			62	
1100	F_g			29	
1112	E_g	2	2		

Figure 2.9.9

Single crystal Raman spectra of $\text{RbTi}(\text{SO}_4)_2 \cdot 12\text{H}_2\text{O}$ between 275 and 1200 cm^{-1} .
Sensitivities: $X'(Z Z)Y'$ 88897 counts sec^{-1} ; $X'(Y'X')Y'$ 1012 counts sec^{-1} ;
 $X'(Z X')Y'$ 1647 counts sec^{-1} (90 (9) K; step size 0.4 cm^{-1} ; spectral bandwidth
2.79 cm^{-1} at 600 cm^{-1} ; integration time: $X'(Z Z)Y'$, 4 seconds; $X'(Y'X')Y'$ and $X'(Z$
 $X')Y'$ 2 seconds. 413 nm radiation, 80 mw power at sample).



2.10 Assignment of the spectra of the rubidium alums between 10 and 275 cm⁻¹

a) The sulphate rotations and translations.

The assignments of these modes are made on the following basis:

- i) The wavenumber of the bands are expected to be insensitive to deuteration of the crystal.
- ii) The low wavenumber single crystal Raman spectra of the caesium selenate α alums Al, Fe, and Cr have been recorded and assigned previously.¹ The bands arising from these modes should shift to lower wavenumber on substitution of selenate for sulphate since the selenate anion is both larger and has a greater mass than the sulphate anion.
- iii) The previously recorded single crystal Raman spectra of the caesium alums,¹ indicate that the sulphate rotations and translations occur below 100 cm⁻¹.

Both lattice modes are predicted to occur with A_g , E_g , and three F_g components. Based on the relative sizes and masses of the anions, the ratio $\nu_{SO_4^{2-}}/\nu_{SeO_4^{2-}}$ is expected to be 1.22 for the translatory mode and 1.12 for the rotary mode. For the caesium aluminium alums, two E_g bands were found below 100 cm⁻¹ at 59 and 75 cm⁻¹ for the sulphate (a β alum) and 49 and 70 cm⁻¹ for the selenate (an α alum); giving $\nu_{SO_4^{2-}}/\nu_{SeO_4^{2-}}$ ratios of 1.20 and 1.07. This being the main basis of assignment of the lower energy band to the anion translation and the higher energy band to the anion rotation. Structural differences between the α and β alums, leading to differences in the field about the anions have formed the basis of the explanation offered for the discrepancy between the calculated and the observed $\nu_{SO_4^{2-}}/\nu_{SeO_4^{2-}}$ ratios.¹

For the RbAlSH and RbAlSD alums, two E_g bands are found below 100 cm⁻¹ and occur at 51 and 76 cm⁻¹ for the hydrate and at 50 and 75 cm⁻¹ for the deuteriate. Comparison with the spectra of CsAlSeH gives ratios for $\nu_{SO_4^{2-}}/\nu_{SeO_4^{2-}}$ of 1.04 and 1.09; both alums being of the same modification. The A_g component for one of these lattice modes occurs around 38 cm⁻¹ for both CsAlSeH and RbAlSH. The other A_g component is also observed; occurring at 93 cm⁻¹ for RbAlSH and 88 cm⁻¹ for

TABLE 2.10.1

Vibrational Frequencies and assignments for $\text{RbAl}(\text{SO}_4)_2 \cdot 12\text{H}_2\text{O}$,
between 20 and 275 cm^{-1} .

ν/cm^{-1}		$X'(Z Z)Y'$	$X'(Y'X')Y'$	$X'(Z X')Y'$	assignment
37	A_g	377	5	11	 tr (SO_4^{2-}) + rot (SO_4^{2-})
51	E_g	529	250	24	
59	F_g	11	3	98	
63	F_g	17	9	157	
76	E_g	434	204	18	
82	F_g	16	5	71	
93	A_g	20		2	
103	F_g	2	1	31	
120	F_g			18	
121	E_g	410	184		rot $[\text{Rb}(\text{OH}_2)_6]^+$
139	F_g	5	1	36	
156	F_g			19	
163	F_g			267	
163	$E_g + A_g$	822	228		rot $[\text{Al}(\text{OH}_2)_6]^{3+}$
171	F_g	17	10	318	
179	F_g		6	73	
181	A_g	52			
193	$A_g + E_g$	551	20	14	$\nu_3[\text{Rb}(\text{OH}_2)_6]^+$
203	F_g	22	7	378	
223	F_g			3	
238	E_g	217	96	13	$\nu_2[\text{Rb}(\text{OH}_2)_6]^+$
246	F_g			25	
258	A_g	132		5	$\nu_1[\text{Rb}(\text{OH}_2)_6]^+$

Figure 2.10.1

Single crystal Raman spectra of $\text{RbAl}(\text{SO}_4)_2 \cdot 12\text{H}_2\text{O}$ between 15 and 300 cm^{-1} .

Sensitivities: $X'(ZZ)Y'$ 12838 counts sec^{-1} ; $X'(Y'X')Y'$ 3887 counts sec^{-1} ;

$X'(ZX')Y'$ 5977 counts sec^{-1} (72 (1) K; step size 0.4 cm^{-1} ; spectral bandwidth

3.02 cm^{-1} at 150 cm^{-1} ; integration time: $X'(ZZ)Y'$ and $X'(Y'X')Y'$, 4 seconds; $X'(Z$

$X')Y'$ 5 seconds. 406 nm radiation, 50 mw power at sample).

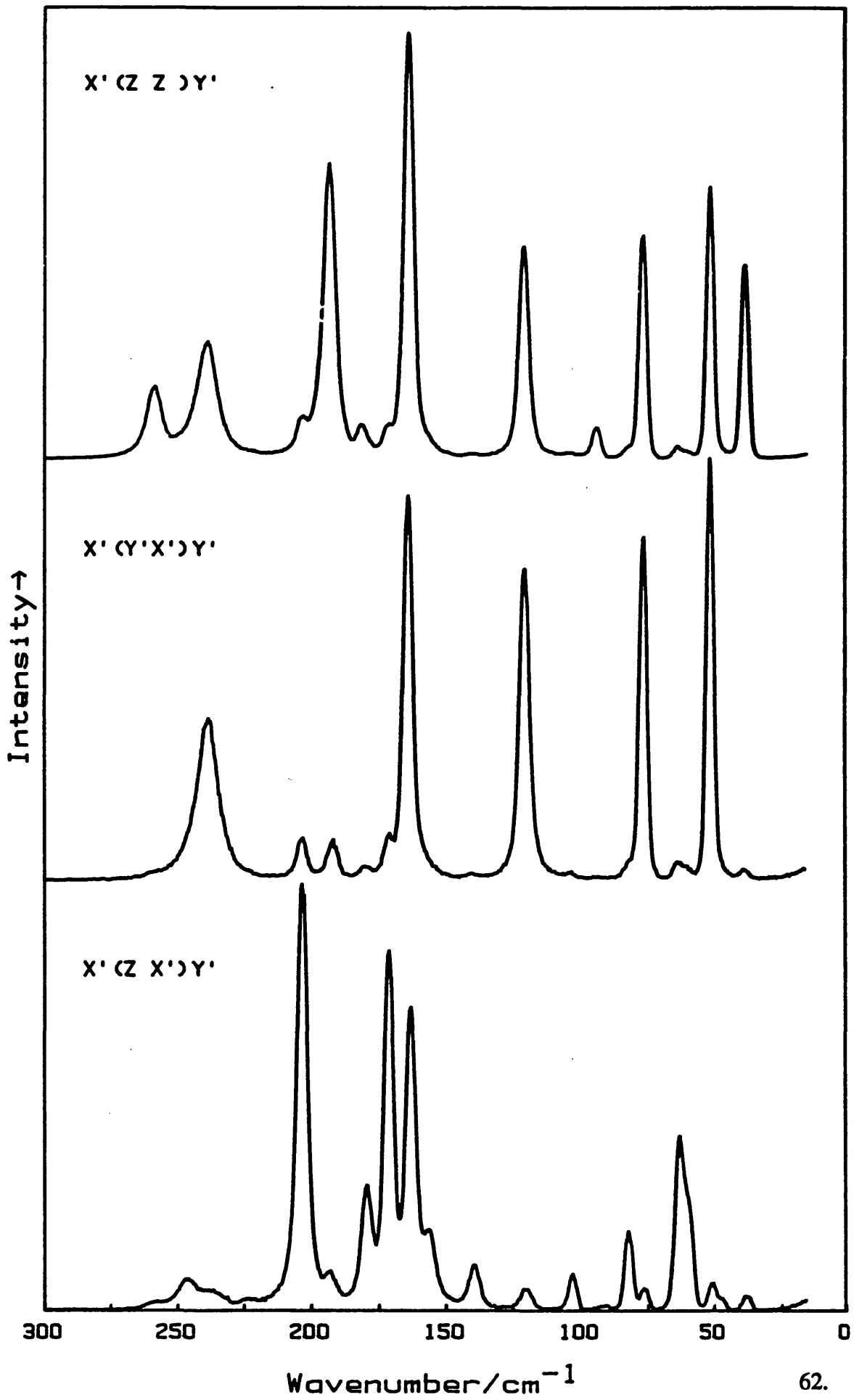


TABLE 2.10.2

Vibrational Frequencies and assignments for $\text{RbAl}(\text{SO}_4)_2 \cdot 12\text{D}_2\text{O}$, between 20 and 275 cm^{-1} .

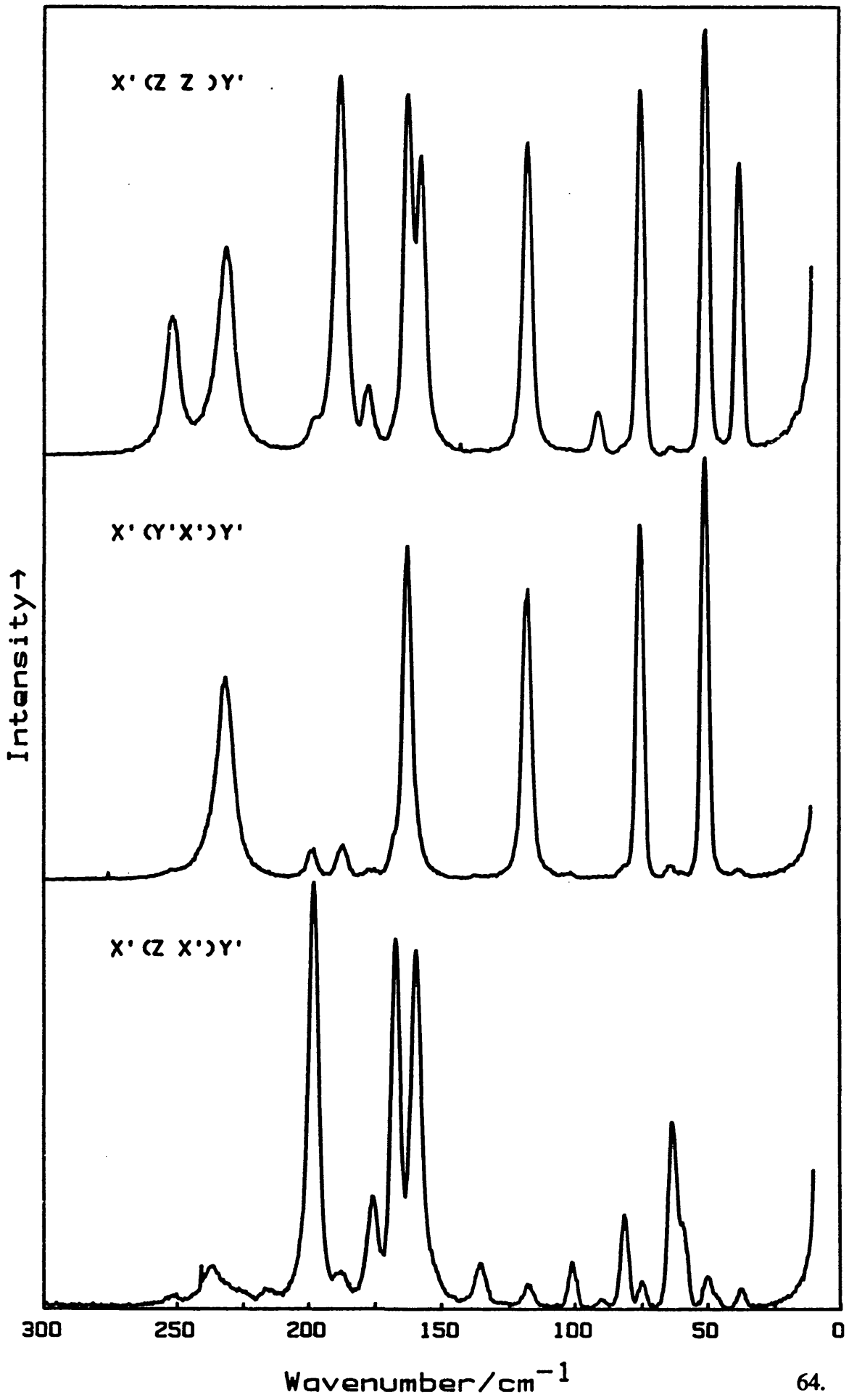
ν/cm^{-1}		$X'(Z Z)Y'$	$X'(Y'X')Y'$	$X'(Z X')Y'$	assignment
37	$A_g (+F_g?)$	300	16	7	 tr (SO_4^{2-}) + rot (SO_4^{2-})
50	E_g	384	122	15	
59	F_g	2	2	30	
63	F_g	5	3	85	
75	E_g	336	102	9	
81	F_g	7	3	42	
91	A_g	38	1	4	
101	F_g			20	
117	E_g	285	84	11	rot [$\text{Rb}(\text{OD}_2)_6$] ⁺
135	F_g			20	
157	A_g	269			
159	F_g			158	
162	E_g	323	97		rot [$\text{Al}(\text{OD}_2)_6$] ³⁺
167	F_g			163	
175	F_g		1	45	
178	A_g	44	1		
187	$A_g + E_g$	327	9	7	$\nu_3[\text{Rb}(\text{OD}_2)_6]$ ⁺
198	F_g	7	7	184	
215	F_g			3	
232	E_g	188	59	5	$\nu_2[\text{Rb}(\text{OD}_2)_6]$ ⁺
237	F_g			17	
251	A_g	126	2	3	$\nu_1[\text{Rb}(\text{OD}_2)_6]$ ⁺

Figure 2.10.2

Single crystal Raman spectra of $\text{RbAl}(\text{SO}_4)_2 \cdot 12\text{D}_2\text{O}$ between 10 and 300 cm^{-1} .

Sensitivities: $X'(Z Z)Y'$ 6027 counts sec^{-1} ; $X'(Y'X')Y'$ 1899 counts sec^{-1} ;

$X'(Z X')Y'$ 2972 counts sec^{-1} (67 (1) K; step size 0.4 cm^{-1} ; spectral bandwidth 3.02 cm^{-1} at 150 cm^{-1} ; integration time 4 seconds; 406 nm radiation, 50 mw power at sample).



CsAlSeH, giving a $\nu\text{SO}_4^{2-}/\nu\text{SeO}_4^{2-}$ ratio of 1.07. Discrepancies between calculated and observed $\nu\text{SO}_4^{2-}/\nu\text{SeO}_4^{2-}$ ratios might be because of different degrees of coupling between the lattice modes in the two alums. In the F_g spectra, where 6 bands are expected, only 3 bands can be assigned as F_g modes with certainty. The other observed bands are likely to occur through leakage of bands of A_g and E_g symmetry.

The E_g and A_g bands corresponding to the translational and rotational modes of sulphate are found in similar positions for the other rubidium α alums. The low wavenumber spectra of RbVSH is analogous to the caesium β alums in that no A_g band is present for the lowest wavenumber lattice mode as is observed for the caesium and rubidium α alums. The low wavenumber spectra of RbTiSH is discussed separately. The $\nu\text{SO}_4^{2-}/\nu\text{SeO}_4^{2-}$ ratios for the sulphate lattice modes of Al, Cr, and Fe give little indication as to the ordering of these modes and assignment is not attempted here.

b) The rotations of the trivalent and monovalent hexa-aqua-cations.

One E_g , one A_g and three bands of F_g symmetry are expected for both sets of lattice modes.

The E_g component for rot $[\text{Cs}(\text{OH}_2)_6]^+$ has been assigned for CsAlSH at 116 cm^{-1} and at 117 cm^{-1} for CsAlSeH. The rot $[\text{Al}(\text{OH}_2)_6]^{3+}$ mode is assigned at 143 and 159 cm^{-1} for the respective alums. Assignments were made on the basis of the variation of the wavenumber of these bands with unit cell size for all the CsM(III)XH alums studied.¹ This is because there will be a relationship between the size of the unit cell and the hydrogen bond strength within. The rubidium alum series is not as robust as the caesium series. Attempts to determine the unit cell of the rubidium alums by powder diffraction techniques were only partially successful. The unit cell dimension was not obtainable for the rubidium alums of Fe, Ti, and In, by powder diffraction methods. These alums, when ground to a powder, are extremely susceptible to acquiring moisture from the atmosphere.

Bands of E_g symmetry are found at 121 cm^{-1} and 163 cm^{-1} for RbAlSH and at 117 and 162 cm^{-1} for RbAlSD. Shifts on deuteration are expected to be similar for these modes. The lower wavenumber band is tentatively assigned as rot $[\text{Rb}(\text{OH}_2)_6]^+$ and the higher wavenumber band as rot $[\text{Al}(\text{OH}_2)_6]^{3+}$ corresponding assignments are

TABLE 2.10.3

Vibrational Frequencies and assignments for $\text{RbIn}(\text{SO}_4)_2 \cdot 12\text{H}_2\text{O}$, between 20 and 275 cm^{-1} .

ν/cm^{-1}		$X'(Z Z)Y'$	$X'(Y'X')Y'$	$X'(Z X')Y'$	assignment
37	A_g	117		23	 tr (SO_4^{2-}) + rot (SO_4^{2-})
47	E_g	183	127	29	
57	F_g		22	48	
63	F_g			40	
74	E_g	154	106		
77	$F_g ?$			19	
93	$A_g + F_g$	64	19	28	
103	E_g	146	101	16	rot $[\text{Rb}(\text{OH}_2)_6]^+$
110	F_g			21	
130	F_g			18	
137	A_g	86			
144	E_g	82	47	19	rot $[\text{In}(\text{OH}_2)_6]^{3+}$
155	A_g	242	20	24	
171	F_g		22	141	
178	A_g	154	2		
188	$F_g + E_g$	sh	31	201	$\nu_5[\text{Rb}(\text{OH}_2)_6]^+$
201	F_g			48	
209	E_g	168	116		$\nu_2[\text{Rb}(\text{OH}_2)_6]^+$
216	F_g			63	
245	A_g	127	3	3	$\nu_1[\text{Rb}(\text{OD}_2)_6]^+$

Figure 2.10.3

Single crystal Raman spectra of $\text{RbIn}(\text{SO}_4)_2 \cdot 12\text{H}_2\text{O}$ between 20 and 300 cm^{-1} .

Sensitivities: $X'(Z Z)Y'$ 5598 counts sec^{-1} ; $X'(Y'X')Y'$ 2861 counts sec^{-1} ;

$X'(Z X')Y'$ 4607 counts sec^{-1} (87 (3) K; step size 0.4 cm^{-1} ; integration time 4 seconds; 514 nm radiation, 30 mw power at sample).

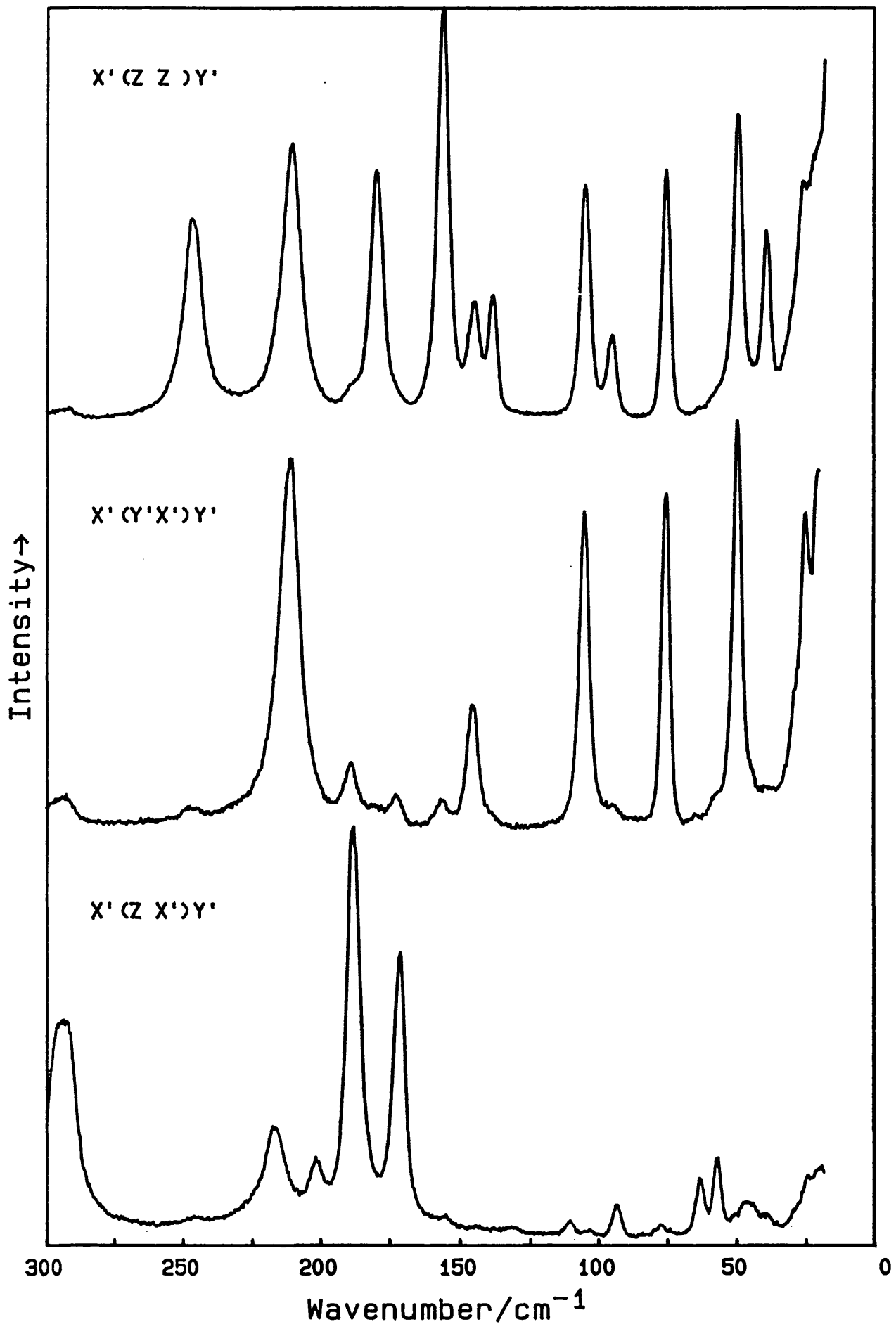


TABLE 2.10.4

Vibrational Frequencies and assignments for $\text{RbGa}(\text{SO}_4)_2 \cdot 12\text{H}_2\text{O}$,
between 20 and 275 cm^{-1} .

ν/cm^{-1}		$X'(Z Z)Y'$	$X'(Y'X')Y'$	$X'(Z X')Y'$	assignment
39	A_g	96	3	7	 tr (SO_4^{2-}) + rot (SO_4^{2-})
46	F_g			10	
49	E_g	135	174	8	
58	F_g	3	3	53	
64	F_g	3	3	39	
77	E_g	131	161	8	
81	F_g			28	
93	A_g	14	1	2	
98	F_g			10	
112	E_g	155	135		rot $[\text{Rb}(\text{OH}_2)_6]^+$
136	F_g			5	
152	F_g			16	
157	$E_g + F_g$	148	118	49	rot $[\text{Ga}(\text{OH}_2)_6]^{3+}$
162	A_g	180	3	3	
166	F_g	sh	3	43	
173	A_g	25			
176	F_g		6	74	
187	A_g	256	sh	8	
190	E_g	sh	14		$\nu_5[\text{Rb}(\text{OH}_2)_6]^+$
201	F_g	7	12	132	
206	F_g			38	
224	F_g			8	
229	E_g	127	100		$\nu_2[\text{Rb}(\text{OH}_2)_6]^+$
235	F_g			30	
256	A_g	102	4	3	$\nu_1[\text{Rb}(\text{OH}_2)_6]^+$

Figure 2.10.4

Single crystal Raman spectra of $\text{RbGa}(\text{SO}_4)_2 \cdot 12\text{H}_2\text{O}$ between 10 and 300 cm^{-1} .
Sensitivities: $X'(Z Z)Y'$ 5297 counts sec^{-1} ; $X'(Y'X')Y'$ 3558 counts sec^{-1} ;
 $X'(Z X')Y'$ 2774 counts sec^{-1} (63 (2) K; step size 0.4 cm^{-1} ; spectral bandwidth
1.79 cm^{-1} at 150 cm^{-1} ; integration time 3 seconds; 514 nm radiation, 80 mw power
at sample).

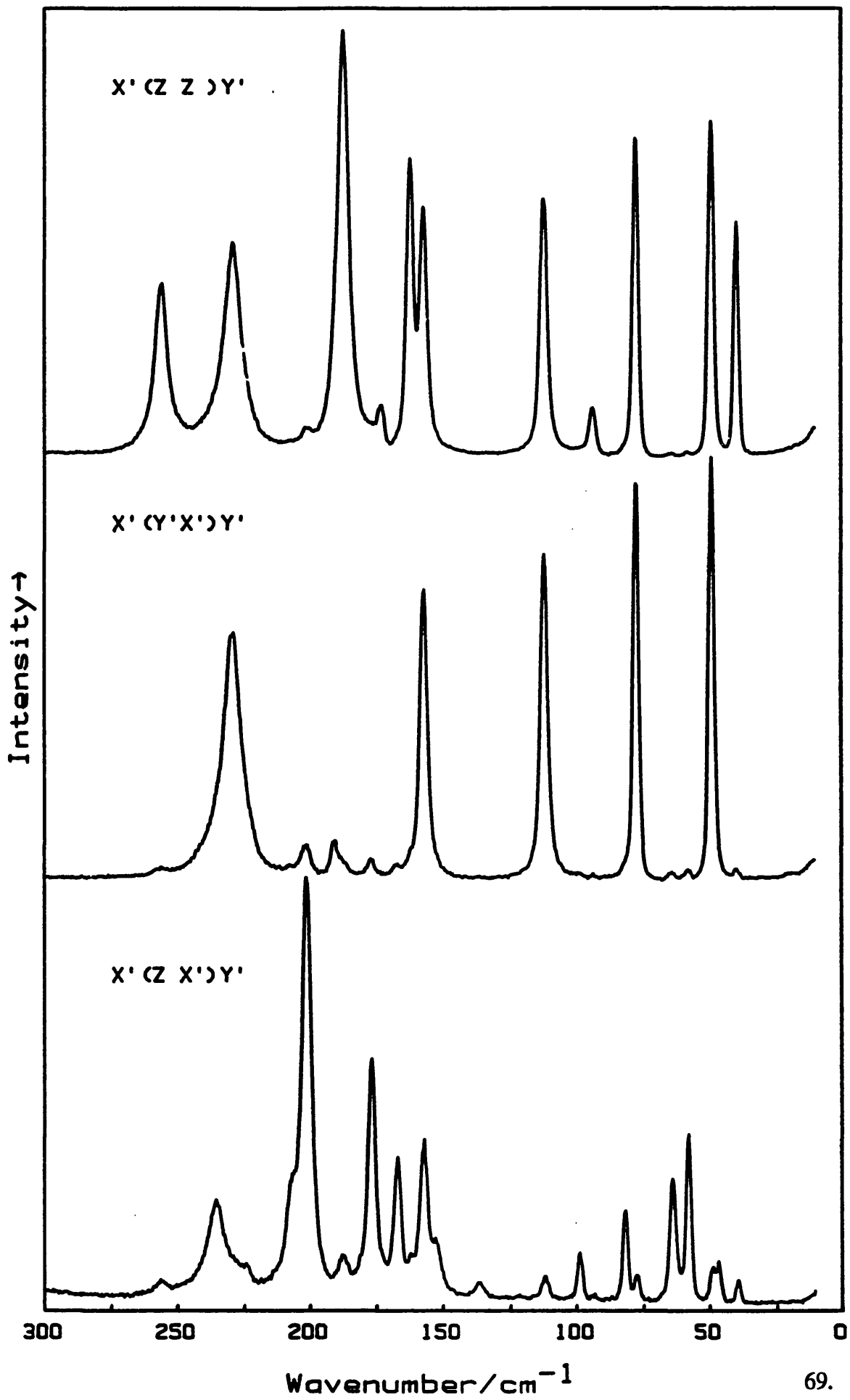


TABLE 2.10.5

Vibrational Frequencies and assignments for $\text{RbFe}(\text{SO}_4)_2 \cdot 12\text{H}_2\text{O}$,
between 20 and 275 cm^{-1} .

ν/cm^{-1}		$X'(Z Z)Y'$	$X'(Y'X')Y'$	$X'(Z X')Y'$	assignment
38	A_g	215			 tr (SO_4^{2-}) + rot (SO_4^{2-})
50	E_g	209	187		
58	F_g	1	10	77	
64	F_g			33	
75	E_g	770	749	15	
81	F_g			26	
86	F_g			15	
94	A_g	16			
97	F_g	4	10	51	
112	E_g	3	3		rot $[\text{Rb}(\text{OH}_2)_6]^+$
120	F_g			3	
154	$E_g (+F_g?)$	sh	30	2	rot $[\text{Fe}(\text{OH}_2)_6]^{3+}$
158	A_g	173	sh		
166	A_g	121	8	2	
175	F_g	3	15	170	
184	A_g	299	10		
189	E_g	sh	27		$\nu_5[\text{Rb}(\text{OH}_2)_6]^+$
196	F_g	15	15	189	
201	F_g	10	15	196	
217	F_g			21	
221	E_g	210	209		$\nu_2[\text{Rb}(\text{OH}_2)_6]^+$
226	F_g			148	
252	A_g	173	2		$\nu_1[\text{Rb}(\text{OH}_2)_6]^+$

Figure 2.10.5

Single crystal Raman spectra of $\text{RbFe}(\text{SO}_4)_2 \cdot 12\text{H}_2\text{O}$ between 25 and 300 cm^{-1} .
Sensitivities: $X'(Z Z)Y'$ 21616 counts sec^{-1} ; $X'(Y'X')Y'$ 17309 counts sec^{-1} ;
 $X'(Z X')Y'$ 5848 counts sec^{-1} (72 (2) K; step size 0.4 cm^{-1} ; spectral bandwidth
2.01 cm^{-1} at 150 cm^{-1} ; integration time 4 seconds; 488 nm radiation, 80 mw power
at sample).

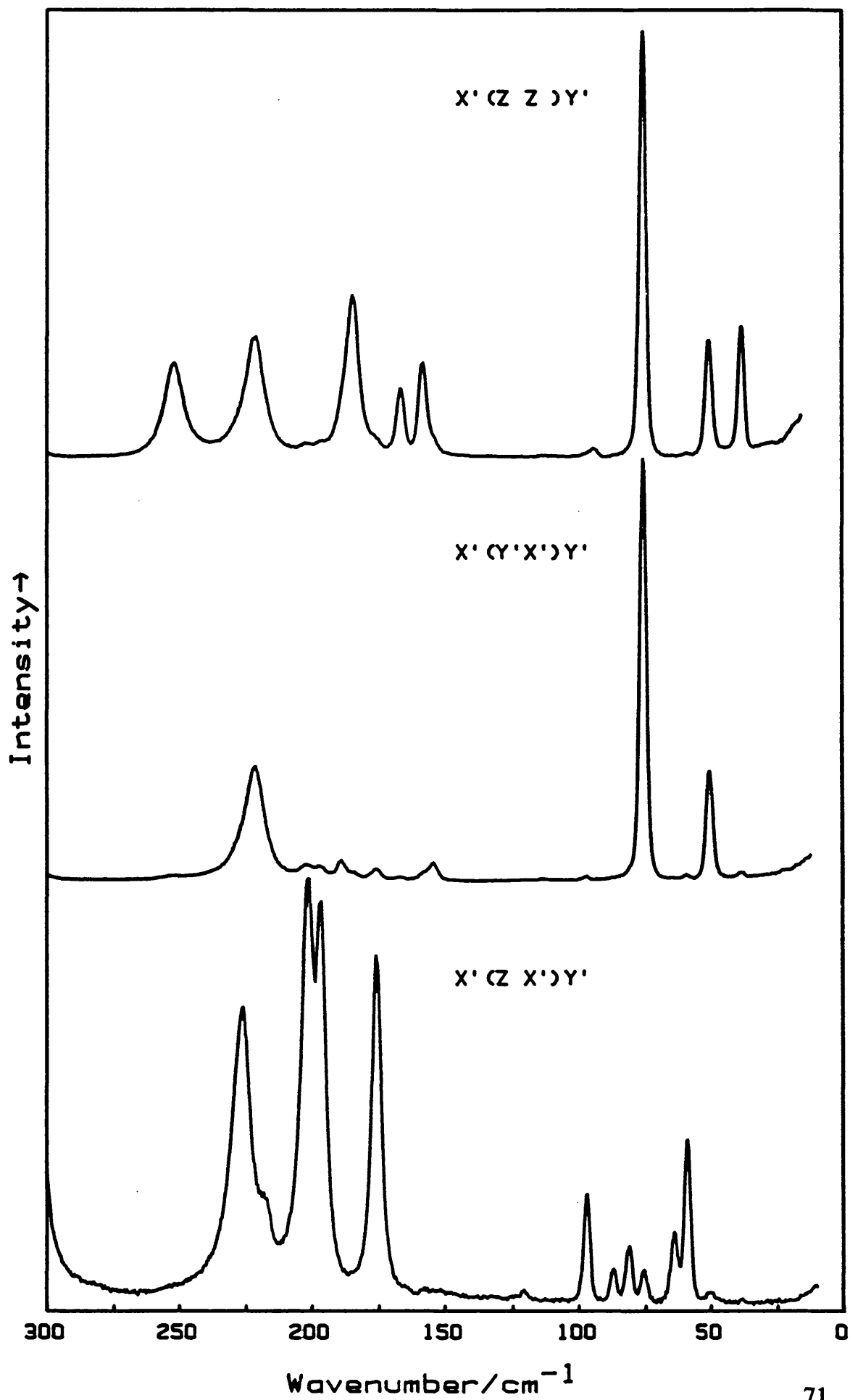


TABLE 2.10.6

Vibrational Frequencies and assignments for $\text{RbCr}(\text{SO}_4)_2 \cdot 12\text{H}_2\text{O}$,
between 20 and 275 cm^{-1} .

ν/cm^{-1}		$X'(Z Z)Y'$	$X'(Y'X')Y'$	$X'(Z X')Y'$	assignment
39	A_g	177			 tr (SO_4^{2-}) + rot (SO_4^{2-})
47	F_g			6	
48	E_g	123	120		
58	F_g	4	8	55	
62	F_g			24	
77	E_g	242	181		
81	F_g			22	
92	A_g	11			
98	F_g		2	9	
102	$A_g?$	4			
106	$A_g?$	4			
113	E_g	13	7		rot $[\text{Rb}(\text{OH}_2)_6]^+$
122	F_g			1	
139	F_g			4	
154	F_g			5	
155	E_g	sh	27		rot $[\text{Cr}(\text{OH}_2)_6]^{3+}$
158	A_g	116			
168	A_g	40		3	
174	F_g		7	44	
184	A_g	158	7		$\nu_5[\text{Rb}(\text{OH}_2)_6]^+$?
202	F_g		13	86	
230	E_g	93	55		$\nu_2[\text{Rb}(\text{OH}_2)_6]^+$
232	F_g			51	
252	A_g	75			$\nu_1[\text{Rb}(\text{OH}_2)_6]^+$

Figure 2.10.6

Single crystal Raman spectra of $\text{RbCr}(\text{SO}_4)_2 \cdot 12\text{H}_2\text{O}$ between 25 and 300 cm^{-1} .

Sensitivities: $X'(Z Z)Y'$ 3860 counts sec^{-1} ; $X'(Y'X')Y'$ 2857 counts sec^{-1} ;

$X'(Z X')Y'$ 1375 counts sec^{-1} (100 (10) K; step size 0.4 cm^{-1} ; spectral bandwidth 2.83 cm^{-1} at 150 cm^{-1} ; integration time 4 seconds; 476 nm radiation, 60 mw power at sample).

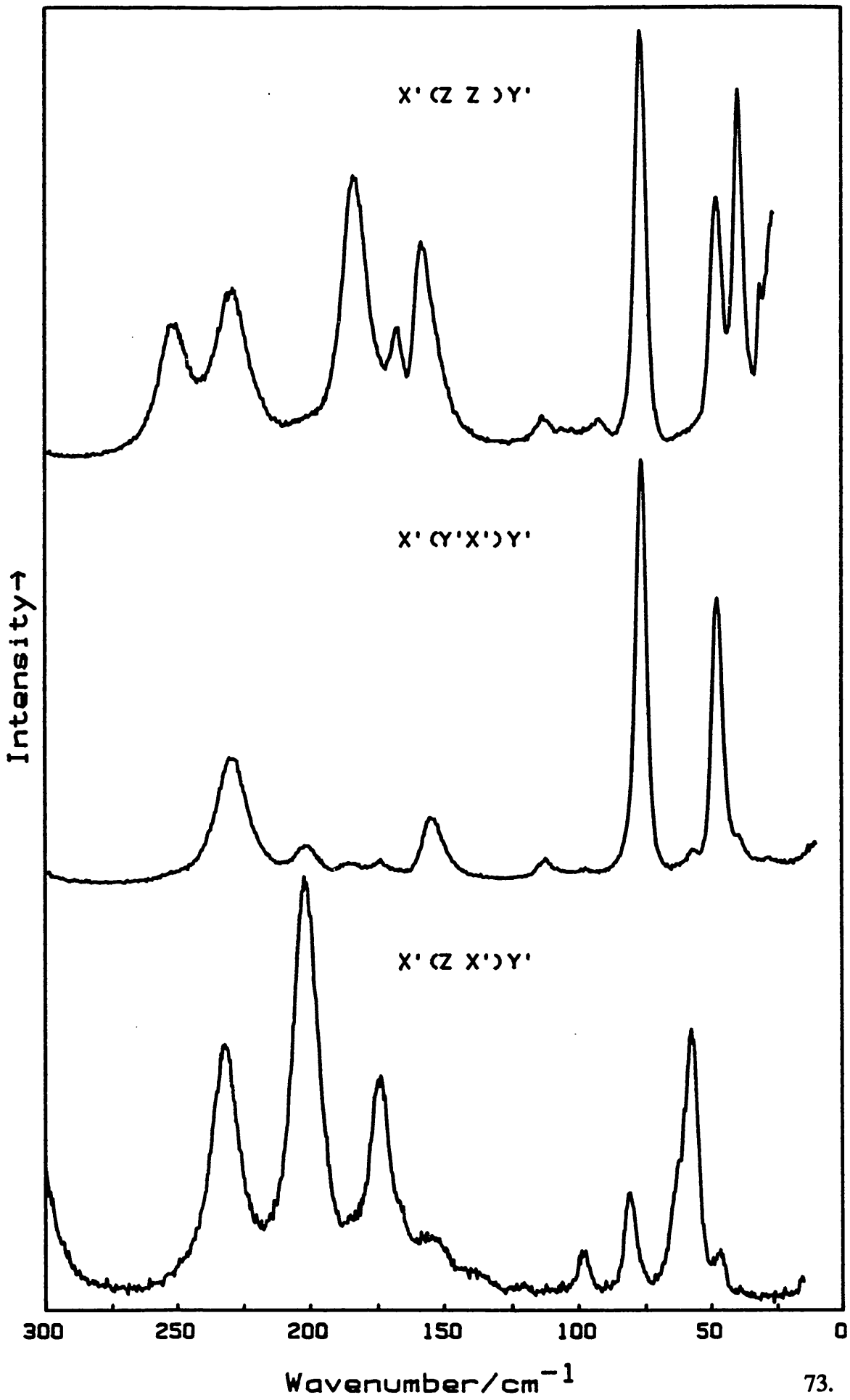


TABLE 2.10.7

Vibrational Frequencies and assignments for $\text{RbV}(\text{SO}_4)_2 \cdot 12\text{H}_2\text{O}$,
between 20 and 275 cm^{-1} .

ν/cm^{-1}		$X'(Z Z)Y'$	$X'(Y'X')Y'$	$X'(Z X')Y'$	assignment
48	E_g	594	381	11	tr (SO_4^{2-}) + rot (SO_4^{2-})
50	F_g			18	
62	F_g			9	
70	F_g			60	
74	E_g	433	289	sh	
82	F_g			7	
95	A_g	54			
107	E_g	58	36		rot [$\text{Rb}(\text{OH}_2)_6$] ⁺
138	E_g	sh	2		rot [$\text{V}(\text{OH}_2)_6$] ³⁺
143?	A_g	15			
151	A_g	59			
162	A_g (+ F_g ?)	333	7	10	
176	A_g	64			
180	F_g			33	
190	E_g	195	106		$\nu_5[\text{Rb}(\text{OH}_2)_6]$ ⁺
190	F_g			127	
208	F_g			85	
210	E_g	1111	703		$\nu_2[\text{Rb}(\text{OH}_2)_6]$ ⁺
211	F_g			118	
220	F_g		sh	117	
245	A_g	147	2	4	$\nu_1[\text{Rb}(\text{OH}_2)_6]$ ⁺

Figure 2.10.7

Single crystal Raman spectra of $\text{RbV}(\text{SO}_4)_2 \cdot 12\text{H}_2\text{O}$ between 25 and 300 cm^{-1} .
Sensitivities: $X'(Z Z)Y'$ 17116 counts sec^{-1} ; $X'(Y'X')Y'$ 10791 counts sec^{-1} ;
 $X'(Z X')Y'$ 2029 counts sec^{-1} (79 (5) K; step size 0.4 cm^{-1} ; spectral bandwidth
3.1 cm^{-1} at 150 cm^{-1} ; integration time 4 seconds; 457 nm radiation, 50 mw power
at sample).

X'(Z Z)Y'

X'(Y'X')Y'

X'(Z X')Y'

Intensity→

300 250 200 150 100 50 0

Wavenumber/cm⁻¹

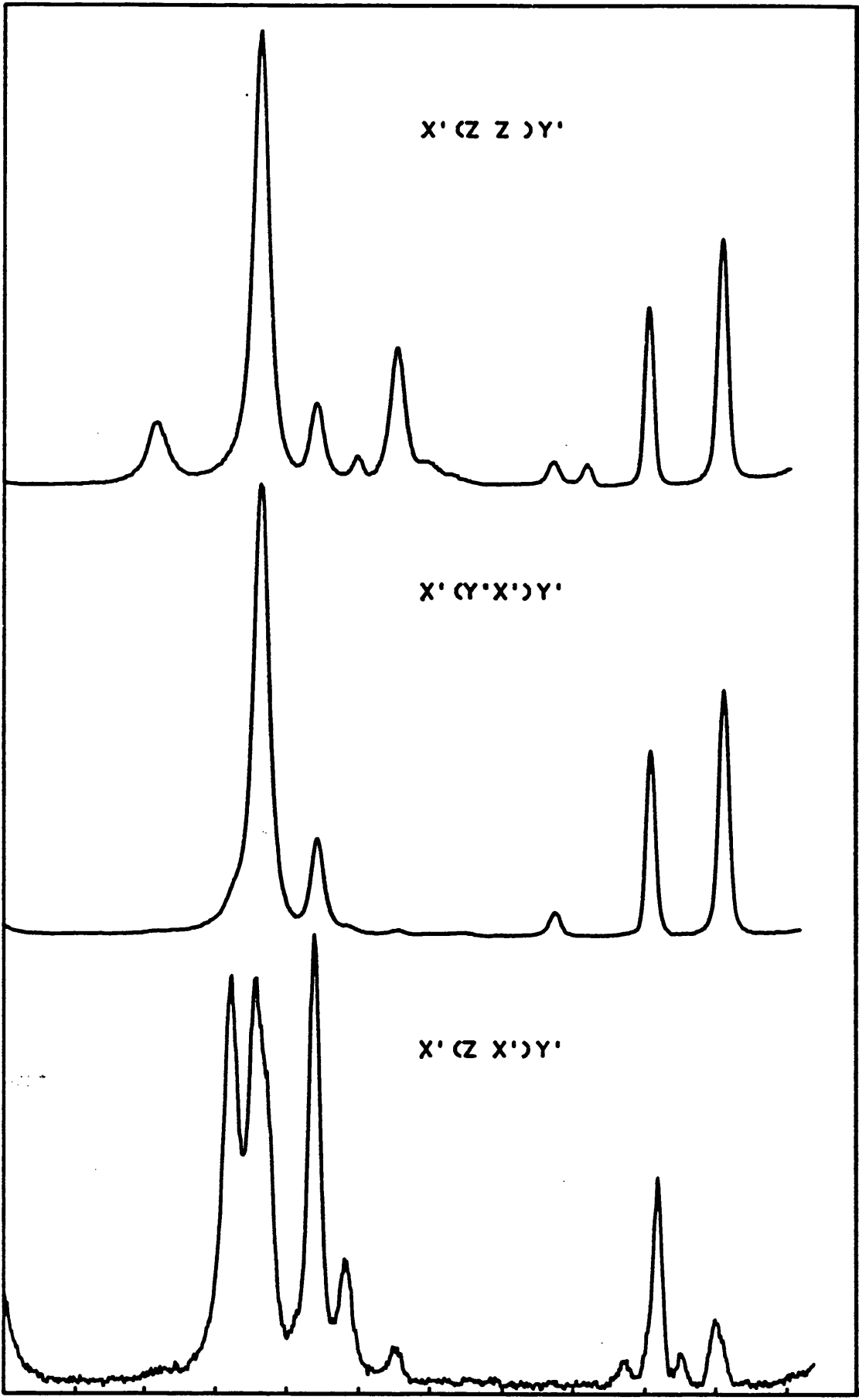


TABLE 2.10.8

Vibrational Frequencies and assignments for $\text{RbV}(\text{SO}_4)_2 \cdot 12\text{D}_2\text{O}$,
between 20 and 275 cm^{-1} .

ν/cm^{-1}		$X'(Z Z)Y'$	$X'(Y'X')Y'$	$X'(Z X')Y'$	assignment
48	E_g	588	391	sh	tr (SO_4^{2-}) + rot (SO_4^{2-})
50	F_g			17	
61	F_g			9	
73	E_g	474	311		
82	F_g			7	
92	A_g	49			
105	E_g	49	32		rot [$\text{Rb}(\text{OD}_2)_6$] ⁺
136	E_g	12	5		rot [$\text{V}(\text{OD}_2)_6$] ³⁺
145	A_g	55	2		
157	A_g	305	9	5	
172	A_g	54			
175	F_g			26	
184	E_g	183	119		$\nu_5[\text{Rb}(\text{OD}_2)_6]$ ⁺
184	F_g			114	
199	F_g			105	$\nu_2[\text{Rb}(\text{OD}_2)_6]$ ⁺
204	E_g	1029	637		
211	F_g			109	
242	A_g	136	2	3	$\nu_1[\text{Rb}(\text{OD}_2)_6]$ ⁺

Figure 2.10.8

Single crystal Raman spectra of $\text{RbV}(\text{SO}_4)_2 \cdot 12\text{D}_2\text{O}$ between 10 and 300 cm^{-1} .
Sensitivities: $X'(Z Z)Y'$ 15885 counts sec^{-1} ; $X'(Y'X')Y'$ 9895 counts sec^{-1} ;
 $X'(Z X')Y'$ 1793 counts sec^{-1} (81 (6) K; step size 0.4 cm^{-1} ; spectral bandwidth
2.32 cm^{-1} at 150 cm^{-1} ; integration time 4 seconds; 457 nm radiation, 60 mw power
at sample).

X' (Z Z) Y'

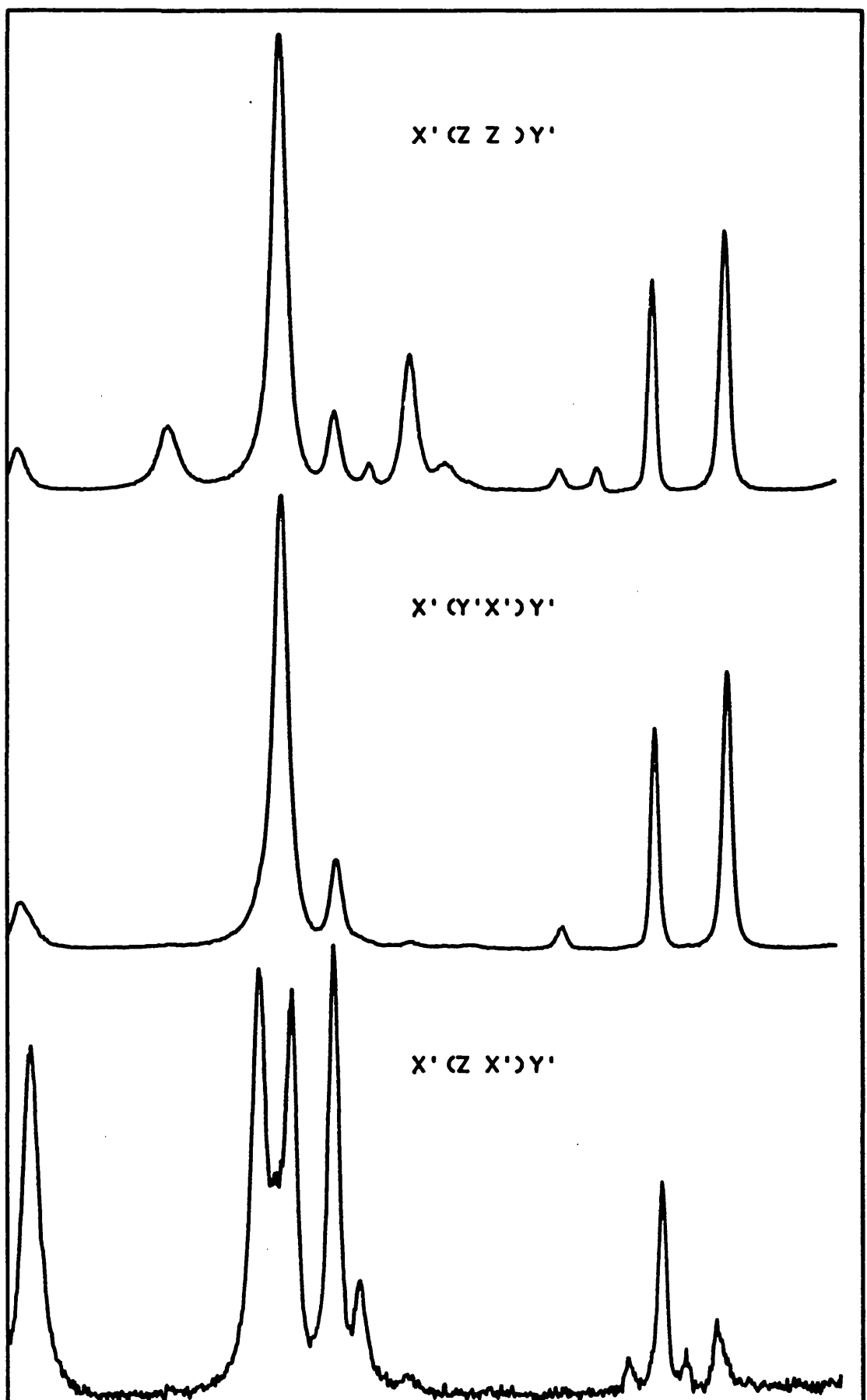
X' (Y' X') Y'

X' (Z X') Y'

Intensity →

300 250 200 150 100 50 0

Wavenumber/cm⁻¹



made for the deuterate. Assignments are entirely based on the analysis of the caesium alums. The rotational modes of the aqua cations are found in similar positions for the other rubidium sulphate alums. However, the relative intensities of the rotational modes compared to the other low wavenumber bands differs greatly with change of trivalent cation indicating extensive coupling which is also found for the caesium alums. The wavenumbers as well as the intensities will also be affected, this casts some doubt as to the ordering of the rotational modes based purely on change of wavenumber with unit cell size. However, the hydrogen bonds to the trivalent hexa-aqua-cation will be stronger than those to the monovalent cation supporting the assignment of the higher wavenumber band to rot $[M(OH_2)_6]^{3+}$.

iii) The internal modes of the rubidium hexa-aqua-cation.

Only the internal modes of the monovalent hexa-aqua-cation remain to be assigned. These are: $\nu_1[Rb(OH_2)_6]^+$, which is expected to occur with one component of A_g symmetry and one of F_g symmetry; $\nu_2[Rb(OH_2)_6]^+$, for which one E_g and two F_g components are predicted; and $\nu_3[Rb(OH_2)_6]^+$, where an A_g , an E_g , and three F_g modes are predicted. For the RbAlSH alum, an A_g band is found at 258 cm^{-1} , 20 wavenumbers from the nearest E_g band. This band is assigned to the $\nu_1[Rb(OH_2)_6]^+$ mode. $\nu_2[Rb(OH_2)_6]^+$ is expected to occur at higher wavenumber than $\nu_3[Rb(OH_2)_6]^+$ as for the trivalent cation. The E_g and F_g bands that occur at 238 and 246 cm^{-1} respectively are assigned to the $\nu_2[Rb(OH_2)_6]^+$ mode. The remaining A_g and E_g modes at 193 cm^{-1} and the F_g mode at 203 cm^{-1} are assigned to $\nu_3[Rb(OH_2)_6]^+$. All three internal modes exhibit similar shifts on deuteration. The internal modes of the $[Rb(OH_2)_6]^+$ cation for the other rubidium sulphate alums are likewise ordered $\nu_1[Rb(OH_2)_6]^+ > \nu_2[Rb(OH_2)_6]^+ > \nu_3[Rb(OH_2)_6]^+$. The ordering of the internal modes is tentative however. This is because the expected ordering $\nu_1 > \nu_2 > \nu_3$, is applicable to a discrete MX_6 unit only. For the $[Rb(OH_2)_6]^+$ cation, the Rb-OH₂ bond distance is *ca.* 3.3 \AA .¹⁵ The water molecules are weakly bound to the Rb⁺ centre, consequently, the internal modes of $[Rb(OH_2)_6]^+$ might be better thought of as water translations.

Of particular interest is the low wavenumber spectra of RbTiSH. The position of the bands show significant variation with temperature most apparent in the lowest wavenumber phonon mode, indicating the onset of a phase transition. This

observation is discussed in detail in chapter 4. The assignment of the RbTiSH spectra is important since identification of the soft modes gives an insight into the nature of the phase transition.

The analysis of the low wavenumber single crystal Raman spectra of the rubidium alums gives no additional information to the assignment of the lattice modes than was available from the caesium alum study. The only modes assigned with confidence are those of the lattice modes of sulphate. However, this study serves only to question the ordering of the tr (SO_4^{2-}) and rot (SO_4^{2-}) modes. Spectra of rubidium selenate alums might aid assignment of these modes.

TABLE 2.10.9

Vibronic Frequencies and assignments for $\text{RbTi}(\text{SO}_4)_2 \cdot 12\text{H}_2\text{O}$,
between 20 and 275 cm^{-1} .

ν/cm^{-1}		$X'(Z Z)Y'$	$X'(Y'X')Y'$	$X'(Z X')Y'$	assignment
34	$E_g + F_g ?$	241	235		$\left. \begin{array}{l} \text{tr} (\text{SO}_4^{2-}) \\ + \\ \text{rot} (\text{SO}_4^{2-}) \end{array} \right\}$
53	F_g			7	
72	F_g			19	
74	E_g	92	73		
96	$A_g + F_g ?$	22		2	
98	$E_g ?$	sh	3		rot $\text{Rb}(\text{OH}_2)_6]^+$?
136	$E_g + F_g$	sh	6	2	rot $\text{Ti}(\text{OH}_2)_6]^{3+}$?
149	A_g	5			
161	$A_g + F_g$	90		5	
168	A_g	sh			
179	E_g	20	17		$\nu_5[\text{Rb}(\text{OH}_2)_6]^+$
185	F_g			42	
202	F_g			sh	
206	E_g	193	139		$\nu_2[\text{Rb}(\text{OH}_2)_6]^+$
213	F_g			34	
243	A_g	30	2	2	$\nu_1[\text{Rb}(\text{OH}_2)_6]^+$

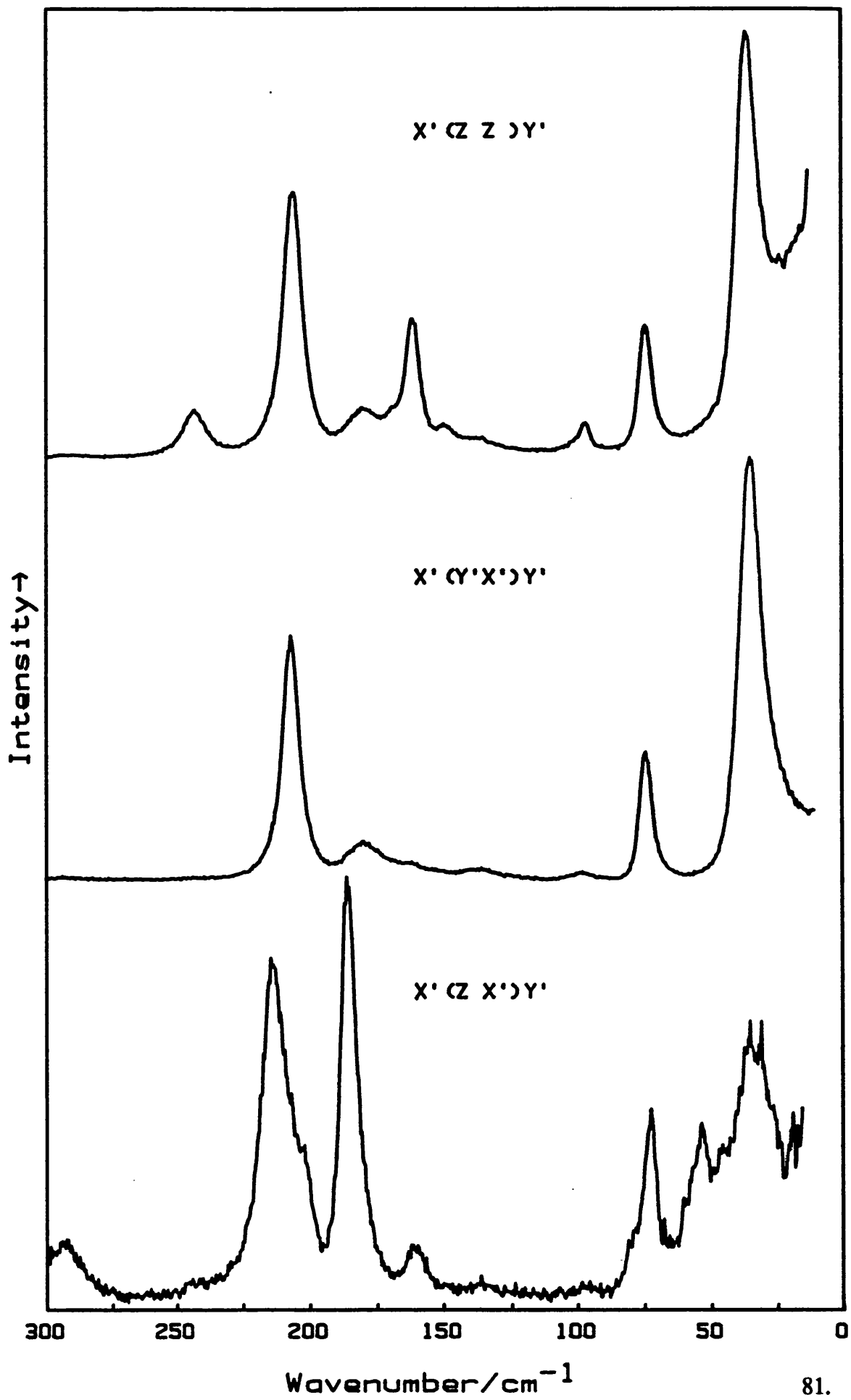
Figure 2.10.9

Single crystal Raman spectra of $\text{RbTi}(\text{SO}_4)_2 \cdot 12\text{H}_2\text{O}$ between 15 and 300 cm^{-1} .

Sensitivities: $X'(Z Z)Y'$ 9679 counts sec^{-1} ; $X'(Y'X')Y'$ 7435 counts sec^{-1} ;

$X'(Z X')Y'$ 1292 counts sec^{-1} (90 (9) K; step size 0.4 cm^{-1} ; spectral bandwidth

2.79 cm^{-1} at 600 cm^{-1} ; integration time: $X'(Z Z)Y'$, 4 seconds; $X'(Y'X')Y'$ and $X'(Z X')Y'$ 2 seconds. 413 nm radiation, 80 mw power at sample).



2.11 Single Crystal Raman Spectrum between 1200 and 4000 cm⁻¹

The internal modes of water are expected to occur in the high wavenumber region of the spectrum, between 1500 and 4000 cm⁻¹.²⁵ There are two distinct water molecules within the lattice each lying on a site of c_1 symmetry. Two stretching modes and one bending mode are expected for each water molecule. Each of these modes gives rise to $A_g + E_g + 3F_g$ Raman active bands.

The wavenumber at which the $\nu(\text{OH})$ stretch occurs is dependent on the O-H force constant which is itself related to the strength of the O-H...O hydrogen bond. The strength of hydrogen bonding is influenced by a number parameters one of which is the $r_{\text{o-o}}$ distance. When the environment about the hydrogen bond is kept constant, it has been shown²⁶ that as the strength of hydrogen bonding is increased *viz.* a reduction of the $r_{\text{o-o}}$ distance, a decrease in the $\nu(\text{OH})$ stretching frequency is observed. For the caesium alum study¹ where extensive x-ray and neutron are available, the ordering of the stretching modes was related to the $r_{\text{o-o}}$ bond distance. The available crystallographic data for the rubidium alums is limited. The discussion of the high wavenumber spectra is therefore confined to that of RbVSH where crystallographic data is available. The high wavenumber spectra of the remaining rubidium sulphate alums are presented in appendix A.1 No assignment is attempted.

Assignment of the Single Crystal Raman spectra of RbVSH between 1200 and 4000 cm⁻¹

Both CsVSH and RbVSH are of the β modification.^{6,15} The ordering of the hydrogen bond lengths is found to be the same for both alums. Assignment of the high wavenumber spectrum of RbVSH is by reference to the available crystallographic data for this alum¹⁵ and by analogy with the high wavenumber spectrum of CsVSH. Since the f.w.h.h. of the bands in this region vary considerably, it is inappropriate to measure the relative intensities of the bands as a function of peak height. Instead the intensities of the bands are termed strong, medium and weak relative to the other bands in the spectrum. The high wavenumber spectra of the crystalline hydrates are complicated by the presence of overtones and combination bands leading to ambiguity

TABLE 2.11.1

Vibrational Frequencies and assignments for $\text{RbV}(\text{SO}_4)_2 \cdot 12\text{H}_2\text{O}$,
between 1200 and 4000 cm^{-1} .

ν/cm^{-1}	Activity	Intensity	Assignment
1224	$E_g + F_g$	w	
1352	$E_g + F_g$	w	
1400	F_g	w	$[\nu_L + \nu_L]$
1416	E_g	w	
1460	F_g	w	
1480	E_g	w	
1596	E_g	m/w	$\nu_2(\text{HOH})$
1680	$E_g + F_g$	m/w	
1726	E_g	w	+
1762	E_g	m/w	
1828	E_g	m/w	$[\nu_L + \nu_L]$
1940	E_g	s	${}^3E_g \leftarrow {}^3A_g$
2144	F_g	w	$\nu_2(\text{HOH})$
2240	F_g	w	
2340	F_g	w	+
2424	$E_g + F_g$	m/w	
2508	E_g	w	$[\nu_L + \nu_L]$
2696	E_g	w	
2788	F_g	w	$\nu(\text{OH}) [\text{V}(\text{OH}_2)_6]^{3+}$
2792	A_g	m/w	
2968	E_g	m	
2976	F_g	s	$\nu(\text{OH}) [\text{V}(\text{OH}_2)_6]^{3+}$
3050	A_g	m	
3096	F_g	w	
3349	F_g	s	
3360	A_g	s	
3368	F_g	s	$\nu(\text{OH}) [\text{Rb}(\text{OH}_2)_6]^{3+}$
3371	E_g	s	
3402	A_g	s	
3416	F_g	w	
3530	$E_g + F_g$	m/w	$[\nu(\text{OH}) + \nu_L]$

ν_L designates an external mode of water,
 $\nu_2(\text{HOH})$ designates the water bending mode,
 $\nu(\text{OH})$ designates an internal mode of water.

Figure 2.11.1

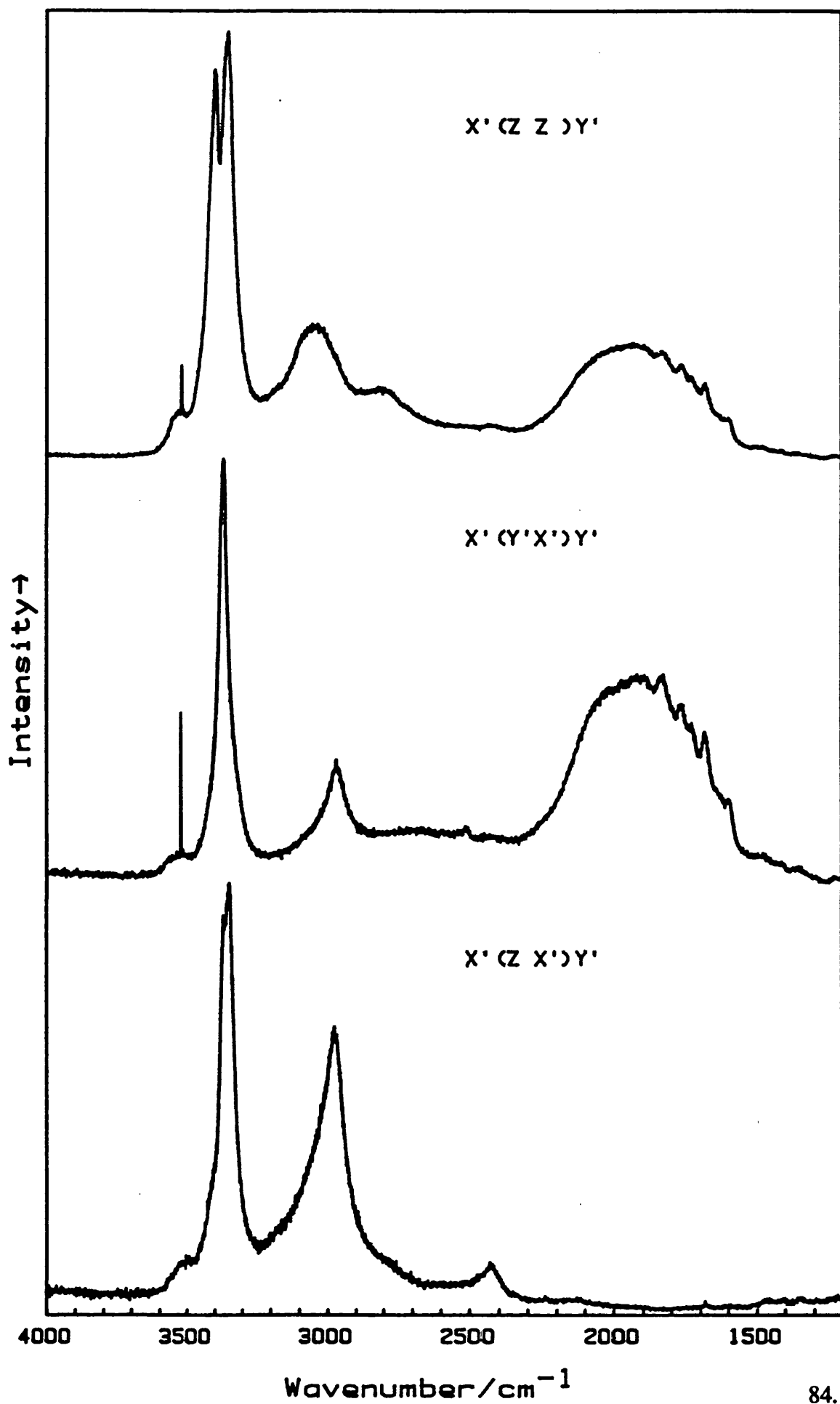
Single crystal Raman spectra of $\text{RbV}(\text{SO}_4)_2 \cdot 12\text{H}_2\text{O}$ between 1200 and 4000 cm^{-1} .

Sensitivities: $X'(Z Z)Y'$ 18011 counts sec^{-1} ; $X'(Y'X')Y'$ 3537 counts sec^{-1} ;

$X'(Z X')Y'$ 3284 counts sec^{-1} (79 (5) K; step size 1 cm^{-1} ; spectral bandwidth

2.39 cm^{-1} at 2600 cm^{-1} ; integration time: $X'(Z Z)Y'$ and $X'(Z X')Y'$ 4 seconds;

$X'(Y'X')Y'$ 7 seconds. 457 nm radiation, 50 mw power at sample).



of assignment.

The RbVSH alum is of particular interest since, unlike the other alums presented in this study, it contains a strong broad band, principally of E_g polarisation, centred around 1940 cm^{-1} . This band is also found for the caesium and ammonium vanadium alums²⁷ where it is assigned as the electronic Raman transition (${}^3E_g \leftarrow {}^3A_g$) between the trigonally split components of the ${}^3T_{1g}(F)$ ground term of the hexa-aqua-vanadium(III) ion. The analogous, strong, broad band found in RbVSH is likewise assigned to this transition. The nature of this transition is discussed in detail in the following chapter.

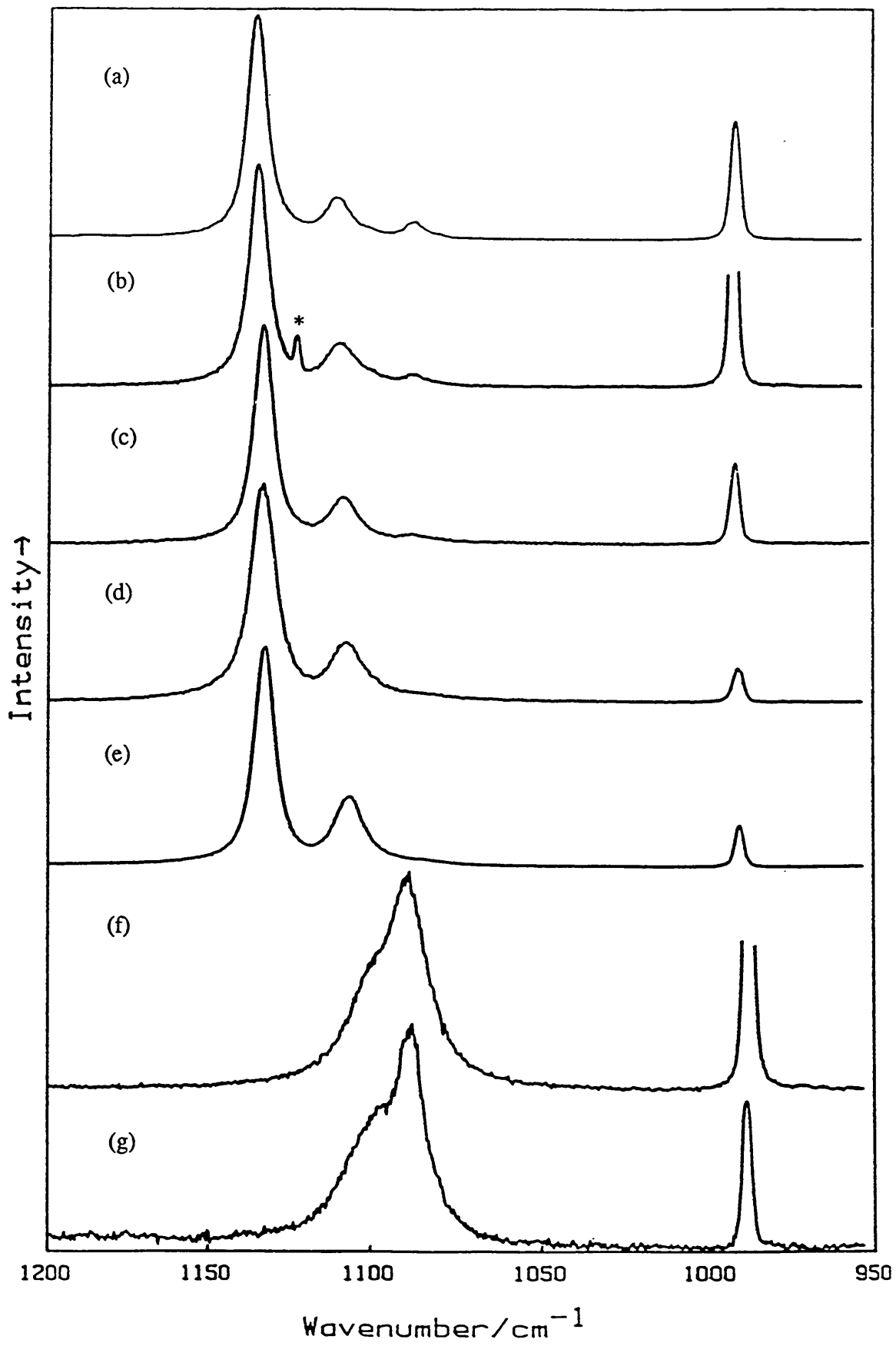
2.12 Discussion

Crystallographic^{6,15-20} and single crystal Raman studies¹⁻⁵ of the caesium alums show a definite correlation between structural modification and the first order phonon spectrum. The difference in the single crystal Raman Spectra of the α and β alums is most apparent in the F_g component of $\nu_3(\text{SO}_4)$.¹⁶ Figure 2.12.1 shows a plot of the F_g component of $\nu_3(\text{SO}_4)$ for the rubidium alums collected in this study. With reference to the Raman and structural data published on the caesium alums, the rubidium sulphate alums of Al, In, Ga, Fe, and Cr are classified as α alums whilst the vanadium and titanium alums belong to the β modification.

The differing alum modifications of the rubidium alums is explained in terms of occupancy of the t_{2g} set rather than size of the trivalent hexa-aqua cation. For the caesium alums, the metal(III)-water bond lengths of Ti, V, Fe, Cr, and Ga have values in between those found for In and Al.⁶ The metal(III)-water bond distances show an inverse relationship with $\nu_1(\text{MO}_6)$ ³ suggesting that the force constant is a reliable guide to the metal(III)-water bond length. The $\nu_1(\text{MO}_6)$ mode for the caesium alums occur at 517 (Ti), 525 (V), 540 (Cr), 523 (Fe), 537 (Ga), 542 (Al), and 505 cm^{-1} (In). The corresponding values for the rubidium alums are 518 (Ti), 531 (V), 540 (Cr), 526 (Fe), 538 (Ga), 545 (Al), and 500 (In). The similar values of the $\nu_1(\text{MO}_6)$ mode for the caesium and rubidium alums suggest that there is little change in the metal(III)-water bond strength on change of monovalent cation, even when this results in a change in the alum type. Since there is little change in the values of the $\nu_1(\text{MO}_6)$ mode on

Figure 2.12.1

The F_g component of the Raman spectrum ($950 - 1200 \text{ cm}^{-1}$) of rubidium alums, $\text{RbM}(\text{SO}_4)_2 \cdot 12\text{H}_2\text{O}$, $M =$ (a) Al, (b) Ga, (c) In, (d) Cr, (e) Fe, (f) Ti, (g) V recorded between 62 and 100 K.



* designates room light emission

substitution of rubidium for caesium, the sizes of the trivalent cations in the rubidium alums follow from the structural data collected on the caesium alums⁶ which shows that the metal(III)-water bond lengths for titanium(III) and vanadium(III) are intermediate between the values of Al and In. It is concluded, therefore, that the size of the trivalent cation is not a factor in determining alum type.

A contributing factor to the stereo-chemical preference for trigonal planar coordination by titanium(III) and vanadium(III) hexa-aqua-cations maybe the magnitude of the interaction between $d\pi$ orbitals on the metal and $p\pi$ orbitals on the water ligand. As the first row transition metal series is traversed, electrons are added to the t_{2g} (π -antibonding) orbitals of the trivalent cation leading to a reduction in the net metal-ligand bond order. However if the absolute magnitude of the π interaction were the driving force for the stereo-chemical preference of the titanium(III) and vanadium(III) hexa-aqua-cations, it would be expected that the chromium(III) hexa-aqua-cation would also show some degree of stereo-chemical preference and this is not observed. The CsCrSH alum belongs to the β modification indicating trigonal planar coordination to the trivalent cation^{17,18} whereas the RbCrSH alum belongs to the α modification indicating trigonal pyramidal co-ordination to the trivalent cation.^{17,20} The position of the $\nu_1(\text{CrO}_6)$ mode is found at 540 cm^{-1} in both alums suggesting that the Cr-O bond is primarily ionic in nature. Neutron diffraction experiments on aqueous solutions of 2.2M chromium(III) perchlorate, have determined the mode of water co-ordination in the $[\text{Cr}(\text{OH}_2)_6]^{3+}(\text{aq})$ cation to be trigonal pyramidal, with the plane of the water molecule making an angle of $34(6)^\circ$ to the CrO_4 plane.²⁸ It is clear, therefore, that the potential energy surface for tilting the plane of the water molecule is shallow and readily influenced by the surroundings.

As well as the magnitude of the π interaction the anisotropy of this interaction must be considered. The highest symmetry that can be achieved for a hexa-aqua-cation is T_h . With this symmetry the degeneracy of the t_{2g} orbitals is accommodated. In the $M^{\text{III}}M^{\text{III}}[\text{SO}_4]_2 \cdot 12\text{H}_2\text{O}$ series, the metal(III) hexa-aqua-cation lies on a site of S_6 symmetry. The t_{2g} orbitals are consequently split into E_g and A_g components. For the metal(III) hexa-aqua-cations Al, Ga, In, Fe and Cr, the extent of splitting of the t_{2g} orbitals does not energetically stabilise or destabilise the system. In the case of Ti and V, however, which have $3d^1$ and $3d^2$ valence configurations respectively, greater

splitting of the t_{2g} orbitals is energetically favourable.

It is concluded, therefore, from the structural modifications adopted by the rubidium alums, that the mode of water co-ordination in the β compared to the α alums leads to greater trigonal field stabilisation energy of the vanadium(III) and titanium(III) hexa-aqua-cations.

REFERENCES

1. S. P. Best, Ph.D Thesis, Sydney University (1983).
2. S. P. Best, J. K. Beattie, and R. S. Armstrong *J. Chem. Soc., Dalton Trans.*, 1655 (1982).
3. S. P. Best, J. K. Beattie, and R. S. Armstrong, *J. Chem. Soc. Dalton Trans.*, 2611 (1984).
4. S. P. Best, J. K. Beattie, and R. S. Armstrong and G. P. Braithwaite, *J. Chem. Soc., Dalton Trans.*, 1771, (1989).
5. S. P. Best, J. K. Beattie, and R. S. Armstrong, *J. Chem. Soc., Dalton Trans.*, 299, (1992).
6. J. K. Beattie, S. P. Best, B. W. Skelton, and A. H. White, *J. Chem. Soc., Dalton Trans.*, 2105 (1981).
7. S. Haussühl, *Z. Kristallogr., Kristallgeom., Kristallphys., Kristallchem.*, **116**, 371, (1961).
8. S. K. Dutta-roy, A. S. Chakravarty, and A. Bose, *Indian J. Phys.*, **33**, 483 (1959).
9. G. F. Dionne, *Can. J. Phys.*, **42**, 2419 (1964).
10. R. S. Halford, *J. Chem. Phys.*, **14**, 8. (1946).
11. D. F. Hornig, *J. Chem Phys.*, **16**, 1063. (1946).
12. G. Herzberg, *Molecular Spectra and molecular structure. Vol. II: Infrared and Raman spectra of polyatomic molecules*, Van Nostrand, Princeton, N. J., (1945).
13. T. E. Jenkins and J. Lewis, *J. Raman Spectrosc.*, **11**, 1. (1981).
14. H. H. Eysel and J. Eckert, *Z. anorg. allg. Chem.*, **424**, 68 (1976).
15. J. K. Beattie, P. Del Favero, S. P. Best, B. W. Skelton and A. H. White, *Aust. J. Chem.*, in press.
16. R. S. Armstrong, J. K. Beattie, S. P. Best, B. W. Skelton, and A. H. White, *J. Chem. Soc., Dalton Trans.*, 1973 (1983).
17. S. P. Best and J. B. Forsyth, *J. Chem. Soc., Dalton Trans.*, 395 (1990).
18. S. P. Best and J. B. Forsyth, *J. Chem. Soc., Dalton Trans.*, 1721 (1990).

19. R. S. Armstrong, J. K. Beattie, S. P. Best, G. P. Braithwaite, P. Del Favero, B. W. Skelton, and A. H. White, *Aust. J. Chem.*, **43**, 393 (1990).
20. A. M. Abdeen, G. Will, W. Schafer, A. Kirfel, M. O. Bargouth, K. Recker, and A. Weiss, *Zeitschrift für Kristallographie*, **157**, 147 (1981).
21. A. Eriksson, J. Lindgren, *J. Mol. Struct.*, **48**, 417 (1978).
22. H. Tanaka, J. Henning, H. D. Lutz, G. Kliche, *Spectrochim. Acta*, **43 A**, 395 (1987).
23. W. Eckers, H. D. Lutz, *Spectrochim. Acta*, **41 A**, 1321, (1985).
24. M. Frindi, M. Peyrard, M. Remoissenet, *J. Phys.*, **C13**, 3493, (1980).
25. H. D. Lutz, *Bonding and Structure of Water Molecules in Solid Hydrates, Structure and Bonding*, **69**, 97, (1988).
26. G. E. Walrafen, M. Abede, F. A. Mauer, S. Block, G. J. Piermarini, and R. Munro, *J. Chem. Phys.*, **77**, 2166 (1982).
27. S. P. Best and R. J. H. Clark, *Chem. Phys. Letts.*, **122**, 401 (1985).
28. R. D. Broadbent, G. W Neilson, and M. Sandstrom, *J. Phys. : Condensed Matter*, **4**, 639, (1992).

Electronic Structure of $[\text{V}(\text{OH}_2)_6]^{3+}$

3.1 Background

The electronic structure of the $[\text{V}(\text{OH}_2)_6]^{3+}$ cation within the $\text{NH}_4\text{V}(\text{SO}_4)_2 \cdot 12\text{H}_2\text{O}$ alum has been probed extensively by magnetic susceptibility measurements both in the 1 - 20 K temperature range^{1,2} and also the 80 - 300 K temperature range.^{3,4}

Of the available measurements, only the results of Fritz and Pinch [2] and Figgis, Lewis, and Mabbs [4] are used for discussion since in these cases the purity of the sample has been checked following magnetic measurements. The susceptibility data can be fitted to a model in which the trigonal field splitting is of the order of 2000 cm^{-1} , with the ${}^3\text{A}_g$ trigonal term lowest in energy.⁴ The splitting between the $\hat{\text{A}}_g$ and $\hat{\text{E}}_g$ spin orbit states which are derived from the ${}^3\text{A}_g$ ground term is found to be 4.9 cm^{-1} .² A model in which the sign of the trigonal field is reversed such that the E_g term is lowest in energy is incompatible with the available experimental data.

A schematic diagram showing the splitting of the ${}^3\text{T}_{1g}$ ground term by a trigonal field and spin-orbit coupling is shown in figure 3.1.1. The energies of the derived states are calculated by applying a simultaneous perturbation by an axial field and spin-orbit coupling to the ${}^3\text{T}_{1g}$ ground term.⁵

Figure 3.1.2 shows the electronic Raman band for RbVSH at 82 K and 4.2 K with both $\text{X}'(\text{Z Z})\text{Y}'$ and $\text{X}'(\text{Y}'\text{X}')\text{Y}'$ activities. Although the signal/noise is poor in the low temperature spectra, it is noted that the low wavenumber component of the electronic band loses intensity on cooling. As the crystal is cooled from 82 to 4.2 K, the transitions from the lowest energy $\hat{\text{E}}_g$ state will lose intensity whilst the transitions from the $\hat{\text{A}}_g$ ground state gain intensity. The loss of the low-energy component of the band on cooling could be suggesting that the transition from the $\hat{\text{A}}_g$ ground state to the $\hat{\text{E}}_g$ state which is lowest lying in the ${}^3\text{E}_g$ manifold does not occur with appreciable intensity. The electronic Raman transition has also been observed for the β alums of CsVSH and NH_4VSH ⁶ and occurs in the same position as found for RbVSH. The

Figure 3.1.1

Splitting of 3T_g term (d^2 transition metal complex) by a trigonal field and spin-orbit coupling. Energies quoted are in units of cm^{-1} and assume that the action of the trigonal field leaves the 3A_g term 1940 cm^{-1} lower in energy than the 3E_g term and that the splitting between the \hat{A}_g and \hat{E}_g spin orbit states which are derived from the 3A_g ground term is 4.9 cm^{-1} .²

Δ denotes the magnitude of trigonal field splitting; λ denotes spin-orbit coupling constant. The parameter 'A' depends on the strength of the crystal field. It is related to the crystal field parameter Dq and the Racah parameter B , by the expression:

$$A = \frac{1.5 - \left(\frac{\sqrt{\frac{105B}{Dq} + 10 + 6Dq}}{4Dq} \right)^2}{1 + \left(\frac{\sqrt{\frac{105B}{Dq} + 10 + 6Dq}}{4Dq} \right)^2}$$

In the weak field limit 'A' tends to the value of 1.5 whereas in the strong field limit A tends to 1, (After Mabbs and Machin [5]).

CUBIC FIELD

TRIGONAL
FIELD

TRIGONAL FIELD +
SPIN-ORBIT COUPLING

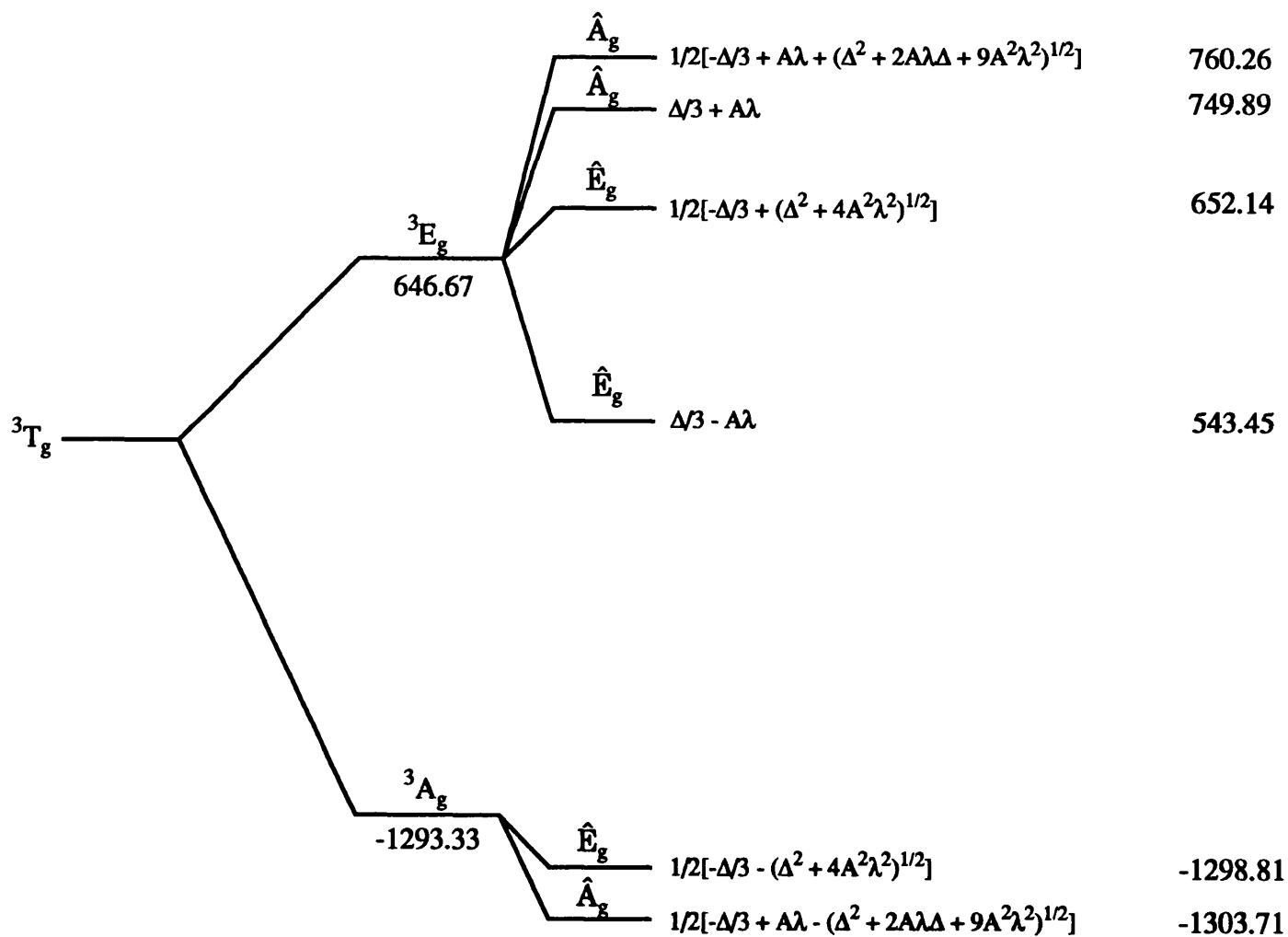
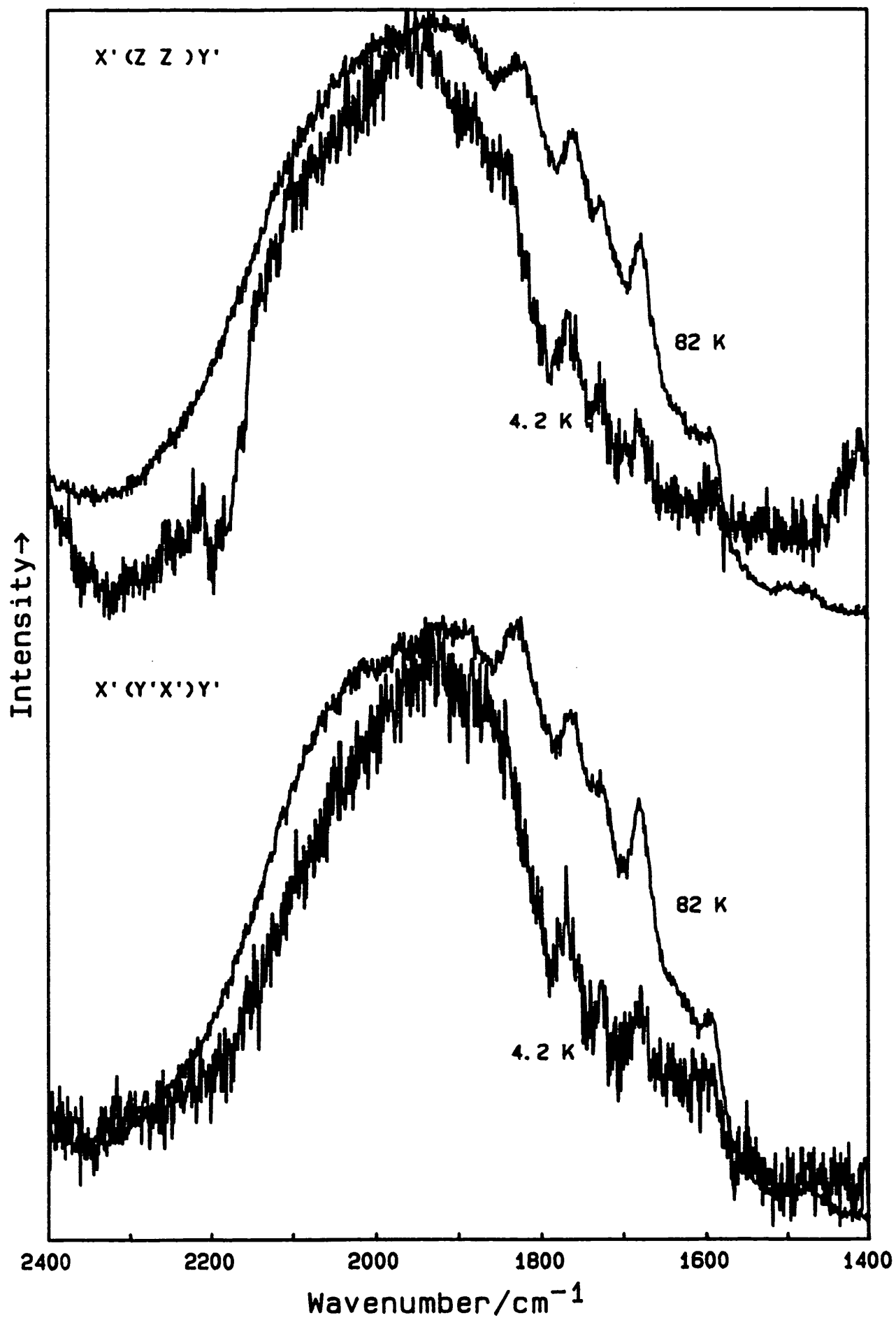


Figure 3.1.2

Electronic Raman band (${}^3E_g \leftarrow {}^3A_g$) for $[V(OH_2)_6]^{3+}$ in RbVSH at 82 and 4.2 K.
Step size 1 cm^{-1} , 457 nm radiation.



profile for the electronic Raman band, recorded at 20 K, for NH_4VSH^6 and CsVSH , differ significantly suggesting that the relative intensities of the spin-orbit coupled transitions are sensitive to substitution of NH_4^+ for Cs^+ . The electronic Raman band of RbVSH recorded at 82 K with $X'(Z Z)Y'$ activity can be fitted to spin-orbit coupled bands arising from a trigonal field of 1940 cm^{-1} . The positions of the bands are constrained to those values predicted by theory⁵ which would give a splitting between the ground \hat{A}_g and \hat{E}_g states of 4.9 cm^{-1} (figure 3.1.3) Although simulation of the spectrum is hampered by vibrational bands occurring on the low wavenumber side of the band, a good fit is achieved with a value of $A\lambda = ca. 103 \text{ cm}^{-1}$. The parameter 'A' depends on $10 Dq$ and the Racah parameter 'B'; the definition of A is given in figure 3.1.1. λ is the spin-orbit coupling constant. An estimate of 'A' can be obtained from the electronic spectrum of NH_4VSH recorded at 10 K by Hitchman *et al.*⁷ From the ratio's of the $T_{1g} \rightarrow T_{2g}$ and $T_{1g} \rightarrow T_{1g}(P)$ transitions, an estimate of Dq/B ⁸ and hence A can be obtained. From the resulting calculations, a value for A of 1.45 is obtained giving a spin-orbit coupling constant of $\lambda = 71 \text{ cm}^{-1}$ (compared to the free ion value of 105 cm^{-1}).

A more comprehensive interpretation of the electronic spectrum of the NH_4VSH alum has been performed by Hitchman *et al.* using an angular overlap model analysis.⁷ It was found that a spin orbit coupling constant of $\lambda = 84 \text{ cm}^{-1}$ and a Racah parameter of $B = 644 \text{ cm}^{-1}$ were needed in order to model the observed electronic and electronic Raman transition energies. The variation of the effective magnetic moment μ with temperature, calculated from parameters derived from the angular overlap model gives excellent agreement with the reported experimental values^{1,2} if an isotropic orbital reduction factor of $\kappa = 0.85$ is used.

The parameters obtained from this angular overlap analysis suggest a significant anisotropic π interaction with the largest interaction being with ligand orbitals normal to the plane of the water molecule.

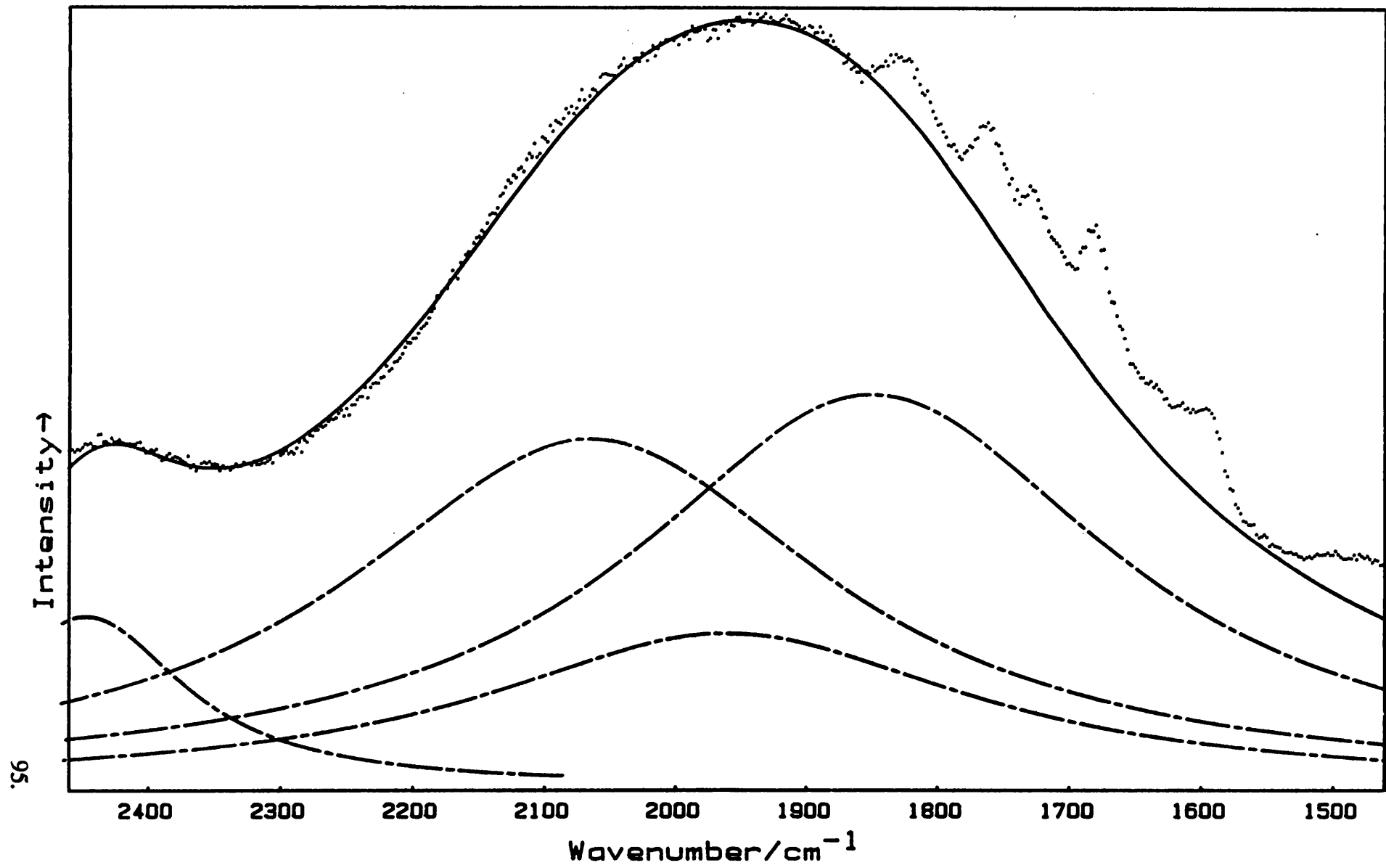
Figure 3.1.3

Simulation of the ${}^3E_g \leftarrow {}^3A_g$ Electronic Raman transition found for RbVSH. Spectrum recorded at 82 K with $A_g + E_g$ activity.

The transition energies of the spin-orbit coupled components are fixed at the values given in figure 3.1.1 which are obtained from a trigonal field splitting of 1940 cm^{-1} .

Peak Positions and Parameters

PEAK POSITION	HEIGHT (0 - 100)	LORENZIAN (100)/ GAUSSIAN (0) MIX	FULL WIDTH HALF HEIGHT	RELATIVE AREAS	ASSIGNMENT
1847 cm^{-1}	71	100	450	34010	Spin-orbit coupled components of ${}^3E_g \leftarrow {}^3A_g$ electronic Raman transition.
1956 cm^{-1}	28	100	450	13410	
2059 cm^{-1}	63	100	450	30180	
2446 cm^{-1}	31	100	180	5940	$\nu_2(\text{HOH}) + \nu_L$



95

3.2 Electronic Structure of $[V(OH_2)_6]^{3+}$ within the mixed alum system $Rb\{Ga/V\}(SO_4)_2 \cdot 12H_2O$

Raman studies presented in the previous chapter indicate that the RbVSH alum is of the β modification. This classification is supported by recent crystallographic data⁹ which indicates that KVSH also crystallises in the β modification. In the previous chapter it was suggested that the mode of water co-ordination in the β compared to the α alums leads to greater trigonal field stabilisation of the $[V(OH_2)_6]^{3+}$ cation. This section reports attempts to perturb the hydration structure whilst monitoring the electronic structure of the $[V(OH_2)_6]^{3+}$ cation.

Mixed alums of the type $Rb\{Ga/V\}(SO_4)_2 \cdot 12H_2O$, with differing proportions of gallium and vanadium, have been synthesised and characterised by Raman spectroscopy. The α alum of RbGaSH was chosen since it has no electronic absorption in the visible and its metal(III)-oxygen bond length is expected to be close to that of the vanadium metal(III)-oxygen bond length in RbVSH. Metal(III)-oxygen bond lengths for vanadium and gallium in the $CsM^{III}SO_4 \cdot 12H_2O$ series are quoted as 1.992 (6) V¹⁰ and 1.944 (3) Ga.¹⁰

i) Preparation of mixed crystals of Rb(Ga/V)SH

Mixed crystals containing the α alum RbGaSH and the β alum RbVSH were prepared either by using the single crystal growing apparatus described in section 2.4, or by dissolving varying amounts of the two alums in sulphuric acid (1 mol dm⁻³) and allowing the alums to co-crystallise at room temperature. Using the latter method, large, deep blue single crystals of the β type were made with vanadium concentrations greater than 25% of the total trivalent cation content. The largest and best quality single crystals were made by using between 10 and 12 cm³ of solvent to three grams of alum. Some of these crystals were cut and polished for single crystal Raman experiments. The concentration of these mixed crystals were determined by Inductively coupled plasma-Atomic Emission spectroscopy (ICP-AES) which is described in Appendix B. It was found that the relative concentration of V and Ga found in the crystals was identical to that found in the bulk solution for all the mixed

alums of the β type made.

With vanadium concentrations $< 20\%$ of the total concentration of trivalent cation present within the bulk solution, mixed alums of the α type are formed, green in colour, though with concentrations of vanadium less than that of the bulk solution. Mixed alums of the α type are also formed for vanadium concentrations between 25 and 40 % with solute/solvent ratios an order of magnitude greater than was used to produce the β alums. Again, the vanadium concentration of the α alums formed was less than that of the bulk solution. The largest vanadium concentration found for any of these vanadium crystals was 20 %.

The solute/solvent ratio has a profound influence on which alum modification is the first to crystallise. Using 12 cm^3 of solvent to 3 grams of alum, β crystals could be made with vanadium concentrations of 20%. These crystals were not thermodynamically stable however, and when disturbed, underwent a phase transition to the α modification. Likewise, α crystals at high vanadium concentrations were seen to undergo a phase change to the β modification over a period of time, the speed at which this occurs depends on the vanadium concentration. After first turning from clear to cloudy, different parts of these crystals were seen to turn blue whereas other parts remained green.

Crystals prepared using the single crystal growing apparatus were of better quality. However, far less control over the composition of the crystals was achieved using this method. Mixed crystals of the α type could be prepared only with vanadium concentrations as high as 6% of the total trivalent cation composition. However only the mixed α crystals prepared by this method were of sufficient quality for single crystal Raman experiments. Photographs of mixed crystals of $\text{Rb}(\text{Ga/V})\text{SH}$ are shown in figures 3.2.1 - 3.2.2.

Figure 3.2.1

Photographs of alum crystals grown using the single crystal growing apparatus described in section 2.4. The crystal on the right is the deep blue crystal of the β alum, RbVSH. The crystal on the left is the green crystal of V^{3+} doped into the α crystal, RbGaSH.

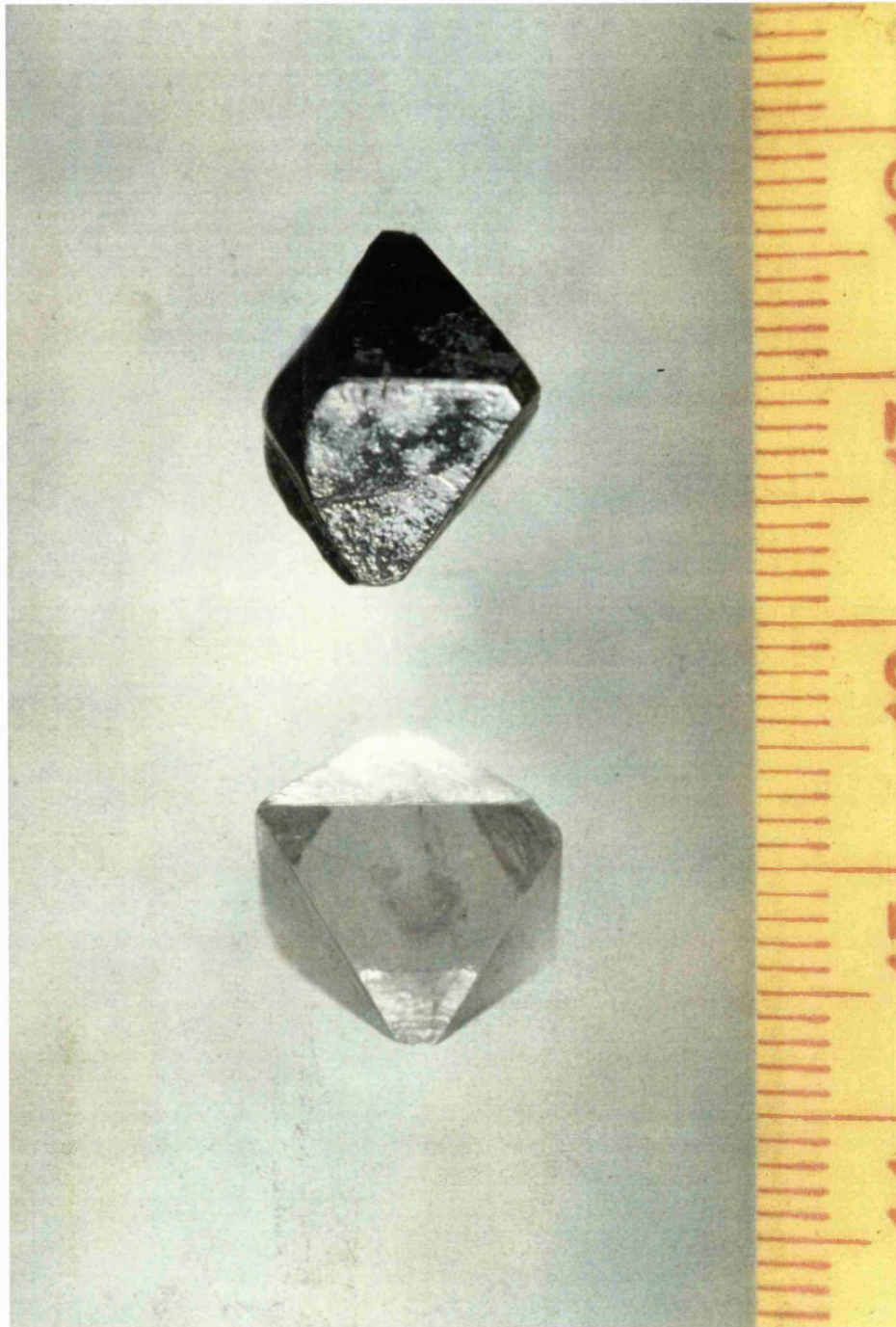


Figure 3.2.2

Photographs of alum crystals made by dissolving 2 g of RbVSH with 4 g of RbGaSH in 8 ml sulphuric acid (1 mol dm^{-3}) and allowing the alums to co-crystallise at room temperature. The crystals are of the α modification. This photograph was taken ca. 1 year after the crystals were made during which time, areas of purple colouration have appeared in the otherwise predominately green crystals. The colour change is interpreted in terms of a localised phase transformation from the α to the β modification.



ii) Electronic Spectra

The electronic spectra, recorded at room temperature, of the α Rb{Ga/V}SH mixed alum containing 6% V and a β Rb{Ga/V}SH mixed alum containing 25 % V are both shown in figure 3.2.3.

A correlation diagram for a first row d^2 transition metal complex in an octahedral field is shown in figure 3.2.4. Two band maxima are observed in the visible region for both electronic spectra presented in figure 3.2.3. These band maxima correlate in octahedral symmetry to the $T_{1g} \rightarrow T_{2g}$ and $T_{1g} \rightarrow T_{1g}(P)$ transitions, in order of increasing energy.

The peak positions for the β alum occur, within experimental error, at the same wavelength as those reported for NH_4VSH .¹² It is well established that the electronic spectrum of a complex is very sensitive to any changes in the metal-ligand bond length.⁸ Thus, the electronic spectrum suggest that the local environment about vanadium(III) changes little from RbVSH to the formation of mixed Rb(Ga/V)SH β alums.

The d-d transitions occur above a sloping baseline. This is probably due to a background peak which occurs in the u.v and whose wing extends into the visible. Such a background peak has been observed in the electronic spectra of "mixed" alums for various other transition metals.¹³ The origin of this peak is yet to be established. It has been shown, however, that the position of the peak is independent of the dopant transition metal(III) cation suggesting that the origin of the peak is a consequence of defects within the lattice rather than on the electronic structure of the cation. The Peak maxima occur at 25800 and 17700 cm^{-1} for the β alum and at 25100 and 16800 cm^{-1} for the α alum. With the two transitions assigned as the $T_{1g} \rightarrow T_{2g}$ and $T_{1g} \rightarrow T_{1g}(P)$ transitions, values of 10Dq and B, the Racah parameter, are calculated as 10Dq = 19040 cm^{-1} , B = 624 cm^{-1} for the β alum and 10Dq = 18090 cm^{-1} , B = 646 cm^{-1} for the α alum. These values could be interpreted in terms of greater delocalisation of electron density onto the water ligand for the β compared to the α alum. However, in view of the large trigonal distortion from octahedral symmetry (for the β alums at least) only a ligand field analysis such as that undertaken by Hitchman *et al.*⁷ is appropriate.

Figure 3.2.3

Single crystal electronic spectra, recorded at room temperature, of an α Rb(Ga/V)SH mixed alum containing 6% V and a β Rb(Ga/V)SH mixed alum containing 25% V. The spectra have been appropriately scaled relative to the spectral frame.

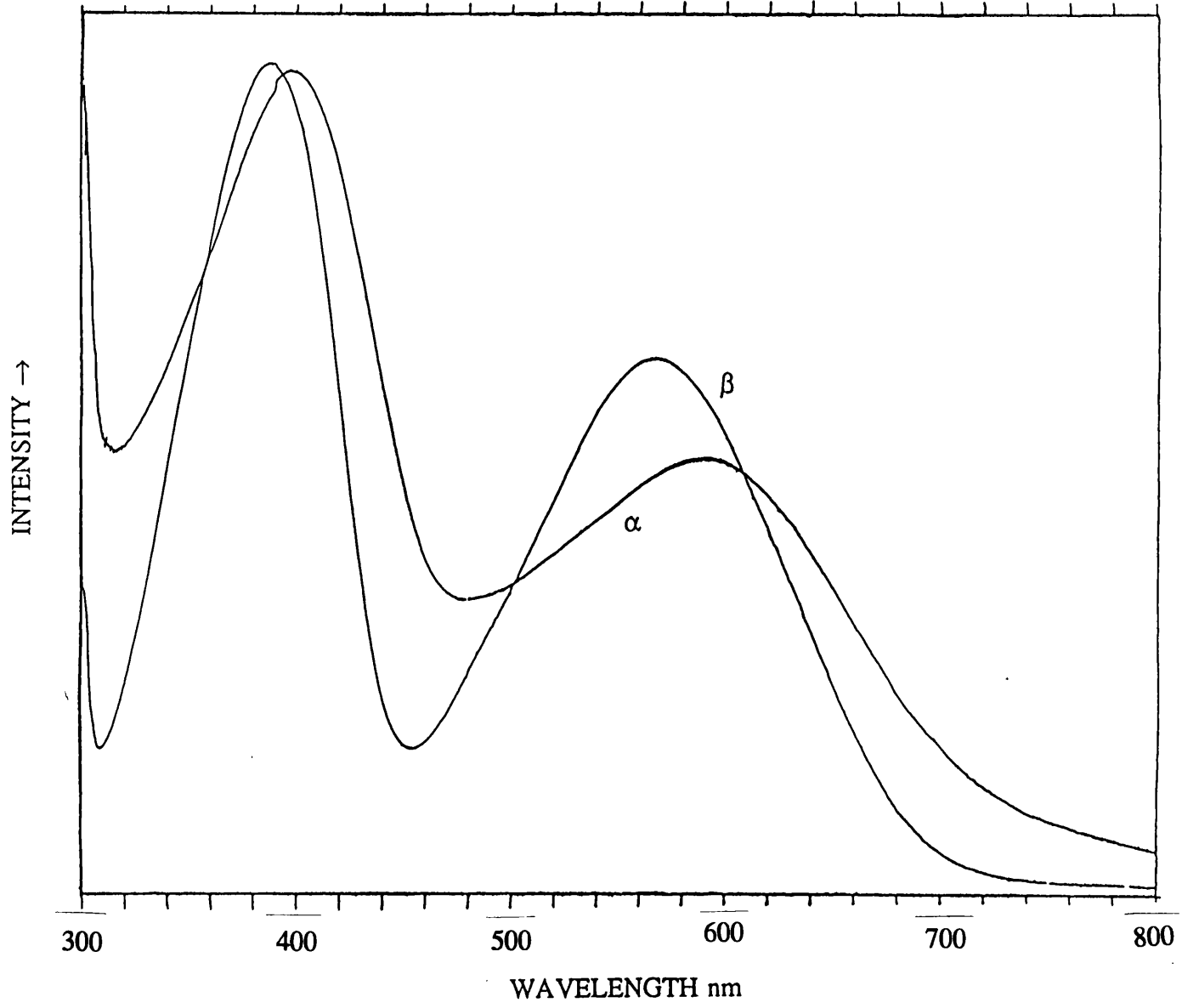
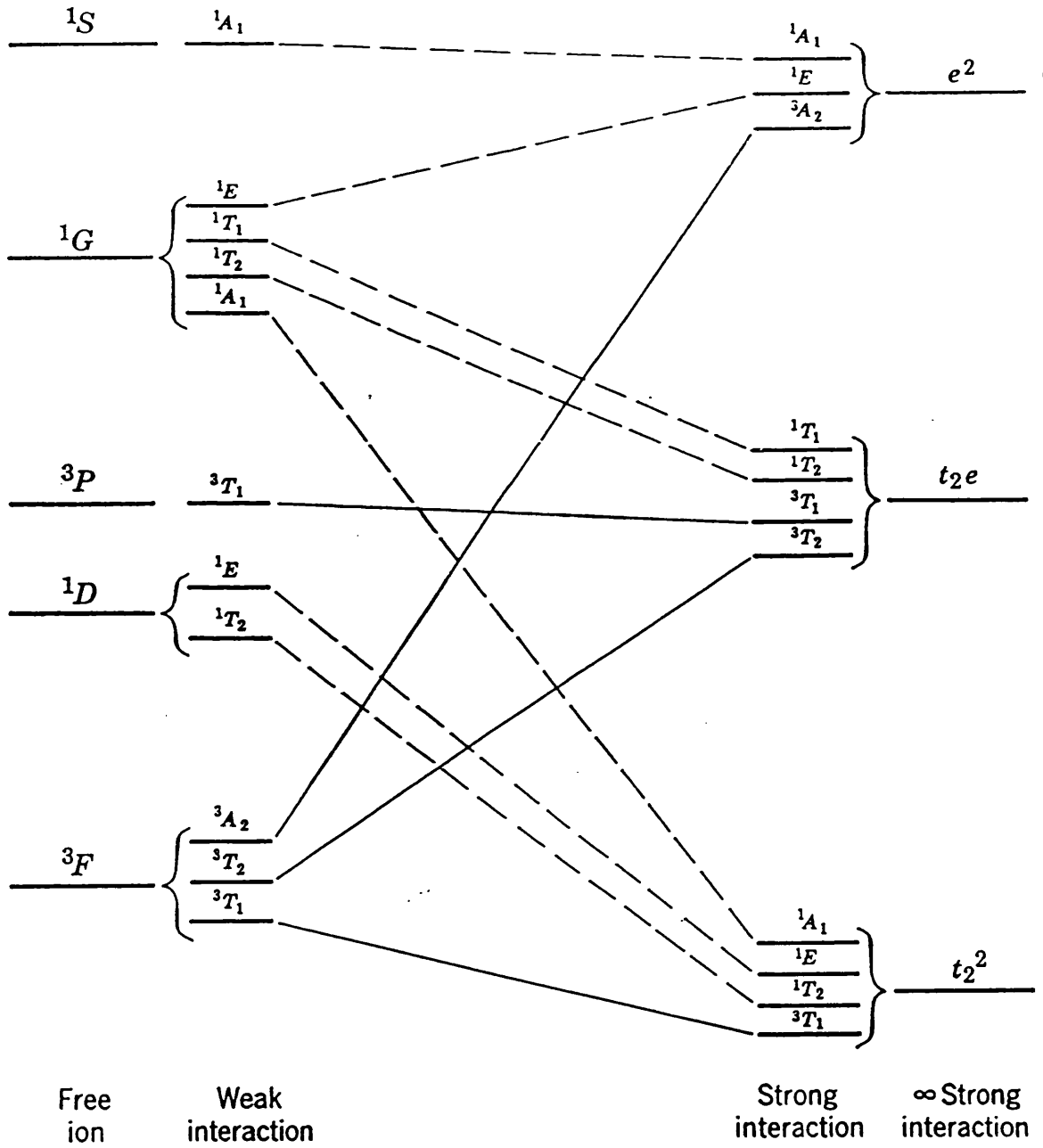


Figure 3.2.4

A correlation diagram for a d^2 ion in an octahedral environment. All states of g type, and this subscript has therefore been omitted. (After F. A. Cotton [11])



iii) Raman Spectra

The Raman spectra of the mixed Rb{Ga/V}SH β alums are all analogous to that of RbVSH. For this reason, only one set of spectra is presented (figures 3.2.5 - 3.2.7). The spectra of " β mix45" were obtained from a mixed alum of the type Rb{Ga/V}SH which crystallises in the β modification and was found by ICP-AES measurements to contain 45.5% (1) V and 54.5% (1) Ga of the total amount of trivalent cation present within the alum.

Both the low and the mid wavenumber spectra of β mix45 are very similar to that of RbVSH, suggesting that with this level of dilution with gallium(III), there are no major structural perturbations of the RbVSH lattice. There are some differences in the relative intensities of the bands in the two spectra. This is most noticeable in the F_g spectra where the number of modes is greatest.

The $\nu_1(\text{MO}_6)$ region, for the spectrum with A_g and E_g activity, is shown in figure 3.2.8. Raman bands at 535 and 565 cm^{-1} are bands of E_g symmetry assigned to ρ_6 and ρ_5 respectively. Two more bands, which are of A_g symmetry are present in the spectrum. These bands occur at 529 and 538 cm^{-1} . The position of these bands are practically coincident with $\nu_1(\text{VO}_6)$ (531 cm^{-1}) and $\nu_1(\text{GaO}_6)$ (538 cm^{-1}) in the RbVSH and RbGaSH alums respectively. The intensity of a band is proportional to its area and is obtained from the equation:¹⁴

$$AREA = \frac{a\pi IW}{2} + \frac{(1-a)\sqrt{\pi/\ln 2}IW}{2}$$

3.2.1

where:

I = maximum band height

a = Lorentzian / Gaussian mixture

W = full width at half height

where $0 \leq a \leq 1$

The ratio of the intensities of $\nu_1(\text{VO}_6) / \nu_1(\text{GaO}_6)$ in the caesium alum study was found to be 0.82.¹⁴ This value was obtained by comparison of the intensity of $\nu_1(\text{MO}_6)$ with that of $\nu_1(\text{SO}_4)$ which was assumed to occur with the same intensity for all the caesium alums studied. The ratio of the intensities of the bands found at 529

Table 3.2.1

Vibrational frequencies and assignments for " β 45mix",
between 20 and 275 cm^{-1} .

ν/cm^{-1}		X'(Z Z)Y'	X'(Y'X')Y'	X'(Z X')Y'	assignment
46	E_g	166	130	sh	tr (SO_4^{2-}) + rot (SO_4^{2-})
51	F_g			7	
62	F_g			17	
69	F_g			34	
70	E_g	149	134		
82	$E_g?$	sh	sh	1	
94	A_g	25			
100	E_g	10	15		
106	E_g	10	15		rot [$\text{Rb}(\text{OH}_2)_6$] ⁺
137	E_g	66	88		rot [$\text{V}(\text{OH}_2)_6$] ³⁺
143?	A_g	7			
151	A_g	28			
162	A_g (+ $F_g?$)	159	7	5	
176	A_g	31			
180	F_g			16	
190	E_g	95	103		ν_5 [$\text{Rb}(\text{OH}_2)_6$] ⁺
190	F_g			62	
208	F_g			42	
210	E_g	548	703		ν_2 [$\text{Rb}(\text{OH}_2)_6$] ⁺
211	F_g			58	
220	F_g		sh	58	
245	A_g	74	2	2	ν_1 [$\text{Rb}(\text{OH}_2)_6$] ⁺

Figure 3.2.5

Single crystal Raman spectra of $\text{Rb}\{\text{V}/\text{Ga}\}(\text{SO}_4)_2 \cdot 12\text{H}_2\text{O}$ between 10 and 300 cm^{-1} . Tervalent cation content from analysis: 45.5(1) % V and 54.5(1) % Ga. Sensitivities: X'(Z Z) Y' 4270 counts sec^{-1} ; X'(Y'X') Y' 3864 counts sec^{-1} ; X'(Z X') Y' 569 counts sec^{-1} (79 (6) K step size 0.4 cm^{-1} ; spectral bandwidth 2.32 cm^{-1} at 150 cm^{-1} ; integration time 4 seconds; 457 nm radiation, 40 mw power at sample).

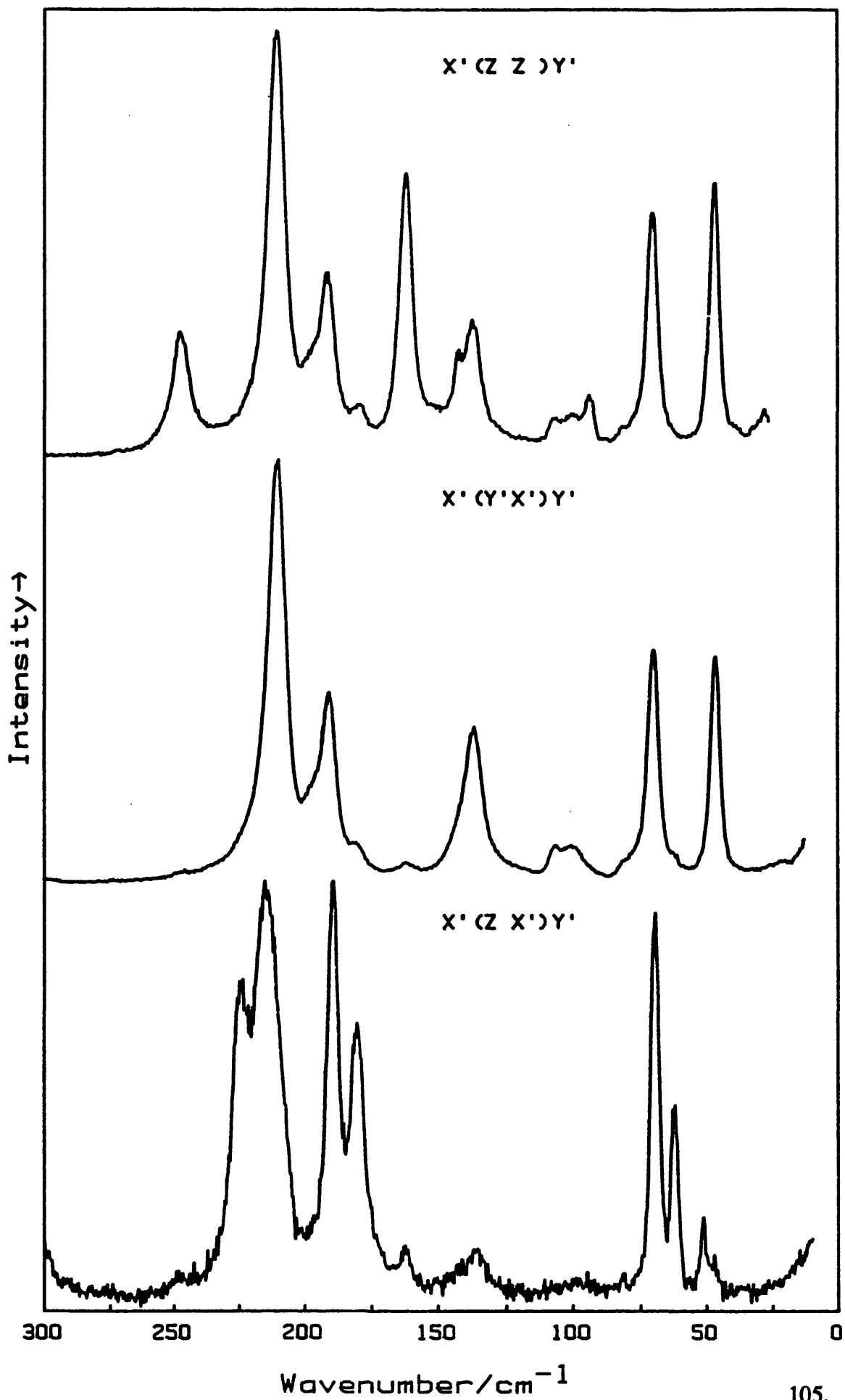


Table 3.2.2

Vibrational Frequencies and assignments for "βmix45";
between 275 and 1200 cm⁻¹.

v/cm ⁻¹		X'(Z Z)Y'	X'(Y'X')Y'	X'(Z X')Y'	assignment
309	F _g			29	v ₅ (MO ₆)
312	E _g	10	19		
319	?	sh	sh	sh	
339	F _g	2	6	15	
431	E _g	145	151		v ₂ (SO ₄ ²⁻) + v ₂ VO ₆
434	F _g	sh	sh	90	
461	F _g		sh	46	
473	E _g	89	108	17	
478	A _g ?	sh			
529	A _g	45			v ₁ (MO ₆)
538	A _g	169			
535	E _g	?	33		ρ ₆
535	F _g			12	
565	E _g	52	38	1	ρ ₅
577	F _g ?			1	
607	F _g		sh	31	v ₄ (SO ₄)
624	E _g	74	97		
625	F _g			35	
680	E _g	41	31	1	ρ ₄
729	F _g			4	ρ ₃
749	F _g			4	
754	E _g	46	58		
796	E _g ?	3	2		
878	E _g (+A _g ?)	22	12		ρ ₂
894	F _g	sh	sh	4	
950	E _g (+A _g)	sh	8		ρ ₁
972	A _g	55			v ₁ (S ¹⁶ O ₃ ¹⁸ O) v ₁ (SO ₄)
988	A _g	5364	203	49	
1088	F _g		29	61	v ₃ (SO ₄)
1093	E _g	25	17		
1099	F _g			15	

Figure 3.2.6

Single crystal Raman spectra of $\text{Rb}\{\text{V}/\text{Ga}\}(\text{SO}_4)_2 \cdot 12\text{H}_2\text{O}$ between 275 and 1200 cm^{-1} . Tervalent cation content from analysis:- 45.5(1) % V and 54.5(1) % Ga. Sensitivities: X'(Z Z)Y' 82323 counts sec^{-1} ; X'(Y'X')Y' 2333 counts sec^{-1} ; X'(Z X') Y' 1849 counts sec^{-1} (79 (6) K; step size 0.4 cm^{-1} ; spectral bandwidth 2.22 cm^{-1} at 600 cm^{-1} ; integration time 4 seconds; 457 nm radiation, 40 mw power at sample).

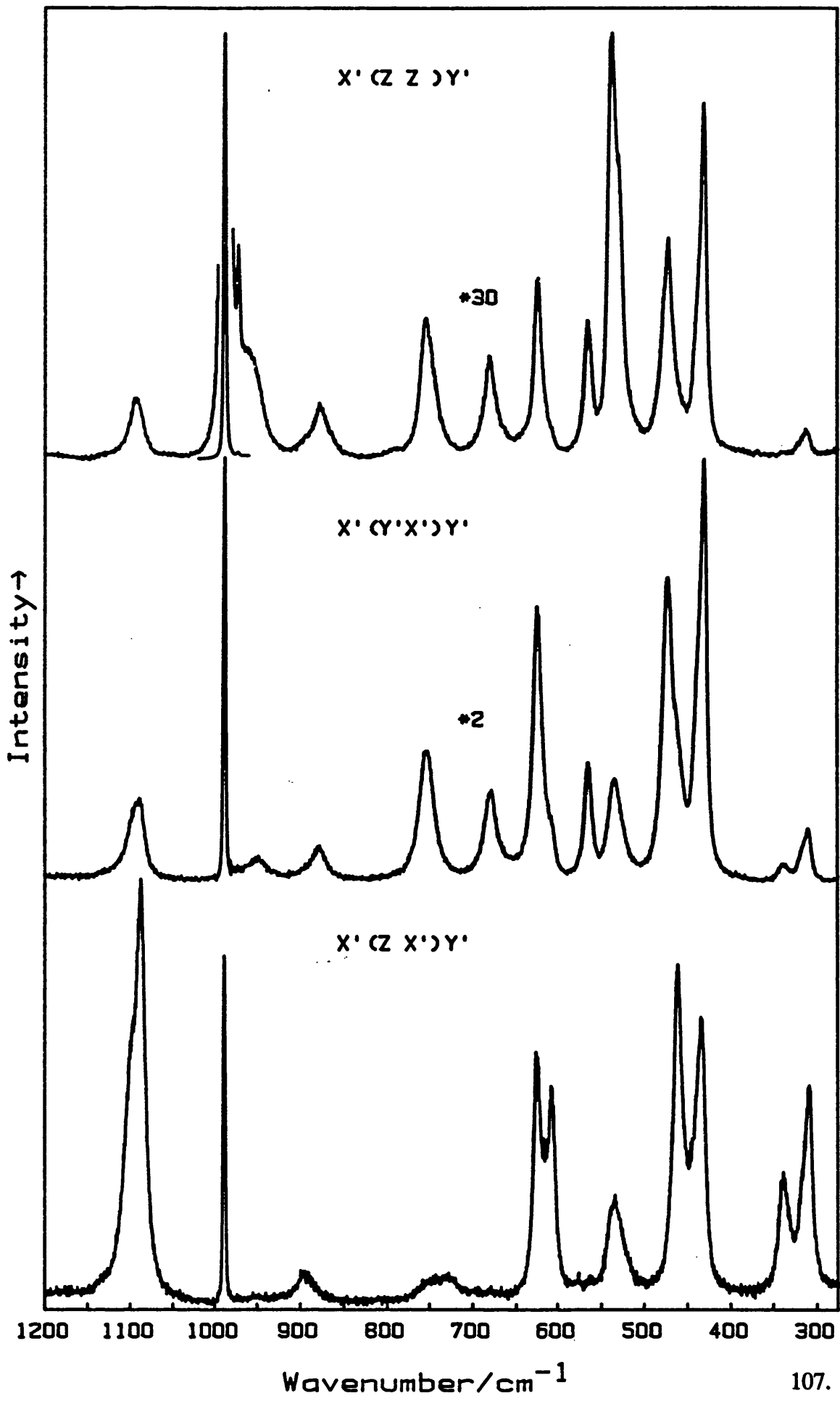


Figure 3.2.7

Single crystal Raman spectra of $\text{Rb}\{\text{V}/\text{Ga}\}(\text{SO}_4)_2 \cdot 12\text{H}_2\text{O}$ β alum between 1200 and 4000 cm^{-1} . Tervalent cation content from analysis:- 45.5(1) % V and 54.5(1) % Ga. Sensitivities: $X'(Z Z)Y'$ 17531 counts sec^{-1} ; $X'(Y'X')Y'$ 6609 counts sec^{-1} ; $X'(Z X')Y'$ 5849 counts sec^{-1} (79 (6) K; step size 1 cm^{-1} ; spectral bandwidth 3.58 cm^{-1} at 2600 cm^{-1} ; integration time 4 seconds; 457 nm radiation, 40 mw power at sample).

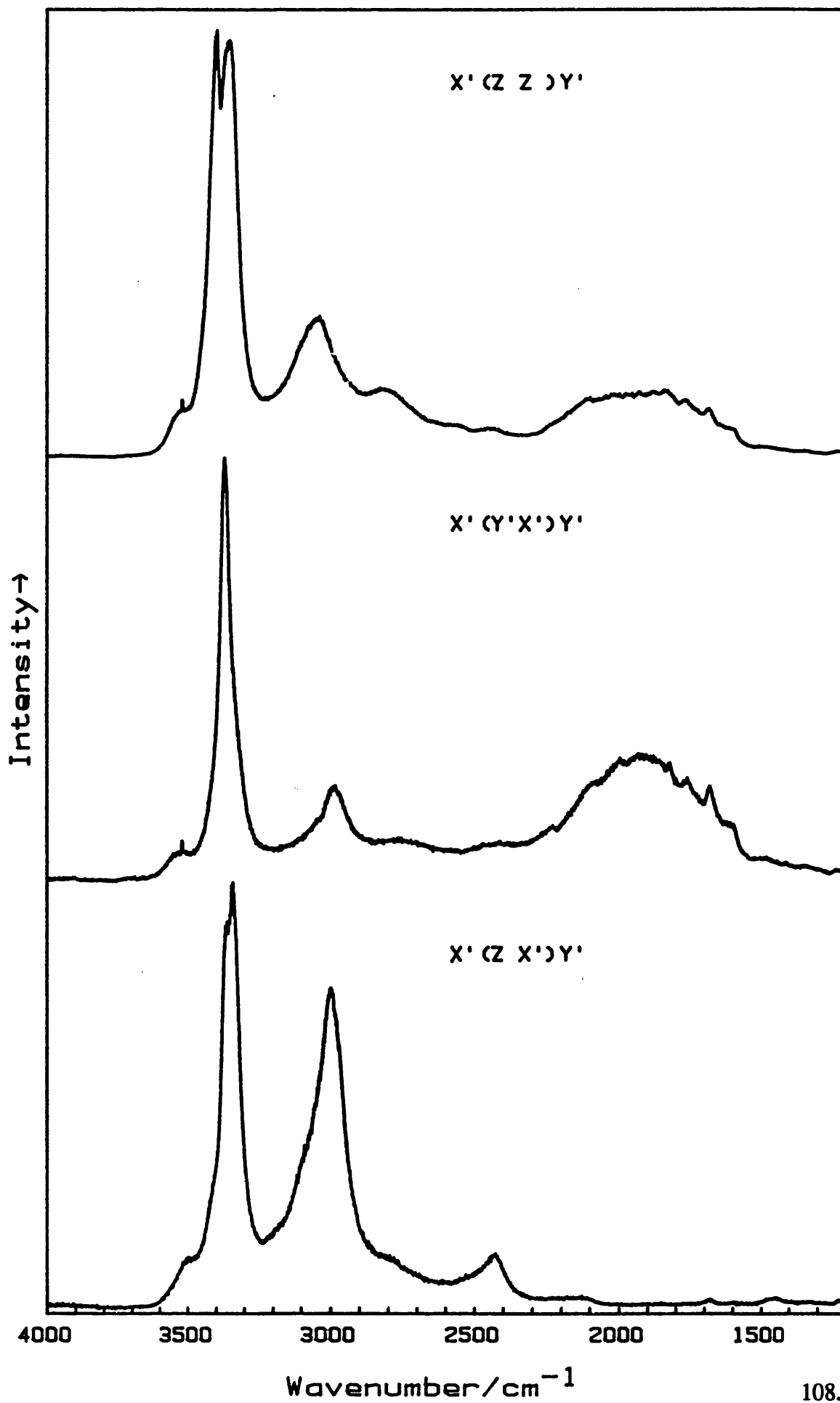
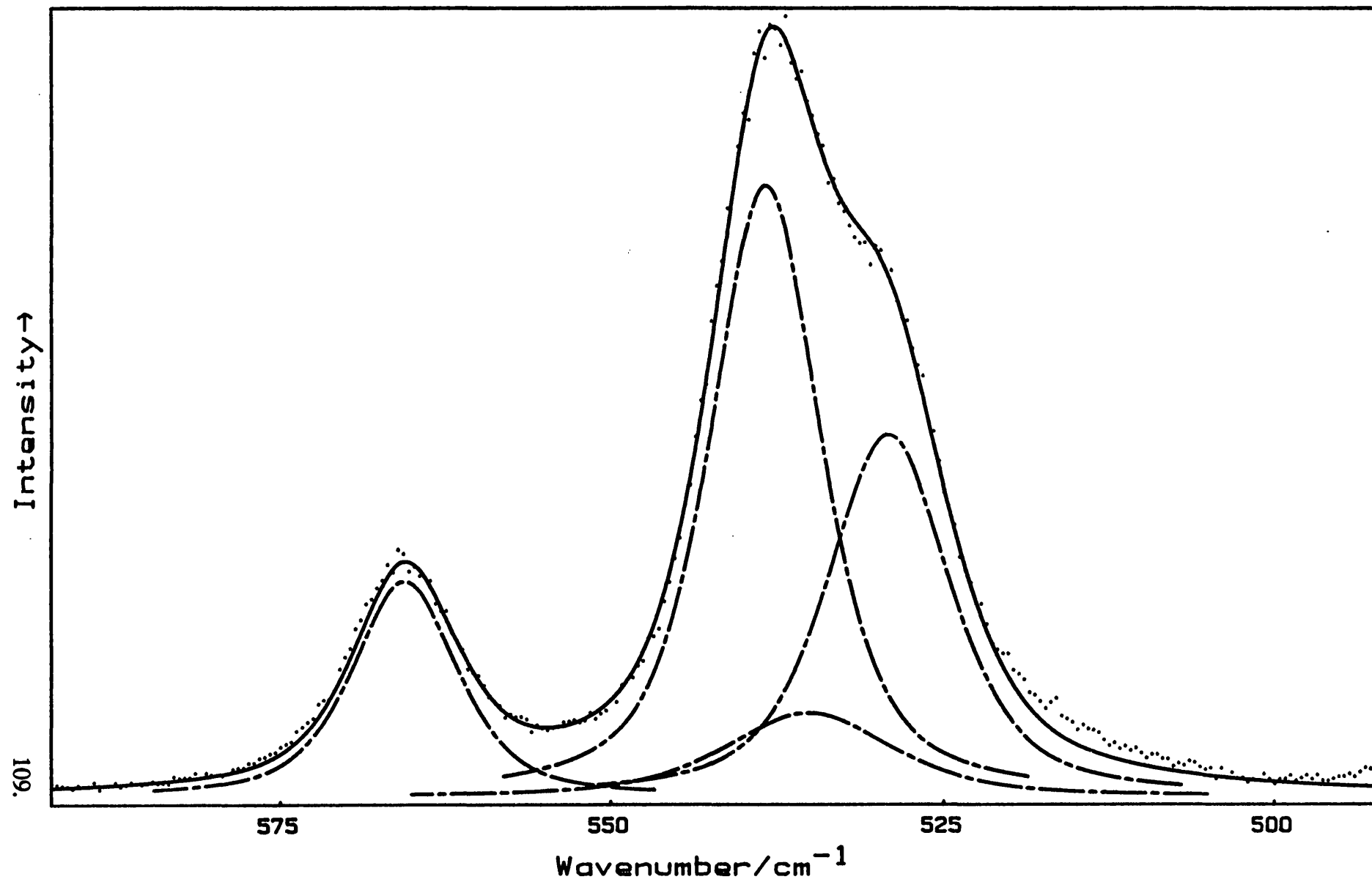


Figure 3.2.8

$\nu_1\text{MO}_6$ region of the $\text{RbV/Ga}(\text{SO}_4)_2 \cdot 12\text{H}_2\text{O}$ "βmix45" extracted from figure. 3.2.6 Tervalent cation content from analysis:- 45.5(1) % V and 54.5(1) % Ga.

Peak Positions and Parameters

PEAK POSITION	HEIGHT (0 - 100)	LORENZIAN (100)/ GAUSSIAN (0) MIX	FULL WIDTH HALF HEIGHT	RELATIVE AREAS	ASSIGNMENT
529 cm^{-1}	47	60	11	655	$\nu_1\text{VO}_6$
535 cm^{-1}	11	60	15	209	ρ_6
538 cm^{-1}	79	60	9.9	991	$\nu_1\text{GaO}_6$
565 cm^{-1}	28	60	9.4	333	ρ_5



and 538 cm^{-1} is 0.66. The calculated ratio of intensities $\nu_1(\text{VO}_6) / \nu_1(\text{GaO}_6)$ for the " β 45mix" crystal, assuming negligible coupling between the $\nu_1\text{MO}_6$ modes is $0.82 \times 45.5 / 54.5 = 0.68$. The $\nu_1(\text{MO}_6)$ region for a mixed $\text{Rb}\{\text{Ga/V}\}\text{SH}$ alum containing 25.3 (2) % V and 74.7 (2) % Ga is shown in figure 3.2.9. The ratio of the intensities of the bands found at 529 and 540 cm^{-1} in this alum = 0.30. The calculated ratio of intensities for $\nu_1(\text{VO}_6) / \nu_1(\text{GaO}_6)$ calculated in the same way as before = 0.28. These results strongly suggest that within this mixed alum, rather than there being a homogeneous metal(III)-water bond distance; the metal(III)-water distance for vanadium and gallium are not significantly different from what they are in the respective pure alums. Further, it is inferred that there is negligible coupling between the $\nu_1(\text{VO}_6)$ and $\nu_1(\text{GaO}_6)$ modes. This may not be surprising in view of the F_g component of $\nu_1(\text{MO}_6)$, which arises purely from factor group coupling, being vanishingly weak in the Raman spectra of all the alums so far studied. One A_g component is also expected for both ρ_6 and ρ_5 . The A_g component for these bands were found to be vanishingly weak in the spectra of RbVSH . It is presumed that this is also the case in the β mixed $\text{Rb}\{\text{Ga/V}\}\text{SH}$ alums.

The high wavenumber spectra show the position of the electronic Raman band to be unchanged from its position in RbVSH suggesting that there is little difference in the immediate environment about vanadium(III) in the " β mix45" and RbVSH alums. Figures 3.2.10 (b) shows the $\nu_3\text{SO}_4$ band for mixed alums of the type $\text{Rb}\{\text{Ga/V}\}\text{SH}$ and $\text{Cs}\{\text{Ga/V}\}\text{SH}$ for differing amounts of gallium and vanadium determined by ICP-AES. Figure 3.2.10 (a) shows the high wavenumber region for these alums. These results clearly show that for vanadium(III) concentrations $\geq 25\%$ of the total amount of trivalent cation, alums of the type $\text{Rb}\{\text{Ga/V}\}\text{SH}$ crystallise in the β alum modification. For all these mixed β alums, the position of the electronic Raman band remains unchanged from that found in RbVSH .

The $\text{Rb}\{\text{Ga/V}\}\text{SH}$ alum containing 6% vanadium crystallises in the α modification. A band resembling an electronic Raman band is not found in the high wavenumber region for this alum. This might be due to a significant change in the electronic structure of the $[\text{V}(\text{OH}_2)_6]^{3+}$ cation or else it may be a consequence of having too little vanadium in the alum; i.e an electronic Raman band could be present in this spectral region but is too weak to be observed. This problem is to some extent

Figure 3.2.9

$\nu_1\text{MO}_6$ region of $\text{RbV/Ga}(\text{SO}_4)_2 \cdot 12\text{H}_2\text{O}$ alum. Tervalent cation content from analysis:- 25.3 (2) % V and 74.7 (2) % Ga.

Peak Positions and Parameters

PEAK POSITION	HEIGHT (0 - 100)	LORENZIAN (100)/ GAUSSIAN (0) MIX	FULL WIDTH HALF HEIGHT	RELATIVE AREAS	ASSIGNMENT
529 cm^{-1}	23	60	10	291	$\nu_1\text{VO}_6$
535 cm^{-1}	16	60	10	101	ρ_6
540 cm^{-1}	88	60	8.6	959	$\nu_1\text{GaO}_6$
565 cm^{-1}	32	60	7.4	150	ρ_5

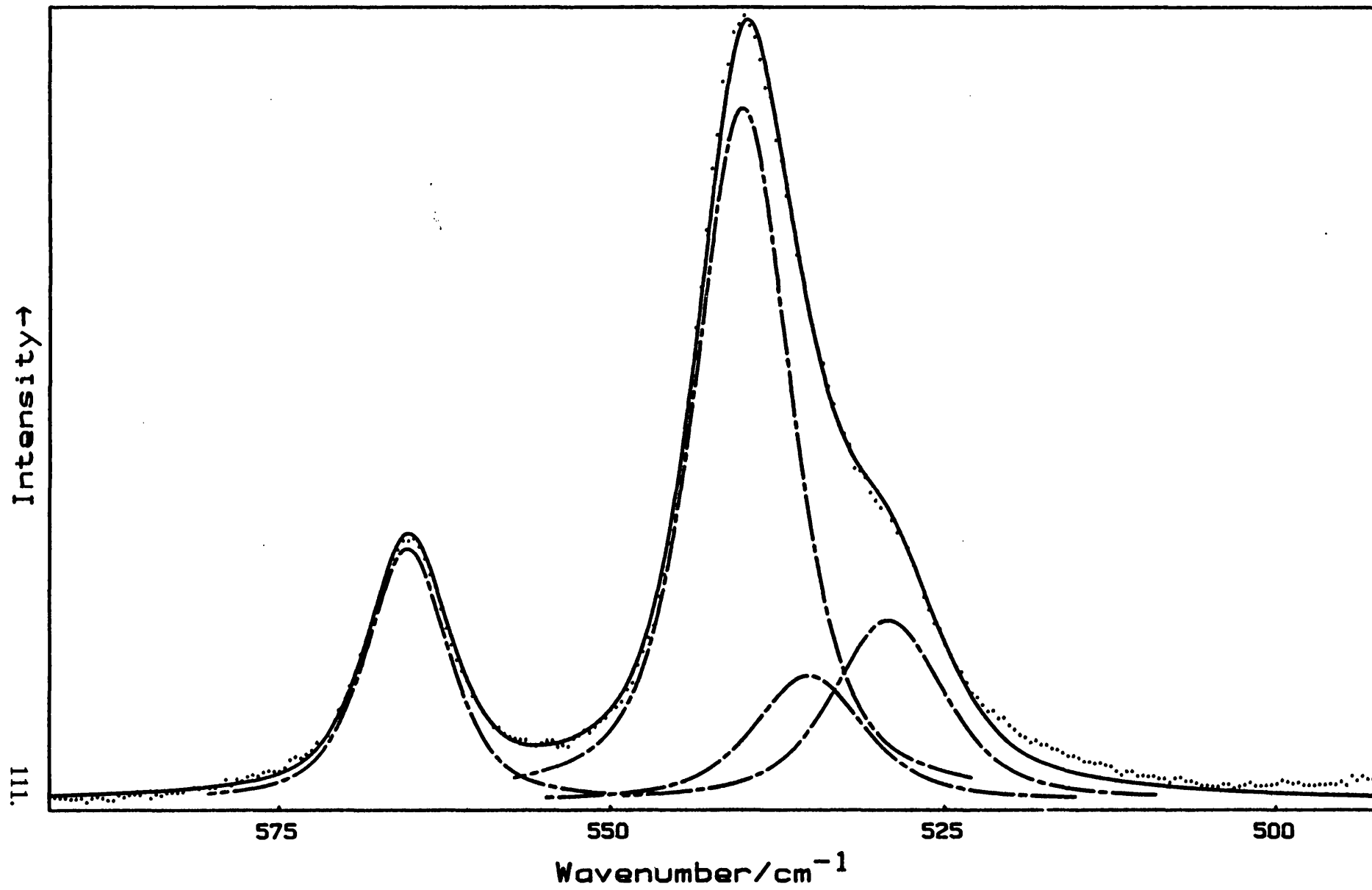
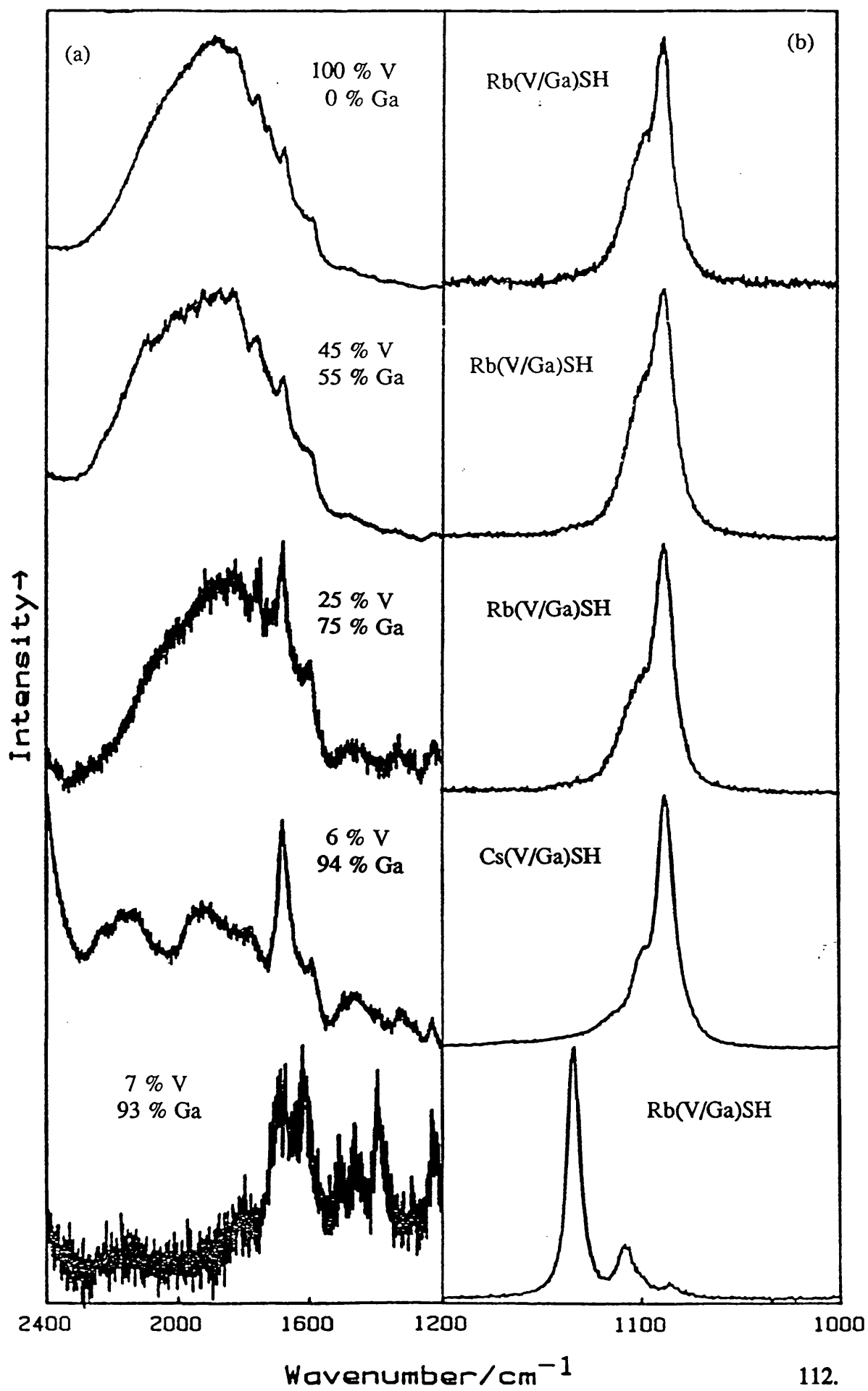


Figure 3.2.10

Single crystal Raman spectra of various $M^I\{Ga/V\}SH$ alums of differing trivalent cation composition.

(a) Spectra of $A_g + E_g$ activity showing the region containing the electronic Raman transition.

(b) Spectra of F_g activity showing region containing $\nu_3(SO_4)^{2-}$.



resolved from the spectra of the β , Cs{Ga/V}SH mixed alum where the vanadium(III) concentration is of a similar magnitude to that found in the α Rb{Ga/V}SH mixed alum. The high wavenumber spectra show a broad band centred at *ca.* 1950 cm^{-1} . Although the band is comparable in intensity to nearby vibrational bands, it is not found in the spectra of the pure alum.¹⁴ It is likely, therefore, that the band originates from the ${}^3E_g \leftarrow {}^3A_g$ vanadium(III) electronic transition. On this evidence it is concluded that the absence of the electronic Raman band for vanadium(III) in an α environment is a consequence of a change in the electronic structure of vanadium(III) on change of alum modification.

The spectra of the Rb{Ga/V}(SO₄).12H₂O alum containing 6% vanadium in the spectral region -100 to 100 cm^{-1} are shown in figure 3.2.11. The lattice modes in this region occur above a background peak. Usually this background can simply be attributed to Rayleigh scattering. The extent of the Rayleigh wing is usually associated with crystal quality. However, the Rayleigh line is symmetric about the exciting line and the intensity of the Rayleigh wing should fall off with increasing wavenumber to the same extent either side of the exciting line. The spectra suggest that there may be additional broad band(s) occurring in this spectral region. These band(s) will occur with greater intensity on the Stokes than the anti-Stokes side of the exciting line. This would be consistent with the greater 'background' intensity in the Stokes side of the spectrum than the anti-stokes side. This is most apparent in the X'(Y'X')Y' scattering experiment showing bands of E_g symmetry. This result is reproducible on change of exciting line (figure 3.2.12 (a)). A variable temperature EPR study of [Cr(OH₂)₆]³⁺ doped into various alum lattices¹⁵ has revealed that the sign of the zero field splitting parameter is negative for the β alums and positive for the α alums. This indicates that for [Cr(OH₂)₆]³⁺ dopant cations, the trigonal field in the α alums is opposite in sign from the β alums.¹⁶ If we assume that the [V(OH₂)₆]³⁺ cation has trigonal symmetry in this environment then electronic bands occurring below 100 cm^{-1} arising from transitions between spin-orbit coupled states can be accounted for by a model in which the trigonal field is less than 50 cm^{-1} with the 3E_g term lowest lying. Table 3.2.3 shows the energy of the spin-orbit states relative to the unperturbed cubic ${}^3T_{1g}$ term for various values of the trigonal field. Although a small trigonal field would leave two spin-orbit states < 100 cm^{-1} above the ground state,

Figure 3.2.11

Single crystal Raman spectra of α RbV/Ga(SO₄)₂·12H₂O alum between -100 and 100 cm⁻¹. Tervalent cation content from analysis: 6.6(6) % V and 93.4(6) % Ga. Sensitivities: X'(Z Z)Y' 1636 counts sec⁻¹; X'(Y'X')Y' 1468 counts sec⁻¹; X'(Z X') Y' 514 counts sec⁻¹ (67 (2) K; step size 0.4 cm⁻¹; spectral bandwidth 2.73 cm⁻¹ at 0 cm⁻¹; integration time 3 seconds; 488 nm radiation, 40 mw power at sample).

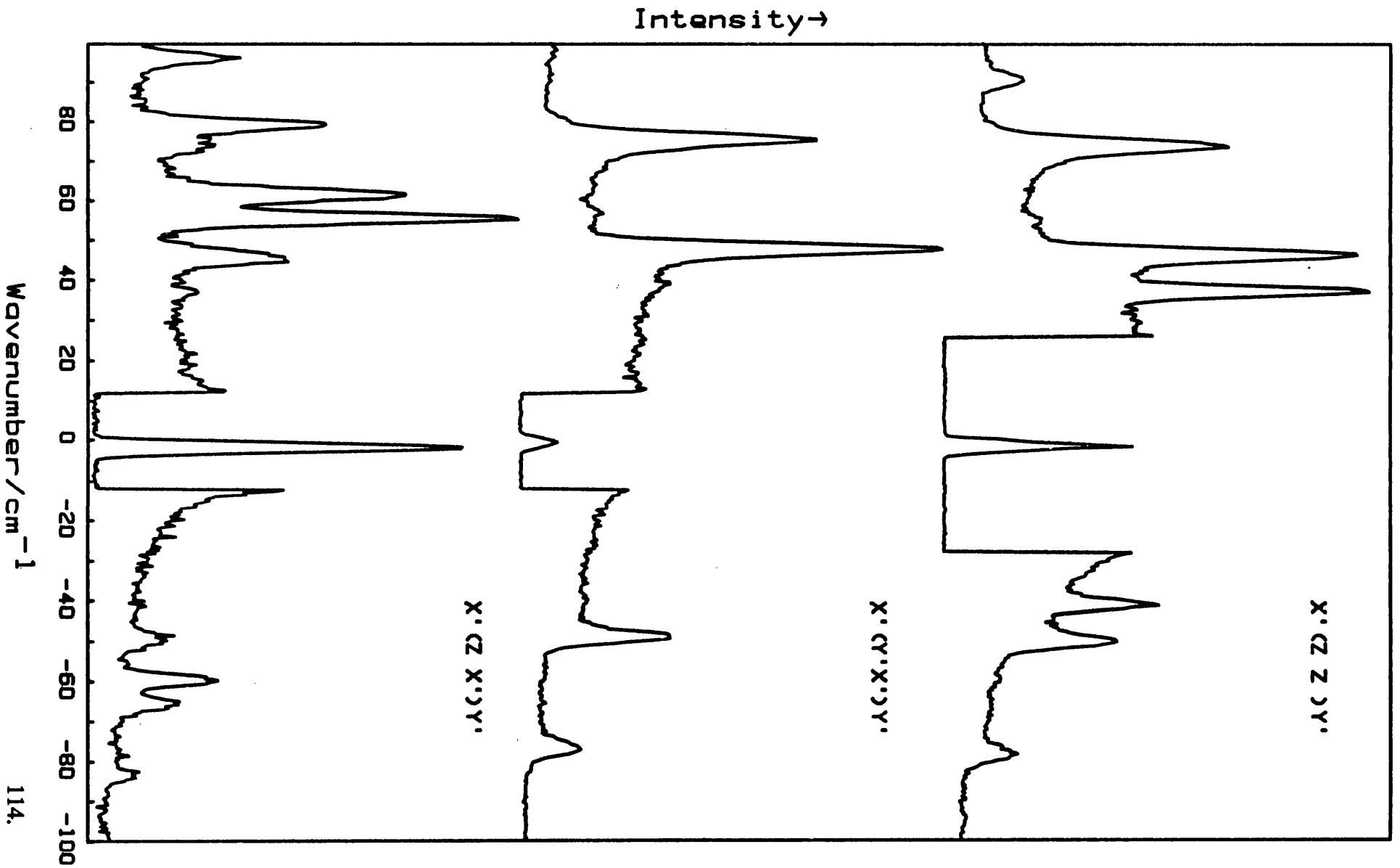


Figure 3.2.12

Single Crystal Raman Spectra between -100 and 100 cm^{-1} showing bands of $A_g + E_g$ activity for:-

- (a) α RbV/Ga(SO₄)₂.12H₂O alum. Tervalent cation content from analysis:- 6.6(6) % V and 93.4(6) % Ga. 406.74 nm excitation.**
- (b) RbV(SO₄)₂.12H₂O alum. 457.94 nm excitation.**
- (c) RbGa(SO₄)₂.12H₂O alum. 514.53 nm excitation**

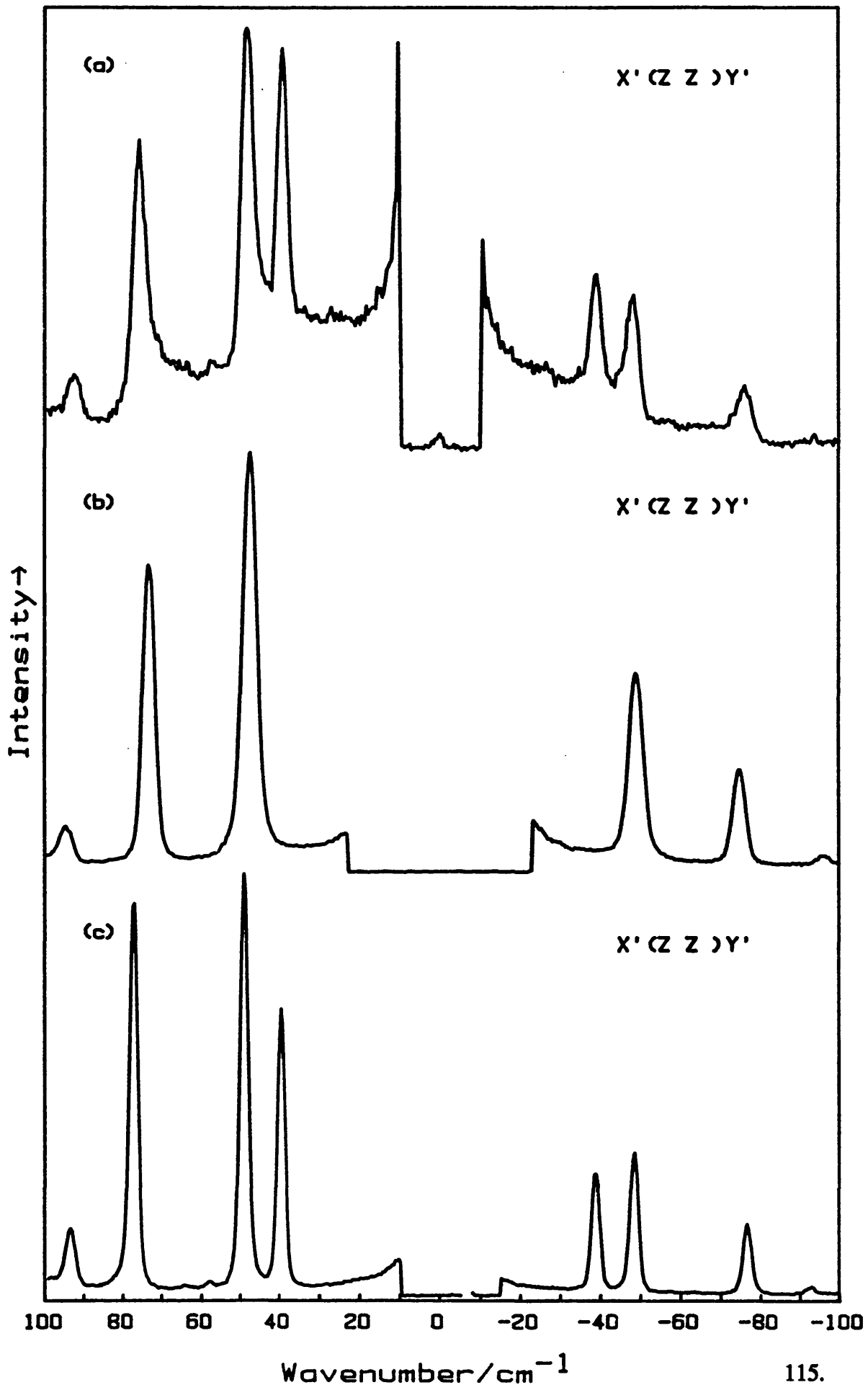


Table 3.2.3

Energy levels for $[\text{V}(\text{OH}_2)_6]^{3+}$ under the action of a trigonal field (with E_g ground term) and spin-orbit coupling.

Orbital Wavefunction	Symmetry	Energies of Spin orbit states / cm^{-1} $\Delta = -30 \text{ cm}^{-1}$	Energies of Spin orbit states / cm^{-1} $\Delta = -100 \text{ cm}^{-1}$	Energies of Spin orbit states / cm^{-1} $\Delta = -150 \text{ cm}^{-1}$
$1/2[-\Delta/3 + A\lambda + (\Delta^2 + 2A\lambda\Delta + 9A^2\lambda^2)^{1/2}]$	A	290	295	302
$1/2[-\Delta/3 + (\Delta^2 + 4A^2\lambda^2)^{1/2}]$	E	151	170	188
$\Delta/3 + A\lambda$	A	135	112	95
$1/2[-\Delta/3 + A\lambda - (\Delta^2 + 2A\lambda\Delta + 9A^2\lambda^2)^{1/2}]$	A	-135	-117	-107
$1/2[-\Delta/3 + (\Delta^2 + 4A^2\lambda^2)^{1/2}]$	E	-141	-137	-138
$\Delta/3 - A\lambda$	E	-155	-178	-195

transitions to spin-orbit states higher in energy would be expected and none are found. If the $[\text{V}(\text{OH}_2)_6]^{3+}$ cation is doped into a lattice where, through constraints of hydrogen bonding, the mode of water co-ordination to the vanadium(III) cation leads to the 3E_g term lowest lying, then according to Jahn-Teller theory,¹⁷ the hexa-aqua-cation will undergo an asymmetric nuclear displacement that will lift the orbital degeneracy leading to an electronic stabilisation of the system. Whether this displacement is static or dynamic will depend on the magnitude of the vibrational energy compared with the energy barrier separating equivalent distorted configurations.¹⁸ Since the electronic ground state of the $[\text{V}(\text{OH}_2)_6]^{3+}$ cation is not Kramers degenerate, the symmetry of the complex when doped into the α lattice is very difficult to determine. EPR measurements, using X-band microwave radiation, of α Rb{Ga/V}SH mixed alums have been undertaken and no resonances that could be attributed to vanadium(III) were found.

The fact that β Rb{Ga/V}SH mixed alums can be prepared with vanadium(III) concentrations as low as 25 % of the total trivalent cation content illustrates the strong preference for $[\text{V}(\text{OH}_2)_6]^{3+}$ to be in a β rather than an α lattice. The α Rb{Ga/V}SH mixed alums degrade over a period of time. Parts of the crystals are seen to turn from green to blue. Photographs of these crystals are shown in figure 3.2.2. A possible interpretation of this observation would be that the $[\text{V}(\text{OH}_2)_6]^{3+}$ cations are migrating through the crystal to form domains where the vanadium(III) concentration is high enough to induce a local phase transformation to the β structure.

This study has established that the electronic structure of the $[\text{V}(\text{OH}_2)_6]^{3+}$ cation is altered on changing its environment from the β to the α alum lattice. However, neither the electronic or the molecular structure of the $[\text{V}(\text{OH}_2)_6]^{3+}$ cation in the α environment have been determined. Further Raman studies at 4.2 K as well as susceptibility measurements might shed further light on this problem.

iv) Powder X-ray diffraction studies

The unit cell parameters for a range of Rb{Ga/V}SH mixed alums have been determined.

The method for the determination of the unit cell parameter for cubic compounds is straight forward and is well described in the literature.¹⁹

For a cubic lattice, the unit cell dimension 'a'; the wavelength of radiation λ ; the Bragg angle θ and the Miller indices of the reflection h, k, and l are related by the equation:

$$\sin\theta = \frac{\lambda(h^2 + k^2 + l^2)}{2a}$$

3.2.2

Accurate cell dimensions are obtained from measurements at high angle. This is because large Bragg angles are very sensitive to small changes in cell dimension. This can be seen by differentiating the Bragg equation:

$$\lambda = 2d\sin\theta \quad 3.2.3$$

$$\frac{\partial(d)}{\partial(\theta)} = \frac{-\lambda\cos\theta}{2\tan\theta}$$

3.2.4

As $\theta \rightarrow 90^\circ$; the rate of change of layer spacing d with angle θ tends to 0. Therefore, an error $\delta\theta$ in θ results in a much smaller error δd in d as $\theta \rightarrow 90$. The high angle reflections were indexed by consideration of the whole diffraction pattern. First, the low angle reflections were indexed and an estimate of the unit cell obtained. The unit cell parameter estimate allowed higher angle reflections to be indexed and a more precise value of the unit cell parameter evaluated. Thus by working up from the low to the high angle reflections the highest angle reflections could be reliably indexed.

There are several effects that may cause powder lines to be displaced from their true positions so that the measured angles are not the true Bragg angles.¹⁹

However, since a small error in θ should produce a vanishingly small error in the unit cell parameter as θ approaches 90° , the systematic errors are minimised for the unit cell parameter determined from a reflection with $\theta = 90^\circ$. Although this is impossible to achieve, since a Bragg angle of 90° corresponds with a reflection directed back into the X-ray beam, it can be done in effect by determining the unit cell parameter from several reflections with differing values of θ and extrapolating the result to $\theta = 90^\circ$ ($1/2[\cos^2\theta/\theta + \cos^2\theta/\sin\theta]$ is often chosen as the extrapolatory function.¹⁹) However, incorrect alignment of the diffractometer can give errors, common to all samples, that cannot be accounted for by extrapolation to $\theta = 90^\circ$.¹⁹ These errors can be corrected for by use of an internal standard.

Figure 3.2.13 shows the powder diffraction pattern for RbVSH. Two sets of scans were recorded. High angle data recorded between 2θ values of 126° and 156° were recorded first, followed by a long scan from 14° to 156° . This was done in order to check that the high angle data was consistent. Figure 3.2.13 (b) shows the two sets of high angle data recorded. The top scan was recorded first; the bottom scan was recorded *ca.* 16 hours later. In this alum, there is negligible change in both the positions and intensities of the high angle data for the two data sets. Figure 3.2.14 shows a plot of unit cell parameters for several high angle reflections versus the function $1/2[\cos^2\theta/\theta + \cos^2\theta/\sin\theta]$. A straight line can be drawn through the points. The unit cell parameter is the value at the intercept which is $12.347(1) \text{ \AA}$. No value of the unit cell obtained from any reflection is greater than 0.001 \AA from the straight line joining the points indicating that this is a precise measurement. Figure 3.2.15 shows the powder diffraction pattern for " β mix45" whose Raman spectra are shown in figures 3.2.5 - 3.2.7. It is noted that there is a slight change in the relative intensities of the peaks from the two scans. This can only mean that there is some change in atomic positions, likely to be a result of either aerial oxidation or acquisition of water from the atmosphere. Similar behaviour was observed for other alums whose diffraction patterns were recorded in this study. The peaks do, however, occur at the same positions for the two scans indicating that within experimental error, there is no change in the unit cell parameter.

Figure 3.2.16 shows a plot of unit cell parameter versus composition. A linear dependence is found. Substituting the smaller $[\text{Ga}(\text{OH})_6]^{3+}$ cation for $[\text{V}(\text{OH})_6]^{3+}$

Figure 3.2.13

Powder X-ray diffraction pattern for RbVSH. Co K α radiation. λ_1 Co K α_1 = 1.788965 Å. λ_2 Co K α_2 = 1.792850 Å. Step size:- 0.025° in 2 θ . Integration time: 15 seconds for high angle scan (the upper diffraction pattern in 3.2.13 (b))
7 seconds for scan over complete range.

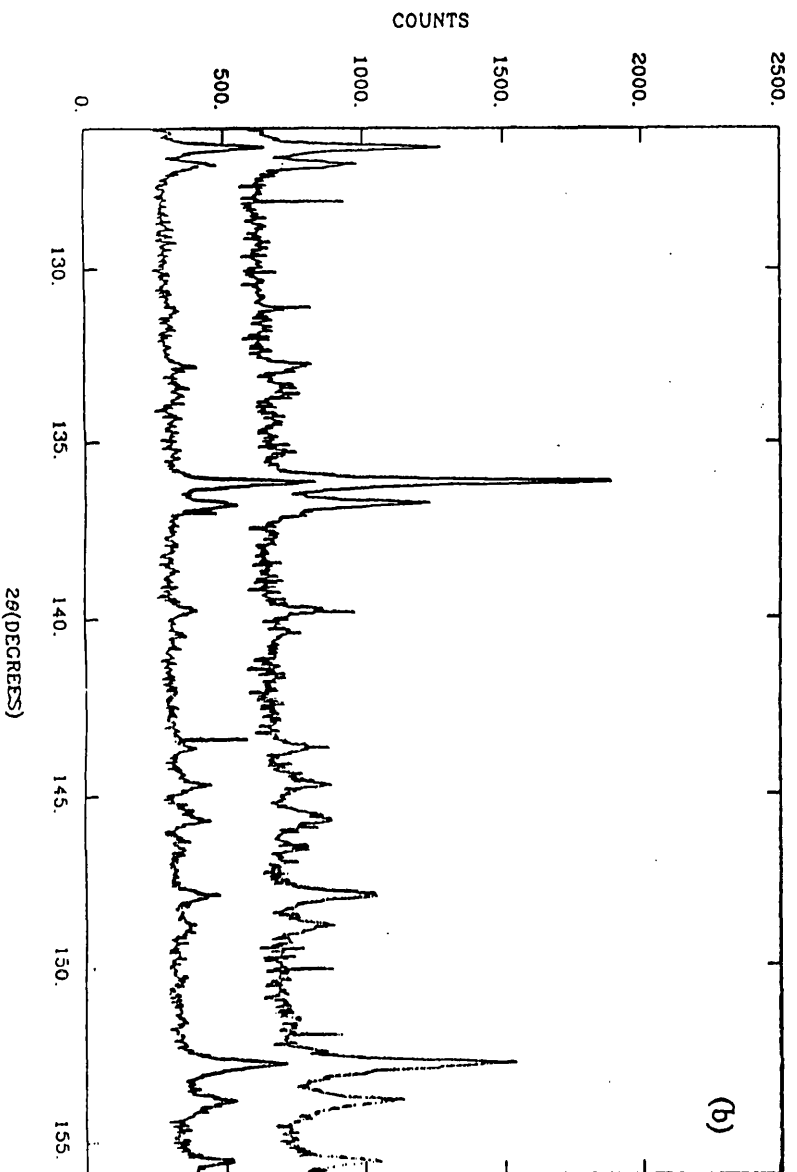
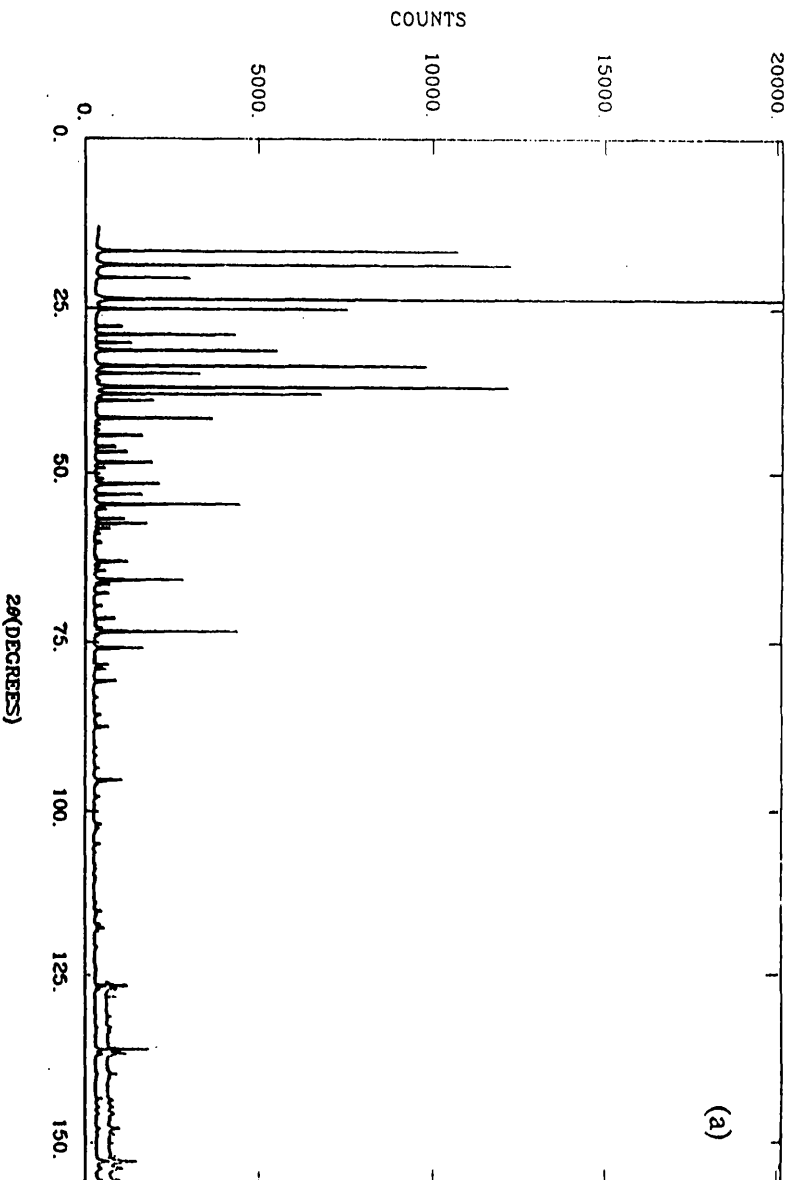


Figure 3.2.14

Plot of unit cell dimension against $1/2[\cos^2\theta/\theta + \cos^2\theta/\sin\theta]$ for high angle reflections of the RbVSH alum. Unit cell dimension at $\theta = 90^\circ$ is 12.347(1) Å.

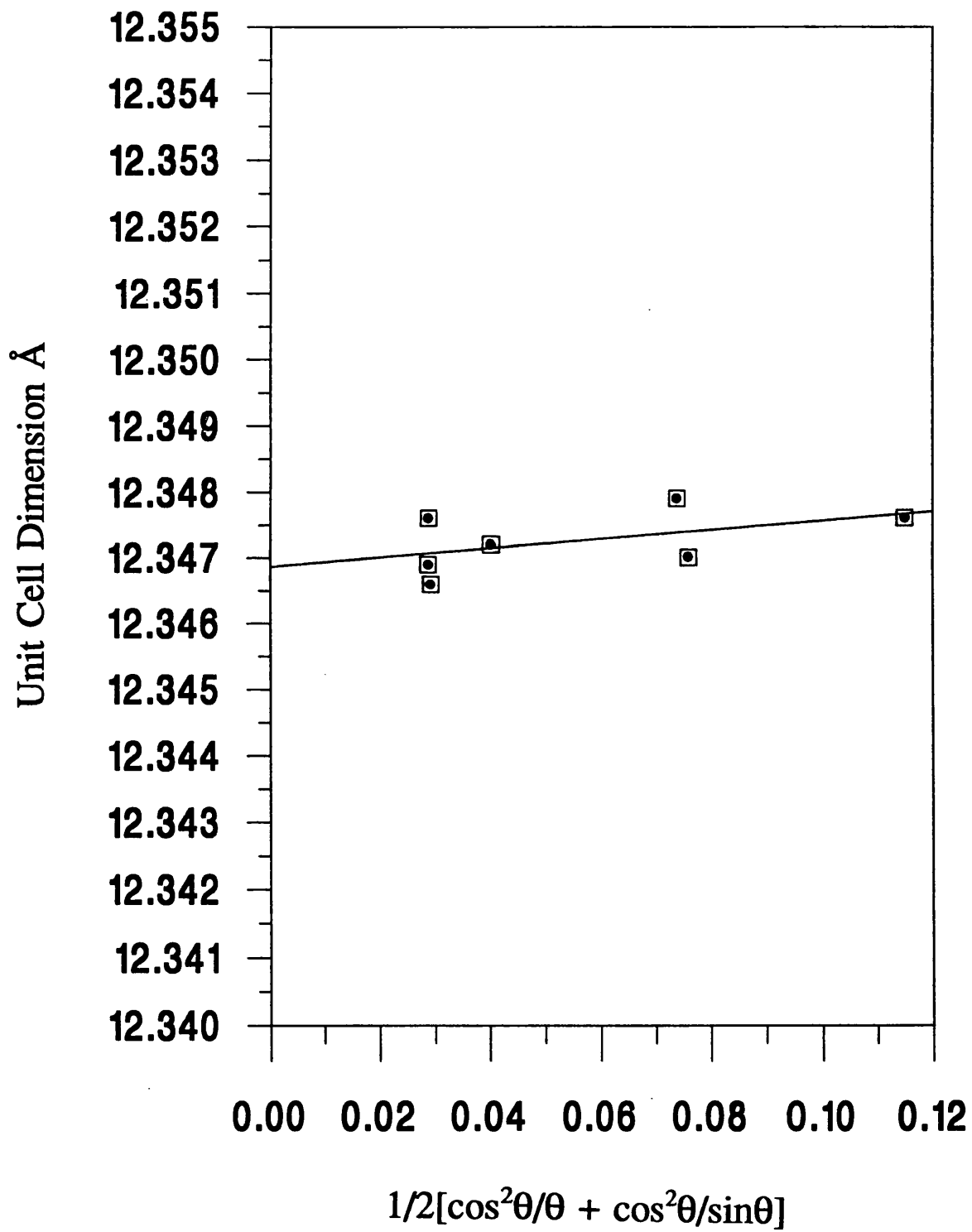


Figure 3.2.15

Powder X-ray diffraction pattern for the $\text{RbV/Ga(SO}_4)_2 \cdot 12\text{H}_2\text{O}$ β alum "βmix45". Tervalent cation content from analysis:- 45.5(1) % V and 54.5(1) % Ga.. Co $K\alpha$ radiation. λ_1 Co $K\alpha_1$ = 1.788965 Å. λ_2 Co $K\alpha_2$ = 1.792850 Å. Step size:- 0.025° in 2θ . Integration time: 15 seconds for high angle scan (the upper diffraction pattern in 3.2.10 (b))
7 seconds for scan over complete range.

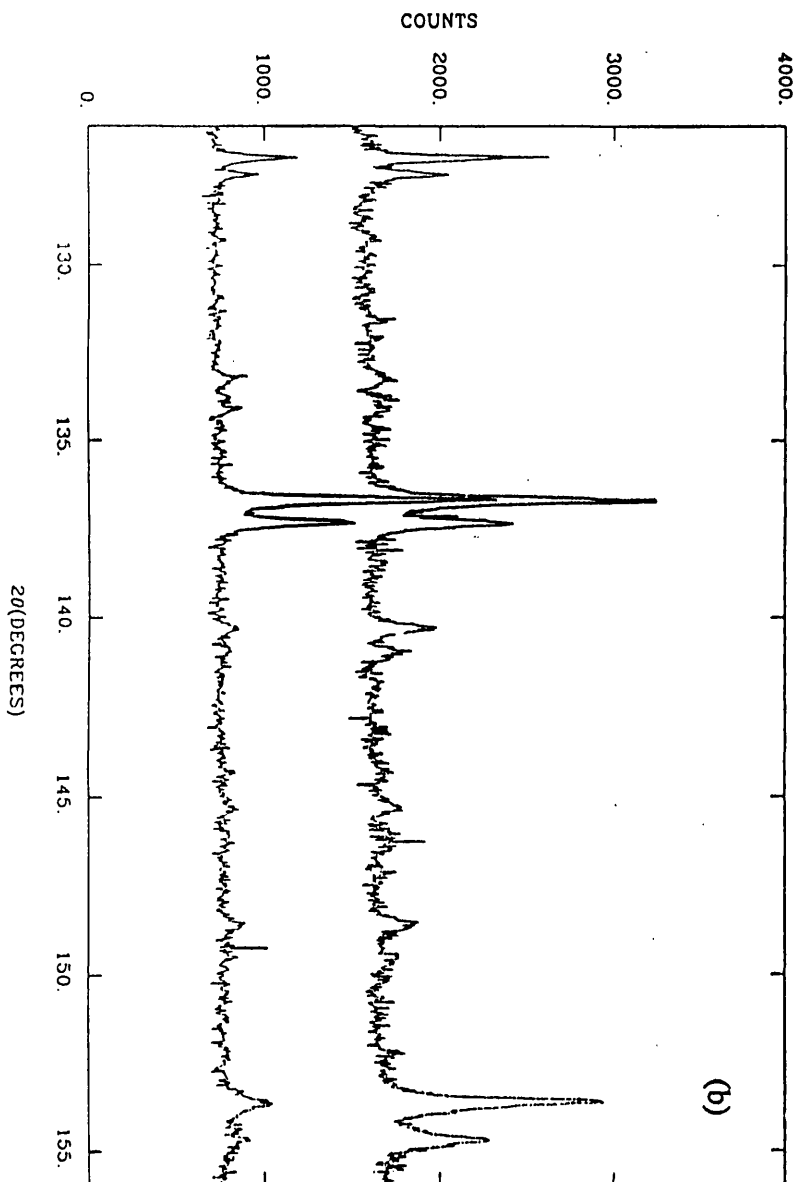
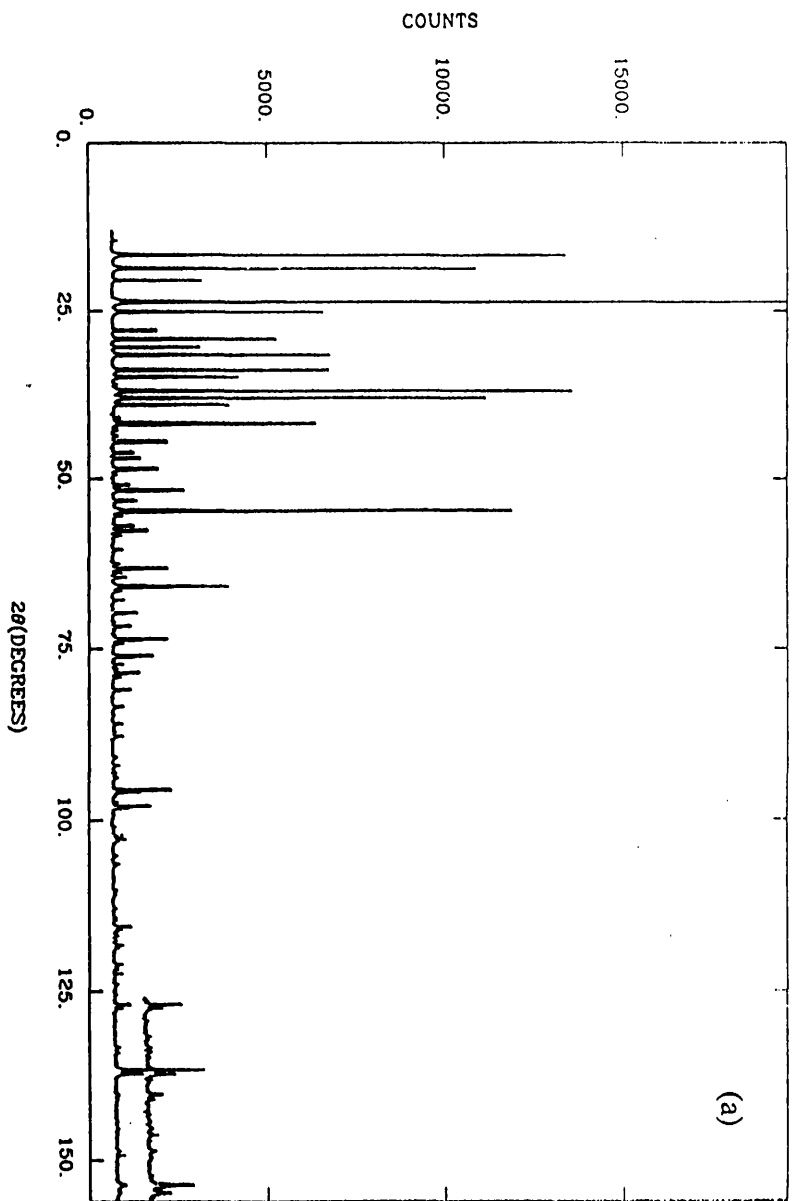
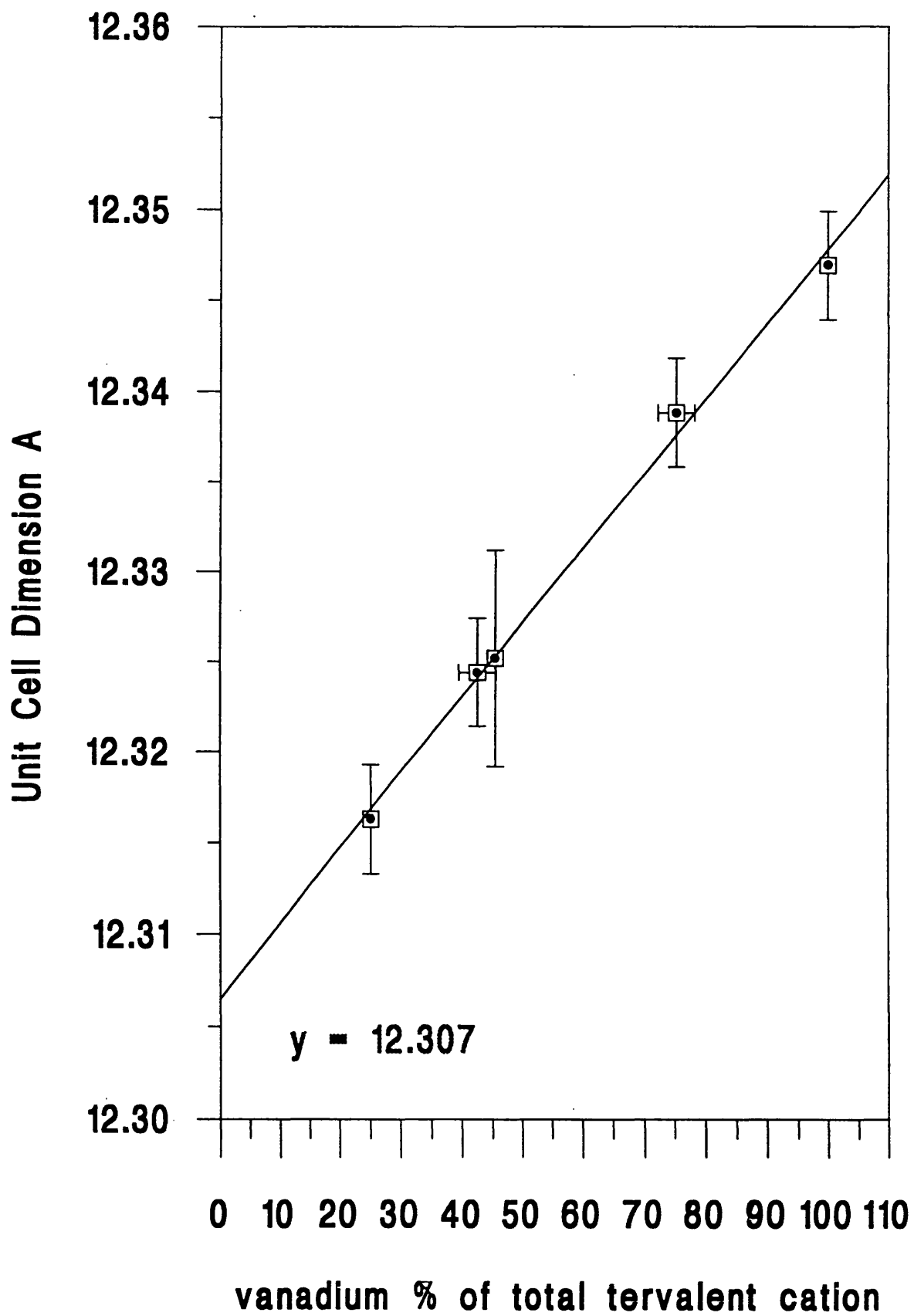


Figure 3.2.16

Plot of unit cell dimension against vanadium composition for the Rb(Ga/V)SH β alum system. The intercept at 12.307 Å is the unit cell dimension of RbGaSH if it were a β alum. 3 σ error margin shown.



leads to a reduction in unit cell size in proportion to the Ga/V ratio. On change of composition of trivalent cation, the reflections move uniformly in position without showing any sign of broadening. This indicates that the $[\text{V}(\text{OH}_2)_6]^{3+}$ and $[\text{Ga}(\text{OH}_2)_6]^{3+}$ cations are uniformly distributed throughout the lattice. If the two different hexa-aqua-cations form separate domains within the mixed alums, then on change of trivalent cation composition, the Bragg reflections for the RbVSH alum would lose intensity and new peaks would emerge. Together with the Raman data, the powder diffraction data sets show that the $[\text{V}(\text{OH}_2)_6]^{3+}$ and $[\text{Ga}(\text{OH}_2)_6]^{3+}$ cations are distributed uniformly throughout the lattice and that their $\text{M}^{\text{III}}\text{-O}$ bond distances are similar to their respective values in the RbVSH and RbGaSH alums. Since the mixed $\text{Rb}\{\text{Ga}/\text{V}\}\text{SH}$ β alums could be formed with vanadium concentrations $> 25\%$ of the total trivalent cation content only, no measurements were possible below this limit. However extrapolation to $\text{V} = 0\%$ and $\text{Ga} = 100\%$ gives the unit cell of the RbGaSH alum if it were a β alum. This value is found to be $12.307(1)$ Å. RbGaSH is an α alum whose unit cell dimension was determined in this study to be $12.270(1)$ Å.

The unit cell dimension of the RbVSH alum is determined from this study to be 12.347 Å. However, the unit cell dimension of the RbVSH alum was found to be 12.367 Å by single crystal X-ray diffraction measurements⁹ suggesting that all the unit cell parameters determined in this study may be subject to the same systematic offset error that cannot be corrected for by extrapolation of the unit cell parameter to $\theta = 90^\circ$.

3.3 Electronic structure of $[V(OH_2)_6]^{3+}$ within the TIVSH alum

The $[Tl(OH_2)_6]^+(aq)$ cation has very different properties to the alkali metal cations in solution. Table 3.3.1 shows a listing of some chemical and physical properties of a selected number of aqua ions. The pK_a extrapolated to infinite dilution is defined as:

$$pK_a = \log_{10} \frac{[M(OH)^{(n-1)+}][H_3O^+]}{[M^{n+}][H_2O]}$$

The Rb^+ and Cs^+ are so weakly acidic that their acid dissociation constants are yet to be satisfactorily measured. Despite the similar ionic radii of the Tl^+ and Rb^+ cations, the $[Tl(OH_2)_6]^+(aq)$ cation is appreciably more acidic.

A solution Raman study²³ of the gallium(III) and thallium(I) sulphate salts in water has identified symmetric modes of vibrations not attributable to that of free water or sulphate. These are found at 470 and 475 cm^{-1} for the thallium(I) and gallium(III) sulphate solutions respectively. These bands were attributed to symmetric forms of vibration within the hydration sheath of the dissolved metal ions.²³ It is unlikely, however, that these bands can be attributed to the symmetric hexa-aqua-cation vibrations. The interpretation of the spectra is greatly complicated by the presence of co-ordinating sulphate and the presence of oxo-anions.

The TIVSH alum was synthesised and studied by Raman spectroscopy in order to see whether, as a consequence of the very different pK_a 's of the Tl^+ and Rb^+ aqua cations, substitution of Tl^+ for Rb^+ might perturb the hydrogen bonding network of the alum lattice, leading to a different hydration and electronic structure for the $[V(OH_2)_6]^{3+}$ cation.

i) Synthesis of TIVSH

TIVSH was made by addition of Tl_2SO_4 to an excess of VCl_3 in sulphuric acid (1 mol dm^{-3}). The alum was left to crystallise at 2°C and then recrystallised from sulphuric acid (1 mol dm^{-3}). Initial crystallisation was precipitated by agitation

Table 3.3.1

Chemical and Physical properties of a selected number of aqua cations in solution

Cation	Hydration enthalpy KJ mol ⁻¹ From Ref [20]	pK _a at infinite dilution From ref [21]	Ionic radii / Å From ref [22]	"Metal-water stretch frequency / cm ⁻¹ "
Cs ⁺	-263.3		1.67	
Rb ⁺	-296.4		1.47	
K ⁺	-321.1		1.33	
Na ⁺	-405.6	14.6 - 14.8	0.97	
Li ⁺	-514.9	13.7 - 14.1	0.68	
Tl ⁺	-326.1	13.3	1.47	470 (Tl ₂ SO ₄ in water) ²³
Ga ³⁺	-4687.1	2.6	0.62	475 (Ga ₂ (SO ₄) ₃ in water) ²³
Cr ³⁺	-4403.7	3.8 - 4	0.63	522 (KCrSH in H ₂ SO ₄ 1 mol dm ⁻³) ¹⁴

of the solution after which formation of the alum was rapid. Large single crystals of the alum were grown by the controlled single crystal growth method described in section 2.4.

ii) Raman Spectra

The complete set of Raman spectra for TlVSH are shown in figures 3.3.1 - 3.3.3. The spectra are practically identical to those of RbVSH and CsVSH. The lattice modes do not move in position on substitution of Tl⁺ for Rb⁺ indicating negligible change in the metal(I)-water strength within the alum lattice.

The external modes of water occur 3 - 18 cm⁻¹ lower in wavenumber in the thallium compared to the rubidium alum. There is no indication, however, of any significant change in wavenumber of the internal modes of water. This suggests that the external modes are more sensitive to the internal modes of water to changes in hydrogen bond strength. On change of monovalent cation from Rb⁺ to Tl⁺, there is a softening of potential about the water molecules within the alum. The wavenumber of the internal modes of [V(OH₂)₆]³⁺ and the electronic Raman transition remain unchanged suggesting essentially no change in the hydration structure of the [V(OH₂)₆]³⁺ cation. The profile of the electronic Raman band is, however, distinctly different from that found in RbVSH and the CsVSH⁶ and NH₄VSH⁶ alums, suggesting that the relative intensities of the spin-orbit coupled transitions are sensitive to the change in monovalent cation. The similarity of the spectra of RbVSH and TlVSH may be either a consequence of the stereo-chemical preference of the two monovalent cations within the alums being similar; or else the stereo-chemical preference of the [V(OH₂)₆]³⁺ cation is strong enough to override any perturbations brought about by the change in monovalent cation. Raman spectra of thallium alums with trivalent cations without a strong stereo-chemical preference (such as Cr³⁺) would be desirable.

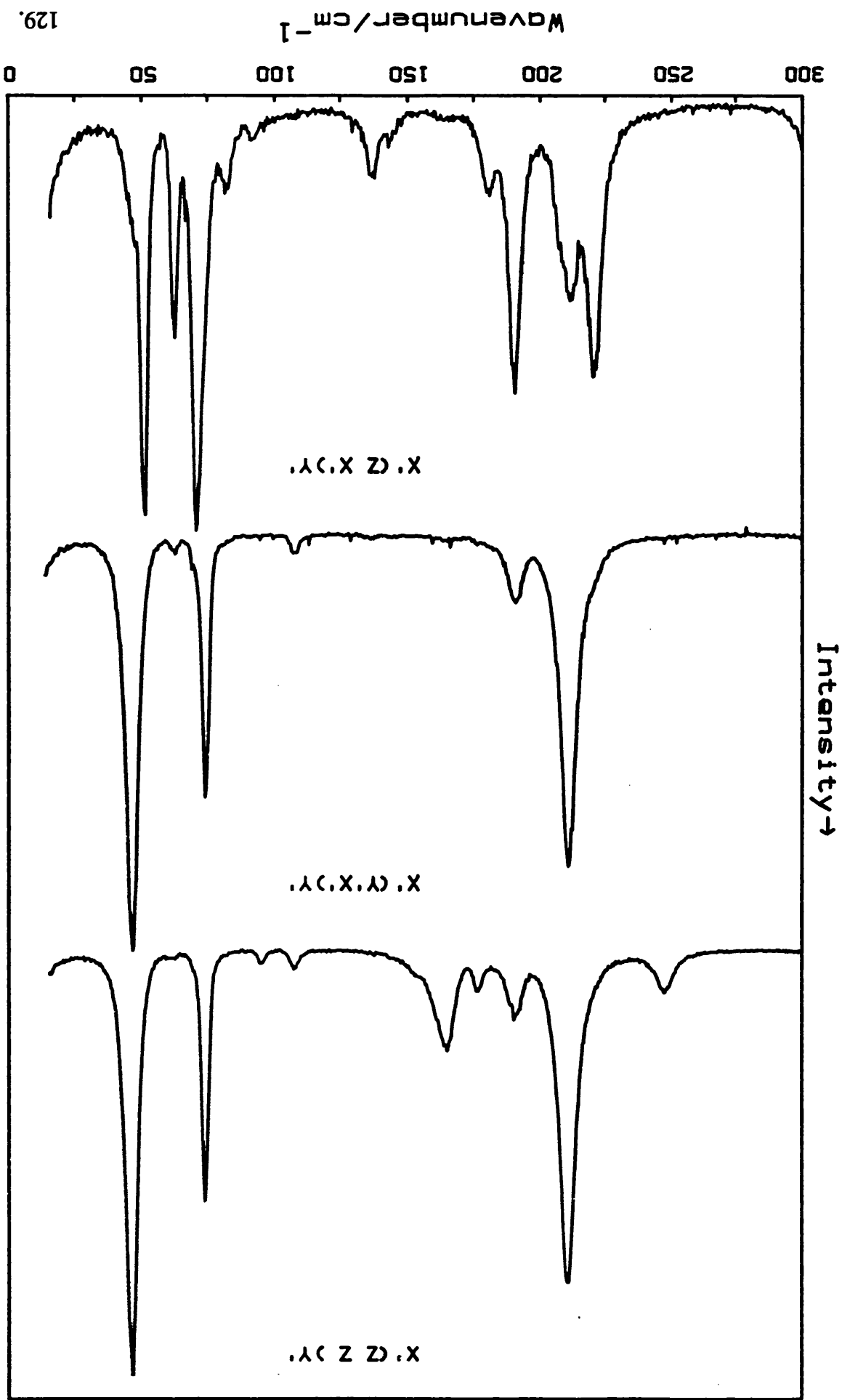
Table 3.3.2

Vibrational frequencies and assignments for $\text{TlV}(\text{SO}_4)_2 \cdot 12\text{H}_2\text{O}$, between 20 and 275 cm^{-1} .

ν/cm^{-1}		$X'(Z Z)Y'$	$X'(Y'X')Y'$	$X'(Z X')Y'$	assignment
46	E_g	382	150	sh	tr (SO_4^{2-}) + rot (SO_4^{2-})
51	F_g			96	
62	F_g	5	3	52	
70	F_g	sh	sh	101	
74	E_g	225	95		
82	F_g	sh	sh	13	
92	F_g			3	
95	A_g	9			
107	E_g	16	7		rot [$\text{Tl}(\text{OH}_2)_6$] ⁺
137	F_g		1	15	
144	F_g			3	rot [$\text{V}(\text{OH}_2)_6$] ³⁺
151	A_g	sh			
164	A_g (+ F_g ?)	159	7	5	
176	A_g	28			
180	F_g			20	
190	F_g			69	
191	E_g	61	21		ν_3 [$\text{Tl}(\text{OH}_2)_6$] ⁺
208	F_g			42	
211	E_g	295	120		ν_2 [$\text{Tl}(\text{OH}_2)_6$] ⁺
211	F_g			45	
221	F_g		sh	65	
248	A_g	35	1	1	ν_1 [$\text{Tl}(\text{OH}_2)_6$] ⁺

Figure 3.3.1

Single crystal Raman spectra of $\text{TlV}(\text{SO}_4)_2 \cdot 12\text{H}_2\text{O}$ between 10 and 300 cm^{-1} .
Sensitivities: $X'(Z Z) Y'$ 5823 counts sec^{-1} ; $X'(Y'X') Y'$ 2355 counts sec^{-1} ;
 $X'(Z X') Y'$ 1614 counts sec^{-1} (102 (5) K; step size 0.4 cm^{-1} ; spectral bandwidth
2.32 cm^{-1} at 150 cm^{-1} ; integration time 4 seconds; 457 nm radiation, 50 mw power
at sample).



129.

Wavenumber/cm⁻¹

0 50 100 150 200 250 300

Intensity →

Table 3.3.3

Vibrational Frequencies and assignments for $\text{TlV}(\text{SO}_4)_2 \cdot 12\text{H}_2\text{O}$, between 275 and 1200 cm^{-1} .

ν/cm^{-1}	$X'(Z Z)Y'$	$X'(Y'X')Y'$	$X'(Z X')Y'$	assignment
305 F_g			48	$\nu_5(\text{VO}_6)$
309 E_g	42	34		
332 F_g		9	33	
431 E_g	483	291		$\nu_2(\text{SO}_4^{2-})$ + $\nu_2\text{VO}_6$
435 F_g			55	
463 F_g			40	
474 E_g	192	120		
528 A_g	275	19		$\nu_1(\text{VO}_6)$
529 E_g	?	19		ρ_6
530 F_g			8	
562 $F_g?$			2	ρ_5
564 E_g	67	30		
608 F_g		sh	18	$\nu_4(\text{SO}_4)$
622 F_g			21	
623 E_g	107	73		
673 E_g	41	31	1	ρ_4
692 F_g			3	
746 F_g			5	ρ_3
752 $E_g (+A_g?)$	135	60		
796 $E_g?$	3	2		?
858 A_g	sh			ρ_2
872 E_g	26	13		
946 A_g	sh			ρ_1
971 A_g	36			$\nu_1(\text{S}^{16}\text{O}_3^{18}\text{O})$ $\nu_1(\text{SO}_4)$
987 A_g	6218	151	28	
1086 F_g		sh	56	$\nu_3(\text{SO}_4)$
1089 E_g	80	49		
1099 F_g			sh	

Figure 3.3.2

Single crystal Raman spectra of $\text{TlV}(\text{SO}_4)_2 \cdot 12\text{H}_2\text{O}$ between 275 and 1200 cm^{-1} .
Sensitivities: X'(Z Z) Y' 95786 counts sec^{-1} ; X'(Y'X') Y' 4494 counts sec^{-1} ;
X'(Z X') Y' 934 counts sec^{-1} (108 (6) K; step size 0.4 cm^{-1} ; spectral bandwidth
2.96 cm^{-1} at 600 cm^{-1} ; integration time 4 seconds; 457 nm radiation, 50 mw power
at sample).

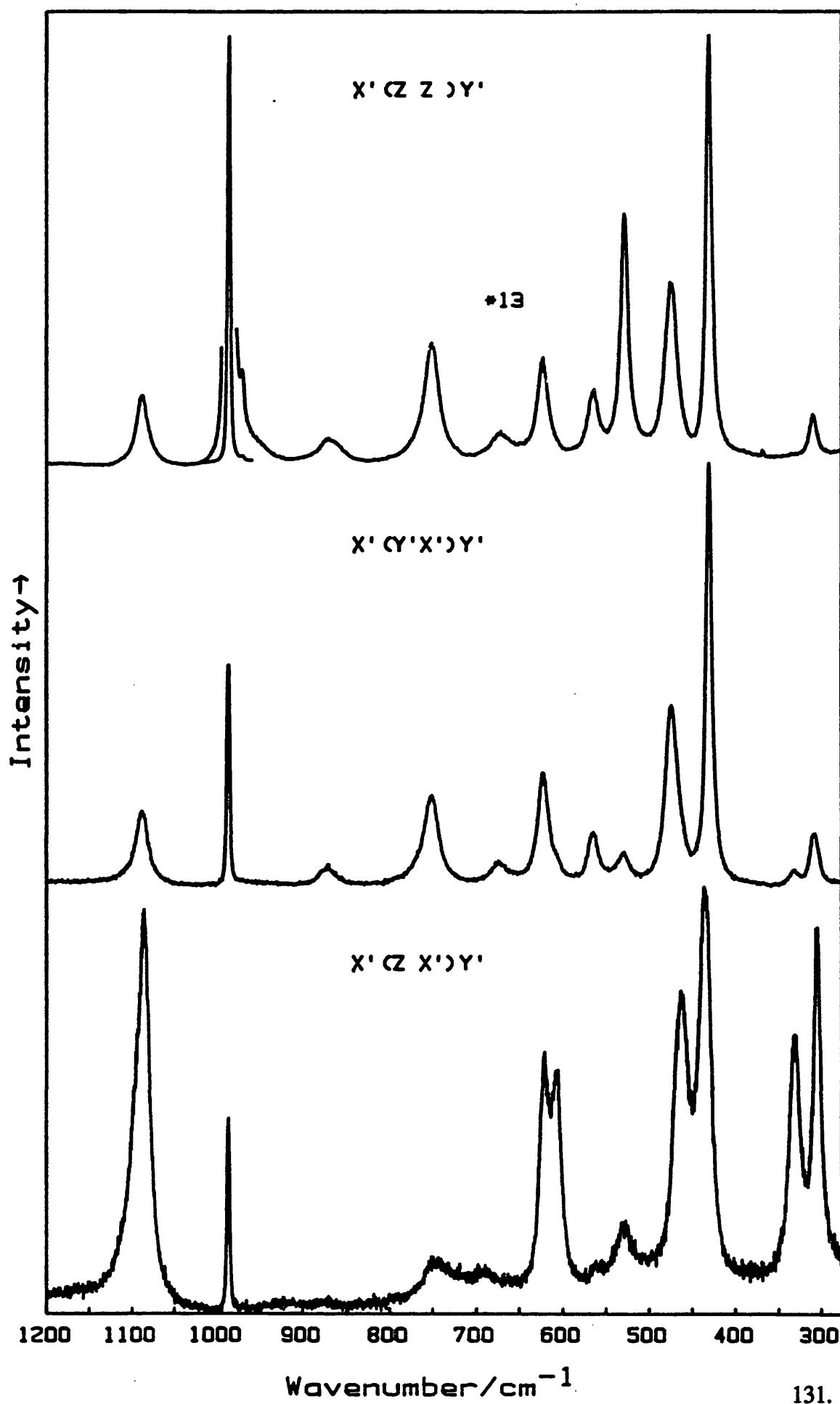


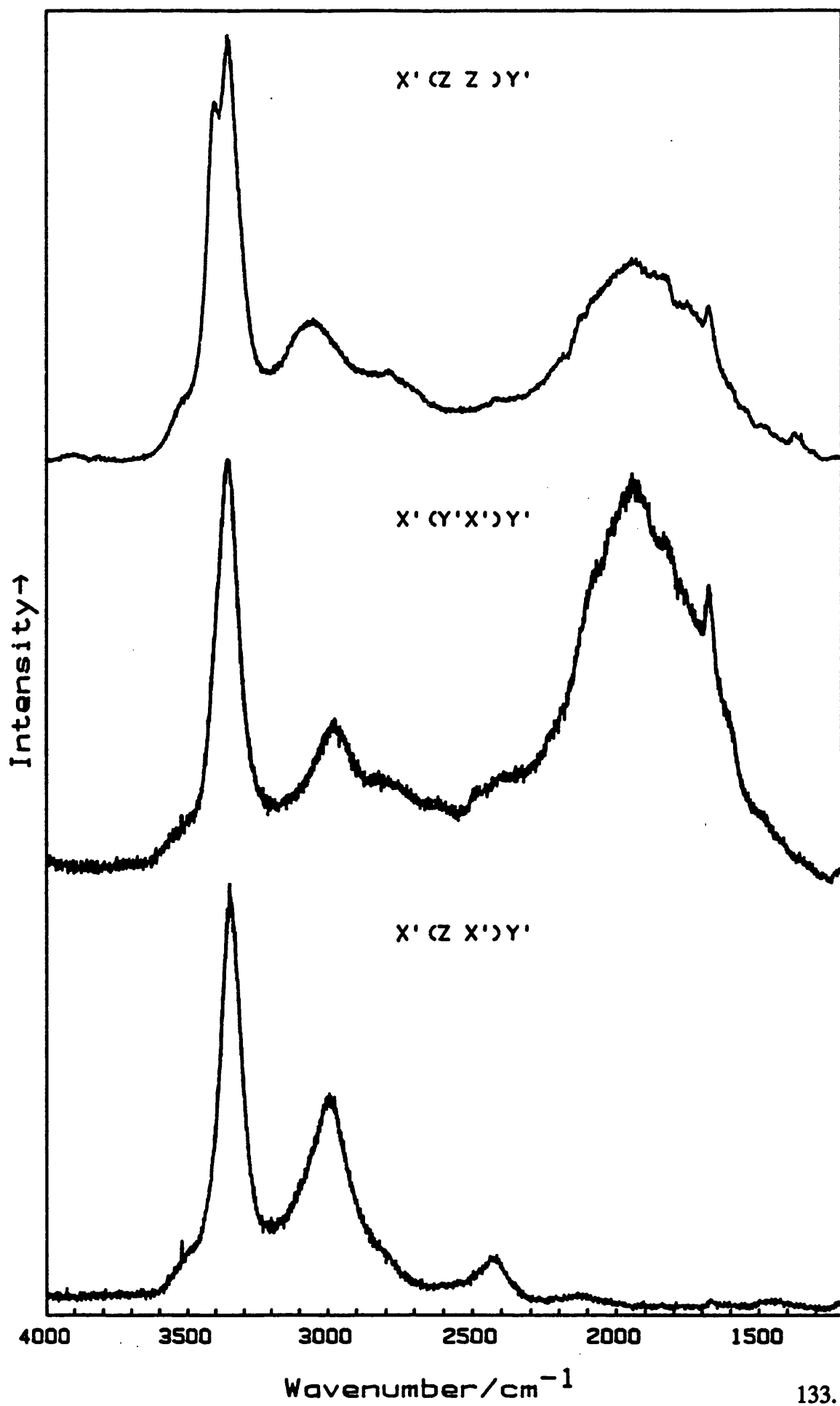
Table 3.3.4

Vibrational frequencies and assignments for $\text{TlV}(\text{SO}_4)_2 \cdot 12\text{H}_2\text{O}$, between 1200 and 4000 cm^{-1} .

ν/cm^{-1}	Activity	Intensity	Assignment	
1220	$E_g + F_g$	w	[$\nu_L + \nu_L$]	
1306	$E_g (A_g?)$	w		
1368	$E_g (A_g?)$	w		
1436	E_g	w		
1456	F_g	w		
1480	E_g	w		
1548	$A_g (E_g?)$	w		$\nu_2(\text{HOH})$
1592	E_g	w		
1672	$E_g + F_g$	m/w		
1744	E_g	w	+	
1762	E_g	m/w		
1828	E_g	m/w	[$\nu_L + \nu_L$]	
1940	E_g	s	Electronic Raman	
2124	$E_g + F_g$	w	$\nu_2(\text{HOH})$	
2196	$A_g (E_g?)$	w		
2240	F_g	w	+	
2392	E_g	w		
2428	$E_g + F_g$	m/w		
2616 ?	E_g	w		[$\nu_L + \nu_L$]
2700	$A_g (E_g?)$	w		$\nu(\text{OH}) [\text{V}(\text{OH}_2)_6]^{3+}$
2784	$E_g + F_g$	m/w		
2976	E_g	m	$\nu(\text{OH}) [\text{V}(\text{OH}_2)_6]^{3+}$	
2992	F_g	s		
3060	A_g	m		
3348	F_g	s	$\nu(\text{OH}) [\text{Tl}(\text{OH}_2)_6]^{3+}$	
3358	E_g	s		
3404	A_g	s		
3524	$E_g + F_g$	m/w	[$\nu(\text{OH}) + \nu_L$]	
3820	A_g	w		
3912	A_g	w		

Figure 3.3.3

Single crystal Raman spectra of $\text{TlV}(\text{SO}_4)_2 \cdot 12\text{H}_2\text{O}$ between 1200 and 4000 cm^{-1} . Sensitivities: $X'(ZZ)Y'$ 7847 counts sec^{-1} ; $X'(Y'X')Y'$ 2376 counts sec^{-1} ; $X'(ZX')Y'$ 2593 counts sec^{-1} (102 (5) K; step size 1 cm^{-1} ; spectral bandwidth 3.58 cm^{-1} at 2600 cm^{-1} ; integration time 4 seconds; 457 nm radiation, 50 mw power at sample).



REFERENCES

1. J. Van der Handel and A. Siegert, *Physica*, **4**, 871 (1937).
2. J. J. Fritz and H. L. Pinch, *J. Amer. Chem. Soc.*, **78**, 6223 (1956).
3. A. S. Chakravarty, *Ind. J. Phys.*, **32**, 447 (1958).
4. B. N. Figgis, J. Lewis, and F. E. Mabbs, *J. Chem. Soc.*, 2480 (1960).
5. F. E. Mabbs and D. J. Machin, *Magnetism and Transition metal complexes*, Chapman and Hall (1973).
6. S. P. Best and R. J. H. Clark, *Chem. Phys. Letts.*, **122**, 401 (1985).
7. M. A. Hitchman, R. G. McDonald, P. W. Smith, and R. Stranger, *J. Chem. Soc., Dalton Trans.*, 1393 (1988).
8. A. B. P. Lever, *Inorganic Electronic Spectroscopy*, (second edition), Elsevier, Amsterdam, (1984).
9. J. K. Beattie, S. P. Best, P. Del Favero, B. W. Skelton and A. H. White, unpublished results.
10. J. K. Beattie, S. P. Best, B. W. Skelton, and A. H. White, *J. Chem. Soc., Dalton Trans.*, 2105 (1981).
11. F. A. Cotton, *Chemical Applications of Group Theory*, John Wiley & Sons press (1990)
12. N. N. Greenwood and A. Earnshaw, *Chemistry of the Elements*, p 1161, Pergamon Press, New York, (1984).
13. R. S. Armstrong and G. P. Braithwaite, unpublished results.
14. S. P. Best, Ph.D Thesis Sydney University (1983).
15. A. Manoogian and A. Leclerc, *J. Chem. Phys.* **63**, 4450, (1975).
16. D. R. McGarvey, *J. Chem. Phys.*, **41**, 3743 (1964).
17. H. A. Jahn and E. Teller, *Proc. Roy. Soc.*, **161**, 220 (1937).
18. F. S. Ham, *Physical Review*, **138**, A1727 (1965).
19. H. Lipson, and H. Steeple, *Interpretation of x-ray powder diffraction patterns*, Macmillan Press (1970).
20. J. Burgess, *Metal Ions in Solution*, Ellis Horwood press (1978)

21. L. G. Sillen and A. E. Martell, *Stability Constants of Metal-ion Complexes*, Special Publications 17 and 25 (Supplement 1), The Chemical Society, London (1964, 1971).
22. *CRC Handbook of Chemistry and Physics*, 64th edition p F-170, CRC press, inc (1983).
23. R. E. Hester and R. A. Plane, *Inorg. Chem.*, **3**, 768 (1964).

The electronic structure of $[\text{Ti}(\text{OH}_2)_6]^{3+}$

4.1 Review

The electronic structure of $[\text{Ti}(\text{OH}_2)_6]^{3+}$ within the alum lattice has been of considerable interest since the early development of the theory of transition metal ions.¹ Because of the extremely fast relaxation time of $[\text{Ti}(\text{OH}_2)_6]^{3+}$ within the lattice,^{2,3} the EPR spectrum of the undiluted alum^{2,4,5} and of $[\text{Ti}(\text{OH}_2)_6]^{3+}$ doped into a diamagnetic β lattice^{6,7} and α lattice^{8,9} can be observed only at temperatures approaching that of liquid helium. Susceptibility measurements on CsTiSH have also been performed in the liquid helium range.^{10,11} At temperatures above 10 K, magnetic susceptibility measurements¹²⁻¹⁶ have been the only means used to probe the electronic structure of the caesium titanium alum.

Table 4.1.1 shown below is a summary of some of the g values obtained for the CsTiSH alum.

Temperature Range	Technique	g values	Reference
80 - 300 K	Magnetic Susceptibility	$g_{\parallel} = 1.88,$ $g_{\perp} = 1.62$	12
100 - 300 K	Magnetic Susceptibility	$g_{\parallel} = 1.92,$ $g_{\perp} = 1.78$	15
1 - 4.2 K	Magnetic Susceptibility	$g_{\text{eff}} = 1.12$	10
2.5 - 4.2 K	EPR	$g_{\parallel} = 1.25,$ $g_{\perp} = 1.14$	4,5

Only the g values from the EPR experiment are determined directly and hence give the most reliable effective g values assuming that the spectra are correctly interpreted. Between 1 and 4.2 K, the susceptibility is found to obey Curie's law.¹⁰

Calculation of the g value follows directly from the Curie constant. The susceptibility measurements above 4.2 K show a complicated variation with temperature.¹¹⁻¹⁶ The g values quoted in this temperature range are calculated indirectly using values of the ligand field parameters that are found to best fit the data.^{12,15}

The discrepancy between the g values calculated from measurements made below 4.2 K and those calculated from measurements above 80 K have yet to be adequately accounted for. It has been suggested¹⁵ that the trigonal field splitting of the $[\text{Ti}(\text{OH}_2)_6]^{3+}$ cation must be reduced drastically on cooling in order to account for the discrepancy in the g values. A model which takes into account second order contributions from the cubic 2E_g term and anisotropic orbital reduction factors has been found to give good agreement with the g values over the whole temperature range but not with a unique set of parameters.¹⁷ In addition, no set of parameters from this analysis were found that could reproduce the variation of the magnetic moment with temperature in the 80 - 300 K temperature range.

A 12 line EPR spectrum has been observed for $[\text{Ti}(\text{OH}_2)_6]^{3+}$ doped into the α lattices of RbAlSH ⁸ or TlAlSH .⁹ This observation was interpreted as resulting from 12 equivalent but differently oriented sites. This was explained as resulting from the larger Ti^{3+} ions forcing localized distortions when they replace Al^{3+} ions giving rise to an orthorhombic type of crystal field. The EPR spectra of Ti^{3+} doped into α host lattices with larger host lattices (eg. CsInSeH) have not been reported but might help to substantiate this interpretation. The EPR spectrum of $[\text{Ti}(\text{OH}_2)_6]^{3+}$ doped into the CsAlSH alum has been reported by separate workers.^{6,7} With the crystal aligned such that one of the four three fold axes is oriented along the magnetic field direction, three lines are observed. In the CsTiSH alum, only one line is reported albeit broad.^{4,5} The interpretation of the EPR spectrum of $[\text{Ti}(\text{OH}_2)_6]^{3+}$ doped into the CsAlSH lattice has been the subject of great contention. It has been proposed¹⁸ that the $[\text{Ti}(\text{OH}_2)_6]^{3+}$ cation exists in 12 differently oriented, but otherwise equivalent, magnetic complexes in both CsTiSH and $[\text{Ti}(\text{OH}_2)_6]^{3+}$ doped into CsAlSH . This claim has been strongly refuted on the grounds that it does not present a realistic model in view of the space group of the CsTiSH alum ($\text{Pa}\bar{3}$) which has 4 $[\text{Ti}(\text{OH}_2)_6]^{3+}$ cations per unit cell.¹⁹ It is also suggested¹⁹ that the experimental evidence offers no support to the claim that there exists 12 magnetic complexes when $[\text{Ti}(\text{OH}_2)_6]^{3+}$ is substituted for $[\text{Al}(\text{OH}_2)_6]^{3+}$

in the CsAlSH lattice. It is interesting to note that with similar dopant concentrations, it is reported that 12 lines can be observed simultaneously with $[\text{Ti}(\text{OH}_2)_6]^{3+}$ doped into an α lattice whereas 12 lines could never be seen simultaneously with $[\text{Ti}(\text{OH}_2)_6]^{3+}$ doped into a β lattice. For the latter case, it is reported by both sets of workers^{6,7} that the intensity of the lines decreases very rapidly as the direction of the magnetic field diverges from the three-fold axis, *i.e.* the line corresponding to g_{\perp} is not observed for $[\text{Ti}(\text{OH}_2)_6]^{3+}$ doped into a β lattice. This intensity difference between $[\text{Ti}(\text{OH}_2)_6]^{3+}$ doped into the β or the α lattice has received little attention in the literature.

An alternative explanation to the EPR spectrum of $[\text{Ti}(\text{OH}_2)_6]^{3+}$ doped into CsAlSH was presented from Shing and Walsh.⁷ Their treatment is shown schematically in figure 4.1.1. The authors suggest that the ${}^2T_{2g}$ term in an octahedral field is stabilised by a dynamic Jahn-Teller distortion as propounded by Ham.²⁰ The authors then move on to consider spin-orbit coupling and finally the trigonal field which they suggest is almost completely eliminated as a consequence of the dynamic Jahn-Teller effect. A quasi-quartet is finally reached from which the 3 transitions are accounted for. A qualitative interpretation of the EPR spectrum of the CsTiSH alum is also given by the authors using this model.²¹ The authors suggest that the trigonal field cancellation in the CsTiSH alum is more complete than for the doped alum leading to a broad, fast relaxing, strain broadened transition.

4.2 Previous assumptions of the symmetry and electronic structure of the $[\text{Ti}(\text{OH}_2)_6]^{3+}$ cation.

In interpreting the electronic structure of $[\text{Ti}(\text{OH}_2)_6]^{3+}$ in the CsTiSH alum or doped into the β alum of CsAlSH, all the authors have made two assumptions. 1. The $[\text{Ti}(\text{OH}_2)_6]^{3+}$ cation retains S_6 symmetry over the whole temperature range. 2. The trigonal field leaves a ground term of A_g symmetry as shown in figure 4.2.1 (a). The basis for assuming that the $[\text{Ti}(\text{OH}_2)_6]^{3+}$ cation retains S_6 symmetry over the whole temperature range must be questioned since no structural data for the alum has been reported below 102 K for the CsTiSH alum. Having assumed trigonal symmetry, the A_g term is assigned as the ground term since this is energetically more favourable to

Figure 4.1.1

(a) EPR spectrum of Ti^{3+} doped into the CsAlSH alum measured at 9.46 GHz and 2.5 K with the external magnetic field direction along a [111] axis. The transitions are assigned as A: $-3/2 \leftrightarrow 1/2$; B: $+3/2 \leftrightarrow 1/2$; C: $+1/2 \leftrightarrow -1/2$. (After Shing and Walsh [7]).

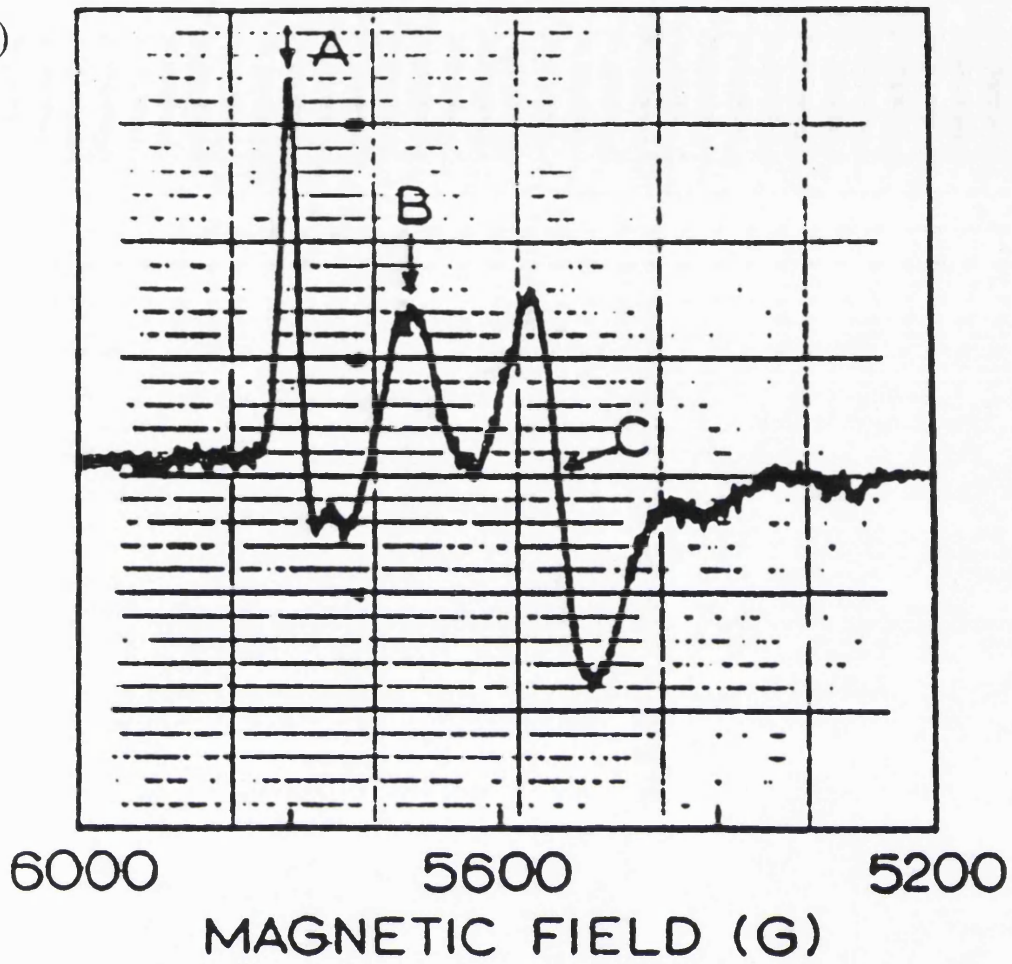
(b) Schematic energy-level diagram after Shing and Walsh,⁷ showing energy levels of Ti^{3+} when doped into the CsAlSH alum in the presence of a magnetic field at 2.5 K. The authors write the trigonal Hamiltonian as:

$$H_{\text{trig}} = 1/3 (\gamma v - (v')^2/\Delta)[3L_z^2 - L(L+1)]$$

after Abou-Ghantous *et al.*²² v is the trigonal field splitting parameter defined as positive when the A_g term is lowest in energy. γ is the vibronic reduction factor, v' is the admixture of an excited vibronic state with the ground state, Δ is the cubic field splitting and L corresponds to the orbital angular momentum quantum number = 1.

The authors propose that the near cancellation of the trigonal field is due to the trigonal field being comparable with and opposite in sign to the second-order effect involving an excited vibronic state. The validity of the model lies with the assumption that the trigonal field leaves the A_g term as the ground state.

(a)



(b)

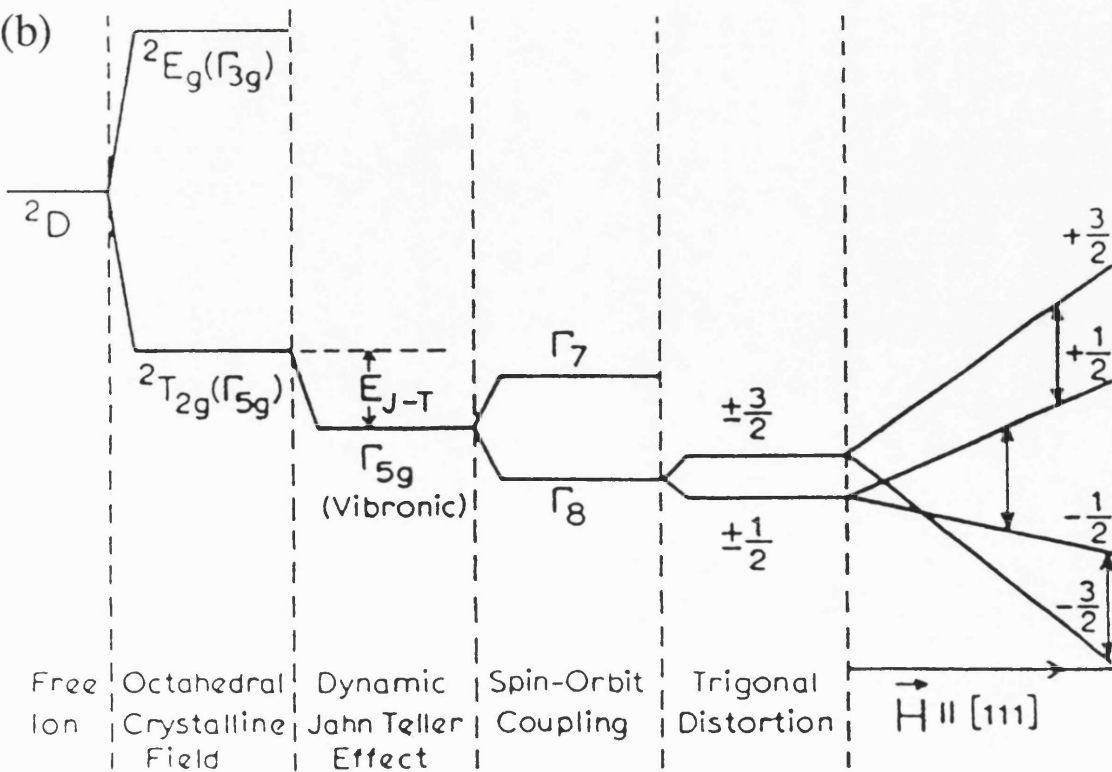
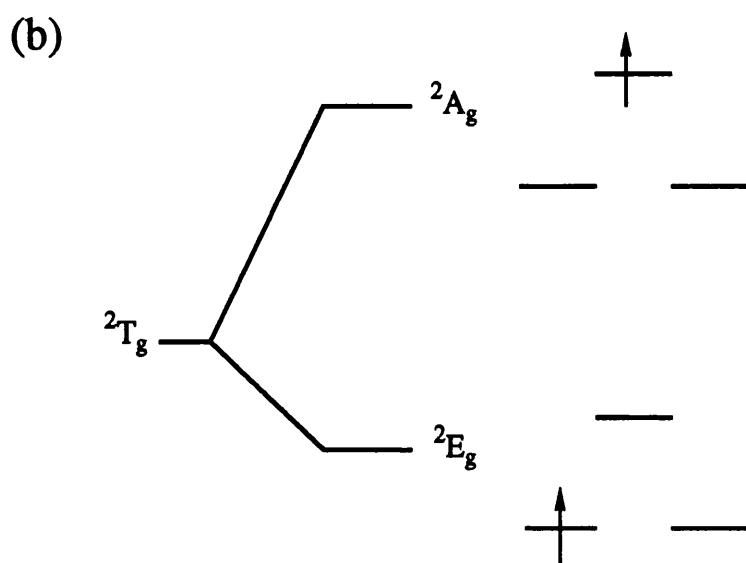
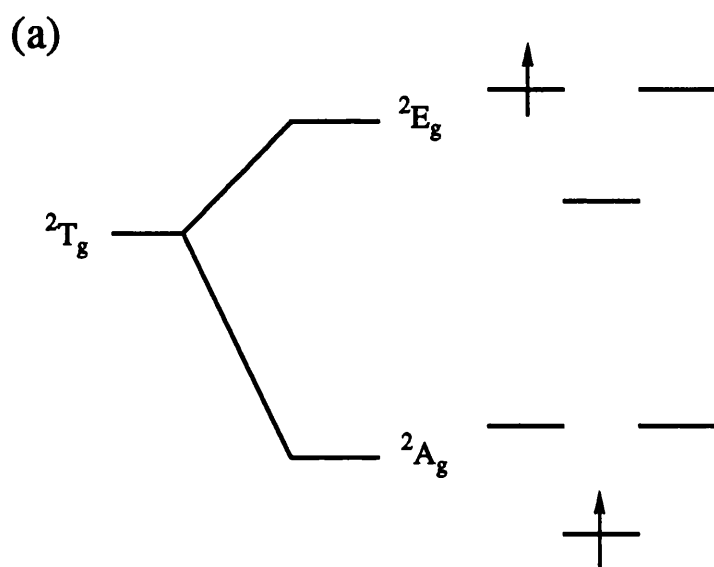


Figure 4.2.1

Splitting of T_g term (T_h) for $[\text{Ti}(\text{OH}_2)_6]^{3+}$ in axial field
Electron configurations in the strong field limit are shown.



when the E_g term is the lower lying and, more importantly, the lowest lying Kramers doublet when the E_g term has $g_{\perp} = 0$ contrary to experiment.^{4,5}

Perturbation theory is the most frequently used method to calculate the magnetic susceptibilities of the ${}^2T_{2g}$ term under the action of a trigonal field and spin-orbit coupling. Treating the trigonal field and spin-orbit coupling as simultaneous perturbations, expressions for the energies of the three Kramers doublets (from the ${}^2T_{2g}$ (O_h) term) may be derived.²³ Table 4.2.1 is reproduced from reference [23] and lists expressions for the first and second order Zeeman coefficients. For transition metal complexes with less than half filled shells, such as titanium(III), the energy levels denoted E_1 and E_2 constitute the lowest energy state for the system when the trigonal field leaves the E_g term lowest (fig 4.2.1 (b)). When the trigonal field is reversed such that the A_g term is lowest lying, as shown in figure 4.2.1 (a), the energy levels E_4 and E_6 are the lowest in energy. From inspection of table 4.2.1, it is seen that for the Kramers doublet with energies E_1 and E_2 , there is no first order Zeeman effect in the perpendicular direction. In the parallel direction it is predicted that there will only be a first order Zeeman effect as a consequence of reduction in the orbital angular momentum as expressed by the modified form of the magnetic moment operator $\hat{\mu} = \beta(k\hat{L} + 2\hat{S})$ where all the terms have their usual meaning. When $k = 1$ the effective magnetic moment, μ , is expected to fall rapidly to zero with decrease in temperature. Levels E_4 and E_6 have non-zero first order Zeeman effects. When the 2A_g term is the ground term, therefore, such a sharp decrease of μ with temperature is not expected.

We propose that the trigonal field leaves the E_g term as the ground term. The available experimental data is explained in terms of the E_g ground term being subject to a dynamic Jahn-Teller distortion at high temperatures freezing out into a static distortion at temperatures approaching that of liquid helium. Vibrational data is presented which indicates that a phase transformation occurs on cooling titanium alum down to liquid helium temperature.

TABLE 4.2.1

First- and second-order Zeeman coefficients for three Kramers doublets derived from ${}^2T_{2g}$ term after perturbation by trigonal field and spin-orbit coupling. $v = \Delta/\lambda$ where λ = spin-orbit coupling constant; Δ = trigonal field splitting parameter, defined as positive when the A_g term is lowest lying and negative when the E_g term is lowest lying. k = the orbital reduction factor taken to be isotropic. Contributions to the susceptibility from the crystal field 2E_g term have been neglected (After Mabbs and Machin [23]).

Energy E_i	$w_i^{(1)}(z)/\beta$	$w_i^{(2)}(z)/\beta$	$w_i^{(1)}(x)/\beta$	$w_i^{(2)}(x)/\beta$
$E_1 = E_2$	$\pm(k-1)$	0	0	$\frac{4}{\lambda} \left[\frac{\left(1 - \frac{k\alpha}{\sqrt{2}}\right)^2}{(1+\alpha^2)(v - \frac{3}{2} - Z)} + \frac{\left(1 - \frac{kb}{\sqrt{2}}\right)^2}{(1+b^2)(v - \frac{3}{2} + Z)} \right]$
$E_3 = E_5$	$\frac{\pm(k+1-\alpha^2)}{(1+\alpha^2)}$	$\frac{2(k+1-\alpha b)^2}{\lambda(1+\alpha^2)(1+b^2)Z}$	$\frac{\pm(\sqrt{2}k\alpha - \alpha^2)}{(1+\alpha^2)}$	$\frac{4}{\lambda} \left[\frac{\left(\frac{k\alpha}{\sqrt{2}} + \frac{kb}{\sqrt{2}} - \alpha b\right)^2}{2Z(1+\alpha^2)(1+b^2)} - \frac{\left(1 - \frac{k\alpha}{\sqrt{2}}\right)^2}{(1+\alpha^2)(v - \frac{3}{2} - Z)} \right]$
$E_4 = E_6$	$\frac{\pm(k+1-b^2)}{(1+b^2)}$	$\frac{-2(k+1-\alpha b)^2}{\lambda(1+\alpha^2)(1+b^2)Z}$	$\frac{\pm(\sqrt{2}kb - b^2)}{(1+b^2)}$	$-\frac{4}{\lambda} \left[\frac{\left(\frac{k\alpha}{\sqrt{2}} + \frac{kb}{\sqrt{2}} - \alpha b\right)^2}{2Z(1+\alpha^2)(1+b^2)} + \frac{\left(1 - \frac{kb}{\sqrt{2}}\right)^2}{(1+b^2)(v - \frac{3}{2} + Z)} \right]$

Where $Z = (v^2 + v + \frac{3}{4})^{\frac{1}{2}}$, $\alpha = [(\frac{1}{2} + v) - (v^2 + v + \frac{3}{4})^{\frac{1}{2}}]/\sqrt{2}$, and $b = [(\frac{1}{2} + v) + (v^2 + v + \frac{3}{4})^{\frac{1}{2}}]/\sqrt{2}$.

$$E_1 = \lambda(v - \frac{1}{2})$$

$$E_2 = \lambda(v - \frac{1}{2})$$

$$E_3 = \frac{\lambda}{2} [(\frac{1}{2} + v) + (v^2 + v + \frac{3}{4})^{\frac{1}{2}}]$$

$$E_4 = \frac{\lambda}{2} [(\frac{1}{2} + v) - (v^2 + v + \frac{3}{4})^{\frac{1}{2}}]$$

$$E_5 = \frac{\lambda}{2} [(\frac{1}{2} + v) + (v^2 + v + \frac{3}{4})^{\frac{1}{2}}]$$

$$E_6 = \frac{\lambda}{2} [(\frac{1}{2} + v) - (v^2 + v + \frac{3}{4})^{\frac{1}{2}}]$$

4.3 The sign of the trigonal field

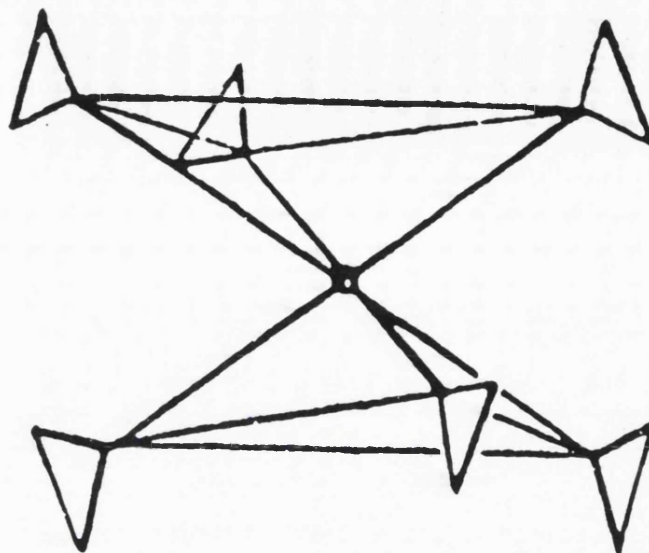
The structure of the $[\text{Ti}(\text{H}_2\text{O})_6]^{3+}$ cation within the CsTiSH alum is greatly affected by the hydrogen bonding constraints within the lattice. When the $[\text{Ti}(\text{H}_2\text{O})_6]^{3+}$ cation is in an environment which has little influence on its optimised geometry, the $[\text{Ti}(\text{H}_2\text{O})_6]^{3+}$ cation will adopt its most stable conformation from electronic and steric considerations alone. Recent, EPR, ENDOR, and electron spin-echo studies on the $[\text{Ti}(\text{D}_2\text{O})_6]^{3+}$ cation in an amorphous 2-propanol/ D_2O glass have established the hydration and electronic structure of the cation in this environment.²⁴ The structure of the complex was found to have high trigonal symmetry, all-vertical D_{3d} , as shown in figure 4.3.1(a). The TiO_6 core is approximately octahedral. The overall symmetry of the complex is realised through the position of the deuterium atoms, the positions of which lie in the D_{3d} mirror planes that contain the oxygen atoms. The EPR spectrum, recorded at X-band, shows the complex to be axially symmetric with $g_{\parallel} = 1.994$ $g_{\perp} = 1.896$. The g values are close to the free ion value implying that the unpaired electron is mainly in the a_{1g} orbital. *Ab initio* MO calculations that include electron correlation effects have been performed on the $[\text{Ti}(\text{D}_2\text{O})_6]^{3+}$ cation in view to relate the electronic and geometrical structure of the cation.²⁵ The optimised geometrical structure is in good agreement with the structure determined experimentally by means of the electron spin-echo modulation analysis. The calculations suggest that the trigonal field leaves a ground term of A_{1g} symmetry with an estimated trigonal field splitting of 5646 cm^{-1} . This form of trigonal distortion is equivalent to the more familiar elongation along the 3-fold axis of the octahedron only in this case the extent of trigonal field stabilisation is determined more by orientation of the water molecular planes relative to the TiO_6 framework than by a change of the Ti-O bond lengths or bond angles. With a trigonal distortion corresponding to an elongation along the 3-fold axis, one would expect the trigonal field splitting diagram to be reversed for the $[\text{V}(\text{H}_2\text{O})_6]^{3+}$ cation which has a ${}^3T_{2g}$ octahedral ground term. On this basis it is predicted that the all-vertical D_{3d} structure will not be the most stable geometry for $[\text{V}(\text{H}_2\text{O})_6]^{3+}$. Neutron Diffraction studies on the triflate salt $[\text{V}(\text{OH}_2)_6][\text{H}_5\text{O}_2][\text{CF}_3\text{SO}_3]_4$ ²⁶ have shown that although occupying a site of only C_1 symmetry, the $[\text{V}(\text{H}_2\text{O})_6]^{3+}$ cation has approximately all-horizontal D_{3d} symmetry as

Figure 4.3.1

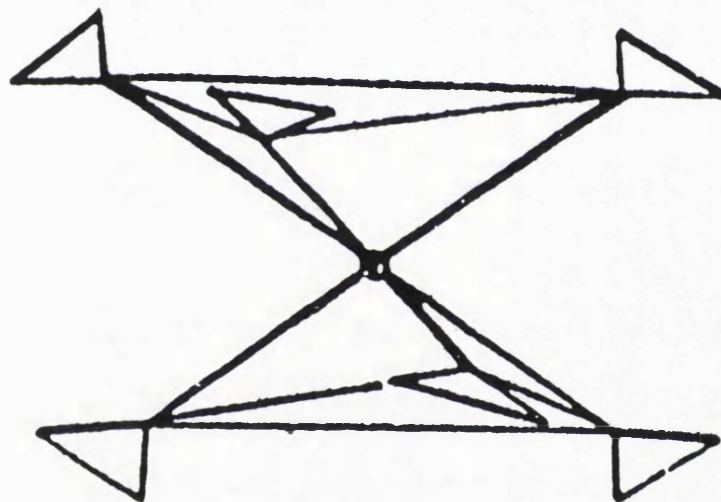
Three symmetry configurations adopted by the $[M(OH_2)_6]^{3+}$ cation.

- (a) The all-vertical D_{3d} structure found for the $[Ti(D_2O)_6]^{3+}$ cation in an amorphous solid of a 2-propanol/ D_2O mixture²⁴ (diagram after Cotton *et al.* [26])
- (b) The all-horizontal D_{3d} structure found for the $[V(OH_2)_6]^{3+}$ cation in the triflate salt $[V(OH_2)_6][H_3O_2][CF_3SO_3]_4$ ²⁶ (diagram after Cotton *et al.* [26])
- (c) The structure of the $[M(OH_2)_6]^{3+}$ cation found in the caesium β alums of Fe,²⁷ Ru,²⁸ Mo,²⁹ Cr,³⁰ and V.³¹ Three-fold axis is out of the plane of the paper (after Best *et al.* [29])

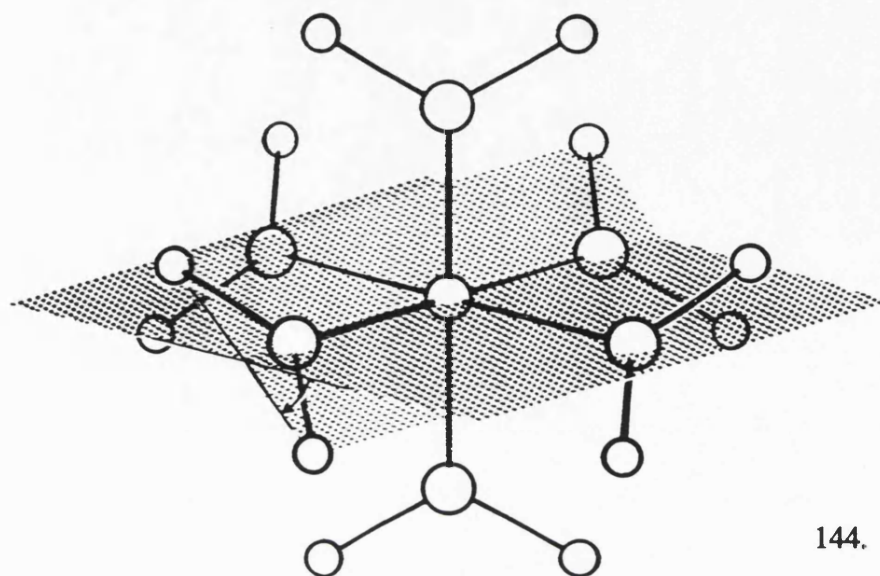
(a)



(b)



(c)



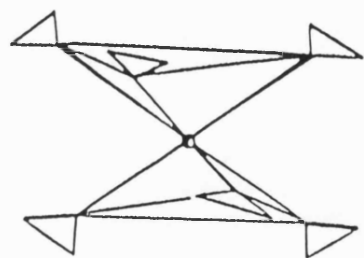
shown in figure 4.3.1(b). This form of trigonal distortion is equivalent to a compression along the 3-fold axis of the octahedron and is in keeping with the electronic preference of the $[\text{V}(\text{H}_2\text{O})_6]^{3+}$ cation. This does not prove, however, that the electronic factor is necessarily the one that determines the structure. It is apparent, however, that the hydration structure of the $[\text{Ti}(\text{OH}_2)_6]^{3+}$ cation is highly correlated to its electronic structure. The best technique available for the determination of the hydration structure of the $[\text{Ti}(\text{OH}_2)_6]^{3+}$ cation, in the undiluted alum lattice, is neutron diffraction. However, no neutron diffraction data is available for the CsTiSH alum. The neutron structures for the caesium sulphate β alums of Fe,²⁷ Ru,²⁸ Mo,²⁹ and Cr,³⁰ have, however, been determined at 15 K and the neutron structure of CsVSH determined at room temperature.³¹ The hydration structure of the $[\text{M}(\text{OH}_2)_6]^{3+}$ cation is found to be similar in each case and is shown in figure 4.3.1(c). The MO_6 core is again, approximately octahedral; the hydrogen atoms define a plane with the metal(III)-oxygen bond vector and are twisted round with respect to the MO_6 framework by angle of between 19 and 22° depending on the electronic structure of the metal(III) centre.³⁰ The cation has overall S_6 symmetry in keeping with the site symmetry within the lattice. The neutron structures are found to be in good agreement with the room temperature X-ray structures of the caesium alums of Fe,³² V,³² Cr,³² Ru,³³ and also the X-ray structure of CsMoSH³⁴ performed at 110 K. X-ray,^{32,35} and neutron²⁷ studies on the alums show clearly that the hydration structure of the $[\text{M}(\text{OH}_2)_6]^{3+}$ cation is dependent on the alum type. This is not surprising since all the hydrogen atoms participate in moderate or strong hydrogen bonds. At present, the only structural data available for any titanium alum is an X-ray structure determination of the CsTiSH alum at 102 K.³⁶ Although the R value for this structure is high (6.6%) the alum is reported to be characteristic of a β alum and isomorphous with the CsAlSH alum. This indicates that the *time averaged* hydration structure of the $[\text{Ti}(\text{OH}_2)_6]^{3+}$ cation at 102 K is similar to that illustrated in figure 4.3.1(c). A significant alteration of the hydration structure, such as the adoption of the all-vertical D_{3d} structure, could not be accommodated with the caesium sulphate β lattice. The single crystal Raman spectrum of CsTiSH³⁷ and RbTiSH³⁸ recorded at 80 K do, however, already show signs of the onset of a phase transition. However, the spectra are not too dissimilar to that of other caesium^{37,39} and rubidium³⁸ β alums. The

available structural and vibrational evidence suggest therefore, that the *time averaged* hydration structure of the $[\text{Ti}(\text{OH}_2)_6]^{3+}$ cation within the CsTiSH alum closely resembles the $[\text{M}(\text{OH}_2)_6]^{3+}$ structure found for the other caesium sulphate β alums (shown in fig. 4.3.1 (c)) in the liquid nitrogen temperature range. Based upon the molecular structure of the $[\text{Ti}(\text{OH}_2)_6]^{3+}$ cation in the β alum lattice, its electronic structure may be predicted using simple angular overlap arguments.³⁰ Figure 4.3.2 shows the relationship between the molecular structure of the $[\text{Ti}(\text{OH}_2)_6]^{3+}$ cation and the energies of the A_g and E_g components derived from the T_g (T_h) term. By rotation of the water molecules about the MO_6 framework, traversing through S_6 symmetry, the *all-vertical* D_{3d} structure is reached where the A_g trigonal field term is the ground term. Calculations from the angular overlap model predict that the magnitude of the trigonal field splitting increases as a function of the angle that the plane of the water molecule makes with the MO_6 framework.^{40,41} Traversing by the other pathway, the *all-horizontal* D_{3d} structure is reached where the E_g term is the lowest lying. Close inspection of the hydration structure of the cation shown in figure 4.3.1 (c) reveals that it is midway between the T_h and all-horizontal D_{3d} structures. For the all-horizontal D_{3d} structure, the water molecules are twisted round by 45° with respect the MO_6 framework. In the alums this angle is found to be between 19° and 22° depending on the electronic structure of the cation.³⁰ On this basis, therefore, we predict the $[\text{Ti}(\text{OH}_2)_6]^{3+}$ cation is constrained within the alum lattice to a structure that yields an E_g ground term. We shall now show that the experimental results for titanium(III) in the alum lattice can be rationalised from this standpoint.

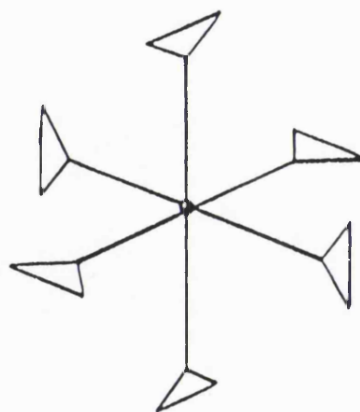
4.4 Jahn-Teller Theory

As Jahn and Teller showed,^{42,43} an electronically degenerate state of a non-linear complex is unstable (except in the case of Kramers degeneracy) with respect to some asymmetric nuclear displacement which acts to lift the degeneracy. The extent of the Jahn-Teller coupling depends on the relative magnitudes of the associated vibrational energies and the Jahn-Teller stabilisation energy. If the coupling between the electrons and such displacements is sufficiently strong relative to the energy of the associated vibrational modes, the complex undergoes a static distortion to a new

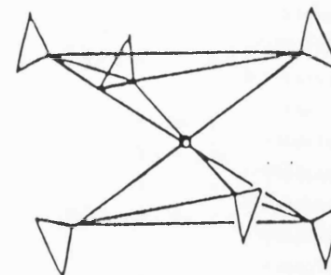
FIGURE 4.3.2



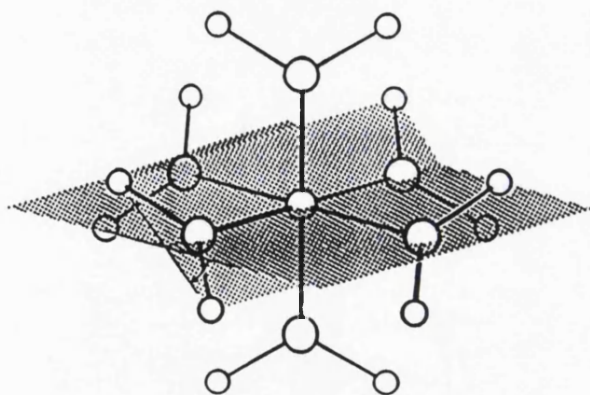
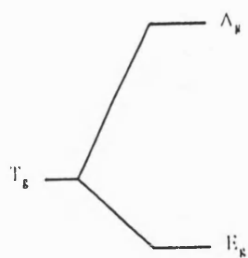
All horizontal
 D_{3d}



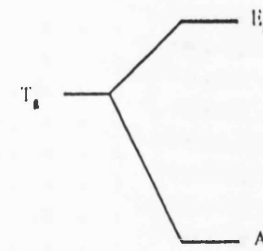
T_h



All Vertical
 D_{3d}



Relationship between the molecular structure and the energies of the A_g and E_g orbital terms for the $[Ti(OH_2)_6]^{3+}$ cation lying on a site of trigonal symmetry.



configuration of minimum energy. If the coupling is less strong, or if the zero-point vibrational energy is comparable with the energy barrier separating equivalent configurations, no static distortion occurs, but the complex exhibits a coupled motion of the electrons and vibrational modes. This situation is referred to as the dynamical Jahn-Teller effect.

Theoretical work concerning the dynamical Jahn-Teller distortion, and the effect that it has on the magnetic properties of a complex, have been most elegantly investigated by Ham for both doubly⁴⁴ and triply²⁰ degenerate orbital ground terms. Ham showed that the dynamical Jahn-Teller effect in a complex may partially quench orbital operators giving rise to spin-orbit interaction, hyperfine interactions, strain etc whilst retaining the symmetry of the symmetrical configuration. Theories which presuppose strong coupling have been pioneered mainly by Bersuker^{45,46} and O'Brien.⁴⁷ These theories are applicable only on approaching the static Jahn-Teller limit where the energy levels of the distorted configurations are effectively treated as Born-Oppenheimer states. A brief outline only of the theories relevant to this discussion is given here. Comprehensive reviews are available on this topic.^{48,49}

The vibronic hamiltonian for an doubly or triply degenerate orbital term coupled to a doubly or triply degenerate vibrational mode may be represented as:

$$H = H_0 + H_{HO} + H_{JT} + H_{JT}^2 + H_{AN}^3 \quad 4.4.1$$

H_0 is the hamiltonian of the degenerate electronic state in the symmetrical configuration; H_{HO} is the harmonic oscillator hamiltonian; H_{JT} and H_{JT}^2 are the linear and quadratic terms represent the Jahn-Teller coupling and H_{AN}^3 is the third-order anharmonicity term. The solution of the vibronic hamiltonian that describes the linear Jahn-Teller coupling, only, of an orbital doublet electronic state to a pair of doubly degenerate vibrational modes Q_e , Q_g in cubic or axial symmetry ($E \otimes e$ problem) within the harmonic approximation is:

$$E_{\pm} = E_0 \pm V\rho + \frac{1}{2}\mu\omega^2\rho^2 \quad 4.4.2$$

where μ is the effective mass of the mode, ω its angular frequency and V the coupling coefficient for linear Jahn-Teller coupling. Equation 4.4.2 plotted as a function of Q_e , Q_g gives the well know "Mexican hat" potential energy surfaces shown in figure 4.4.1(a). Equation 4.4.2 has rotational symmetry about the origin. The configurations of minimum energy on the lower sheet in figure 4.4.1(a) are all the points on the circle $\rho = V/\mu\omega^2$. This minimum defines the Jahn-Teller energy E_{JT} :

$$E_{JT} = V^2/2\mu\omega^2 \quad 4.4.3$$

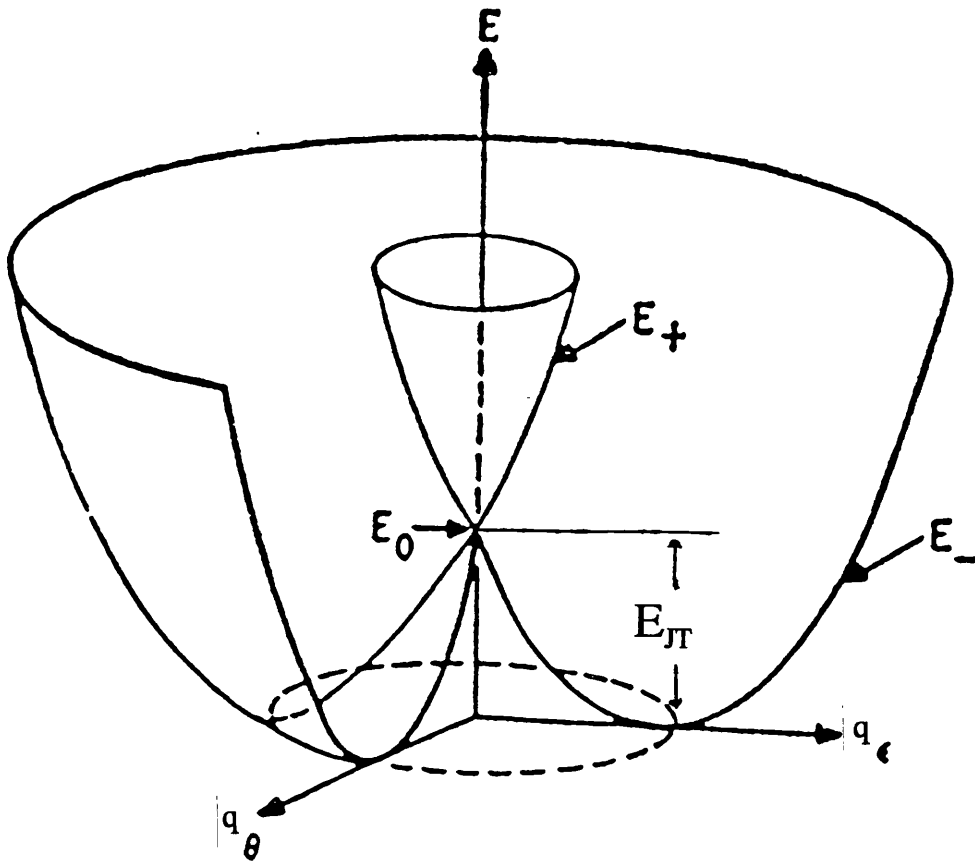
which is the amount by which the system is lowered when the system is distorted from the symmetrical configuration to a point at the bottom of the trough. Irrespective of the value of V , the vibronic states, so far as symmetry considerations are concerned are identical with those of the original electronic orbital doublet state when Jahn-Teller effects are ignored. This treatment is limited to linear Jahn-Teller coupling. This coupling should be more important than higher order effects if the Jahn-Teller coupling is weak with respect to the vibrational energy available to the system *i.e.* when the Jahn-Teller effect is dynamic. However, considering only linear Jahn-Teller coupling leads to an infinity of static distortions. Inclusion of the quadratic and cubic terms leads to warping of the bottom of the potential-energy trough giving three equivalent minima as shown in figure 4.4.1(b). In the limit of strong Jahn-Teller coupling where $E_{JT} \gg \hbar\omega$, the distortion becomes static yielding three equivalent configurations. In transcending from the dynamic to the static model the complex is thought to undergo "pulsating deformations".⁴⁶ That is to say the complex rapidly interconverts from one minimum to another *viz.* tunnelling through the potential barriers of the minima. Since there will be a finite overlap of the wavefunctions of the respective potential wells, the energy levels of the minima perturb one another leading to a small energy separation between the ground state and the first vibronic excited state. For the $E \otimes e$ problem, this "tunnelling splitting" leads to a doublet ground state and singlet excited state.⁴⁹ The magnitude of the tunnelling splitting, δ , diminishes as the height of the potential barrier is increased and is inversely proportional to the lifetime τ of the distorted configuration. The tunnelling theory is applicable on approaching the strong coupling limit only. In this instance, $\delta \ll \hbar\omega$, *ie.* the frequency

Figure 4.4.1

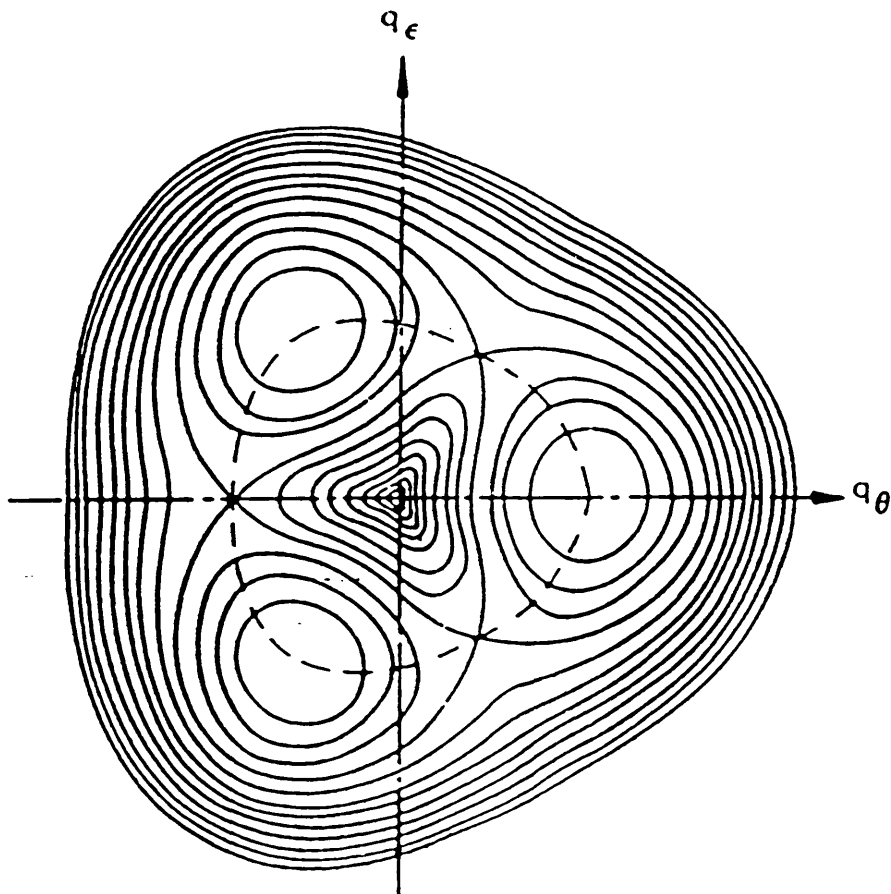
(a) Potential-energy surface for an electronic E term linearly coupled to E displacements (After F. S. Ham [44]).

(b) Equipotential section of potential-energy surface for $E \otimes e$ problem taking into account quadratic and cubic terms of the vibronic hamiltonian (after Bersuker and Polinger [48]).

(a)



(b)



of pulsating distortions of the molecule is much less than the frequency of ordinary vibrations undergone in the distorted configurations. Tunnelling splitting can have a dramatic effect on the magnetic behaviour of a Jahn-Teller system since the vibronic levels mix under the magnetic field. Figure 4.4.2 shows the variation of the energy levels of the ground state $E \otimes e$ problem with respect to the external magnetic field strength. The form of the EPR and magnetic susceptibility data obtained for a system of this kind will depend on the strength of the magnetic field applied to the system and the orientation of the distortion axis with respect to the magnetic field direction. For the case shown in figure 4.4.2, the external magnetic field is applied along a distortion axis where the anisotropic Zeeman interaction is greatest. In this instance, the external magnetic field has the effect of depressing the pulsations, locking the system in the minimum along the field direction. As a consequence of increase in magnetic field strength, therefore, the system is induced into making the transition from a dynamic to a static Jahn-Teller system.

4.5 Raman spectra of CsTiSH and RbTiSH

i) 10 - 275 wavenumber range

The wavenumbers of the lattice modes are found to have a strong temperature dependence in both the rubidium and caesium⁵⁰ titanium alums. Figure 4.5.1 shows bands of E_g symmetry in the wavenumber range -100 to 250 cm^{-1} at temperatures between 80 and 200 K for the RbTiSH alum. Assignments for the RbTiSH alum in this spectral region at 80 K are listed in chapter 2, table 2.10.9. The band found at 200 cm^{-1} at 200 K, tentatively assigned to $\nu_2(\text{RbO}_6)$ moves to 202 cm^{-1} at 125 K and to 206 cm^{-1} , at 80 K. The band found at 40 cm^{-1} at 200 K, tentatively assigned to a translational mode of sulphate, moves to lower wavenumber on cooling. As with the $\nu_2(\text{RbO}_6)$ mode, the position of the band changes more rapidly as the crystal is cooled to 80 K. The band assigned to the $\text{tr}(\text{SO}_4)^{2-}$ mode is found at 39 cm^{-1} at 125 K and at 34 cm^{-1} at 80 K. The changes in this spectral region become even more pronounced as the crystal is cooled to liquid helium temperatures. Figure 4.5.2 shows bands of all symmetries in the wavenumber range -100 to 250 cm^{-1} between 4 and

Figure 4.4.2

Energy levels of the ground state $E \otimes e$ problem in a magnetic field parallel to the distortion axis taking into account tunnelling splitting. Magnetic-dipole allowed transitions in regions I to III are shown by means of arrows (after Bersuker [49]). The Zeeman interaction arising from the excited singlet vibronic state is isotropic whereas the Zeeman splitting of the ground state is anisotropic and is a maximum along the distortion axes.

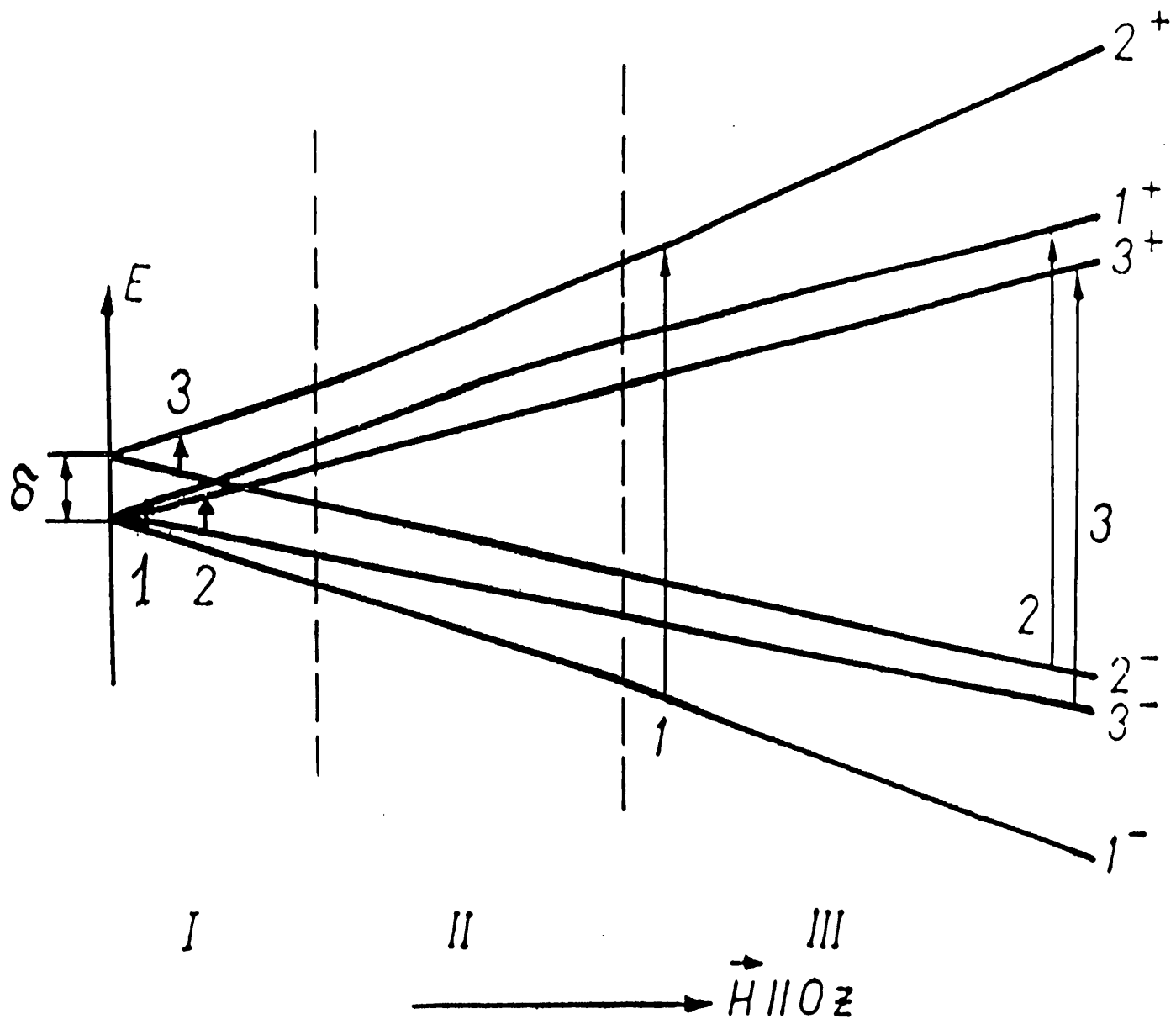


Figure 4.5.1

Single crystal Raman spectra of $\text{RbTi}(\text{SO}_4)_2 \cdot 12\text{H}_2\text{O}$ showing bands of E_g symmetry in the wavenumber range -100 to 250 cm^{-1} at temperatures of 80 , 125 and 200 K

Step size 0.4 cm^{-1} ; spectral bandwidth 2.93 cm^{-1} at 75 cm^{-1} ; integration time: 2 seconds, 413 nm radiation, 80 mw power at sample).

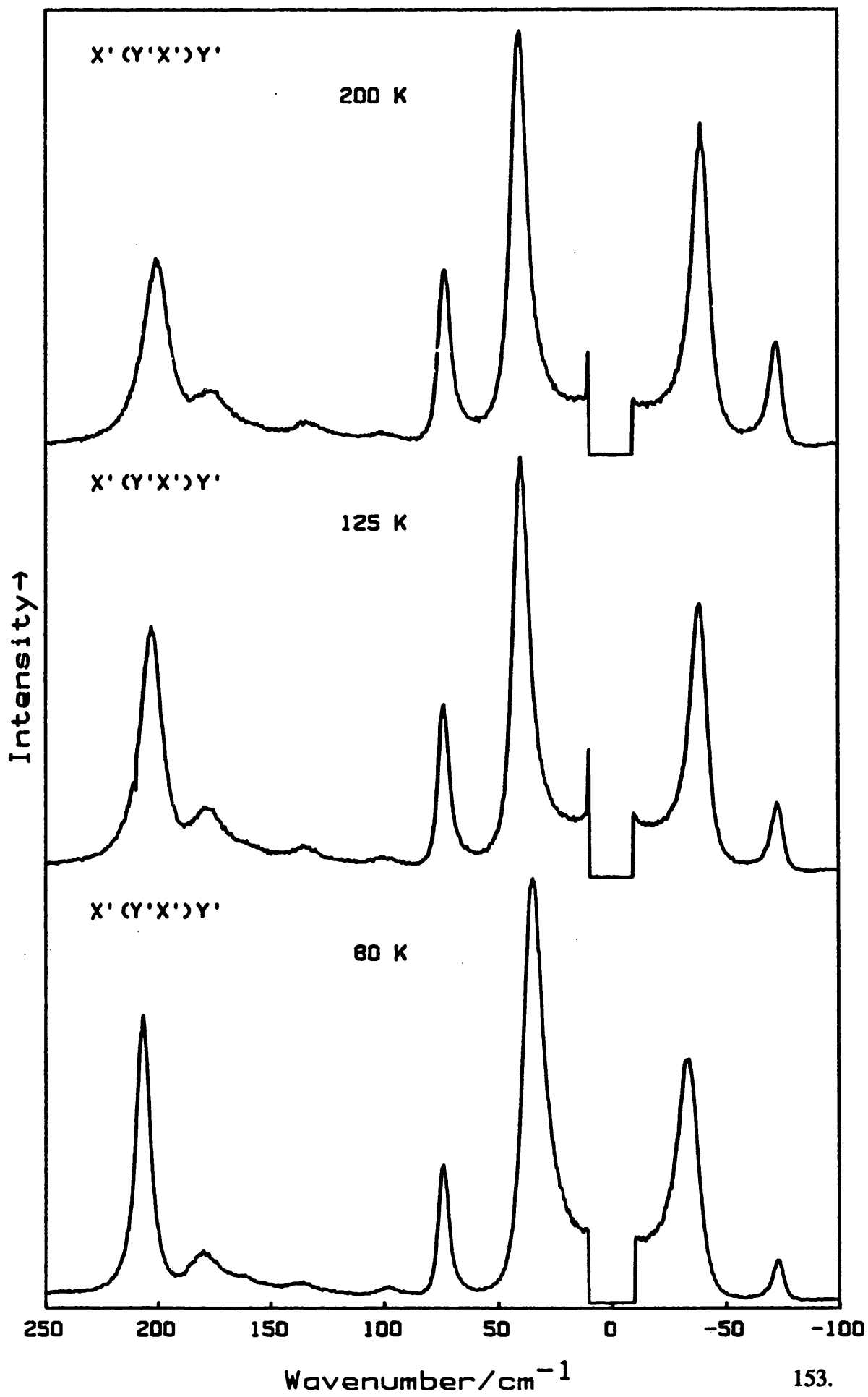
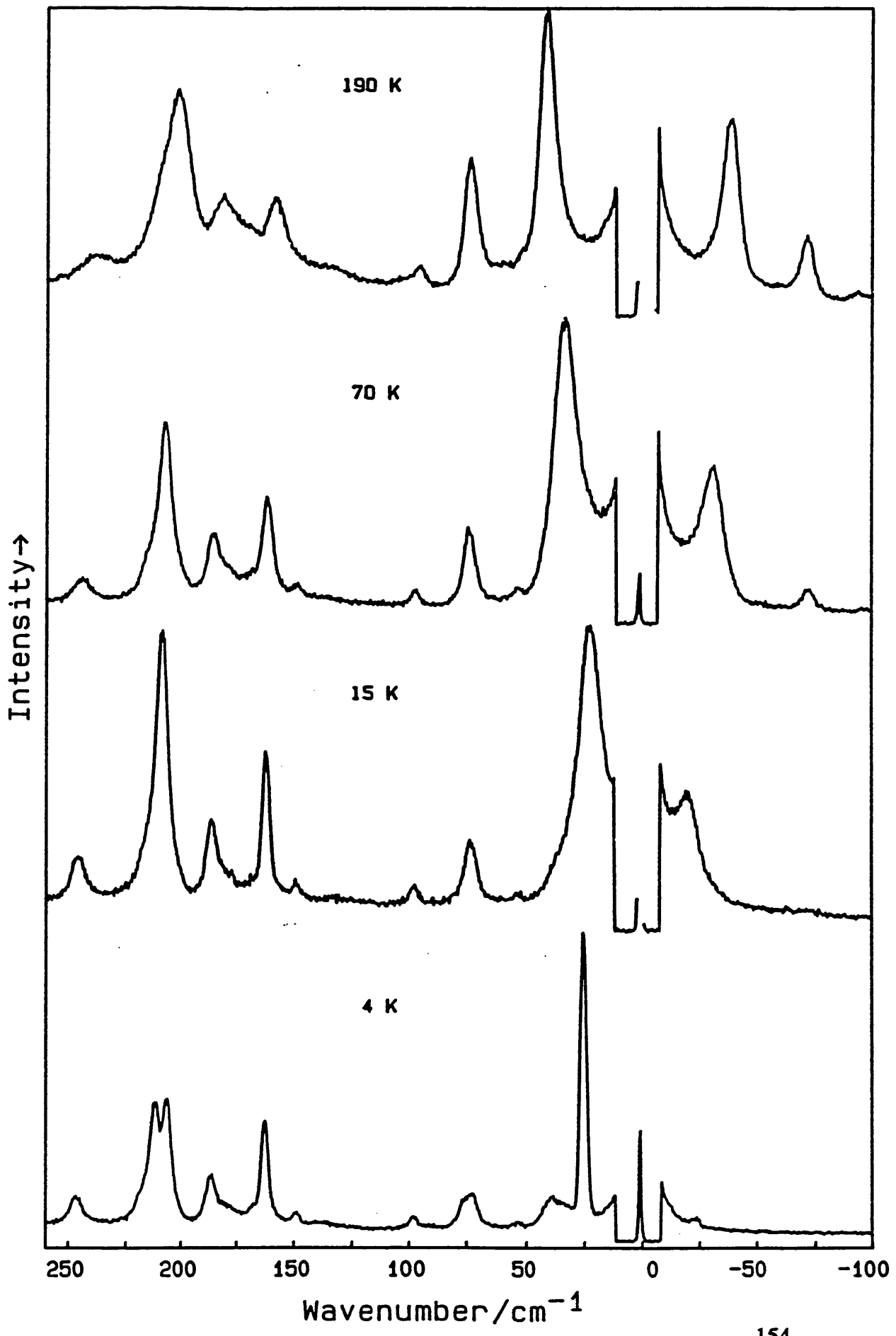


Figure 4.5.2

Single crystal Raman spectra of $\text{RbTi}(\text{SO}_4)_2 \cdot 12\text{H}_2\text{O}$ showing bands of all symmetries in the wavenumber range -100 to 250 cm^{-1} at temperatures of 4, 15, 70, and 190 K. Step size 0.4 cm^{-1} ; spectral bandwidth 2.93 cm^{-1} at 75 cm^{-1} ; integration time: 2 seconds, 413 nm radiation, 25 mw power at sample).



200 K. The band due to the soft mode corresponding to $\text{tr}(\text{SO}_4)^{2-}$ is found at 22 cm^{-1} at 15 K, 18 cm^{-1} lower than its wavenumber at 200 K. On cooling from 15 K to 4 K the band sharpens and moves to 25 cm^{-1} . The sharpening of the soft mode is an indication that at this temperature, 4 K, the phase transition is near completion. Analogous behaviour is also observed for the CsTiSH alum⁵⁰ but data is yet to be recorded over a large wavenumber and temperature range. No such behaviour is observed for any other first row transition metal ion.

ii) 275 - 1200 wavenumber range

The mid-wavenumber Raman spectra of the RbTiSH alum recorded at 80 K is shown in chapter 2, figure 2.9.9, with corresponding assignments in table 2.9.9. The Raman spectra of the rubidium and caesium³⁷ alums are analogous. The mid-wavenumber region of the titanium alums are similar to that of other β alums.³⁷ There are differences however which are indicative of the onset of a phase transition.

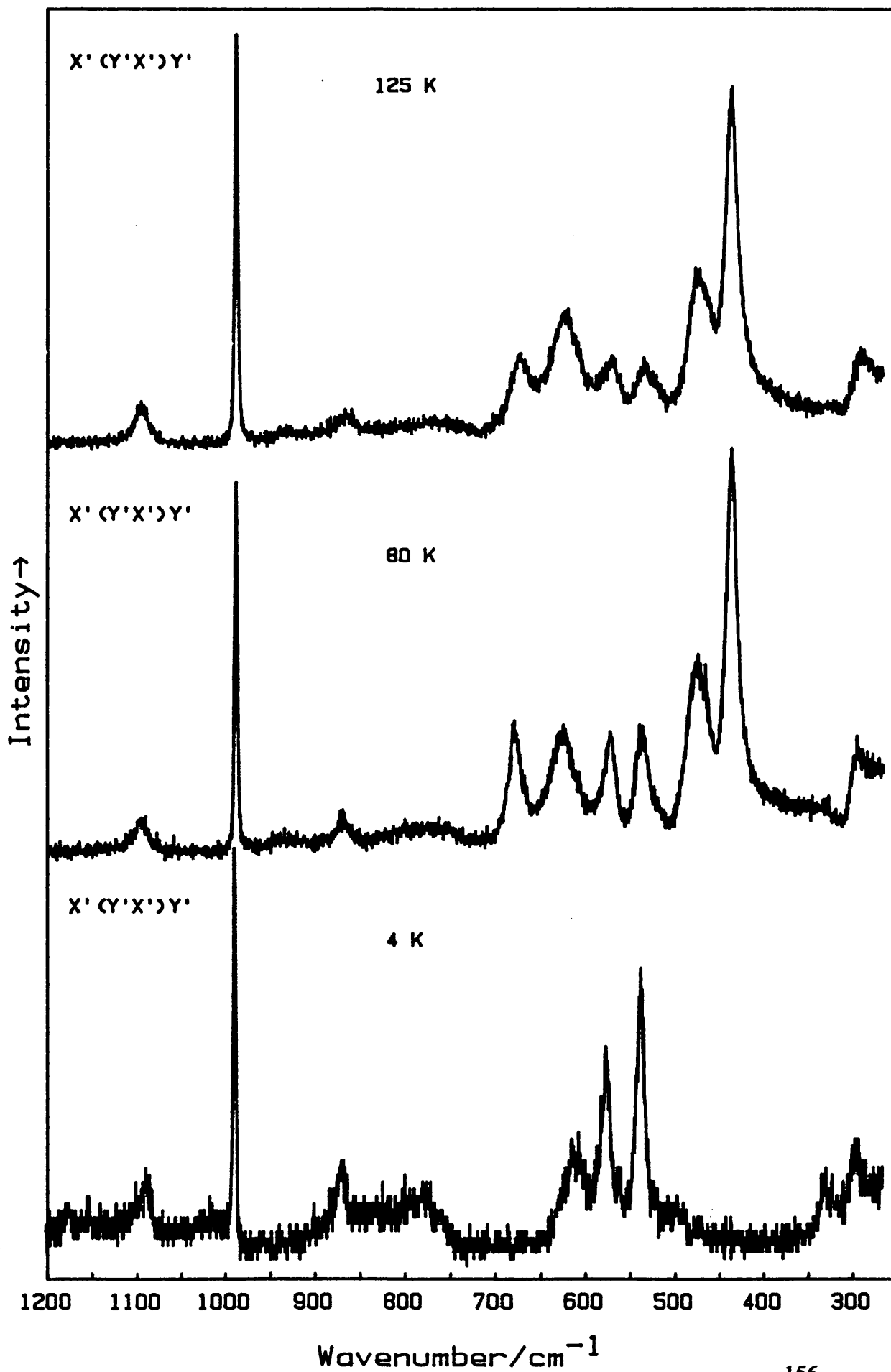
A number of modes observed show considerable broadening, most evident in the external modes of water. For the caesium alum single crystal Raman study,^{37,51} a good correlation is found between the wavenumber of the six external modes of water and the size of the unit cell for all the alums of the same modification except that of CsTiSH where the external modes associated with the $[\text{Ti}(\text{OH})_6]^{3+}$ cation are anomalous both in wavenumber and profile.

There is a dramatic change in the mid-wavenumber spectra of the RbTiSH alum on cooling to liquid helium temperatures. Figure 4.5.3 shows E_g spectra in the wavenumber range 265 to 1200 cm^{-1} . Bands found at 677, 473 and 435 cm^{-1} in the spectra recorded at 80 K were assigned in chapter 2 as phonon modes corresponding to ρ_4 , and coupled components of $\nu_2(\text{TiO}_6)^{3+} + \nu_2(\text{SO}_4)^{2-}$ respectively.

These bands are not present or else occur with vanishingly weak intensity in the spectra recorded at 4 K. A new peak is found at *ca.* 328 cm^{-1} . Assignment of this band to a phonon mode is not attempted because of the limited available data. A schematic representation of the $\nu_2(\text{MO}_6)$ mode is shown in figure 2.7.1. In the course of the vibration, the hexa-aqua-cation is subject to a tetragonal distortion. The orbital degeneracy will be lifted and the system stabilised.

Figure 4.5.3

Single crystal Raman spectra of $\text{RbTi}(\text{SO}_4)_2 \cdot 12\text{H}_2\text{O}$ showing bands of E_g symmetry in the wavenumber range 250 to 1200 cm^{-1} at temperatures of 4, 80, and 125 K. Spectra at 80 and 125 K: step size 0.4 cm^{-1} ; Integration time: 2 seconds, 413 nm radiation, 80 mw power at sample. Spectrum at 4 K step size 0.4 cm^{-1} ; Integration time: 1 second, 406 nm radiation, 35 mw power at sample.



The Raman spectra of the caesium and rubidium titanium alums can be interpreted in terms of the $[\text{Ti}(\text{OH}_2)_6]^{3+}$ cation transcending from a dynamic Jahn-Teller complex to the static limit on cooling to 4 K. At room temperature, excited vibrational levels are thermally populated and the Jahn-Teller coupling is not sufficiently strong to cause a static asymmetric displacement of the complex. As the temperature is lowered, the excited vibrational states are depopulated and the system falls into the lowest possible potential energy minima. At 4 K the spectra suggest that the phase transition is near completion indicating that the Jahn-Teller coupling is strong compared with the zero-point energies of the phonon modes within the lattice. A displacement along the $\nu_2(\text{TiO}_6)$ normal co-ordinate is a likely candidate for the asymmetric displacement that gives the greatest Jahn-Teller energy stabilisation making this problem appropriate to the $E \otimes e$ description. Such a distortion would induce structural perturbations throughout the lattice. Evidence for such perturbations is seen clearly from the dramatic change in the low wavenumber spectra with temperature. Within the titanium alum lattice there exists a highly directional hydrogen bonding network. All the Jahn-Teller centres are therefore correlated to one another and distortions that were equivalent on considering the free Jahn-Teller centre only, are no longer so. Assuming there are four $[\text{Ti}(\text{OH}_2)_6]^{3+}$ cations per unit cell each with 3 possible distortion directions there will be 81 possible distortion combinations for the unit cell. Some of these arrangements will be equivalent and also, more energetically favourable than other arrangements. When viewing the crystal as the macroscopic body it is predicted that in the static limit, there will be an ordering of the $[\text{Ti}(\text{OH}_2)_6]^{3+}$ cations throughout the lattice. This is known as the co-operative Jahn-Teller effect. Since it is predicted that long range ordering will remain on undergoing the phase transformation, the system can readily be studied by diffraction techniques.

4.6 Magnetic data

In order to test the proposed model, the published EPR and magnetic data has to be satisfactorily accounted for with the trigonal field reversed from what was previously supposed. We are aware of four groups of authors who have made magnetic susceptibility measurements for CsTiSH in the 80 - 300 K temperature range.^{11,12,14,16} Of these data sets we choose the set published by Figgis, Lewis and Mabbs¹² with which to work. This is because a comprehensive data set is presented and the authors report that every precaution to prevent oxidation of titanium(III) to diamagnetic titanium(IV) has been taken and the specimens analyzed after measurement to check that such oxidation had not taken place.

Two data sets were recorded by these authors. These are presented in figure 4.6.1. along with the best fit achieved by the authors. The parameters used to get the best fit were $\Delta = 350 \text{ cm}^{-1}$, $\lambda = 93 \text{ cm}^{-1}$, and $|k| = 0.7$; $|k|$ being the orbital reduction factor taken to be isotropic.

Although the two data sets have different offsets, they have the same curvature. Figures 4.6.2 and 4.6.3 show the best fit that we have achieved with a negative trigonal field (E_g ground term) and isotropic orbital reduction factor for the two data sets. Using anisotropic orbital reduction factors gave little improvement to the fit. The theoretical fit matches the experimental data very well in the temperature range 300 to 140 K. Below this, the effective magnetic moment derived from the parameters is predicted to fall off much faster than is observed. The variation of μ_{eff} with temperature in the 80 - 300 K region can be accounted for by a model in which the action of the trigonal field leaves an E_g ground term which is subject to Jahn-Teller distortion. The theoretical fit follows from Van Vleck's susceptibility formula and uses expressions for the first and second order Zeeman coefficients given in table 4.2.1. This approach assumes that the $[\text{Ti}(\text{OH})_6]^{3+}$ cation is undergoing vibrations described within the S_6 point group only. If the complex is under going ordinary vibrations within the distorted configurations, then the expressions for the Zeeman coefficients shown in table 4.2.1 will not be valid as the $[\text{Ti}(\text{OH})_6]^{3+}$ cation is better thought of as rapidly interconverting between rhombic configurations. This will have the effect of lifting the orbital degeneracy of the ground state resulting in χ_{\perp} being

Figure 4.6.1

Plot of effective magnetic moment, μ_{eff} against temperature.

Data sets 1 and 2 are the experimental data sets obtained from susceptibility measurements by Figgis, Lewis and Mabbs.¹² Theoretical fit is the best fit to the experimental data achieved by the authors. Parameters used for fit are:

Orbital reduction factor, $k, = 0.7$; Trigonal field splitting, $\Delta, = + 350 \text{ cm}^{-1}$ (A_g term ground state); Spin-orbit coupling constant, $\lambda, = 93 \text{ cm}^{-1}$.

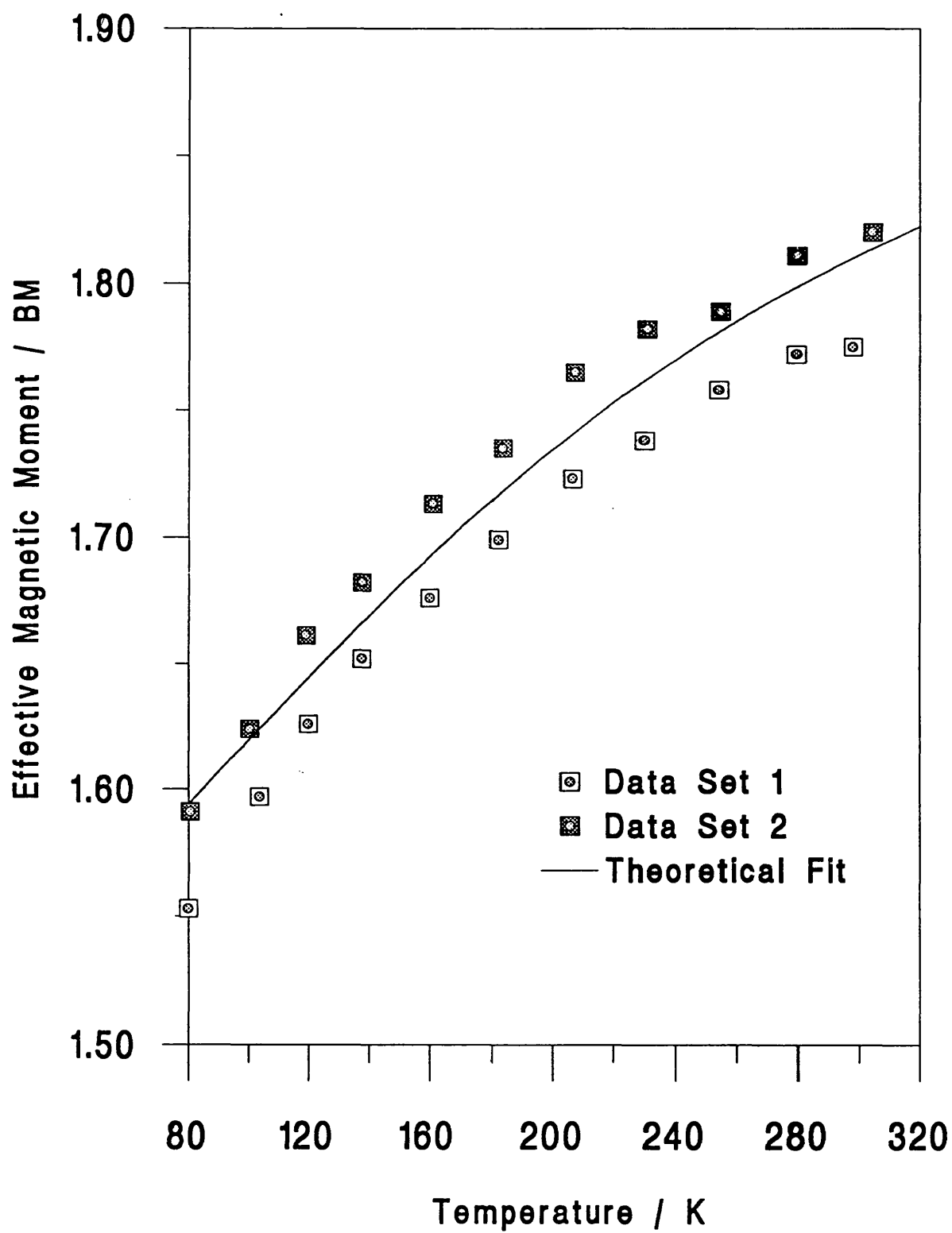


Figure 4.6.2

Plot of effective magnetic moment, μ_{eff} against temperature.

Data sets 1 and 2 are the experimental data sets obtained from susceptibility measurements by Figgis, Lewis and Mabbs.¹² Theoretical fit is the best fit to data set 1 with negative trigonal field and isotropic orbital reduction factor. Parameters used for fit are: $k_{\parallel} = 0.66$; $\Delta = -2400 \text{ cm}^{-1}$; $\lambda = 91 \text{ cm}^{-1}$.

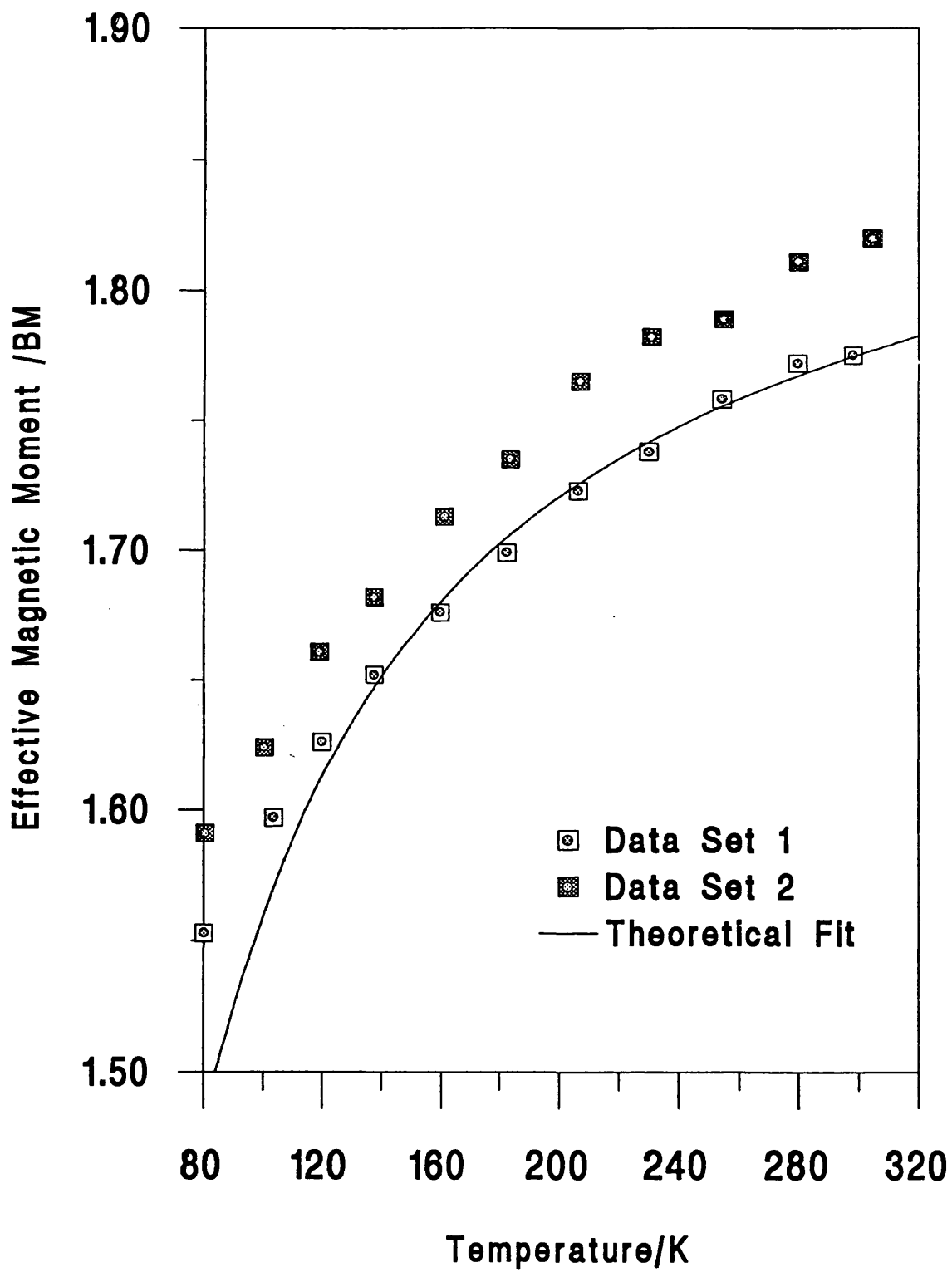
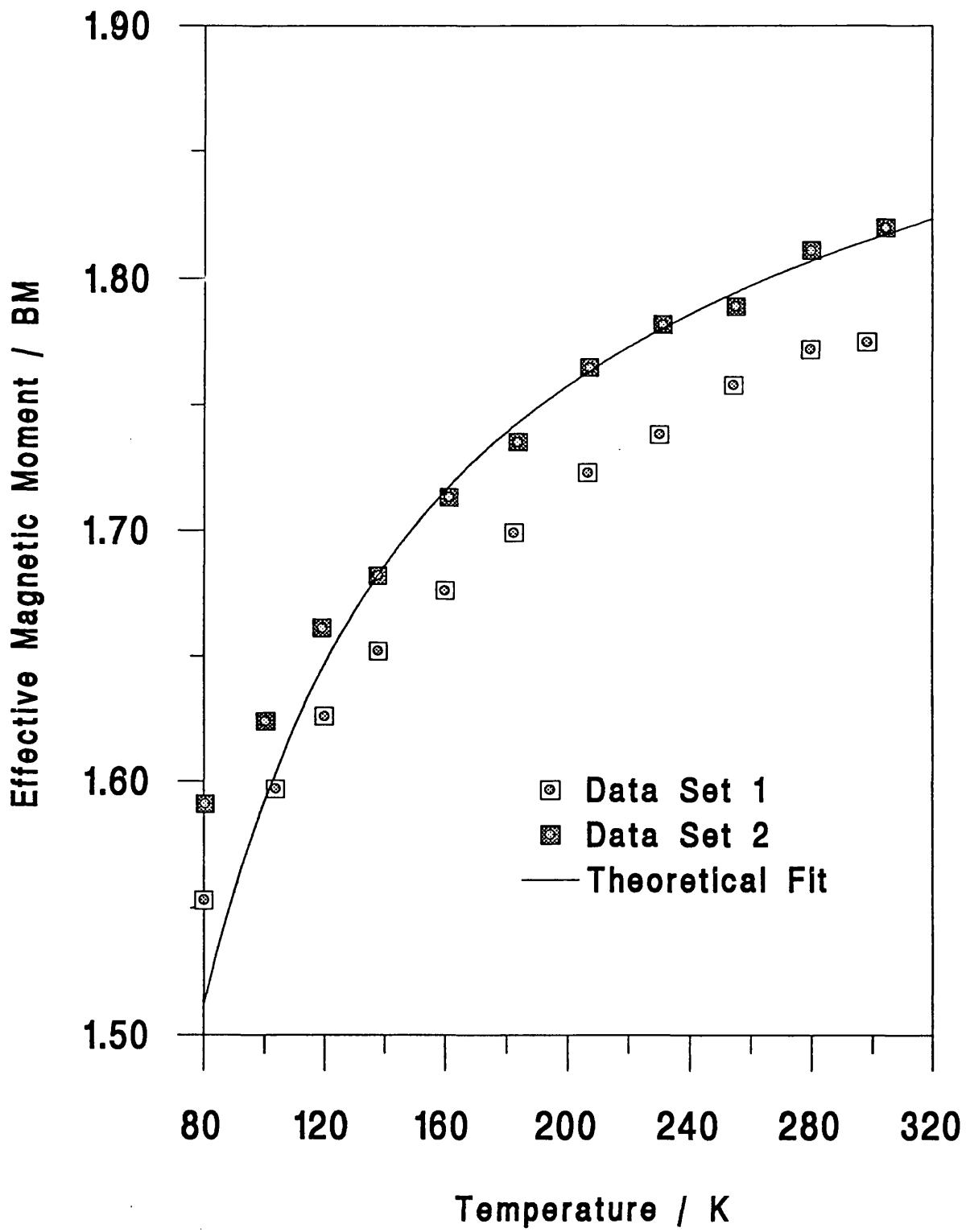


Figure 4.6.3

Plot of effective magnetic moment, μ_{eff} against temperature.

Data sets 1 and 2 are the experimental data sets obtained from susceptibility measurements by Figgis, Lewis and Mabbs.¹² Theoretical fit is the best fit to data set 2 with negative trigonal field (E_g term ground state) and isotropic orbital reduction factor. Parameters used for fit are: $k = 0.76$; $\Delta = -2400 \text{ cm}^{-1}$ (E_g term ground state); $\lambda = 85 \text{ cm}^{-1}$.



non-zero for the ground state Kramers doublet. This would account for the departure, below 140 K, of the experimentally determined values of the effective magnetic moment with those calculated from the model assuming axial symmetry with a 2E_g ground term. The trigonal field splitting used in both these fits was -2400 cm^{-1} . In the vanadium alums of NH_4^+ ,⁵² Cs^+ ,⁵² and Rb^+ ,⁵³ the trigonal field splitting is found to be ca. 1940 cm^{-1} by Raman spectroscopy. Since titanium(III) has a more diffuse 3d radial function than vanadium(III), we would expect a trigonal field splitting for titanium(III) of at least this magnitude. However, no electronic Raman band has yet been found for either RbTiSH^{38} or CsTiSH .⁵¹

Magnetic susceptibility measurements on the CsTiSH alum have been made in the 1.0 - 4.2 K temperature range by Benzie and Cooke.¹⁰ These authors also report that the sample was analyzed after the experiment as a check on the titanium(III) content of the alum. The susceptibility is found to follow Curie's law in this temperature region. No Weiss constant is detected. An effective g value of 1.12 is obtained from the "spin only" susceptibility formula. The deviation from the "free-spin" Lande g value of 2 is interpreted as arising from a relatively small separation between the ground state and the higher orbital energy levels. At temperatures above 4.2 K, the experimental results are found to deviate from Curie's law,¹¹ this behaviour is also interpreted in terms of a low lying excited state. Recently we have undertaken susceptibility measurements on the CsTiSD alum in the liquid helium temperature range at very high fields using a SQUID magnetometer. The results are presented in figure 4.6.4. The experimental data is found to follow the Curie-Weiss law. Curie and Weiss constants of $C_M = 0.2091\text{ (K mole}^{-1}\text{ emu}^{-1}\text{)}$ and -1.4368 (K) are respectively obtained giving an effective g value of 0.41 from the susceptibility formula:-

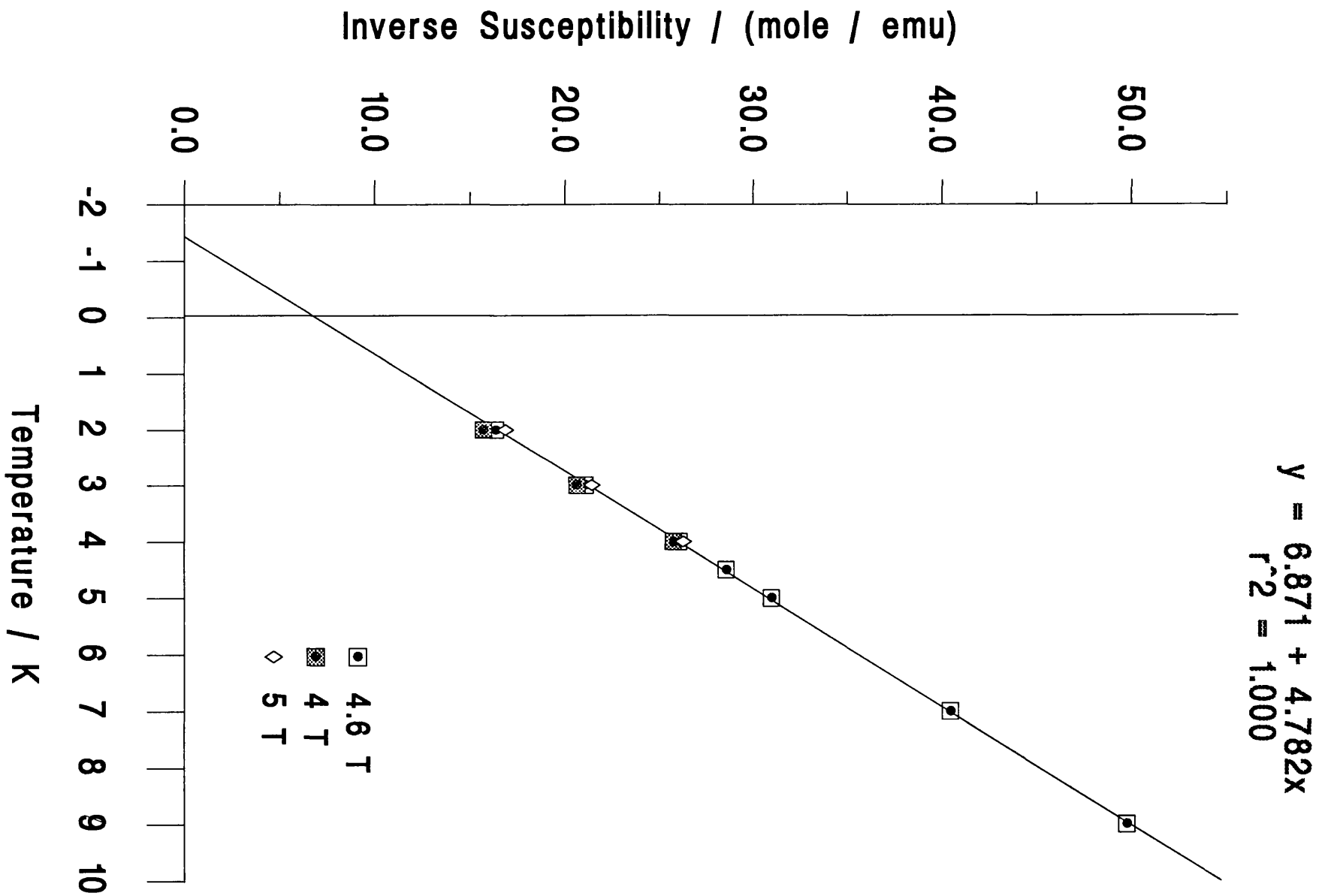
$$\chi T = \frac{Ng^2\beta^2s(s+1)}{3k}$$

4.6.1

where $\chi_M =$ Susceptibility $\text{J T}^{-2}\text{mole}^{-1}$; T = Temperature K; N = Avogadro's constant mole^{-1} ; $\beta =$ Bohr Magneton JT^{-1} ; k = Boltzmann's constant J K^{-1} ; s = spin quantum number = 1/2.

Figure 4.6.4

Plot of inverse susceptibility against temperature for CsTiSD alum. Data collected on Squid Magnetometer (Sheffield).



At fields of 5 T and temperatures as low as 2 K, there is no sign that the system approaches magnetic saturation. The data was collected with fields of 4, 4.6, and 5 T in the temperature range of 2 - 9 K. No deviation from the Curie-Weiss law is found in this experimental range.

The magnetic behaviour of CsTiSD found in this study is very different to that reported by Benzie and Cooke¹⁰ for CsTiSH in the same temperature range. The g value is considerably lower and an appreciable Weiss constant is detected. The negative Weiss constant found may be suggesting an antiferromagnetic ordering of the spins. Since this system is magnetically dilute, this would be surprising. Both the EPR spectrum of CsTiSH and CsTiSD have been recorded at X-band and the g values for the deuterate found to be slightly higher than those for the hydrate⁵ (CsTiSH:- $g_{\parallel} = 1.25$ (2) $g_{\perp} = 1.14$ (2); CsTiSD:- g approximately isotropic = 1.31 (2)) The low effective g value for CsTiSD found in this study (0.41) may be a consequence of oxidation of titanium(III) as no check on the titanium(III) content of the sample was made. It is also possible, however, that the different magnetic behaviour is a result of the very different experimental conditions used for the two experiments. At the time when the magnetic data for CsTiSD was collected it was assumed that the alum was cubic over the whole temperature range. Since the magnetic properties of cubic compounds are isotropic, the alum was introduced into the sample chamber as a single crystal rather than as a powder. The Raman data suggest that there is a structural change on approaching temperatures of liquid helium. In the absence of structural data in this temperature range, it cannot be presumed that the alum remains cubic. In addition, since the two data sets were measured at very different field strengths, the data sets are not directly comparable since the magnitude of the external magnetic field can have a profound effect on the static/dynamic nature of the Jahn-Teller complex. According to Bersuker,⁴⁹ in the limit where the tunnelling splitting approximation is valid, the three equivalent minima of an $E \otimes e$ complex will be non-equivalent in the presence of an external magnetic field. As a result, the complex is subject to a Zeeman-induced transition from a dynamic to a static Jahn-Teller complex. This effect will be of greatest magnitude when a tetragonal axis of the complex is aligned with the field direction. The strong external field will then have the effect of depressing the pulsations, locking the system in the minimum along the

field direction. In the CsTiSH alum, the tetragonal axes of the TiO_6 octahedron are practically coincident with the unit cell axes. For an $E \otimes e$ complex within a co-operative Jahn-Teller system, the distortion minima are non-equivalent before the application of an external magnetic field. The effect that an external magnetic field might have on the structure of the CsTiSH lattice will depend on the co-operative nature of the system and the strength of the field. It is possible that the presence of a strong magnetic field along the unit cell axes could induce a change in the co-operative arrangement of the $[\text{Ti}(\text{OH}_2)_6]^{3+}$ cations within the lattice favouring a ferrodistorptive interaction.

4.7 Concluding remarks

The interpretation of the X-band EPR spectrum of CsTiSH and $[\text{Ti}(\text{OH}_2)_6]^{3+}$ doped into CsAlSH by Walsh and co-workers²¹ assumes, that within the β alum lattice, the $[\text{Ti}(\text{OH}_2)_6]^{3+}$ cation is subject to a trigonal distortion which leaves the A_g ground term lowest lying. Symmetry considerations cast doubt over this supposition. Our analysis suggests that an explanation for the anomalous EPR spectra should be within the confines of the $E \otimes e$ description. The three bands observed along each of the three-fold axes in the EPR spectrum of $[\text{Ti}(\text{OH}_2)_6]^{3+}$ doped into CsAlSH may be a consequence of splitting of the vibronic states due to an external perturbation such as random strain. In this instance the appearance of the EPR spectrum is very sensitive to the relative magnitudes of the Zeeman, the tunnelling and the strain splittings.⁵⁴ EPR measurements at other microwave frequencies of Ti^{3+} doped into various alum lattices might shed further light on this problem. EPR measurements using a range of microwave frequencies may also give an indication of the magnitude of the tunnelling splitting since the EPR spectrum of the distorted configuration can only be observed if its lifetime is greater the measurement time of interaction *i.e.* $> 10^{-9}$ s.

The variation of μ_{eff} with temperature can be accounted for over the 80 - 300 K temperature range assuming no deviation from trigonal symmetry with an A_g ground term.¹² The same data set can also be accounted for with a model in which the action of the trigonal field leaves an E_g ground term which is subject to a Jahn-Teller distortion. The susceptibility measurements within this temperature range, therefore,

offer no unique description of the electronic structure of the $[\text{Ti}(\text{OH}_2)_6]^{3+}$ cation.

The X-ray diffraction structure of CsTiSH determined by Sygusch at 102 K³⁶ shows it to be characteristic of a β alum. It is reported that the structure exhibits a high degree of perfection and there is no distortion of the water octahedron surrounding the Ti^{3+} cation. However, the question arises whether the rapid interconversion of the $[\text{Ti}(\text{OH}_2)_6]^{3+}$ cation between lower symmetry configurations would be detectable by x-ray crystallography. The time averaged structure of the $[\text{Ti}(\text{OH}_2)_6]^{3+}$ cation would retain the full trigonal symmetry even if the complex is undergoing ordinary vibrations within the distorted configurations. In this instance X-ray diffraction measurements would indicate no distortion of the water octahedron surrounding the Ti^{3+} cation with the diffuseness of the water molecules being accounted for by thermal smearing.

The available magnetic and EPR data for the CsTiSH alum is still poorly understood. It is clear, however, that static crystal field theory is unable to adequately account for the experimental observations. Structural data collected in the liquid helium temperature range is vital to understanding the electronic structure of the $[\text{Ti}(\text{OH}_2)_6]^{3+}$ cation within the alum lattice.

REFERENCES

1. J. H. Van Vleck, *J. Chem. Phys.*, **7**, 61 (1939).
2. D. Bijl, *Proc. Phys. Soc. A.*, **63**, 407, (1950).
3. A. Jesion, Y. H. Shing, and D. Walsh, *Physical Review*, **35**, 51 (1975).
4. B. Bleaney, G. S. Bogle, A. H. Cooke, R. J. Duffus, M. C. M. O'Brien, and K. W. H. Stevens, *Proc. Phys. Soc. (London)*, A **255**, 145. (1955).
5. B. V. Harrowfield, *Phys. Abstr.*, **75**, 594, No. 10288 (1972).
6. G. A. Woonton and J. A. Mackinnon, *Can. J. Phys.*, **46**, 59, (1968).
7. Y. H. Shing and D. Walsh, *Phys. Rev. Letts.*, **33**, 1067, (1974).
8. G. F. Dionne, *Can. J. Phys.*, **42**, 2419, (1964). *Phys. Rev.*, **137**, A743, (1965).
9. J. A. Mackinnon and G. F. Dionne, *Can. J. Phys.*, **44**, 2329 (1966).
10. R. J. Benzie and A. H. Cooke, *Proc. Roy. Soc. (London)*, A, **68**, 57, (1951).
11. J. A. Mackinnon and J. L. Bickerton, *Can. J. Phys.*, **48**, 814 (1970).
12. B. N. Figgis, J. Lewis and F. E. Mabbs, *J. Chem. Soc.*, 2473 (1963).
13. A. Bose, A. S. Chakravarty, and R. Chatterjee, *Indian Journal Physics*, **33**, 325 (1959).
14. S. K. Dutta-Roy, A. S. Chakravarty, and A. Bose, *Indian Journal Physics*, **33**, 483, (1959).
15. A. Bose, A. S. Chakravarty, and R. Chatterjee, *Proc. Roy. Soc. (London)*, A, **255**, 145 (1960).
16. J. Van der Handel, Thesis, Leiden, (1940).
17. H. M. Gladney and J. D. Swalen, *J. Chem. Phys.*, **42**, 1999, (1965).
18. A. Manoogian, *Can. J. Phys.*, **48**, 2577, (1970).
19. G. F. Dionne, *Can. J. Phys.*, **50**, 2232, (1972).
20. F. S. Ham, *Physical Review*, **138**, A1727 (1965)
21. A. Jesion, Y. H. Shing, and D. Walsh, in *Proceedings of the Eighteenth Colloques Ampere*, Nottingham, England, 9-14 Sept, ed. E. R. Andrew and C. A. Bates (Univ. of Nottingham Press, Nottingham, England, p.561) (1974).
22. M. Abou-Ghantous, C. A. Bates, and K. W. H. Stevens, *J. Phys., C: Solid State Physics*, **1**, 325 (1974).

23. F. E. Mabbs and D. J. Machin, *Magnetism and Transition Metal Complexes*, London Chapman and Hall Press (1973).
24. H. Tachikawa, T. Ichikawa, and H. Yoshida, *J. Amer. Chem. Soc.*, **112**, 977 (1990).
25. H. Tachikawa, T. Ichikawa, and H. Yoshida, *J. Amer. Chem. Soc.*, **112**, 982 (1990).
26. F. A. Cotton, C. K. Fair, G. E. Lewis, G. N. Mott, F. K. Ross, A. J. Schultz, and J. Williams, *J. Amer. Chem. Soc.*, **106**, 5319, (1984).
27. S. P. Best and J. B. Forsyth, *J. Chem. Soc.*, Dalton Trans, 395 (1990).
28. S. P. Best and J. B. Forsyth, *J. Chem. Soc.*, Dalton Trans, 3507 (1990).
29. S. P. Best and J. B. Forsyth, P. L. W. Tregenna-Piggott, *J. Chem. Soc.*, Dalton Trans, 2711 (1993).
30. S. P. Best and J. B. Forsyth, *J. Chem. Soc.*, Dalton Trans, 1721 (1990).
31. J. K. Beattie, S. P. Best, F. Moore, and A. H. White, *Aust. J. Chem.*, in press
32. J. K. Beattie, S. P. Best, B. W. Skelton, A. H. White, *J. Chem. Soc.*, Dalton Trans, 2105 (1981).
33. J. K. Beattie, P. de Favero, and A. H. White, unpublished work.
34. M. Brorson, M. Gajhede, *Inorg Chem.*, **26**, 2109 (1987).
35. R. S. Armstrong, J. K. Beattie, S. P. Best, B. W. Skelton, A. H. White, *J. Chem. Soc.*, Dalton Trans, 1973 (1983).
36. J. Sygusch, *Acta Cryst.*, B30, 662 (1974).
37. S. P. Best, J. K. Beattie, and R. S. Armstrong, *J. Chem. Soc.*, Dalton Trans, 2611 (1984).
38. This work, Chapter 2
39. S. P. Best, R. S. Armstrong, and J. K. Beattie, *J. Chem. Soc.*, Dalton Trans, 1655 (1982).
40. E. Larsen and G. N. La Mar, *J. Chem. Educ.*, **51**, 633 (1974).
41. C. Daul and A. Goursot, *Inorg. Chem.*, **24**, 3554 (1985).
42. H. A. Jahn and E. Teller, *Proc. Roy. Soc. (London)*., A161, 220 (1937).
43. H. A. Jahn, *Proc. Roy. Soc. (London)*., A164, 117 (1938).
44. F. S. Ham, *Physical Review*, **166**, 2, 307 (1968).

45. I. B. Bersuker, *Zh. Eksperim. i Teor. Fiz.*, **43**, 1315 (1962).
[English transl.: *Soviet Phys. -JETP*, **16**, 933 (1963)].
46. I. B. Bersuker, *Zh. Eksperim. i Teor. Fiz.*, **44**, 1239 (1963)
[English transl.: *Soviet Phys. -JETP*, **17**, 836 (1963)].
47. M. C. M. O'Brien, *Proc. Roy. Soc. (London)*, **A281**, 323 (1964).
48. The dynamical Jahn-Teller Effect in localised systems (ed Yu. E. Perlin and M. Wagner), Elsevier, Amsterdam (1984)
49. I. B. Bersuker, *The Jahn-Teller effect and vibronic interactions in modern chemistry*, Plenum Press, New York (1984).
50. R. S. Armstrong, unpublished results.
51. S. P. Best, Ph.D Thesis, Sydney University (1983).
52. S. P. Best and R. J. H. Clark, *Chem. Phys. Letts.*, **122**, no 4, 401 (1985).
53. This work, chapter 3.
54. R. W. Reynolds and L. A. Boatner, *Phys. Rev. B.*, **12**, 4735 (1975).

POLARISED NEUTRON DIFFRACTION STUDY OF CsMoSD

5.1 Introduction

The neutron scattering cross section has contributions from nuclear and magnetic components. Nuclear scattering is the process by which the neutron is scattered by the nuclei giving Bragg like diffraction. Neutrons are also, however, scattered in a magnetic material on account of the interaction of the magnetic moment of the neutron with the magnetic fields within the material.

Magnetic fields within a material are produced almost entirely by electrons with unpaired spins. Since core electrons are paired they contribute little to magnetic scattering. Thus, magnetic neutron scattering is sensitive to only those electrons which can be used in chemical bonding.

A brief overview of the theory of nuclear and magnetic scattering will now be given. Comprehensive accounts on this topic are available in the literature.^{1,2,3}

5.2 Theory of Neutron scattering

Nuclear scattering

We begin by defining the scattering cross section of the nucleus as:

$$\begin{aligned}\sigma &= \frac{\text{outgoing flux of scattered neutrons}}{\text{incident neutron flux}} \\ &= \frac{\text{interactions per second}}{\text{neutron flux per cm}^2 \text{ per second}} \quad \text{cm}^2 \quad 5.2.1\end{aligned}$$

For nuclear scattering which is isotropic, the cross section of a single nucleus is related to the scattering length b (which may be positive or negative)

$$\sigma = 4\pi b^2 \quad 5.2.2$$

The scattering from a sample is not generally isotropic.

For elastic scattering, it is convenient to define a differential cross section per unit solid angle, $d\sigma/d\Omega$ which is composed of two terms, an incoherent term which is isotropic, and a coherent term which is not.

$$\frac{d\sigma}{d\Omega} = \left(\frac{d\sigma}{d\Omega}\right)_{coh} + \left(\frac{d\sigma}{d\Omega}\right)_{incoh}$$

5.2.3

Coherent scattering from a nucleus is scattering which is coherent with that of other nuclei and which can therefore produce interference.

The resultant neutron state can be represented by a plane wave $e^{i\mathbf{x}\cdot\mathbf{R}}$ where \mathbf{x} is the scattering vector, and \mathbf{R} is the distance from the point of measurement to the origin at which the nucleus is considered to be rigidly fixed.

For elastic nuclear scattering from an assembly of N atoms of one element each having position vector \mathbf{R}_N .

$$\left(\frac{d\sigma}{d\Omega}\right)_{coh} = \left[b \sum_N e^{i\mathbf{x}\cdot\mathbf{R}_N} \right]^2$$

5.2.4

For scattering from a crystal this reduces to:

$$\left(\frac{d\sigma}{d\Omega}\right)_{coh} = \frac{N(2\pi)^3}{v_o} \sum_{\tau} \delta(\mathbf{x} - \tau) |F_N(\mathbf{x})|^2$$

5.2.5

v_0 is the volume of the unit cell; N , the number of unit cells in the sample, χ is the scattering vector and τ is a reciprocal lattice vector $\tau_{hkl} = 2\pi/d_{hkl}$. The δ function defines the Bragg condition. $F_N(\chi)$ is the nuclear structure factor:

$$F_N(\chi) = \sum_N b_N e^{i\chi \cdot R_N} e^{-W_N(\chi)}$$

5.2.6

$\exp(-W_N(\chi))$ is the Debye-Waller factor and arises from atomic vibrations. It is both angular and temperature dependent.

Measurement of $(d\sigma/d\Omega)_{coh}$ allows the nuclear structure factors to be determined. From the nuclear structure factors, the structure can be determined.

Magnetic Scattering

In a true paramagnetic substance, the magnetic moments of the atoms, which arise from their unpaired electronic moments, are completely uncoupled from each other and are randomly orientated in direction. The magnetic scattering is then incoherent. At low temperatures in the presence of a strong external magnetic field the paramagnets tend to align themselves in the direction of the field. The magnetic scattering is then coherent. In analogy with nuclear scattering

$$\left(\frac{d\sigma}{d\Omega}\right)_{coh} = \frac{N(2\pi)^3}{v_0} \sum_{\tau} \delta(\chi - \tau) |F_M(\chi)|^2$$

5.2.7

The magnetic structure factor, which is the fourier transform of the magnetisation density, is analogous to the nuclear structure factor:

$$F_M(\chi) = q_N p_N \sum_N e^{i\chi \cdot R_N} e^{-W_N(\chi)}$$

5.2.8

p is the magnetic scattering length:

$$p_N = \left(\frac{\gamma e^2}{mc^2} \right) \frac{g}{2} \langle S_N \rangle f_N(\chi)$$

5.2.9

Where γ is the gyromagnetic ratio of the neutron, m is the mass of the electron, c is the speed of light, e is the charge of the electron and g is the Landé g factor. The sum is over the magnetic ions in the magnetic unit cell. The n^{th} ion has effective spin S_N , form factor f_N and Debye-Waller factor $\exp[-W_N(\chi)]$

The form factor is a measure of the scattering power of an atom or ion for a particular reflection. When radiation is scattered by particles that are very small compared to the wavelength of radiation, the scattered radiation has approximately the same intensity in all directions as in the case of nuclear neutron scattering. When the radiation is scattered by particles with linear dimensions comparable to the wavelength of incoming radiation, destructive interference will occur, increasing with scattering angle. Since magnetic scattering occurs from electrons in the outer orbits of an atom, the form factor for magnetic scattering is expected to fall off more sharply than for X-rays, as illustrated in figure 5.2.1 (a).

q is the magnetic interaction vector defined by

$$q = \boldsymbol{\kappa}(\boldsymbol{\kappa} \cdot \mathbf{K}) - K$$

5.2.10

where \mathbf{K} is a unit vector in the direction of the magnetic spins.

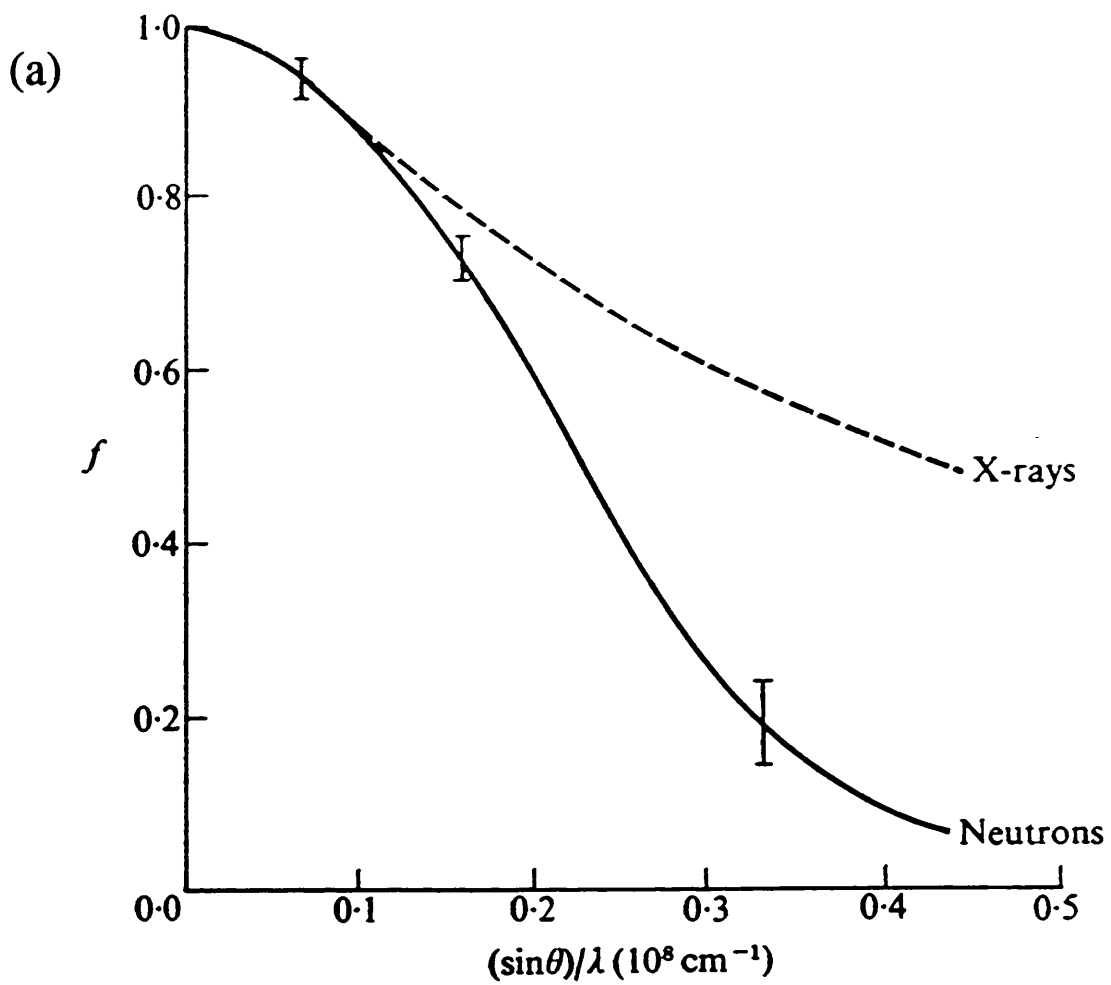
It follows from the definition that q lies in the plane of $\boldsymbol{\kappa}$ and \mathbf{K} and is perpendicular to $\boldsymbol{\kappa}$ and of magnitude $\sin\alpha$ where α is the angle between $\boldsymbol{\kappa}$ and \mathbf{K} .

The basis of the polarised beam experiment is shown diagrammatically in figure 5.2.1 (b). Let a magnetic field be applied to a material which is orientated suitably in space to give both a Bragg and a magnetic reflection from the shaded hkl plane and let the field be sufficiently intense to produce saturation so that all the magnetic moments are pointed vertically upwards. $\boldsymbol{\lambda}$ is a unit vector in the direction of the spin of the incident neutron. For an unpolarised neutron beam, $\boldsymbol{\lambda}$ can take all

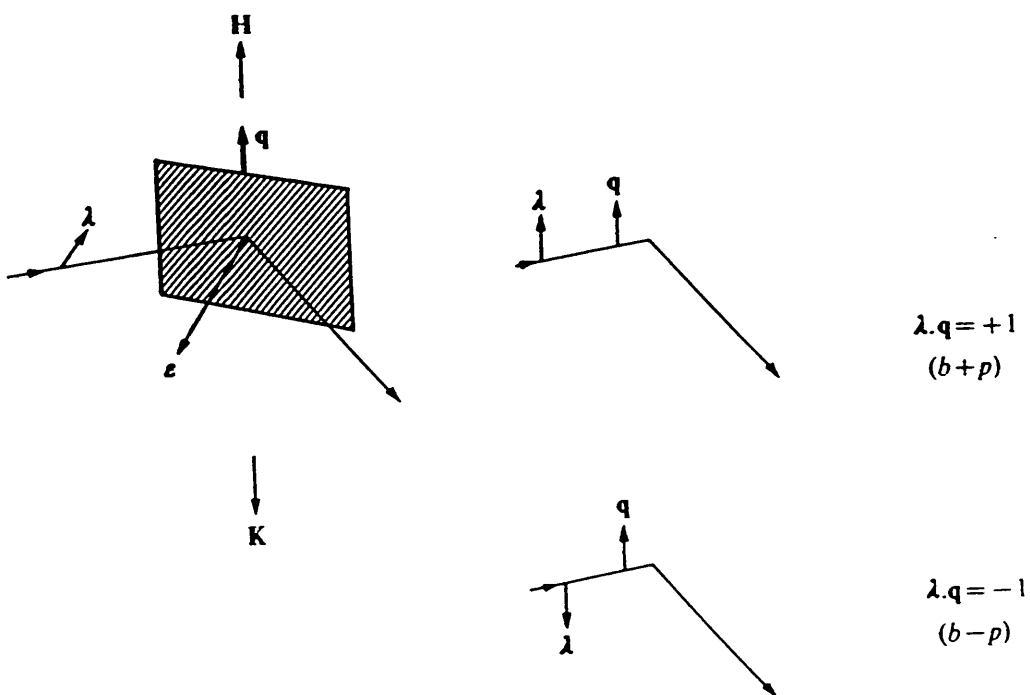
Figure 5.2.1

(a) Variation of the amplitude form factor f for the Mn^{2+} ion with $(\sin\theta/\lambda)$, as deduced from experimental measurements of paramagnetic scattering by MnF_2 . For comparison the more slowly varying curve for X-ray scattering by a manganese atom is also shown. (After C. G. Shull *et al.* [4]).

(b) Values of the product $\lambda \cdot \mathbf{q}$ for the upward and downward neutron polarisation states when a magnetic field \mathbf{H} produces a vertical alignment of spins. \mathbf{K} is the magnetic spin vector which is the reverse of the magnetisation. (After G. E Bacon [1])



(b)



possible directions. For the circumstances shown in the diagram, it is useful to consider the unpolarised beam as the sum of two completely polarised beams; one with the neutron spin directed upwards in the direction of H and q , the other downwards. For a Bravais lattice, the total scattering cross section can be expressed in terms of nuclear and magnetic scattering lengths:

$$\left(\frac{d\sigma}{d\Omega}\right)_{coh} = \left[\sum_N e^{i\mathbf{x}\cdot\mathbf{R}_N}\right]^2 (b^2 + 2bp\lambda\cdot\mathbf{q} + p^2)$$

5.2.11

When λ is in the direction of q , $\lambda\cdot q = 1$ and the expression becomes:

$$\left(\frac{d\sigma}{d\Omega}\right)_{coh} = \left[\sum_N e^{i\mathbf{x}\cdot\mathbf{R}_N}\right]^2 (b + p)^2$$

5.2.12

When the direction of λ is opposite to that of q , $\lambda\cdot q = -1$ and the expression becomes:

$$\left(\frac{d\sigma}{d\Omega}\right)_{coh} = \left[\sum_N e^{i\mathbf{x}\cdot\mathbf{R}_N}\right]^2 (b - p)^2$$

5.2.13

It is the ratio of the intensities in these two experiments that is measured in a polarised neutron experiment.

The so called flipping ratio is equal to:

$$R = (b + p)/(b - p)$$

5.2.15

R can only differ from unity if there are magnetic and nuclear contributions to the reflection. Whether R is > 1 or < 1 depends on the sign of the magnetic structure factor relative to the nuclear structure factor.

Thus, for centrosymmetric structures, where the structure factors are real, the phase of the structure factor can readily be determined directly from the experiment.

The fourier transform of the magnetic structure factors gives the magnetisation density. The g values obtained for $[\text{Mo}(\text{OH}_2)_6]^{3+}$ doped into the CsInSH alum are $g_{\parallel} = 1.954$ and $g_{\perp} = 1.950$.⁵ This compares with the calculated free ion value of $g = 2/5$ and the spin only value of $g = 2.0023$ indicating that the orbital angular momentum is almost completely quenched by the ligand field. In this instance, the magnetisation density approximates to the spin density.

5.3 Experimental

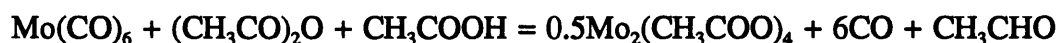
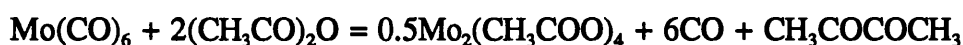
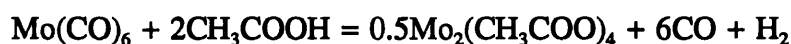
Preparation of $\text{CsMo}(\text{SO}_4)_2 \cdot 12\text{D}_2\text{O}$

The alum was prepared by hydrolysis of the compound $\text{Na}_3(\text{Mo}(\text{HCO}_2)_6)$ in strong acid, giving the aqua ion within a few minutes.⁶ This method was found to be successful in producing crystals of CsMoSH approximately 1 mm^3 in volume.

$\text{Na}_3(\text{Mo}(\text{HCO}_2)_6)$ was prepared from $(\text{NH}_4)_2(\text{MoCl}_5(\text{H}_2\text{O}))$ which is itself prepared from $\text{Mo}_2(\text{CH}_3\text{COO})_4$. The synthesis of these compounds is described below.

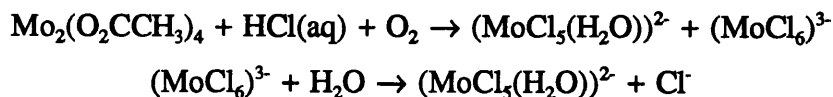
i) Preparation of Tetrakis(aceto)dimolybdenum.⁷ $\text{Mo}_2(\text{CH}_3\text{COO})_4$

Reflux of molybdenum hexa-carbonyl, $\text{Mo}(\text{CO})_6$, with glacial acetic acid and acetic anhydride in diglyme (2-methoxy ethyl ether) gave $\text{Mo}_2(\text{CH}_3\text{COO})_4$ on cooling which is a characteristic yellow, needle-like compound.



ii) Aquapentachloromolybdate(III).⁸ $(\text{NH}_4)_2(\text{MoCl}_5(\text{H}_2\text{O}))$

$\text{Mo}_2(\text{O}_2\text{CCH}_3)_4$ and NH_4Cl were mixed with HCl (12 mol dm^{-3}). The slurry was warmed to boiling point and evaporated until a brick-red crystalline solid appeared. After cooling the solid was dried and weighed.



iii) Sodium hexakis(formato)molybdate(III). $\text{Na}_3(\text{Mo}(\text{HCO}_2)_6)$

$(\text{NH}_4)_2(\text{MoCl}_5(\text{H}_2\text{O}))$ was dissolved in an aqueous solution containing sodium formate (7 mol dm^{-3}) and formic acid (0.1 mol dm^{-3}). A light green precipitate formed on leaving the solution to cool overnight.

iv) Caesium Molybdenum Sulphate.⁶ $\text{CsMo}(\text{SO}_4)_2 \cdot 12\text{H}_2\text{O}$

$\text{Na}_3(\text{Mo}(\text{HCO}_2)_6)$ was applied to a cold solution of Cs_2SO_4 in p-toluenesulfonic acid (2 mol dm^{-3}). The greenish yellow solution rapidly became black; bright yellow crystals of CsMoSH were formed on leaving the reaction mixture at 275 K overnight.

Partially deuteriated (90% D atom) crystals of the alum were formed by addition of $\text{Na}_3(\text{Mo}(\text{HCO}_2)_6)$ to p-toluenesulfonic acid (2 mol dm^{-3}) in deuterium oxide. Re-crystallisation by heating and cooling leads to the solution rapidly turning black through oligomerisation leading to a significant loss of product. Recrystallisation and deuterium enrichment were achieved in the process used to produce large single crystals described in chapter 2 section 2.4. This uses a thermal gradient technique in which the lower part of the apparatus, containing the polycrystalline material is held at a higher temperature than the upper part of the apparatus. It was found that large crystals of CsMoSD could be grown by maintaining the two water baths at temperatures of 2 and 15° C with the seed crystal positioned close to the meniscus surface. A 41 mg crystal, octahedral in appearance was used for both the unpolarised and polarised neutron experiments.

Structure of $\text{CsMo}(\text{SO}_4)_2 \cdot 12\text{D}_2\text{O}$

The structure of $\text{CsMo}(\text{SO}_4)_2 \cdot 12\text{D}_2\text{O}$ was determined using data collected on the D9 four-circle diffractometer at the Institut Laue Langevin, Grenoble. The intensities of the reflections were extracted using the program RETREAT.⁹ The standard deviations in the observed moduli of the structure factors were estimated

from the agreement among equivalents, generally two or three in number, or the counting statistics whichever was highest. The weighted least-squares refinement (Cambridge Crystallographic Subroutine Library¹⁰) converged to give excellent final R, and weighted R factors. A single scattering length for deuterium sites was allowed to vary in the refinement, the extent of deuterium substitution was then obtained using the known scattering lengths of hydrogen (-3.741 fermi) and deuterium (6.674 fermi).

A summary of the data collection and analysis parameters is given in table 5.3.1. Atomic fractional cell coordinates and thermal parameters are assembled in table 5.3.2 and a listing of bond lengths and angles are given in table 5.3.3.

The general features of the structure of the $\text{CsMo}(\text{SO}_4)_2 \cdot 12\text{D}_2\text{O}$ alum is in good agreement with a previous X-ray structural investigation performed at 110 K.¹¹ The alum has a structure typical of the β alum modification which has been previously described.^{13,14} The structure of the $[\text{Mo}(\text{OD}_2)_6]^{3+}$ cation is shown in figure 5.3.1. Whilst the MoO_6 core is approximately octahedral the deuterium atoms occur in positions that gives the complex overall S_6 symmetry. The mode of water coordination is approximately trigonal planar with the deuterium atoms tilted out of the MoO_4 plane by $1.8(1)^\circ$. The D_2O molecule is found to be twisted by $19.7(1)^\circ$ away from the MoO_6 framework.¹⁵

Figure 5.3.1

Molecular structure of the $[\text{Mo}(\text{OD}_2)_6]^{3+}$ cation within the $\text{CsMo}(\text{SO}_4)_2 \cdot 12\text{D}_2\text{O}$ alum.

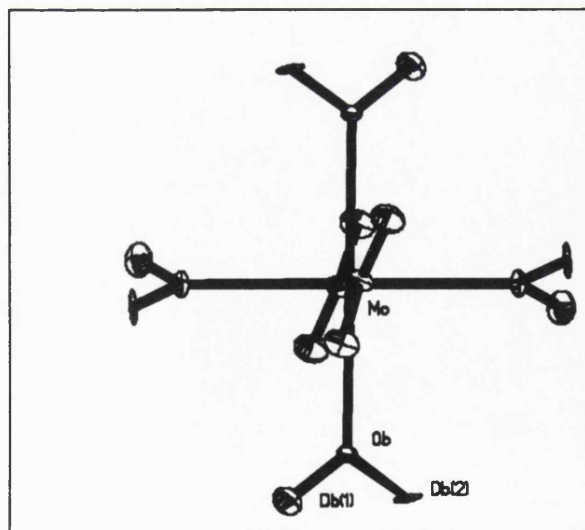
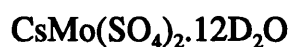


TABLE 5.3.1.

Data collection and analysis parameters.



formula weight	661.0
sample temperature	15.0 (1) K
sample weight / mg	41
a / Å	12.436(3)
volume / Å ³	1923.3(10)
space group	Pa $\bar{3}$
wavelength	0.8344 (3) Å
max (sin θ/λ) / Å ⁻¹	0.85
total no. reflections	1768
no. unique reflections	609
no. used in refinement	607
no. variables	74
scattering length (H/D)/ fermi	6.21(1)
% deuterium	95.5(2)
R-factor	0.013
weighted R-factor	0.012
goodness of fit (χ^2)	1.67
χ^2 on repeated measurements	1.5
R (F ²) on repeated measurements	1.5
χ^2 on equivalent measurements	5.3
R (F ²) on equivalent measurements	2.0

TABLE 5.3.2

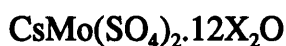
Atomic fractional cell coordinates, isotropic (B_{iso}) and anisotropic thermal parameters* for $CsMo(SO_4)_2 \cdot 12D_2O$.

ATOM	x	y	z	B_{iso}	B11	B22	B33	B23	B13	B12
Cs	0.50000	0.50000	0.50000	0.27(1)						
Mo	0.00000	0.00000	0.00000	0.26(1)						
S	0.32737(7)	0.32737	0.32737		0.23(2)			0.01(2)		
O(1)	0.25858(4)	0.25858	0.25858		0.51(1)			-0.08(1)		
O(2)	0.28158(4)	0.33337(4)	0.43694(4)		0.58(1)	0.50(1)	0.35(1)	0.03(1)	0.16(1)	0.00(1)
O(a)	0.05425(4)	0.20560(4)	0.34022(4)		0.56(2)	0.64(2)	0.45(2)	-0.04(1)	0.00(1)	0.01(1)
D(a1)	0.01058(5)	0.22763(5)	0.27915(5)		1.17(2)	1.72(2)	1.01(2)	0.06(2)	-0.30(1)	0.13(2)
D(a2)	0.12759(5)	0.21874(5)	0.31703(5)		0.82(2)	1.78(2)	1.40(2)	-0.01(2)	0.10(1)	-0.00(1)
O(b)	0.16840(3)	-0.00197(4)	-0.00115(4)		0.30(1)	0.49(1)	0.85(1)	0.19(1)	0.01(1)	0.01(1)
D(b1)	0.21525(5)	-0.06282(4)	0.02238(5)		0.90(2)	0.96(2)	1.41(2)	0.20(2)	-0.04(1)	0.19(1)
D(b2)	0.21184(5)	0.06060(5)	-0.02337(5)		0.92(2)	0.94(2)	1.49(2)	0.21(1)	0.09(1)	-0.19(1)

* Thermal parameters are in units of Å^2

TABLE 5.3.3

Bond lengths (Å) and angles (°) which define the coordination environments.



	X = D	X = H
i) SO_4^{2-}		
S-O(1)	1.482(2)	[1.478(1)] [‡]
S-O(2)	1.479(2)	[1.478(1)]
O(1)-S-O(2)	109.8(1)	[109.83(5)]
O(2)-S-O(2)	109.1(1)	[109.11(8)]
ii) $[\text{M}(\text{OX}_2)_6]^{3+}$		
M-O(b)	2.094(1)	[2.089(1)]
O(b)-M-O(b)	91.1(1)	[91.00(6)]
iii) Cs^+		
Cs-O(2)	3.505(1)	[3.509(1)]
Cs-O(a)	3.308(1)	[3.311(1)]
O(2)-Cs-O(2')	40.2(1)	
O(a)-Cs-O(a')	60.0(1)	[60.02(4)]
O(2)-Cs-O(a)	65.6(1)	
O(2)-Cs-O(a')	78.6(1)	
O(2)-Cs-O(a'')	80.5(1)	[80.49(3)]
iv) the water molecules		
O(a)-X(a1)	0.973(1)	[0.68(4)]
O(a)-X(a2)	0.970(1)	[0.75(4)]
O(b)-X(b1)	0.999(1)	[0.75(3)]
O(b)-X(b2)	0.987(1)	[0.80(3)]
X(a1)-O(a)-X(a2)	104.2(1)	[101(5)]
X(b1)-O(b)-X(b2)	111.1(1)	[110(4)]
v) the hydrogen bonds		
X(a1)--O(2)	1.802(1)	
X(a2)--O(1)	1.851(1)	
X(b1)--O(a)	1.606(1)	
X(b2)--O(2)	1.654(1)	
O(a)-X(a1)--O(2)	174.1(1)	[170(4)]
O(a)-X(a2)--O(1)	171.4(1)	[173(3)]
O(b)-X(b1)--O(a)	176.8(1)	[176(3)]
O(b)-X(b2)--O(2)	178.2(1)	[175(3)]

[‡] Obtained from a 110 K X-ray study of $\text{CsMo}(\text{SO}_4)_2 \cdot 12\text{H}_2\text{O}$ ¹¹

Polarised Neutron Apparatus

A schematic representation of a polarised neutron diffractometer is shown in figure 5.3.2 .

Polarised beams are produced by materials for which $p = b$ for a given reflection. The Heusler alloy, Cu_2MnAl , is frequently used, and polarisation efficiencies of ≥ 99 percent may be obtained. The polarisation is retained by use of magnetic guide fields. At some point in this path a "spin-flipper" is introduced whose function is to reverse the polarisation of the neutron beam.

The crystal was mounted in the D3 diffractometer at the Institut Laue-Langevin. The sample was held at a temperature of 1.8 K and subjected to a field of 4.6 Tesla for a period of two weeks during which time 197 unique reflections were obtained. Figure 5.3.4 shows a plot of the structure factors against $(\sin\theta/\lambda)$. Reflection $F_M(000)$ is included. This corresponds to the bulk magnetisation of the sample. Its value was determined from susceptibility measurements made using a SQUID magnetometer. This experiment is described in section 5.7.

5.4 Programs used to refine the data

Two different programs were used, ASRED, which is able to expand the magnetisation density as a function of chemical orbitals placed on the atoms and MOLLY, which describes the magnetisation density as a multipole expansion.

ASRED

ASRED was originally written by B. N. Figgis and G. A. Williams¹⁶ and later modified by P. A. Reynolds. A description of the formalism used in ASRED is given in the literature¹⁷ a brief summary of which is given here.

For the $[\text{Mo}(\text{OD}_2)_6]^{3+}$ cation, which lies on a site of trigonal symmetry within the CsMoSD unit cell, the 4d atomic orbitals may be written as:

Figure 5.3.2

A schematic representation of a polarised neutron diffractometer. (After P. J. Brown [3])

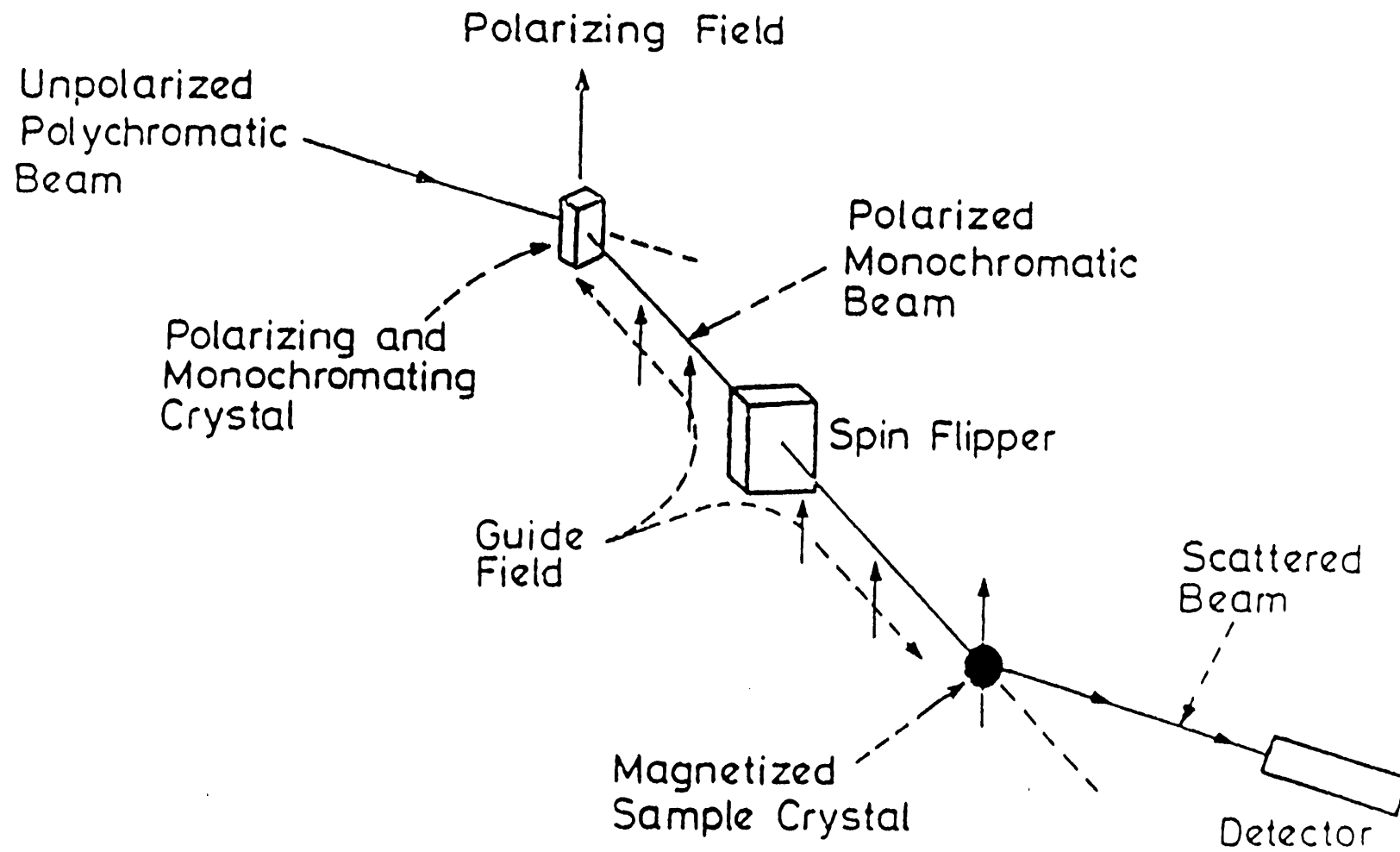
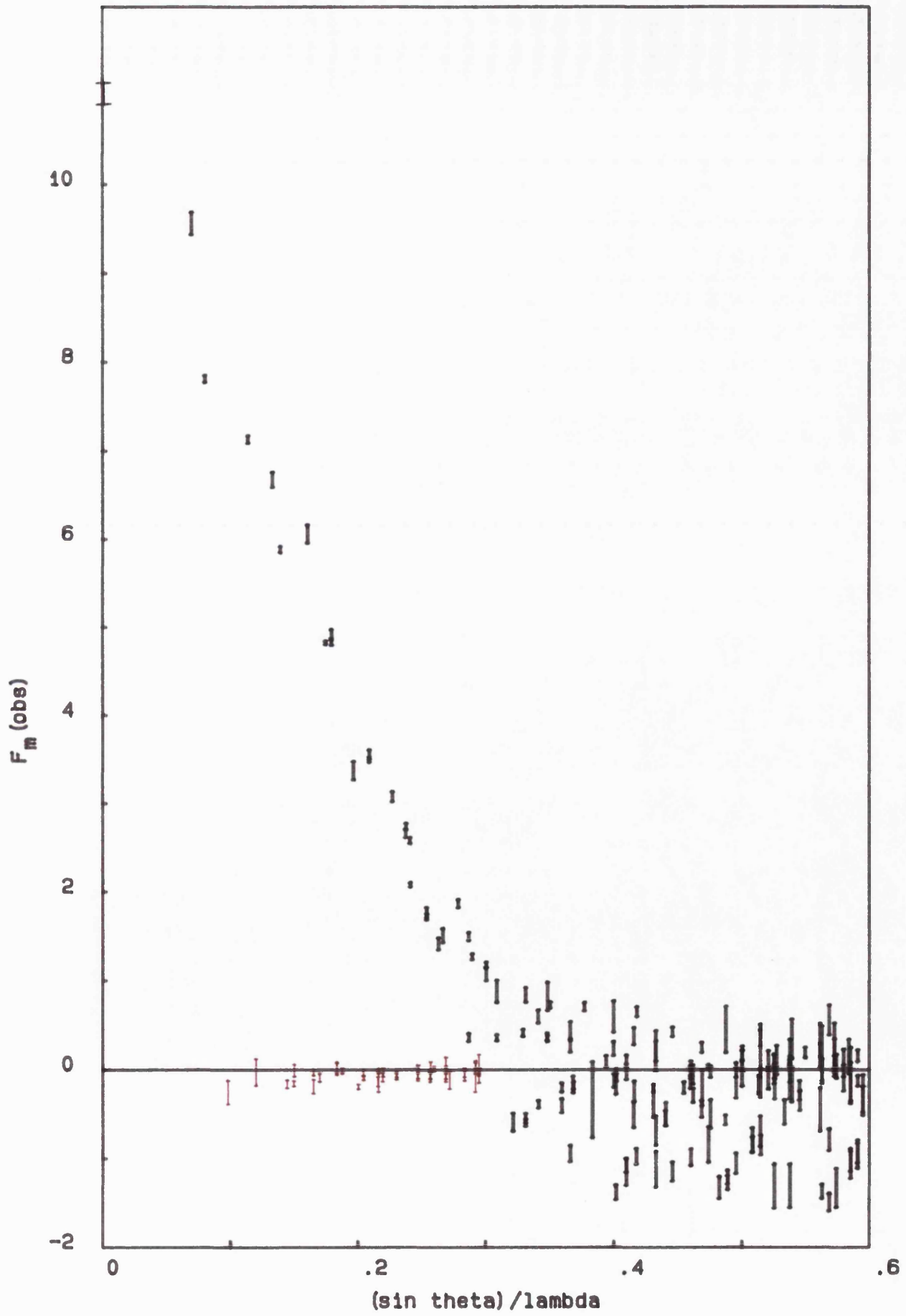


Figure 5.3.4

Plot of magnetic structure factors obtained for $\text{CsMo}(\text{SO}_4)_2 \cdot 12\text{D}_2\text{O}$ against $(\sin \theta)/\lambda$. The molybdenum atoms lie on the corners and faces of the cubic unit cell such that they define a face centred cubic arrangement. The reflection conditions for an atom on this site are $h + k, h + l, k + l = 2n$, *ie.* the Miller indices have to be either all even or all odd. These reflections are shown in black whereas the mixed reflections are shown in red. The all even and all odd reflections do not decrease uniformly in intensity with $(\sin \theta)/\lambda$. It is immediately apparent, therefore, that the magnetisation density is not spherically distributed about the Mo atom. Some of the mixed reflections have non-zero values. Intensity in the mixed reflections cannot arise from magnetisation density at the molybdenum site implying that there must be some spin transfer to the surrounding water ligands.



$$\begin{aligned}
|a_g\rangle &= d_{z^2} \\
|e_g^+(\pi)\rangle &= \sqrt{1/3}d_{x^2-y^2} + \sqrt{2/3}d_{zx} \\
|e_g^-(\pi)\rangle &= \sqrt{1/3}d_{xy} - \sqrt{2/3}d_{yz} \\
|e_g^+(\sigma)\rangle &= \sqrt{2/3}d_{x^2-y^2} - \sqrt{1/3}d_{zx} \\
|e_g^-(\sigma)\rangle &= \sqrt{2/3}d_{xy} + \sqrt{1/3}d_{yz}
\end{aligned}$$

5.4.1

taking the 3-fold axis of the molecule as the z quantisation axis.

In octahedral symmetry, $e_g(\sigma)$ and a_g correlate with t_{2g} whilst $e_g(\pi)$ correlates with the e_g orbital set. With populations p_{a_g} , $p_{e_g\sigma}$, and $p_{e_g\pi}$ the electron density ρ can be represented by:

$$\begin{aligned}
\rho &= [p_{a_g}][\langle a_g | a_g \rangle] + \\
& [p_{e_g\sigma}a^2 + p_{e_g\pi}(1 - a^2)][\langle e_g^+(\sigma) | e_g^+(\sigma) \rangle + \langle e_g^-(\sigma) | e_g^-(\sigma) \rangle] + \\
& [p_{e_g\sigma}(1 - a^2) + p_{e_g\pi}a^2][\langle e_g^+(\pi) | e_g^+(\pi) \rangle + \langle e_g^-(\pi) | e_g^-(\pi) \rangle] + \\
& [2a\sqrt{1 - a^2}(p_{e_g\sigma} - p_{e_g\pi})][\langle e_g^+(\sigma) | e_g^+(\pi) \rangle + \langle e_g^-(\sigma) | e_g^-(\pi) \rangle]
\end{aligned}$$

5.4.2

where 'a' is a mixing parameter. The electron density is represented by four populations (first term in brackets) P_{z^2} , $P_{E_g\sigma}$, $P_{E_g\pi}$ and $P_{E_g\sigma\pi}$; and four overlap densities (second term in brackets). The scattering factors for these overlap densities are evaluated as a function of spherical harmonics and the Hartree-Fock 4d radial distribution function which is listed in tabular form in the International Tables of Crystallography.¹⁸

The associated populations P_{z^2} , $P_{E_g\pi}$, $P_{E_g\sigma}$ and $P_{E_g\sigma\pi}$ are determined from least squares refinement.

For atoms on a site of very low symmetry such as the oxygen and deuterium atoms within the $[\text{Mo}(\text{OD}_2)_6]^{3+}$ complex, sp hybrid orbitals are centred on the atoms that best reflect the local bonding symmetry.

MOLLY

In the least squares refinement program "MOLLY" the electron density is expanded by a procedure first suggested by Stewart.¹⁹ A series of nuclear-centred spherical harmonic functions, truncated at a level chosen by practical considerations, are placed on each atom and the electron density described as linear combinations of the nuclear centred multipoles. MOLLY was written by N. K. Hansen and first described in 1978.²⁰ The program was written for analysis of high resolution X-ray data where the core electrons are considered to be positioned symmetrically around the atom and the valence density expanded as a multipole series. The aspherical atomic density distribution ρ_{atomic} is represented by:

$$\rho_{\text{atomic}}(r) = P_c \rho_{\text{core}} + P_v \kappa'^3 \rho_{\text{valence}}(\kappa' r) + \sum_{l=0}^4 R_l(r) \sum_{m=-l}^l P_{lm} Y_{lm}$$

5.4.3

Here P_c , P_v and P_{lm} are population coefficients. The total number of electrons associated with one atom is equal to $P_c + P_v + P_{00}$, since the higher terms with $l \neq 0$ integrate to zero when integrated over all space.

The radial density functions ρ_{core} and ρ_{valence} are described using the core and valence Hartree - Fock (HF) scattering factor tables normalised to one electron which are listed in the international tables of crystallography¹⁸ or calculated from theoretical wavefunctions.²¹ The valence function is allowed to expand and contract by adjustment of the variable radial parameter κ' . The radial functions $R_l(r)$ of the other terms can be described either by HF wavefunctions or analytical, Slater type functions of the form:

$$R_l(r) = \frac{\zeta^{n_l + 3}}{(n_l + 2)!} \kappa'^3 r^{n_l} \exp(-\zeta r)$$

5.4.4.

where in principle n_1 can take any positive integer value. Starting values of the orbital exponent ζ are modified by a variable parameter κ'' , such that $\zeta' = \kappa''\zeta$.

5.5 RESULTS

ASRED refinements

ASRED refinements are discussed first. The refinements are represented by means of schematic diagrams to aid visualisation.

The magnetisation density about Mo is described using the populations and associated overlap densities described in equation 5.4.2. In all initial refinements performed, $P_{E\pi\sigma}$ was found to have a negligible population. $P_{E\pi\sigma}$ was subsequently fixed at zero and not refined upon in all the refinements that are shown here. The negligible population of $P_{E\pi\sigma}$ implies little mixing of the wavefunctions represented by $e_g(\sigma)$ and $e_g(\pi)$. In this instance $P_{E\sigma}$ corresponds to $p_{e\sigma}$ and $P_{E\pi}$ corresponds to $p_{e\pi}$ so that the populations corresponding to the 4d atomic orbitals are associated with the wavefunctions expressed in equation 5.4.1.

The magnetisation density about the ligand is expanded by means of sp hybrid orbitals placed on the ligand.

The weighted R factor and χ^2 values quoted give an indication of the quality of the model fits to the experimental data and are defined as:

$$R = \frac{\sum |F_o - |F_c||}{\sum F_o}, \quad R_w = \frac{\sum w|F_o - |F_c||}{\sum \sqrt{w}F_o}, \quad \chi^2 = \sqrt{\frac{\sum w(F_o - |F_c|)^2}{M-N}}$$

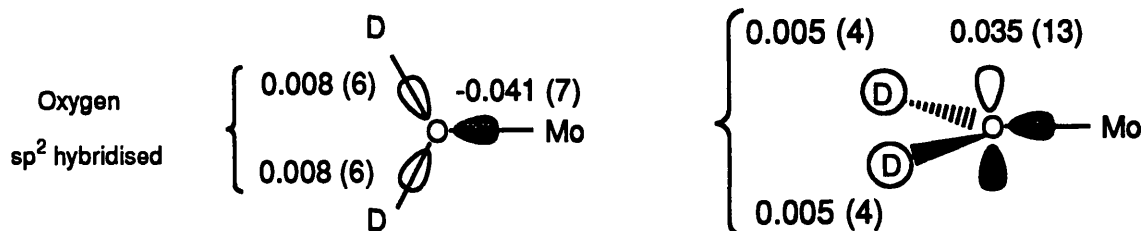
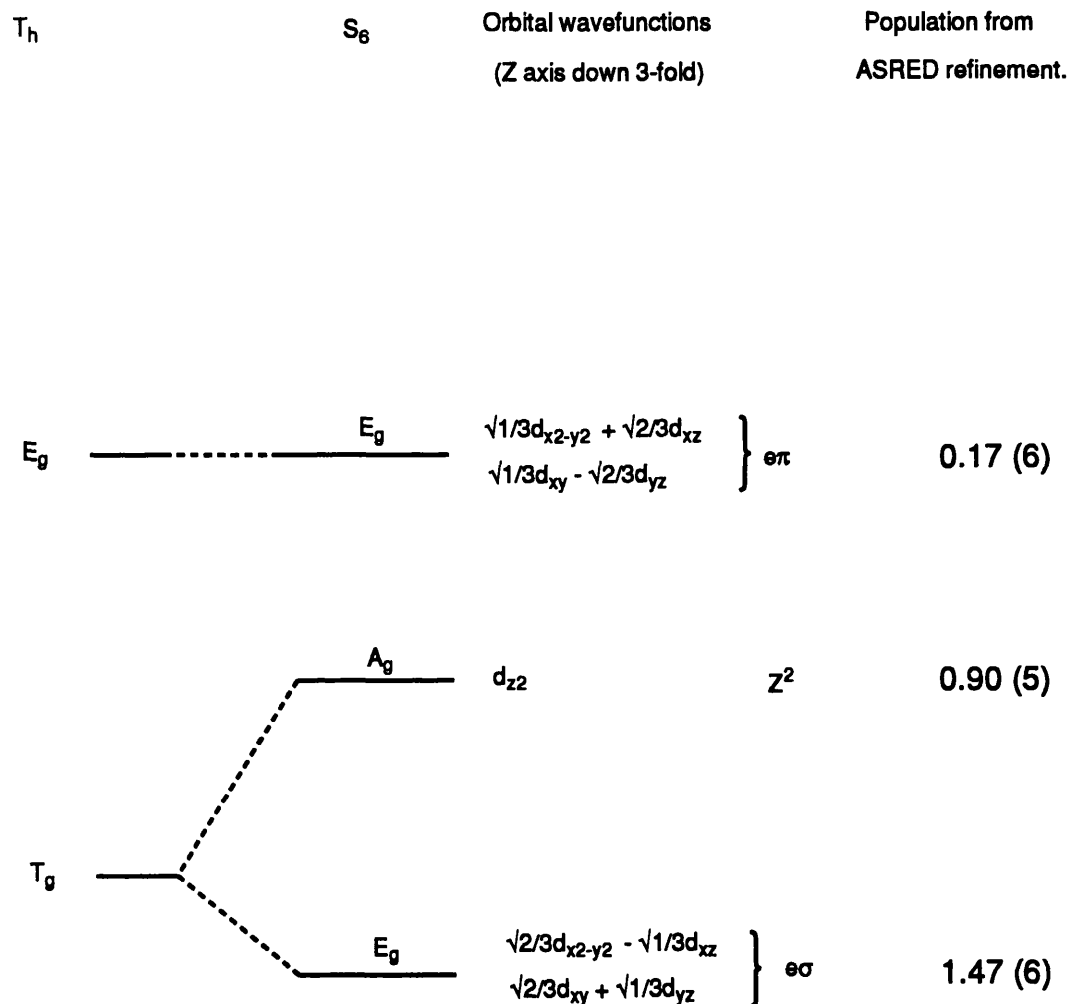
N = Number of reflections used in refinement, M = Number of parameters refined.

| 5.5.1

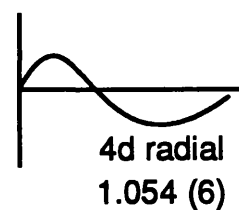
In **Refinement 1**, shown schematically in figure 5.5.1, the oxygen atom is treated as sp^2 hybridised with the co-ordinate system constrained to the MO_6 framework such that one hybrid orbital lies exactly along the oxygen-molybdenum bond vector. In this and subsequent refinements it was found that the sp^2 hybridised orbitals pointing towards the deuterium atoms had small and roughly equal values and could be constrained together with little effect on the values of the other parameters

Figure 5.5.1

**ASRED
REFINEMENT 1.**



Number of reflections used in refinement	198
Number of parameters	8
Experimental $F_M(000)$ and E.S.D	11.08 (0.05)
Calculated $F_M(000)$	10.65
Weighted Residual Index R_w	0.0867
chi squared χ^2	3.84



or the goodness of fit on the model. Constrained parameters are represented by means of brackets. The deuterium atoms are represented by 1s functions and are likewise constrained as indicated. This refinement shows appreciable spin density for the z^2 and $e\sigma$ functions (correlating to T_g in T_h symmetry). Some spin is transferred to the ligand (populations quoted are per water molecule) but the E.S.D's are large and the anisotropy of the spin about the oxygen is poorly defined. The $\chi^2 = 3.84$ and $R_w = 8.67\%$ values indicate that there is a poor fit of the experimental structure factors and the structure factors calculated from the model. Table 5.5.1 shows a comparison between the experimental and the calculated structure factors.

Purging of the data.

Reflections are rejected on the basis of their 'spin up' and 'spin down' intensities, the ratio of which are used in conjunction with the nuclear structure factors to calculate the magnetic structure factors. Reflections are rejected on two criteria.

1. If either of the spin up or spin down intensities are weak, the error in the flipping ratio will be large leading to a large error for the magnetic structure factor so the reflection is rejected.
2. Because of multiple scattering, nuclear structure factors that are weak carry relatively large systematic errors. Magnetic structure factors which are calculated in conjunction with low values of nuclear structure factors are therefore rejected.

Out of a data set containing 197 reflections, 58 were rejected leaving 139 from which to model the data. It is stressed that reflections were rejected using criteria established from previous polarised neutron diffraction studies²² and no reflections were rejected on the basis of their poor agreement with the model.

Refinement 2 has the same parametisation as Refinement 1, but uses the culled reflection data set. Comparison of Refinement 2 with Refinement 1 shows that χ^2 and R_w have dropped to 1.47 and 3.37 % respectively. More significantly, all the E.S.D's have halved. The anisotropy of the spin about the oxygen is now better defined. The two hybrid orbitals pointing towards the deuterium atoms that are constrained together have negligible populations. Significant positive spin is, however, found in the p-type

TABLE 5.5.1

Comparison between experimental structure factors and those calculated by ASREDD for basis setup described in Refinement 1. $F_{\text{obs}} - F_{\text{calc}} > 0.3$ are shown in bold. Weighted R value for 198 reflections = 8.67 % Goodness of fit $\sigma^2 = 3.84$.

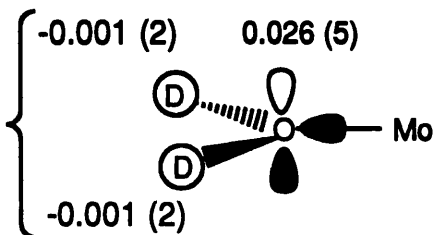
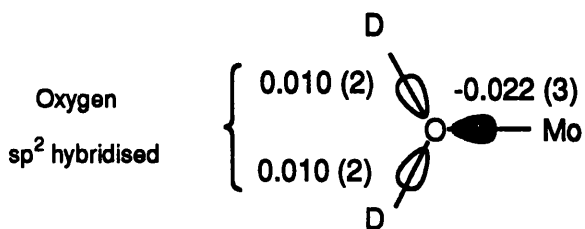
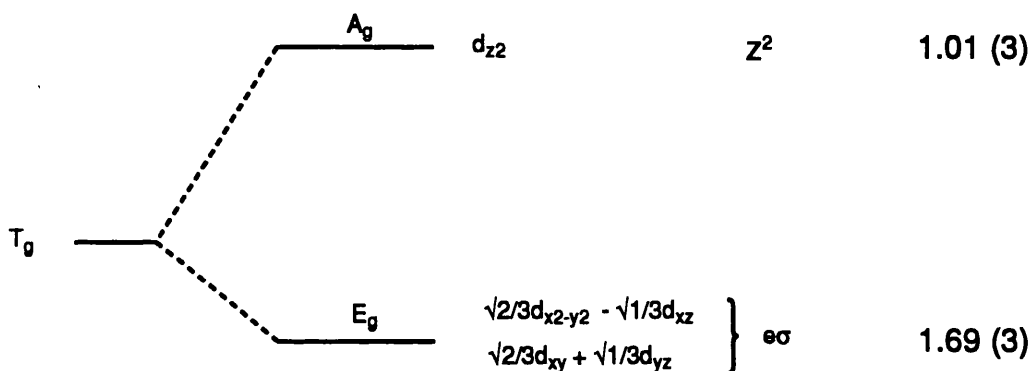
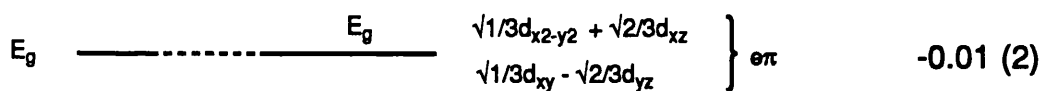
H	K	L	F_{obs}	F_{calc}	SIG F_{obs}	$F_{\text{obs}} - F_{\text{calc}}$	H	K	L	F_{obs}	F_{calc}	SIG F_{obs}	$F_{\text{obs}} - F_{\text{calc}}$
0	0	0	11.0800	10.6506	0.0500	0.4294	1	3	1	6.6842	6.3869	0.0826	0.2973
4	1	0	-0.0292	-0.0458	0.0304	0.0166	2	3	1	-0.0060	-0.0097	0.0677	0.0036
0	2	0	7.8187	8.6848	0.0367	-0.8661	3	3	1	4.8351	4.6542	0.0187	0.1809
2	2	0	7.1388	7.1292	0.0398	0.0096	4	3	1	-0.0335	-0.0186	0.0346	-0.0149
4	2	0	4.8347	4.5919	0.0298	0.2429	5	3	1	2.6709	2.6858	0.0430	-0.0150
6	2	0	1.7741	1.7834	0.0545	-0.0093	7	3	1	0.3655	0.4813	0.0340	-0.1158
8	2	0	-0.5376	-0.3778	0.0526	-0.1598	11	3	1	-0.9779	-0.6360	0.0916	-0.3419
10	2	0	-1.1410	-0.8287	0.1499	-0.3123	13	3	1	-1.3001	-0.7822	0.2431	-0.5178
12	2	0	-1.2002	-0.9152	0.0763	-0.2850	1	4	1	-0.0862	-0.0394	0.0437	-0.0468
14	2	0	-0.7793	-0.9218	0.1216	0.1425	2	4	1	0.0106	-0.0347	0.0653	0.0453
2	3	0	-0.1584	-0.0688	0.0437	-0.0895	3	4	1	-0.0890	-0.1190	0.0245	0.0300
4	3	0	-0.1875	-0.1239	0.0261	-0.0636	4	4	1	-0.0752	-0.0068	0.0313	-0.0684
6	3	0	-0.0593	-0.1255	0.0725	0.0662	6	4	1	0.0170	-0.0034	0.0617	0.0204
0	4	0	6.0680	5.4801	0.1023	0.5879	1	5	1	3.5744	3.4801	0.0384	0.0943
2	4	0	4.9309	4.6120	0.0506	0.3188	2	5	1	-0.0249	0.0008	0.0490	-0.0227
4	4	0	3.0862	3.1191	0.0537	-0.0329	3	5	1	2.7480	2.6529	0.0360	0.0951
8	4	0	-0.1913	-0.1739	0.0486	-0.0174	4	5	1	0.0117	-0.0013	0.0268	0.0130
10	4	0	-0.6757	-0.4948	0.1635	-0.1809	5	5	1	1.5052	1.6422	0.0431	-0.1370
12	4	0	-0.7859	-0.5899	0.1388	-0.1960	7	5	1	0.3784	0.3411	0.0369	0.0373
14	4	0	-1.0085	-0.6601	0.1263	-0.3484	9	5	1	-0.4982	-0.3343	0.1439	-0.1639
2	5	0	-0.1353	-0.0848	0.1097	-0.0505	11	5	1	-0.5591	-0.3667	0.0531	-0.1924
4	5	0	-0.0718	-0.1521	0.0599	0.0803	1	6	1	0.0264	-0.0388	0.0272	0.0652
0	6	0	2.0877	2.0340	0.0226	0.0537	2	6	1	-0.0569	-0.0301	0.0482	-0.0268
2	6	0	1.7253	1.7526	0.0324	-0.0274	3	6	1	-0.1165	-0.1151	0.0979	-0.0014
4	6	0	1.2778	1.2570	0.0304	0.0207	4	6	1	-0.1256	-0.0088	0.1224	-0.1167
6	6	0	0.6033	0.5553	0.0710	0.0480	5	7	1	0.3688	0.4760	0.0422	-0.1072
8	6	0	-0.1251	-0.2073	0.1401	0.0823	7	7	1	0.3573	0.3085	0.0331	0.0488
10	6	0	-0.4332	-0.3022	0.0934	-0.1311	9	7	1	-0.1302	-0.2491	0.0738	0.1190
2	7	0	0.0576	-0.0734	0.0427	0.1310	11	7	1	0.0098	-0.1397	0.1597	0.1494
0	8	0	-0.5818	-0.5004	0.1006	-0.0815	1	9	1	-0.9346	-0.8578	0.0903	-0.0768
2	8	0	-0.5897	-0.4376	0.0385	-0.1521	3	9	1	-0.3293	-0.6269	0.4248	0.2976
4	8	0	-0.3963	-0.2436	0.0762	-0.1526	5	9	1	-0.2366	-0.2998	0.1130	0.0632
6	8	0	-0.0784	-0.1535	0.0412	0.0751	7	9	1	-0.0194	-0.1897	0.0703	0.1703
8	8	0	-0.1943	-0.2592	0.0632	0.0649	9	9	1	-0.0168	-0.0836	0.1014	-0.0783
10	8	0	0.2185	-0.1077	0.2974	0.3262	11	9	1	0.1888	0.0940	0.1622	0.0949
12	8	0	-0.0842	-0.0557	0.1465	-0.0285	1	11	1	1.1404	-0.9796	0.1051	-0.1609
0	10	0	-1.0732	-1.0483	0.0796	-0.3240	3	13	1	0.0827	-0.8620	0.0324	0.9447
2	10	0	-1.0732	-0.9146	0.0763	-0.1587	7	11	1	-0.2088	-0.1505	0.1105	-0.0583
4	10	0	-1.1121	-0.5644	0.1998	-0.5477	9	11	1	0.2299	0.0343	0.2990	0.1956
6	10	0	-0.1964	-0.2626	0.2010	0.0661	1	13	1	-1.3013	-1.0906	0.2480	-0.2107
8	10	0	-0.1408	-0.1300	0.1598	-0.0108	3	13	1	0.0827	-0.8620	0.0324	0.9447
0	12	0	-1.3189	-1.1390	0.1219	-0.1799	5	13	1	-0.4393	-0.5188	0.2418	0.0795
2	12	0	-1.2639	-1.0132	0.0778	-0.2506	7	13	1	-0.3253	-0.2463	0.1448	-0.0791
4	12	0	-0.8314	-0.6744	0.0841	-0.1570	2	2	2	5.8908	5.9026	0.0343	-0.0119
6	12	0	-0.1623	-0.3470	0.1936	0.1847	2	3	2	-0.1850	-0.0594	0.0769	-0.1256
8	12	0	0.0802	-0.1226	0.1510	0.2028	3	3	2	-0.0094	-0.0337	0.0291	0.0243
0	14	0	-1.3608	-1.1094	0.0772	-0.2514	4	3	2	-0.1308	-0.0942	0.0525	-0.0367
2	14	0	-1.4811	-1.0026	0.0975	-0.4786	5	3	2	-0.0782	-0.0056	0.0406	-0.0726
4	14	0	9.5728	9.0240	0.1249	0.5489	3	4	2	3.3786	3.9116	0.1034	-0.5330
1	1	1	-0.2521	-0.0224	0.1310	-0.2298	2	4	2	-0.0140	-0.0089	0.0271	-0.0050
2	1	1	-0.0247	-0.0213	0.1493	-0.0034	4	4	2	2.5890	2.7370	0.0327	-0.1480
3	2	1	-0.1528	-0.0723	0.0282	-0.0804	5	4	2	-0.0003	-0.0135	0.0436	0.0133
4	2	1	0.0260	-0.0017	0.0617	0.0277	6	4	2	1.1830	1.2487	0.0330	-0.0657
5	2	1	-0.0823	-0.0853	0.0459	0.0029	8	4	2	-0.1576	-0.0895	0.0925	-0.0681
6	2	1	-0.0574	-0.0016	0.0411	-0.0559	10	4	2	-0.5367	-0.3798	0.0842	-0.1568
7	2	1	0.0131	-0.0771	0.1563	0.0902	12	4	2	-0.8388	-0.4878	0.1096	-0.3510

H	K	L	F _{obs}	F _{calc}	SIG F _{obs}	F _{obs} - F _{calc}	H	K	L	F _{obs}	F _{calc}	SIG F _{obs}	F _{obs} - F _{calc}
14	4	2	-0.9591	-0.5720	0.1402	-0.3871	5	7	5	0.6048	0.4156	0.1752	0.1892
2	5	2	-0.0471	-0.0717	0.0352	0.0246	7	7	5	0.4307	0.2323	0.0514	0.2094
3	5	2	-0.0458	-0.0353	0.0511	-0.0105	9	7	5	0.1056	0.1250	0.1141	-0.0195
4	5	2	0.0199	-0.1143	0.1200	0.1343	11	7	5	0.2812	0.1597	0.2439	0.1215
5	5	2	-0.0136	-0.0107	0.0263	-0.0029	5	9	5	0.0541	0.0756	0.0507	-0.0215
2	6	2	1.5146	1.5720	0.0776	-0.0574	7	9	5	0.1680	0.1454	0.0553	0.0226
4	6	2	1.0834	1.1921	0.0734	-0.1087	9	9	5	0.1986	0.2157	0.0558	-0.0171
6	6	2	0.7348	0.5910	0.0326	0.1438	5	11	5	-0.0037	0.0296	0.0760	-0.0333
8	6	2	-0.0365	-0.0956	0.0635	0.0591	7	11	5	0.2263	0.1538	0.0723	0.0726
10	6	2	-0.4913	-0.1926	0.1582	-0.2987	5	13	5	-0.2781	-0.1459	0.2242	-0.1322
12	6	2	-0.2253	-0.2509	0.1081	0.0256	6	6	6	0.6593	0.4319	0.0519	0.2274
2	8	2	-0.3816	-0.3049	0.0405	-0.0768	6	8	6	0.2543	0.1839	0.0553	0.0704
4	8	2	-0.1678	-0.1091	0.0427	-0.0587	8	8	6	0.3613	0.1792	0.0896	0.1821
6	8	2	0.1198	-0.0263	0.0485	0.1461	10	8	6	0.5665	0.2614	0.1675	0.3051
8	8	2	-0.0494	-0.1311	0.1057	0.0817	6	10	6	0.1124	0.1649	0.1616	-0.0525
10	8	2	-0.0863	-0.0060	0.1261	-0.0803	6	12	6	0.1642	0.0876	0.0609	0.0766
12	8	2	-0.0607	0.0210	0.3130	-0.0817	7	7	7	0.4562	0.1975	0.2612	0.2587
2	10	2	-0.9684	-0.7016	0.0876	-0.2668	7	9	7	0.2171	0.2150	0.1279	0.0021
4	10	2	-0.4914	-0.3817	0.1286	-0.1097							
6	10	2	-0.0161	-0.1177	0.0623	0.1017							
8	10	2	0.1026	-0.0099	0.1116	0.1125							
10	10	2	0.0425	0.1670	0.1319	-0.1245							
2	12	2	-1.0455	-0.7988	0.1132	-0.2466							
4	12	2	-0.6850	-0.4939	0.1707	-0.1910							
6	12	2	-0.3434	-0.2072	0.1070	-0.1361							
8	12	2	-0.1287	-0.0140	0.2162	-0.1147							
2	14	2	-1.3227	-0.8229	0.2182	-0.4998							
4	14	2	-0.9133	-0.5605	0.1287	-0.3527							
3	3	3	3.4935	3.5174	0.0167	-0.0239							
4	4	3	0.0275	-0.0220	0.0603	0.0495							
5	4	3	-0.0641	-0.0598	0.0560	-0.0043							
3	5	3	1.4217	2.1472	0.0648	-0.7256							
4	5	3	-0.0305	-0.0118	0.0516	-0.0187							
5	5	3	0.8889	1.4286	0.1240	-0.5397							
7	5	3	0.2778	0.4089	0.0737	-0.1311							
9	5	3	-0.3418	-0.1376	0.1850	-0.2042							
11	5	3	-0.0365	-0.1854	0.1395	0.1489							
13	5	3	0.0676	-0.3621	0.0920	0.4297							
3	6	3	-0.0149	-0.0556	0.0372	0.0407							
3	7	3	0.4187	0.4684	0.0390	-0.0496							
5	7	3	0.4378	0.4189	0.1047	0.0190							
7	7	3	0.3818	0.1086	0.0942	0.2732							
11	7	3	-0.0291	0.0118	0.1012	-0.0409							
3	9	3	-0.1164	-0.3417	0.0735	0.2253							
5	9	3	-0.1984	-0.0694	0.0412	-0.1290							
7	9	3	0.0390	0.0100	0.0239	0.0290							
9	9	3	0.1022	0.0864	0.0773	0.0158							
11	9	3	0.1548	0.2141	0.1918	-0.0593							
3	11	3	-0.8334	-0.4208	0.2002	-0.4126							
5	11	3	0.2416	-0.1303	0.0251	0.3719							
7	11	3	-0.0836	0.0364	0.2371	-0.1200							
4	4	4	1.8751	2.0414	0.0462	-0.1663							
4	6	4	0.8490	1.0354	0.0801	-0.1864							
6	6	4	0.7161	0.6066	0.0454	0.1095							
8	6	4	0.2184	0.0981	0.2248	0.1203							
10	6	4	-0.1400	0.0177	0.1698	-0.1577							
12	6	4	0.0075	-0.0658	0.1202	0.0733							
4	8	4	0.0992	0.0878	0.0606	0.0114							
6	8	4	0.2148	0.1490	0.1107	0.0658							
10	8	4	0.3517	0.1571	0.2196	0.1946							
4	10	4	-0.2826	-0.1211	0.0772	-0.1615							
6	10	4	0.0028	0.0743	0.0811	-0.0715							
10	10	4	-0.1170	0.2818	0.0564	-0.3989							
4	12	4	-0.4676	-0.2434	0.1346	-0.2242							
6	12	4	0.1747	-0.0264	0.3194	0.2011							
5	5	5	0.8311	1.0490	0.1579	-0.2178							

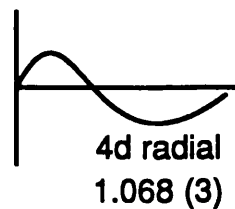
Figure 5.5.2

**ASRED
REFINEMENT 2.**

T_h S_6 Orbital wavefunctions
(Z axis down 3-fold) Population from
ASRED refinement.



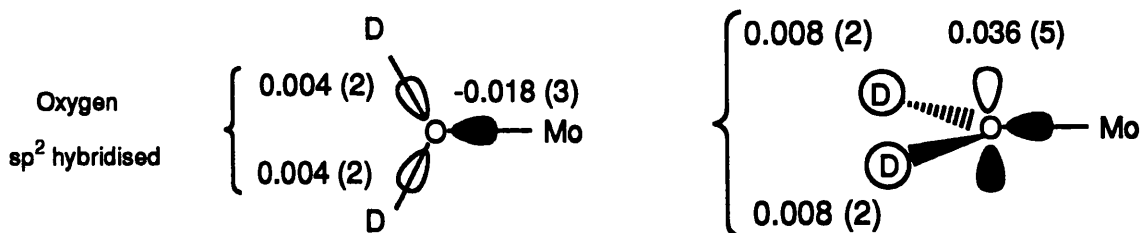
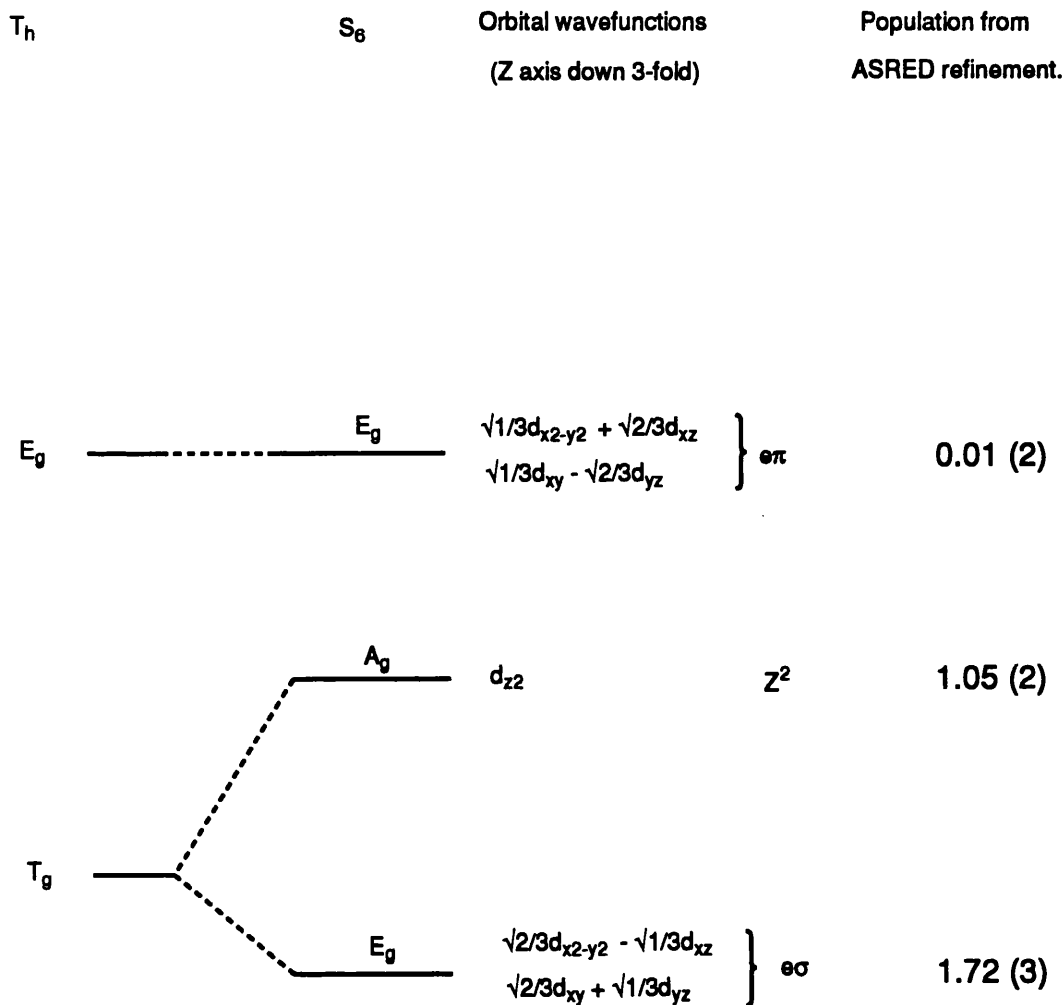
Number of reflections used in refinement	140
Number of parameters	8
Experimental $F_M(000)$ and E.S.D	11.08 (0.05)
Calculated $F_M(000)$	11.27
Weighted Residual Index R_w	0.0337
chi squared χ^2	1.47



orbital normal to the plane of the water molecule indicating some degree of covalency. The hybrid orbital pointing along the metal-oxygen bond has a significant negative value, indicative of spin polarisation effects. The value of the $F_M(000)$ reflection, calculated by ASRED for this refinement, is 11.27 BM which is in bad agreement with the experimental value of 11.08 (0.05). The experimental value was determined from susceptibility measurements on CsMoSD using a SQUID magnetometer at the University of Sheffield. This experiment is described in the section 5.7. Susceptibility measurements obtained for other alums, using the same apparatus, suggest that the experimental value of $F_M(000)$ obtained for CsMoSD may be systematically in error. In addition, the $[\text{Mo}(\text{OD}_2)_6]^{3+}$ cation is extremely susceptible to oxidation and no check on the molybdenum(III) content was made after measurement. In **Refinement 3** a greater E.S.D has been given to $F_M(000)$. The experimental value of $F_M(000)$ is now 11.08 (0.5) as compared to 11.08 (0.05) in Refinement 2, this has the effect of giving the 'reflection' ten times less weighting, with dramatic results. χ^2 and R_w are now 1.24 and 3.19% indicating that the model from this refinement gives a better fit to the experimental data. The calculated value of $F_M(000)$ has now risen to 12.14 BM as a result of giving the experimental value less weighting. This value is, however, unacceptable. Since molybdenum(III) has a less than half filled 4d shell the spin-orbit coupling constant is positive and any orbital contribution to the magnetic moment would act against the spin so that $F_M(000)$ is < 12 at magnetic saturation. In addition, saturation is not quite reached at the temperature and field at which the experiment was undertaken (see section 5.7). In **Refinement 4**, an additional parameter is introduced on Mo. Spin is now allowed to occupy a 5s orbital on the metal. It is found that with this additional function, χ^2 and R_w can be maintained at values obtained in Refinement 3 whilst keeping $F_M(000)$ constrained to a realistic value. As the weighting on the experimentally determined value of $F_M(000)$ is increased the calculated value of $F_M(000)$ drops and the diffuse 5s function takes on an increasingly negative value. The model is further improved by letting the 5s radial function contract or expand. The radial expansion/contraction parameter finds a value of 1.5 (2) as shown in **Refinement 5**. A comparison between the observed structure factors and those calculated in this refinement is given in table 5.5.2.

Figure 5.5.3

**ASRED
REFINEMENT 3.**



Number of reflections used in refinement	140
Number of parameters	8
Experimental $F_M(000)$ and E.S.D	11.08 (0.5)
Calculated $F_M(000)$	12.14
Weighted Residual Index R_w	0.0319
chi squared χ^2	1.24

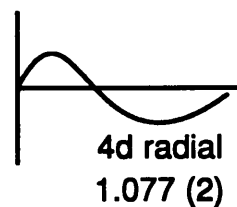
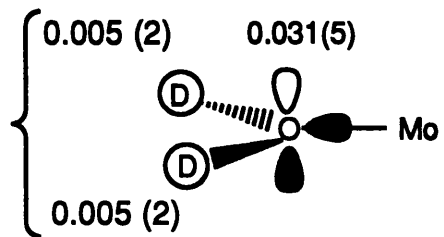
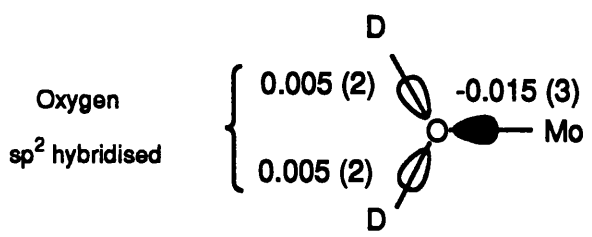
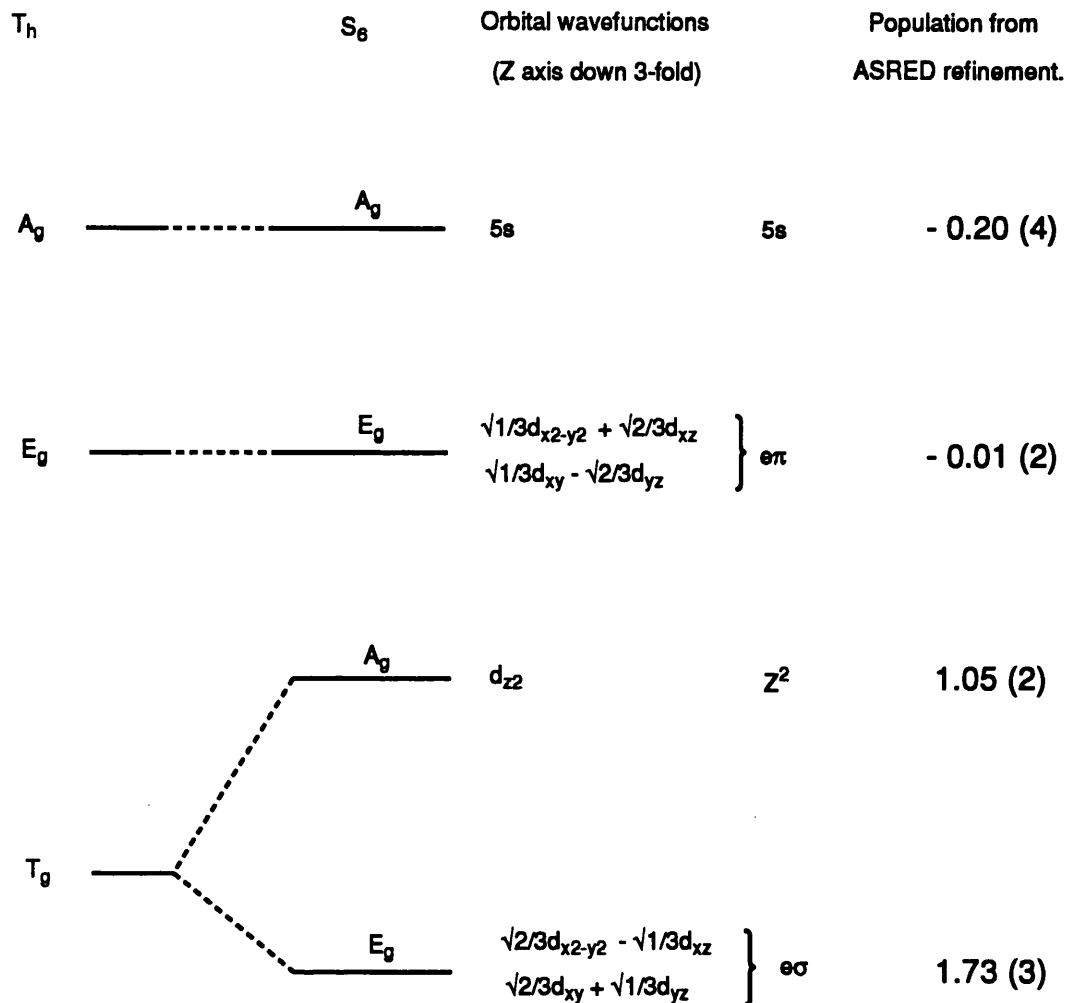


Figure 5.5.4

**ASRED
REFINEMENT 4.**



Number of reflections used in refinement	140
Number of parameters	9
Experimental $F_M(000)$ and E.S.D	11.08 (0.05)
Calculated $F_M(000)$	11.14
Weighted Residual Index R_w	0.0305
chi squared χ^2	1.33

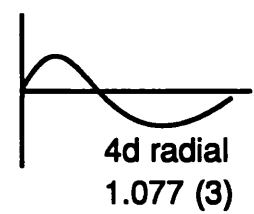
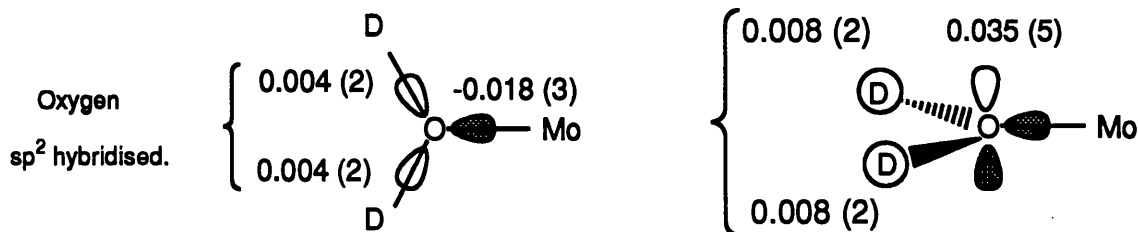


Figure 5.5.5

**ASRED
REFINEMENT 5.**

T_h	S_6	Orbital wavefunctions (Z axis down 3-fold)	Population from ASRED refinement.
A_g	A_g	5s	5s - 0.14 (4)
E_g	E_g	$\left. \begin{array}{l} \sqrt{1/3}d_{x^2-y^2} + \sqrt{2/3}d_{xz} \\ \sqrt{1/3}d_{xy} - \sqrt{2/3}d_{yz} \end{array} \right\} e\pi$	- 0.04 (2)
	A_g	d_{z^2}	z^2 1.03 (2)
T_g	E_g	$\left. \begin{array}{l} \sqrt{2/3}d_{x^2-y^2} - \sqrt{1/3}d_{xz} \\ \sqrt{2/3}d_{xy} + \sqrt{1/3}d_{yz} \end{array} \right\} e\sigma$	1.68 (3)



Number of reflections used in refinement	140
Number of parameters	10
Experimental $F_M(000)$ and E.S.D	11.08 (0.05)
Calculated $F_M(000)$	11.10
Weighted Residual Index R_w	0.0291
chi squared χ^2	1.27

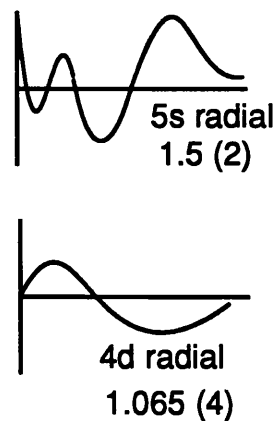


TABLE 5.5.2

Comparison between the observed structure factors and those calculated by ASRED in Refinement 5. $R_w = 2.91\%$ $\sigma^2 = 1.27$ for 140 unique reflections.

H	K	L	F_{obs}	F_{calc}	SIG	F_{obs}	$F_{obs} - F_{calc}$	H	K	L	F_{obs}	F_{calc}	SIG	F_{obs}	$F_{obs} - F_{calc}$
0	0	0	11.0800	11.0999	0.0500	-0.0199		9	5	1	-0.4982	-0.3977	0.1439	-0.1005	
4	2	0	4.8347	4.7949	0.0298	0.0399		11	5	1	-0.5591	-0.4905	0.0531	-0.0685	
6	2	0	1.7741	1.7958	0.0545	-0.0217		1	6	1	0.0264	-0.0405	0.0272	0.0669	
8	2	0	-0.5376	-0.5136	0.0526	-0.0240		2	6	1	-0.0569	-0.0335	0.0482	-0.0234	
12	2	0	-1.2002	-1.1474	0.0763	-0.0528		2	7	1	-0.0346	0.0019	0.0344	-0.0365	
14	2	0	-0.7793	-1.0475	0.1216	0.2682		5	7	1	0.3573	0.3291	0.0331	0.0282	
2	3	0	-0.1584	-0.0679	0.0437	-0.0905		7	7	1	0.2409	0.0990	0.0764	0.1420	
4	3	0	-0.1875	-0.1295	0.0261	-0.0579		9	7	1	-0.1302	-0.1651	0.0738	0.0349	
6	3	0	-0.0593	-0.1393	0.0725	0.0801		11	7	1	0.0098	-0.1253	0.1597	0.1351	
0	4	0	6.0680	5.8384	0.1023	0.2296		5	9	1	-0.2366	-0.3593	0.1130	0.1227	
2	4	0	4.9309	4.8405	0.0506	0.0903		7	9	1	-0.0194	-0.0867	0.0703	0.0673	
4	4	0	3.0862	3.1352	0.0537	-0.0490		9	9	1	-0.1618	-0.0120	0.1014	-0.1498	
8	4	0	-0.1913	-0.2409	0.0486	0.0495		11	9	1	0.1888	0.1307	0.1622	0.0581	
10	4	0	-0.6757	-0.7000	0.1635	0.0243		1	11	1	-1.1404	-1.3026	0.1051	0.1622	
12	4	0	-0.7859	-0.7405	0.1388	-0.0454		7	11	1	-0.2088	-0.1357	0.1105	-0.0731	
14	4	0	-1.0085	-0.7406	0.1263	-0.2679		9	11	1	0.2299	0.0599	0.2990	0.1700	
2	5	0	-0.1353	-0.0859	0.1097	-0.0494		1	13	1	-1.3013	-1.2622	0.2480	-0.0391	
0	6	0	2.0877	2.1199	0.0226	-0.0322		5	13	1	-0.4393	-0.5731	0.2418	0.1338	
2	6	0	1.7253	1.7807	0.0324	-0.0555		7	13	1	-0.3253	-0.2129	0.1448	-0.1124	
4	6	0	1.2778	1.2169	0.0304	0.0609		2	3	2	-0.1850	-0.0668	0.0769	-0.1182	
6	6	0	0.6033	0.6353	0.0710	-0.0320		3	4	2	-0.0140	-0.0026	0.0271	-0.0114	
10	6	0	-0.4332	-0.3276	0.0934	-0.1057		4	4	2	2.5890	2.6704	0.0327	-0.0814	
2	7	0	0.0576	-0.0730	0.0427	0.1306		5	4	2	-0.0003	-0.0072	0.0436	0.0070	
2	8	0	-0.5897	-0.5717	0.0385	-0.0179		6	4	2	1.1830	1.1967	0.0330	-0.0136	
4	8	0	-0.3963	-0.3295	0.0762	-0.0668		10	4	2	-0.5367	-0.5883	0.0842	0.0516	
8	8	0	-0.1943	-0.1074	0.0632	-0.0869		12	4	2	-0.8388	-0.6501	0.1096	-0.1887	
12	8	0	-0.0842	-0.0046	0.1465	-0.0796		14	4	2	-0.9591	-0.6684	0.1402	-0.2907	
0	10	0	-1.3723	-1.3787	0.0796	0.0064		2	5	2	-0.0471	-0.0813	0.0352	0.0342	
2	10	0	-1.0732	-1.2383	0.0763	0.1651		3	5	2	-0.0458	-0.0375	0.0511	-0.0083	
4	10	0	-1.1121	-0.7844	0.1998	-0.3277		5	5	2	-0.0136	-0.0078	0.0263	-0.0058	
6	10	0	-0.1964	-0.2763	0.2010	0.0798		6	6	2	0.7348	0.6516	0.0326	0.0832	
8	10	0	-0.1408	-0.0698	0.1598	-0.0709		8	6	2	-0.0365	-0.0137	0.0635	-0.0228	
0	12	0	-1.3189	-1.3879	0.1219	0.0690		12	6	2	-0.2253	-0.2849	0.1081	0.0596	
2	12	0	-1.2639	-1.2674	0.0778	0.0036		2	8	2	-0.3816	-0.4481	0.0405	0.0665	
4	12	0	-0.8314	-0.8464	0.0841	0.0150		4	8	2	-0.1678	-0.2008	0.0427	0.0330	
6	12	0	-0.1623	-0.3672	0.1936	0.2049		6	8	2	0.1198	0.0665	0.0485	0.0532	
8	12	0	0.0802	-0.0845	0.1510	0.1647		10	8	2	-0.0863	0.0359	0.1261	-0.1222	
0	14	0	-1.3608	-1.2409	0.0772	-0.1198		12	8	2	-0.0607	0.0541	0.3130	-0.1148	
2	14	0	-1.4811	-1.1488	0.0975	-0.3323		2	10	2	-0.9684	-1.0094	0.0876	0.0410	
4	14	0	-1.0612	-0.8076	0.1519	-0.2536		4	10	2	-0.4914	-0.5940	0.1286	0.1026	
2	2	1	-0.0247	-0.0240	0.1493	-0.0007		6	10	2	-0.0161	-0.1378	0.0623	0.1218	
4	2	1	0.0260	0.0013	0.0617	0.0247		8	10	2	0.1026	0.0359	0.1116	0.0667	
5	2	1	-0.0823	-0.0928	0.0459	0.0105		10	10	2	0.0425	0.1838	0.1319	-0.1413	
6	2	1	-0.0574	-0.0007	0.0411	-0.0567		4	12	2	-0.6850	-0.6599	0.1707	-0.0251	
2	3	1	-0.0060	-0.0096	0.0677	0.0036		6	12	2	-0.3434	-0.2327	0.1070	-0.1107	
3	3	1	4.8351	4.8278	0.0187	0.0073		8	12	2	-0.1287	0.0131	0.2162	-0.1419	
4	3	1	-0.0335	-0.0194	0.0346	-0.0141		4	14	2	-0.9133	-0.6547	0.1287	-0.2586	
5	3	1	2.6709	2.6837	0.0430	-0.0129		3	3	3	3.4935	3.5052	0.0167	-0.0117	
7	3	1	0.3655	0.4222	0.0340	-0.0567		5	4	3	-0.0641	-0.0675	0.0560	0.0034	
11	3	1	-0.9779	-0.9047	0.0916	-0.0733		7	5	3	0.2778	0.4341	0.0737	-0.1563	
1	4	1	-0.0862	-0.0409	0.0437	-0.0452		9	5	3	-0.3418	-0.1948	0.1850	-0.1470	
2	4	1	0.0106	-0.0386	0.0653	0.0492		3	6	3	-0.0149	-0.0609	0.0372	0.0461	
6	4	1	0.0170	-0.0030	0.0617	0.0200		3	7	3	0.4187	0.3847	0.0390	0.0340	
1	5	1	3.5744	3.6321	0.0384	-0.0577		7	7	3	0.3818	0.2595	0.0942	0.1223	
2	5	1	-0.0249	0.0043	0.0490	-0.0292		11	7	3	-0.0291	0.0180	0.1012	-0.0471	
3	5	1	2.7480	2.6573	0.0360	0.0907		5	9	3	-0.1984	-0.1161	0.0412	-0.0823	
4	5	1	0.0117	0.0033	0.0268	0.0084		9	9	3	0.1022	0.1458	0.0773	-0.0436	
7	5	1	0.3784	0.3829	0.0369	-0.0045		11	9	3	0.1548	0.2399	0.1918	-0.0850	

H	K	L	F _{obs}	F _{calc}	SIG F _{obs}	F _{obs} - F _{calc}
3	11	3	-0.8334	-0.6663	0.2002	-0.1671
7	11	3	-0.0836	0.0507	0.2371	-0.1343
4	4	4	1.8751	1.8925	0.0462	-0.0174
6	6	4	0.7161	0.6918	0.0454	0.0244
12	6	4	0.0075	-0.0667	0.1202	0.0741
4	8	4	0.0992	0.0558	0.0606	0.0434
10	8	4	0.3517	0.2199	0.2196	0.1319
4	10	4	-0.2826	-0.2564	0.0772	-0.0262
6	10	4	0.0028	0.0942	0.0811	-0.0914
4	12	4	-0.4676	-0.3496	0.1346	-0.1179
7	7	5	0.4307	0.4437	0.0514	-0.0130
9	7	5	0.1056	0.2701	0.1141	-0.1646
5	9	5	0.0541	0.1288	0.0507	-0.0748
7	9	5	0.1680	0.2981	0.0553	-0.1300
9	9	5	0.1986	0.3250	0.0558	-0.1264
5	11	5	-0.0037	0.0155	0.0760	-0.0192
7	11	5	0.2263	0.2258	0.0723	0.0005
5	13	5	-0.2781	-0.1303	0.2242	-0.1478
6	6	6	0.6593	0.6457	0.0519	0.0136
6	8	6	0.2543	0.4069	0.0553	-0.1526
8	8	6	0.3613	0.3989	0.0896	-0.0376
10	8	6	0.5665	0.3902	0.1675	0.1763
6	12	6	0.1642	0.1667	0.0609	-0.0026
7	9	7	0.2171	0.4134	0.1279	-0.1964

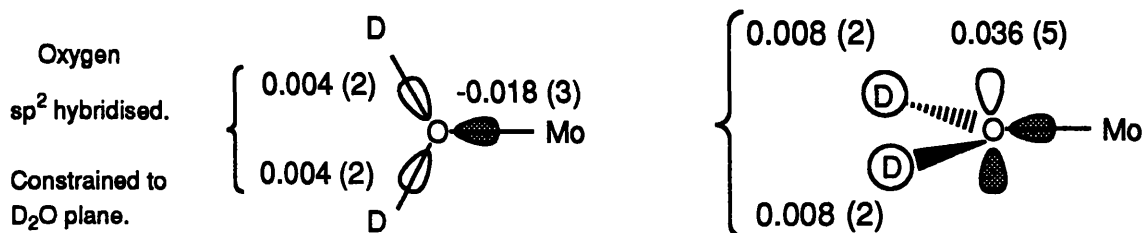
The polarised neutron data collected for CsMoSD can be adequately modelled treating the oxygen atom as sp^2 hybridised. In this instance small but significant spin is transferred to the ligand where it is concentrated in the p-type orbital normal to the water plane.

For purposes of commenting on the water bonding symmetry, it is instructive to compare this model with other models in which bonding symmetry is altered. **Refinement 6** has the same parametisation setup as Refinement 5 except that the sp^2 co-ordinate system is constrained to the positions of the deuterium atoms which lie out of the MoO_4 plane by $1.8 (1)^\circ$. Compared with the set of quantisation axes in Refinement 5, three hybrid orbitals now lie exactly in the plane of the water molecule. This results in the two hybrid orbitals giving a closer match to the oxygen-deuterium bonds but the hybrid orbital pointing towards Mo now makes an angle of 1.8° with the Mo-O bond vector. The populations of the parameters are practically unchanged from Refinement 5 reflecting the fact that the deuterium atoms very nearly form a plane with the molybdenum and oxygen atoms. In **Refinement 7**, the parametisation setup on Mo is unchanged from that of Refinement 5, however the bonding symmetry about the oxygen atom is changed to sp^3 hybridised with hybrid lobes pointing as close as possible along the oxygen-deuterium bonds. χ^2 and R_w are significantly higher than for Refinement 5 indicating that the spin density about the oxygen is modelled more effectively by treating the oxygen as sp^2 hybridised. This is because for this sp^3 hybridised refinement, there is no available hybrid orbital with which to model the negative spin density along the molybdenum-oxygen bond. In **Refinement 8**, the oxygen atom is treated as sp^3 hybridised with respect to the MO_6 framework such that one sp^3 lobe is directed along the molybdenum-oxygen bond and the other three hybrid orbitals point in positions that would match a trigonal pyramidal co-ordination of the water molecules with the oxygen-deuterium bond vectors each making an angle of 55° to the MoO_4 plane. In **Refinement 9**, the sp^3 framework is rotated around the molybdenum-oxygen bond by 180° from its position in Refinement 8. It is expected that the choice of bonding symmetry chosen in Refinements 8 and 9 would be more applicable when the water co-ordination is not planar but the deuterium atoms are tilted out of the MoO_4 plane by 55° . Although not representing a chemically feasible model, the goodness of fit of these refinements is only

Figure 5.5.6

**ASRED
REFINEMENT 6.**

T_h	S_6	Orbital wavefunctions (Z axis down 3-fold)	Population from ASRED refinement.
A_g	A_g	5s	5s - 0.14 (4)
E_g	E_g	$\left. \begin{array}{l} \sqrt{1/3}d_{x^2-y^2} + \sqrt{2/3}d_{xz} \\ \sqrt{1/3}d_{xy} - \sqrt{2/3}d_{yz} \end{array} \right\} e\pi$	- 0.04 (2)
		d_{z^2}	z^2 1.02 (2)
T_g		$\left. \begin{array}{l} \sqrt{2/3}d_{x^2-y^2} - \sqrt{1/3}d_{xz} \\ \sqrt{2/3}d_{xy} + \sqrt{1/3}d_{yz} \end{array} \right\} e\sigma$	1.68 (3)



Number of reflections used in refinement	140
Number of parameters	10
Experimental $F_M(000)$ and E.S.D	11.08 (0.05)
Calculated $F_M(000)$	11.10
Weighted Residual Index R_w	0.0290
chi squared χ^2	1.27

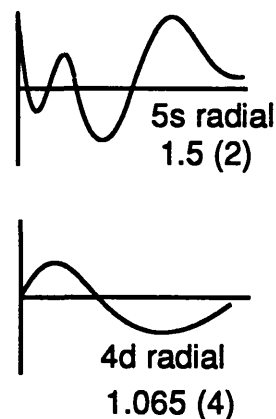
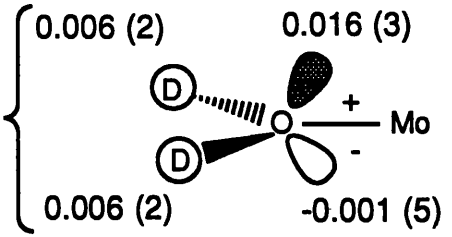
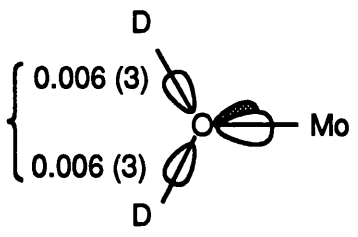


Figure 5.5.7

**ASRED
REFINEMENT 7.**

T_h	S_6	Orbital wavefunctions (Z axis down 3-fold)	Population from ASRED refinement.
A_g	A_g	5s	5s - 0.20 (4)
E_g	E_g	$\left. \begin{array}{l} \sqrt{1/3}d_{x^2-y^2} + \sqrt{2/3}d_{xz} \\ \sqrt{1/3}d_{xy} - \sqrt{2/3}d_{yz} \end{array} \right\} e\pi$	- 0.06 (3)
		d_{z^2}	z^2 1.06 (3)
T_g		$\left. \begin{array}{l} \sqrt{2/3}d_{x^2-y^2} - \sqrt{1/3}d_{xz} \\ \sqrt{2/3}d_{xy} + \sqrt{1/3}d_{yz} \end{array} \right\} e\sigma$	1.73 (4)

Oxygen
 sp^3 hybridised
Constrained to
 D_2O Plane.



Number of reflections used in refinement	140
Number of parameters	10
Experimental $F_M(000)$ and E.S.D	11.08 (0.05)
Calculated $F_M(000)$	11.09
Weighted Residual Index R_w	0.0345
chi squared χ^2	1.51

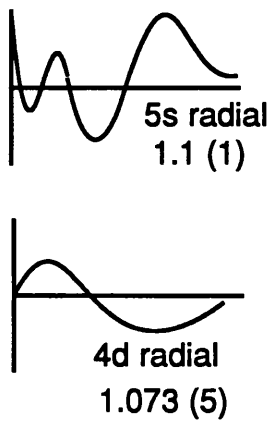
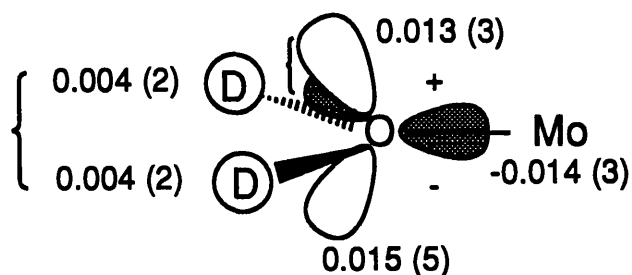


Figure 5.5.8

**ASRED
REFINEMENT 8.**

T_h	S_6	Orbital wavefunctions (Z axis down 3-fold)	Population from ASRED refinement.	
A_g	A_g	5s	5s	- 0.11 (4)
E_g	E_g	$\left. \begin{array}{l} \sqrt{1/3}d_{x^2-y^2} + \sqrt{2/3}d_{xz} \\ \sqrt{1/3}d_{xy} - \sqrt{2/3}d_{yz} \end{array} \right\} e\pi$		- 0.05 (3)
	A_g	d_{z^2}	z^2	1.04 (3)
T_g	E_g	$\left. \begin{array}{l} \sqrt{2/3}d_{x^2-y^2} - \sqrt{1/3}d_{xz} \\ \sqrt{2/3}d_{xy} + \sqrt{1/3}d_{yz} \end{array} \right\} e\sigma$		1.68 (3)

Oxygen
 sp^3 hybridised
Constrained to
 MO_6 framework.



Number of reflections used in refinement	140
Number of parameters	10
Experimental $F_M(000)$ and E.S.D	11.08 (0.05)
Calculated $F_M(000)$	11.10
Weighted Residual Index R_w	0.0310
chi squared χ^2	1.36

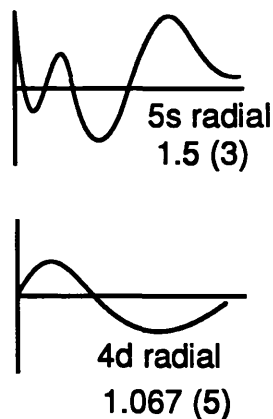
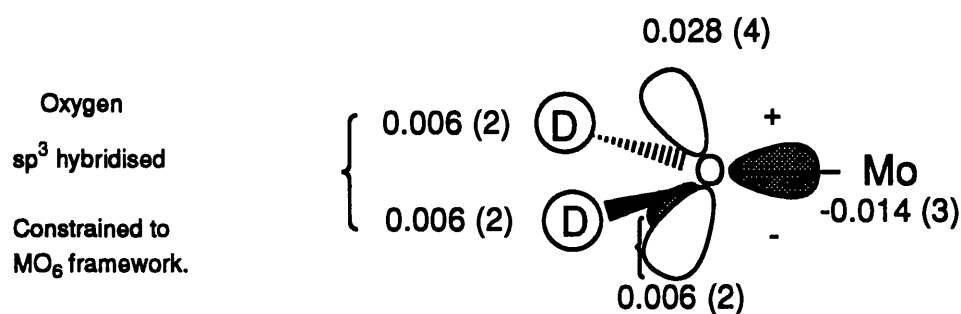
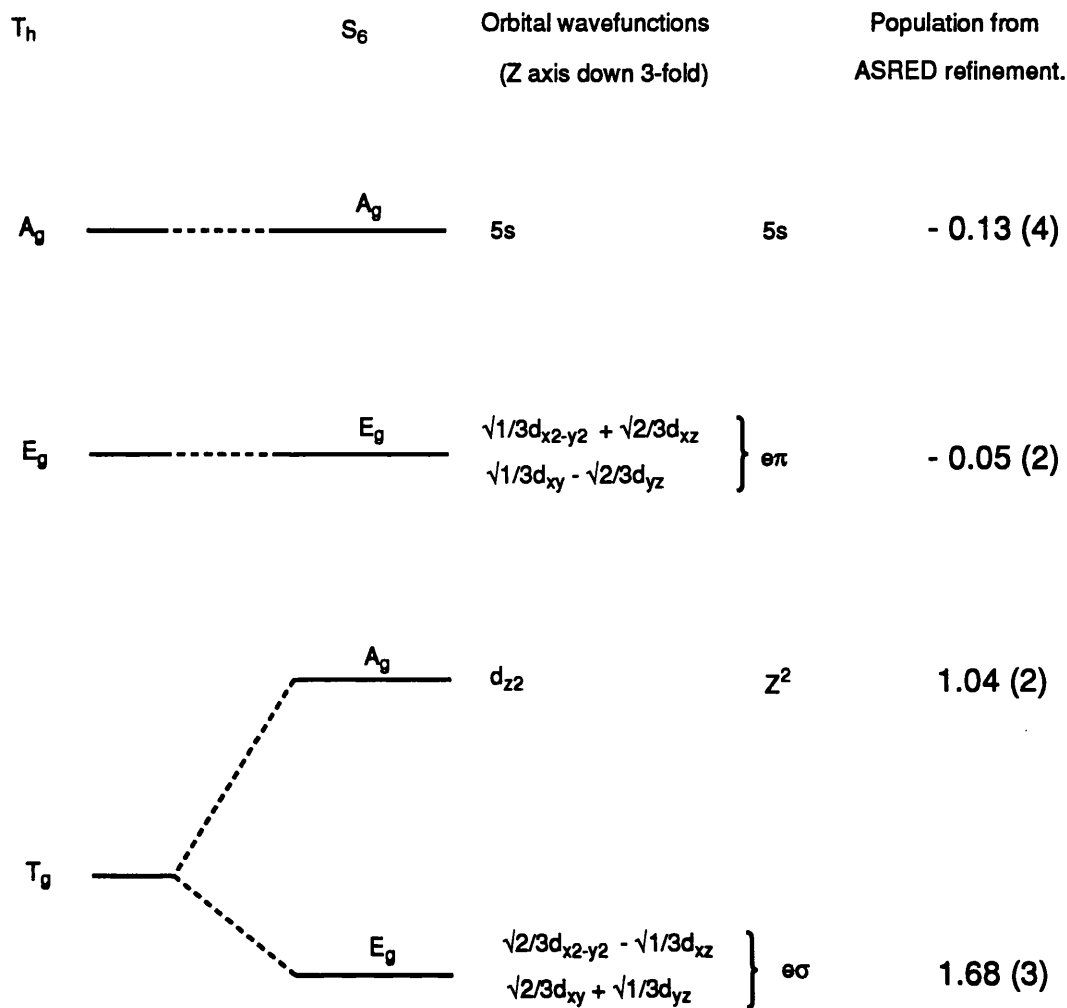
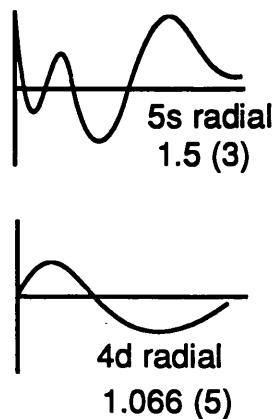


Figure 5.5.9

**ASRED
REFINEMENT 9.**



Number of reflections used in refinement	140
Number of parameters	10
Experimental $F_M(000)$ and E.S.D	11.08 (0.05)
Calculated $F_M(000)$	11.10
Weighted Residual Index R_w	0.0298
chi squared χ^2	1.30



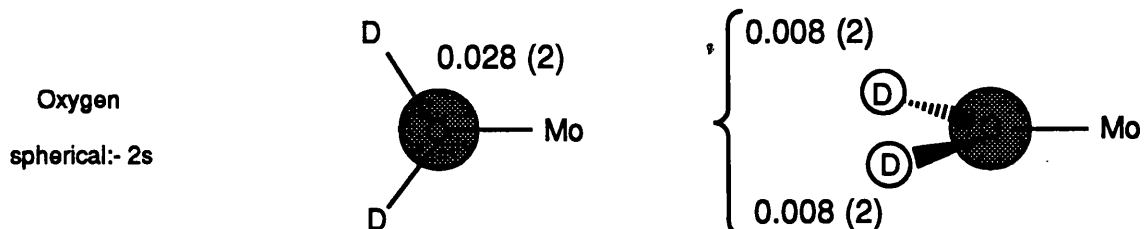
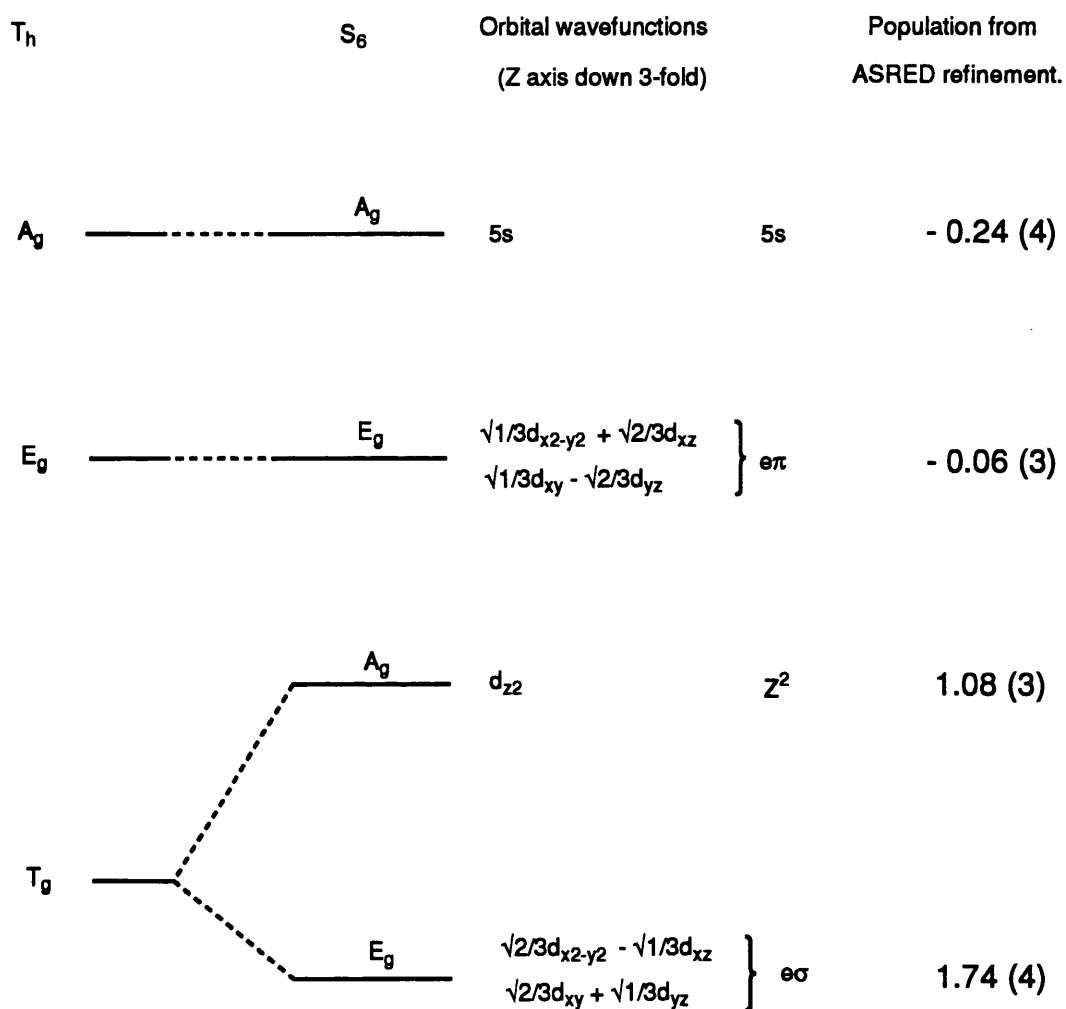
marginally worse than for the sp^2 hybridised model. In addition these refinements are instructive in that they suggest that the spin is not symmetrically distributed about the water plane. **Refinement 10** models the spin distribution about the oxygen by a 2s orbital. The high χ^2 and R_w values demonstrate that to describe the spin density distribution about the oxygen using a spherical model is inappropriate.

Refinements 11 - 14

These are refinements of theoretical structure factors. The structure factors were calculated by Sean Howard²³ from a spin restricted Hartree-Fock calculation using the basis set LANL1-DZ.²⁴ The ab initio code used for the calculation was GAUSSIAN 90.²⁵ Since the structure factors were calculated from a spin restricted HF calculation, no spin density can arise from electron paired orbitals; thus the calculation does not account for electron - electron correlation effects. The calculation is instructive, however, in describing how the unpaired electron density is distributed throughout the complex. In all refinements of the theoretical structure factors, it was found that a satisfactory refinement could be achieved only with a highly contracted spherical function placed at the Mo site. This function was given a gaussian radial dependence. In all refinements of the theoretical structure factors, this function was found to have a very small but well defined negative population. The significance of this function is not apparent. As for the experimental data set, the best fit to the theoretical magnetisation density is achieved when the oxygen is treated as sp^2 hybridised as shown in **Refinement 11**. The theoretical model predicts that some spin is transferred to the ligand where it is concentrated normal to the plane of the water molecule. For comparison, **Refinements 12-14** show refinements in which the oxygen is treated as sp^3 hybridised with differing axes of quantisation.

Figure 5.5.10

**ASRED
REFINEMENT 10.**



Number of reflections used in refinement	140
Number of parameters	8
Experimental $F_M(000)$ and E.S.D	11.08 (0.05)
Calculated $F_M(000)$	11.09
Weighted Residual Index R_w	0.0356
chi squared χ^2	1.55

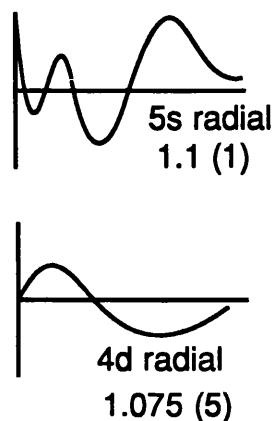
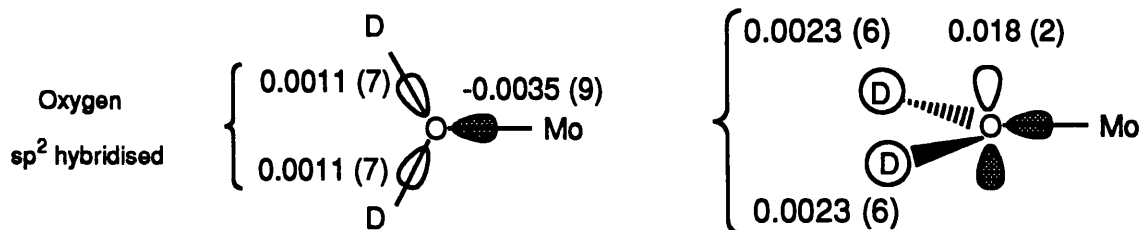
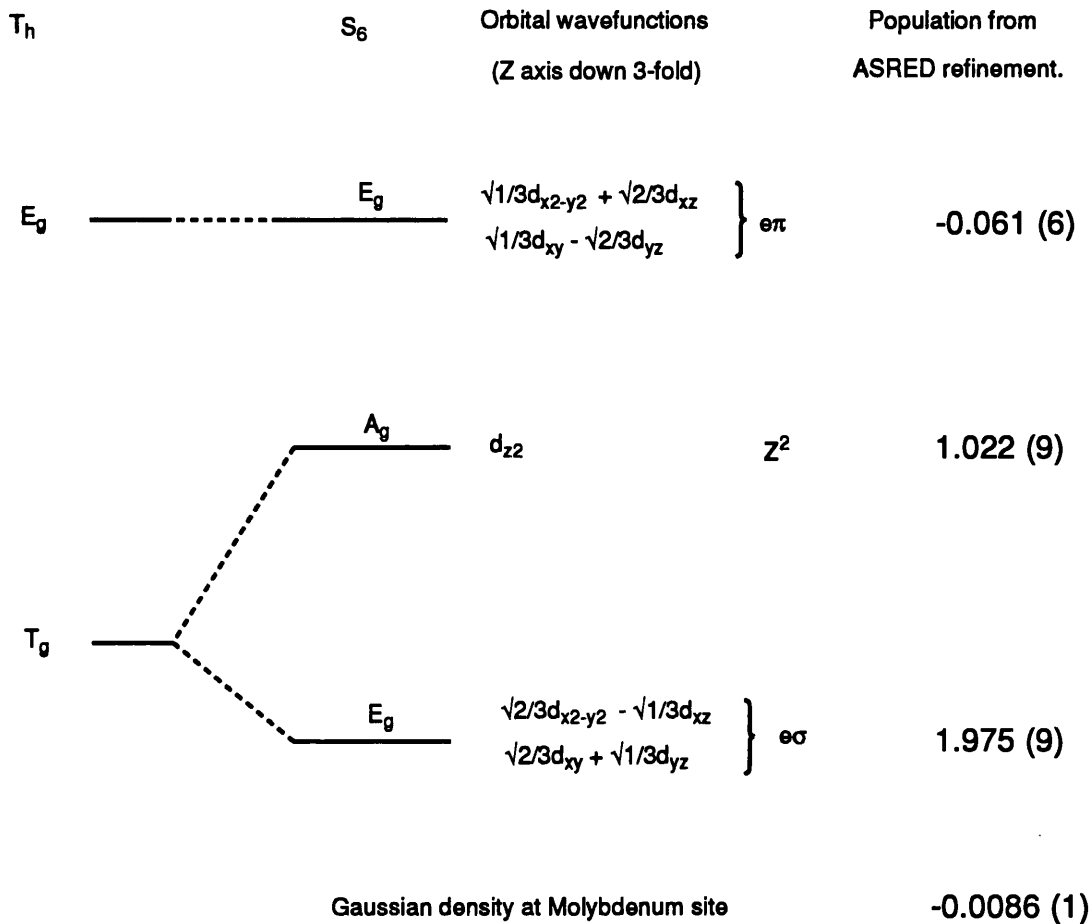


Figure 5.5.11

**ASRED
REFINEMENT 11.**

**Theoretical Structure
Factors**



Number of reflections used in refinement	198
Number of parameters	9
Theoretical $F_M(000)$	12.00
Calculated $F_M(000)$	12.06
Residual Index R	0.0212
chi squared χ^2	-

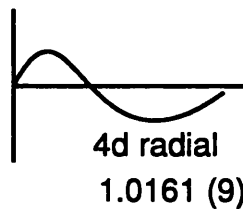
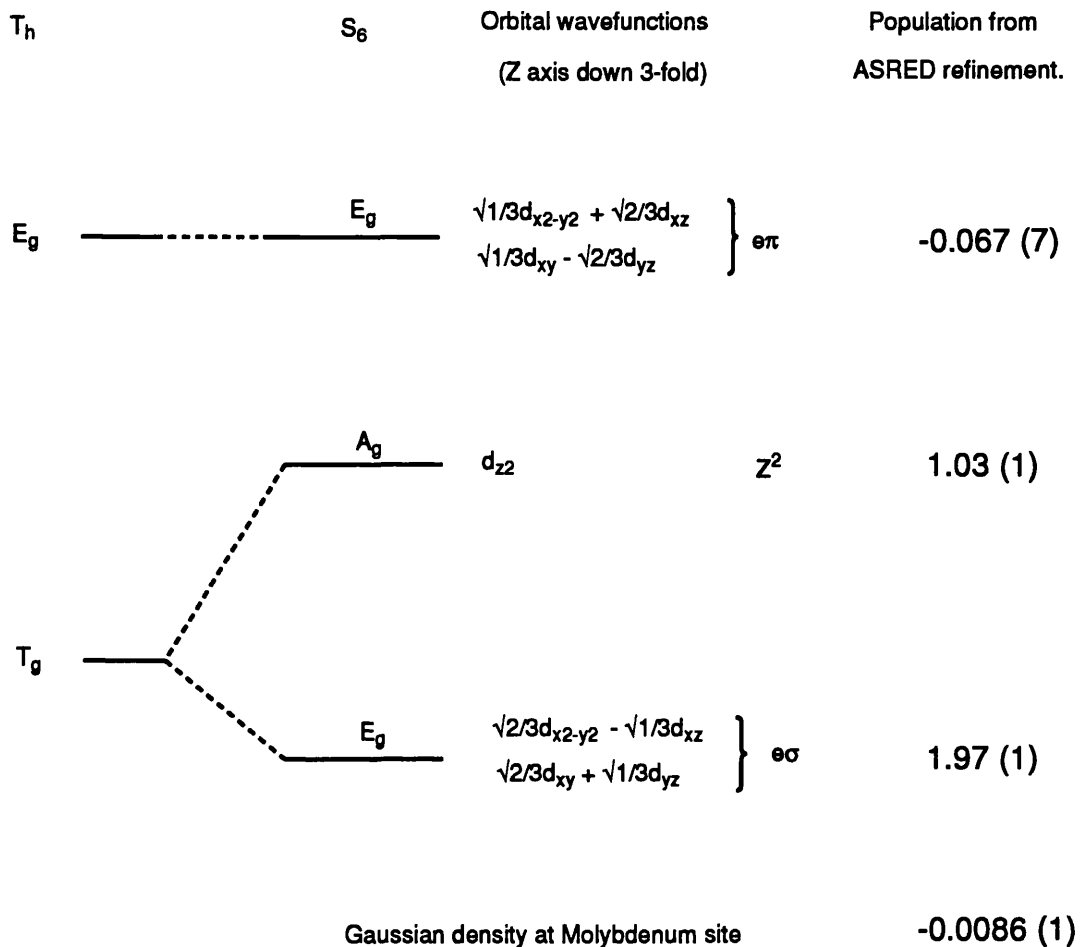


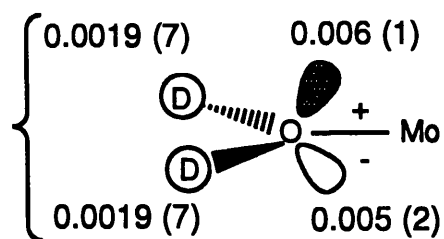
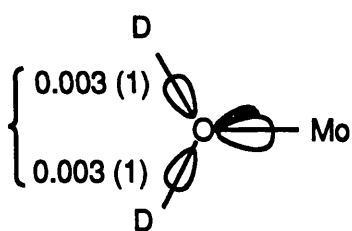
Figure 5.5.12

**ASRED
REFINEMENT 12.**

**Theoretical Structure
Factors**



Oxygen
 sp^3 hybridised
Constrained to
deuterium atom
positions.



Number of reflections used in refinement	198
Number of parameters	9
Theoretical $F_M(000)$	12.00
Calculated $F_M(000)$	12.05
Residual Index R	0.0246
chi squared χ^2	-

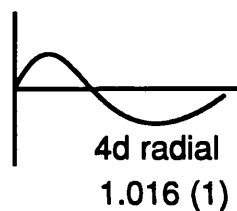
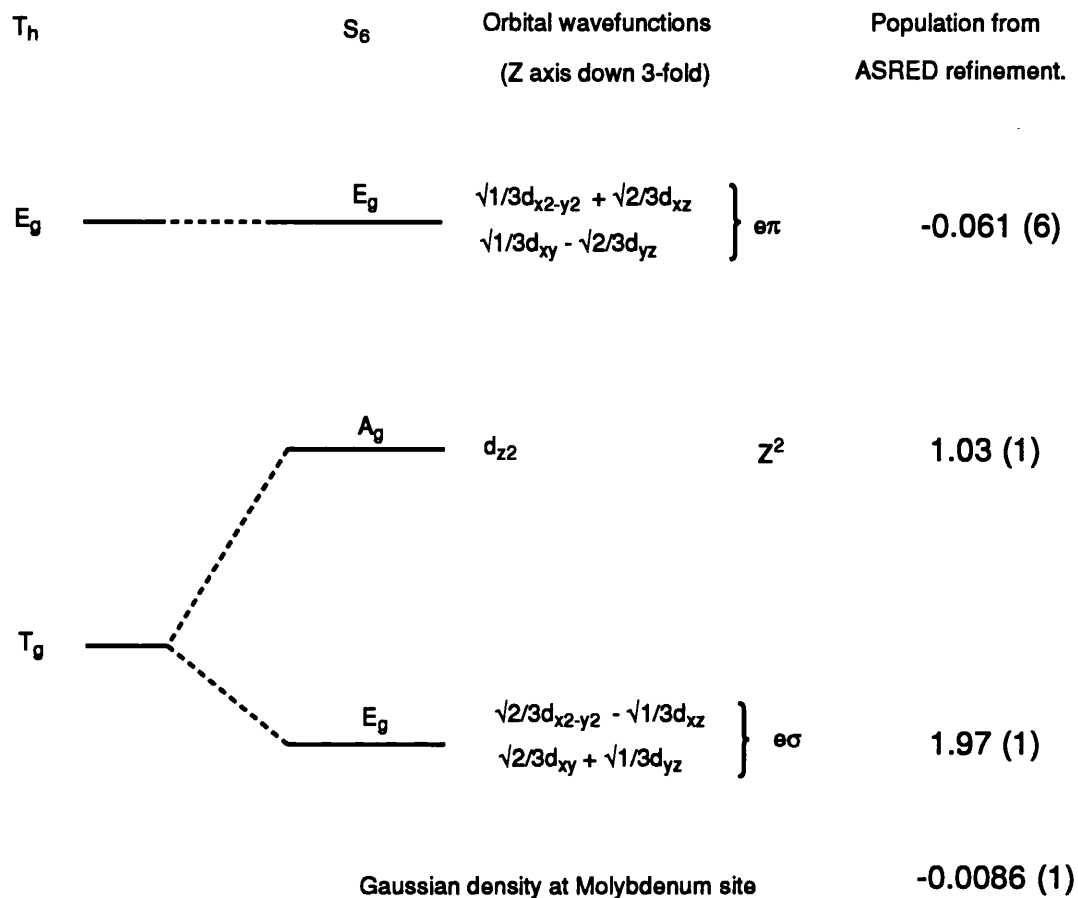


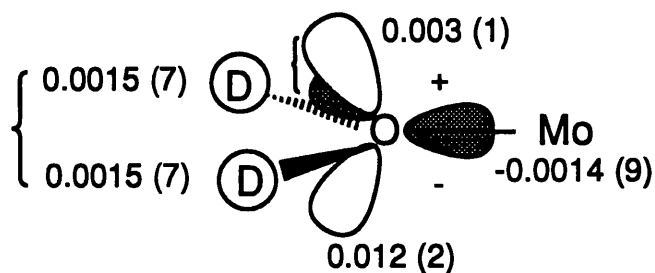
Figure 5.5.13

**ASRED
REFINEMENT 13.**

**Theoretical Structure
Factors**



Oxygen
 sp^3 hybridised
Constrained to
 MO_6 framework.



Number of reflections used in refinement	198
Number of parameters	9
Theoretical $F_M(000)$	12.00
Calculated $F_M(000)$	12.04
Residual Index R_w	0.0227
chi squared χ^2	-

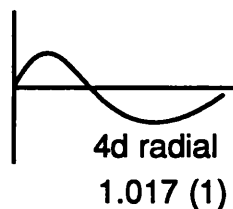
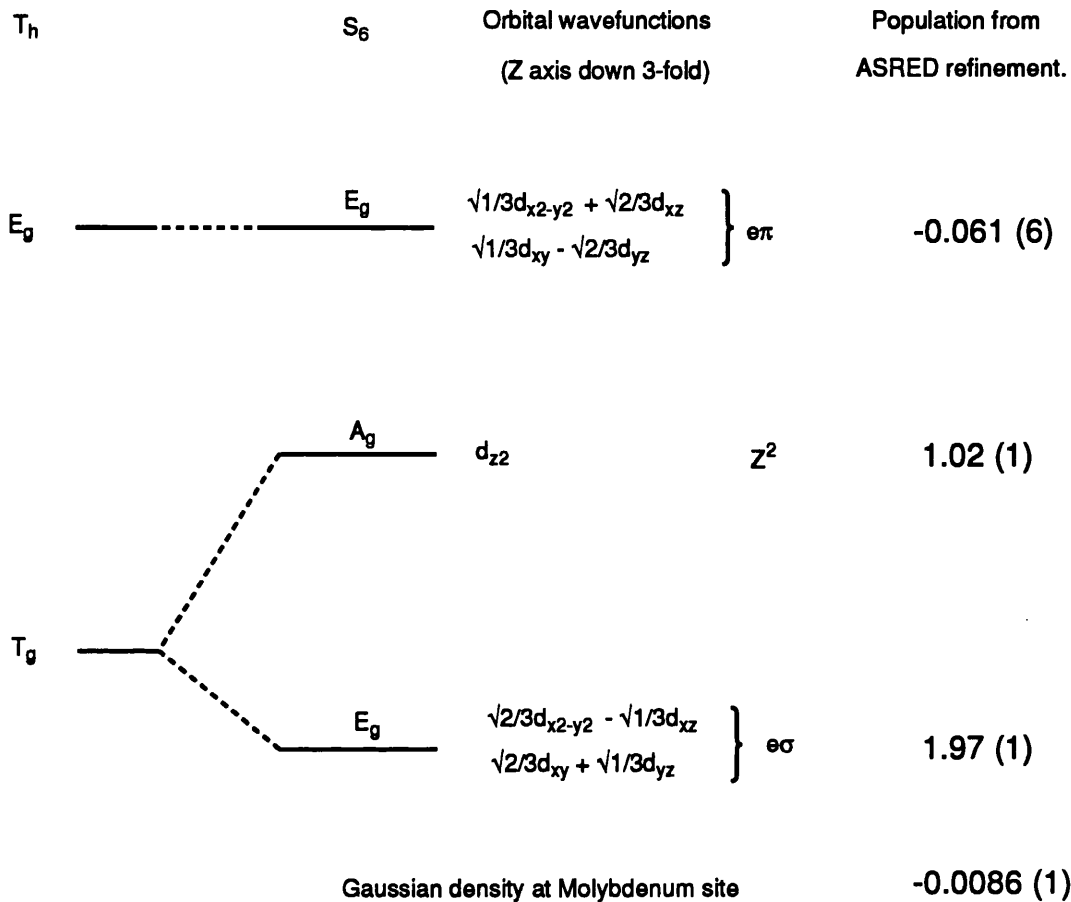


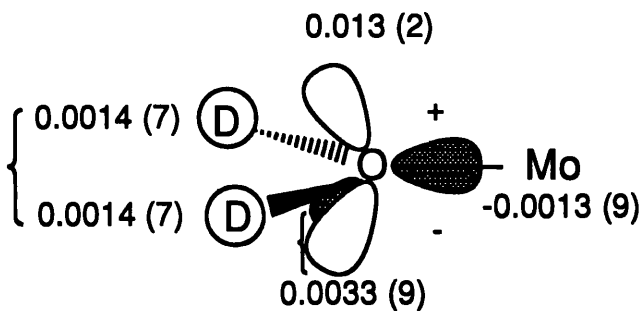
Figure 5.5.14

**ASRED
REFINEMENT 14.**

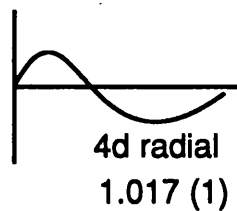
**Theoretical Structure
Factors**



Oxygen
 sp^3 hybridised
Constrained to
 MO_6 framework.



Number of reflections used in refinement	198
Number of parameters	9
Experimental $F_M(000)$ and E.S.D	12.00
Calculated $F_M(000)$	12.05
Residual Index R	0.0234
chi squared χ^2	-



MOLLY Refinements

The nuclear centred multipoles

The multipoles which can be used to expand the magnetisation density for an atom on a site of trigonal symmetry are restricted²⁶ to those shown in figure 5.5.15. The magnetisation density about molybdenum(III) was expanded as a linear combination of the allowed multipoles shown. The radial dependence of the 4d wavefunction for molybdenum(III) is listed in tabular form in the international tables on crystallography V.4.¹⁸

It was found that there was a significant improvement in the fit when an additional monopole was placed on the molybdenum cation. The additional monopole was given a Slater-type radial dependence as described in eq 5.4.4.

The oxygen and deuterium atoms lie on sites of c_1 symmetry. The multipoles that may be placed on these atoms are not restricted by symmetry. Monopoles were placed on each of the ligand atoms to represent the valence density. Dipoles were placed on the oxygen to express the deformation of the magnetisation density about the oxygen. MOLLY uses Slater-type radial functions for the deformation multipoles. The starting values of η_1 and ζ were left at the program default values recommended by Hansen and Coppens.²⁰

The refinements are again represented schematically to aid visualisation.

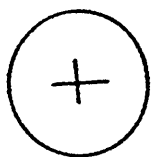
MOLLY was written for the purpose of refining high resolution X-ray diffraction data. There are drawbacks to refining polarised neutron diffraction data with MOLLY. Since all phase information is lost in an X-ray diffraction experiment, MOLLY refines on the modulus of the structure factor. Information regarding the phase of the reflection, which is obtained from the PND experiment, is thus lost and the phase has to be recalculated. Additionally, the bulk magnetisation which is left as an experimental variable in ASRED, has to be given a fixed value in MOLLY and so is effectively given infinite weight. Refinement of the data with MOLLY was not as successful as with ASRED. It was found that more parameters were needed in order to achieve a refinement comparable in R_w and χ^2 . In order to describe adequately the anisotropy of the spin distribution in the bonding region of the

Figure 5.5.15

The multipole description of the magnetisation density is expressed in terms of a series expansion in real spherical harmonics γ_{lm} . The symmetry allowed multipoles for an atom on a site of trigonal symmetry²⁶ are shown in bold.

$\gamma_{lm\pm}$

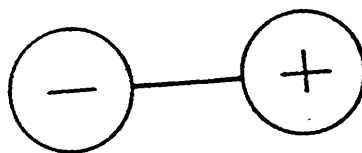
00



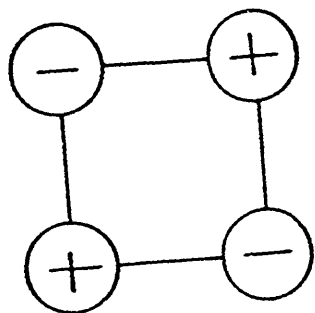
monopole

$\gamma_{lm\pm}$

11+
11-
10



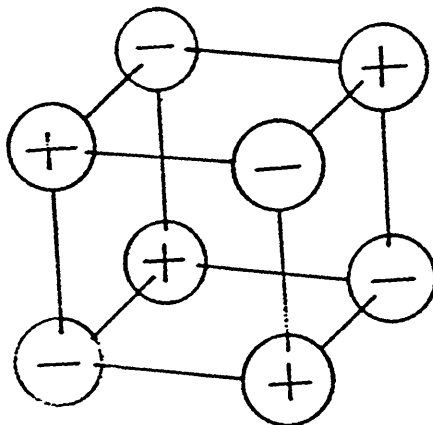
dipole



quadrupole

$\gamma_{lm\pm}$

20
21+
21-
22+
22-



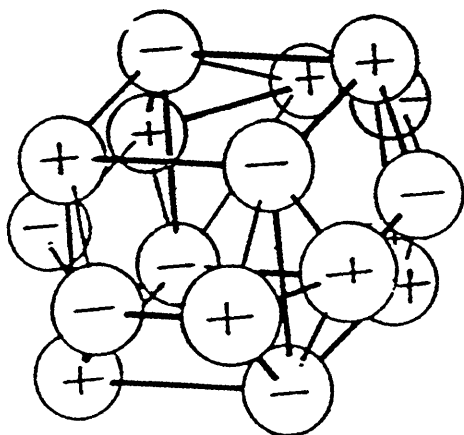
octupole

$\gamma_{lm\pm}$

30
31+
31-
32+
32-
33+
33-

$\gamma_{lm\pm}$

40
41+
41-
42+
42-
43+
43-
44+
44-



hexadecapole

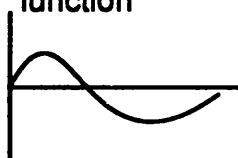
complex, a dummy hydrogen atom was placed along the molybdenum - oxygen bond. When the bonding spin density was described just by means of dipoles placed on the oxygen atom, the populations of the oxygen dipoles converged to values which depended on their given starting values indicating that the populations from these refinements are not reliable. In contrast, the multipole populations from **Refinement A**, which includes the dummy hydrogen, converge to the same values regardless of the starting populations. The need for the dummy hydrogen atom arises since one monopole placed on the oxygen is unable to describe both the 'up' spin on the oxygen and the 'down' spin in the bonding region which arises because of electron-electron correlation effects. It was found that the optimum position of the dummy hydrogen atom, in terms of achieving the best fit, was 0.785 the way along the molybdenum - oxygen bond vector going towards the oxygen. The dummy atom was given a large isotropic thermal parameter of $B_{iso} = 3.95$ to give the negative spin density a large thermal smearing. In total, 20 parameters were needed in order to obtain a consistent refinement with acceptable values of R_w and σ^2 . This many parameters gives a rather confusing picture of the spin density distribution throughout the complex. Large positive and negative charges are found for the oxygen and dummy hydrogen monopoles respectively. Only the dipoles along the Mo-O bond and normal the water plane have significant populations. Expanding the magnetisation density by means of a multipole expansion is a more rigorous approach than by the model-dependent orbital description. However translating from multipole populations to a chemically meaningful model is not trivial. Little chemical information can be obtained from these multipole refinements. **MOLLY Refinement B** is a refinement of the structure factors calculated from a spin restricted calculation. Inclusion of the dummy hydrogen and κ radial parameters gave little improvement to the R value and so were not included in the refinement. It was found, however, in analogy to the ASRED refinements, that a better fit was achieved by contracting the Slater-type monopole placed on the molybdenum site. n_1 and ζ were changed from values of 4 and 12 (used in refinement of the experimental data) to 1 and 20 resulting in the R value dropping from 3 to 2.5 %. However, the anisotropy of the spin distribution about the oxygen remains undefined since the populations of the oxygen dipoles converge to values dependent on their given starting values.

Figure 5.5.16

MOLLY REFINEMENT A

Number of reflections used in refinement	139
Number of parameters	20
Fixed value of Bulk magnetisation	11.08
Weighted Residual Index R_w	2.81
chi squared χ^2	1.14

Molybdenum
multipole radial
function



$$\kappa' = \kappa'' = 0.97 \text{ (1)}$$

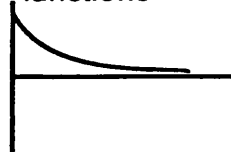
Oxygen
multipole radial
functions



$$\kappa' = 0.82 \text{ (2)}$$

$$\kappa'' = 0.83 \text{ (3)}$$

Dummy Hydrogen
multipole radial
functions



$$\kappa' = 1.11 \text{ (4)}$$

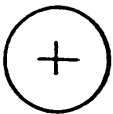
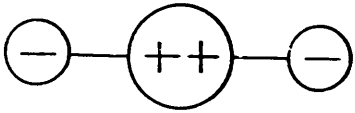
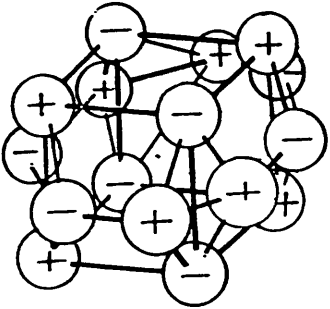
$$\kappa'' = 1.34 \text{ (7)}$$

Atomic Fractional cell coordinates and isotropic (B_{iso}) thermal parameter for dummy hydrogen.

X	Y	Z	B_{iso}
0.1322	-0.00155	-0.0089	3.95

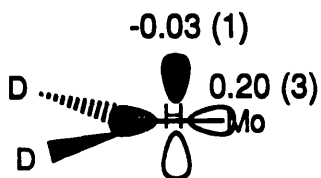
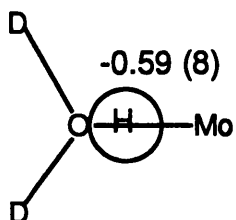
MOLLY REFINEMENT. A.
Experimental Structure Factors

**Molybdenum centred
spherical harmonics**

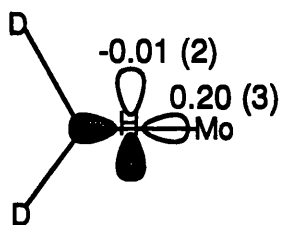
	MONOPOLE	$\gamma_{l,m}$
		(0,HF) 2.42 (6)
		(0,ST) -0.024 (7)
	QUADRUPOLE	(2, 0) 0.01 (2)
	HEXADECAPOLE	(4, 0) 0.34 (3)
		(4,+3) 0.41 (2)
		(4,-3) 0.14 (12)

DUMMY HYDROGEN MULTIPOLES

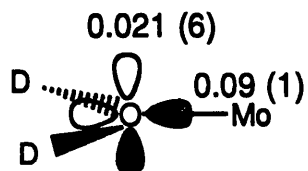
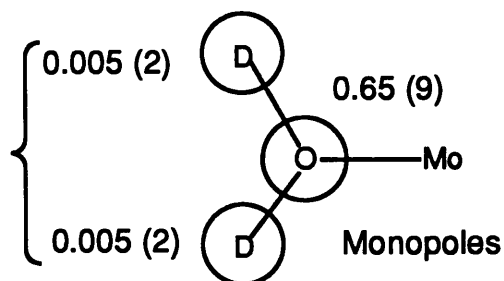
Monopole



Dipoles



LIGAND MULTIPOLES



Dipoles

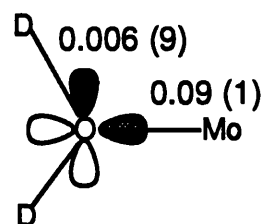
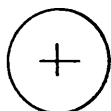


Figure 5.5.17

MOLLY REFINEMENT. B.
Theoretical Structure Factors

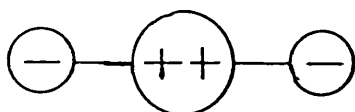
Molybdenum centred
spherical harmonics

$\gamma_{l,m}$
(0, HF) 2.947 (5)



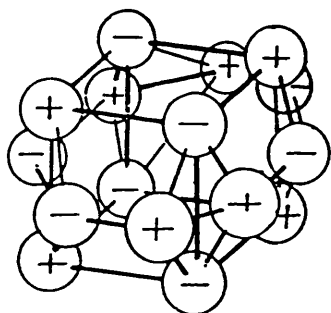
MONOPOLE

(0, ST) -0.056 (1)



QUADRUPOLE

(2, 0) -0.007 (5)



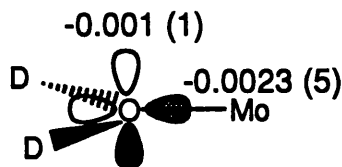
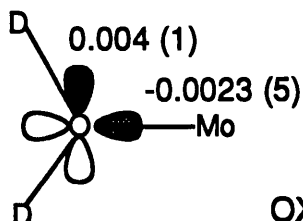
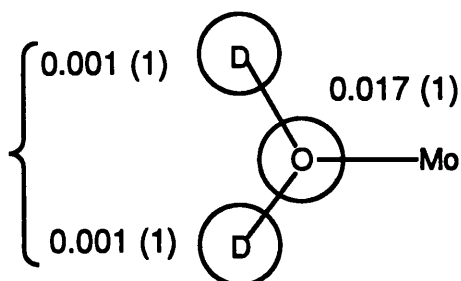
HEXADECAPOLE

(4, 0) 0.31 (2)

(4, +3) 0.45 (1)

(4, -3) -0.03 (2)

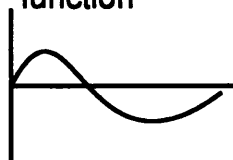
LIGAND CENTRED
MONOPOLES



OXYGEN DIPOLES

Number of reflections used in refinement	197
Number of parameters	12
Fixed value of Bulk magnetisation	12.00
Residual Index R	2.47
chi squared χ^2	-

Molybdenum
multipole radial
function



$\kappa' = \kappa'' = 0.984 (1)$

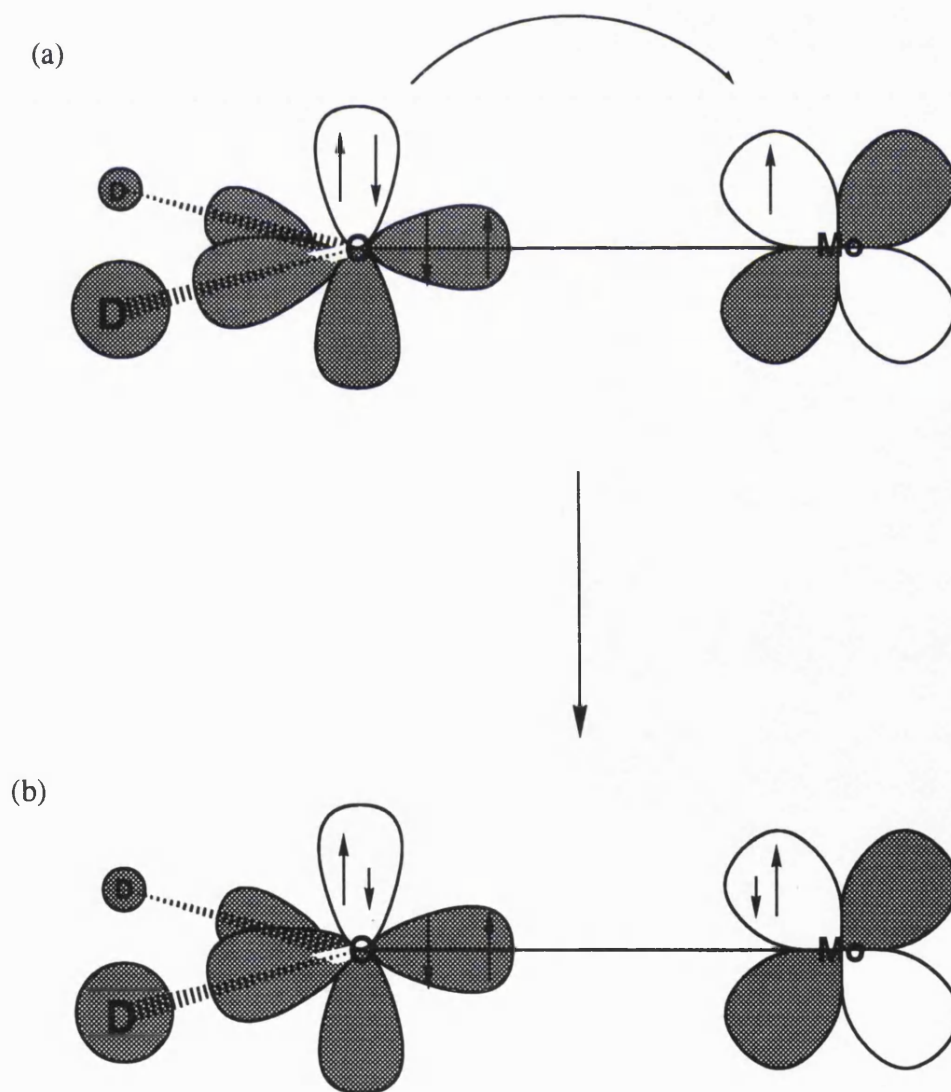
5.6 Discussion

Refinement of the polarised neutron diffraction data for the CsMoSH alum consistently shows that spin density is found to occupy t_{2g} -like orbitals on the metal with small, but significant spin transfer to the ligand, this being concentrated normal to the plane of the water molecule. The data is best modelled treating the oxygen atom as sp^2 hybridised, reflecting the local bonding symmetry. If we define spin on Mo as being 'up' then 'up' spin is found in the 2p orbital on the oxygen which is normal to the plane of the water molecule and 'down' spin is found in the hybrid orbital along the Mo-O bond. Figure 5.6.1 shows how these observations can be interpreted in terms of simple concepts of chemical bonding. In figure 5.6.1(a) the molybdenum(III)-water bond is shown with no orbital interaction and in figure 5.6.1(b) a covalent interaction is shown. In the formation of a covalent bond, 'down' spin is transferred from an oxygen lone pair to the 'up' spin half-filled 4d Mo orbitals. As a result, there is apparent transfer of spin from Mo to the surrounding water molecules. 'Up' spin transferred to the ligand is found mainly in the 2p orbital normal to the plane of the water molecule rather than in molecular orbitals within the plane of the water molecule. This observation is in agreement with refinement of the theoretical structure factors calculated from a spin-restricted Hartree-Fock calculation. The larger out-of-plane than in-plane π bonding can be explained by the better overlap and energy matching of the t_{2g} -like orbitals on Mo with the 2p orbitals on the oxygen atoms rather than with the in-plane π sp^2 orbitals and deuterium 1s orbitals. The hybrid orbital on the oxygen atom pointing towards the metal is part of the σ bonding network and becomes polarised due to electron correlation effects. Negative spin density found in σ bonded water orbitals repeats similar observations found for $[M(OD_2)_6]^{2+}$ aqua cations.²⁷ *Ab initio* calculations by Chandler *et al.*²⁸ on various transition metal ion complexes indicate that the balancing positive density in the spin-paired, but polarised σ system resides quite close to the metal nucleus. Spin density which resides close to the Mo nucleus is unlikely to be resolved into t_{2g} and e_g components at our experimental resolution. Thus we might expect an increase in the populations representing the t_{2g} orbitals as well as the parameter which represents spin occupying the e_g orbitals. The corresponding increase in the e_g population is

Figure 5.6.1

Schematic diagram showing the orbital interactions which mediate the covalency and spin polarisation effects within the $[\text{Mo}(\text{OH}_2)_6]^{3+}$ cation. The oxygen atom is treated as sp^2 hybridised.

Diagram (a) shows no orbital interaction (b) is with some degree of interaction which indirectly leads to transfer of 'up' spin from t_{2g} -like orbitals on Mo to p-type orbitals on the oxygens. 'Down' spin found in the hybrid orbital pointing along the Mo-O bond is accounted for by electron correlation effects.



outweighed by the negative spin found in the outer σ 4d region which can be ascribed as resulting from charge transfer from the water ligands into the metal 4d orbitals which subsequently becomes polarised. The 4d- e_g population is found to be -0.04 (2) in Refinement 5.

Both the π and σ molybdenum(III)-water interactions are adequately modelled treating the oxygen as sp^2 hybridised. Since the deuterium atoms very nearly form a plane with the molybdenum and oxygen atoms; it makes little difference whether the oxygen atom valence orbitals are aligned with the Mo-O bond vector (as in ASRED Refinement 5) or whether the sp^2 co-ordinate system is constrained to the D_2O plane as in ASRED Refinement 6 (resulting in the sp^2 σ hybrid making an angle of 1.8° to the molybdenum(III)-oxygen bond vector) Constraining the oxygen atom to be sp^3 hybridised with respect to the D_2O plane as in Refinement 7, the sp^3 hybrid orbitals give a better match to the experimental D-O-D bond angle than by treating the oxygen atom as sp^2 hybridised. The experimental D-O-D bond angle is 111° ; the sp^3 -O- sp^3 bond angle is 109.5° whereas the angle between the sp^2 hybrid orbitals is 120° . The two remaining sp^3 hybrid orbitals almost exactly bisect the molybdenum(III)-oxygen bond. These two sp^3 hybrids are able to model the 'up' spin transferred to the ligand as a consequence of the π interaction. However, there is no molecular orbital pointing along the molybdenum(III)-oxygen bond with which to model the negative spin found in the σ sp^2 -lone pair orbital. Consequently, the R_w and χ^2 values are appreciably higher for the sp^3 hybridised model. In both ASRED Refinements 8 and 9 the oxygen atom is sp^3 hybridised with an sp^3 hybrid orbital aligned with the Mo-O bond vector. The other three hybrid orbitals point in positions that would match a trigonal pyramidal co-ordination of the water molecules with the oxygen-deuterium bond vectors each making an angle of 55° to the MoO_4 plane. With these bonding constraints, the σ and π interaction are both modelled adequately although the fit is not quite as good as the sp^2 case above. It is interesting to note, however, that in all three sp^3 refinements, spin is found to be asymmetrically distributed about the water plane. More spin is consistently found on the side of the water plane where the M-O-D bond angle is 178.2° . These refinements suggest that although the spin is concentrated in a molecular orbital normal the water plane, the spin is not symmetrically distributed either side of the plane as is required for the sp^2 hybridised

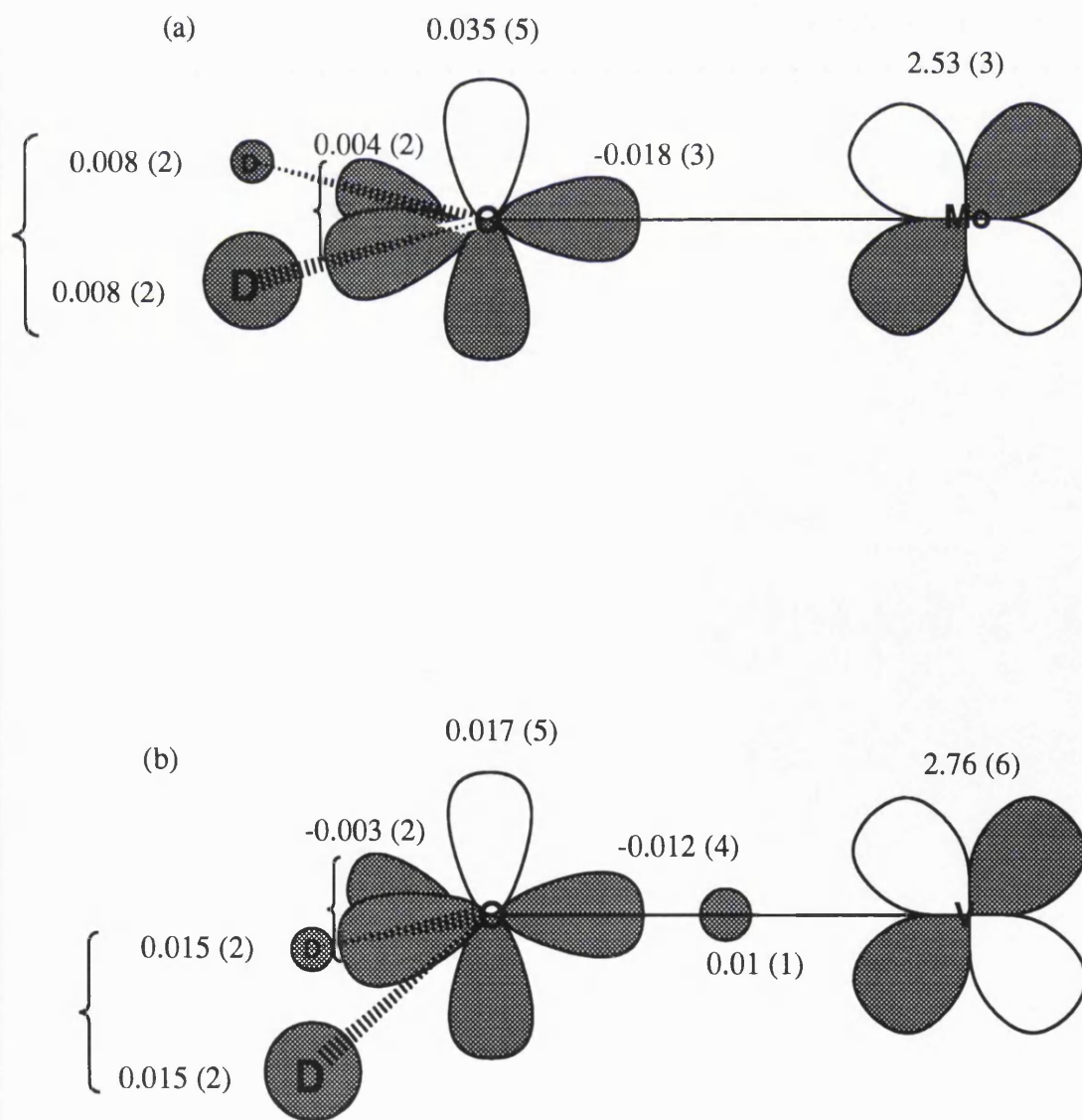
model.

No other polarised neutron study of a trivalent hexa-aqua-cation has yet been published. It is instructive, however, to compare the spin distribution throughout the $[\text{Mo}(\text{OD}_2)_6]^{3+}$ cation with that of the $[\text{V}(\text{OD}_2)_6]^{2+}$ cation in the ammonium-vanadium Tutton salt.²⁷ The ammonium-vanadium Tutton salt is monoclinic with space group $P2_1/a$.²⁹ Although possessing only a centre of inversion, the VO_6 core is approximately octahedral with the deuterium atoms inclined at *ca.* 40° to the VO_4 plane. Despite the large tilt angle, it was found that there was little difference in the goodness of fit between treating the oxygen atom as sp^2 or sp^3 hybridised (hybrid orbital co-ordinate system constrained to MO_6 framework rather than the D_2O plane). The sp^2 refinement for the $[\text{V}(\text{OD}_2)_6]^{2+}$ cation is compared with ASRED Refinement 5 of the CsMoSD PND refinements in which the oxygen atom is also treated as sp^2 hybridised constrained to the MO_6 framework. Ten parameters were used in the refinement of the p.n.d data for $\text{ND}_4\text{V}(\text{SO}_4)_2 \cdot 6\text{D}_2\text{O}$ including a gaussian function placed at the mid-point of each V-O bond to model the overlap density. The net amount of spin transferred to the water molecules is 5.8 % for $[\text{V}(\text{OD}_2)_6]^{2+}$ and 8.9 % for $[\text{Mo}(\text{OD}_2)_6]^{3+}$. Although greater covalency is expected for Mo^{3+} compared to V^{2+} , these values are not directly comparable in view of the differing modes of water coordination. The spatial spin distribution about the water ligand is shown schematically in figure 5.6.2. It is seen that significant spin is found on the deuterium atoms for the $[\text{V}(\text{OD}_2)_6]^{2+}$ cation which are the only functions left to model the in-plane π bonding. The move from out-of-plane to in-plane π -bonding from $[\text{Mo}(\text{OD}_2)_6]^{3+}$ to $[\text{V}(\text{OD}_2)_6]^{2+}$ can be accounted for by the greater tilt of the plane of the water molecule out of the MO_4 plane. This angle is 40° and 1.8° for the $[\text{V}(\text{OD}_2)_6]^{2+}$ and $[\text{Mo}(\text{OD}_2)_6]^{3+}$ cations respectively. As the tilt angle is increased, so will the in-plane π interaction increase on account of the better overlap with the t_{2g} -like orbitals on the metal.

In order to adequately model the p.n.d data collected for the CsMoSD alum, it was found necessary to place a diffuse function at the Mo site. This function, which was given a 5s radial dependence, is consistently found to have a negative population. For $[\text{V}(\text{OD}_2)_6]^{2+}$, a negative population was found for a '4d- e_g ' function placed at the vanadium site; this was interpreted in terms of indirect evidence of substantial charge transfer from the water ligands into the metal e_g orbitals. The

Figure 5.6.2

Spin distribution about the water molecule in (a) $[\text{Mo}(\text{OD}_2)_6]^{3+}$ and (b) $[\text{V}(\text{OD}_2)_6]^{2+}$ cation. Oxygen sp^2 hybridised w.r.t MO_6 framework. Only the total spin on the metal is shown. Populations for $[\text{V}(\text{OD}_2)_6]^{2+}$ are from Deeth *et al.* [27].



negative population resulting from effects of spin polarisation. Such an interpretation may also be appropriate here. The function may also, however, be correcting for deficiencies of the experimental data set. It would be useful to compare the experimental model with refinements of structure factors calculated from spin unrestricted Hartree-Fock calculations.

In ASRED Refinement 5, a population of 0.008 (2) is found on each deuterium atom. The significance of this population is also treated with caution. Unlike the population in the 2p orbital normal to the oxygen atom, a significant population is not always found on the deuterium atoms. In Refinement 2, -0.022 (3) spins are found in the hybrid orbital along the Mo-O bond, 0.026 (5) spins in the 2p orbital normal to the water plane, 0.0095 (23) in the two in-plane hybrid orbitals and -0.001 (2) spins on each deuterium atom. A slightly positive spin found in the two in-plane hybrid orbitals and a negative spin on the deuterium atoms would be in keeping with spin polarisation considerations. However, once the $F_M(000)$ reflection is given less weighting and finds a higher value as in Refinement 3 or else the weighting on $F_M(000)$ is left unchanged but a 5s function is placed on Mo, as in Refinements 4 and 5, then the populations on the ligand take on very different values. In Refinement 5, the ligand populations are -0.018 (3) spins in the hybrid orbital along the Mo-O bond, 0.035 (5) spins in the 2p orbital normal to the water plane, 0.004 (2) in the two in-plane hybrid orbitals and 0.008 (2) spins on each deuterium atom. Refinement 5 differs from Refinement 2 in having a 5s orbital at the molybdenum site which is allowed to expand and contract. Since the population on the deuterium atoms becomes significant only when the 5s function is introduced, the population cannot be taken as 'real' despite being above the 3 E.S.D level.

5.7 Spin Paramagnetism of CsM(III)SD alums of Ti, Ru, V, Mo, Cr and Fe at Low Temperatures and Strong Magnetic Fields.

The $F_M(000)$ reflection corresponds to the magnetisation of the unit cell and this, while inaccessible to diffraction experiments, can be determined from susceptibility measurements.

Susceptibility measurements were undertaken using a SQUID magnetometer at the University of Sheffield. SQUID stands for 'Superconducting Quantum Interference Device'. A description of this experimental technique is provided elsewhere.^{30,31}

A theoretical prediction of the variation of the magnetic moments of paramagnetic compounds with respect to field and temperature has been given by Brillouin.³²

In this analysis, it is assumed that all excited multiplet states are $\gg kT$ above the ground state and that the M_J levels are degenerate before the application of the external magnetic field. By summing the magnetisation over all the M_J magnetic sub-levels, whose populations are found according to Boltzmann statistics, the bulk magnetisation, M (Bohr magnetons / ion) is calculated to be:

$$M = J g_J F(J,y) \quad 5.7.1$$

where $F(J,y)$ is the Brillouin function:

$$F(J,y) = (1 + 1/2J) \coth[(1 + 1/2J)y] - 1/2J \coth(y/2J) \quad 5.7.2$$

where $y = J g_J \mu_B H/kT$

μ_B is the Bohr magneton, H the field strength, k = Boltzmann constant, T = temperature and g_J = the Landé g factor.

$$g_J = 1 + \frac{J(J + 1) + S(S + 1) - L(L + 1)}{2J(J + 1)} \quad 5.7.3$$

At magnetic saturation, where all the atomic moments are aligned with the field, $F(J,y) = 1$ so that the 5.7.1 becomes:

$$M_{\text{sat}} = J g_J \quad 5.7.4$$

the "spin only" version of which reads:

$$M_{\text{sat}} = S g \quad 5.7.5$$

where any orbital contribution is absorbed into the g factor.

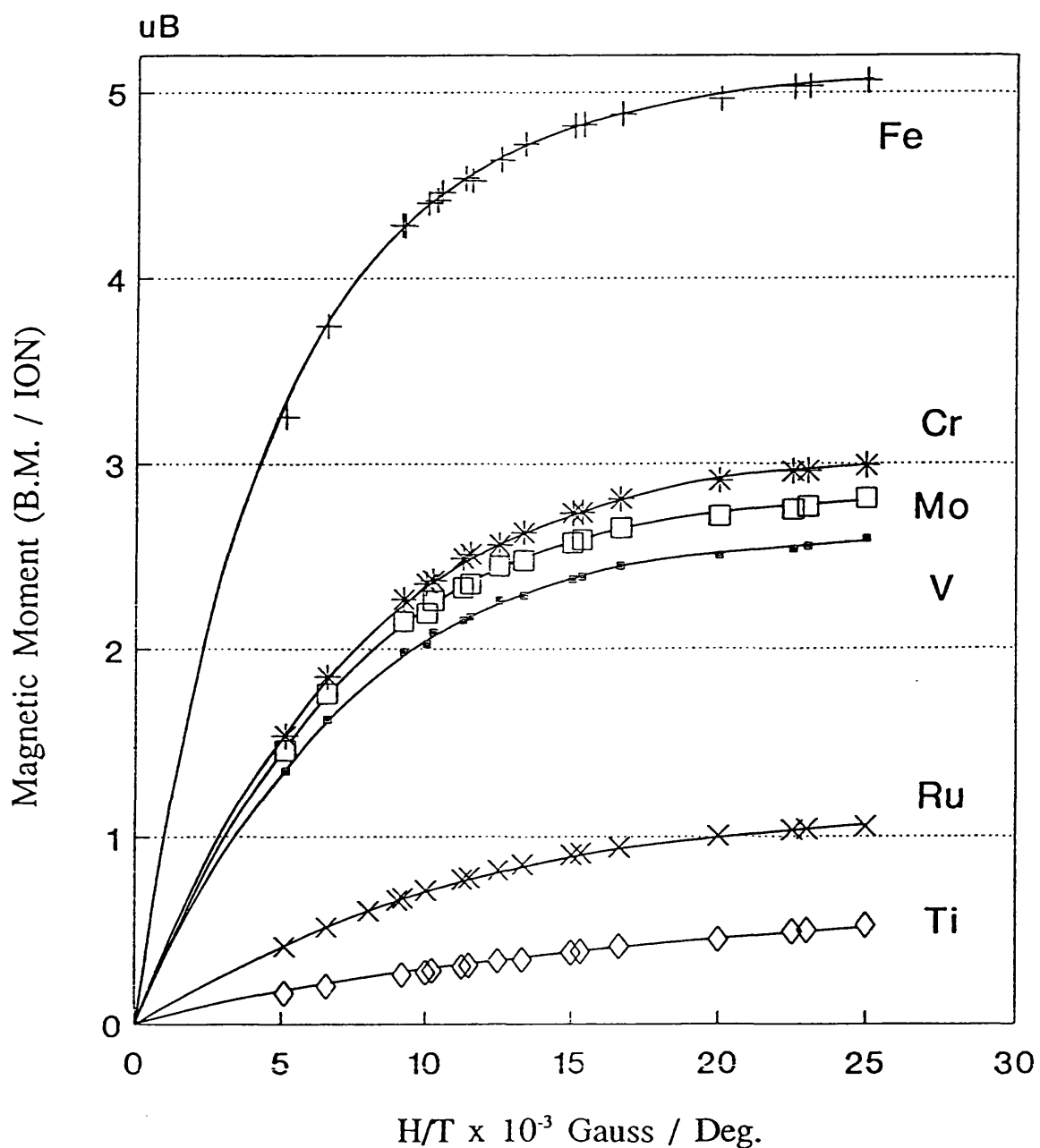
Susceptibility measurements at values of H/T approaching that of magnetic saturation have previously been undertaken on the alums of KCrSH and NH_4FeSH .³³ In this earlier study, it was found that the variation of magnetisation with H/T for iron(III) (${}^6\text{S}_{5/2}$ free ion) in NH_4FeSH alum followed almost exactly that predicted by the Brillouin function. The experimental results for chromium(III) (${}^4\text{F}_{3/2}$ free ion) within KCrSH show a close compatibility with the Brillouin function where $g = 2$ ($L = 0$) indicating almost complete quenching of orbital angular momentum by the ligand field.

The results of the present study are summarised in figure 5.7.1 where magnetisation (BM / ion) is plotted against $H/T \times 10^{-3}$ (Gauss / Deg)

For molybdenum(III), the magnetisation at saturation for the free ion ($L = 3$, $g = 2/5$) = 0.6 BM / ion. The spin only ($L = 0$, $g = 2$) value of the magnetisation = 3 BM / ion. Any residual orbital angular momentum acts to reduce the magnetisation from the spin-only value so that $M_{\text{sat}} \leq 3$. For ruthenium(III), which has the low-spin $4d^5$ valence configuration (${}^2\text{D}_{5/2}$ free ion) any residual angular momentum would act to add to the spin-only value of the magnetisation so that $M_{\text{sat}} \geq 1$. Incomplete quenching of angular momentum by the ligand field is the likely explanation as to why the magnetisations for $[\text{Mo}(\text{OD}_2)_6]^{3+}$ and $[\text{Ru}(\text{OD}_2)_6]^{3+}$ do not converge exactly to the spin-only values. The magnetisation for CsFeSH reaches a value above 5 BM / ion. This is rather puzzling since the free ion ground state for iron(III) is an orbital singlet (${}^6\text{S}_{5/2}$) so that the question of incomplete quenching of orbital angular momentum does not arise. The results obtained for CsVSD alum are also surprising since vanadium(III) has a less than half-filled 3d shell, so M_{sat} would be expected to be < 2 . At the value of H/T of 25×10^{-3} Gauss / Deg, however, the moment is at a value of 2.6 BM / ion. The results obtained for the CsTISD alum are curious since there is no indication of the onset of magnetic saturation even at values of H/T of

FIGURE 5.7.1

Plot of magnetic moment (bulk magnetisation) per ion vs H/T for $\text{CsM}^{\text{III}}(\text{SO}_4)_2 \cdot 12\text{D}_2\text{O}$ where $\text{M}^{\text{III}} = \text{Ti, Ru, V, Mo, Cr, and Fe}$. The magnetic moments were calculated from susceptibility measurements undertaken on a SQUID magnetometer at the University of Sheffield.



25×10^{-3} Gauss / Deg. This data set is discussed, appropriately, in chapter 4.

The Polarised Neutron Diffraction experiment for CsMoSD was performed at 1.8 K and 4.6 T. The magnetisation of the alum under these conditions, determined from this study, = 2.77 (BM / ion). This gives a value of 11.08 (BM / unit cell) for the $F_M(000)$ magnetic reflection.

CsMoSD is extremely unstable with respect to oxidation. Left open to air, the alum rapidly turns from pale yellow to black as molybdenum(III) is oxidised to molybdenum(V). Such oxidation would lead to a reduction in the total magnetic moment of the alum. Although every attention was paid to prevent oxidation whilst performing the experiment, the sample was not analyzed after the measurement to check that oxidation of Mo^{3+} had not taken place. On this basis alone, the experimental value is not wholly reliable and should be repeated.

The magnetic behaviour of CsFeSD, and CsVSD at low temperatures and high fields is incompatible with simple crystal field theory. The data set obtained for CsVSD seems particularly unlikely. A possible source of error that could lead to such a result would be in the weighing of the sample. These data sets should be reproduced before any inferences are to be made from these measurements. All data sets presented here were recorded on the same day using the same apparatus. The data sets recorded for CsFeSD and CsVSD suggest that the value of $F_M(000)$ obtained for the CsMoSD may be systematically in error.

The EPR spectrum of $[Mo(OH_2)_6]^{3+}$ doped into the CsInSH alum has recently been recorded at 6 K and the Spin Hamiltonian parameters reported.⁵ The quoted g values are $g_{\parallel} = 1.954$ and $g_{\perp} = 1.950$ giving $g_{eff} = 1.951$. The zero field splitting is found to be 1.15 cm^{-1} . With a field of 4.6 T, the Zeeman splitting is ca. 5 cm^{-1} . Therefore, since the zero field splitting is comparable with the Zeeman splitting, calculation of the magnetisation using the g values and the Brillouin function is incorrect. A crystal field calculation of the magnetisations undertaken by Philip Reynolds³⁴ gave an estimate of $F_M(000)$ of 11.30 (BM / unit cell) at 4.6 T and 1.8 K. Using the $F_M(000)$ value of 11.30 instead of the experimental value of 11.08 gave a slightly improved fit to all refinements although with little effect on the values of the parameters or the E.S.D's.

REFERENCES

1. G. E. Bacon, *Neutron diffraction*, Clarendon Press, 3rd edition (1975).
2. B. C. Tofield, *The study of covalency by Magnetic Neutron Scattering, Structure and Bonding*, **21**, 1 (1975).
3. P. J. Brown, *Portgal. Phys* - **13**, fasc, 1-2, p 1-22, (1982).
4. C. G. Shull, W. A. Strauser and E. O. Wollan, *Phys Rev.*, **83**, 333 (1951).
5. C. J. H Jacobsen and E. Pedersen, *Inorg. Chem.*, **30**, 4477 (1991).
6. M. Brorson and C. E. Schaffer, *Acta Chem. Scand.* A40: 358 (1985).
7. G. Holste and H. Schafer, *Z. annorg. allg. Chem.* **391**, 263 (1972).
8. J. V. Brencic and F. A. Cotton, *Inorg. Synth*, **13**, 170 (1972).
9. M. S. Lehmann, W. F. Kuhs, G. J. McIntyre, C. Wilkinson, and J. R. Allibon *J. Appl. Cryst.*, **22**, 562, (1989).
10. P. J. Brown and J. C. Mathewman, Rutherford Appleton Laboratory Report RAL-97-010 (1987).
11. M. Brorson and M. Gajhede, *Inorg. Chem.*, **26**, 2109 (1987).
12. S. P. Best and J. B. Forsyth. *J. Chem. Soc., Dalton Trans.*, 3507, (1990).
13. S. P. Best and J. B. Forsyth. *J. Chem. Soc., Dalton Trans.*, 395, (1990).
14. J. K. Beattie, S. P. Best, B. W. Skelton and A. H. White, *J. Chem. Soc., Dalton Trans.*, 2105 (1981).
15. S. P. Best, J. B. Forsyth, and P. L. W. Tregenna-Piggott, *J. Chem. Soc. Dalton Trans.*, 2711 (1993).
16. B. N. Figgis, E. S. Kucharski, G. A. Williams, *J. Chem. Soc. Dalton Trans.*, 1515 (1980).
17. B. N. Figgis, and P. A. Reynolds, *Inorg. Chem.*, **24**, 1864 (1985).
18. International Tables for Crystallography, **4**, D. Reidel Publishing company, (1985).
19. R. F. Stewart, *J. Chem. Phys.*, **58**, 1668 (1973).
20. N. K. Hansen and P. Coppens, *Acta. Cryst.*, **A34**, 909 (1978).
21. E. Clementi and C. Roetti, *Atomic Tables, Nuclear Tables*, **14**, (1974).
22. B. N. Figgis, J. B. Forsyth, and P. A. Reynolds, *Inorg. chem.*, **26**, 101 (1987).
23. Sean Howard, Department of chemistry, University of Cardiff.

24. P. J. Hay, W. R. Wadt, *J. Chem. Phys.*, **82**, 270 (1985).
W. R. Wadt, P. J. Hay, *J. Chem. Phys.*, **82**, 284 (1985).
P. J. Hay, W. R. Wadt, *J. Chem. Phys.*, **82**, 299 (1985).
25. Gaussian 90, Revision F, M. J. Frisch, M. Head-Gordon, G. W. Trucks, J. B. Foresman, H. B. Schlegel, K. Raghavachari, M. Robb, J. S. Binkley, C. Gonzalez, D. J. Defrees, D. J. Fox, R. A. Whiteside, R. Seeger, C. F. Melius, J. Baker, R. L. Martin, L. R. Kahn, J. J. P. Stewart, S. Topiol, and J. A. Pople, Gaussian Inc., Pittsburgh PA, 1990.
26. P. Coppens and E. D. Stevens, Reciprocal Space Analysis of Electron Densities, in *Electron and Magnetisation Densities in Molecules and Crystals*, NATO Advanced Study Institutes Series, Ed. P. Becker (1980).
27. R. J. Deeth, B. N. Figgis, J. B. Forsyth, E. S. Kucharski, and P. A. Reynolds, *Proc. R. Soc. Lond.*, A **421**, 153 (1989).
28. G. S. Chandler, B. N. Figgis, R. A. Phillips, P. A. Reynolds, and G. A. Williams, *Proc. R. Soc. Lond.*, A **384**, 31 (1982).
29. R. J. Deeth, B. N. Figgis, J. B. Forsyth, E. S. Kucharski, and P. A. Reynolds, *Aust. J. Chem.*, **41**, 1289 (1988).
30. C. J. O'Connor., *Magnetochemistry - Advances in Theory and Experimentation*, *Prog. Inorg. Chem.*, **29**, 203 (1982).
31. J. Crangle, *Solid State Magnetism*, Edward Arnold Press, (1991).
32. L. Brillouin, *J. Phys. et radium*, **8**, 74 (1927).
33. W. E. Henry, *Phys. Rev.*, **88**, 559 (1952).
34. Philip Reynolds, University of Western Australia, Perth, Private communication.

Electronic Structure of $[\text{Cr}(\text{OH}_2)_6]^{3+}$

6.1 Introduction

CW EPR (Continuous Wave Electron Paramagnetic Resonance) and ESEEM (Electron Spin Echo Envelope Modulation) experiments have been undertaken on $^{50}\text{Cr}(^{17}\text{OH}_2)_6^{3+}$ doped into the CsGaSH lattice in order to develop these experiments as complementary techniques to polarised neutron diffraction for determining the spin distribution within the $[\text{Cr}(\text{OH}_2)_6]^{3+}$ cation.

In order to determine directly both the magnitude and orbital occupancy of unpaired electron density on an atom using resonance techniques, the atom must possess a nuclear spin. ^{17}O is the only isotope of oxygen to possess a nuclear spin. The ^{17}O nucleus has a spin of 5/2 with an electric quadrupole moment of $-0.026 \times 10^{-24} \text{ cm}^2$.¹ The low natural abundance of the ^{17}O nucleus (0.0374%) makes it necessary to make measurements on ^{17}O enriched samples. ^{50}Cr was used because it does not possess a nuclear spin so that all observed hyperfine interactions can unambiguously be accredited with the ligand nuclei.

6.2 Synthesis of single crystals of $[\text{Cr}(\text{OH}_2)_6]^{3+}$ doped into $\text{M}^1\text{Ga}(\text{SO}_4)_2 \cdot 12\text{H}_2\text{O}$ [$\text{M}^1 = \text{Cs}$ or Rb]

The natural abundance single crystals were prepared by co-crystallisation of the chromium alum with the host alum. Chromium concentrations between 0.5 and 1% of the total trivalent hexa-aqua-cation concentration were used in the experiments. This concentration was chosen since for the cw EPR experiments, this was found to be the optimum concentration for detection and line width.

Crystals containing isotopically pure ^{50}Cr surrounded by water molecules enriched in ^{17}O were prepared by recrystallisation of $[\text{Cs}(\text{OH}_2)_6]^{+} [^{50}\text{Cr}(^{17}\text{OH}_2)_6]^{3+} (\text{SO}_4)_2$ in triflic acid (1 mol dm^{-3}) with a solution of the host alum in sulphuric acid (1 mol dm^{-3}). $\text{Cs}^{50}\text{CrSH}$ (2 mg) was dissolved in $20 \times 10^{-2} \text{ cm}^3$ of ^{17}O enriched water (62.5

% atom) which was 1 mol dm^{-3} in triflic acid. The solution was sealed in a 2 mm diameter bore capillary. The length of the capillary was approximately 3 times that of the length of the solution. The capillary was subsequently immersed in a beaker of water and heated on a steam bath at 80°C for 72 hours to allow the equilibration of ^{17}O enriched H_2O with the inner co-ordination sphere of the chromium(III) hexa-aqua-cation. The length and bore of the capillary were chosen to ensure that the capillary could be sealed without loss of solution to evaporation in the process of sealing, and also to ensure that when heating to 80°C as little as possible of the solution went into the vapour phase. It was found in preliminary experiments, that if the volume of the capillary was too large then the effective increase in sulphate concentration of the solution, on heating the contents to 80°C , ultimately lead to sulphate anions displacing water molecules from the first co-ordination sphere. It is for this reason the non co-ordinating acid triflic acid was used, rather than sulphuric acid. After heating on a steam bath, the contents of the capillary were added to a solution of the host alum. The doped alum crystallised on cooling.

6.3 Techniques employed for the execution of Single Crystal E.P.R experiments

The samples crystallise as thick plates with predominant (111) type faces. Samples were mounted on a quartz rod and placed in a quartz tube. The crystal morphology greatly aided alignment of the sample with respect to the magnetic field direction. The cw EPR spectra were collected at Bristol university using a Bruker-ESP300E EPR spectrometer. An automatic 2 circle goniometer was used for these measurements. Using this facility, the spectrometer could be programmed to collect spectra at regular intervals of the desired increment accurate to $1/6$ th of a degree. The ESEEM spectra were collected on a Bruker spectrometer at University College London, the crystals were mounted the same way.

6.4 CW EPR

A free electron has a magnetic moment \mathbf{m} which interacts with the magnetic field \mathbf{B} such that the energies of the electron along the field direction (z axis) are restricted to the eigenvalues of the operator $-\mathbf{m}\cdot\mathbf{B} = -g_e\beta B s_z$ where g_e , the Landé g-factor, is equal to 2.0023 for a free electron, s_z is the component of spin down the z axis and β is the Bohr magneton. The corresponding energies are $-g_e\beta B m_s$ with $m_s = +1/2$ or $-1/2$. If the system is irradiated and the magnetic field varied, there will come a point where the resonance condition is reached such that:

$$h\nu = E(1/2) - E(-1/2) = g_e\beta B \quad 6.4.1$$

when a resonant absorption is observed. In commercial EPR spectrometers, frequencies of *ca.* 9.5 GHz (X-band) are frequently used and the magnetic field swept over a wide field range; resonance usually occurring in the range of 500 - 6000 Gauss.

Spin Hamiltonian and the g factor

The true hamiltonian for a paramagnetic substance contains terms other than the effect of the magnetic field on the electron spin:

e.g
$$H = -g_e\beta s\cdot B - \beta l\cdot B + \dots \quad 6.4.2$$

The first term is the operator representing the effect of the magnetic field on the electron spin and the second term represents the interaction of the applied field with the orbital angular momentum (operators representing other terms such as spin-orbit interaction, hyperfine coupling, nuclear Zeeman interaction etc have been omitted at this stage for clarity).

The spin Hamiltonian is an effective Hamiltonian in which the effect of the orbital operators have been absorbed into various parameters. Any orbital angular momentum that the electron may have is absorbed into the g parameter, so that 6.4.2 becomes:

$$H_{\text{spin}} = -\beta s \cdot g \cdot B \quad 6.4.3$$

For one electron systems, the spin quantum number is represented by $m_s = \pm 1/2$. Cr^{3+} has 3 unpaired electrons. For Cr^{3+} the spins of the 3 unpaired electrons couple together to give an effective spin quantum number $M_s = 3/2$.

Within the alum lattice, the Cr^{3+} cations lie on sites of trigonal symmetry. As a consequence of both the trigonal field and spin orbit coupling, the degeneracy of the M_s states are already broken before the application of the external magnetic field.² If $h\nu$ is much greater than the magnitude of the zero field splitting (ZFS), the system can still be described as spin 3/2 with the effect of the ZFS treated as a perturbation. On the other hand, when the microwave energy is small compared to the ZFS, then each doublet must be considered as having its own spin of 1/2. The principal values of the ZFS for Cr^{3+} doped into the CsGaSH are -731.7 and $-670.1 \cdot 10^{-4} \text{ cm}^{-1}$ at 300 and 4.2 K respectively.³ For measurements at X-band ($h\nu = 0.3 \text{ cm}^{-1}$) these values approach the case where $h\nu \gg \text{ZFS}$. The Cr^{3+} cation can be orientated with respect to the magnetic field in such a way that the ZFS is a maximum, this axis of the molecule is denoted the z axis. When the molecule is orientated with the z axis perpendicular to the field in the xy plane, then the ZFS is a minimum. The principal value of the ZFS is denoted D and is determined when the z axis of the paramagnet is orientated along the field; the ZFS spin Hamiltonian in this orientation has the form:⁴

$$H_{\text{spin}} = g_1 \beta \hat{S}_z H_z + D[\hat{S}_z^2 - 1/3 S(S + 1)]. \quad 6.4.4$$

where S is the effective spin and S_z is the component of S down the z axis.

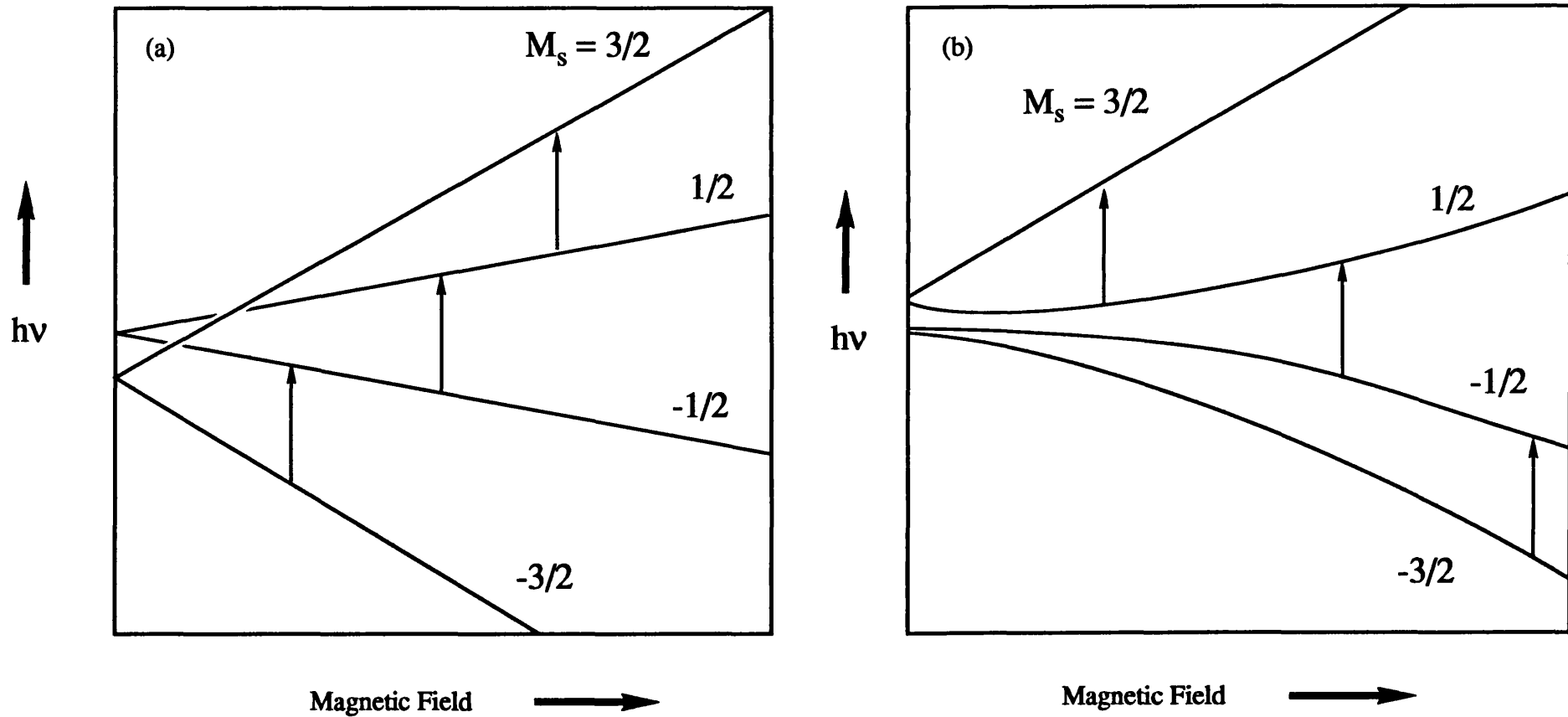
Figure 6.4.1 shows energy level diagrams for Cr^{3+} in an axial field.

The selection rules are $\Delta M_s = \pm 1$ so that 3 magnetic dipole allowed transitions are observed at any orientation. With the z axis of the paramagnet orientated along the field and in the limit where $h\nu \gg |D|$, then the central resonance corresponds to g_1 and the two other resonances are split symmetrically around this position by a separation equal to $2D/g_1\beta$.⁴

The complete spin Hamiltonian describing the ground term energies of the $[\text{}^{50}\text{Cr}(\text{}^{17}\text{OH}_2)_6]^{3+}$ paramagnet within the alum lattice is given by:

FIGURE 6.4.1

Energy level diagram of Cr^{3+} doped into the CsGaSH lattice showing magnetic dipole allowed transitions within the ${}^4A_{2g}$ manifold. (a) The direction of the external magnetic field is parallel to the principal ZFS direction, (b) the direction of the external magnetic field is perpendicular to the principal ZFS direction.



$$\begin{aligned}
H_{\text{Spin}} = & \\
& -\beta\mathbf{S}\cdot\mathbf{g}\cdot\mathbf{B} + \mathbf{S}\cdot\mathbf{D}\cdot\mathbf{S} + \\
& [\mathbf{S}\cdot\mathbf{A}\cdot\mathbf{I}]_{17\text{O}} + [\mathbf{L}\cdot\mathbf{Q}\cdot\mathbf{I}]_{17\text{O}} + [g_n\beta_n\mathbf{B}\cdot\mathbf{I}]_{17\text{O}} + \\
& [\mathbf{S}\cdot\mathbf{A}\cdot\mathbf{I}]_{1\text{H}} + [g_n\beta_n\mathbf{B}\cdot\mathbf{I}]_{1\text{H}}
\end{aligned} \tag{6.5.5}$$

The first term represents the electron Zeeman interaction and the second term represents the zero field splitting. The remaining terms arise as a consequence of the spins of the ^{17}O and ^1H nuclei. \mathbf{A} is the hyperfine coupling tensor, \mathbf{Q} is the quadrupole tensor and \mathbf{I} the nuclear spin operator. For completeness the nuclear Zeeman terms have been included although they do not affect the transition energies.

Aims of CW EPR study

In order to determine the spatial spin distribution, the orientation of the $[\text{}^{50}\text{Cr}(\text{}^{17}\text{OH}_2)_6]^{3+}$ cation with respect to the magnetic field must be known. This requires an understanding of the cw EPR spectra and the assignment of the Zeeman transitions to a given $[\text{}^{50}\text{Cr}(\text{}^{17}\text{OH}_2)_6]^{3+}$ cation at differing orientations to the external magnetic field direction. The cw spectra of these systems have been recorded and assigned previously.^{3,5} The g values and the ZFS parameter D , were determined in this study.

CW spectra of $[\text{}^{50}\text{Cr}(\text{}^{17}\text{OH}_2)_6]^{3+}$ doped into the CsGaSH alum were collected prior to the collection of the ESEEM spectra. Two complete sets of spectra with different crystal alignments, were recorded at 6° increments through 180° rotations. With the aid of simulations,⁶ the orientations of the four $[\text{}^{50}\text{Cr}(\text{}^{17}\text{OH}_2)_6]^{3+}$ cations that are within the unit cell could be determined with respect to the magnetic field direction. This provided the information necessary for the design of the ESEEM experiments.

Interpretation of cw ESR spectra

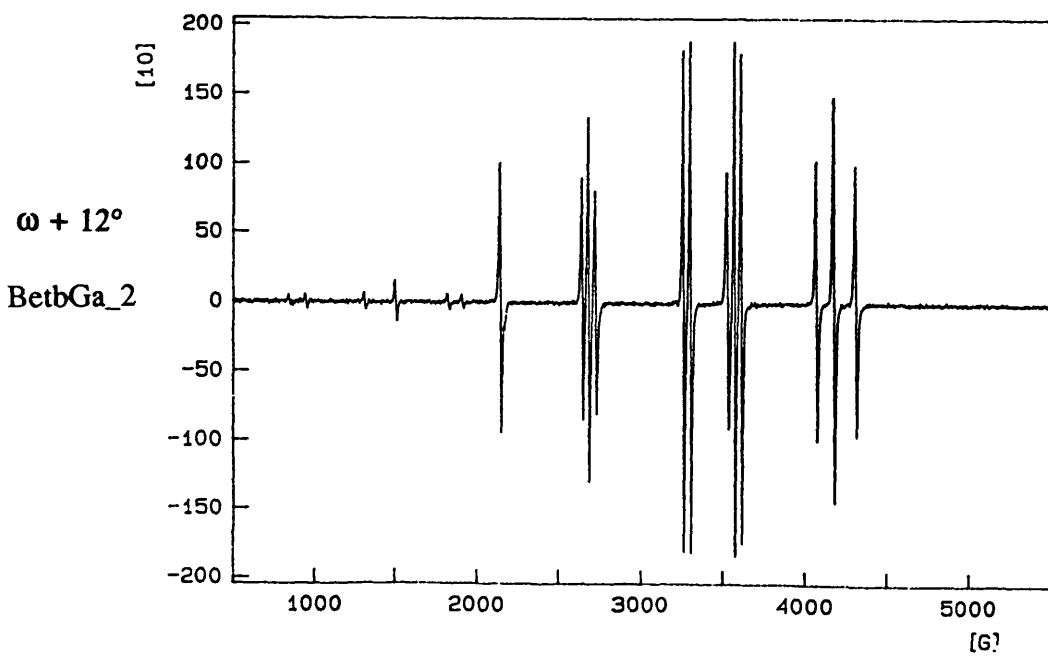
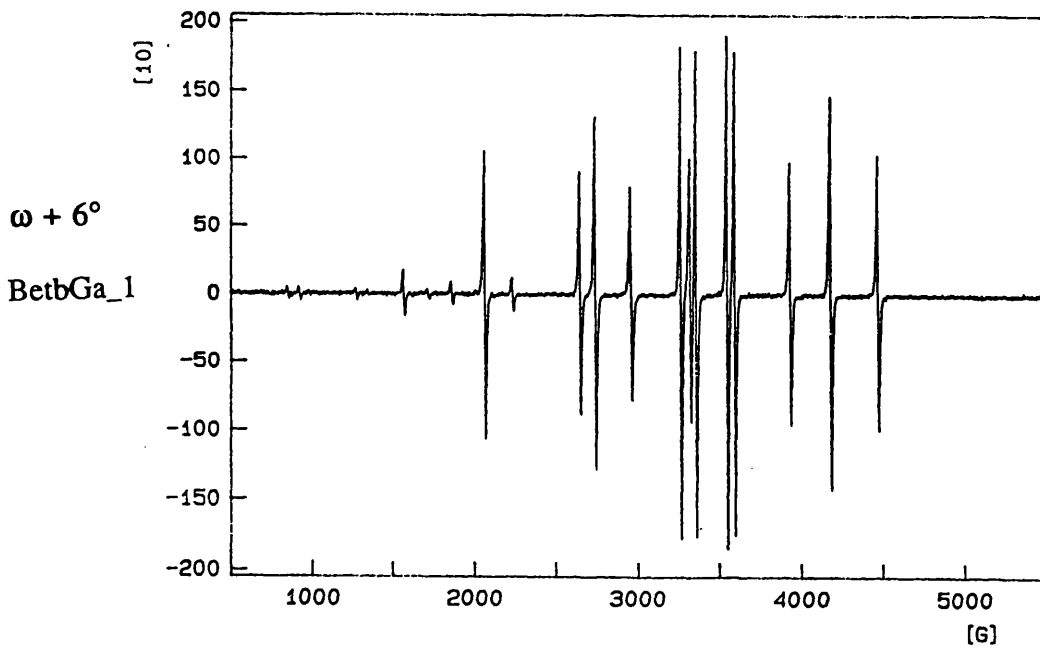
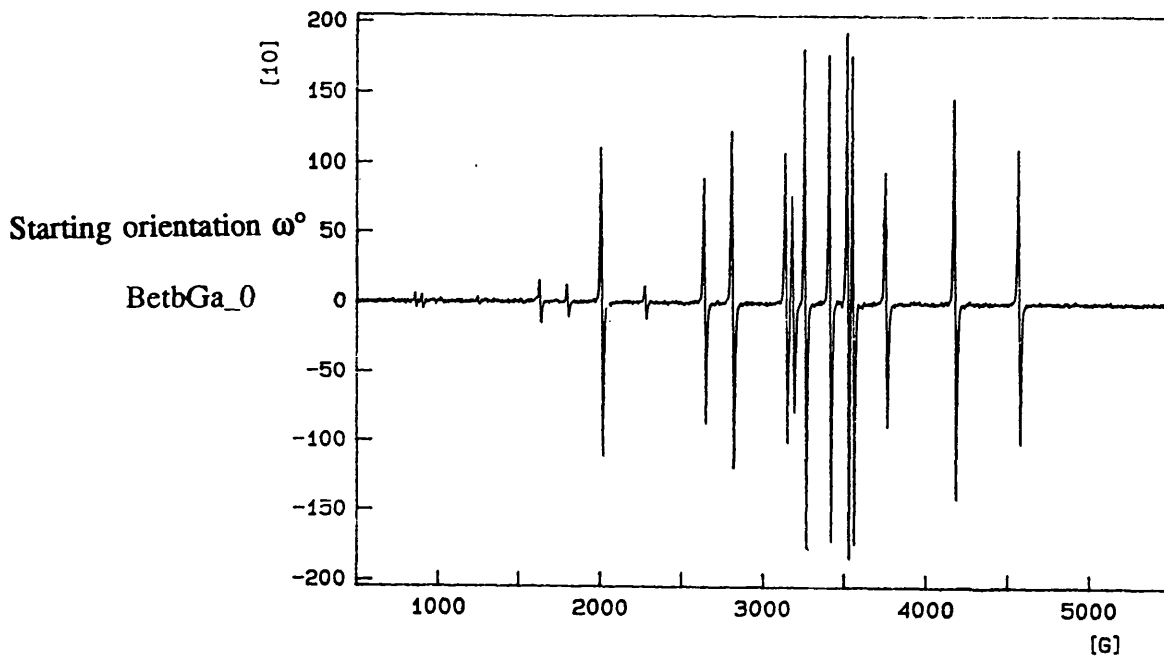
The hexa-aqua-cations are positioned within the CsGaSH unit cell such that each metal-oxygen bond lies close to the crystallographic axes (0.52°); all metal-oxygen bonds are equivalent by symmetry, the oxygen-metal-oxygen bond angle is 90.6° .⁷ There are 4 molecular units per unit cell with the trivalent cation occupying sites of S_6 symmetry. The oxygen and hydrogen atoms, however, occupy general positions of C_1 symmetry. Relative to one of the four hexa-aqua-cations within the unit cell, the other three are generated first by a translation then a reflection in the crystallographic axes. For the S_6 point group, the highest axis of rotation is the C_3 axis of which there is only one. The principal axes of the four trivalent cations within the unit cell are coincident with the crystallographic 3-fold axes of the cubic unit cell.

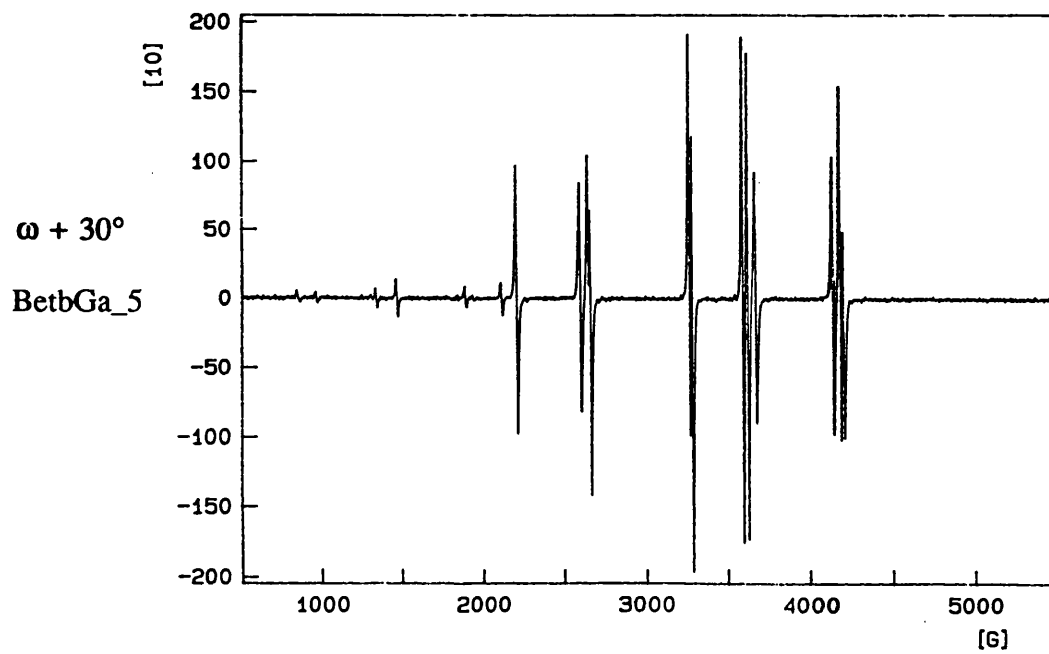
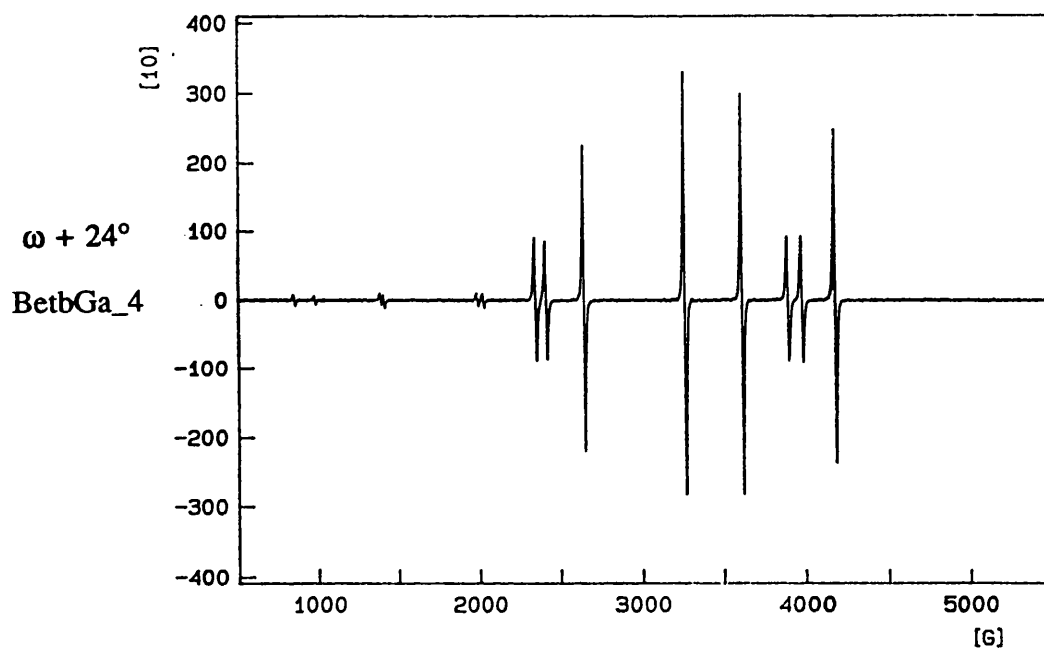
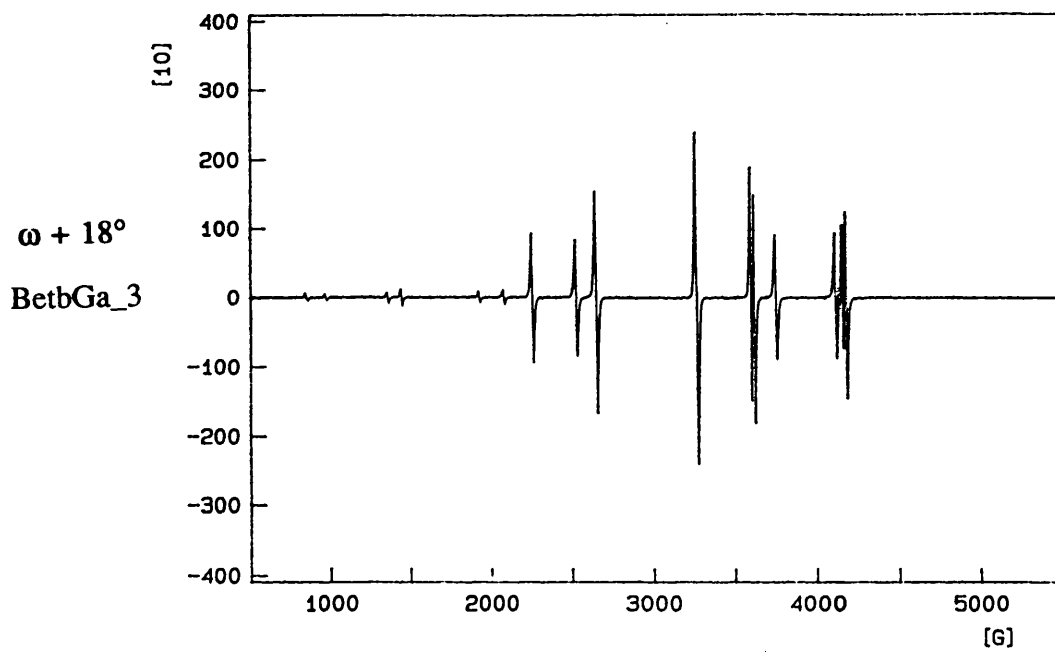
A selection of the set of spectra labelled $BetbGa_$ are shown in figure 6.4.2. The crystal orientation was such that a crystallographic 3-fold axis was normal to the direction of the field, this being the axis of rotation. Spectra were collected at 6° incrementations.

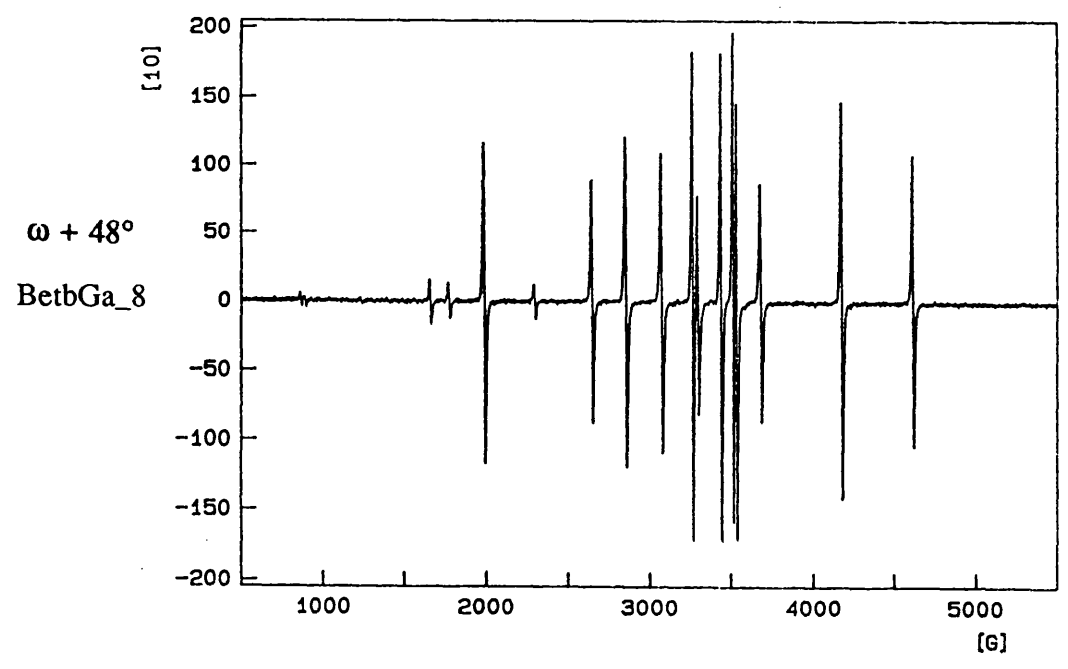
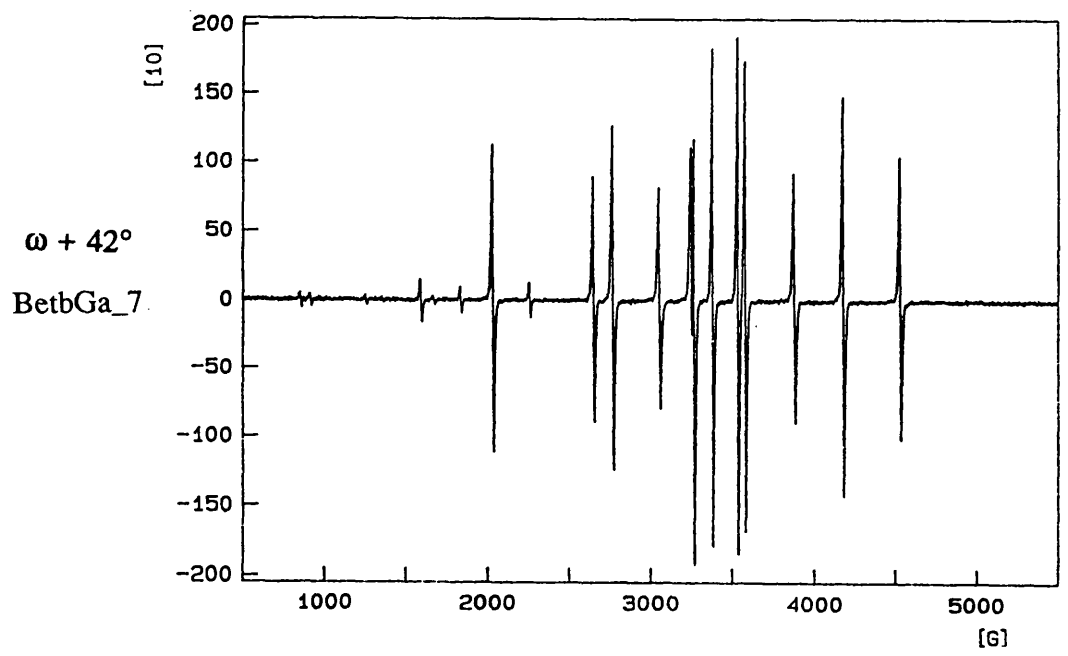
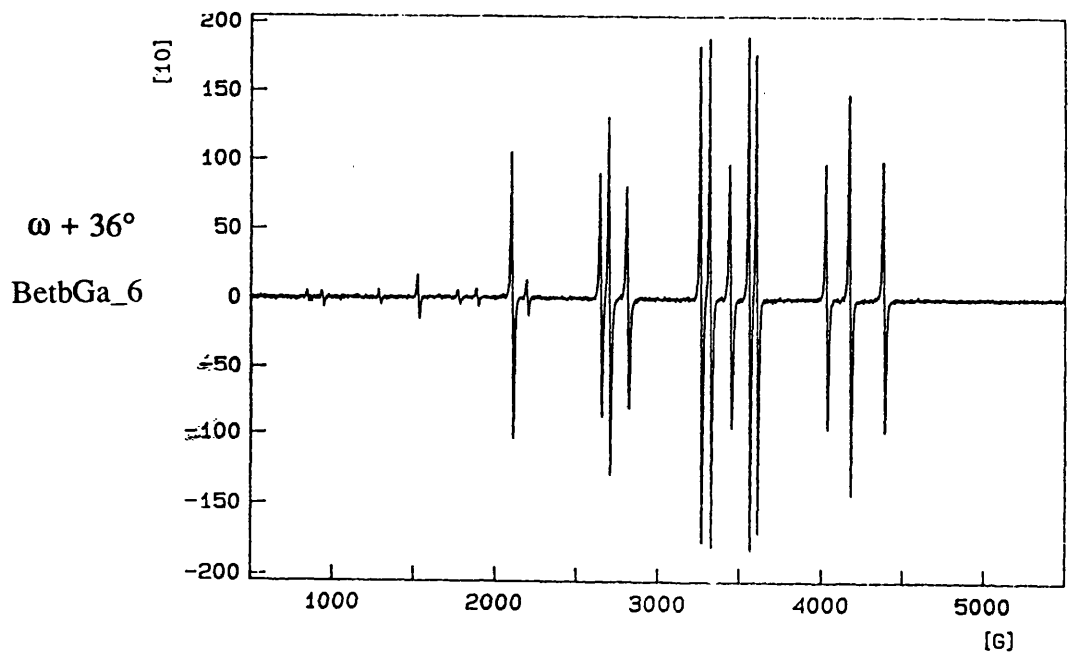
Three intense lines are found in all the spectra which do not vary in intensity and position. They occur at *ca.* 2650 G, 3280 G, and 4190 G. These transitions are assigned as the $1/2 \leftrightarrow 3/2$, $-1/2 \leftrightarrow 1/2$, $-3/2 \leftrightarrow -1/2$ ΔM_S transitions for the $[Cr(OH_2)_6]^{3+}$ cation within the unit cell whose principal axis is aligned with the axis of rotation. The principal ZFS direction of the $[Cr(OH_2)_6]^{3+}$ cation is therefore directed along a crystallographic three fold axis in accordance with previous studies.^{3,5} From the symmetry of the unit cell, another 3 equivalent ZFS directions lie along the 3 remaining three-fold axes of the unit cell. The angle that the three-fold axes make to one another is 70.5° . Figure 6.4.3 shows the orientation, with respect to the magnetic field direction, of the 4 principal ZFS directions, for this crystal alignment. The cosine of the angle which any of the four principal ZFS directions make with the field direction, is given by the product $\cos\theta\cos\phi$. θ is the angle that the principal ZFS directions make with the plane which is normal to the axis of rotation, denoted plane 'A'. For direction '4' in figure 6.4.3 this angle = 90° ; for directions '1', '2', and '3' this angle is necessarily 19.5° . ϕ is the angle that the projection of the ZFS directions in plane 'A' make with the field direction. These angles are shown for direction '2'

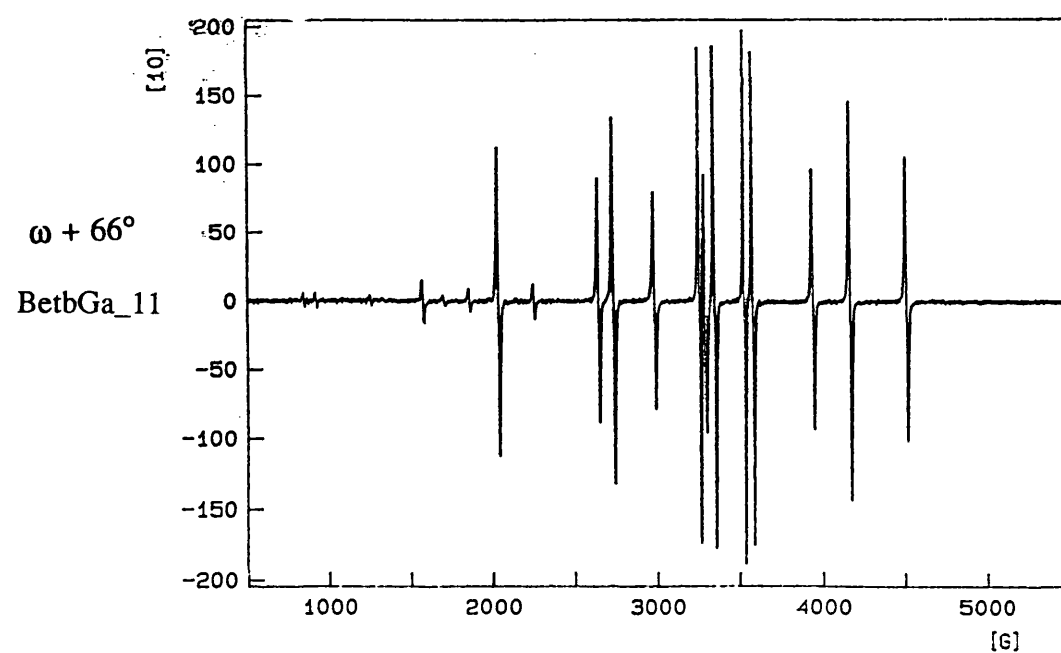
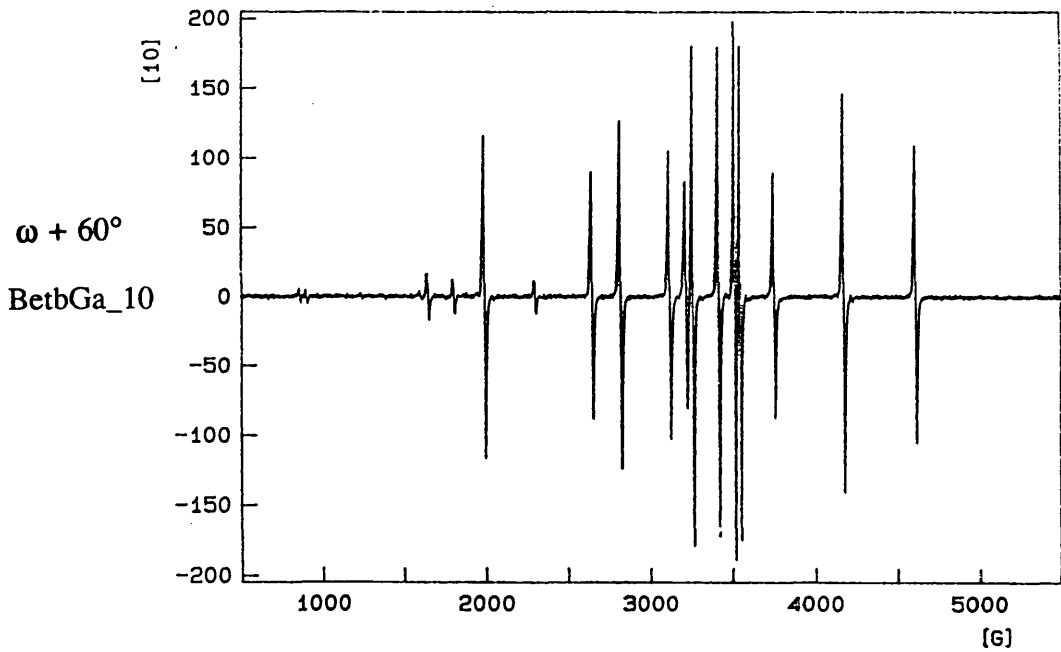
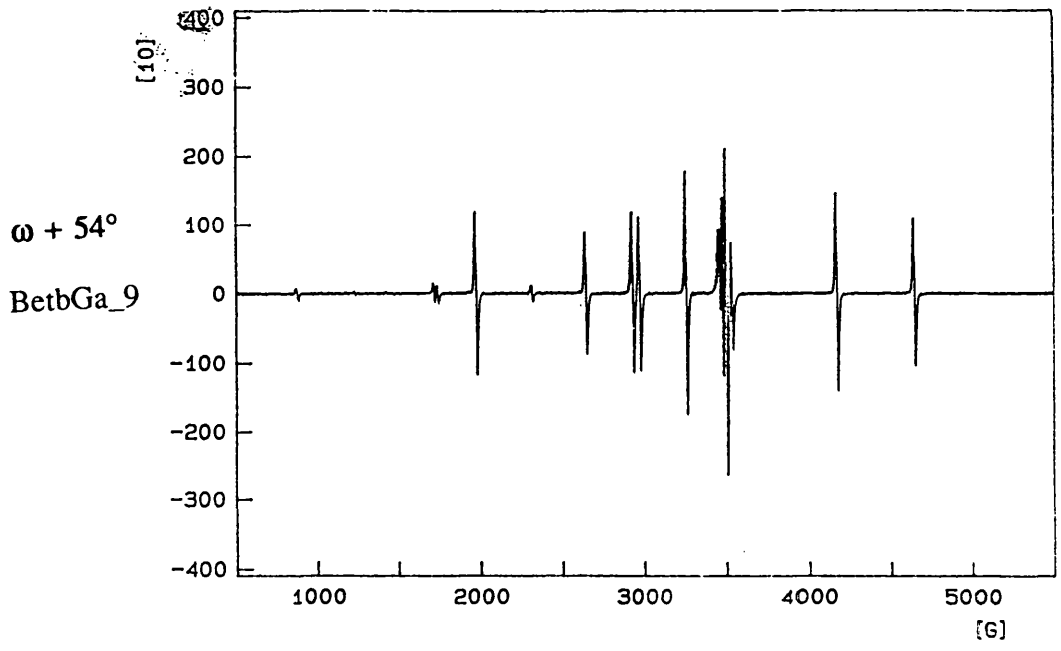
Figure 6.4.2

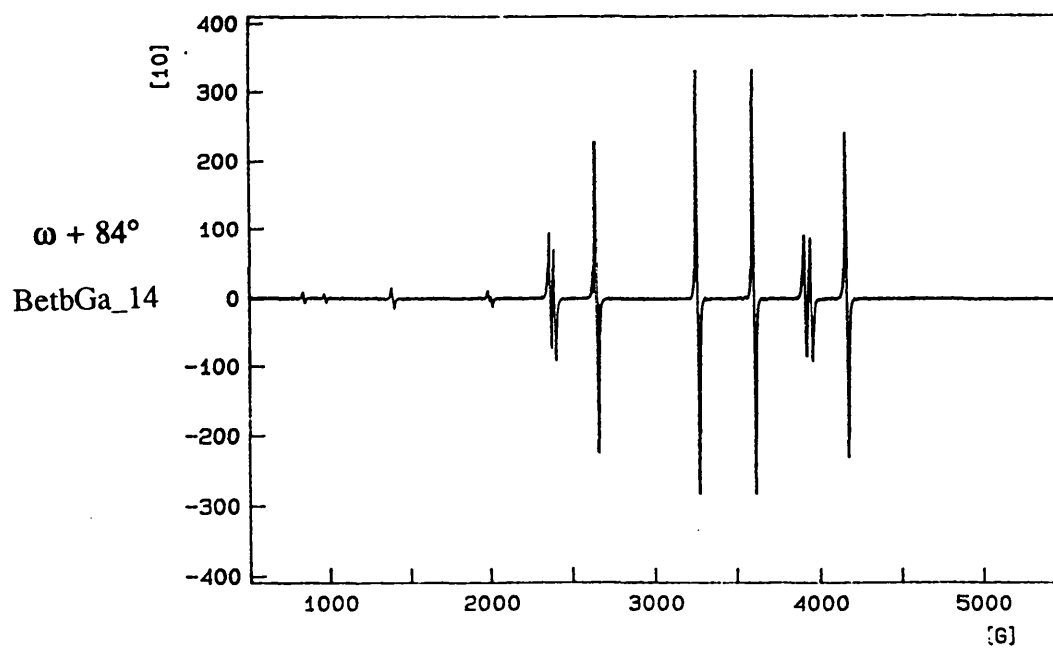
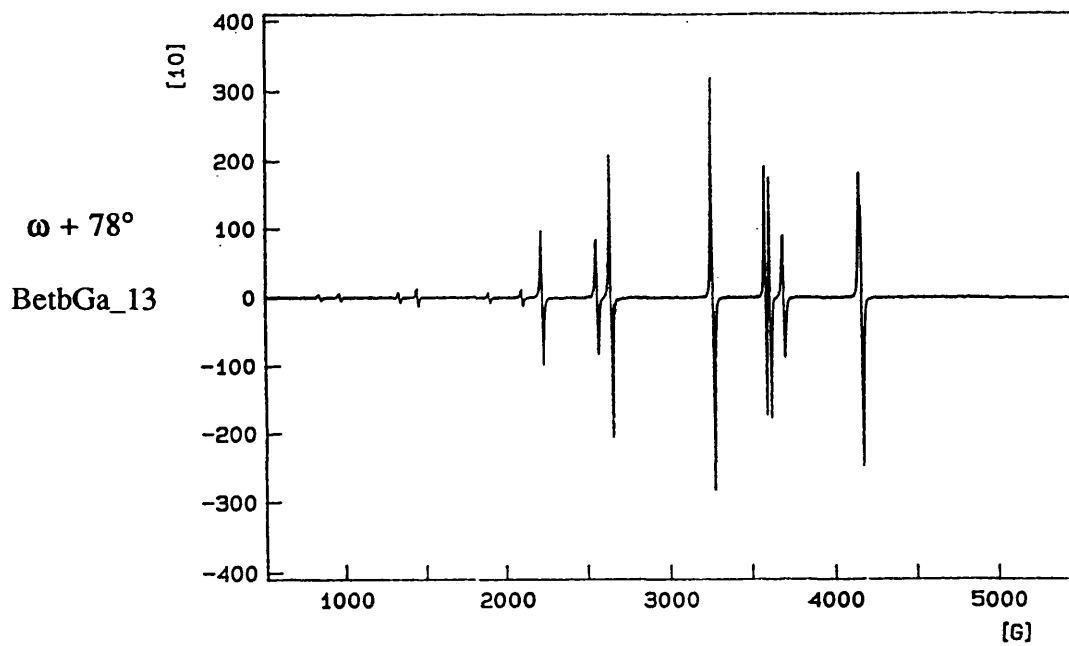
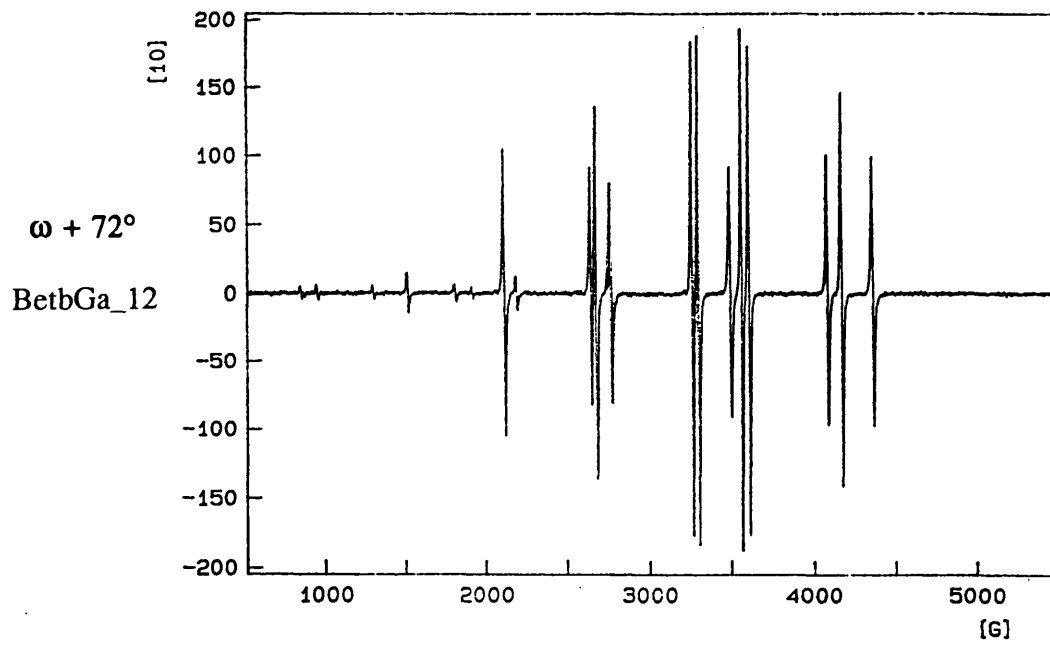
Oriented Single Crystal cw-EPR Spectra of $[^{50}\text{Cr}(^{17}\text{OH}_2)_6]^{3+}$ doped into $\text{CsGa}(\text{SO}_4)_2 \cdot 12\text{H}_2\text{O}$ alum. BetbGa data set. Three fold axes aligned normal to the field. Crystal rotated about this axis in 6° incrementations.

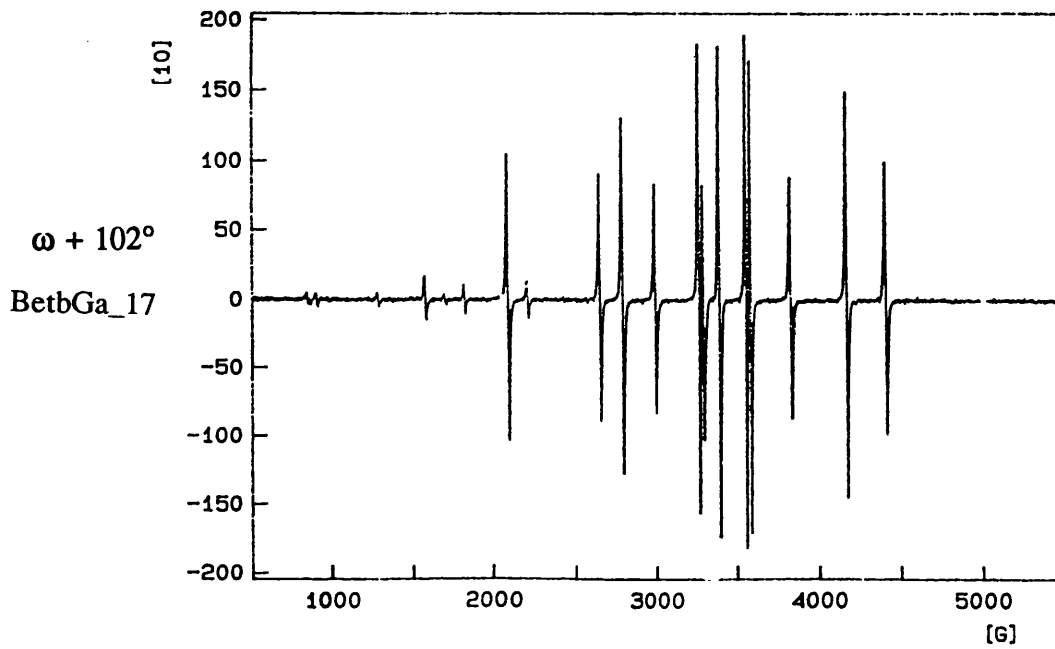
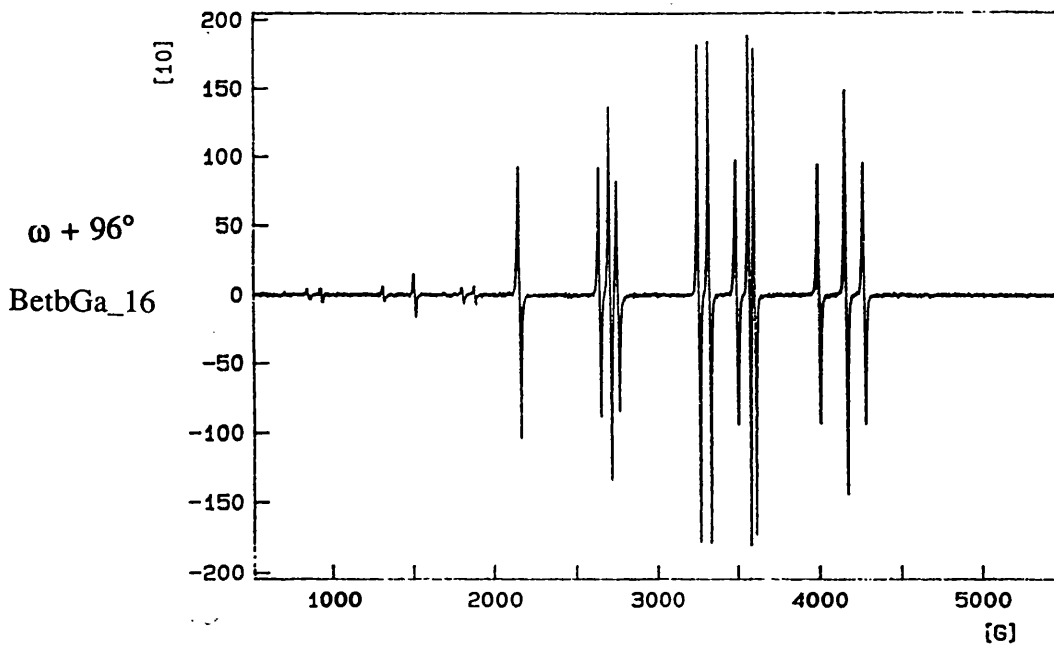
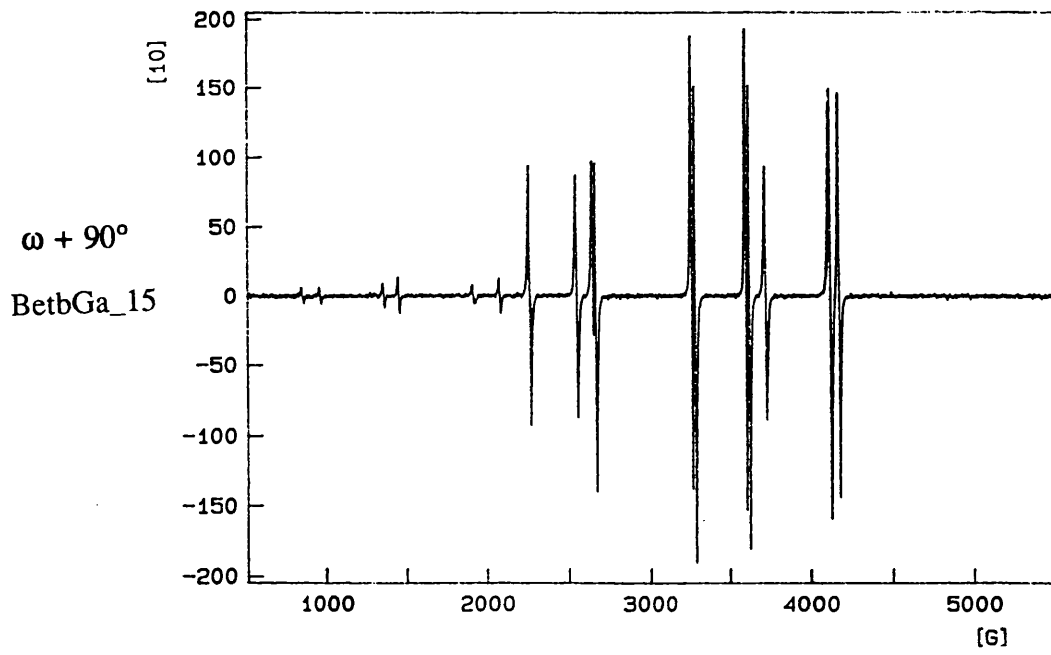


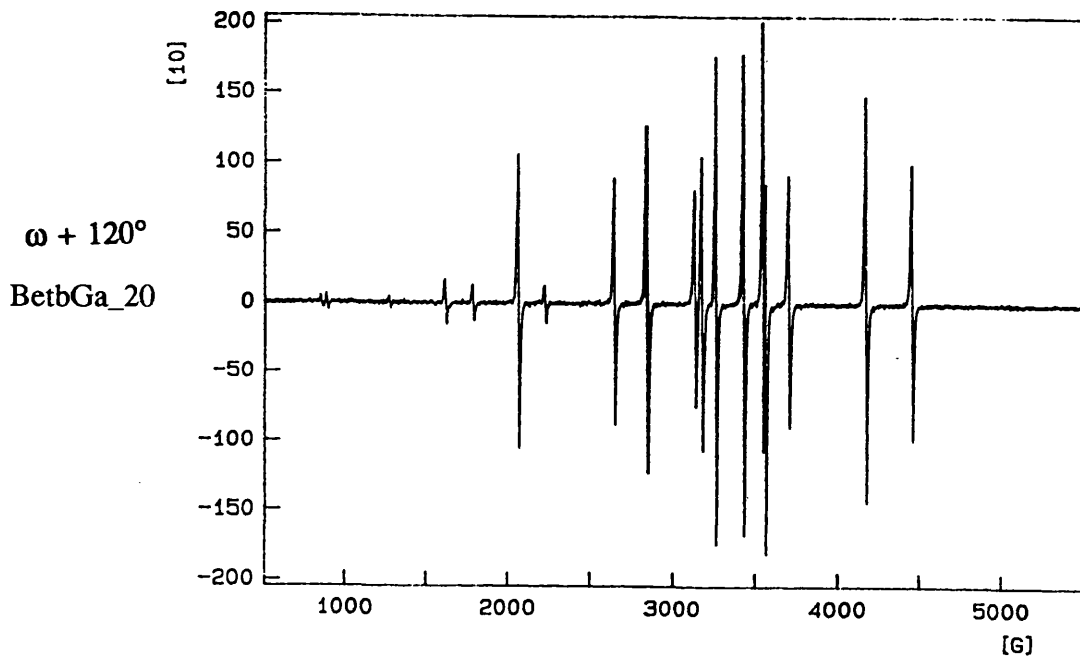
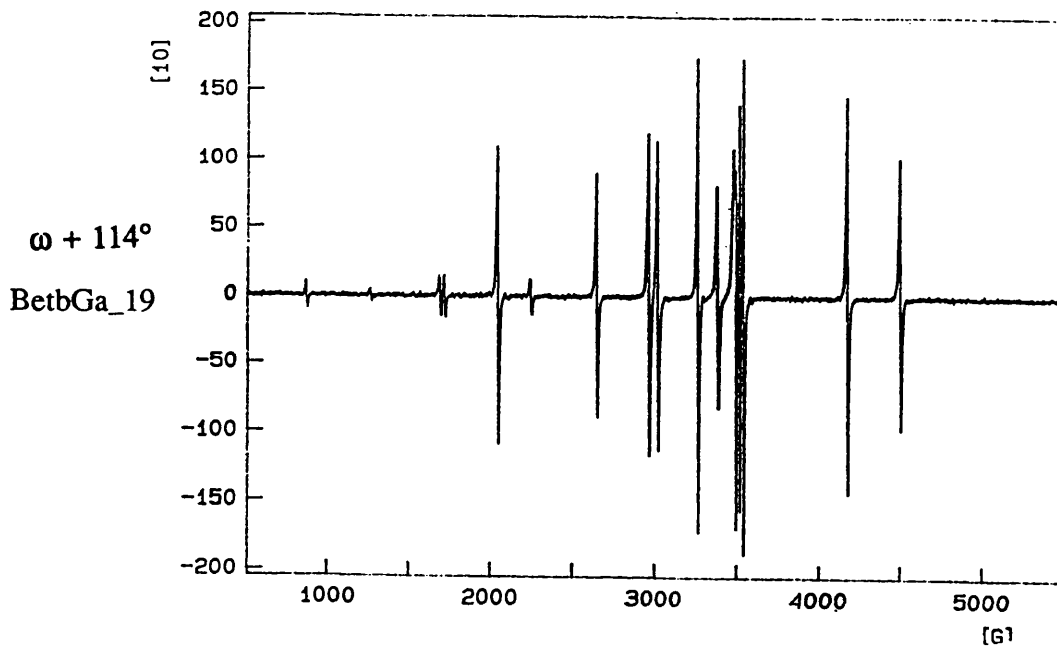
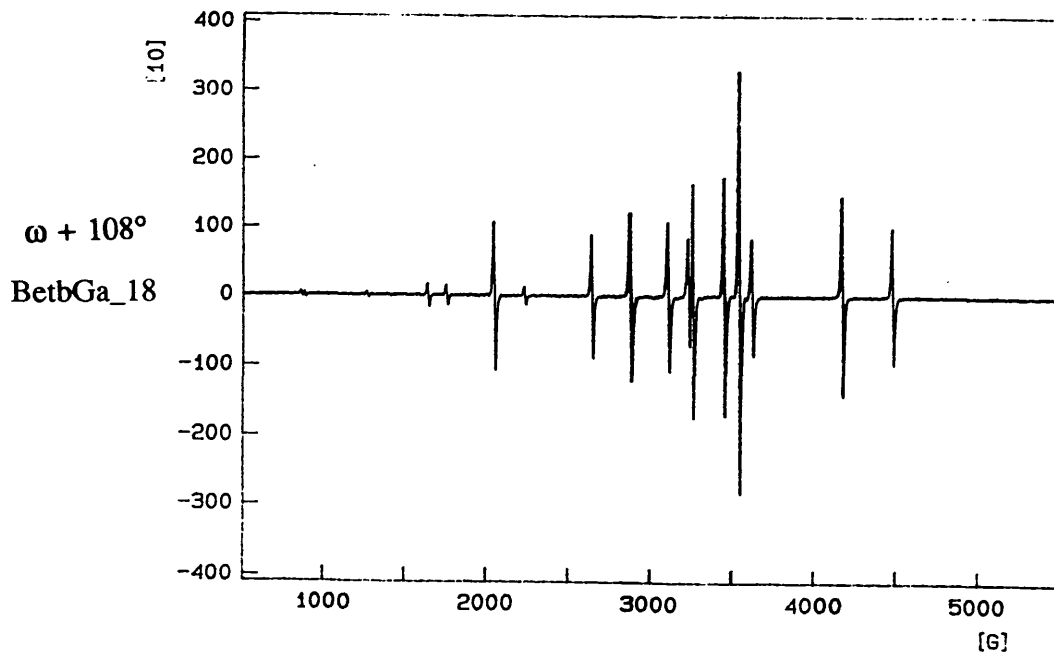


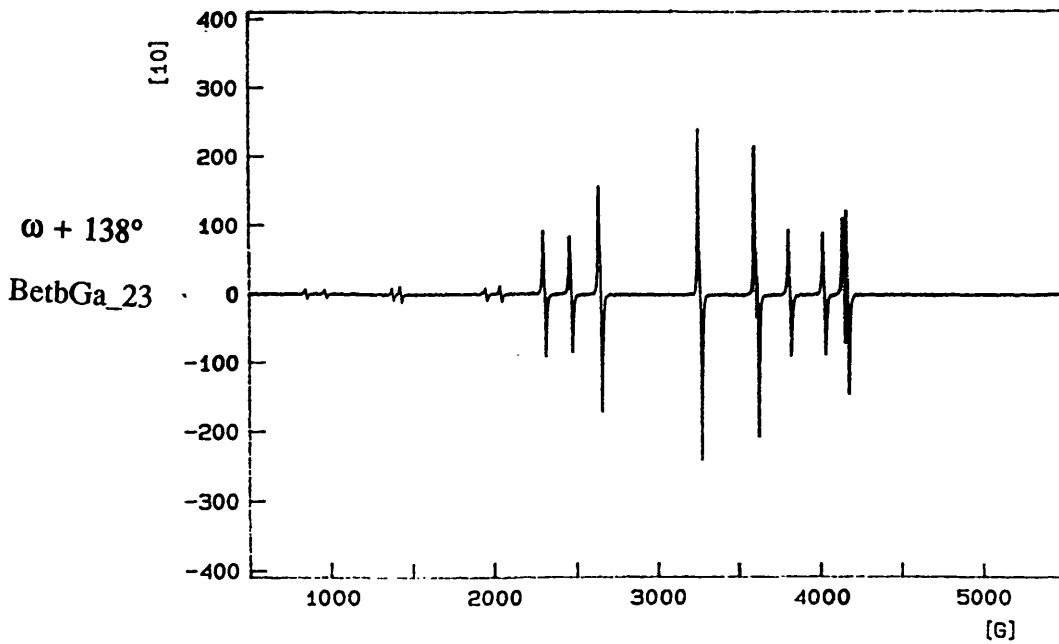
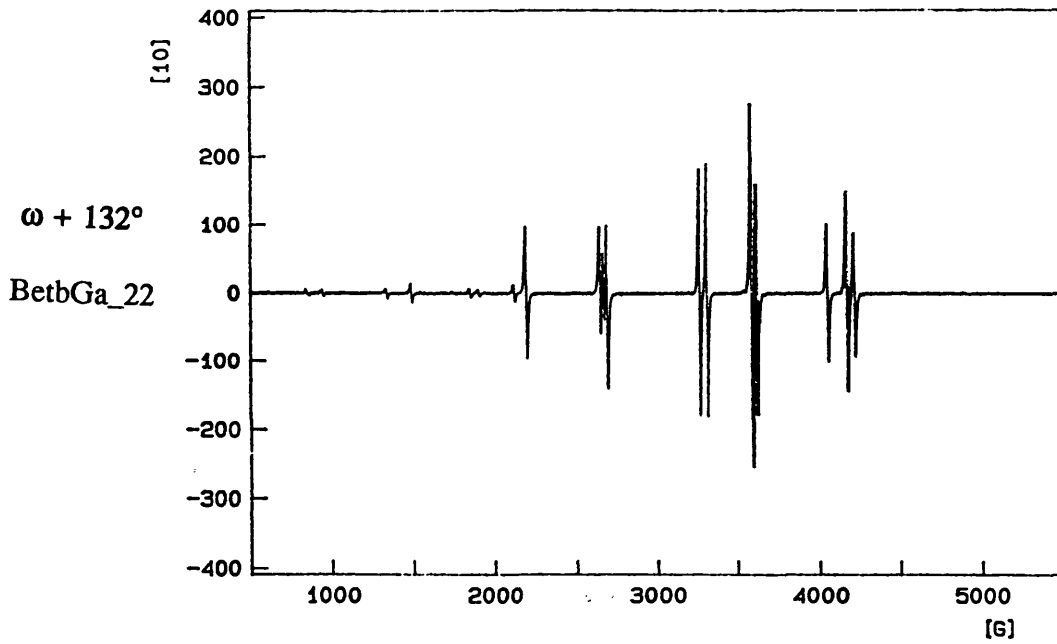
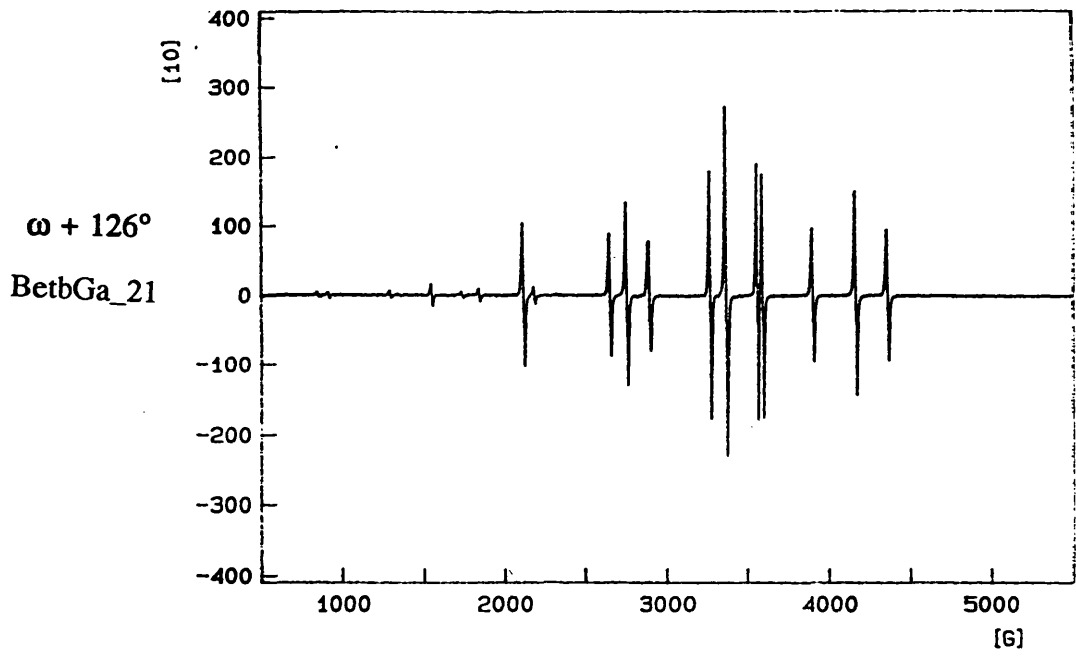


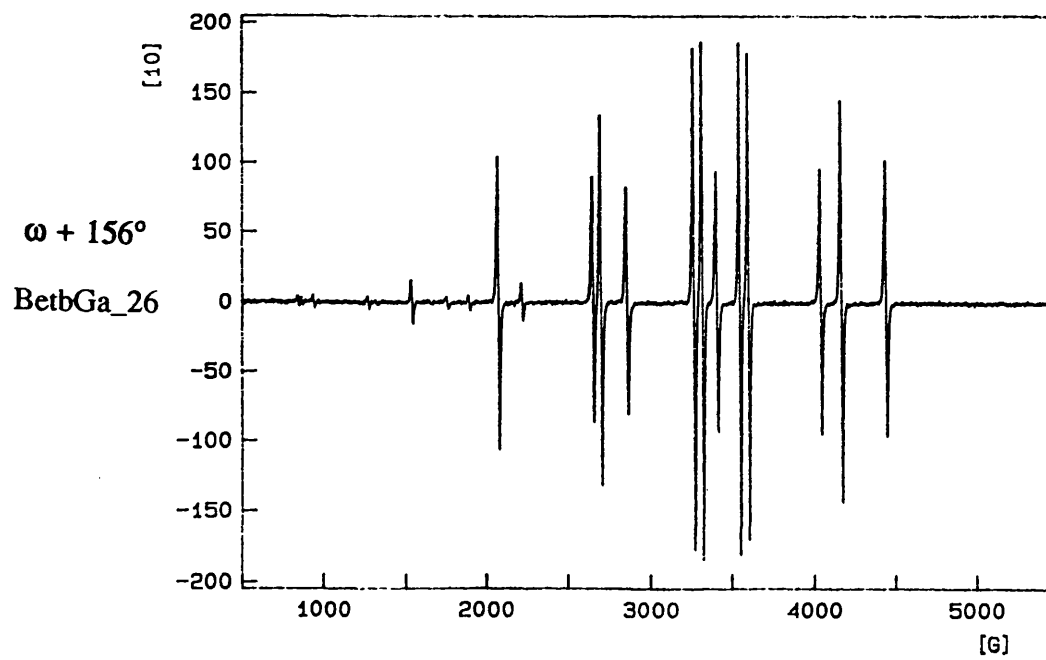
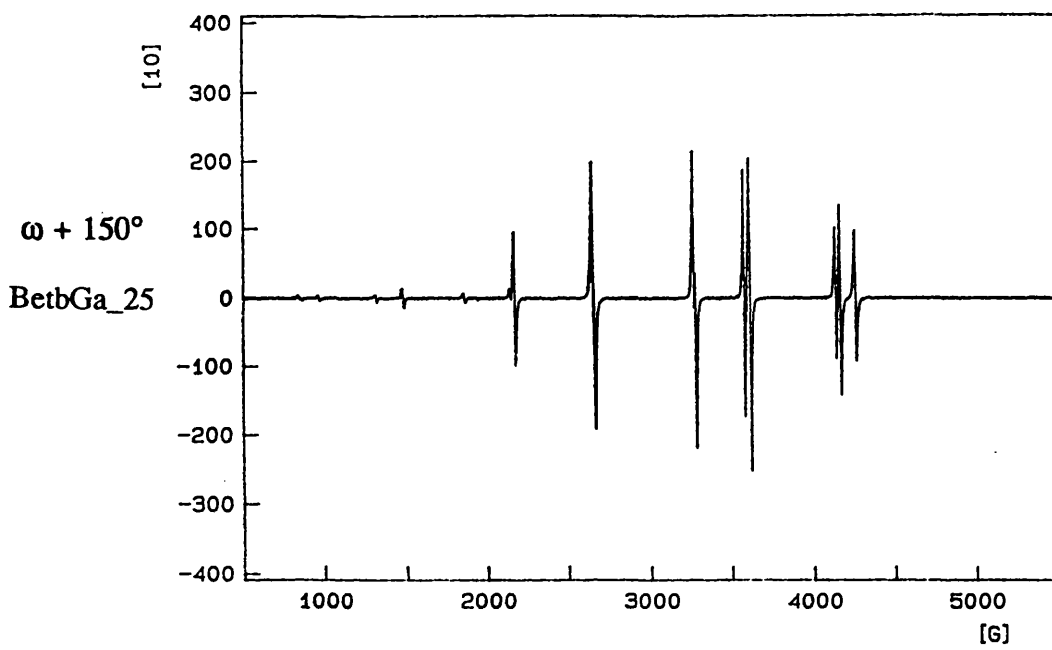
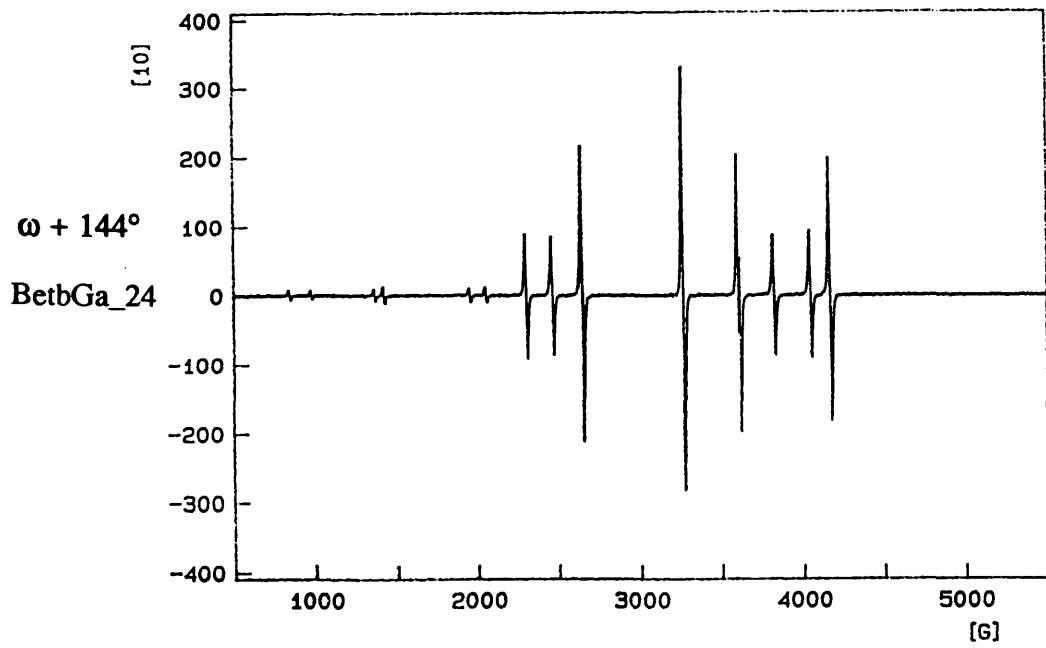


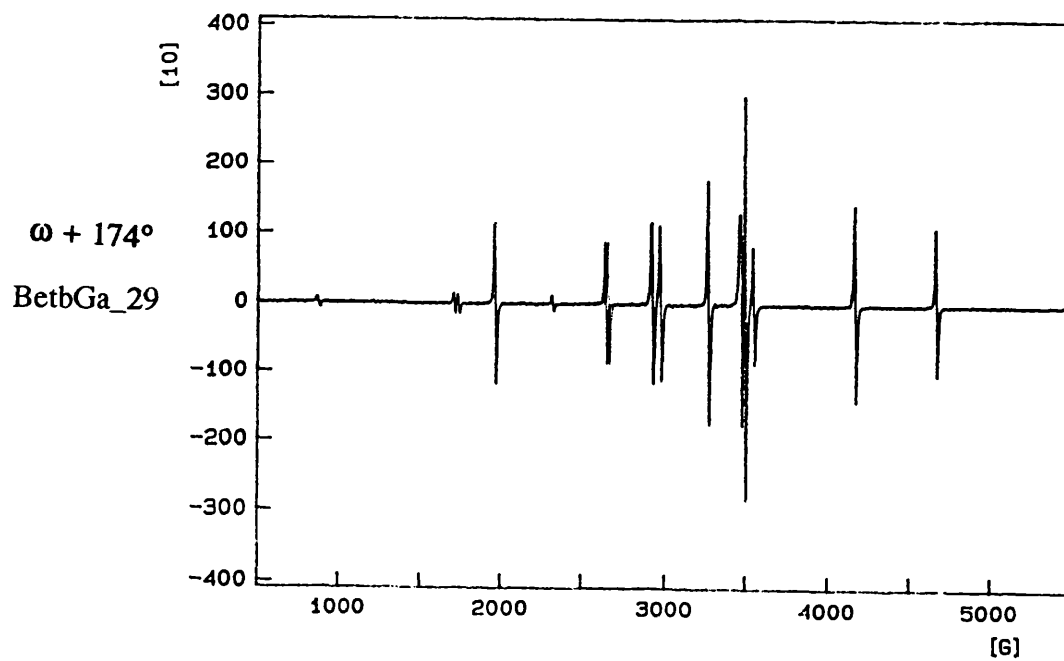
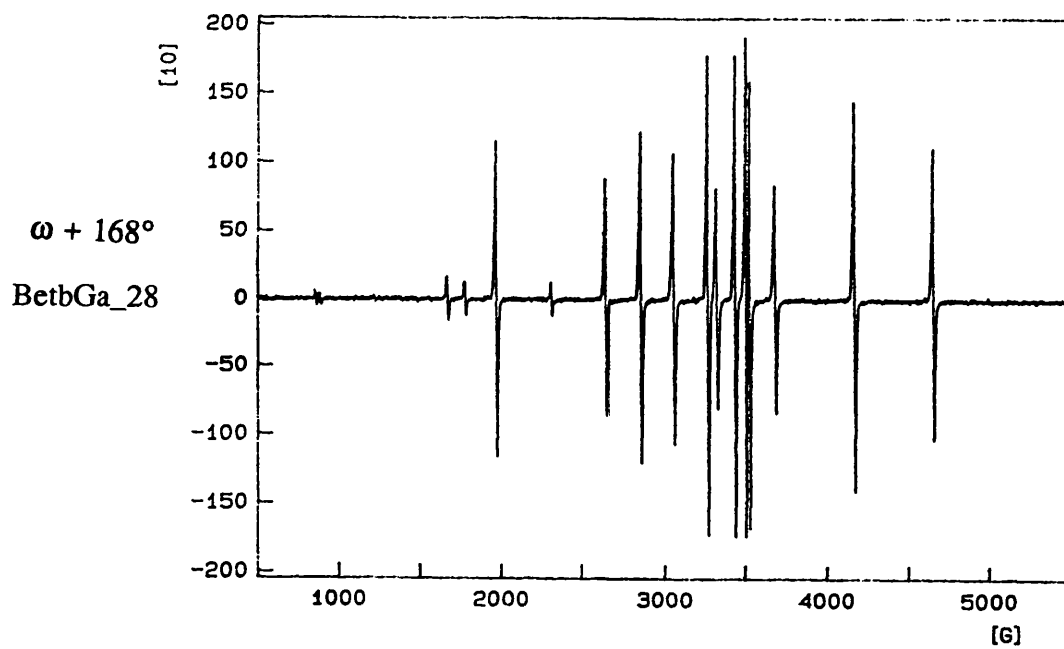
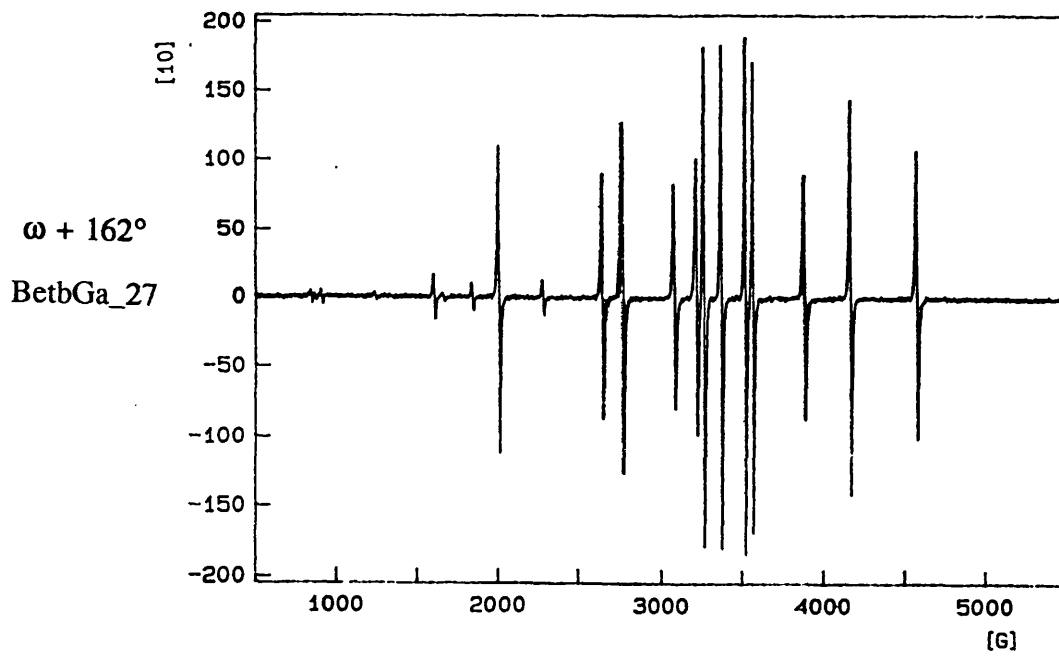












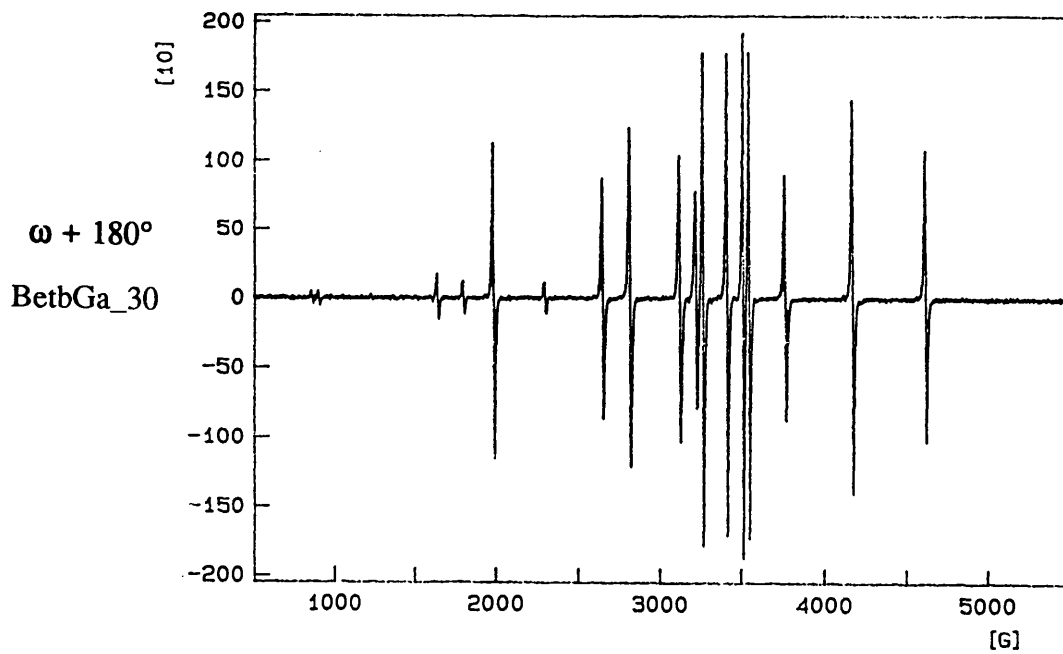
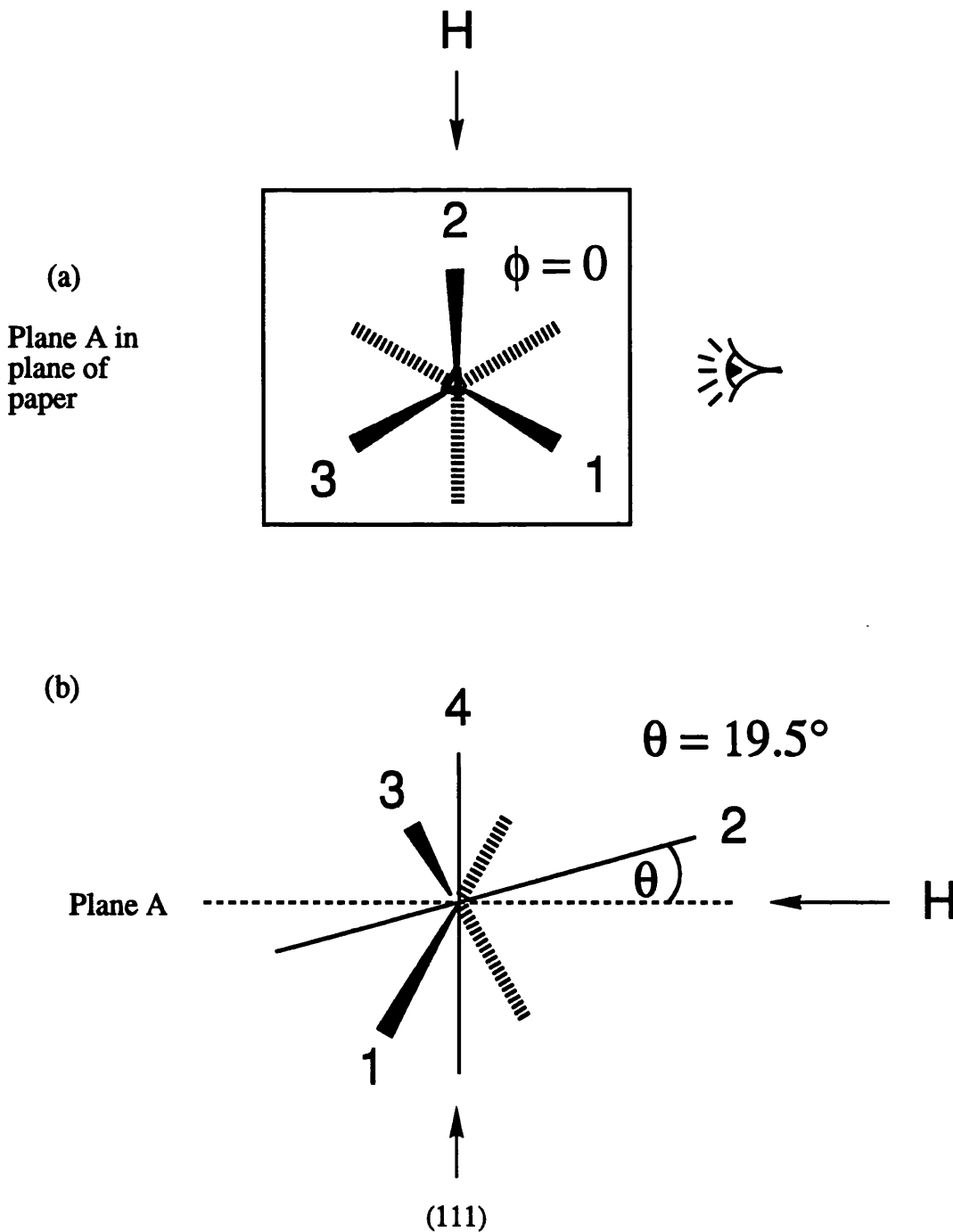


FIGURE 6.4.3

Orientation of the principal ZFS directions, with respect to the external magnetic field, for the 4 paramagnets within the unit cell.

The principal ZFS direction associated with paramagnet 4, lies along the (111) direction which is the axis of rotation for the Be_2Ga_3 data set. The cosine of the angle that each principal ZFS direction makes with the field direction is given by the product $\cos\phi\cos\theta$. Angles ϕ and θ are shown for the principal ZFS direction of paramagnet 2.



in figure 6.4.3. Looking down the axis of rotation as in 6.4.3 (a), the three principal ZFS directions make an angle of 120° to one another when projected into plane A.

From the starting orientation ω the first spectrum in which the lines are seen to converge is BetaGa_4 which is at angle $\{\omega + 24\}^\circ$. Lines converge towards the positions which correspond to a paramagnet having its principle ZFS value normal to the field. This pattern is repeated every 60° . This corresponds to positions shown in figures 6.4.4 (a); 6.4.4 (b); 6.4.4 (c). The principal direction of the D tensors are shown as projections in plane A. 30° on, at angle $\{\omega + 54\}^\circ$, the lines are again seen to converge. This spectrum corresponds to the orientations illustrated in figures, 6.4.5 (a), 6.4.5 (b), and 6.4.5 (c). Again the spectra repeat at 60° intervals. These spectra show the highest field line, which arises from a $[\text{Cr}(\text{OH})_6]^{3+}$ cation having its principal ZFS direction making the smallest possible angle with the field direction (19.5°) with this crystal orientation.

Another set of spectra were recorded, labelled BetaGa_ (figure 6.4.6) for which the crystal orientation was such that a (111) direction is aligned with the field. As with the previous set of spectra, the axis of rotation of the crystal is normal to the field. When one of the 4 principal ZFS directions is aligned with the field, the remaining 3 principal ZFS directions all necessarily make an angle of 70.5° with the field direction. This condition is met when the angle of rotation is $\{\omega' + 6\}^\circ$ where ω' is the initial alignment angle. The field strengths of the Zeeman transitions in this spectrum are in close agreement with those predicted from spectral simulations.

The precise location of the principal ZFS directions for the three remaining paramagnets cannot be easily determined from this crystal orientation. Projecting the principal ZFS directions into the plane which is normal to the field direction, the principal ZFS directions could have two limiting orientations as shown in figures 6.4.7 (a) and (b). For the limiting case shown in figure 6.4.7 (a), the spectra would repeat after 71° or 109° , depending on the direction of rotation. This is not observed. Alternatively, there could be an arrangement as in figure 6.4.7 (b). In this conformation we would expect, after a 90° rotation from BetaGa_1 to have two of the principal ZFS directions normal to the field direction and two making an angle of 35° . No convergence is observed after 90° . It is therefore inferred that the alignment of the crystal with respect to the magnetic field in the BetaGa_ data set is somewhere

FIGURE 6.4.4

Principal ZFS directions of the 4 paramagnets within the unit cell shown as projections in plane A. In this instance, the orientation of the crystal with respect to the field direction is that observed in spectrum BetbGa_4. The spectra repeat in 60° cycles.

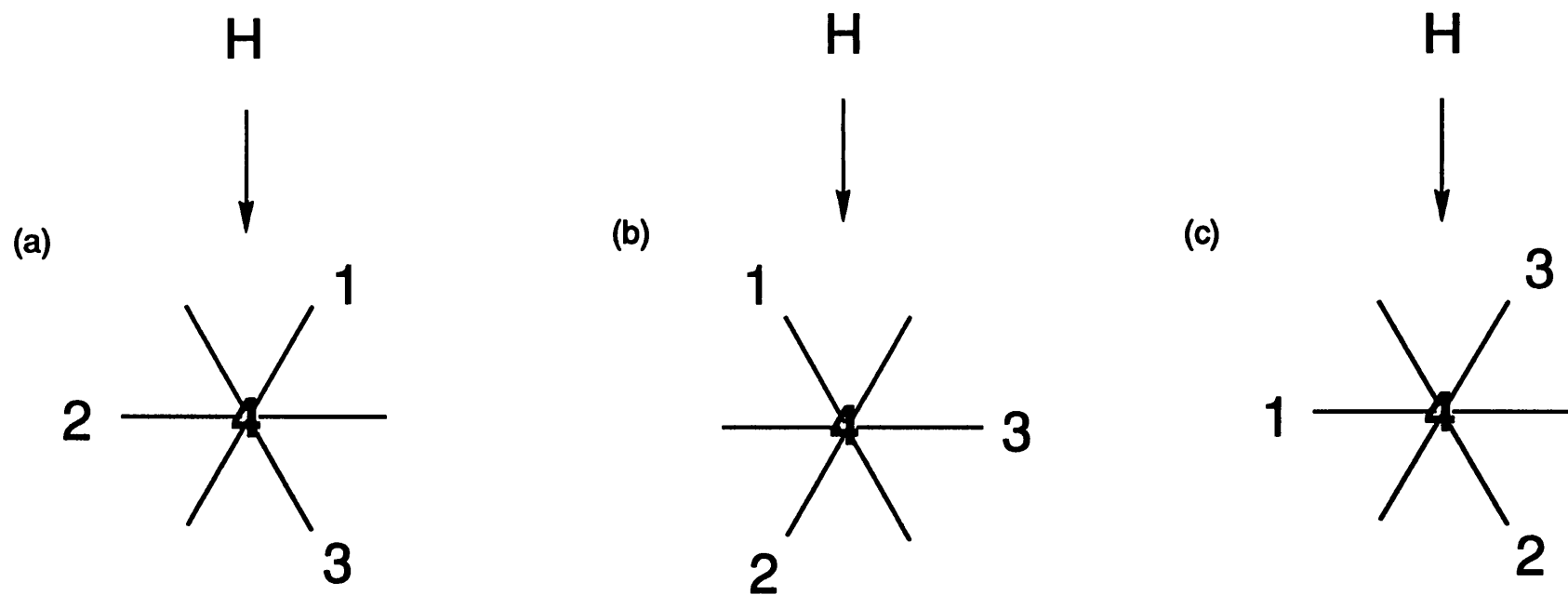


FIGURE 6.4.5

Principal ZFS directions of the 4 paramagnets within the unit cell shown as projections in plane A. In this instance, the orientation of the crystal with respect to the field direction is that observed in spectrum BetbGa_9. The spectra repeat in 60° cycles.

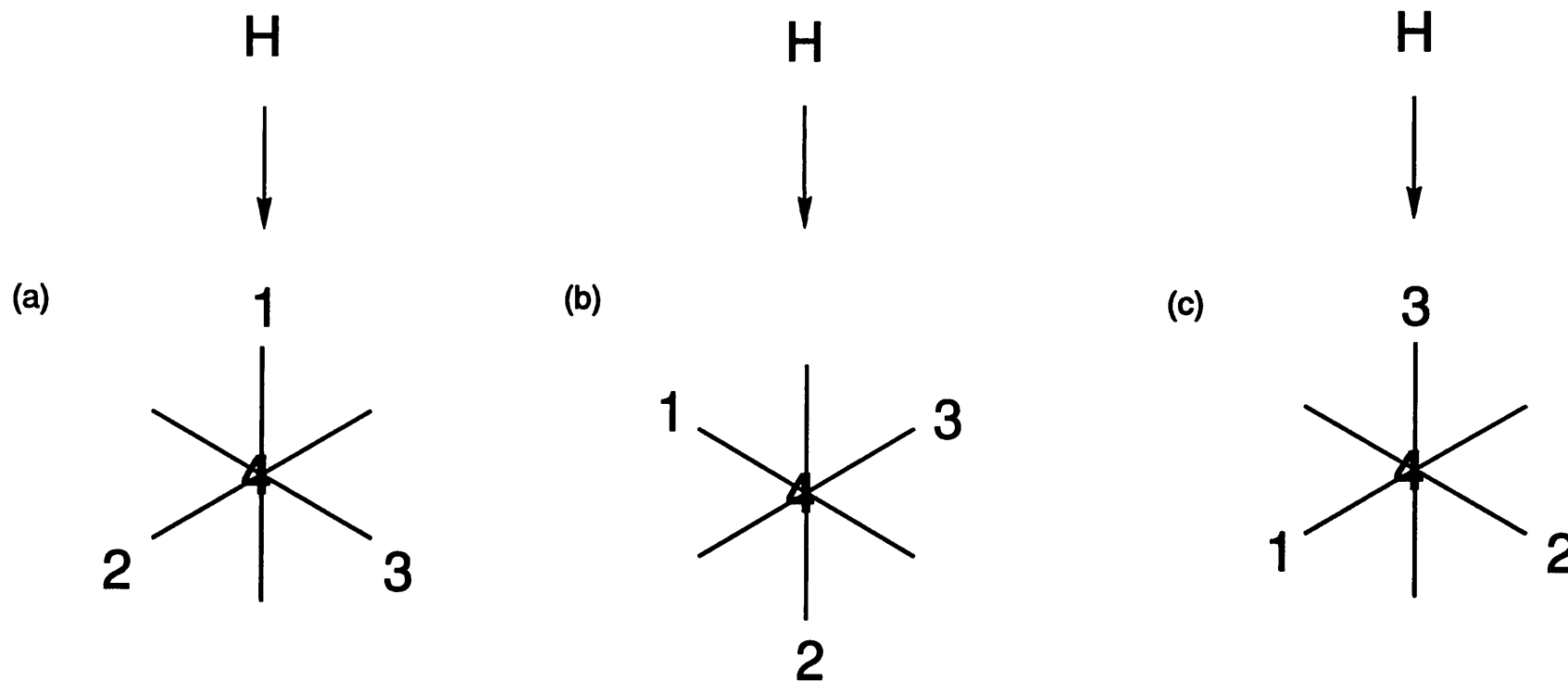
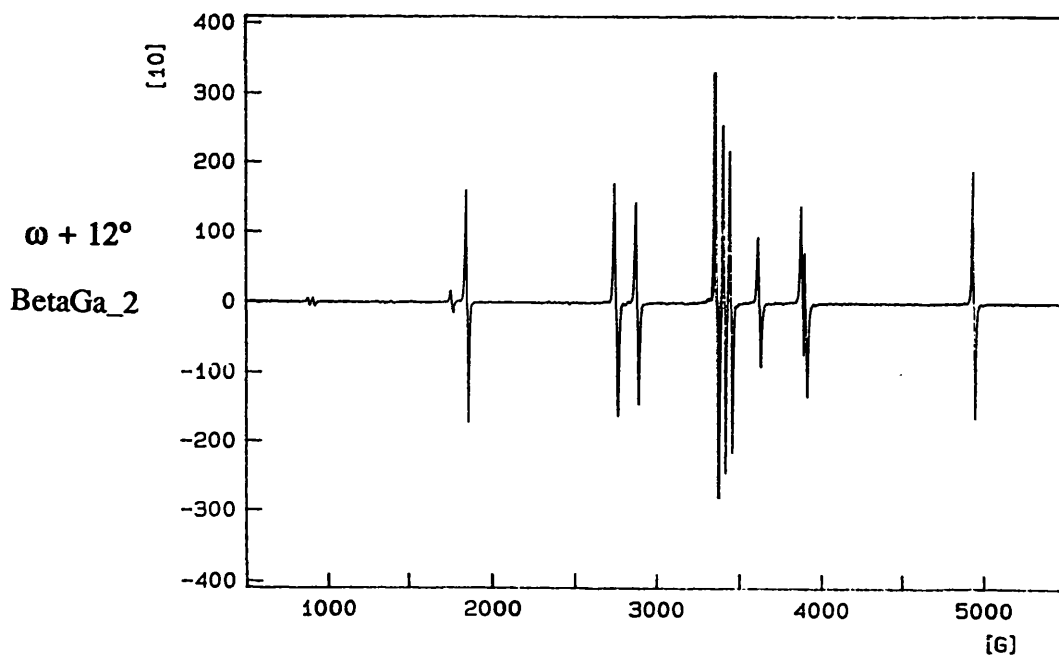
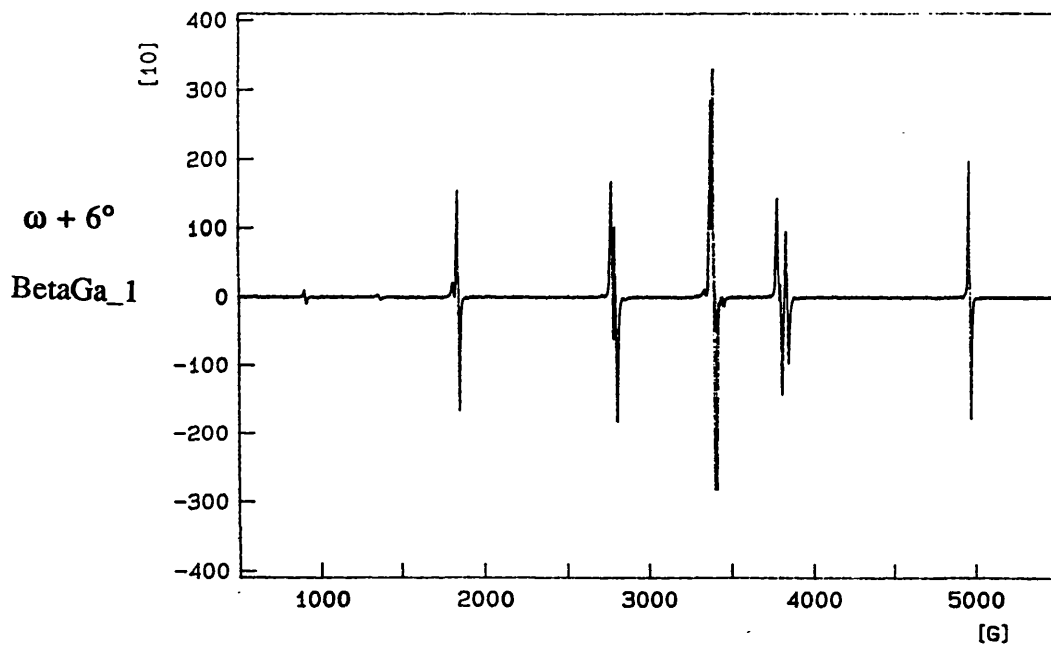
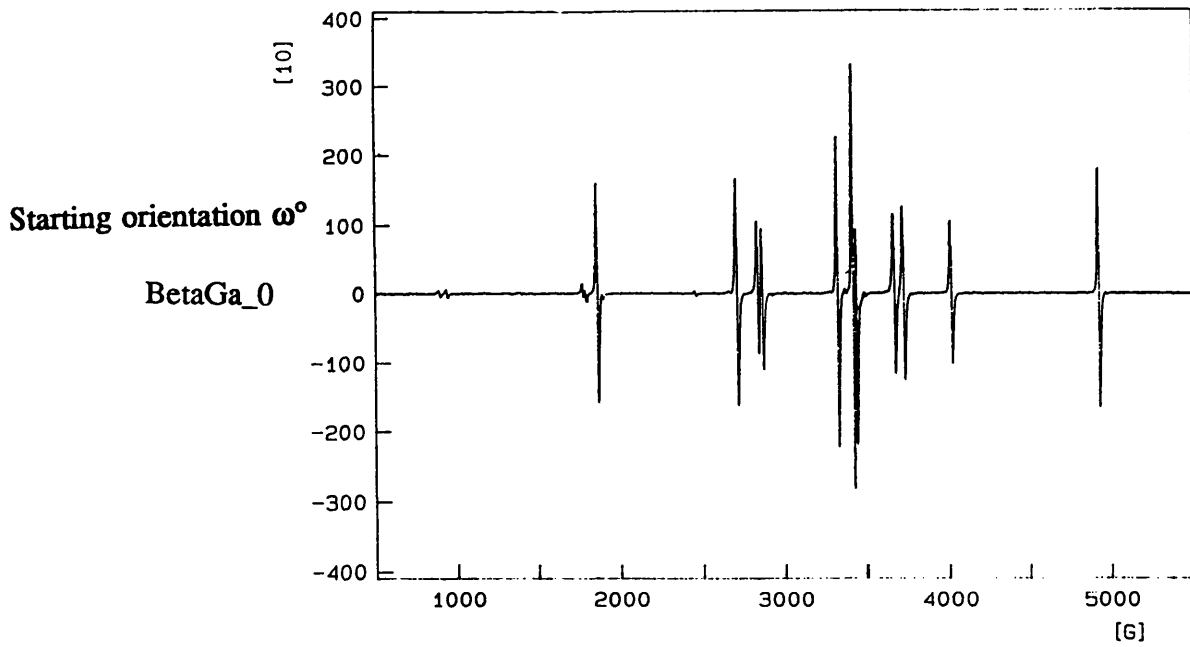
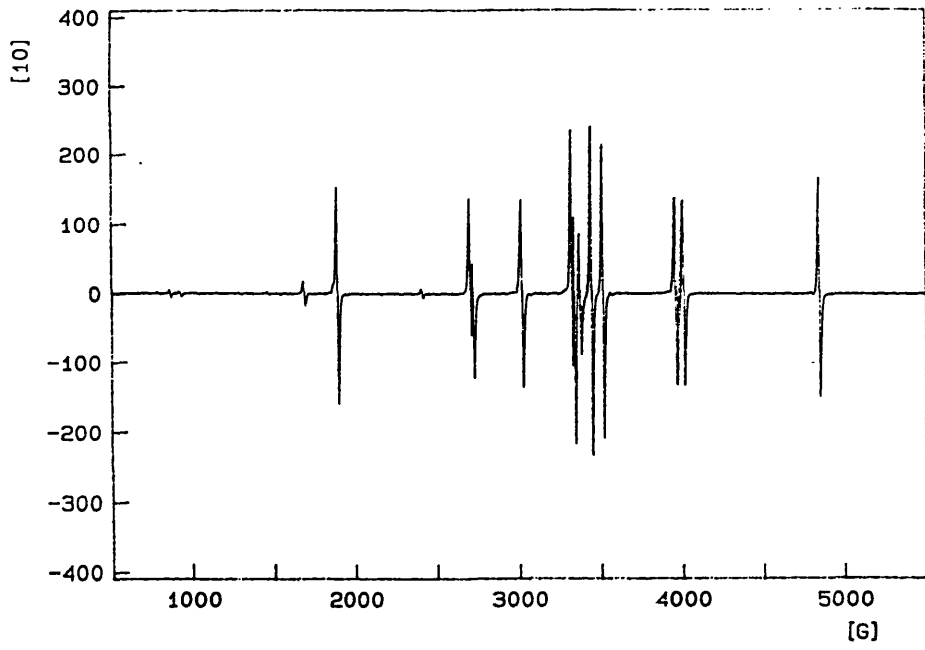


Figure 6.4.6

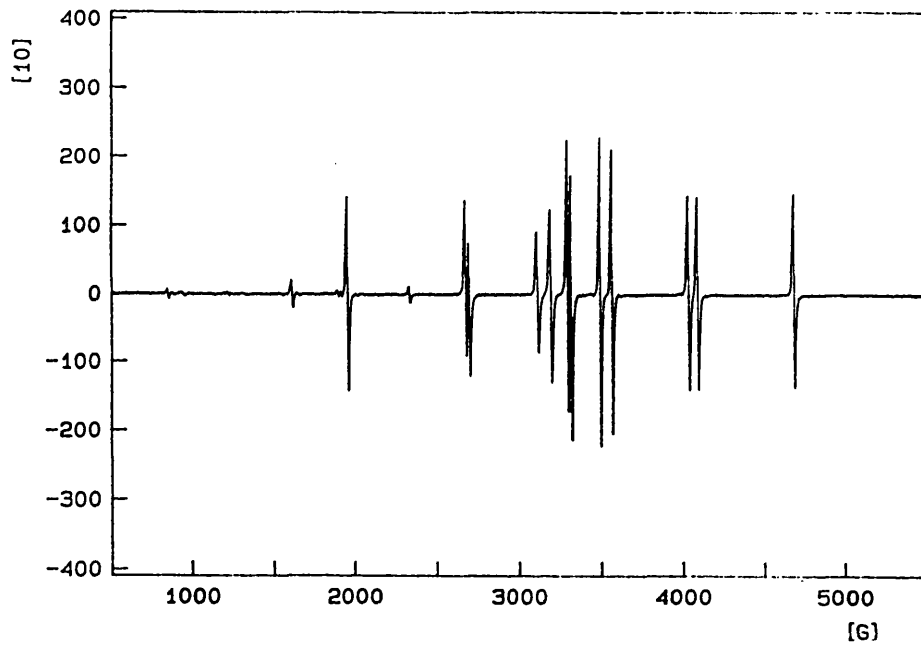
Oriented Single Crystal cw-EPR Spectra of $[^{50}\text{Cr}(^{17}\text{OH}_2)_6]^{3+}$ doped into $\text{CsGa}(\text{SO}_4)_2 \cdot 12\text{H}_2\text{O}$ alum. BetaGa data set. Three fold axis aligned in the direction of the external magnetic field (BetaGa_1) and rotated in 6° incrementations; the axis of rotation being normal to the field direction.



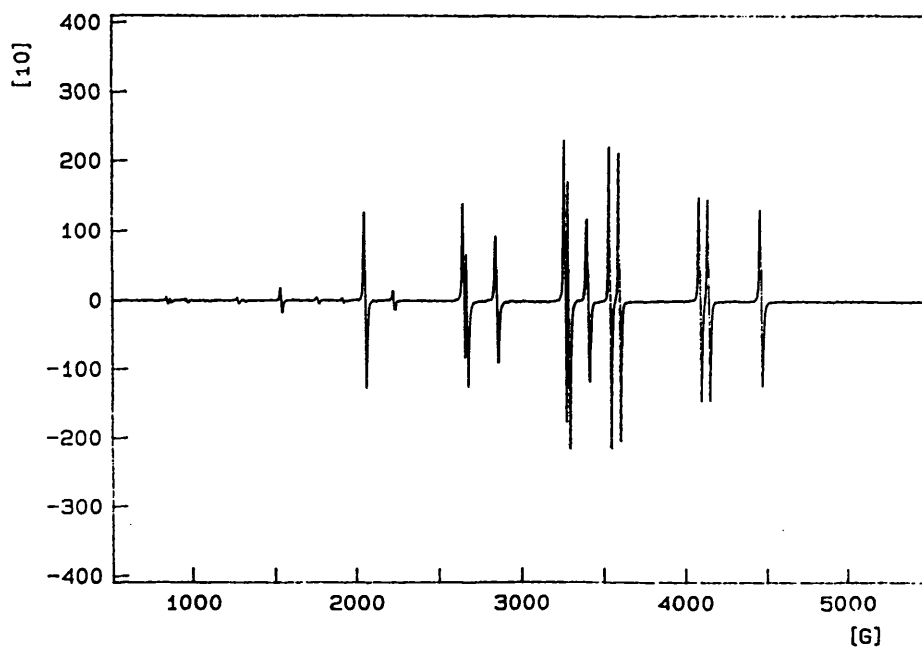
$\omega + 18^\circ$
BetaGa_3

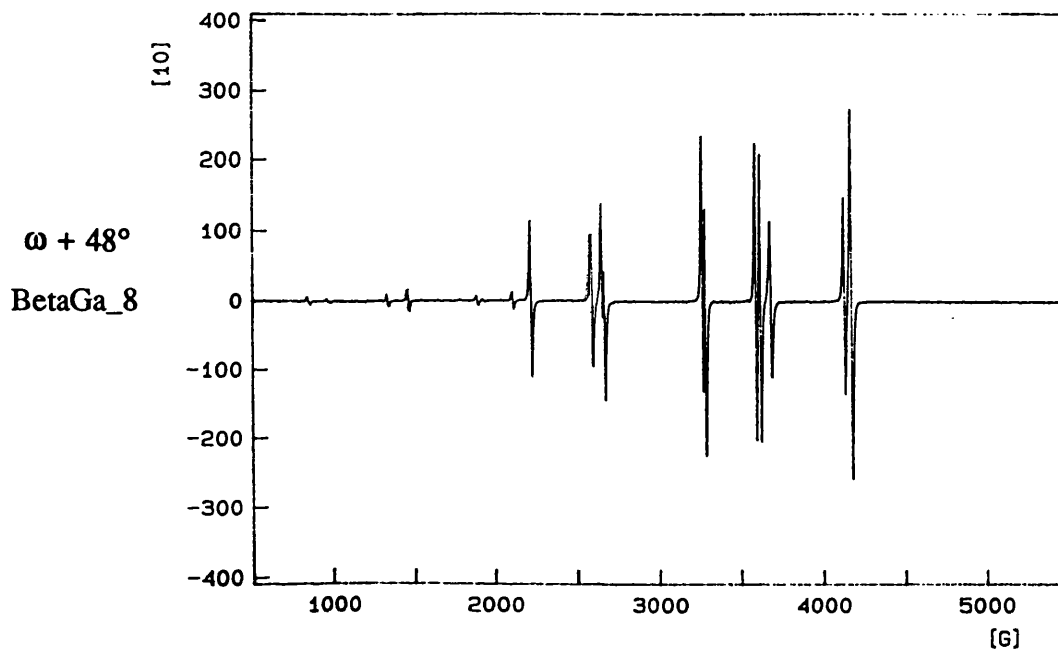
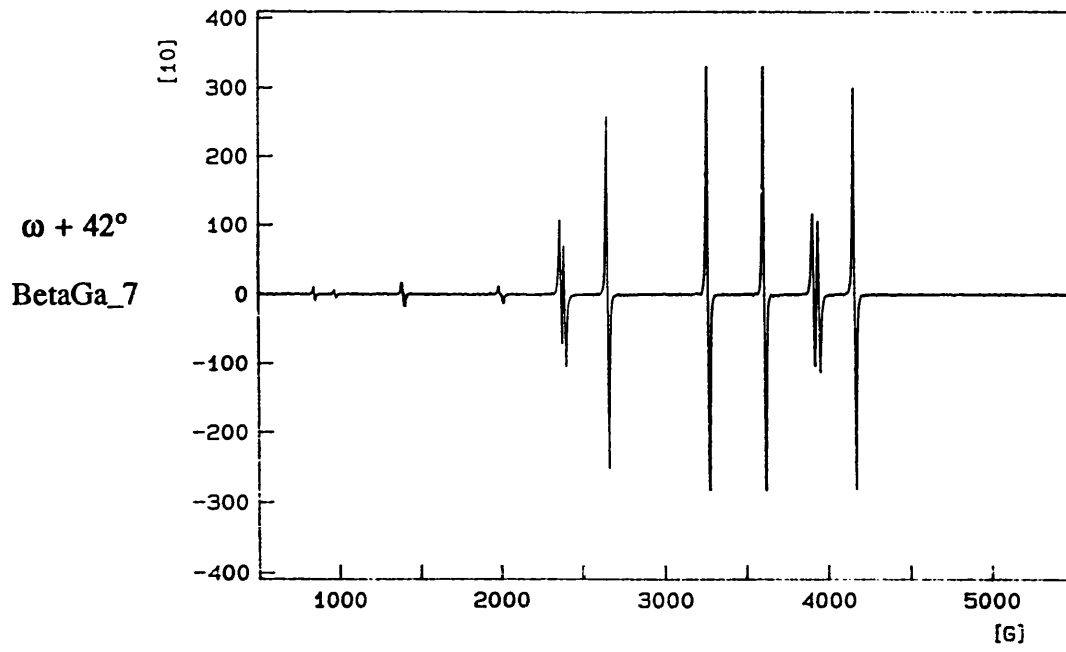
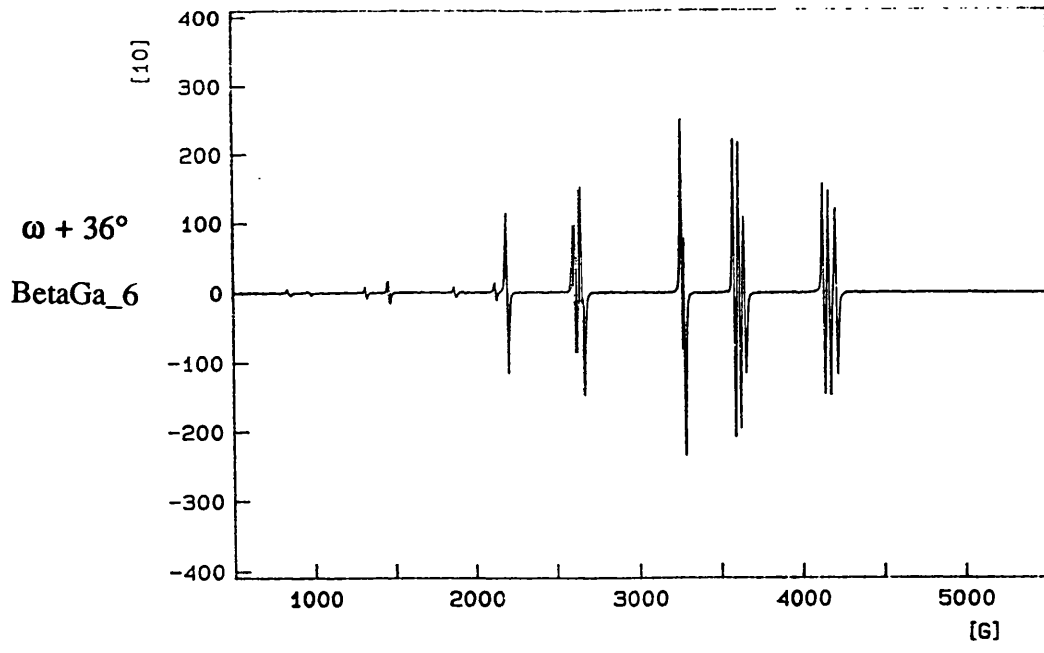


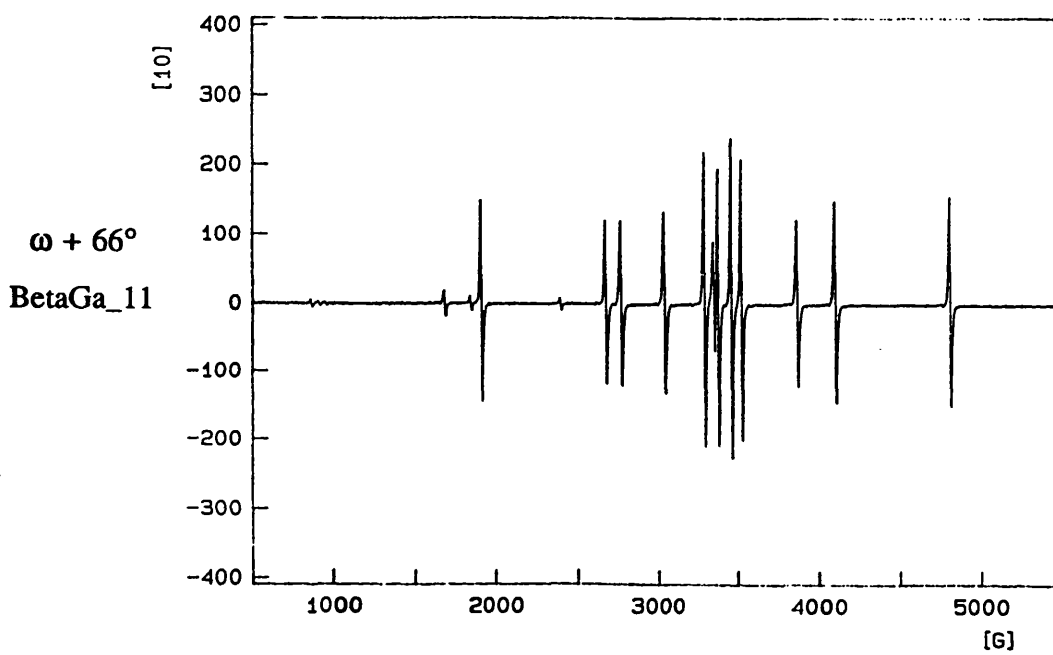
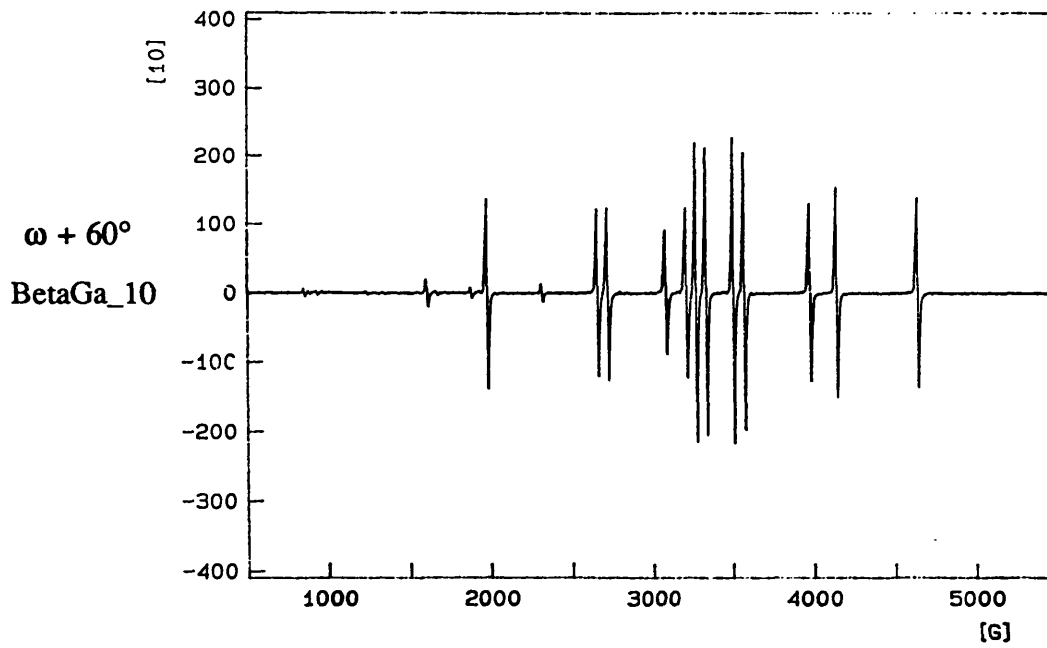
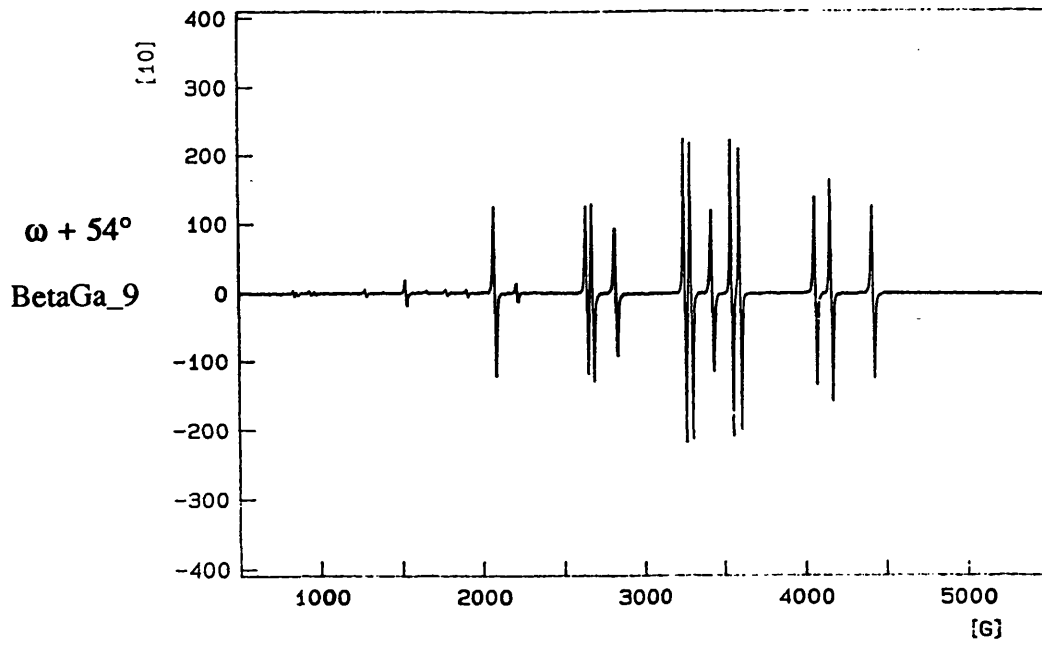
$\omega + 24^\circ$
BetaGa_4

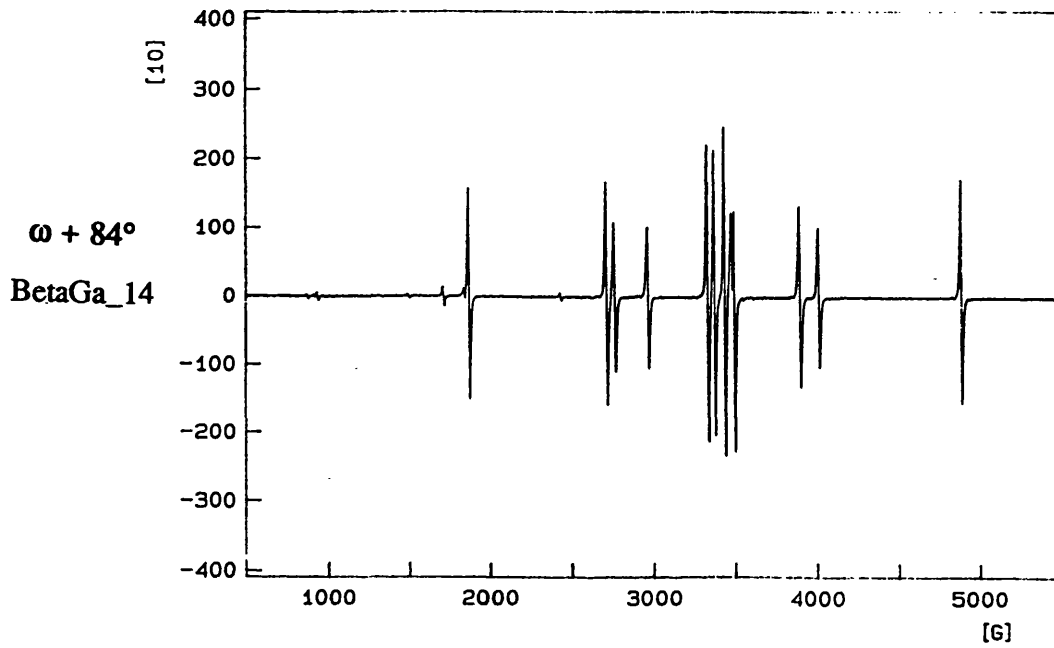
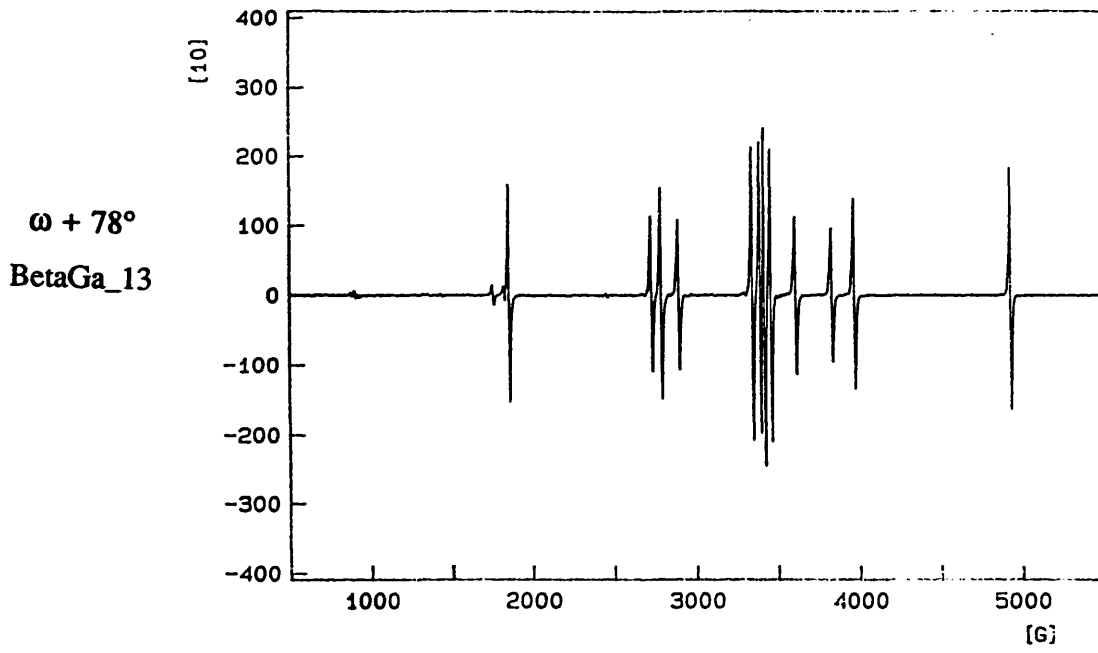
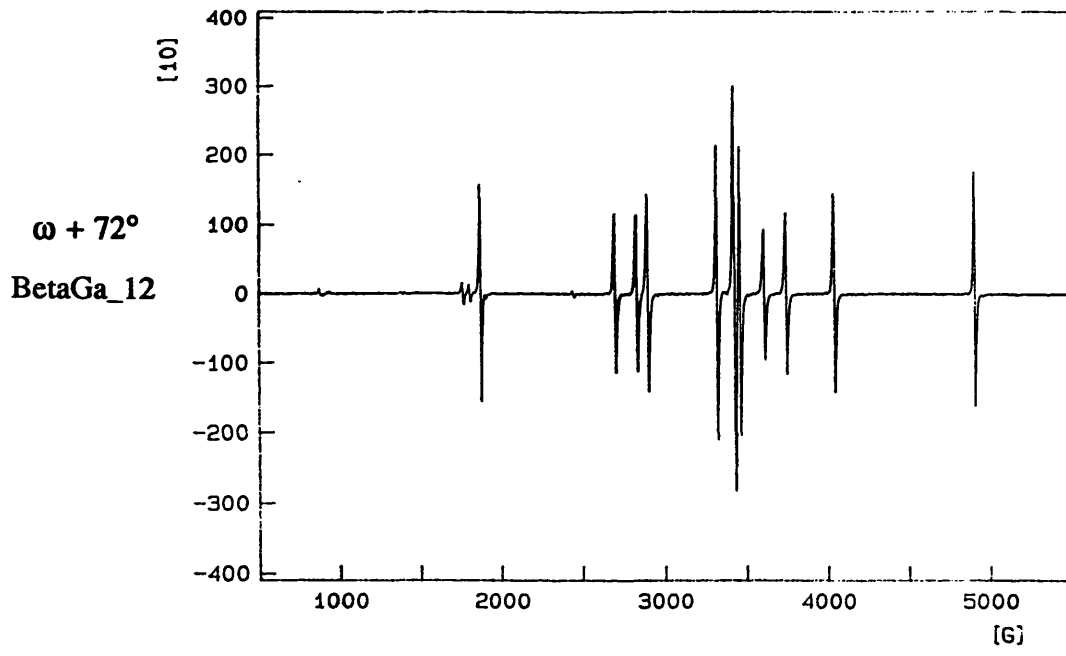


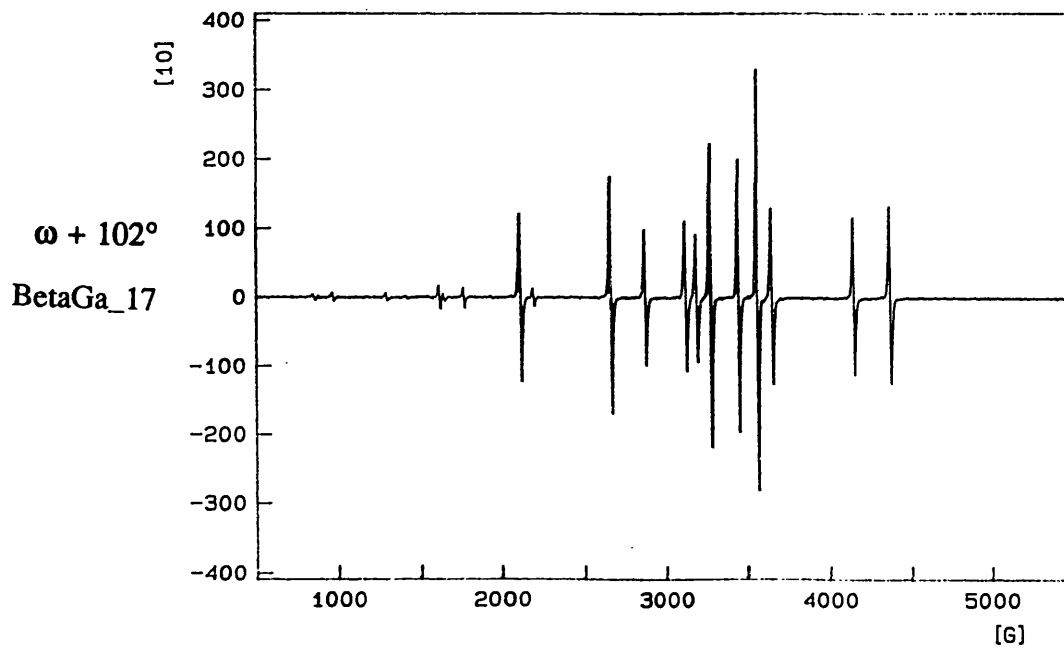
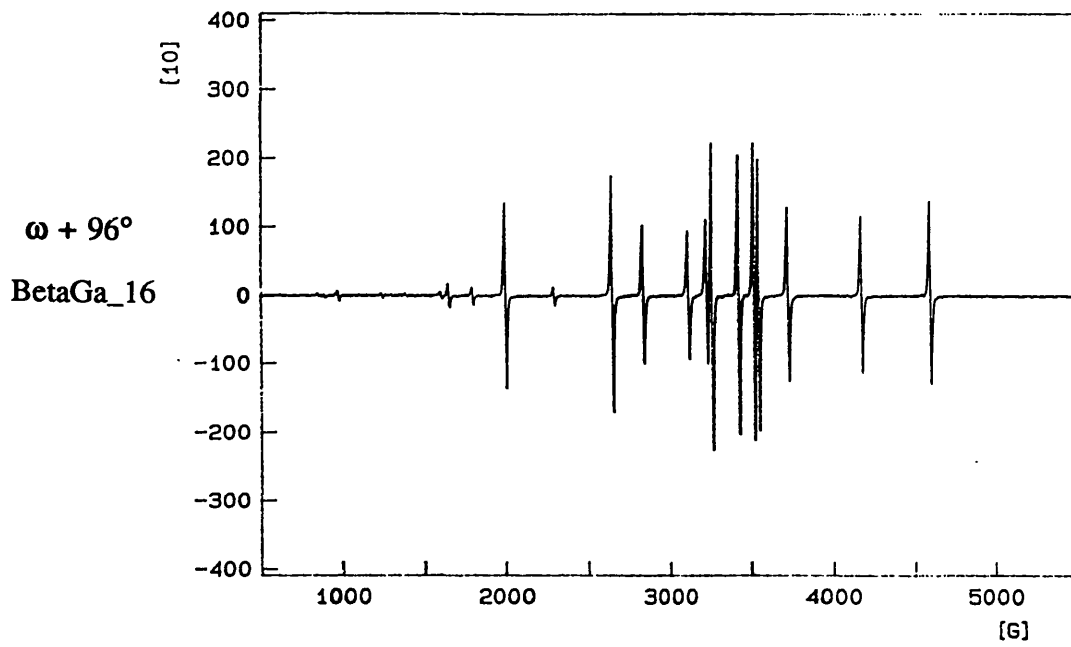
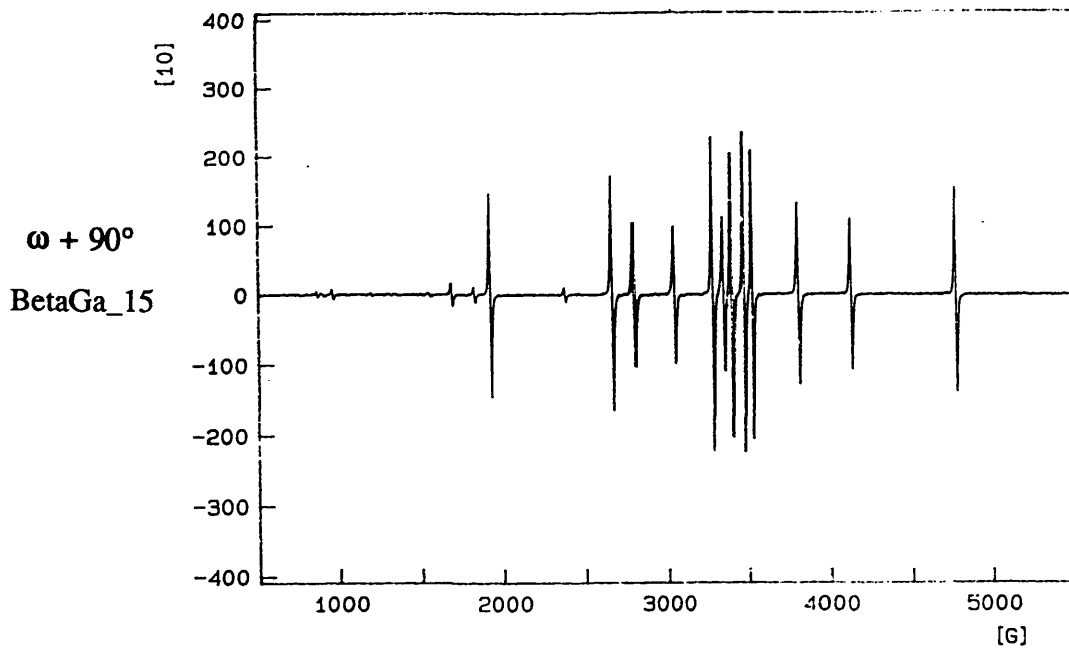
$\omega + 30^\circ$
BetaGa_5

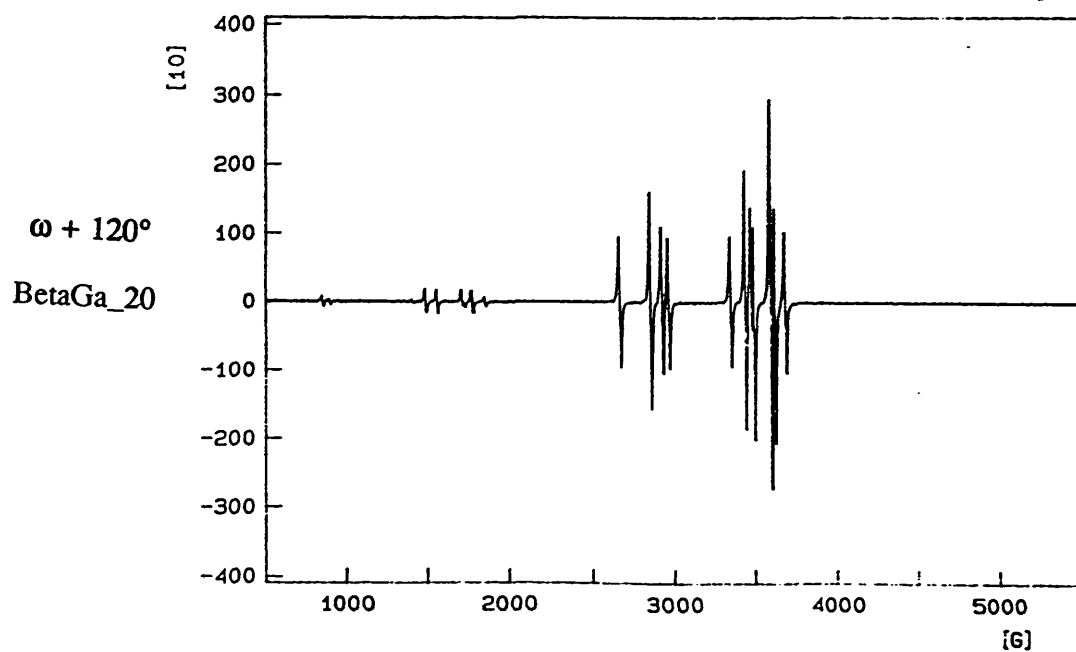
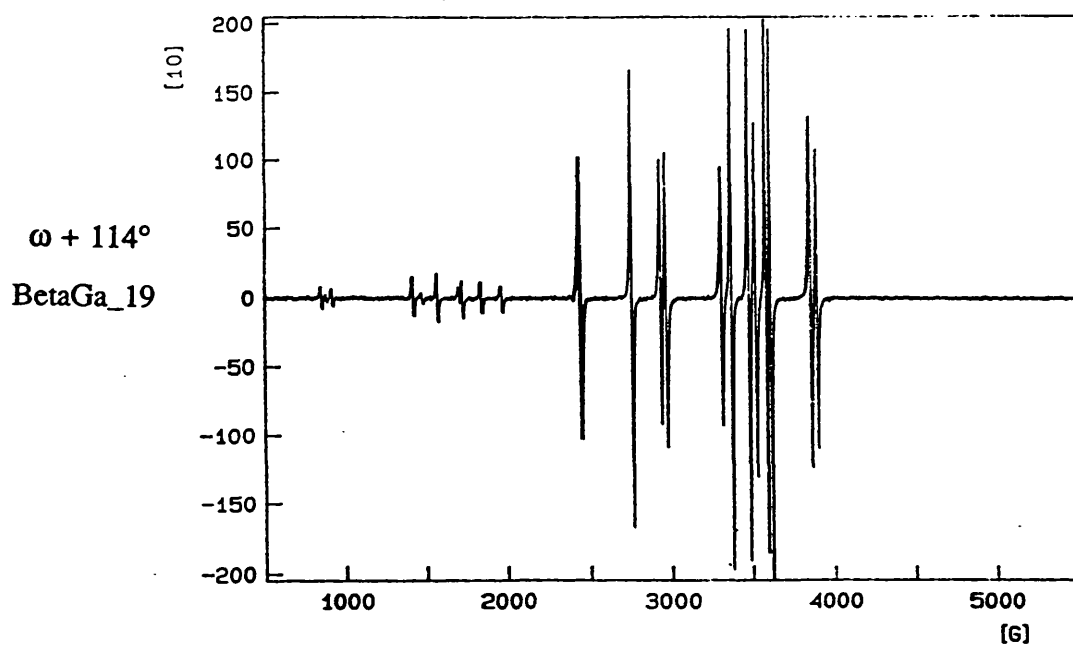
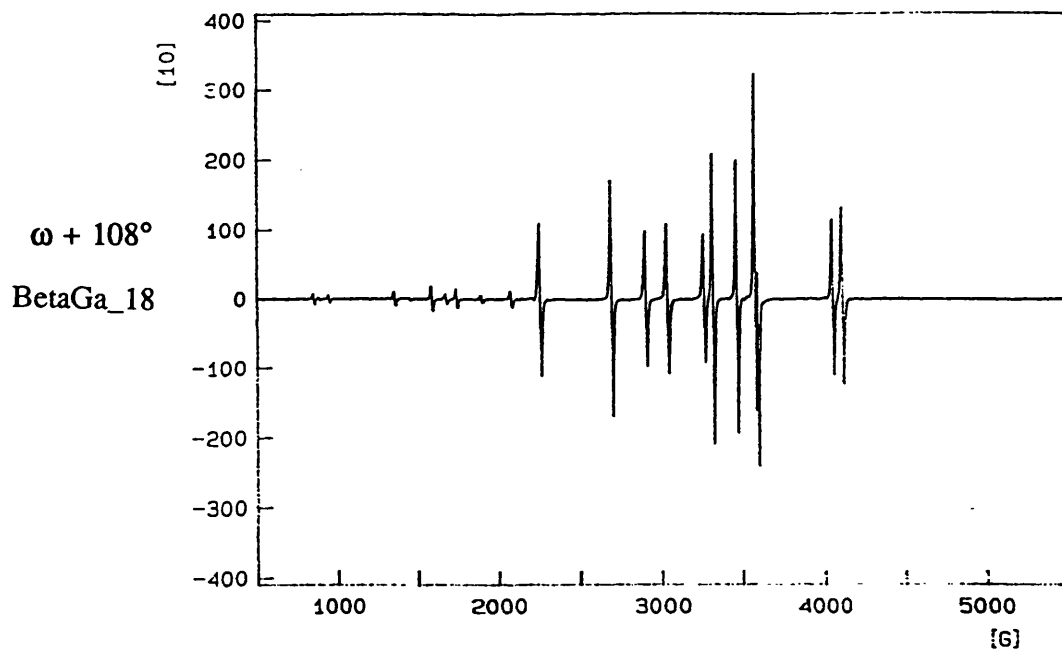


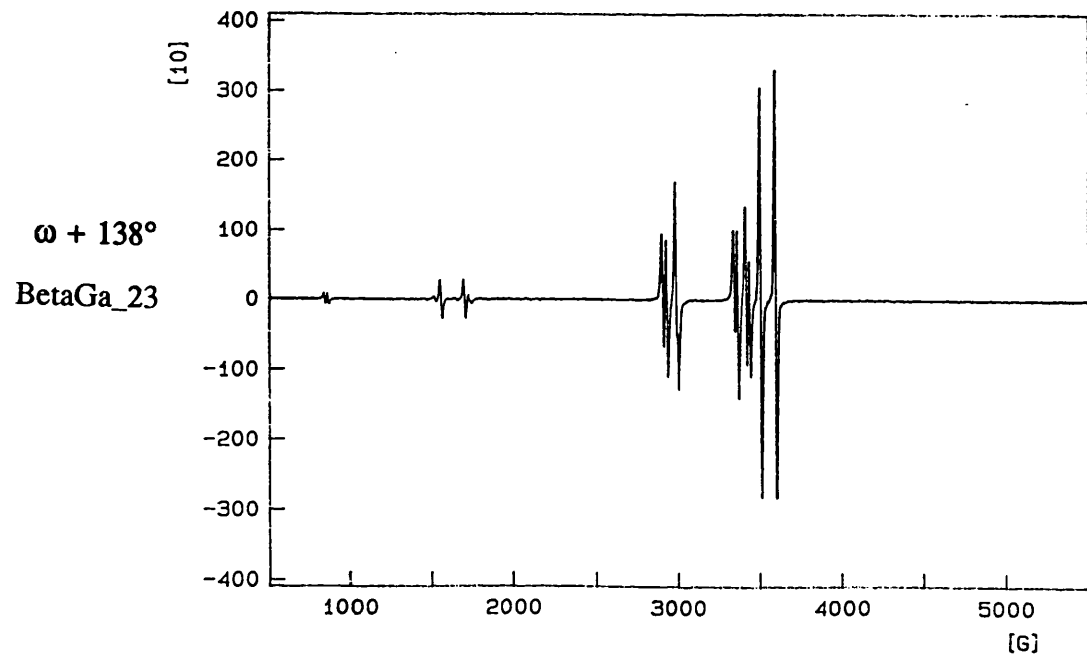
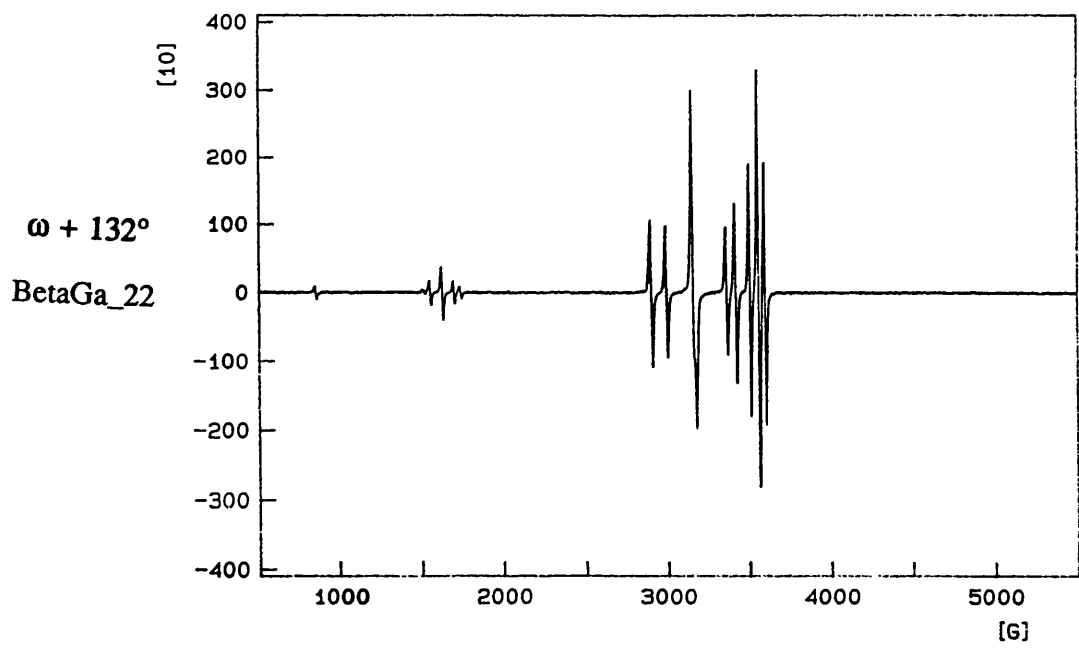
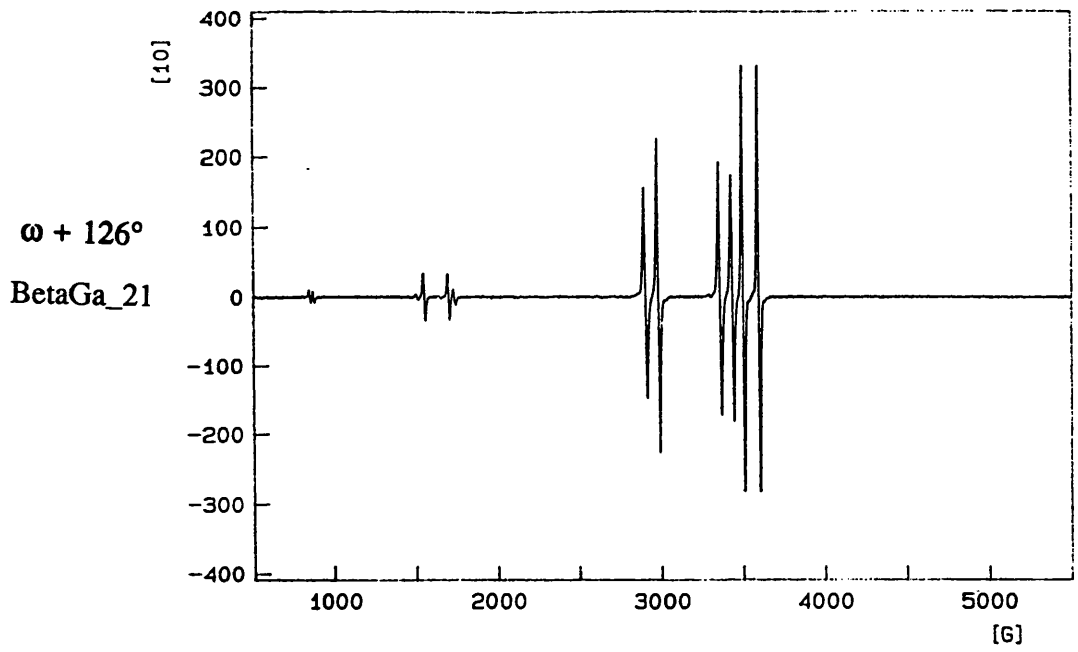


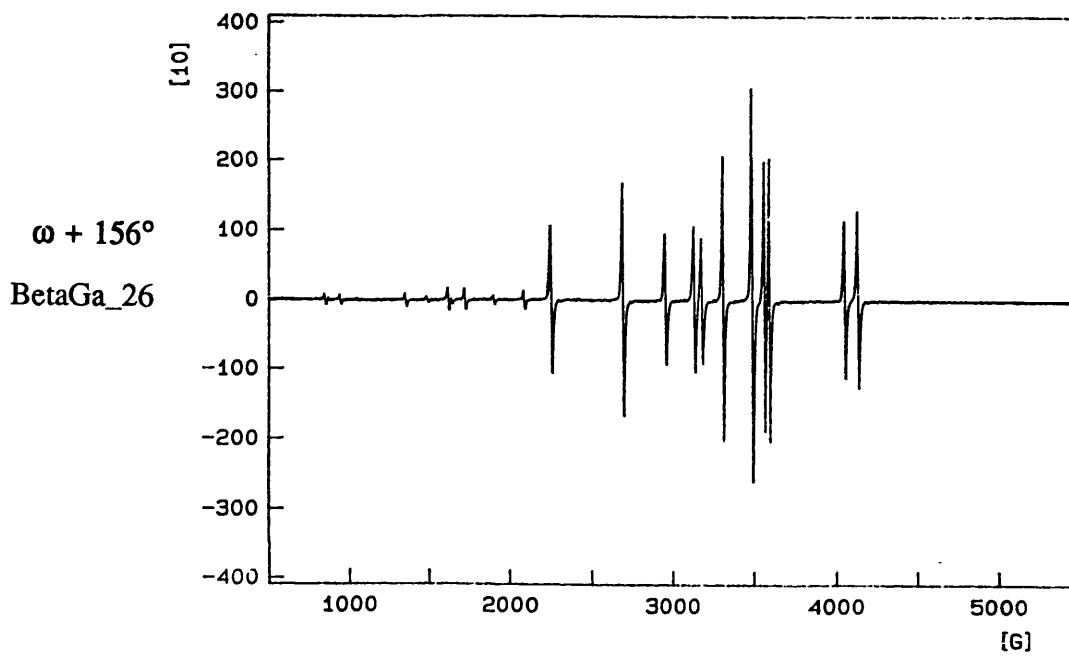
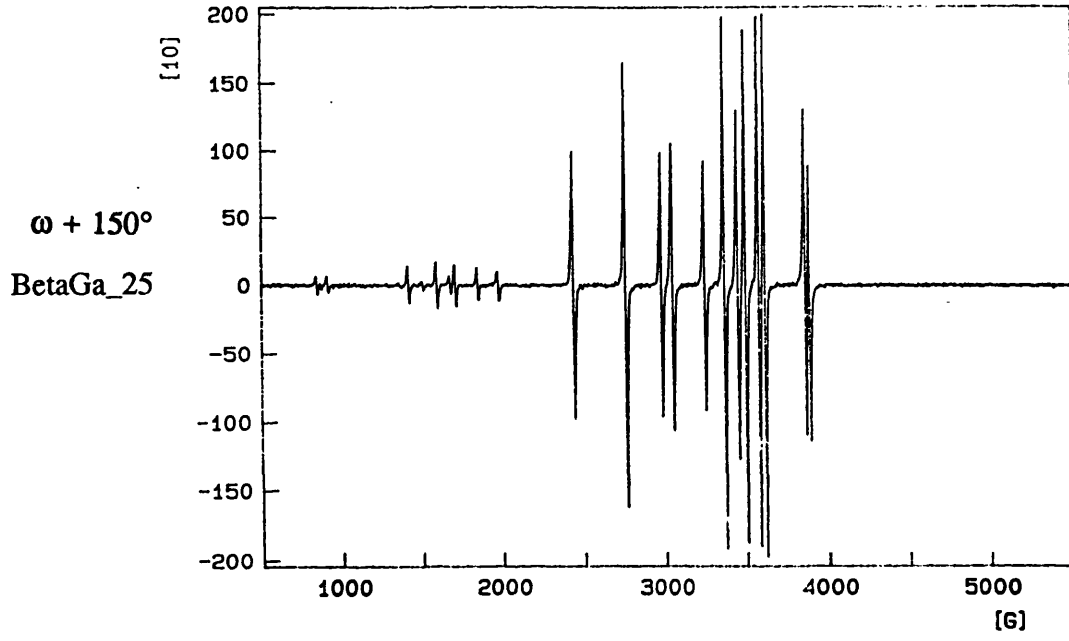
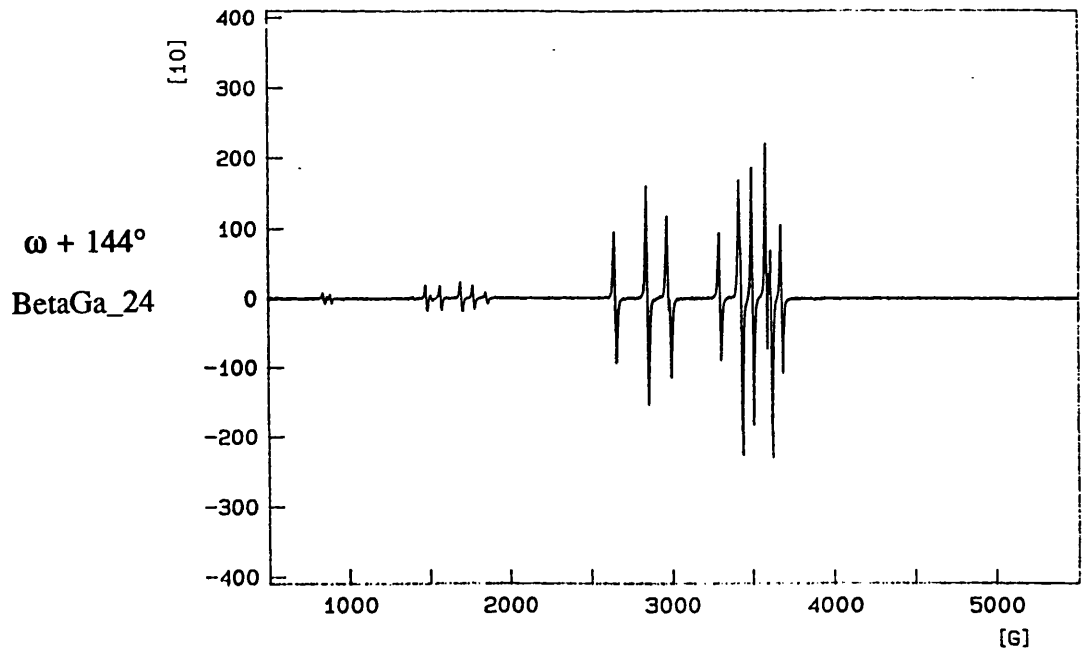


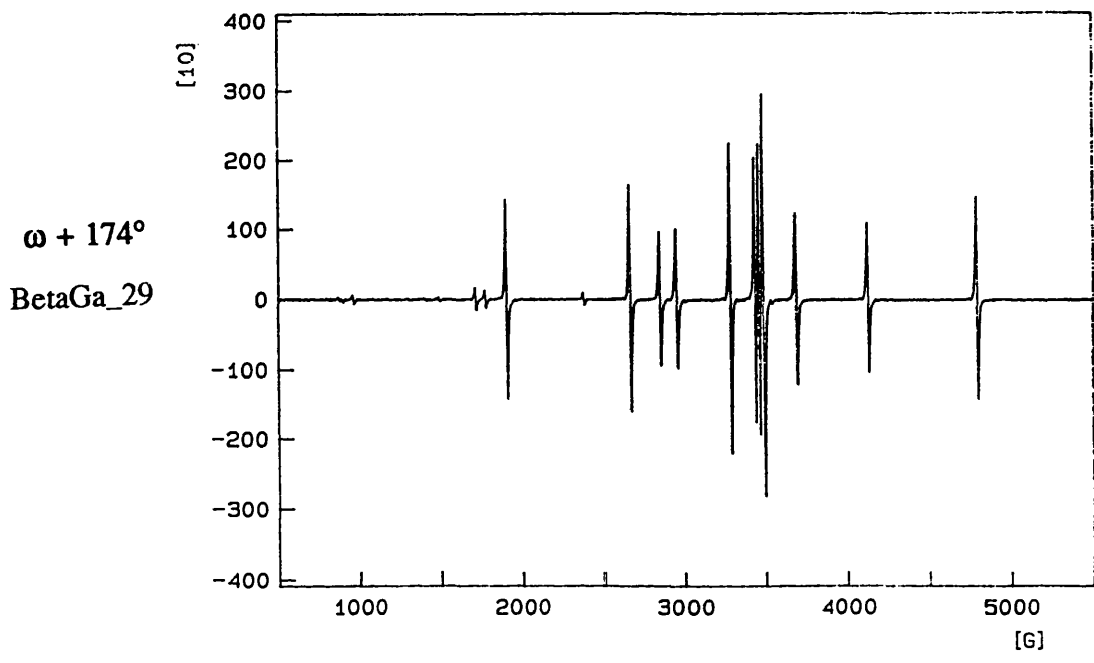
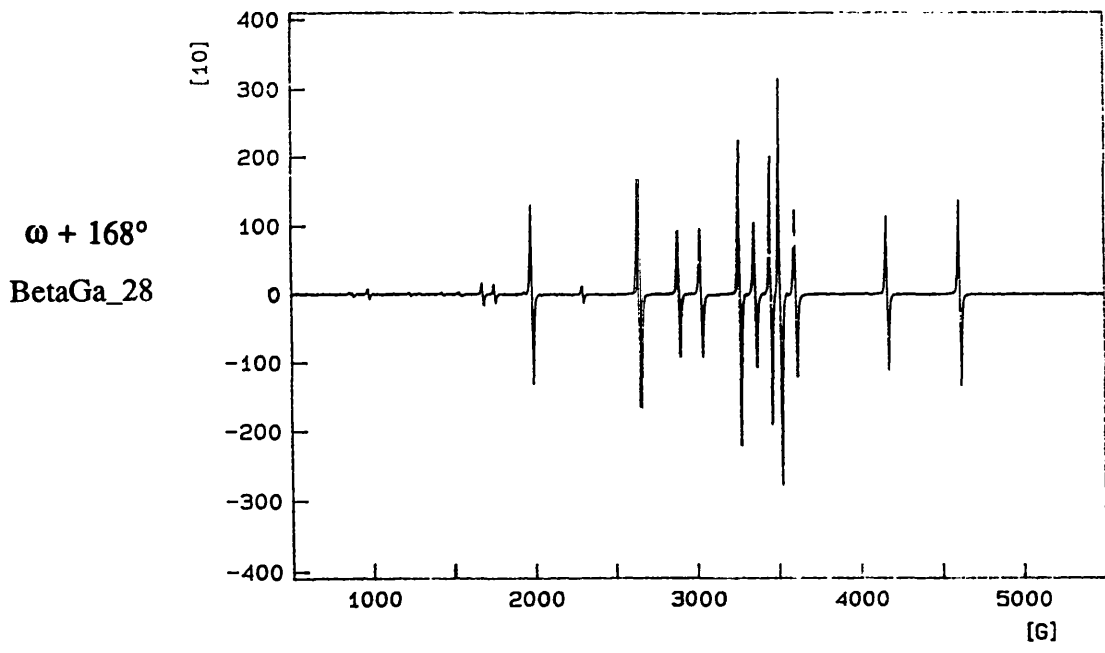
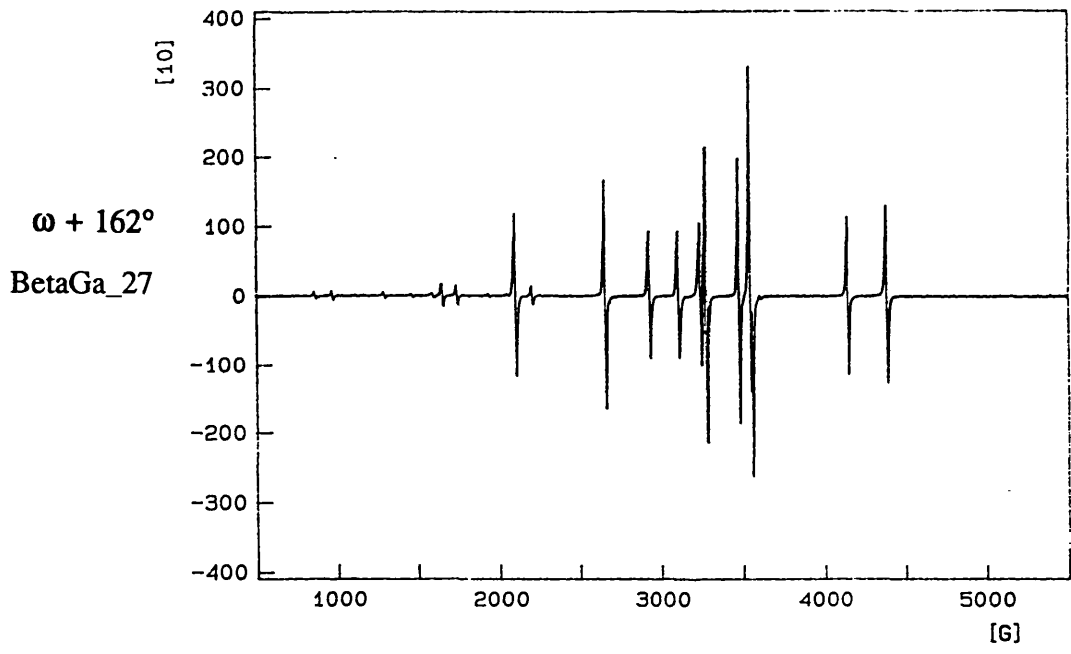












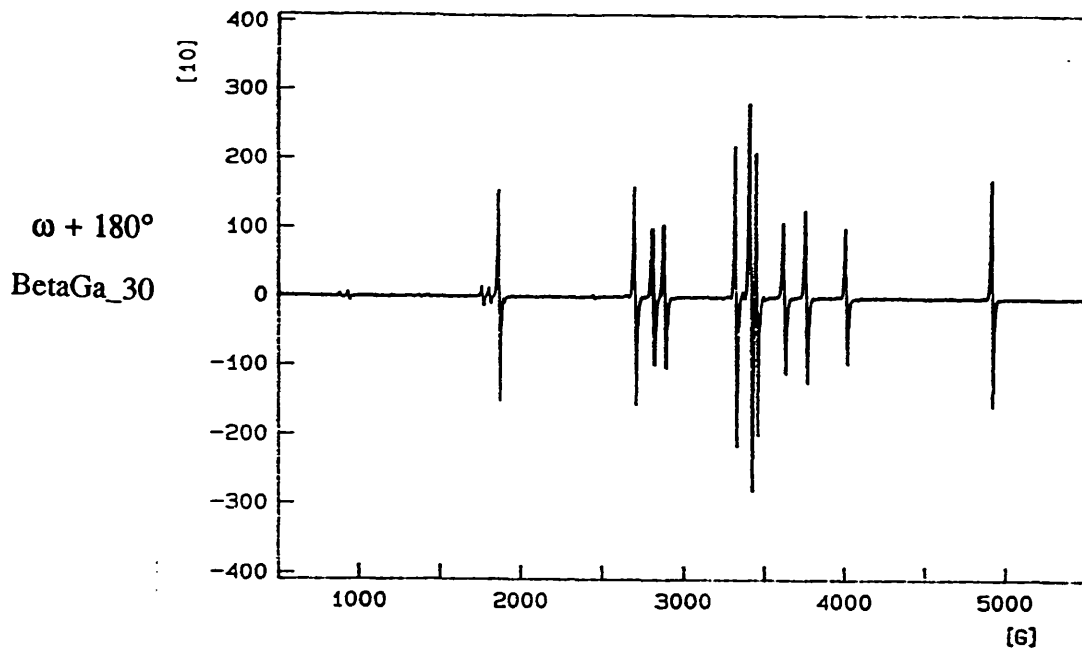
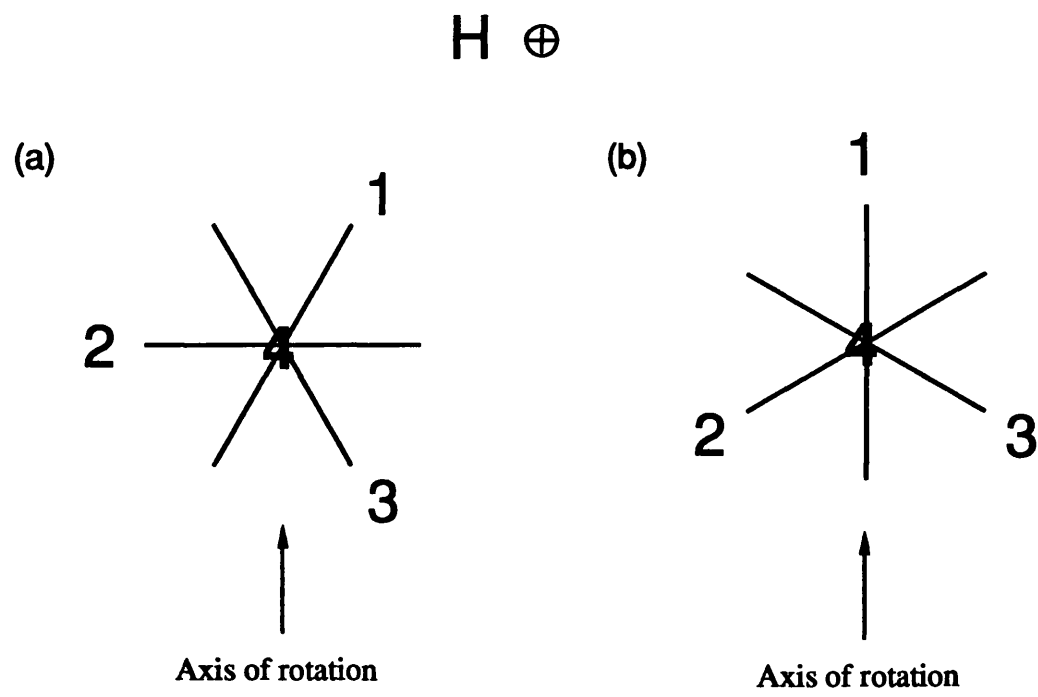


FIGURE 6.4.7

With the principle ZFS of one of the 4 paramagnets aligned with the field, two limiting orientations of the magnetic unit cell with respect to the field direction are shown. For a crystal orientation as shown in figure (a), the spectra would repeat after 71° or 109° , depending on the initial direction of rotation, and then in 109° cycles after that. For a crystal orientation as shown in figure (b), the principal ZFS direction for 2 of the 4 paramagnets will be normal to the field after a 90° rotation.

The external magnetic field direction is out of the plane of the paper.



between the two limiting orientations.

The cw EPR spectra have been assigned at differing crystal orientations to the external magnetic field direction. The sample behaves as a well ordered single crystal with no obvious signs of twinning. It was concluded that the three intense lines corresponding to the $1/2 \leftrightarrow 3/2$, $-1/2 \leftrightarrow 1/2$, $-3/2 \leftrightarrow -1/2$ ΔM_s transitions ($H \perp$ to Z axis) occurring at *ca.* 2650 G, 3280 G, and 4190 G in all the spectra of the Betb-Ga set were to be used in the ESEEM study. This is because their positions remain unchanged on rotation of the crystal about the three-fold axis; they do not overlap with other lines for a large portion of a 90° rotation segment; and with this crystal orientation the positions of all the Zeeman lines can be used to determine accurately the orientations of the 4 paramagnets within the unit cell with respect to the external magnetic field direction.

6.5 The Spin Echo Phenomenon

No hyperfine transitions were able to be observed in the cw spectra presented above. This is because the hyperfine coupling constants are not large enough to allow resolution of the individual spin packets which leads to the observation of one inhomogeneously broadened band. The ^{17}O nucleus has a spin of $5/2$ and can modify the EPR spectra by three distinct interactions: isotropic hyperfine coupling; anisotropic hyperfine coupling and quadrupolar coupling. The isotropic coupling arises from the Fermi contact interaction whereby the unpaired electron has a non-zero probability of being found at the nucleus. The Fermi contact interaction can arise only as a consequence of the unpaired electron occupying an orbital with 's character' since all other atomic orbitals have a nodal surface at the origin. The isotropic hyperfine coupling constant for a single unpaired electron occupying a 2s orbital on an ^{17}O atom is given as - 4628 MHz.⁸ At X-band with $g = 2$, this corresponds to a field of *ca.* 1650 Gauss. The line widths in the cw data set, determined by the relaxation properties of the system and by inhomogeneous broadening, are between 20 and 40 Gauss. These line widths are similar to those of the natural abundance cw-EPR spectra. We conclude therefore that if a significant amount of spin is transferred to the water ligand in the $[\text{}^{50}\text{Cr}(\text{}^{17}\text{OH}_2)_6]^{3+}$ complex then the form of the molecular orbital

which the unpaired electron occupies has insufficient 's' character for the coupling to be resolved at the resolution of the cw experiment.

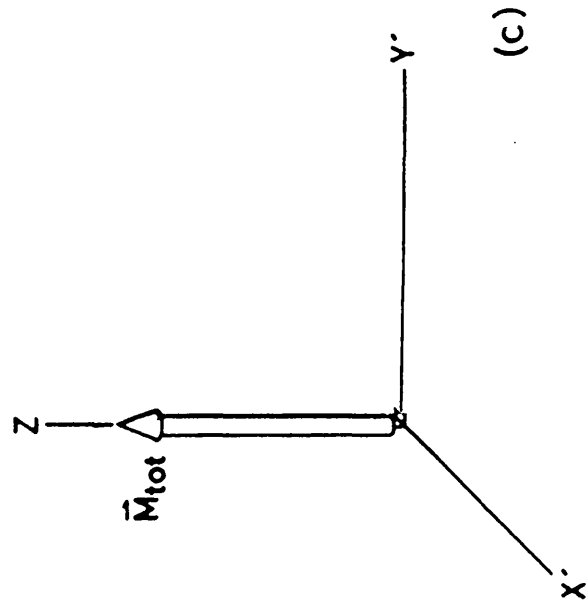
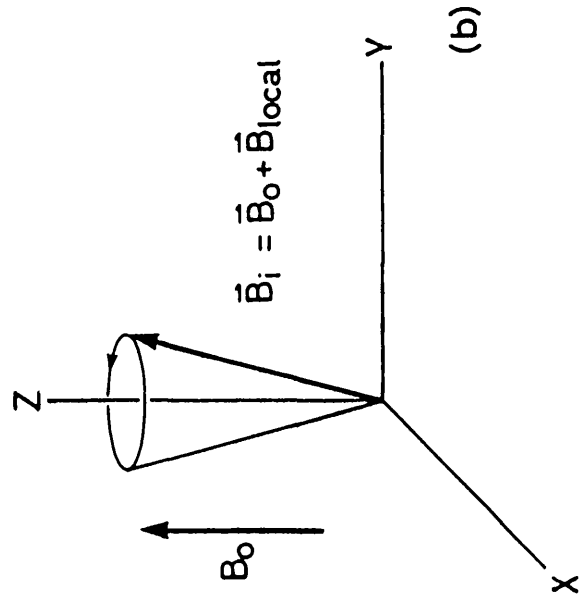
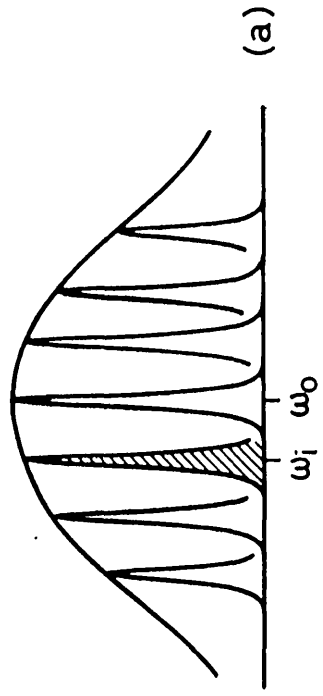
The anisotropic hyperfine coupling arises as a consequence of the interaction of the electron and nuclear dipoles. For an unpaired electron residing in a 2p orbital on an oxygen atom with mass number 17, this coupling is calculated to be *ca.* 50 G at X-band with $g = 2$.⁸ If *ca.* 10% of the total unpaired electron density occupies 2p orbitals on the oxygen atoms, then the coupling constant will be of the order 2 - 3 G and will not be able to be resolved at the resolution of the cw experiment.

The last interaction to be considered is that of the quadrupolar interaction. Nuclei with spins $I \geq 1$ possess a quadrupole moment as well as a dipole moment. The quadrupole interaction, measured by the quadrupole coupling tensor, is the product of the nuclear quadrupole moment and the electric field gradient (EFG), at the nucleus, due to *all* surrounding electrons. This interaction occurs as a consequence of the charge being non-spherically distributed about the nucleus. If the charge distribution about the quadrupolar nucleus is cubic, then the EFG at the nucleus will be zero and no quadrupolar interaction will occur. The quadrupolar interaction can, potentially, give valuable information on the distribution of *charge* throughout the $[\text{}^{50}\text{Cr}(\text{}^{17}\text{OH}_2)_6]^{3+}$ complex. If there is a concentration of charge in the Cr-O bonding region, then the EFG at the ^{17}O nucleus will be non-zero and the magnitude of the quadrupolar coupling is a measure of the electron concentration in the Cr-O bond. This is in contrast to the hyperfine coupling which measures the unpaired electron distribution only. Potentially, if the hyperfine and quadrupolar interaction tensors can be determined, a wealth of chemical information may be obtained. The next section describes how the hyperfine and quadrupolar coupling constants may be extracted using time resolved EPR techniques.

A resonance absorption observed in cw spectra can be thought of as an inhomogeneously broadened line consisting of homogenous spin packets (fig. 6.5.1 (a)). The magnetic moment of each spin packet M_i experiences a static magnetic field B_i and precesses about B_i with frequency ω_i (fig 6.5.1 (b)). ω_i is the resonance frequency also known as the Larmor frequency. Due to inhomogeneous broadening, there is a distribution of ω_i around the centre frequency ω_0 for which, resonance occurs at B_0 , the static external magnetic field. At this point, it is convenient to look

Figure 6.5.1

(a) The EPR line of paramagnetic centre in a solid can be regarded as an inhomogeneously broadened line consisting of homogenous spin packets. Each spin packet experiences a magnetic field B_1 and precesses about B_1 with Larmor frequency ω_1 (b) In the frame of reference that rotates about B_0 with frequency ω_0 , each spin packet M_1 precesses about B_0 with frequency $\omega'_1 = \omega_1 - \omega_0$. The resultant bulk magnetisation, M_{tot} , is aligned along B_0 (c). Adapted from diagrams after C.P Keijzers, E.J. Reijerse, and J. Schmidt [9].



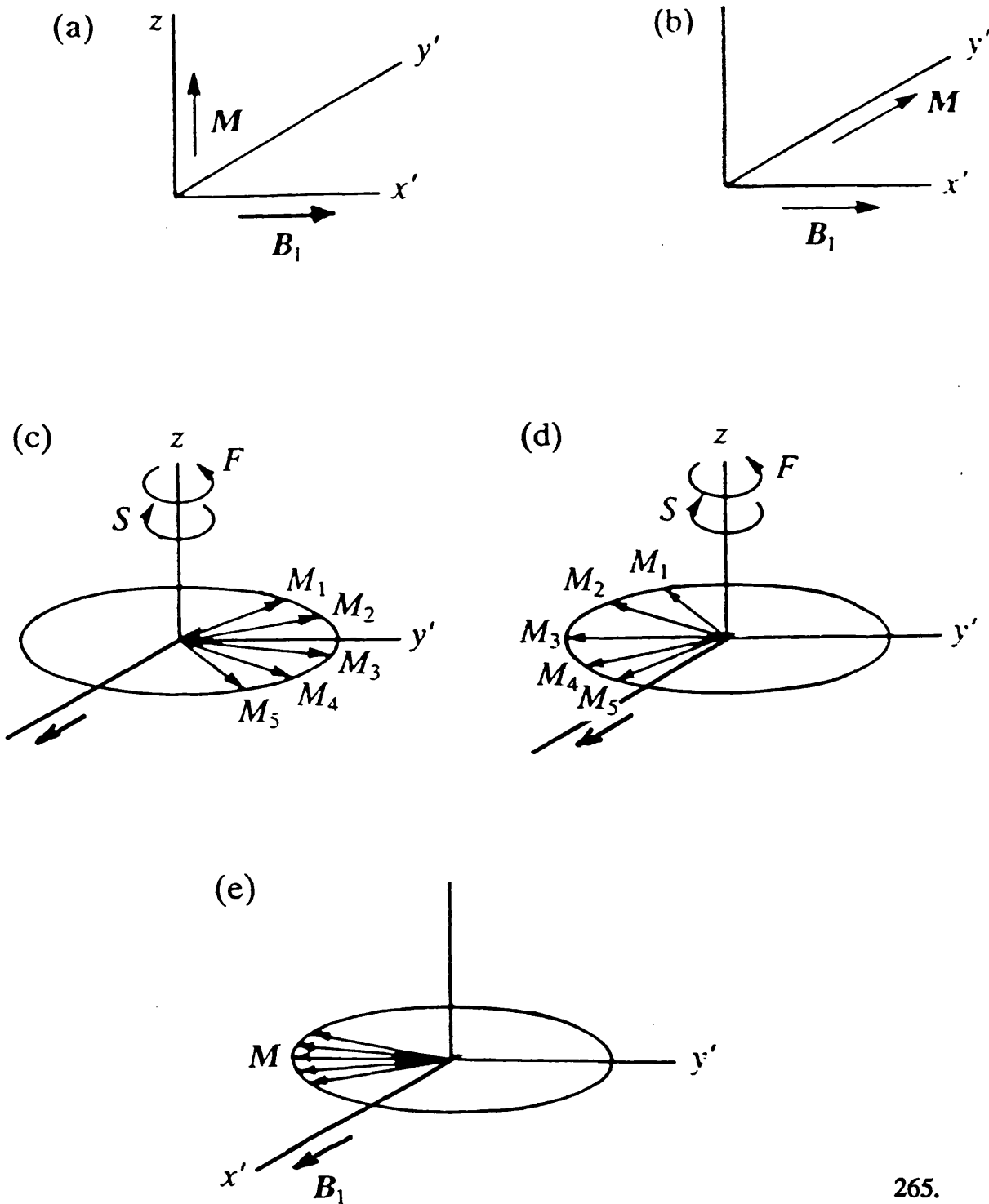
upon the magnetisation in a frame of reference that rotates around the direction of the external magnetic field B_0 with frequency ω_0 , defined as the z axis. The precession frequency of the spin packet M_i relative to that of ω_0 is $\omega'_i = \omega_i - \omega_0$ and the resultant bulk magnetic moment is aligned along the z axis as shown in figure 6.5.1 (c).

Figure 6.5.2 describes the two-pulse echo experiment in schematic form. Microwave radiation is applied with frequency ω_0 and polarised in the $x'y'$ plane. In the rotating frame, B_1 is a stationary field defined along the x' axes (fig. 6.5.2(a)). If the spread of microwave radiation is larger than the spread in Larmor frequencies, then the resonance condition is met for all spin packets and their corresponding magnetic moments will precess around B_1 in the zy' plane. When the duration of the microwave radiation is just enough to flip the magnetisations M_i into the $x'y'$ plane (fig. 6.5.2(b)), the pulse is defined as a $\pi/2$ pulse. Since the different spin packets have different offset frequencies ω'_i , they will start to dephase immediately in the $x'y'$ plane (fig. 6.5.2(c)). This process is known as the free induction decay (FID). In a typical ESE experiment dephasing is complete within 50 ns. From this FID an echo can be generated by means of a second microwave pulse. If after a time τ after the first pulse, a second pulse lasting twice as long as the first is generated, then this will have the effect reflecting the dephased pattern in the $x'z$ plane (fig. 6.5.2(d)). The original precession frequencies and directions remain unaltered so that the spin packets refocus after the same time τ into a macroscopic magnetic moment which produces the "two pulse" echo (fig. 6.5.2 (e)). Inhomogeneities can be the result of crystal defects as well as small hyperfine couplings. The echo signal can be used to obtain the EPR spectrum by recording the echo height as a function of the magnetic field. Such a field swept ESE spectrum is similar to the conventional cw-EPR spectrum except that the lines have an absorption shape instead of the familiar first derivative.

The amplitude of two pulse echoes do not always decay smoothly as a function of τ . Very often the decay is not monotonic but is modulated with clearly defined periodicity. The modulations are a consequence of the precision of the nuclear magnetic moments which give rise to variations in the local field seen by the electron. This causes the phase of the electron to lag or lead according to the stage reached in the nuclear precessional cycle leading to an interference effect. In order for the nuclear modulation effect to be observed, the microwave field pulse must be

FIGURE 6.5.2

Schematic diagram showing the origin of the two-pulse echo in the rotating frame of reference. (a) and (b) are before and after the 90° pulse; (c) and (d) before and after the 180° pulse. F denotes the direction of rotation of the faster spin packets M_1 and M_2 ; S denotes the direction of rotation of the slower spin packets M_4 and M_5 . (e) phase convergence of the spin packets. (After Mims [10])



large enough to encompass the hyperfine splittings of the electron spin states. It can be shown^{9,11} that the microwave field must simultaneously induce both the allowed ($\Delta M_s = 1, \Delta M_I = 0$) and forbidden ($\Delta M_s = 1, \Delta M_I = 1$) transitions in order for the nuclear modulation effect to be observed. This effect is known as "branching of transitions". The "forbidden transitions" become "slightly allowed" as a consequence of mixing of eigenstates *viz.* hyperfine interaction. Figure 6.5.3 shows transitions between hyperfine states labelled by the electron and spin quantum numbers $|M_s, M_I\rangle$. In the limit where the nuclear Zeeman interaction is much greater than the hyperfine interaction, the wavefunctions for the resultant states represented in figure 6.5.3 are:¹²

$$\begin{aligned}
 |\Psi(\pm \frac{1}{2}, \pm \frac{1}{2})\rangle &= |\pm \frac{1}{2}, \pm \frac{1}{2}\rangle + \frac{1}{2} \frac{[A_{xz} \mp iA_{yz}]}{2g\beta B_0 \pm A_{zz}} |\mp \frac{1}{2}, \pm \frac{1}{2}\rangle \\
 &\quad - \frac{1}{2} \frac{[A_{xz} \mp iA_{yz}]}{2g\beta B_0 \pm A_{zz}} |\pm \frac{1}{2}, \mp \frac{1}{2}\rangle \\
 &\quad + \frac{[A_{xx} \mp A_{yy} + 2iA_{xy}]}{g\beta B_0 - g_n\beta_n B_0} |\mp \frac{1}{2}, \mp \frac{1}{2}\rangle \\
 |\Psi(\pm \frac{1}{2}, \mp \frac{1}{2})\rangle &= |\pm \frac{1}{2}, \mp \frac{1}{2}\rangle - \frac{1}{2} \frac{[A_{xz} \mp A_{yz}]}{2g\beta B_0 \mp A_{zz}} |\mp \frac{1}{2}, \mp \frac{1}{2}\rangle \\
 &\quad + \frac{1}{2} \frac{[A_{xz} \pm iA_{yz}]}{2g\beta B_0 \mp A_{zz}} |\pm \frac{1}{2}, \pm \frac{1}{2}\rangle \\
 &\quad + \frac{[A_{xx} + A_{yy}]}{g\beta B_0 + g_n\beta_n B_0} |\mp \frac{1}{2}, \pm \frac{1}{2}\rangle
 \end{aligned}$$

6.5.1

where the principal directions of A are allowed to have any orientation.

The ratio of forbidden to allowed probabilities is given by:¹²

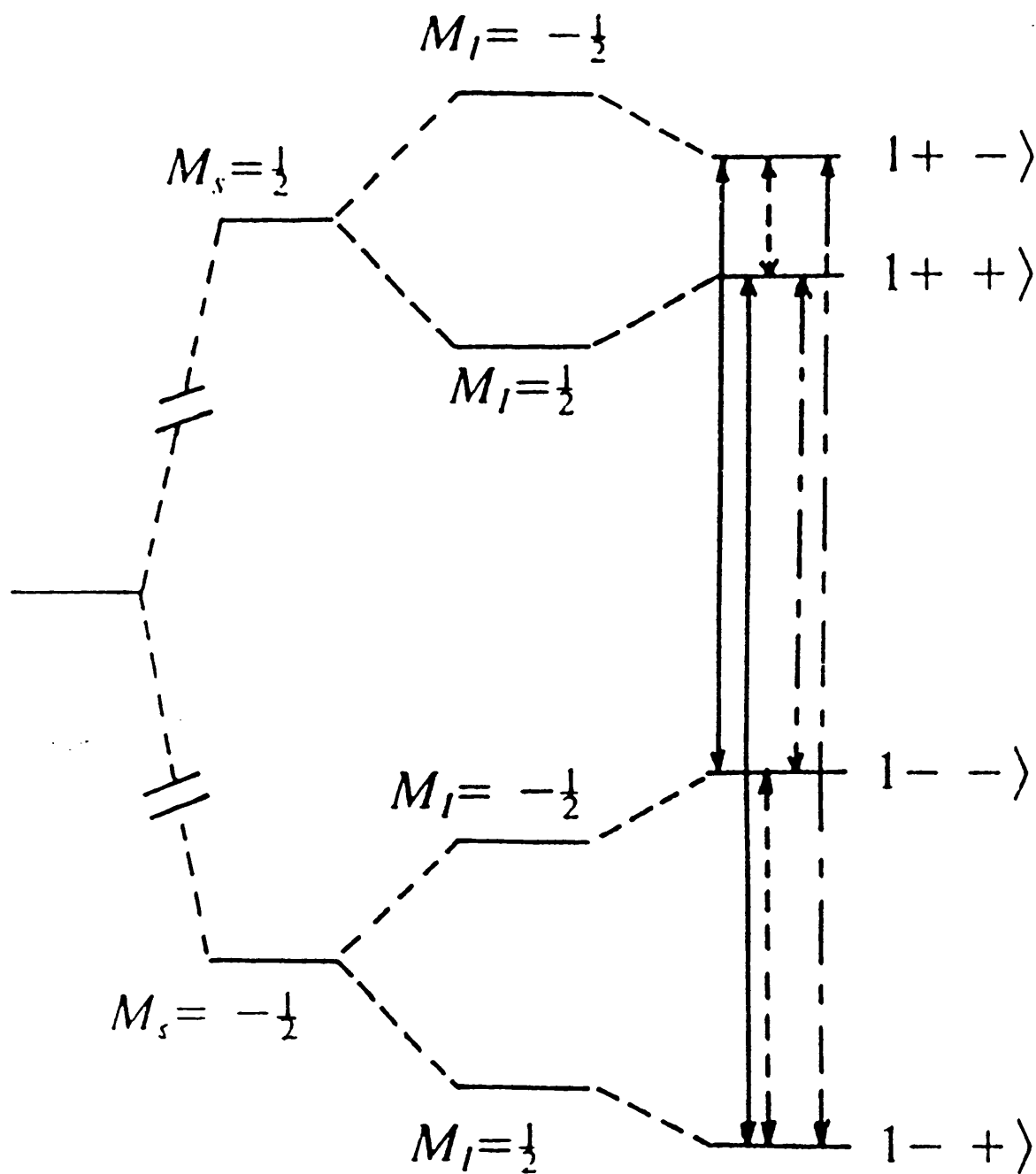
$$\frac{I_{\text{forbidden}}}{2I_{\text{allowed}}} = \frac{A_{xz}^2 + A_{yz}^2}{8g^2\beta^2 B_0^2}$$

6.5.2

All the symbols have their usual meaning. When the hyperfine interaction is isotropic, no mixing of states, which leads to the forbidden transitions becoming slightly allowed, occurs. The nuclear modulation effect is a consequence, therefore, of

FIGURE 6.5.3

Energy level diagram for $S = I = 1/2$ where the nuclear Zeeman interaction is much greater than the hyperfine interaction. States are labelled $|M_S M_I\rangle$ where $+$ $\equiv 1/2$ and $- \equiv -1/2$. First-order allowed transitions ———; first-order forbidden transitions - - - -; 'ENDOR' transitions -----. (After Pilbrow [12])



anisotropic coupling (eg a dipolar interaction) and is observable only in the limit where the nuclear Zeeman interaction is much greater than the hyperfine interaction.

In practice, the nuclear modulation effect is measured using a three pulse experiment as this has some advantages over the two-pulse experiment.⁹ For three-pulse echoes (stimulated echoes), all of which are $\pi/2$ pulses, the first two pulses are spaced by a time τ while the third pulse is spaced a time T after the second. The echo envelope is recorded by setting τ to fixed value and varying T . The three-pulse echo modulation function for an $S = 1/2$, $I = 1/2$ system (*i.e* for a system whose energy levels are described in figure 6.5.3) is given by:¹¹

$$V(\tau, T) = 1 - 1/2k\{\sin^2 1/2\omega_r\tau[1 - \cos\omega_r(\tau + T)] + \sin^2 1/2\omega_s\tau[1 - \cos\omega_s(\tau + T)]\} \quad 6.5.3$$

where ω_r and ω_s are the superhyperfine intervals in the upper and lower manifolds respectively and k is the depth parameter, defined in reference 11. The anisotropic hyperfine coupling constants can then be extracted from the modulation decay, the fourier transform of which gives peaks at the nuclear spin transition or ENDOR frequencies. If $\omega_r\tau$ is equal to an integer then the $\cos\omega_r(\tau + T)$ term vanishes and vice versa. Thus, τ can be set at values that can attenuate either the hyperfine frequencies in the lower or the upper manifold.

ESEEM SPECTRA

Two-pulse echo induced absorption spectra, and three-pulse nuclear modulation experiments have been performed. As for the cw spectra, the field strengths of all the observed transitions in the two-pulse echo induced absorption spectra allow the orientations of the four $[^{50}\text{Cr}(^{17}\text{OH}_2)_6]^{3+}$ cations to be determined with respect to the external magnetic field direction.

Single crystal experiments were undertaken on $[^{50}\text{Cr}(^{17}\text{OH}_2)_6]^{3+}$ doped into the CsGaSH lattice. The crystal was orientated in the same position as for the BetbGa_ cw data set. Two-pulse echo induced absorption spectra were first recorded. The three-pulse nuclear modulation experiments were then recorded for the three $\Delta M_s =$

± 1 transitions corresponding to the hexa-aqua-cation whose principal ZFS direction is normal to the field. These transitions correspond to $1/2 \leftrightarrow 3/2$, $-1/2 \leftrightarrow 1/2$, $-3/2 \leftrightarrow -1/2$, ΔM_S transitions. τ values of 112, 136 and 200 ns were used in these experiments. The apparatus was attenuated to give a microwave pulse width of approximately 6 G. A complete data set for just one orientation is presented in figures 6.5.4 - 6.5.10.

The two-pulse echo-induced absorption spectrum presented here, shows the Zeeman lines to have an irregular band shape. Some of the Zeeman lines are seemingly split into two bands of unequal intensities. This observation repeats for the other two-pulse absorption sweep spectra recorded which are not presented. cw spectra were recorded at room temperature after these measurements and no splitting of the lines observed suggesting that the irregular band shape is not a consequence of an irreversible crystal defect induced on cooling. A possible explanation for this observation would be that there is a reversible phase transition on cooling which results in more than four possible orientations for the $[^{50}\text{Cr}(^{17}\text{OH}_2)_6]^{3+}$ cations within the magnetic unit cell. This explanation seems unlikely however, since the reported cw spectra of this system recorded at 300 and 4.2 K³ give no indication that the Zeeman lines become split on cooling. A more likely explanation would be that the irregular band shape found in the echo-induced absorption sweep is an artefact of the modulation experiment. Direct comparison of cw EPR with echo-induced absorption spectra is not wholly justified since the general appearance of the Zeeman lines in the modulation experiment may have a very marked dependence on the width of the microwave pulse relative to the width of the inhomogeneously broadened band. As a consequence of increase in pulse width, the resonance condition will be met over a wider field range leading to an apparent broadening of the band. Likewise the appearance of the absorption sweep may differ markedly from the corresponding cw spectra since in the modulation experiment, the echo intensity will depend on both the total magnetisation from all the spin packets contained within the pulse and also the transverse relaxation efficiency which may vary across an inhomogeneously broadened band.

The modulation and fourier transform recorded for the $1/2 \leftrightarrow 3/2$ transition at 2812 Gauss are shown in figures 6.5.5 and 6.5.6. The nuclear transition frequency for

FIGURE 6.5.4

Two-pulse echo induced absorption sweep of $[^{50}\text{Cr}(^{17}\text{OH}_2)_6]^{3+}$ doped into CsGaSH recorded at a temperature of 3.8 K. Crystal orientated with one crystallographic three-fold axis normal to the field direction.

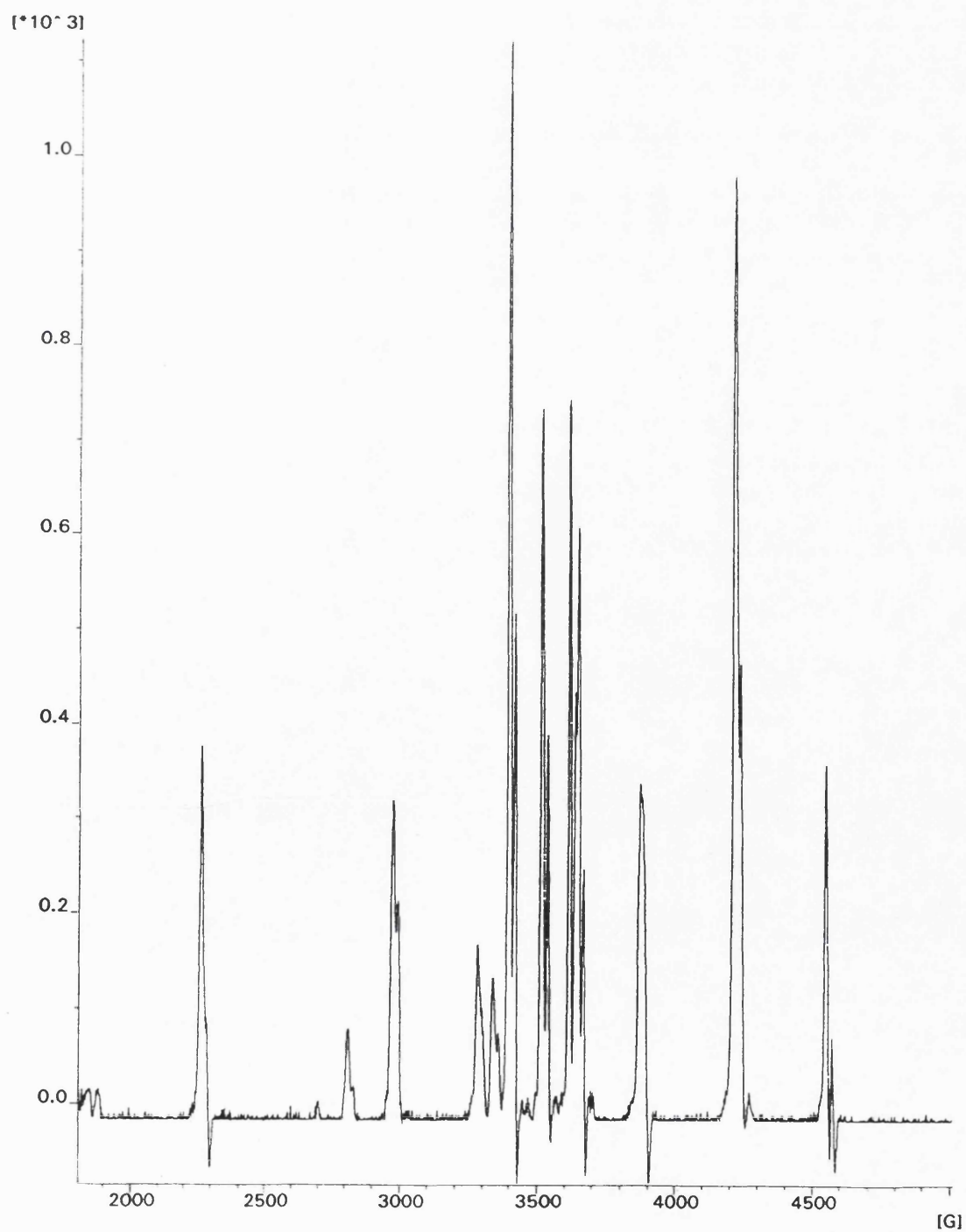


FIGURE 6.5.5

Three-pulse electron spin echo nuclear modulation spectra recorded for the $1/2 \leftrightarrow 3/2$ transition of the $[\text{}^{50}\text{Cr}(\text{}^{17}\text{OH}_2)_6]^{3+}$ paramagnet, doped into CsGaSH, whose principal ZFS direction is normal to the field. Spectra recorded at a field of 2812 Gauss and a temperature of 3.9 K with τ values of 112, 136 and 200 ns.

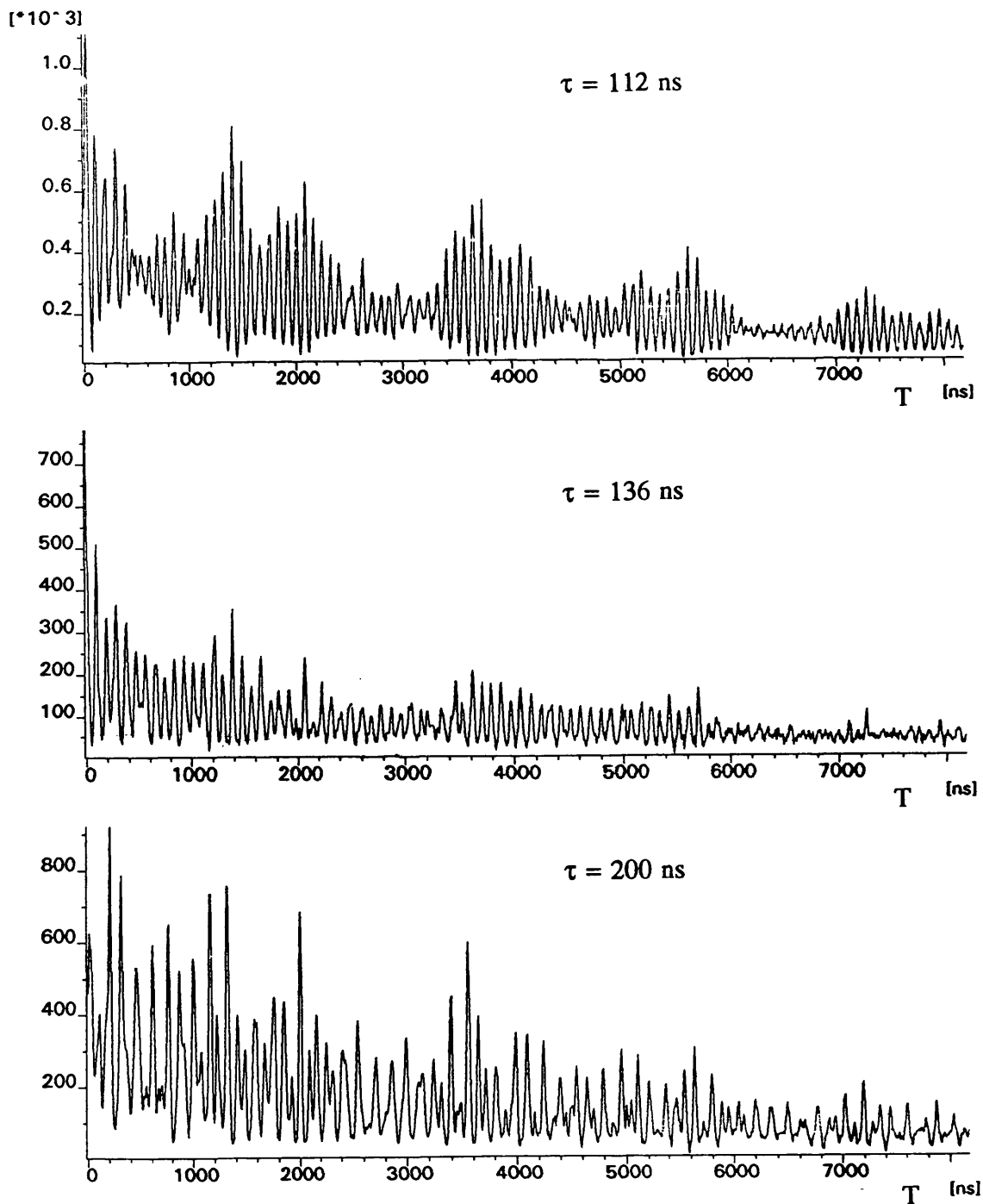


FIGURE 6.5.6

Fourier transforms of the ESEEM spectra recorded for the $1/2 \leftrightarrow 3/2$ transition of the $[^{50}\text{Cr}(^{17}\text{OH}_2)_6]^{3+}$ paramagnet, doped into CsGaSH, whose principal ZFS direction is normal to the field. Spectra recorded at a field of 2812 Gauss and a temperature of 3.9 K with τ values of 112, 136 and 200 ns.

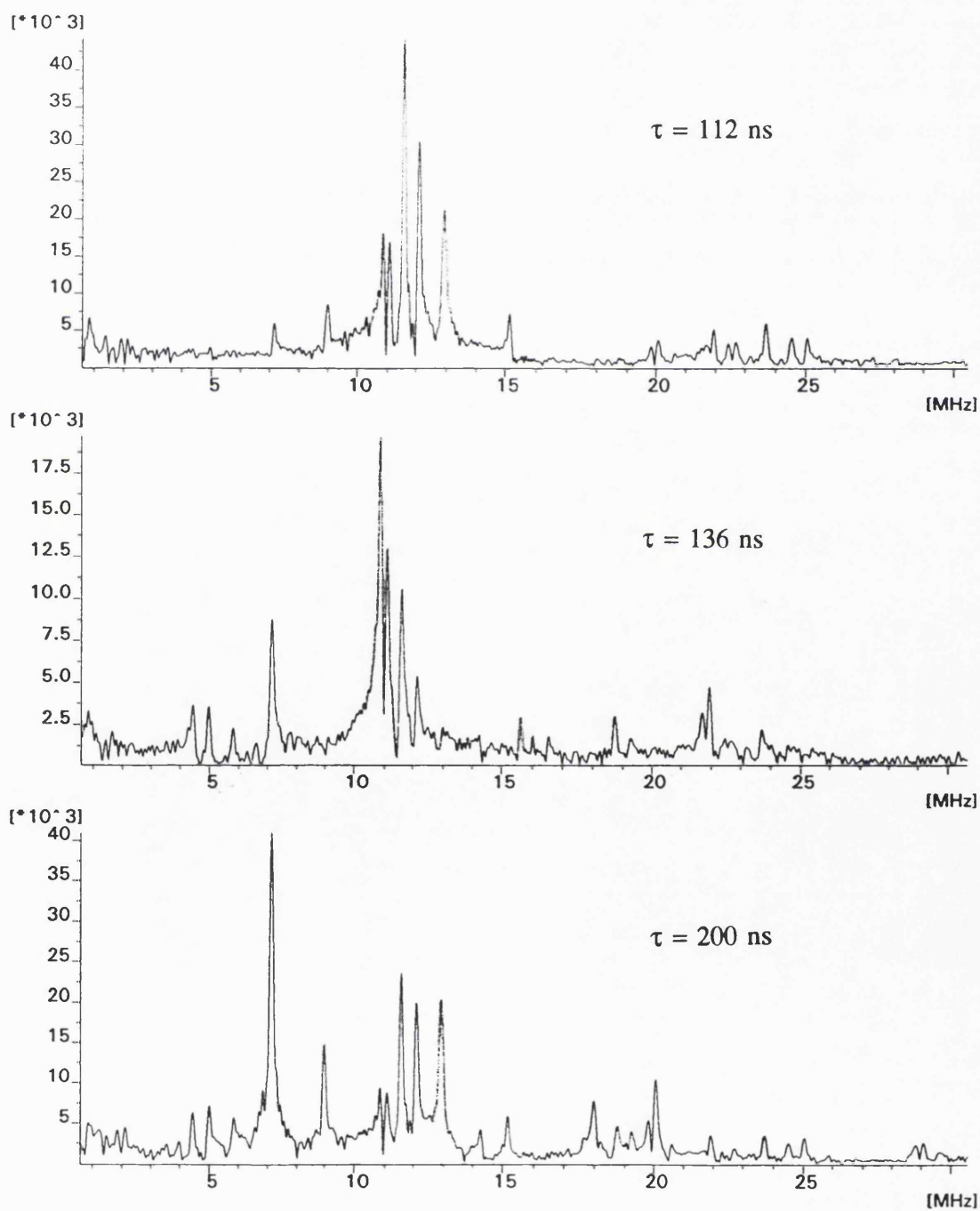


FIGURE 6.5.7

Three-pulse electron spin echo nuclear modulation spectra recorded for the $-1/2 \leftrightarrow 1/2$ transition of the $[^{50}\text{Cr}(^{17}\text{OH}_2)_6]^{3+}$ paramagnet, doped into CsGaSH, whose principal ZFS direction is normal to the field. Spectra recorded at a field of 3419 Gauss and a temperature of 3.9 K with τ values of 112, 136 and 200 ns.

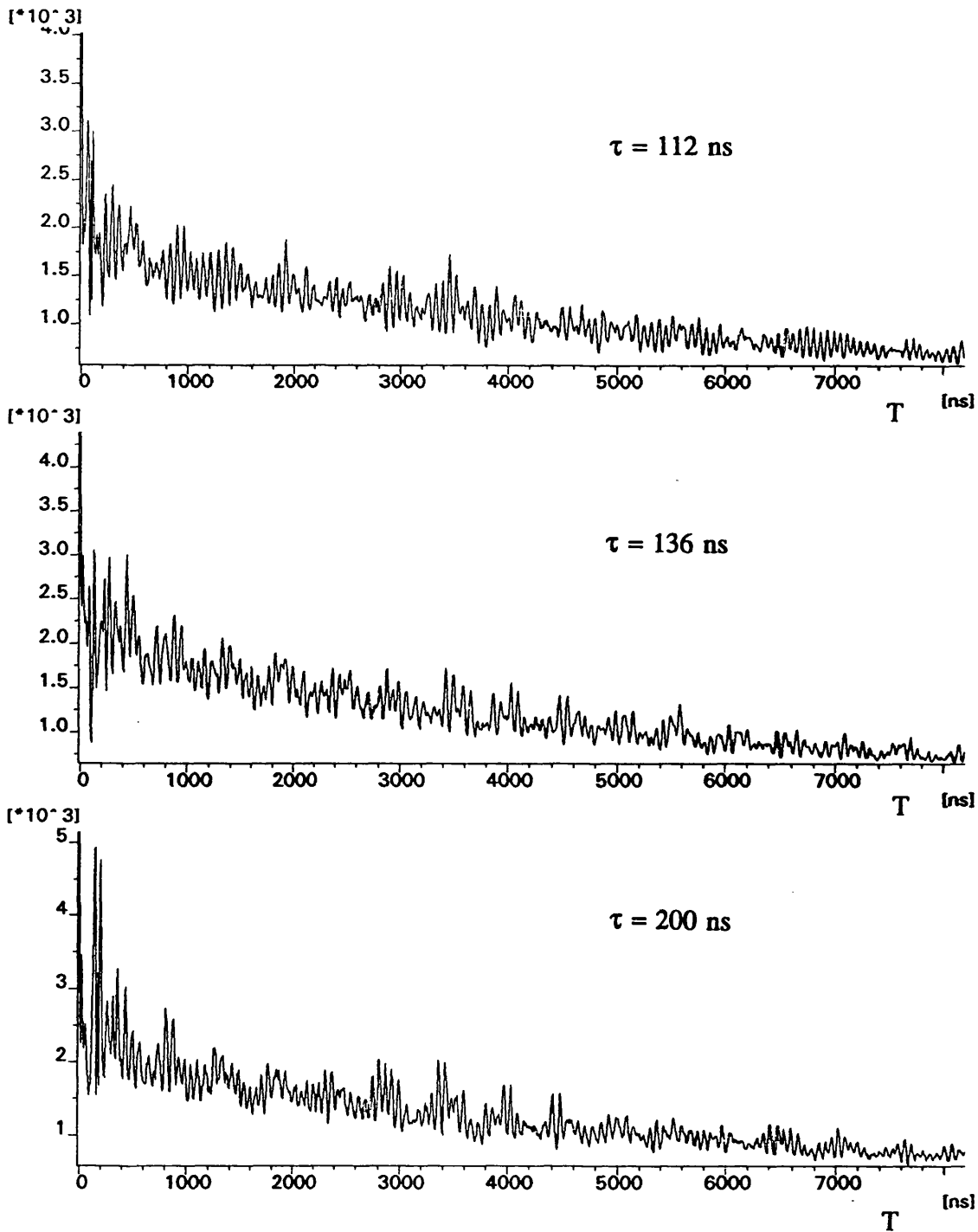


FIGURE 6.5.8

Fourier transforms of the ESEEM spectra recorded for the $-1/2 \leftrightarrow 1/2$ transition of the $[\text{}^{50}\text{Cr}(\text{}^{17}\text{OH}_2)_6]^{3+}$ paramagnet, doped into CsGaSH, whose principal ZFS direction is normal to the field. Spectra recorded at a field of 3419 Gauss and a temperature of 3.9 K with τ values of 112, 136 and 200 ns.

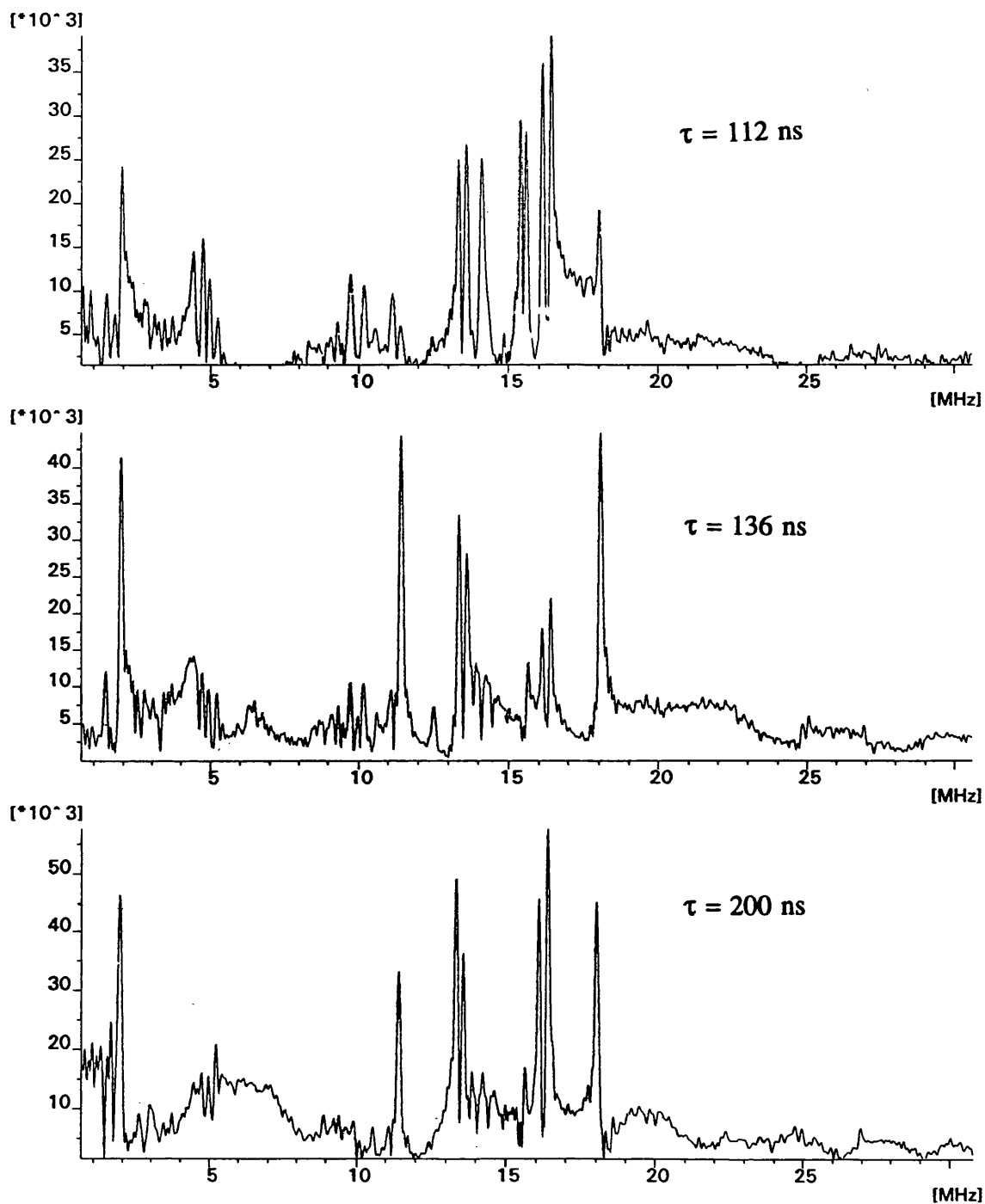


FIGURE 6.5.9

Three-pulse electron spin echo nuclear modulation spectra recorded for the $-3/2 \leftrightarrow -1/2$ transition of the $[^{50}\text{Cr}(^{17}\text{OH}_2)_6]^{3+}$ paramagnet, doped into CsGaSH, whose principal ZFS direction is normal to the field. Spectra recorded at a field of 4240 Gauss and a temperature of 3.9 K with τ values of 112, 136 and 200 ns.

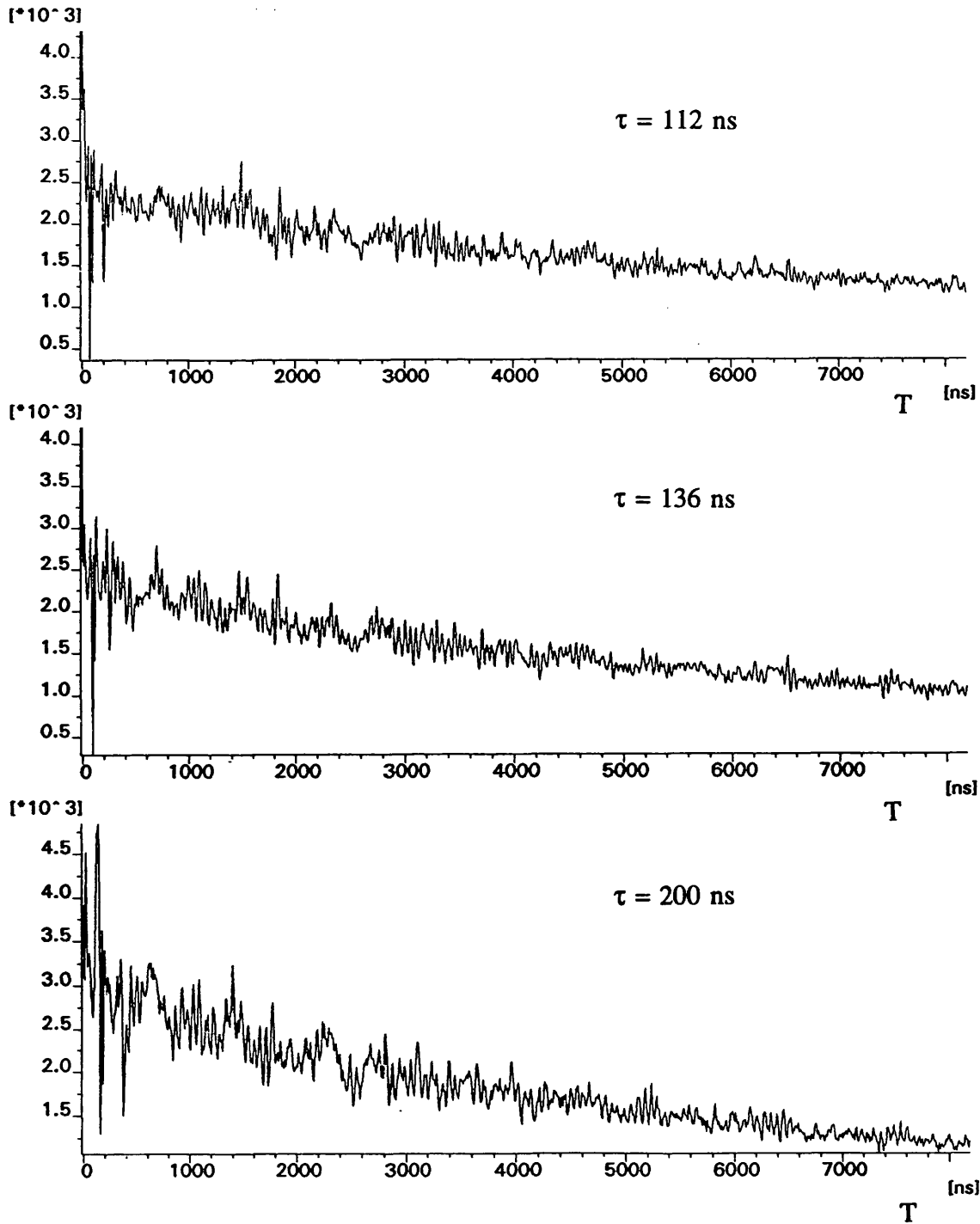
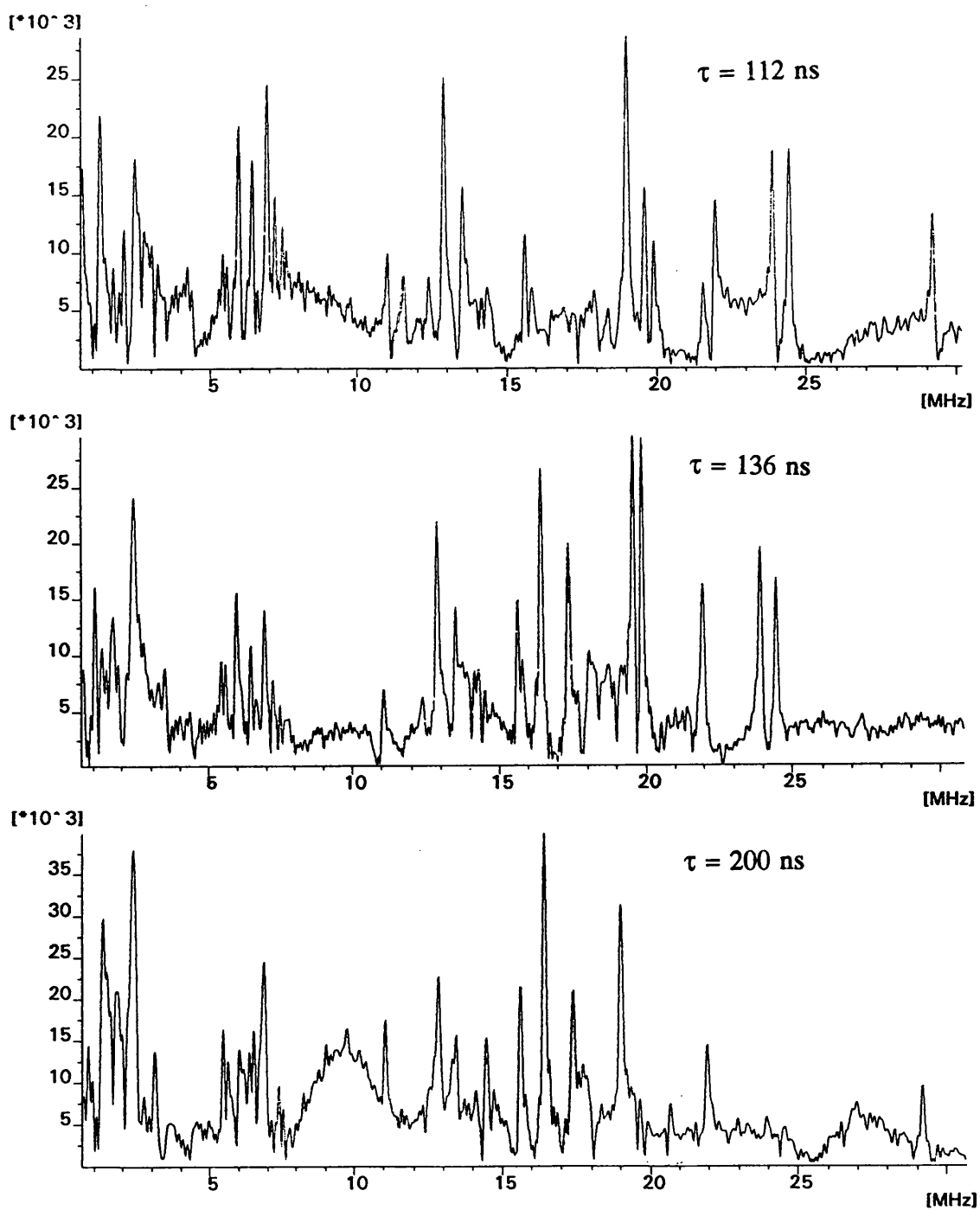


FIGURE 6.5.10

Fourier transforms of the ESEEM spectra recorded for the $-3/2 \leftrightarrow -1/2$ transition of the $[\text{}^{50}\text{Cr}(\text{}^{17}\text{OH}_2)_6]^{3+}$ paramagnet, doped into CsGaSH, whose principal ZFS direction is normal to the field. Spectra recorded at a field of 4240 Gauss and a temperature of 3.9 K with τ values of 112, 136 and 200 ns.



the proton (ENDOR frequency) is 14.90218 MHz for a 3500 G field.¹ The modulations shown in figure 6.5.5 were recorded at a field of 2812 G so that the ENDOR frequency of the proton will occur at *ca.* 12 MHz [(2812/3500 G) X 14.90218 MHz]. The group of peaks centred around 12 MHz in the fourier transform are attributed to proton hyperfine coupling which is due to a distant dipolar interaction between the protons and the unpaired electron density on the metal. On increasing τ from 112 to 136 to 200 ns, the proton hyperfine peaks decrease in intensity relative to the peak at *ca.* 7 MHz which is attributed to coupling from the ¹⁷O nucleus. The suppression of hyperfine transitions by an appropriate choice of τ are well illustrated by these spectra.

The ENDOR frequency for the ¹⁷O nucleus is 1.6, 2.0 and 2.4 MHz for fields of 2812, 3419 and 4240 Gauss respectively. The fourier transforms of the modulations show an increasing number of hyperfine transitions for the higher field $\Delta M_s = \pm 1$ transitions, with more lines centred around the ¹⁷O ENDOR frequency. The three Zeeman transitions from which the three-pulse modulation spectra were recorded correspond to the $1/2 \leftrightarrow 3/2$, $-1/2 \leftrightarrow 1/2$, $-3/2 \leftrightarrow -1/2$ ΔM_s transitions of a paramagnet whose principle ZFS direction is orientated normal to the field. It is well established that the transition probabilities between super hyperfine energy levels within Cr³⁺ systems depend explicitly on the ΔM_s transition which is used to obtain the nuclear modulation.¹³ Therefore, extraction of hyperfine coupling constants from multi-electron systems using time resolved EPR techniques is not a trivial task. Recent theoretical advances¹⁴ have led to analytical expressions for the ESEEM frequencies and amplitudes of multi-electron systems coupled to $I = 1/2$ nuclei. In this treatment, the spin system is described in terms of a set of noninteracting two-level systems. The total ESEEM spectrum is then calculated as a weighted superposition of the subspectra. The underlying assumption in this analysis is that $h\nu \gg ZFS \gg$ microwave pulse width. In the limit where $h\nu \gg ZFS$, the electron spin states can conveniently be labelled by their M_s quantum numbers which simplifies the analysis. If $ZFS \gg$ microwave pulse width, then it is unlikely that two-level systems with a common level are both close to resonance. Consequently, this restricts attention to single-photon microwave transitions. This treatment was shown to account for the observed spectral behaviour of ¹⁵N and ³¹P nuclei coupled to Mn²⁺ in

a guanosine diphosphate (GDP) complex with the protein *N-ras* p21.¹⁴ A similar treatment might also be appropriate for calculation of the superhyperfine coupling constants in the $[^{50}\text{Cr}(^{17}\text{OH}_2)_6]^{3+}$ complex. At this juncture, the chemical information that can be obtained from this experiment is limited. The peaks centred about the ^{17}O ENDOR frequency are evidence of dipolar coupling arising from the ^{17}O nucleus. This form of coupling can arise as a consequence of unpaired electron density occupying a 2p-type orbital on the oxygen. In addition, however, there will be a dipolar interaction involving the ^{17}O nuclei and unpaired electron density on the metal so that nothing can be said about the amount of spin residing on the oxygen atom without detailed calculation and spectral simulation.

6.6 Electronic and Emission spectra of chromium(III) within the alum lattice.

The luminescence observed from chromium(III) as an impurity within the alum lattice has been a subject of study ever since the early development of crystal field theory.¹⁵⁻¹⁸ However, the assignment of the luminescence and an understanding of the spectral changes with alum type has required crystallographic¹⁹ and Raman²⁰ data which has only recently been obtained. This section presents a brief review of research undertaken in this area since it is of relevance to this work.

The luminescence spectra recorded for the β alum of CsCrSH and the α alum of RbCrSH are presented in figure 6.6.1. The luminescence is attributed to the ${}^2E \rightarrow {}^4A_2$ (O_h) transition. The electronic origin is found at 14943 cm^{-1} for RbCrSH with an observed splitting of 3 cm^{-1} attributable to the zero field splitting of the 2E excited state. For CsCrSH, the electronic origin is found 460 cm^{-1} lower in energy. High resolution electronic spectroscopy of CsCrSH¹⁸ has permitted an estimate of 120 cm^{-1} for the zero field splitting of the excited state for this alum. According to the analysis by Macfarlane,² the splitting of the 2E term depends predominately on the magnitude of the trigonal field splitting v and spin orbit coupling λ , increasing in proportion to both these parameters.

Recent work by Armstrong and Berry,²¹ in which the luminescence of chromium(III) has been studied in a number of alum lattices, has allowed a qualitative account of the spectra to be given in terms of the mode of water co-ordination to the chromium(III) centre. An account of their inferences is given here.

The Tanabe-Sugano diagram for chromium(III) is shown in figure 6.6.2. Since the ${}^2E \rightarrow {}^4A_2$ transition is an intra t_{2g} transition, its energy does not depend on $10Dq$ (the crystal field splitting parameter) as is apparent in the Tanabe-Sugano diagram. The electronic origin of chromium(III) within the β alum CsCrSH is found 460 cm^{-1} lower in energy than the corresponding transition of the α alum of RbCrSH. This is interpreted by Armstrong and Berry²¹ as a consequence of a greater reduction in the Racah parameter, B , from the free ion value, for the chromium(III) hexa-aqua complex in the β compared to the α environment. Reduction of the Racah parameter from the free ion value is viewed as arising from an expansion of the t_{2g} orbitals on complexation, which leads to a reduced interelectronic repulsion. Armstrong and

Figure 6.6.1

Luminescence from (a) the α alum of RbCrSH, (b) the β alum of CsCrSH. The intense bands found at 14483 cm^{-1} for the β alum and at 14940 cm^{-1} for the α alum are assigned as the non-phonon, electronic origin energies for chromium(III) ${}^2E_g \rightarrow {}^4A_{2g}$ emission. The origin is split by *ca.* 3 cm^{-1} for RbCrSH. For CsCrSH the splitting of the 2E_g term is too large for the emission from the upper level to be observed. Assignment of the vibrational structure is given in reference [21].

Spectra recorded between 12435.21 and 15435.21 cm^{-1} (Absolute wavenumbers)
Sensitivities: RbCrSH: $151245\text{ counts sec}^{-1}$; CsCrSH: $91466\text{ counts sec}^{-1}$; 80 K; step size 1 cm^{-1} ; integration time: 1 second; 514.53 nm radiation, 10 mw power at sample).

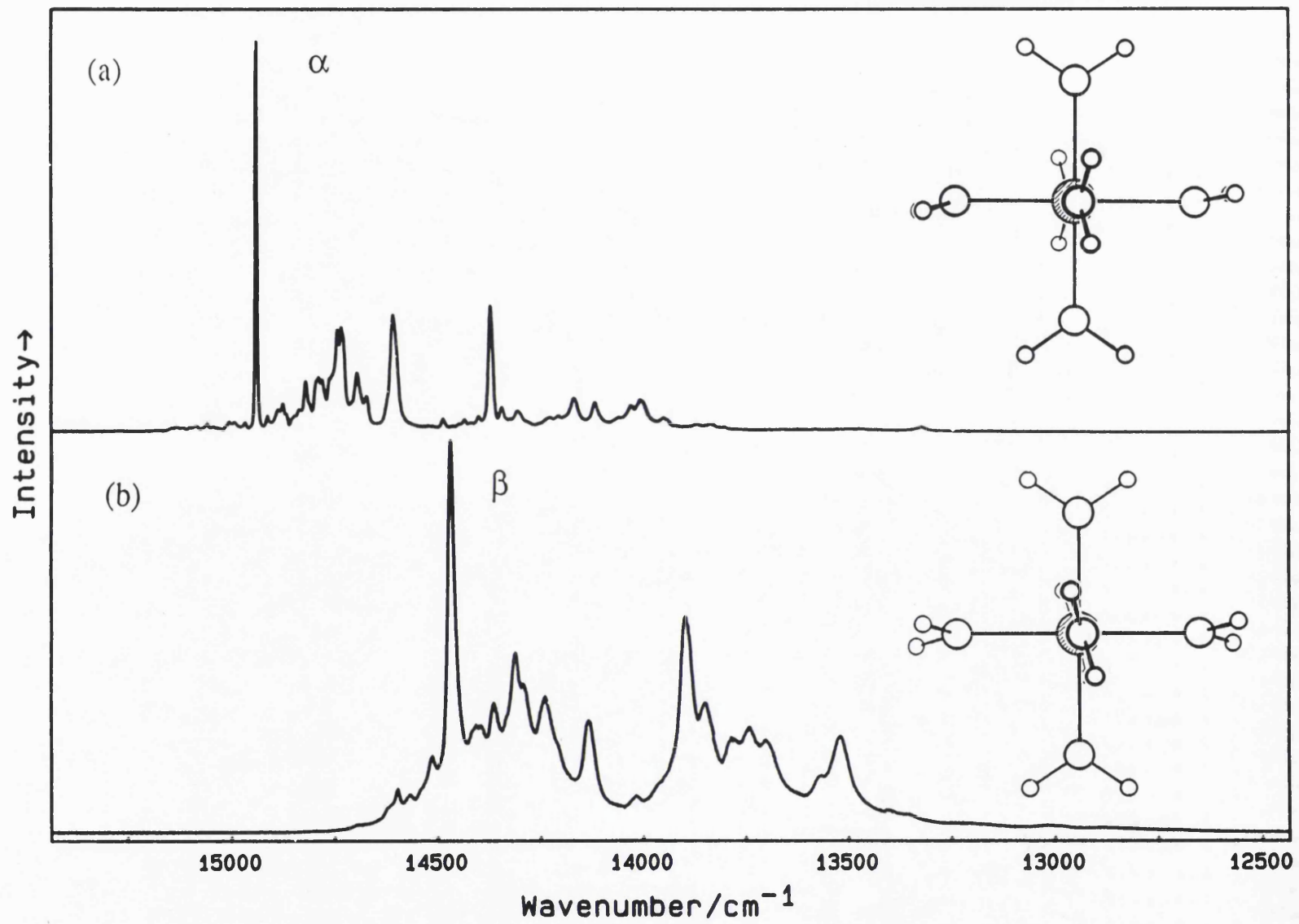
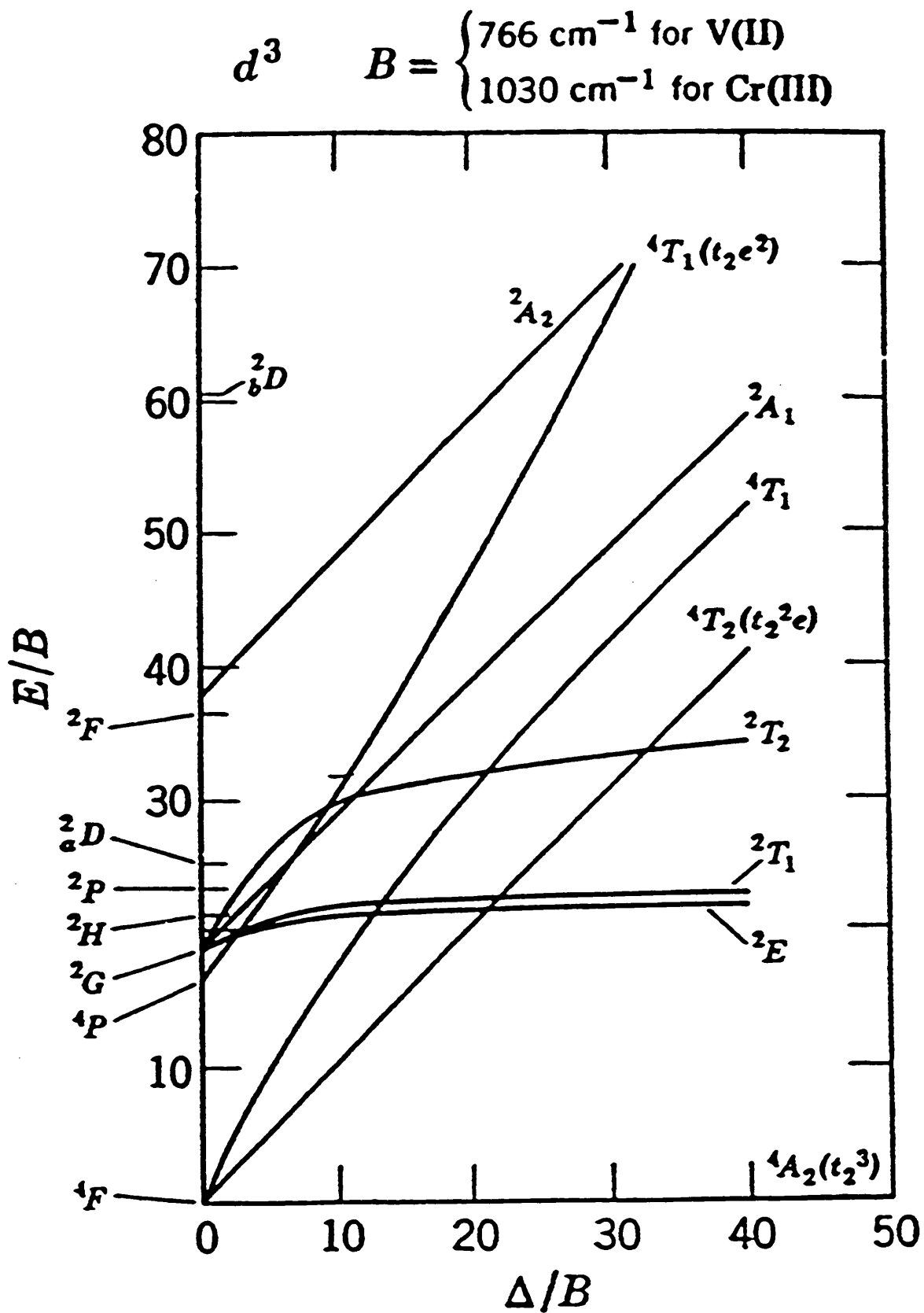


FIGURE 6.6.2

Energy level diagram for d^3 configuration in octahedral symmetry. (After Tanabe and Sugano [22])



Berry infer, therefore, that there is a greater degree of π overlap for the $[\text{Cr}(\text{OH}_2)_6]^{3+}$ cation in the β compared to the α environment. However, the formation of molecular orbitals involving the metal d- and ligand p-orbitals is also thought to reduce spin-orbit coupling through damping of orbital angular momentum.²³ Greater π overlap would therefore act to reduce the splitting of the ${}^2\text{E}$ term. In order to account for the greater splitting of the ${}^2\text{E}$ term for the β compared to the α alums Armstrong and Berry²¹ conclude that the mode of water co-ordination the chromium(III) centre found in the β alum of CsCrSH compared to the α alum of RbCrSH leads to a greater trigonal field.

In summary, the luminescence of chromium(III) within the alum lattice suggests there is greater π bonding within the $[\text{Cr}(\text{OH}_2)_6]^{3+}$ complex for β compared with α modes of water co-ordination and that the π interaction within the β alums must be highly anisotropic in order to account for the large splitting of the ${}^2\text{E}_g$ term.

REFERENCES

1. Bruker Almanac (1993)
2. R. M. Macfarlane, *J. Chem. Phys.*, **47**, 2066 (1967).
3. A. G. Danilov and A. Manoogian, *Phys. Rev.*, **B6**, 4097 (1972).
4. F. E. Mabbs and D. Collison, *Electron Paramagnetic Resonance of d Transition Metal Compounds*, Elsevier Amsterdam (1992).
5. A. Manoogian and A. Leclerc, *J. Chem. Phys.*, **63**, 4450 (1975).
6. CW spectral simulations performed by D. Collison Manchester University.
7. J. K. Beattie, S. P. Best, B. W. Skelton, A. H. White, *J. Chem. Soc., Dalton Trans*, 2105 (1981).
8. J. E. Wertz, J. R. Bolton, *Electron Spin Resonance, Elementary Theory and Practical Applications*, McGraw-Hill inc, (1972).
9. *Pulsed EPR: A new field of applications* Ed. C.P Keijzers, E.J. Reijerse, and J. Schmidt, Koninklijke Nederlandse Akademie van Wetenschappen (1989).
10. W. B. Mims, in *Electron Paramagnetic resonance* Ed. S. Geschwind, Chapter 4, Plenum Press, New York (1972).
11. W. B. Mims and J. Peisach, in *Biological Magnetic Resonance*, Ed. L. J. Berliner and J. Reuben, p 213, Plenum Press, New York (1981).
12. J. R. Pilbrow, *Transition ion Electron Paramagnetic Resonance*, Clarendon Press, Oxford, (1990).
13. D. Grischkowsky and S. R. Hartmann, *Phys. Rev.*, **B2**, 60 (1970).
14. R. G. Larsen, C. J. Halkides, D. J. Singel, *J. Chem. Phys.*, **98**, 6704 (1993).
15. H. Bohm, *Ann. Physik.*, **32**, 521 (1938).
16. G. J. Goldsmith and F. V. Shallcross, *J. Mol. Spectry.*, **16**, 296 (1965).
17. Y. Uesaka, T. Ban and I. Tsujikawa, *J. Phys. Soc., Japan*, **30**, 228 (1971).
18. L. Grabner, R. A. Forman, E. Y. Wong, *Phys. Rev. B*, **6**, 797 (1972).
19. S. P. Best and J. B. Forsyth, *J. Chem. Soc., Dalton Trans*, 395 (1990).
20. S. P. Best, J. K. Beattie, and R. S. Armstrong, *J. Chem. Soc., Dalton Trans*, 2611 (1984).
21. R. S. Armstrong and A. Berry, unpublished results.
22. Tanabe and Sugano, *J. Phys. Soc. Jpn.*, **9**, 753 (1954).
23. M. Gerloch and J. R. Miller, *Progr. Inorg. Chem.*, **10**, 1 (1968).

APPENDICES

Appendix A

**Single crystal Raman spectra of rubidium alums
between 1200 and 4000 cm^{-1}**

Figure A.1

Single crystal Raman spectra of $\text{RbV}(\text{SO}_4)_2 \cdot 12\text{D}_2\text{O}$ between 1200 and 4000 cm^{-1} .
Sensitivities: $X'(Z Z)Y'$ 52997 counts sec^{-1} ; $X'(Y'X')Y'$ 23807 counts sec^{-1} ;
 $X'(Z X')Y'$ 14582 counts sec^{-1} (81 (6) K; step size 1 cm^{-1} ; spectral bandwidth
3.58 cm^{-1} at 2600 cm^{-1} ; integration time 4 seconds; 457 nm radiation, 60 mw power
at sample).

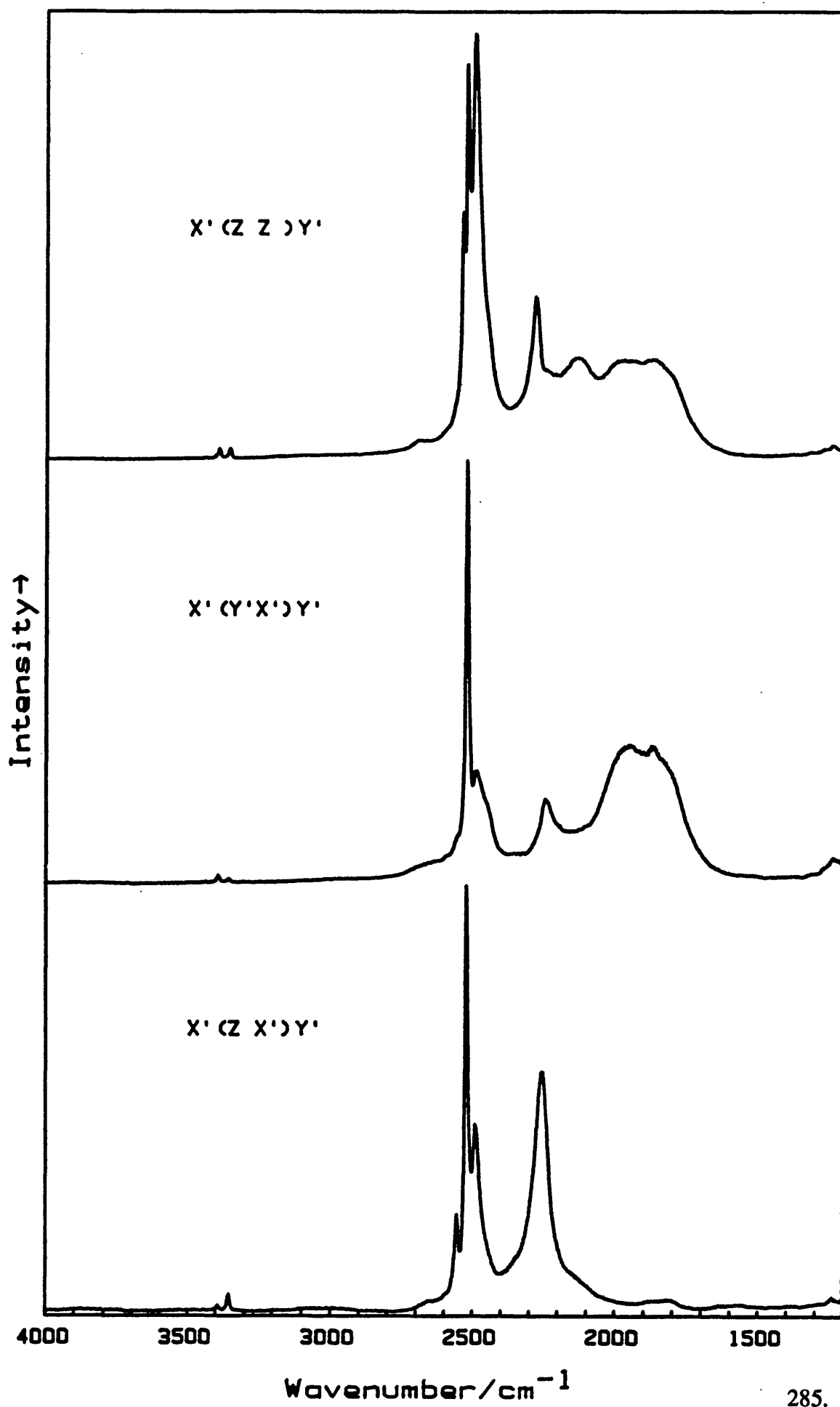


Figure A.2

Single crystal Raman spectra of $\text{RbTi}(\text{SO}_4)_2 \cdot 12\text{H}_2\text{O}$ between 1200 and 4000 cm^{-1} .
Sensitivities: $X'(Z Z)Y'$ 70747 counts sec^{-1} ; $X'(Y'X')Y'$ 12322 counts sec^{-1} ;
 $X'(Z X')Y'$ 10703 counts sec^{-1} (90 (9) K; step size 1 cm^{-1} ; spectral bandwidth
6.12 cm^{-1} at 2600 cm^{-1} ; integration time: $X'(Z Z)Y'$ 4 seconds, $X'(Y'X')Y'$ 1.5
seconds, $X'(Z X')Y'$ 2 seconds; 413 nm radiation, 80 mw power at sample).

X' (Z Z)Y'

X' (X'X')Y'

X' (Z X')Y'

Intensity →

4000 3500 3000 2500 2000 1500

Wavenumber/cm⁻¹

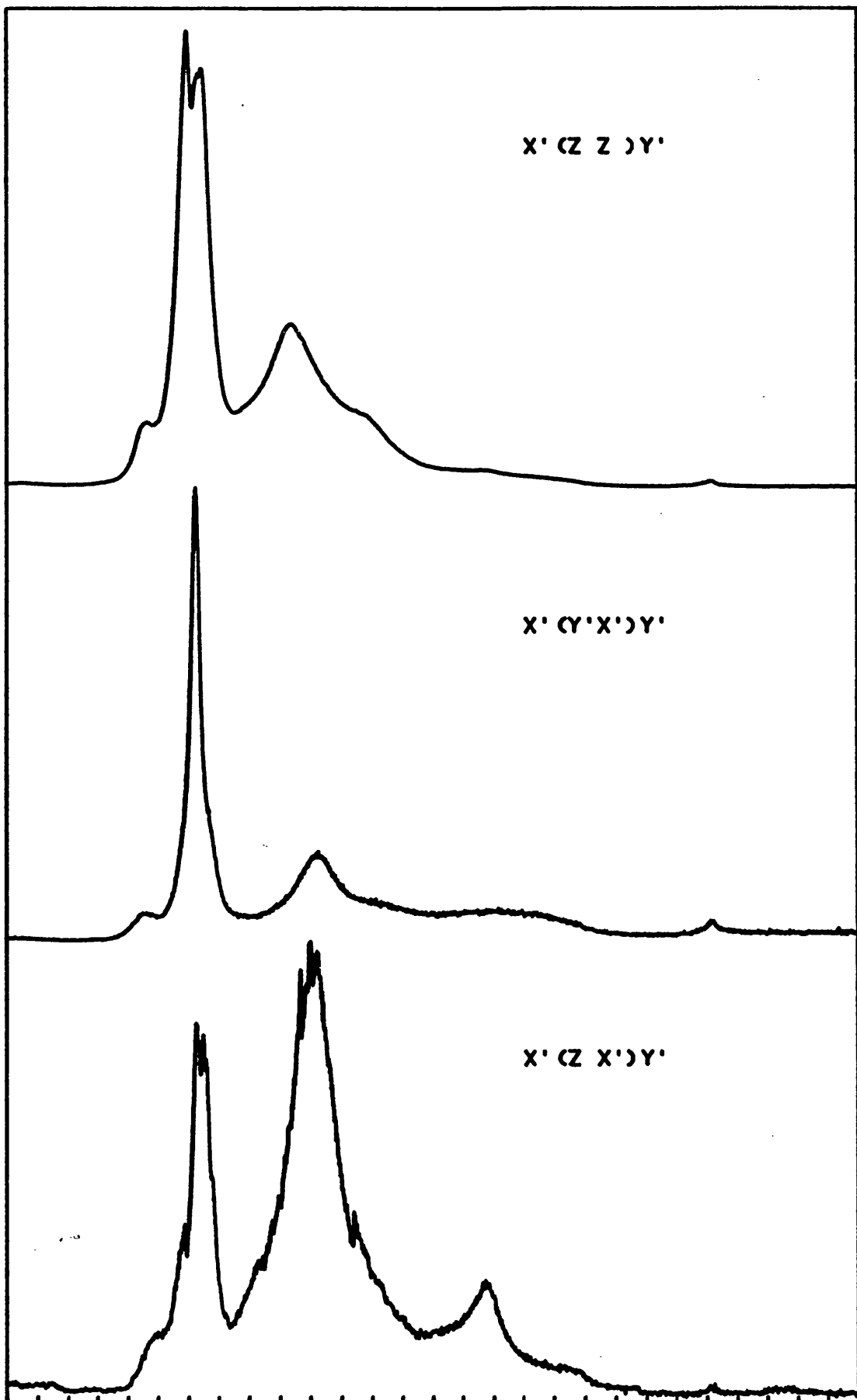


Figure A.3

Single crystal Raman spectra of $\text{RbCr}(\text{SO}_4)_2 \cdot 12\text{H}_2\text{O}$ between 1200 and 4000 cm^{-1} .
Sensitivities: $X'(Z Z)Y'$ 11589 counts sec^{-1} ; $X'(Y'X')Y'$ 3102 counts sec^{-1} ;
 $X'(Z X')Y'$ 2481 counts sec^{-1} (100 (10) K; step size 1 cm^{-1} ; spectral bandwidth
4.32 cm^{-1} at 2600 cm^{-1} ; integration time 4 seconds; 476 nm radiation, 60 mw power
at sample).

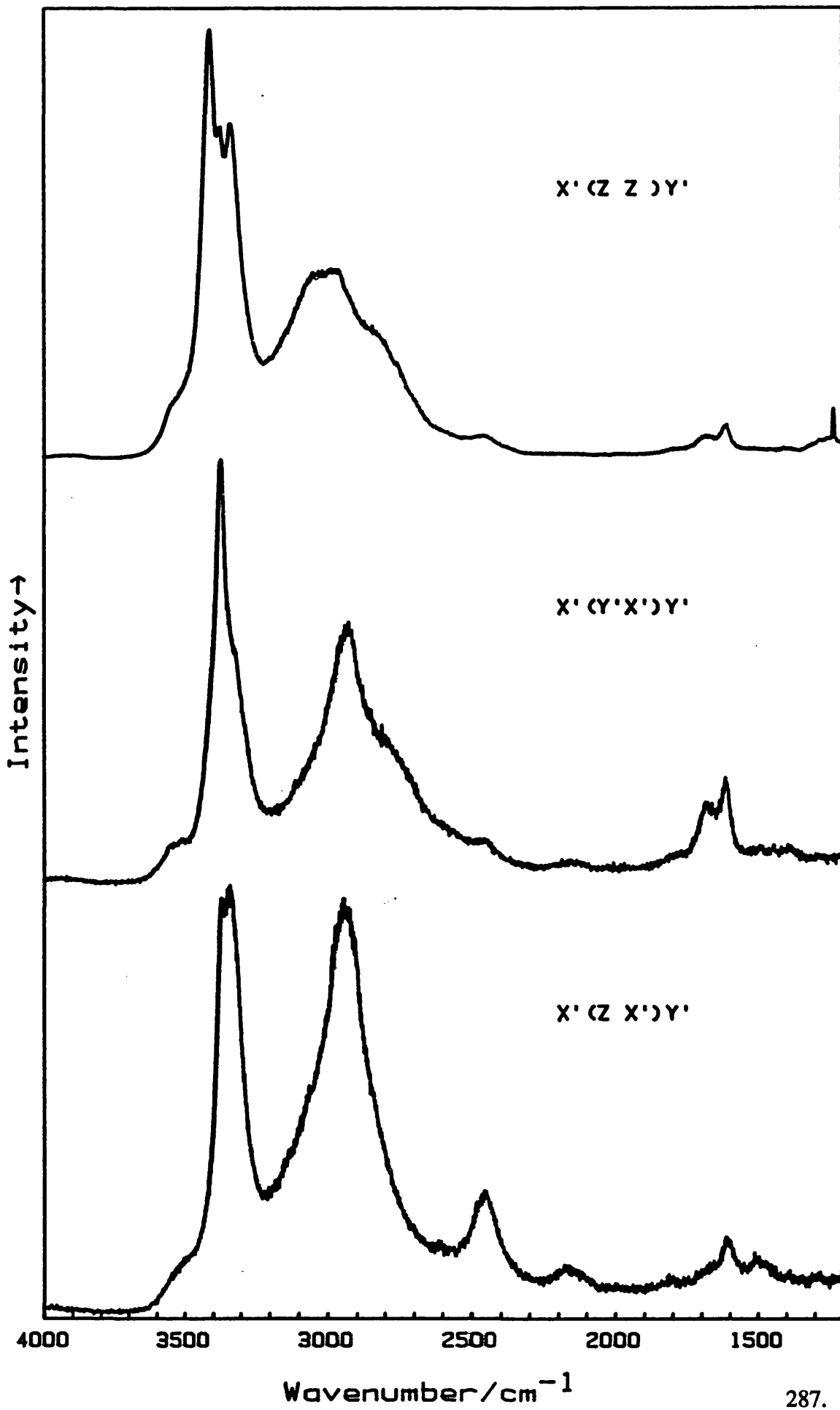


Figure A.4

Single crystal Raman spectra of $\text{RbGa}(\text{SO}_4)_2 \cdot 12\text{H}_2\text{O}$ between 1200 and 4000 cm^{-1} .
Sensitivities: $X'(Z Z)Y'$ 11387 counts sec^{-1} ; $X'(Y'X')Y'$ 4535 counts sec^{-1} ;
 $X'(Z X')Y'$ 4810 counts sec^{-1} (63 (2) K; step size 1 cm^{-1} ; spectral bandwidth:
 $X'(Z Z)Y'$ and $X'(Y'X')Y'$ 1.78 cm^{-1} , $X'(Z X')Y'$; 1.34 cm^{-1} at 2600 cm^{-1} ;
integration time 2 seconds; 514 nm radiation, 80 mw power at sample).

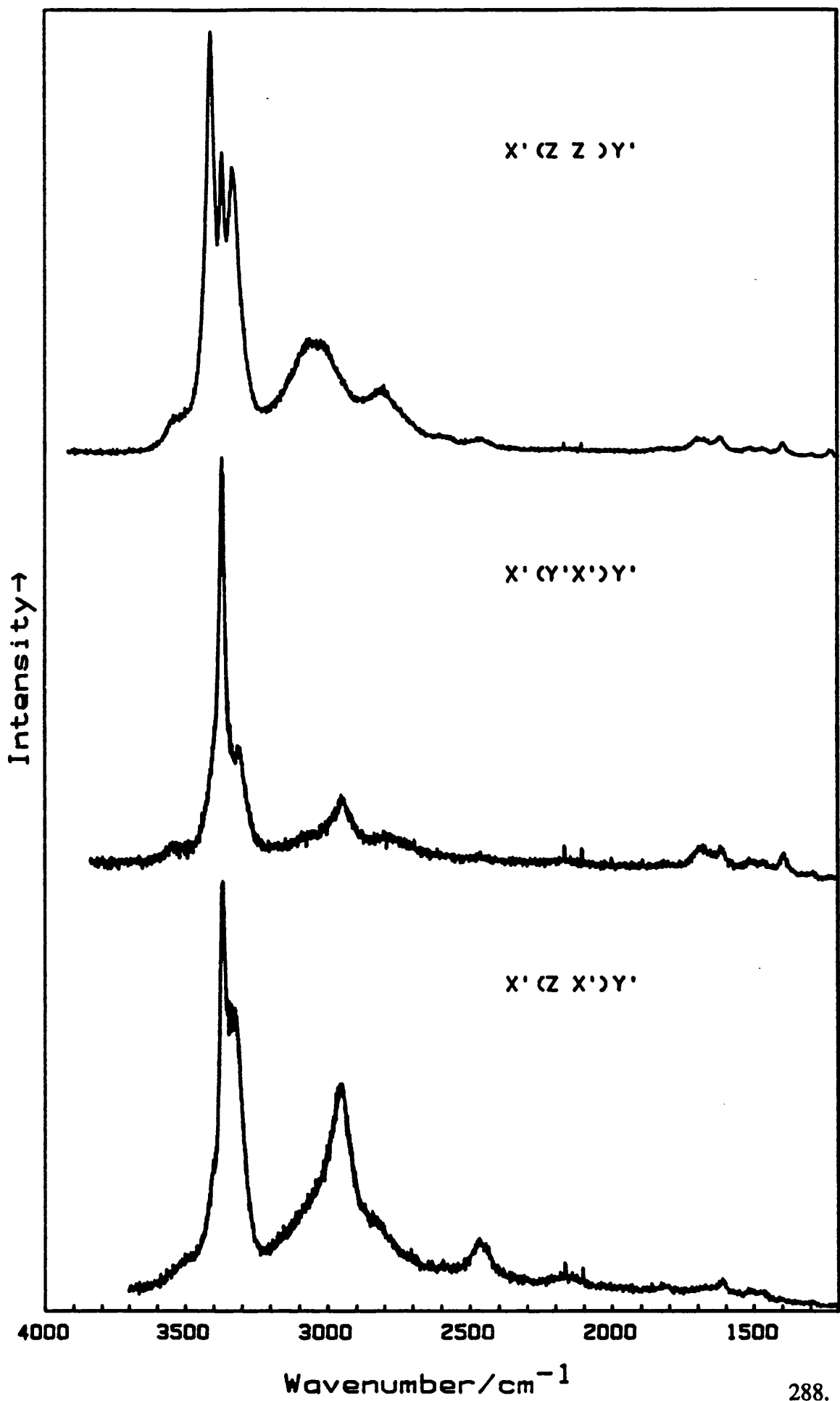


Figure A.5

Single crystal Raman spectra of $\text{RbFe}(\text{SO}_4)_2 \cdot 12\text{H}_2\text{O}$ between 1200 and 4000 cm^{-1} .
Sensitivities: $X'(Z Z)Y'$ 25234 counts sec^{-1} ; $X'(Y'X')Y'$ 7943 counts sec^{-1} ;
 $X'(Z X')Y'$ 7671 counts sec^{-1} (72 (2) K; step size 1 cm^{-1} ; spectral bandwidth
2.03 cm^{-1} at 2600 cm^{-1} ; integration time 4 seconds; 488 nm radiation, 80 mw power
at sample).

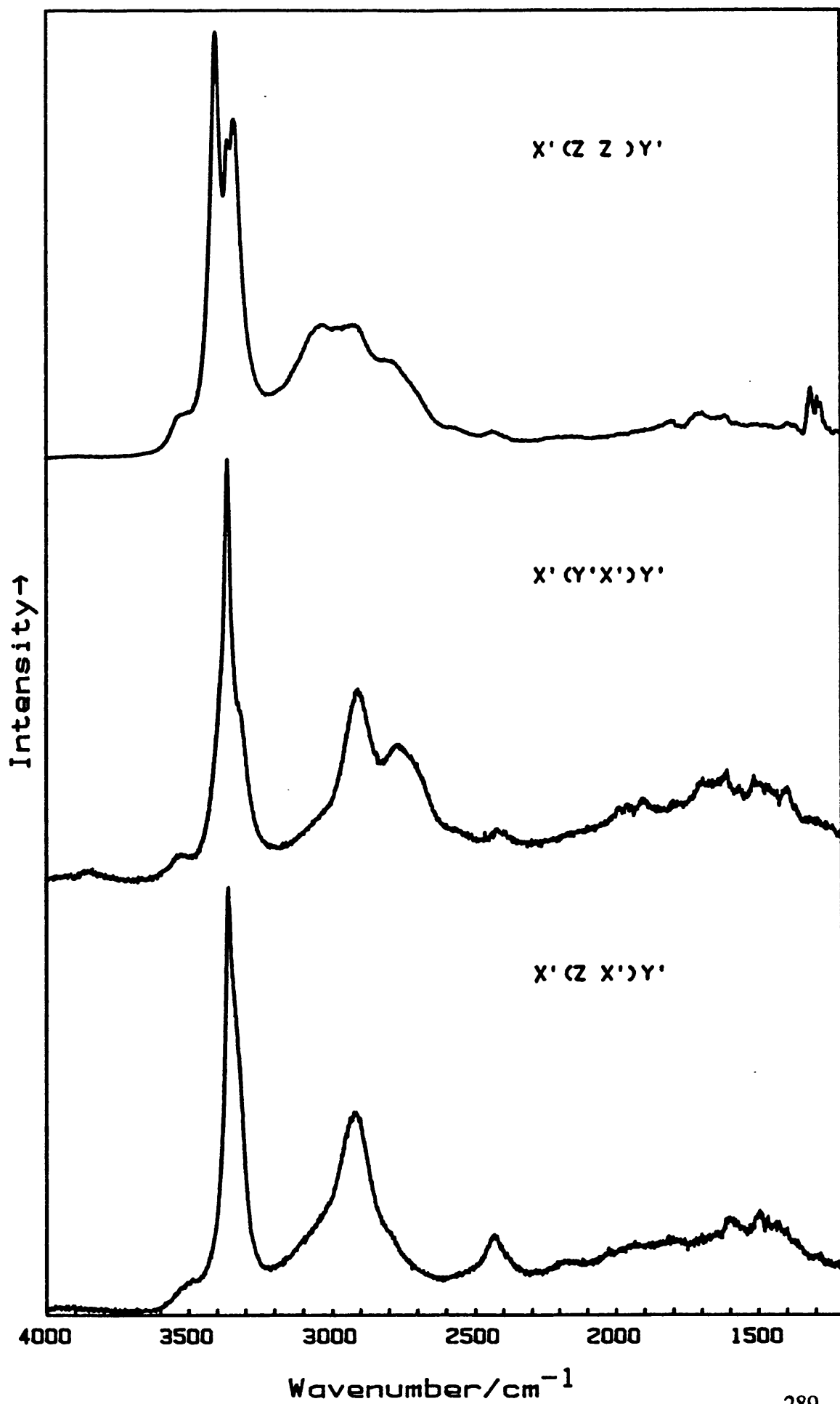


Figure A.6

Single crystal Raman spectra of $\text{RbAl}(\text{SO}_4)_2 \cdot 12\text{H}_2\text{O}$ between 1200 and 4000 cm^{-1} .
Sensitivities: X'(Z Z)Y' 8851 counts sec^{-1} ; X'(Y'X')Y' 2069 counts sec^{-1} ;
X'(Z X')Y' 3150 counts sec^{-1} (72 (1) K; step size 1 cm^{-1} ; spectral bandwidth
2.39 cm^{-1} at 2600 cm^{-1} ; integration time: 4 seconds. 406 nm radiation, 50 mw power
at sample).

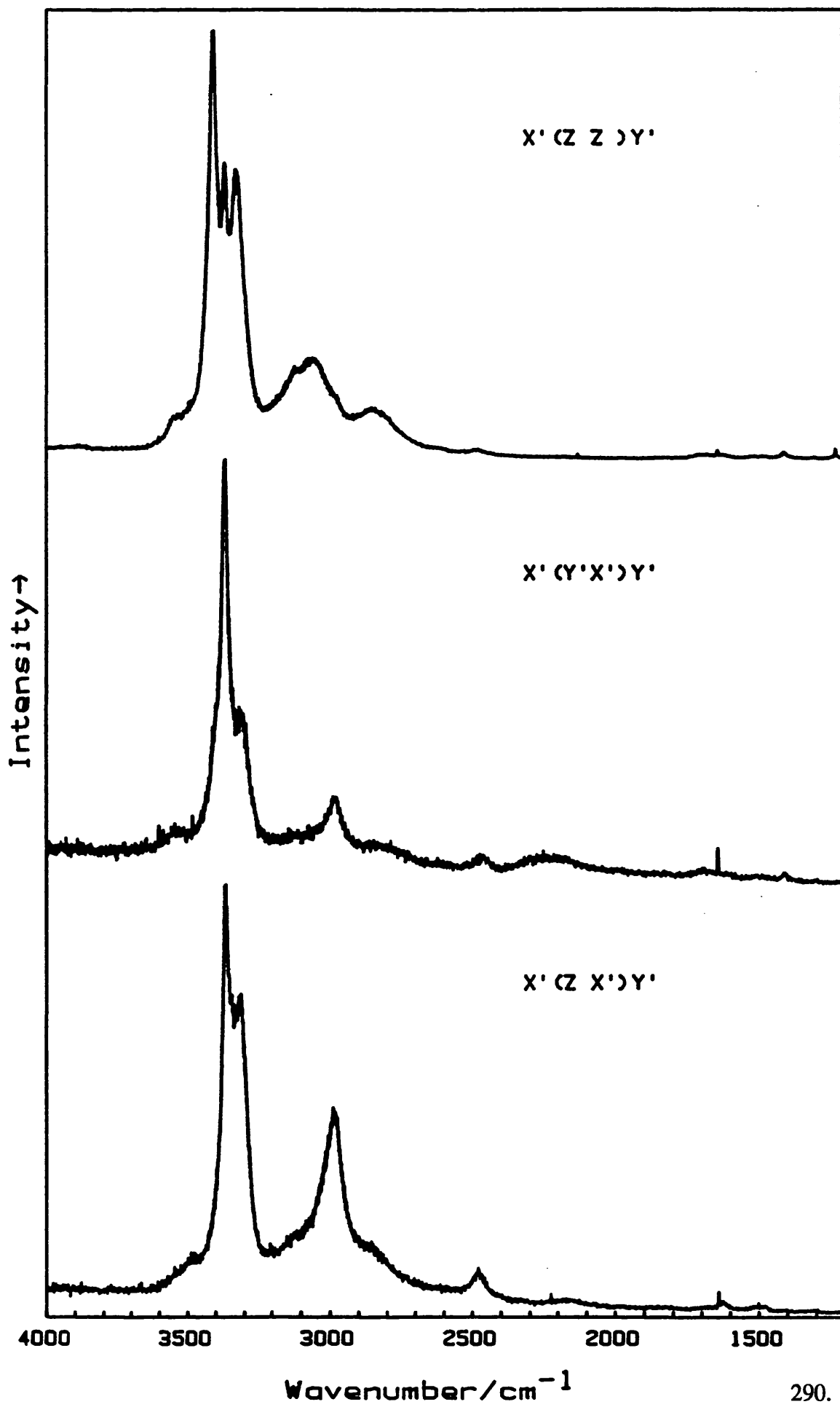


Figure A.7

Single crystal Raman spectra of $\text{RbAl}(\text{SO}_4)_2 \cdot 12\text{D}_2\text{O}$ between 1200 and 4000 cm^{-1} .
Sensitivities: X'(Z Z)Y' 10668 counts sec^{-1} ; X'(Y'X')Y' 1570 counts sec^{-1} ;
X'(Z X')Y' 8282 counts sec^{-1} (67 (1) K; step size 1 cm^{-1} ; spectral bandwidth
2.39 cm^{-1} at 2600 cm^{-1} ; integration time 4 seconds; 406 nm radiation, 50 mw power
at sample).

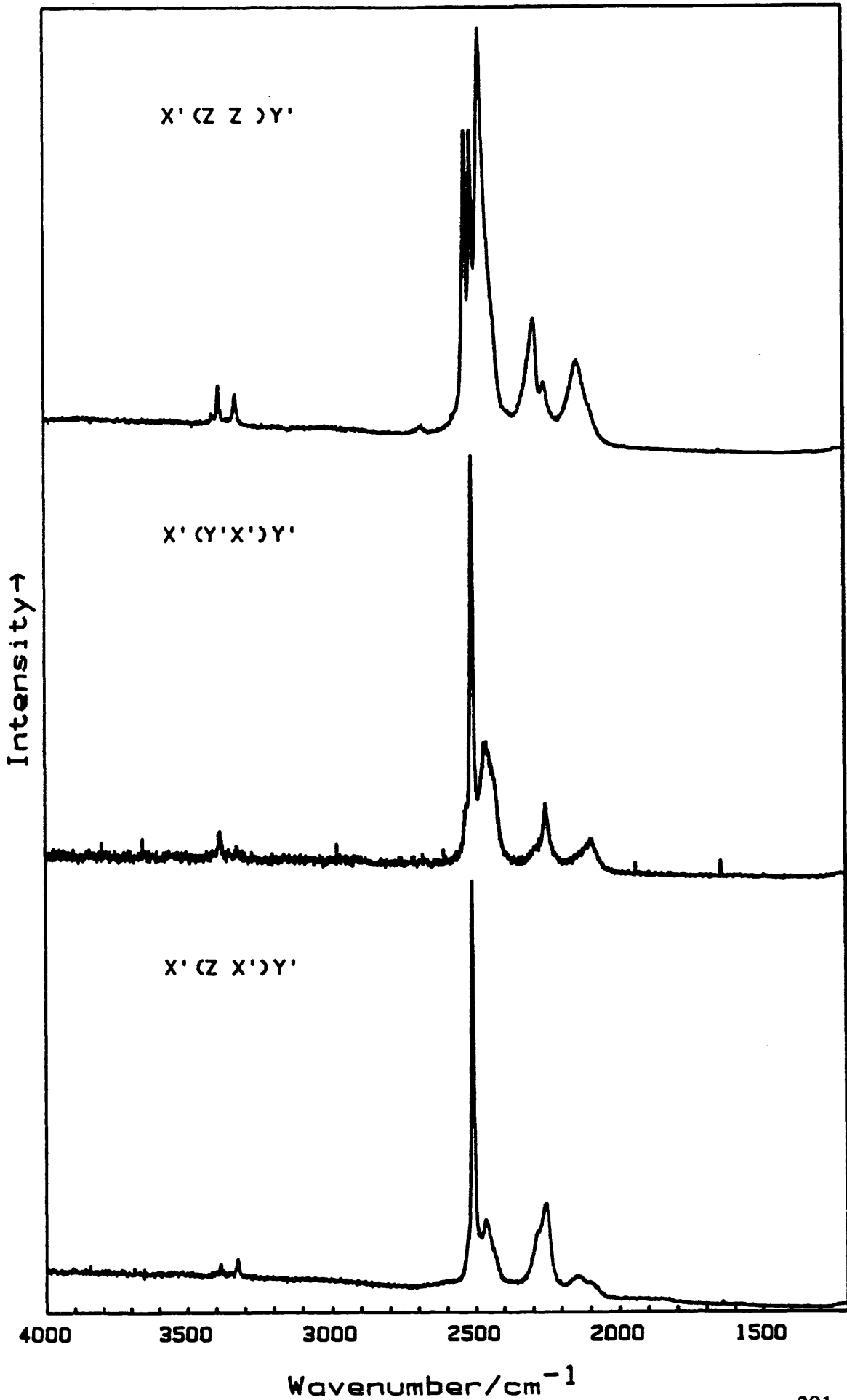


Figure A.8

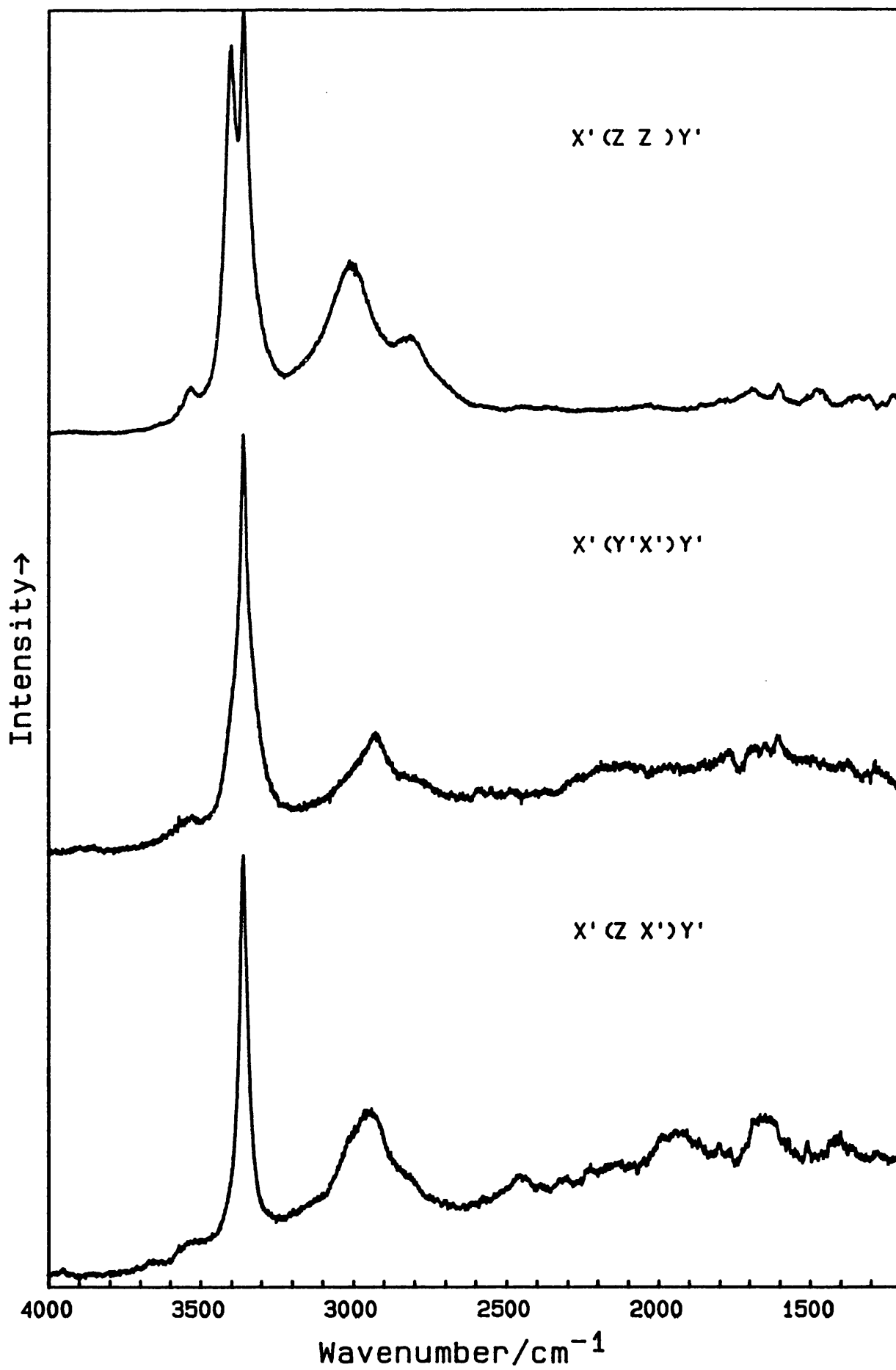
Single crystal Raman spectra of $\text{RbIn}(\text{SO}_4)_2 \cdot 12\text{H}_2\text{O}$ between 1200 and 4000 cm^{-1} .

Sensitivities: $X'(Z Z)Y'$ 11706 counts sec^{-1} ; $X'(Y'X')Y'$ 4804 counts sec^{-1} ;

$X'(Z X')Y'$ 6089 counts sec^{-1} (87 (3) K; step size 1 cm^{-1} ; spectral bandwidth

1.78 cm^{-1} at 2600 cm^{-1} ; integration time: $X'(Z Z)Y'$ and $X'(Z X')Y'$ 4 seconds,

$X'(Y'X')Y'$ 3 seconds. 514 nm radiation, 30 mw power at sample).



INDUCTIVELY COUPLED PLASMA - ATOMIC EMISSION SPECTROSCOPY

The method is based on Atomic Emission Spectroscopy (AES) coupled with an Inductively Coupled Plasma (ICP) source.

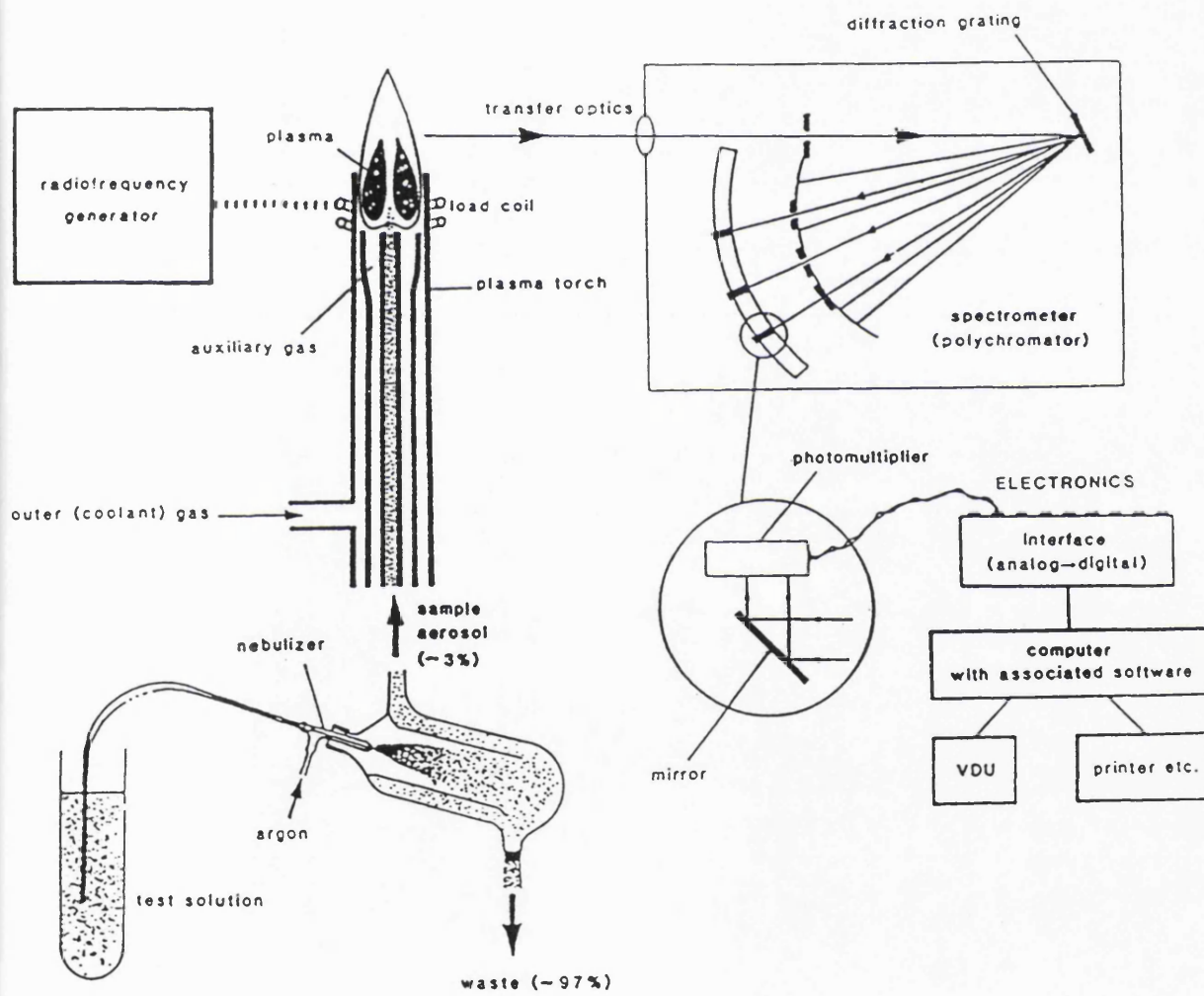
By inductively coupling a gas (argon is most often used) with a high frequency field, a high energy ionised gas, known as a plasma, is formed. The resulting plasma has an internal energy temperature of between 6000 - 10000 K. The plasma flame desolvates, dissociates, atomises and excites the elements present into a highly excited ionised state when a solution of the sample is injected through its centre. This results in the emission of electromagnetic radiation of unique frequencies for the given elements. The radiation emitted from the plasma is directly proportional to the concentration of the elements typically over 5 orders of magnitude. The radiation is passed to an optical emission spectrometer which separates the radiation into the unique frequencies corresponding to the different elements present. The intensity of the radiation is converted to an electrical signal by a photo-multiplier in the spectrometer. The intensity of this electrical signal is compared to previous measured intensities of samples of known concentration for the different elements and concentrations computed.

Figure B.1 shows a schematic diagram of a conventional simultaneous ICP-AES system. The first stage in the analysis of any sample is its introduction into the ICP torch. Liquid sampling is the normal method of sample introduction; the pneumatic nebulizer is the most commonly used device. The solution to be analyzed is converted into fine droplets; it is an aerosol of these fine droplets in argon which is injected into the flame. If the viscosity of a set of standard and unknown solutions is not the same then it is possible that this could result in different flow rates into the plasma torch leading to erroneous readings. For this reason all standard and unknown solutions were made up in H_2SO_4 (1 mol dm^{-3}).

A plasma is a gas in which atoms are present in an ionised state. When a high frequency current flows through a coil, a rapidly varying magnetic field within the coil

Figure B.1

Schematic diagram of a conventional simultaneous ICP system. [After M. Thompson and J. N. Walsh., A handbook of Inductively Coupled Plasma - Atomic Emission Spectroscopy. Blackie Press, Glasgow, 1989]



is generated. An ionised gas flowing through the coil cuts the lines of magnetic flux resulting in Joule (ohmic) heating. This interaction (inductive coupling) of the oscillating magnetic field with the ionised gas generates the ICP flame. To initiate electrical conductivity in the gas as it flows through the coil, a Tesla spark is used. Inductive heating of the flowing gas then maintains the gas 'burning' at temperatures of between 6000 - 10000 K.

The emitted energy is proportional to the concentration of ions at low ionic concentrations (0.1 to 1000 ppm). At high concentrations of sample, however, emitted photons will be absorbed by the same emitting ions, the observed radiation for the appropriate number of ions will consequently be reduced. The advantage of using the ICP source rather than more conventional lower temperature excitation systems is that since more of the sample is excited, concentration and signal are proportional to a higher concentration. The high local temperature is also responsible for the precise determination of concentration of sample at very low concentrations.

This technique was used for analysis of the trivalent cation composition for alum crystals of the type $\text{Rb}\{\text{Ga/V}\}(\text{SO}_4)_2 \cdot 12\text{H}_2\text{O}$ (chapter 3). Solutions were made up in the concentration region of between 1 -100 ppm (mg/litre). The relation between concentration and signal was found to be linear. An estimate of the error in trivalent cation composition was obtained from discrepancies in the independently calculated vanadium and gallium percentages. For the " β mix45" crystal whose Raman spectra are presented in figures 3.2.1 - 3.2.3, the independently calculated values for the % of trivalent cation were found to be 45.5% V and 54.4% Ga.